D5.1.2 BEACON
Bentonite Mechanical Evolution

Synthesis of results from task 5.1

DELIVERABLE (D5.1.2)
Report

Author(s): J. Talandier (Andra) with contribution from G. Scaringi, D. Mašín, J. Kruis, T. Koudelka, T. Krejčí, P. Poskas, A. Narkuniene, D. Justinavicius, A. Gens, L. He, D. Ruiz Restrepo, M. Åkesson, O. Kristensson, D. Malmberg, R K Newson, K E Thatcher, S J Benbow, L. Zdravkovic, G. Ghiadistri, D. Potts, A. Tsiampousi, J. A. Bosch, A. Ferrari, L. Laloui, V. Kumar, H. Shao, H. Gharbieh, V.-M. Pulkkanen, L. Asensio, V. Navarro, L. Gramegna, R. Charlier, S. Tachibana

Reporting period: e.g. 01/12/18 – 31/05/20

Date of issue of this report: **30/06/2019**

Start date of project: **01/06/17** Duration: 48 Months

This project receives funding from the Euratom research and training programme 2014-2018 under grant agreement No 745 942		
Dissemination Level		
PU	Public	

REVIEW

Name	Internal/Project/External	Comments

DISTRIBUTION LIST

Name	Number of copies	Comments
Athanasios Petridis (EC) Christophe Davies (EC) Beacon partners		

Content

1 Introduction

The overall objective of the project is to evaluate the performance of an inhomogeneous bentonite barrier. Inhomogeneities are mainly due to initial distribution of dry density in link with technological voids, the simultaneous use of several forms of bentonite (for example, blocks and pellets), the setting up in granular form… Some external solicitations could also lead to heterogeneous evolution of these bentonite based engineered barriers such as non-uniform water flow or anisotropic stress field.
Understanding of swelling clay properties and fundamental processes that lead to its homogenization as well as improvement of capabilities for numerical modelling are essential for the assessment of the hydromechanical evolution and the resulting performances of the engineered barriers.
The purpose of WP5 is to contribute to improvement of numerical models. In this work package, several tests are proposed from small size tests (centimeters) to field scale experiments (several meters). The idea is to start with simple tests and progressively increase the complexity in terms of scale, coupled processes and initial/boundary conditions.
This report contains the synthesis of results obtained by the partners involved in WP5 on the first set of tests. Three tests have been proposed pick up from WP2 inventory work:

- Swelling pressure tests for compacted plugs with free volume available – TEST B1.7 from Clay Technology AB, SKB
- Swelling pressure tests for pellets mixture – TEST B1.16 from CEA, Andra
- Swelling pressure tests for block and pellets structure – TEST B1.6 from Posiva

The specification of the tests are defined in details in report D5.1.1. The conditions of the tests are well control but in each test, heterogeneity is Introduced: in the first one, by having a void in the cell, in the second one, by dealing with a pellets mixture, and in the last one by having two layers of bentonite: block and pellets mixture.
For each test, the results obtained by the partners are presented and compared with the measurements. An analysis is proposed at several levels:

- Which part of the test or physical processes are the most difficult to model for all partners?
- How the heterogeneities in the bentonite are handle by the models?
- Are the initial and boundary conditions taken into account are similar for all partners? Are the parameters used comparable?

- Is it possible to identify some relevant parameters, which need a particular effort in terms of experimental characterisation?
- Is it possible to deduce from this exercise the advantages and disadvantages of the methods and models used?

2 Models

In this paragraph, a brief description of the models used in the tests is proposed. A more detail report has been produced for Work Package 3: D3.1 - Description of the constitutive models available at the start of the project. This Deliverable presents the constitutive models available at the start of the project for the different modelling teams involved both in Work Package 3 and 5.

2.1 ICL

The constitutive model used for numerical simulation is the Imperial College Double Structure Model (IC DSM), Ghiadistri (2019). Developed for compacted, highly expansive clays, this model takes into account two levels of structure, the macro-structure and the micro-structure, which are both elastoplastic. The model is implemented in the bespoke finite element code ICFEP (Potts & Zdravkovic, 1999, 2001), which is used in all simulations presented here. The outline of the IC DSM model formulation and the summary of model input parameters are given in the BEACON Deliverable 3.1.

The Soil-Water Retention (SWR) model used in the analysis is similar to van Genuchten (1980), expressed in terms of degree of saturation and matric suction, s:

$$S_r = \left\{\frac{1}{1 + [\alpha(s - s_{des})]^n}\right\}^m \left(1 - S_{r,0}\right) + S_{r,0} \qquad (1)$$

where:

- s is the current value of suction;
- s_{des} is the value of suction at de-saturation;
- $S_{r,0}$ is the residual degree of saturation;
- α, n and m are fitting parameters controlling the shape of the retention curve. The dimension of parameter α is 1/stress so that the product $s \cdot \alpha$ is dimensionless.

The model imposes that the degree of saturation is at 100% when $s = s_{des}$. Usually, s_{des} is considered equal to the air-entry value of suction, s_{air}, used in the constitutive model.

The permeability model used allows for the logarithm of permeability to vary linearly with suction from its initial value k_{sat}, corresponding to suction s_1, to a limiting value k_{min}, corresponding to suction s_2. The magnitude of permeability corresponding to the current suction level s can, therefore, be obtained from the following equation:

$$\log k = \log k_{sat} - \frac{s - s_1}{s_2 - s_1} \log\left(\frac{k_{sat}}{k_{min}}\right) \qquad (2)$$

For values of suction smaller than s_1 the permeability is equal to k_{sat}, whereas for suction levels higher than s_2 the permeability is equal to k_{min}.

2.2 BGR

The simulations of the test cases 1a01, 1b and 1c were performed with OpenGeoSys 5 (OGS5 Ver. 5.7.1) (Kolditz et al. 2012), a free, multi-platform, scientific modelling package for coupled thermo-hydro-mechanical-chemical (THMC) processes in fractured and porous media. This report contains the documentation of the modelling and simulation of the three homogenization experiments.

2.2.1 Mechanical model

The simulations were performed using a linear poroelastic model with linear swelling/shrinkage model for the mechanical process and a two-phase flow model with Richards' approximation for the flow process. Isothermal conditions were assumed in all the simulations. In the mechanical model, the change in swelling pressure $\left(\Delta\boldsymbol{\sigma}_{\mathrm{sw}}\right)$ is linearly proportional to the change in the water saturation $\left(\Delta S^w\right)$ and a maximum swelling pressure$\left(\sigma_{\mathrm{max,sw}}\right)$, given by the equation

$$\Delta\boldsymbol{\sigma}_{\mathrm{sw}} = -\boldsymbol{\sigma}_{\mathrm{max,sw}} \Delta S^w \mathbf{I}. \qquad (1)$$

The swelling is pressure considered in the stress tensor for the momentum balance of the solid phase. In a system without gravitational acceleration, the coupled momentum balance equation accounts for the effect of the changes in fluid pressure $\left(p^w\right)$ and the saturation driven swelling on the mechanics. It is given by the divergence of the stresses

$$\nabla \cdot \left(\boldsymbol{\sigma}_{\text{eff}} - \alpha_{\text{Biot}} \chi p^w \mathbf{I} - \Delta \boldsymbol{\sigma}_{\text{sw}}\right) = 0 . \tag{2}$$

Where χ is the Bishop's parameter, which is a function of saturation and together with the Biot coefficient controls the coupling between fluid pressure and the mechanical stresses through the effective stress concept. For test case 1a01, the Bishop's parameter is set equal to the fluid saturation. For test cases 1b and 1c, the Bishop's parameter is chosen to be a cubic function of the saturation.

2.2.2 Flow model

The fluid flow is modelled by the Richards' approximation (Richards 1931) of the two-phase flow equation under isothermal conditions in deforming porous media (Lewis and Schrefler 1998):

$$\phi \frac{\partial S^w}{\partial t} + S^w \left(\frac{\phi}{K^w} + \frac{\alpha_{\text{Biot}} - \phi}{K^s}\right) \frac{\partial p^w}{\partial t} + \nabla \cdot \left(\mathbf{q}^w\right) + S^w \alpha_{\text{Biot}} \nabla \cdot \frac{\partial \mathbf{u}}{\partial t} = 0 \tag{3}$$

In the above equations

- $\phi[\text{-}]$: the porosity,
- $S^w[\text{-}]$: the saturation of the water phase,
- $t[\text{s}]$: the time,
- $p^w[\text{Pa}]$: the fluid pressure
- $\rho^w \left[\frac{\text{kg}}{\text{m}^3}\right]$: the density of the water phase,
- $\rho^s \left[\frac{\text{kg}}{\text{m}^3}\right]$: the density of the solid phase,
- $K^w[\text{Pa}]$ and $K^s[\text{Pa}]$: the compressibility of the water and the solid phases,
- $\alpha_{\text{Biot}}[\text{-}]$: the Biot coefficient defined by

$$\alpha_{\text{Biot}} = 1 - \frac{K^{skel}}{K^s} , \tag{4}$$

- $K^{skel}[\mathrm{Pa}]$: the compressibility of the solid skeleton,
- $\mathbf{u}[\mathrm{m}]$: the displacement field vector,
- $\mathbf{g}\left[\frac{\mathrm{m}}{\mathrm{s}^2}\right]$: the gravitational acceleration vector,
- $\mathbf{I}[\text{-}]$: the identity matrix,
- $\mathbf{q}^w\left[\frac{\mathrm{m}}{\mathrm{s}}\right]$: is the flux of the water phase, given by Darcy's law for multiphase flow

$$\mathbf{q}^w = -k_{\mathrm{rel,w}} \frac{\mathbf{k}}{\mu}\left(\nabla p^w - \rho^w \mathbf{g}\right) \tag{5}$$

- $\mu\left[\frac{\mathrm{kg}}{\mathrm{m \cdot s}}\right]$: the dynamic viscosity,
- $\mathbf{k}\left[\mathrm{m}^2\right]$: the intrinsic permeability tensor,
- $k_{\mathrm{rel,w}}[\text{-}]$: the relative permeability of the water phase.

In the above stated coupled linearly poroelastic equation the changes in the fluid pressure and saturation are coupled to the deformation in the solid phase. The equation considers the compressibility of both the solid and fluid phases and, together with the Biot coefficient, the distribution of stresses between the two phases. The stress $(\boldsymbol{\sigma})$ and strain $(\boldsymbol{\varepsilon})$ tensors are related by the elasticity matrix $(\mathbf{C})$ with the constitutive equation

$$\boldsymbol{\sigma}_{\mathrm{tot}} = \underline{\underline{\mathbf{C}}} : \grave{\mathbf{o}} \tag{6}$$

The total stresses $(\boldsymbol{\sigma}_{\mathrm{tot}})$ and the effective $(\boldsymbol{\sigma}_{\mathrm{eff}})$ stresses are related by

$$\boldsymbol{\sigma}_{\mathrm{tot}} = \boldsymbol{\sigma}_{\mathrm{eff}} - \alpha_{\mathrm{Biot}} \chi p^w \mathbf{I} \tag{7}$$

With the strains defined as a function of the displacement gradients

$$\grave{\mathbf{o}} = \tfrac{1}{2}(\nabla \mathbf{u} + \nabla^{\mathrm{T}} \mathbf{u}) \tag{8}$$

The changes in porosity, void ratio and water content arising from the mechanical evolution were calculated in the post-processing step for experiment 1a01. For experiments 1b and 1c, the porosity model was implemented in the code. The void ratio and the water content were calculated from the porosity and saturation in the post-processing step. For systems with change in total volume, such as system under unconstrained swelling, the change in porosity is calculated using the initial porosity, the Biot coefficient and the divergence of the displacements by the expression (Nermoen et al. 2015):

$$\phi_{\text{new}} = \frac{\phi_{\text{old}} + \alpha_{\text{Biot}} \nabla \cdot u_i}{1 + \nabla \cdot u_i} \tag{9}$$

For systems under constrained swelling or for systems under small deformations where $1+\nabla \cdot u_i \approx 1$, the denominator in (9) can be neglected. In this case the change in porosity is given by

$$\phi_{\text{new}} = \phi_{\text{old}} + \alpha_{\text{Biot}} \nabla \cdot u_i \tag{10}$$

In both cases, the inclusion of the Biot coefficient allows to consider compressibility of the grains. Bentonite shows a multiscale porosity structure, in which the inter-aggregate porosity is greatly influenced by the dry compaction (Lloret et al. 2003; Lloret and Villar 2007). Moreover, due to swelling under constrained volume, a further reduction of porosity can be expected. Since the models were simulated without using a multiscale porosity-structure model, the Biot coefficient was chosen in a way which would imply a compressible microscructure.

The void ratio (e) is calculated from the porosity using the expression

$$e = \frac{\phi}{1-\phi} \tag{11}$$

The volumetric water content (Θ) is calulated from the porosity and the saturation using

$$\Theta = \phi \cdot S^w \tag{12}$$

The gravimetric water content $(\Theta_{\text{gr}})$is calculated from the volmetric water content using the bulk specific gravity (SG).

$$\Theta = \Theta_{\text{gr}} \cdot \text{SG} \tag{13}$$

The capillary pressure(p_c) - saturation (S^w) relation is given by the van Genuchten function (1980) (cf. Figure 3-15):

$$S_{\text{eff}} = \frac{S^w - S^w_{\text{res}}}{1 - S^w_{\text{res}}} = \left(1 + (\alpha p_c)^n\right)^m \tag{14}$$

$$p_c = \begin{cases} 0 & S^w > S^w_{\max} \\ \dfrac{\rho^w g}{\alpha}\left(S_{\text{eff}}^{-\frac{1}{m}} - 1\right)^{\frac{1}{n}} & S^w_{\text{res}} < S^w < S^w_{\max} \\ p_{c,\,\max} & S^w < S^w_{\text{res}} \end{cases} \tag{15}$$

$$m = 1 - \frac{1}{n} \tag{16}$$

$$k_{\text{rel}}^{w} = \left(S^{w}\right)^{3} \tag{17}$$

Where S^w is the liquid phase saturation, S_{res}^{w} and $S_{\max}^{w}$ are the residual and maximum liquid phase saturations respectively and m is the van Genuchten shape factor.

2.3 ClayTech

The approach taken by Clay Technology for analysing these tests has been to apply and to develop the Hysteresis Based Material (HBM) model (Börgesson et al. 2018; Dueck et al. 2018). The original version of this model describes the hydromechanical behaviour of bentonite for water saturated conditions, and this version had recently been implemented in Comsol Multiphysics. This code was therefore used as a tool for analysing Test 1a.

For water unsaturated conditions, on the other hand, a first version of the material model defined for isotropic conditions, was developed as part of the D3.1 deliverable (Åkesson et al. 2018). Subsequently, a first definition for non-isotropic conditions was made as part of the current work. This model was in turn used to develop numerical solutions for simple 1D geometries, implemented in the MathCad software, which were used for analysing Test 1b and 1c. Wall friction between the bentonite and the test equipment had an significant impact of the behaviour of Test 1c, and effort was therefore taken to include such a mechanism in the analysis.

Three versions of the Hysteresis Based Material (HBM) are described in the first three section: isotropic model for saturated conditions (2.3.1.1); principal direction model for saturated conditions (2.3.1.2); and non-isotropic model for unsaturated conditions (2.3.1.3). A model for wall friction is described in the subsequent section (2.3.1.4). Finally, constitutive laws for water transport are described in the last section (2.3.2)

2.3.1 Material model

2.3.1.1. *The Isotropic HBM model for saturated conditions*

The chemical potential of the clay water (μ) was used as a starting point for the stress-stain relations of the model. This can be described as a function the water content (w) and the *pressure* (p):

$$\mu = \mu_0 + RT\ln\big(RH(w)\big) + v_c p \tag{2-1}$$

where μ_0 is the chemical potential of a reference state, R is the universal gas constant, T is the absolute temperature, v_c is the molar volume of the clay water, and RH is the relative humidity of the clay at free swelling conditions. In the case of water saturated conditions RH can be described as a function of the void ratio instead of the water content. The relation above can then be rearranged as:

$$-\frac{\mu-\mu_0}{v_0} = -\frac{RT}{v_0}\ln\big(RH(e)\big) - \frac{v_c}{v_0}p \tag{2-2}$$

where v_0 is the molar volume of bulk water. The term on the left hand side can be identified as *suction* (s), while the first term on the right side from here on is denoted the *clay potential* (Ψ). Assuming that v_0 and v_c are equal, this can simply be expressed as:

$$s = \Psi(e) - p. \tag{2-3}$$

It should be noted that the suction corresponds to the RH in an external gas phase. Correspondingly, it corresponds to the negative value of an external water pressure. This means that the clay potential is defined in a similar way as an *effective stress*. It should also be noted that this description is based on the assumptions that the osmotic effect of any solution in the water can be disregarded and that the temperature is constant. It also assumes an *isotropic* stress state. Moreover, the description doesn't include any path dependence. This is taken into account by introducing a *void ratio history*, which from here on simply is denoted with $e(t)$, which means that equation (2-18) can be replaced with:

$$s = \Psi(e, e(t)) - p. \tag{2-4}$$

The clay potential function is here written on the following form:

$$\Psi\big(e, e(t)\big) = \Psi_M(e) + \Psi_{\Delta/2}(e)f(e(t)) \tag{2-5}$$

where Ψ_M, $\Psi_{\Delta/2}$ and f are denoted the *mid-line*, the *half allowed span*, and the *path variable*, respectively. It can be noted that Ψ_M, and $\Psi_{\Delta/2}$ are defined as functions of the void ratio, whereas f is a variable, with values between -1 and +1, which depends on the void ratio history. The clay potential is thus confined to a region with two bounding lines: $\Psi_M + \Psi_{\Delta/2}$ (the consolidation line) and $\Psi_M - \Psi_{\Delta/2}$ (the swelling line; see Figure 2-1).

The path variable (f) is obtained by integration over time,

$$f = f_0 + \int_{t_0}^{t} \frac{\partial f}{\partial e} \dot{e} \, d\tau \, , \tag{2-6}$$

where the differential is given by,

$$\frac{\partial f}{\partial e} = -\frac{K'}{1 + e_0}(1 + \mathrm{sgn}(\dot{e}) f). \tag{2-7}$$

K' is an introduced parameter, the sign of the time derivative of the void ratio determines whether the value of f changes asymptotically towards 1 or -1. The sign function is defined as:

$$\mathrm{sgn}(x) = \begin{cases} -1 & \text{if} \quad x < 0 \\ 0 & \text{if} \quad x = 0 \\ 1 & \text{if} \quad x > 0 \end{cases} . \tag{2-8}$$

Finally, it is in many cases necessary to define a relation between suction and the density of water thereby generalizing the compressibility of water (β) to "negative pore pressures":

$$\rho_w(s) = \rho_{w0} \exp(-\beta s). \tag{2-9}$$

Since the density of water is related to both water content and void ratio ($\rho_w = \rho_s w / e$), this means that the increment in suction is given by increments in water content and void ratio by the following simple relation:

$$ds = \frac{1}{\beta}\left(\frac{de}{e} - \frac{dw}{w}\right). \tag{2-10}$$

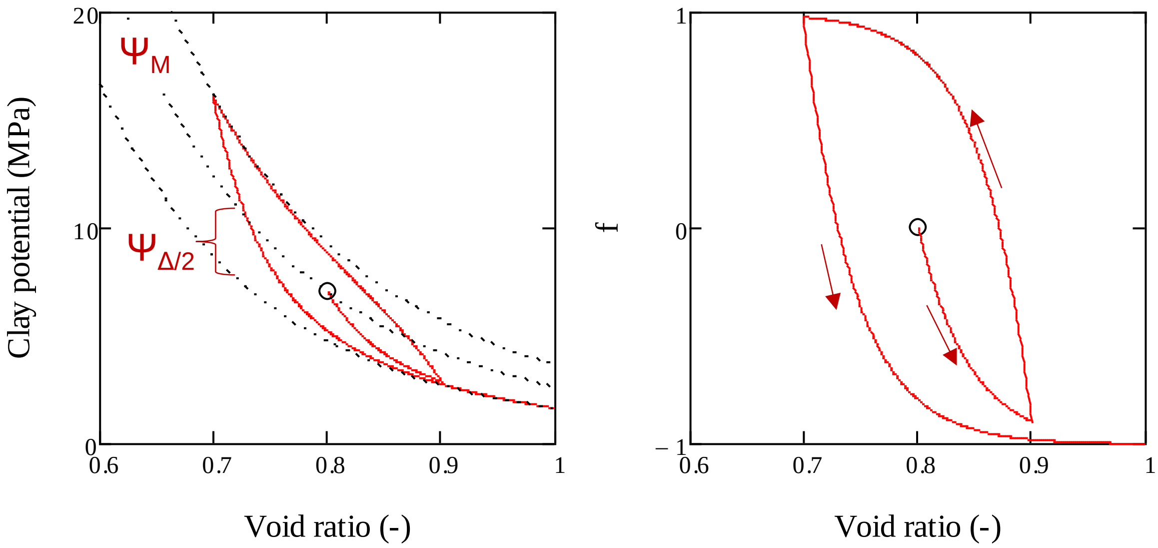

Figure 2-1 ***Clay potential and path variable (f) versus void ratio. Right graph shows an example of the path variable for a case with swelling, followed by consolidation and followed by swelling. Left graph shows the same path mapped on the region for the clay potential.***

2.3.1.2. *Principal direction model for saturated conditions*

This model is designed for the case when the principal directions correspond to the Cartesian basis $\{\boldsymbol{e}_1, \boldsymbol{e}_2, \boldsymbol{e}_3\}$.

$$
\begin{gathered}
-\boldsymbol{\sigma} = \boldsymbol{\psi} - s\mathbf{1} \\
\boldsymbol{\psi} = \tilde{\psi}_M(\varepsilon_v)\mathbf{1} + \tilde{\psi}_{\Delta/2}(\varepsilon_v)\boldsymbol{f} \\
\boldsymbol{f} = \boldsymbol{f}_0 + \int_{t_0}^{t} \frac{\partial \boldsymbol{f}}{\partial \boldsymbol{\varepsilon}} \dot{\boldsymbol{\varepsilon}}\, d\tau
\end{gathered}
\tag{2-11}
$$

The path dependent variable is a second order tensor,

$$
\boldsymbol{f} = f_{11}\boldsymbol{e}_1 \otimes \boldsymbol{e}_1 + f_{22}\boldsymbol{e}_2 \otimes \boldsymbol{e}_2 + f_{33} \otimes \boldsymbol{e}_3 \otimes \boldsymbol{e}_3\,, \tag{2-12}
$$

and its derivative with respect to strain is given by,

$$
\begin{gathered}
\frac{\partial \boldsymbol{f}}{\partial \boldsymbol{\varepsilon}} = \frac{\partial f_{11}}{\partial \varepsilon_{11}} \boldsymbol{e}_1 \otimes \boldsymbol{e}_1 \otimes \boldsymbol{e}_1 \otimes \boldsymbol{e}_1 + \frac{\partial f_{22}}{\partial \varepsilon_{22}} \boldsymbol{e}_2 \otimes \boldsymbol{e}_2 \otimes \boldsymbol{e}_2 \otimes \boldsymbol{e}_2 + \\
\frac{\partial f_{33}}{\partial \varepsilon_{33}} \boldsymbol{e}_3 \otimes \boldsymbol{e}_3 \otimes \boldsymbol{e}_3 \otimes \boldsymbol{e}_3\,,
\end{gathered}
\tag{2-13}
$$

The differential equation for the path variable in Eq (2-7) is generalized for the three principal directions:

$$
\frac{\partial f_{\alpha\alpha}}{\partial \varepsilon_{\alpha\alpha}} = -K(\tilde{\kappa}(\boldsymbol{f}, \dot{\varepsilon}_{\alpha\alpha}) + \operatorname{sgn}(\dot{\varepsilon}_{\alpha\alpha}) f_{\alpha\alpha})\,, \tag{2-14}
$$

where $\alpha = \{1,2,3\}$ and no summation convention is to be used. It should be noted the parameter K is three times higher than K' in Eq (2-7), and the "1-term" is replaced with the $\tilde{\kappa}$-function:

$$
\tilde{\kappa}(\boldsymbol{f}, \dot{\varepsilon}_{\alpha\alpha}) = 1 - \Phi(\tilde{\gamma}(\boldsymbol{f}, \dot{\varepsilon}_{\alpha\alpha}))\tilde{\gamma}(\boldsymbol{f}, \dot{\varepsilon}_{\alpha\alpha}), \tag{2-15}
$$

where Φ is the Heaviside step function, and the $\tilde{\gamma}$-function is defined as:

$$
\tilde{\gamma}(\boldsymbol{f}, \dot{\varepsilon}_{\alpha\alpha}) = f_T + \operatorname{sgn}(\dot{\varepsilon}_{\alpha\alpha}) f_P, \tag{2-16}
$$

Where f_T and f_P represents the "half-distance" and "mid-point" between the largest and smallest f-value, respectively:

$$
f_T = \frac{\max(f_{ij}) - \min(f_{ij})}{2}\,, \quad f_P = \frac{\max(f_{ij}) + \min(f_{ij})}{2}\,, \tag{2-17}
$$

The purpose of the $\tilde{\kappa}$- and the $\tilde{\gamma}$-function is to limit the *maximum difference* between the f-values in different directions to 1, thereby making sure that the shear strength of the material is taken into account.

2.3.1.3. *Non-isotropic model for unsaturated conditions*

A first definition of the HBM model for unsaturated isotropic conditions was presented by Åkesson et al. (2018). The following presentation is focused on the material model necessary for solving the problem at hand, i.e. unsaturated non-isotropic conditions, without explaining the derivation of the different parts. For simplicity, compressive stresses are defined as larger than zero.

Thermodynamic relation for chemical potential of clay water

A corner stone of the models is the relation between the suction (s), the stress (σ_i) in the i-direction and the clay potential (Ψ_i) also for the i-direction. Since unsaturated conditions are considered, the stress is divided with the so-called contact area fraction (a), which equals one at saturated conditions, but which is lower than one for unsaturated conditions (see below):

$$s + \frac{\sigma_i}{\alpha} = \Psi_i \tag{2-18}$$

Clay potential function

The clay potential for a specific void ratio (e) is assigned a value in an interval, defined by two functions (Ψ_M and $\Psi_{\Delta/2}$), and the actual state within this interval is specified with the so-called path variable (f_i) with values between -1 and +1. Since unsaturated conditions are considered, the void ratio is replaced with the micro void ratio (e_m):

$$\Psi_i(e_m, f_i) = \Psi_M(e_m) + f_i \cdot \Psi_{\Delta/2}(e_m) \tag{2-19}$$

The micro void ratio is related to the water content (w), the particle density (ρ_s) and the water density (ρ_w) as $e_m = w \cdot \rho_s / \rho_w$.

Path variable derivative

The path variable is obtained by integration of the derivative with respect to the strain in the same direction. Since unsaturated conditions are considered, the strain is replaced with the micro strain (ε_i^m):

$$\frac{\partial f_i}{\partial \varepsilon_i^m} = -K(\tilde{\kappa}(\boldsymbol{f}, \dot{\varepsilon}_i^m) + \mathrm{sgn}(\dot{\varepsilon}_i^m) f_i) \tag{2-20}$$

where the κ-function is defined in the same way as for saturated conditions, see (2-15), (2-16) and (2-17).

Water density

The density of water is defined as a function of suction, thereby generalizing the compressibility of water (β) to "negative pore pressures".

$$\rho_w(s) = \rho_{w0} \exp(-\beta s) \tag{2-21}$$

Contact area function

The contact area fraction is assumed to be related to the fraction between water saturated grains (1+e_m) and the total volume (1+e). This ratio is reduced as a power law with the exponent γ:

$$\alpha(e_m, e) = \left(\frac{1+e_m}{1+e}\right)^{\gamma} \tag{2-22}$$

Interaction functions

The introduction of a second (micro) void ratio has called for the introduction a relation between three variables. Åkesson et al. (2018) tentatively defined such a relation as two partial derivatives of the pressure with respect to the void ratio and the water content.

This is here modified as a relation between the stress in the i-direction (σ_i), the (macroscopic) strain in the i-direction (ε_i), and the water content (w):

$$d\sigma_i = \frac{\partial \sigma_i}{\partial \varepsilon_i} d\varepsilon_i + \frac{\partial \sigma_i}{\partial w} dw \tag{2-23}$$

The two derivatives: $\partial\sigma_i/\partial\varepsilon_i$ and $\partial\sigma_i/\partial w$, are very similar to the original definitions and written as:

$$\frac{\partial \sigma_i}{\partial \varepsilon_i} = -\frac{\ln\left[\frac{\sigma_i}{\Psi(e_m, f)}\right]}{\ln\left[\frac{1+e_m}{1+e}\right]} \frac{\alpha(e_m, e)\Psi(e_m, f_i)}{1+e}(1+e_0) \tag{2-24}$$

and:

$$\frac{\partial \sigma_i}{\partial w} = -\frac{\partial \sigma_i}{\partial \varepsilon_i}\frac{\partial \varepsilon_i}{\partial w} \tag{2-25}$$

in which:

$$\frac{\partial \varepsilon_i}{\partial w} = \frac{e_{sat}(\sigma_i, f_i) - e}{e_{sat}(\sigma_i, f_i)\frac{\rho_w(0)}{\rho_s} - e_m\frac{\rho_w(s)}{\rho_s}} \cdot \frac{1}{(1+e_0)} \tag{2-26}$$

The basis for these derivatives was described by Åkesson et al. (2018).

Strain relations

A relation between macroscopic and microscopic strains is tentatively defined with the following matrix:

$$\begin{pmatrix} d\varepsilon_1^m \\ d\varepsilon_2^m \\ d\varepsilon_3^m \end{pmatrix} = \begin{pmatrix} 1 & -\xi & -\xi \\ -\xi & 1 & -\xi \\ -\xi & -\xi & 1 \end{pmatrix} \begin{pmatrix} d\varepsilon_1 \\ d\varepsilon_2 \\ d\varepsilon_3 \end{pmatrix} \quad (2\text{-}27)$$

The diagonal elements are equal to one and the value of the non-diagonal elements should equal zero at saturated conditions which means the two strain vectors are identical for that condition. Moreover, the non-diagonal elements can be assumed to be -1/2 at dry conditions, mimicking a condition with constant volume. Taken together, the non-diagonal elements can tentatively be defined as half the value of the degree of gas saturation:

$$\xi = S_g/2 = (e - e_m)/2e \quad (2\text{-}28)$$

It can be noted that the microscopic strains are not related to the micro void ratio (2-27), as was proposed for the isotropic version the unsaturated model (Åkesson et al. 2018).

2.3.1.4. *Wall friction*

The friction between the bentonite and the circumferential surface of the test equipment, has an influence of the overall stress balance along the bentonite specimen. This relation can be expressed as:

$$\frac{d\sigma_1}{dx} + \frac{2}{r} \cdot \tau = 0 \quad (2\text{-}29)$$

where σ_1 is the axial stress, τ is the shear stress and r is the radius of the specimen. It should be noted that τ is here defined to have positive values when acting in the negative x direction.

The shear stress is determined by the displacement (u) and the normal stress (σ_2). For small displacements, the shear stress is given as the product of the displacement and the shear module (K_s). If the shear stress reaches the value of the product between the normal stress and the tangent of the friction angle (φ), then the shear stress will be limited to this value. If the direction of the displacement is reversed, then the direction (i.e. the sign) of the shear stress will also be reversed; at first related to the displacement and subsequently to the normal stress (Figure 2-2). This behaviour can be described in the following incremental form:

$$\Delta\tau = \begin{cases} \Delta u \cdot K_s & \text{if } |\tau| < \sigma_2 \cdot \tan(\varphi) \vee \tau \cdot \Delta u < 0 \\ \mathrm{sign}(\Delta u) \cdot \Delta\sigma_2 \cdot \tan(\varphi) & \text{otherwise} \end{cases} \quad (2\text{-}30)$$

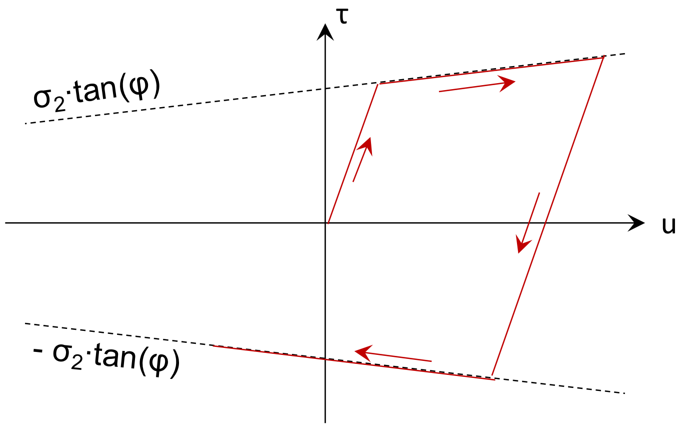

Figure 2-2 Stress path illustrating the relation between the displacement (u) and the shear stress (τ).

2.3.2 Water transport

The transport of liquid water is generally described with Darcy´s law for unsaturated conditions. The mass flux is thus given by the suction gradient, the hydraulic conductivity (K) defined as a function of the void ratio and the degree of saturation, the density of water and the unit weight of water (γ_w):

$$j = \rho_w \cdot K_H \frac{\partial s}{\partial x} \qquad (2\text{-}31)$$

The hydraulic conductivity is here divided with the unit weight: $K_H = K/\gamma_w$, where γ_w=10^{-2} MPa·m^{-1}.

Water can also be transported through vapor diffusion, and this process was added to the Darcy´s flux for the analysis of Test 1b. The diffusion of water vapor is described as driven by the gradient of the water mass fraction in the gas phase (ω) following the constitutive laws implemented in Code_Bright:

$$j_v = -\rho_g \cdot n(1 - S_l) \cdot D_m^w \frac{\partial \omega}{\partial x} \qquad (2\text{-}32)$$

where $D_m^w = \tau \cdot 5.9 \cdot 10^{-6} \cdot T^{2.3} \cdot (p_g)^{-1}$ (m^2/s), where τ is the vapor tortuosity and T is the temperature. This expression is transformed so that this transport is described as driven by gradients in suction instead:

$$\frac{\partial \omega}{\partial x} = \frac{d\omega}{dP_v} \frac{dP_v}{ds} \frac{\partial s}{\partial x} \qquad (2\text{-}33)$$

It should be noted that this is only valid for isothermal conditions.

The two first factors on the right side can be expressed as:

$$\frac{d\omega}{dP_v} \approx \frac{M_w}{P_g M_a} \qquad \& \qquad \frac{dP_v}{ds} = -\frac{M_w}{\rho_w RT} \cdot P_v \tag{2-34}$$

Taken together, the diffusive water flux can be described as:

$$j_v = n(1 - S_l) \cdot D_m^w \frac{M_w}{RT} \frac{\rho_v}{\rho_w} \frac{ds}{dx} \tag{2-35}$$

The vapor density is related to suction in accordance with Kelvin´s equation as:

$$\rho_v = exp\left[\frac{-s \cdot M_w}{\rho_w RT}\right] \cdot \rho_v^{sat} \tag{2-36}$$

where the saturated vapor density (ρ_v^{sat}) for 20 ºC is 0.0173 kg/m³.

2.4 EPFL

2.4.1 ACEMG – TS constitutive model

ACMEG-TS is formulated using an elastoplastic framework based on Hujeux's critical state model for saturated soils (Hujeux, 1979). In order to accommodate behaviour in unsaturated state, Bishop's effective stress and suction are used as state parameters. Bishop's coefficient is taken equal to the degree of saturation, leading to:

$$\boldsymbol{\sigma}' = \boldsymbol{\sigma} - [S_r u_w + (1 - Sr)u_a]\mathbf{I} = \boldsymbol{\sigma}^{\mathrm{n}} - S_r s\mathbf{I} \tag{1}$$

where $\boldsymbol{\sigma}'$ is the effective stress tensor, $\boldsymbol{\sigma}$ is the total stress tensor, S_r is the degree of saturation, u_w is water pressure; u_a is air pressure; $s = u_a - u_w$ is suction and $\boldsymbol{\sigma}^{\mathrm{n}} = \boldsymbol{\sigma} - u_a\mathbf{I}$ is the net stress tensor. Using the effective stress principle allows to express the material deformation as:

$$\mathrm{d}\boldsymbol{\varepsilon}^{\mathrm{e}} = \mathbf{C}^{\mathrm{e}} : \mathrm{d}\boldsymbol{\sigma}' \tag{2}$$

where $\boldsymbol{\varepsilon}^{\mathrm{e}}$ is the elastic strain tensor and $\mathbf{C}^{\mathrm{e}}$ is the secant elastic compliance tensor. To allow for irreversible deformation the strain tensor is divided as (isothermal conditions):

$$\mathrm{d}\boldsymbol{\varepsilon} = \mathrm{d}\boldsymbol{\varepsilon}^{\mathrm{e}} + \mathrm{d}\boldsymbol{\varepsilon}^{\mathbf{p}} \tag{3}$$

being $\mathrm{d}\boldsymbol{\varepsilon}$ the total strain increment and $\mathrm{d}\boldsymbol{\varepsilon}^{\mathrm{p}}$ the plastic strain increment.

Elastic strains will be induced as long as the stress increment lies inside the yield surface. In such case the response is governed by the elastic compliance $\mathbf{C}^{\mathrm{e}}$

$$\mathbf{C}^{\mathrm{e}} = C^{e}_{ijkl} = G\left(\delta_{ik}\delta_{jl} + \delta_{il}\delta_{jk}\right) + \left(K - \frac{2}{3}G\right)\delta_{ij}\delta_{kl} \tag{4}$$

where G is the shear modulus and K the bulk modulus. These moduli depend on the mean effective stress p' to express a non-linear elastic response as

$$G = G_{ref}\left(\frac{p'}{p'_{ref}}\right)^{n^e} \qquad K = K_{ref}\left(\frac{p'}{p'_{ref}}\right)^{n^e} \tag{5}$$

where G_{ref} and K_{ref} are the shear and bulk modulus respectively at a reference pressure p'_{ref} and n^e is a material parameter controlling the nonlinear behaviour.

In non-isothermal conditions, additional elastic strains are induced by temperature changes according to

$$\mathrm{d}\boldsymbol{\varepsilon}^{\mathrm{e}} = \mathbf{C}^{\mathrm{e}}\colon \mathrm{d}\boldsymbol{\sigma}' - \left(\frac{1}{3}\beta_s \mathbf{I}\right)\mathrm{d}T = \mathbf{C}^{\mathrm{e}}\colon \mathrm{d}\boldsymbol{\sigma}' - \boldsymbol{\beta}_T \mathrm{d}T \tag{6}$$

where $\boldsymbol{\beta}_T$ is the thermal expansion coefficient tensor and β_s is given by

$$\beta'_s = \beta'_{s0}\left(1 - \frac{T - T_0}{100}\right)\frac{p'_{cr0}}{p'} \tag{7}$$

where β'_{s0} is the thermal expansion coefficient at a reference temperature T_0 and p'_{cr0} is the initial critical state pressure at the reference temperature.

If the effective stress state reaches the yield surface, plastic strains will develop. These might be induced by two mechanisms one isotropic and another one deviatoric, developing respectively isotropic $\mathrm{d}\boldsymbol{\varepsilon}^{\mathrm{p}}_{\mathrm{iso}}$ and deviatoric $\mathrm{d}\boldsymbol{\varepsilon}^{\mathrm{p}}_{\mathrm{dev}}$ plastic strains. Thus plastic strain is decomposed as

$$\mathrm{d}\boldsymbol{\varepsilon}^{\mathrm{p}} = \mathrm{d}\boldsymbol{\varepsilon}^{\mathrm{p}}_{\mathrm{iso}} + \mathrm{d}\boldsymbol{\varepsilon}^{\mathrm{p}}_{\mathrm{dev}} \tag{8}$$

each mechanism corresponds to a different yield surface f whose expressions are respectively

$$f_{iso} = p' - p'_c r_{iso} = 0 \tag{9}$$

$$f_{dev} = q - Mp'[1 - b\ln\left(\frac{p'd}{p'_c}\right)]r_{dev} \tag{10}$$

Where p'_c is the preconsolidation pressure, q is the deviatoric stress, M is the slope of the critical state line in the $(p'-q)$ plane; b is a material parameter defining the shape of the deviatoric yield surface; $d=\frac{p'_c}{p'_{cr}}$ with p'_{cr0} the critical state pressure; r_{iso} and r_{dev} correspond to the degrees of plastification for each mechanism, allowing for plastic strains within the yield limits. It can be readily observed that both mechanisms are coupled by means of the preconsolidation pressure p'_c.
Preconsolidation pressure depends on the volumetric plastic strain, temperature and suction as follows

$$p'_c=\begin{cases} p'_{c0}\exp\left(\beta\varepsilon_v^p\right)\left[1-\gamma_T\log\left({}^{T}/_{T_0}\right)\right] & \text{if } \ s<s_e \\ p'_{c0}\exp\left(\beta\varepsilon_v^p\right)\left[1-\gamma_T\log\left({}^{T}/_{T_0}\right)\right]\left[1+\gamma_S\log(s/s_e)\right] & \text{if } \ s>s_e \end{cases} \tag{11}$$

where β is the plastic compressibility modulus (slope of the $\varepsilon_v^p-\ln p'_c$ relation, where $\varepsilon_v^p\ =\frac{1}{3}tr(\boldsymbol{\varepsilon})$); s_e is the air entry suction value; and γ_T and γ_s account for the evolution of elastic domain with suction and temperature. The flow rule of the isotropic mechanism is associated whereas that for the deviatoric mechanism can be non-associated. Thus the plastic potentials have the following form:

$$g_{iso}=p'-p'_c r_{iso}=0 \tag{12}$$

$$g_{dev}=q-\frac{\alpha}{\alpha-1}Mp'\left[1-\frac{1}{\alpha}\left(\frac{p'd}{p'_c}\right)^{\alpha-1}\right]=0 \tag{13}$$

where α is a non-associativity parameter. The magnitude of plastic strains depends on the derivatives of these potentials as follows

$$\mathrm{d}\boldsymbol{\varepsilon}^{\mathrm{p}}_{\mathrm{iso}}=\mathrm{d}\lambda^p_{iso}\frac{\partial g_{iso}}{\partial\boldsymbol{\sigma}'} \tag{14.a}$$

$$\mathrm{d}\boldsymbol{\varepsilon}^{\mathrm{p}}_{\mathrm{dev}}=\mathrm{d}\lambda^p_{dev}\frac{\partial g_{dev}}{\partial\boldsymbol{\sigma}'} \tag{14.b}$$

where λ^p_{iso} and λ^p_{dev} are the plastic multipliers which are determined following Prager's consistency condition extended to multi-dissipative materials:

$$\begin{gathered}\mathrm{d}\mathbf{F}=\frac{\partial\mathbf{F}}{\partial\boldsymbol{\sigma}'}:\mathrm{d}\boldsymbol{\sigma}'+\frac{\partial\mathbf{F}}{\partial\boldsymbol{\pi}}\cdot\frac{\partial\mathbf{F}}{\partial\boldsymbol{\pi}}\cdot\mathrm{d}\boldsymbol{\lambda}^p\leq\mathbf{0}, \\ \mathrm{d}\boldsymbol{\lambda}^p\geq\mathbf{0},\qquad \mathrm{d}\mathbf{F}\cdot\mathrm{d}\boldsymbol{\lambda}^p=0\end{gathered} \tag{15}$$

where $\mathbf{F}=(f_{iso}\ \ f_{dev})$ is the yield surface vector, $\boldsymbol{\pi}=(p'_c\ \ r_{iso}\ \ r_{dev})$ is the vector of internal variables and $\boldsymbol{\lambda}^p=(\lambda^p_{iso}\ \ \lambda^p_{dev})$ is the plastic multiplier vector.

In order to account for unsaturated conditions, a relationship between degree of saturation and suction is introduced. An elastoplastic approach is used to model water retention, which includes hysteretic behaviour controlled by two yield surfaces corresponding to drying and wetting paths. Desaturation (or saturation) is induced when suction reaches either the wetting limit or the drying limit, satisfying respectively

$$f_{wet} = s_d s_{hys} - s \quad \text{and} \quad f_{dry} = s - s_d \tag{16}$$

Where f_{dry} and f_{wet} stand for the yield activated during a wetting or drying process respectively, s_d is the drying yield limit which during a desaturation/saturation process (i.e. $f_{dry} = 0$ or $f_{wet} = 0$) remains equal to the actual value of s; and s_{hys} a material parameter controlling the size of the water retention hysteresis.

If the initial state is saturated, s_{d0} is equal to the air entry suction s_{e0} and increases when suction exceeds this value according to the following hardening law

$$s_d = s_e \exp(-\beta_h \Delta S_r) \tag{17}$$

where β_h is the slope of the retention curve in the $(S_r - \ln s)$ plane. The same process is activated for a wetting path in the opposite way (expression (16)). Thus, expression (17) describes the hardening process that leads to changes in S_r. A limit condition is imposed so that when S_r reaches the residual degree of saturation s_d is kept constant.

To account for the dependency of water retention on dry density and temperature, s_e is taken as a function that depends on the material state as

$$s_e = s_{e0}[1 - \theta_T \log\left(\frac{T}{T_0}\right) - \theta_E \log(1 - \varepsilon_v)] \tag{18}$$

where s_{e0} is the initial air entry suction, and θ_T and θ_E describe the evolution of air entry suction with temperature and volumetric strain respectively.

2.4.2 Water flow formulation

For the sake of concisness, only the equations that relate to the evolution of permeability with degree of saturation and deformation are reported here. For a complete description of the multi-phase flow formulation under general non-isothermal conditions used in LAGAMINE the reader is refered to Collin et al., (2002).

Water flow is modelled by means of Darcy's law:

$$\mathbf{q}_w = -\frac{k_{rw}\mathbf{k}_f}{\mu_w}[\mathrm{grad}(p_w) + g\rho_w \mathrm{grad}(z)] \tag{19}$$

Where $\mathbf{q}_w$ is the vector of water flux, $\mathbf{k}_w$ is the tensor of intrinsic permeability, k_{rw} is the relative permeability, μ_w is water viscosity, p_w is water pressure, g is the gravity acceleration, ρ_w is water density and z is the elevation in global coordinates. In the present case it will be considered that permeabilty tensor is isotropic, i.e.:

$$\mathbf{k}_f = \mathbf{I}k_f \tag{20}$$

Where

$$k_f = k_{rw}\frac{\mu_w}{\rho_w g} \tag{21}$$

k_{rw} is the relative permeability which evolves with the degree of saturation, S_r as follows

$$k_{rw} = k_{sat}\frac{(S_r - S_{res})^{C_{KW1}}}{(1 - S_{res})^{C_{KW2}}} \tag{22}$$

Where k_{sat} is the permeability at saturated state, C_{KW1} and C_{KW2} are material parameters and S_{res} is the residual degree of saturation.
The influence of deformation on the intrinsic permeability is taken into account by means of the Kozeny-Karman formula:

$$k_f = k_{f,0}\frac{(1 - n_0)^M}{n_0^N}\frac{n^N}{(1 - n)^M} \tag{23}$$

Where $k_{f,0}$ is the initial intrinsic permeability, n stands for porosity, n_0 is the initial porosity and $M$and N are material parameters.

2.5 LEI

2.5.1 COMSOL Multiphysics model

For the modelling of hydro-mechanical (HM) response of hydration of bentonite material under three different tests Richard‘s equation was applied for the water flow modelling. Wetting induced swelling was modelled as linear elastic deformations and its impact on porosity change. HM model included couplings to consider impact of mechanical deformations on water balance, porosity change impact on specific moisture capacity, on storage coefficient, on permeability, on air entry pressure.

2.5.2 CODE_BRIGHT model

The finite element code, CODE-BRIGHT (COuple DEformation BRIne Gas and Heat Transport) (UPC, 2017) was used for numerical simulations of the experiments "Test 1a01" and "Test 1b" considering coupled hydro-mechanical problem for multiphase process in unsaturated porous media. The Barcelona Basic Model (Alonso et al., 1990) has been adopted for the mechanical constitutive behaviour of analysed material. It is carried out by the Thermo-elastoplastic model for soils taking into account the variation of stress-stiffness with suction and variation of swelling potential with stresses and suction. For hydraulic process, advective flow of water phase is described by Darcy law (air flow is neglected - gas phase pressure is constant P_{gas}=0). The tensor of intrinsic permeability is supposed to depend on porosity according to Kozeny's model. The relative permeability and retention curve of analysed material is derived from the van Genuchten model.

2.6 Quintessa

Amongst the measurements that are regularly made of the properties of bentonite are three common data sets:

- The swelling pressure of the bentonite versus dry density;
- Suction versus water content;
- Void ratio versus vertical stress for loading and unloading (oedometer tests).

These three data sets were available for a 70/30 by mass MX-80 bentonite / sand mixture during the DECOVALEX-2015 project. Comparison of these three data sets showed that a curve of the form:

$$p = p_0 * \exp\left(\frac{-e}{\lambda}\right) \quad (1)$$

can be fit to all three data sets, using the same values of parameters p_0 and λ for each data set. For swelling pressure versus dry density data (Figure 2-3), p [Pa] is swelling pressure and e [-] is void ratio which is converted to dry density (ρ_{dry} [Mg/m^3]) using the equation:

$$e = \frac{1 - {}^{\rho_{dry}}/_{\rho_{grain}}}{{}^{\rho_{dry}}/_{\rho_{grain}}} \tag{2}$$

where ρ_{grain} [Mg/m³] is the density of the solid grains (2.77 Mg/m³).

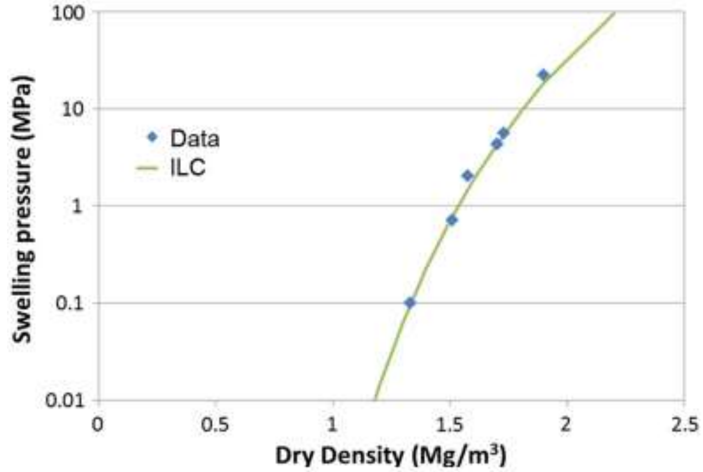

Figure 2-3 ***Swelling pressure data for the final dry density of bentonite in a 70/30 bentonite/sand mixture (Wang et al. 2012) plotted against the Internal Limit Curve (Equation 1, parameterised to fit the swelling data).***

For suction versus water content data, the same equation can be applied, but now p [Pa] is suction and water content is calculated from void ratio assuming that all pore space is filled with water (Figure 2-4).

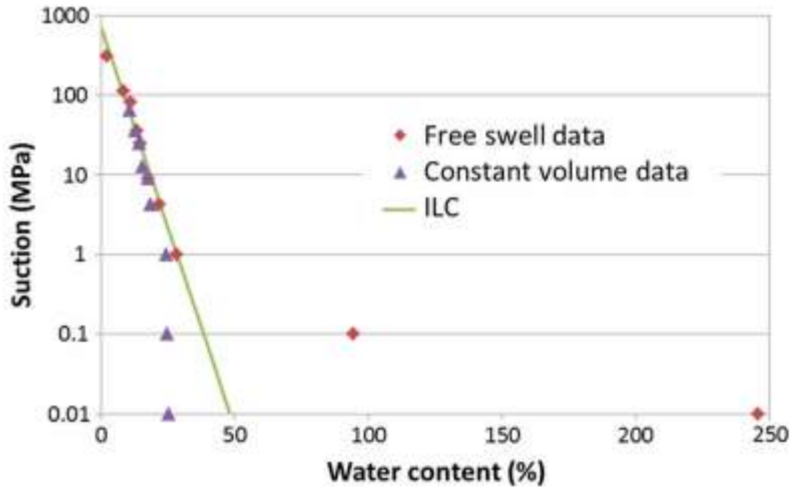

Figure 2-4 ***Water retention data for free swelling and constant volume samples (Wang et al. 2013a) alongside the ILC curve modified to give saturated water content for a given dry density, but using the same parameters as Figure 2-3.***

Finally, the same equation can be plotted with data from oedometer tests, with p [Pa] equal to vertical stress (Figure 2-5).

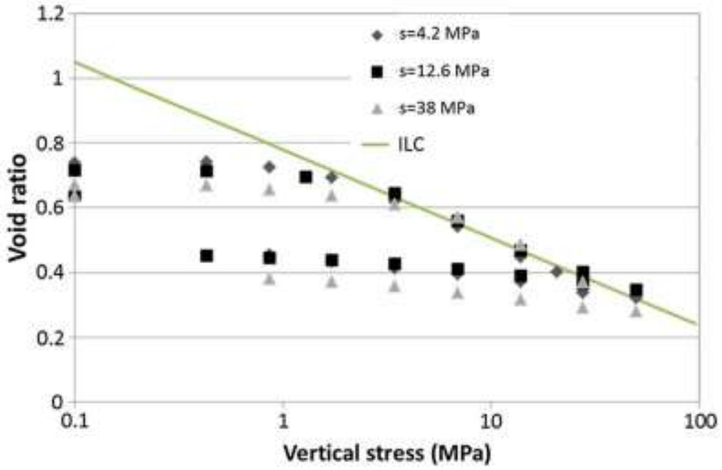

Figure 2-5 Data from the oedometer tests at a constant initial dry density (Wang et al. 2013a) plotted with the ILC, using the same parameterisation for the ILC as inFigure 2-3 and Figure 2-4.

In Figure 2-3, Figure 2-4 and Figure 2-5, the ILC line has the same parameter values for p_0 and λ. For the swelling data (Figure 2-3), the curve fits the data well. For the water retention data (Figure 2-4), the curve fits free swell data at lower water contents well (in this regime, the fixed volume swell data also fits the curve). The two free swell data points at water contents > 50% show much higher suctions that the ILC curve would suggest and we hypothesise that this is due to a different mechanism causing suction at higher water contents. The ILC curve also fits the virgin consolidation part of the oedometer test well (Figure 2-5). These observations suggest that for a given dry density of bentonite there is a limiting stress that the sample can support, be that stress due to swelling, compaction or suction.

These observations, alongside a suggestion given by Dueck (2004) that suction (Ψ) in bentonite is related to free swelling suction (Ψ^{free}) and stress (σ) by

$$\Psi = \Psi^{\text{free}} - \sigma, \quad (3)$$

form the background to the model.

The ILM is based on Richards' equation for the hydraulics, momentum balance for the mechanics and the Modified Cam Clay (MCC) model (Roscoe and Burland 1968) to represent plastic deformation. Thermal processes were later coupled to the model, which are based on the diffusion equation.

The mechanical problem is expressed in terms of conservation of momentum, which is otherwise referred to as the Navier equation (Howell et al. 2009):

$$\rho \frac{\partial^2 \bar{u}}{\partial t^2} = \nabla \bar{\bar{\sigma}} - \rho \bar{g} \tag{4}$$

where ρ [kg/m³] is the solid density, $\bar{u}$ [m] is the displacement vector, t [s] is time, $\bar{\bar{\sigma}}$ [MPa] is the stress tensor and $\bar{g}$ [m/s²] is the vector of the acceleration due to gravity. The equation effectively ensures a local force balance for pseudo-steady state. The stress vector [$\bar{\sigma}$] assumes a pseudo-steady state and is given by:

$$\bar{\sigma} = \bar{\bar{S}}(\bar{\varepsilon} - \bar{\gamma}) - P \tag{5}$$

where $\bar{\bar{S}}$ [MPa] is the elastic stiffness matrix, $\bar{\varepsilon}$ [-] is the strain vector, $\bar{\gamma}$ [-] represents arbitrary additional strains, e.g. swelling strain and plastic strain, and P [MPa] is fluid pressure.

For swelling bentonite at a constant temperature, it is assumed that there are two additional sources of strain: swelling strains due to changes in water content of the bentonite and plastic strains due to plastic failure of the bentonite. Swelling strains are discussed later as they are coupled to the hydraulics.

Plastic strains are calculated according to the MCC model. The plastic yield surface is given by:

$$\left[\frac{q}{M}\right]^2 + p'(p' - p_c) = 0 \tag{6}$$

whilst the virgin consolidation line in the MCC model, which describes how the yield surface changes with stress, has the equation:

$$v = \Gamma - C \ln p' \tag{7}$$

where v [-] is the specific volume ($v = 1 + e$, where e [-] is the void ratio), p' [MPa] is the effective confining stress, q [MPa] is deviatoric stress, p_c [MPa] is the pre-consolidation pressure (which is a point on the virgin consolidation line) and M, Γ and C [-] are all constant parameters. The plastic strain is calculated as the derivative of the plastic yield surface.

The hydraulic problem is expressed in terms of conservation of mass:

$$\frac{\partial}{\partial t}\left(\theta \rho_f \varphi\right) = -\nabla \cdot (\rho_w v) + Q \qquad (8)$$

where θ [-] is porosity, ρ_f [kg/m^3] is fluid (water) density, φ [-] is saturation, v [m/s] is the fluid velocity and Q [kg/m^3/s] is a source or sink.

A number of different formulations can be used to represent the fluid migration in the ILM, including full multiphase flow. In the models described below, Richards' equation has been chosen. Richards' equation can be used where gas flow is very fast compared to water flow, so that gas flow does not need to be solved for in the equations. It was found that model results using Richards' equation were as good as full multiphase flow, but since gas flow was not represented, fewer free parameters were required:

$$u = -\frac{k}{\mu}\nabla(P_w + \rho g z) \qquad (9)$$

where k [m^2] is the effective permeability tensor, μ [Pa s] is the fluid viscosity and z (m) is height. Permeability varies with water saturation (S_w [$-$]) in the model as S_w^4.

Water pressure (P_W [MPa]) is calculated by subtracting the net suction (Ψ [MPa]) from the gas pressure (P_g [MPa]):

$$P_W = P_g - \Psi. \qquad (10)$$

Suction is determined from the Internal Limit Curve (ILC).

To calculate the net suction when the sample is not swelling freely, an approach modified from that suggested by Dueck (2004) (Equation 10) has been adopted. The net suction is the free swell suction minus stress, but localised according to stress direction, following the argument that bentonite interlayers will be constrained in terms of their water content most significantly by the plate normal stress. This is calculated in three principal directions in the model as:

$$\Psi_{nn} = {\Psi_{nn}}^{free} - \sigma_{nn} \quad \text{for} \quad n = i, j, k \tag{11}$$

where σ_{nn} is the stress component nn, with the total suction given by:

$$\Psi = \frac{1}{3}(\Psi_{ii} + \Psi_{jj} + \Psi_{kk}). \tag{12}$$

The water content in the three directions is constrained such that the net suction in each of the three directions is equal. The conceptual model behind considering water content and suction in three directions is that the bentonite grains are oriented in random directions such that a third of the grains are aligned to each principal direction.

Note that this suction model is a significant departure from conventional models used with Richards' equation where suction is defined purely as a function of fluid saturation. The approach shown above allows stress to be coupled into the suction relationship directly, at the expense of always enforcing a strict constraint on volume conservation of the water.
Not enforcing such a volume constraint (although local and global mass balance is retained at all times), as one might do for a conventional porous material, is justified on the basis of recent work (Jacinto et al. 2012) which suggests that when water is present as a crystalline phase in the bentonite inter-layers, the density of that water may depart significantly from the equivalent liquid water density due to the presence of charged ions in the bentonite, allowing water molecules to sit closely together. Hence water saturation could exceed unity in the models in order to obtain the necessary mass in the $\theta\rho_f\varphi$ term in (8), which assumes a fixed fluid density.

In the ILM, swelling strain is calculated based on the change in water content in the bentonite. Swelling strain is calculated in the three principal directions as follows:

$$\epsilon_{nn}^{swell} = \frac{\frac{a}{3}(w_{nn} - w_0)m_s}{\rho_w V_{comp}} \tag{13}$$

where w_0 is the initial water content [kg/kg], w_{nn} is the water content in the direction nn, m_s is the mass of solids [kg], ρ_w is the density of water [kg/m^3], V_{comp} is the compartmental volume [m^3] in the numerical discretisation and a is a swelling efficiency term which reflects that not all additional water will cause a volume increase, some will just fill void space in the sample. The calculation is considered in three principal directions following the conceptual model that bentonite grains are aligned principally in one of the three directions. The amount of stress in the three principal directions is different, so the free suction, and therefore water content, will be different in the three directions; however, the net suction (free suction minus stress) will be the same in each direction.

2.7 ULG

2.7.1 Hydraulic model

The unique relationship between suction and the degree of saturation or water content ((Brooks & Corey, 1964); (van Genuchten, 1980)) does not suit the hydraulic behaviour of highly expansive soils such as bentonite. Indeed, in the case of compacted bentonites, the material swells significantly upon wetting, resulting in important changes in dry density. Consequently, the dependency of the water retention curve on the dry density of the material is a major issue.

Hence, a new model is proposed and implemented and it is currently adopted in Liège (Dieudonnè, 2016).

Based on the abovementioned information, the model is formulated in terms of water ratio e_w reference, which is expressed as the superposition of a contribution from the water stored in the micropores e_{wm} and a second contribution from the water contained in the macropores e_{wM}:

$$e_w = e_{wm} + e_{wM} \tag{2.1}$$

This model takes into account the evidence of the different water retention mechanisms, namely adsorption in the microstructure (inter-layer porosity and inter-particle porosity) and capillary storage in the inter-aggregate porosity (see Figure 2-6).

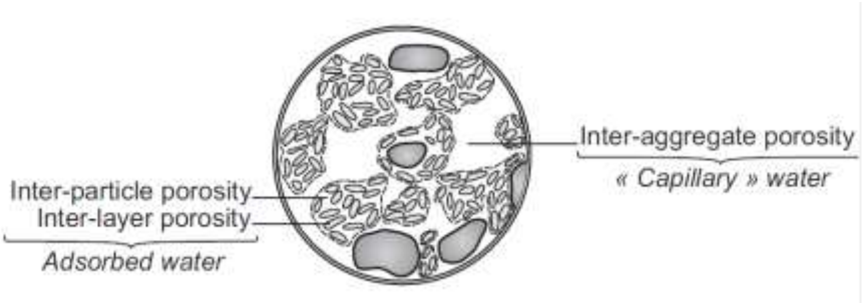

Figure 2-6 Conceptual representation of the structure of compacted bentonite (in black) and the different water storage mechanisms (in blue) (modified after Gens & Alonso (Gens & Alonso, 1992); (Jacinto, Villar, & Ledesma, 2012).

The degree of saturation S_r is then expressed as:

$$S_r = \frac{e_w}{e} = \frac{e_m}{e} S_{rm} + \frac{e_M}{e} S_{rM} \tag{2.2}$$

where e_m and $e_M = e - e_m$ are respectively the microstructural and macrostructural void rations, and S_{rm} and S_{rM} the microstructural and macrostructural degrees of saturation. The degrees of saturation are therefore not additive, as the global degree of saturation is obtained by the sum of the microstructural and macrostructural degrees of saturation, weighted by the corresponding volumetric fractions.
In the following, thermodynamic equilibrium between the microstructure and macrostructure is assumed. Accordingly, the current value of suction applies to both structural levels.

2.7.1.1. ***Microstructural water retention domain***

Water in the microstructure is mainly stored by adsorption. Several adsorption isotherms have been proposed in the literature by the community of physicists. Dubinin's isotherm is adopted to describe the water retention behaviour of the microstructure. Its equation takes the following form:

$$\Omega_{wm} = \Omega_m exp\left\{-\left[\frac{RT}{\beta_D E_0} ln\left(\frac{u_v^0}{u_v}\right)\right]^{n_{ads}}\right\} \tag{2.3}$$

where Ω_{wm} is the volume of water adsorbed in the micropores at temperature T and relative pressure u_v/u_v^0, R is the universal gas constant ($= 8{:}314\, J/mol \cdot K$), and Ω_m is the total volume of the micropores, n_{ads} is a specific parameter of the system, called heterogeneity factor. β_D is termed similarity constant and $E = DE_0$ is the characteristic adsorption energy for the given system. E_0 is the characteristic energy of adsorption for a reference vapour for which $\beta_D = 1$.

By dividing both sides of equation 2.3 by the volume of solid particles Ω_s, it yields:

$$\mathrm{e}_{wm} = \mathrm{e}_m exp\left\{-\left[\frac{RT}{\beta_D E_0} ln\left(\frac{u_v^0}{u_v}\right)\right]^{n_{ads}}\right\} \quad (2.4)$$

Moreover, assuming relative humidity RH being function of relative pressure u_v/u_v^0, in terms of suction s:

$$RH = \frac{u_v^0}{u_v} = exp\left(\frac{-sM_w}{RT\varrho_w}\right) \quad (2.5)$$

where M_w is the molecular mass of water $(= \ 0{:}\,018\,kg/mol)$ and ϱ_w its density. Gathering the constant parameters, the following expression is finally adopted for the micro-structural water retention domain:

$$e_{wm}(s, e_m) = \mathrm{e}_m exp[-(C_{ads}s)^{n_{ads}}] \quad (2.6)$$

Where n_{ads} and C_{ads} are material parameters controlling respectively the curvature of the water retention curve in the high suction range and the dependency on the rate of desaturation of the soil. C_{ads} also reads:

$$C_{ads} = \frac{M_w}{\varrho_w \beta_D E_0} \quad (2.7)$$

2.7.1.2. *Macrostructural water retention domain:*

The van Genuchten (van Genuchten, 1980) water retention model has been successfully used to model the water retention behaviour of a wide variety of soils. It is generally expressed as:

$$S_r(s) = \left[1 + \left(\frac{s}{\alpha}\right)^n\right]^{-m} \quad (2.8)$$

where m and n are material parameters, and α is related to the air-entry value s_{AE}. Alternatively, the van Genuchten equation may expressed in terms of water ratio e_w:

$$e_w(s, e) = e\left[1 + \left(\frac{s}{\alpha}\right)^n\right]^{-m} \quad (2.9)$$

In this model, the van Genuchten equation is selected to model the macrostructural water retention domain. Accordingly, the void ratio e is replaced by the macrostructural void ratio $e_M = e - e_m$, and the macrostructural water retention model reads:

$$e_{wM}(s,e) = (e - e_m)\left[1 + \left(\frac{s}{\alpha}\right)^n\right]^{-m} \quad (2.10)$$

In order to represent the influence of the bentonite structure on the air-entry value, the parameter α is assumed to depend on the macrostructural void ratio. The following law is adopted:

$$\alpha = \frac{A}{e - e_m} \quad (2.11)$$

where A controls the dependence of the air-entry pressure on the macrostructural void ratio.

2.7.1.3. ***Microstructure evolution***

In order to take into account the variation of microstructure due to saturation degree change, the following equation is written:

$$e_m = e_{m0} + \beta_0 e_w + \beta_1 e_w^2 \quad (2.12)$$

Where e_{m0} is the microstructural void ratio for the dry material ($e_w = 0$) and β_0 and β_1 are parameters that quantify the swelling potential of the aggregates.

2.7.1.4. ***Water permeability evolution***

Given the double structure of compacted bentonite, the water permeability evolution is modelled as follows:

$$K_w = K_{w0}\frac{e_M^N}{(1 - e_M^N)^M}\frac{(1 - e_{M0})^N}{e_{M0}} \quad (2.13)$$

where K_{w0} is a reference permeability measured on a material with a reference macroscopic void ratio e_{M0}.
By using equation 2.13, one implicitly assumes that water flow takes place essentially in the macro-pores of the material. Although this hypothesis cannot

be directly checked using experimental techniques, some evidences tend to validate it.

Via this strategy, an additional hydro-mechanical and multi-scale coupling is added in the hydro-mechanical formulation of the model. Indeed, the saturated water permeability turns out to be affected by the mechanical deformation through the void ratio e and by microstructure evolution through e_m, since the macrostructural void ratio reads $e_M = e - e_m$.

2.7.2 Mechanical model

The Barcelona Basic Model (BBM) was chosen for its well-known robustness and capacities. Its formulation in terms of net stress and suction allows an easier calibration than other models formulated using an effective stress.

It was proposed by Alonso (Alonso, Gens, & Josa, A constitutive model for partially saturated soils, 1990), who pioneered the development of mechanical constitutive models for partially saturated soils. Most of the existing models for unsaturated soils rely indeed on the concepts developed in the BBM. The idea behind the model is the extension of an existing model for saturated soils to unsaturated conditions.

Accordingly, the behaviour of unsaturated soils should be modelled consistently and full saturation considered as a limiting case. Therefore, the Barcelona Basic Model consists in the extension of the Modified Cam-Clay Model (Roscoe & Burland, 1968) to unsaturated conditions, by using suction as an additional stress variable. It is formulated adopting net stress σ and suction s as stress variables.

It is worth reminding the definition of net stress $\boldsymbol{\sigma}$:

$$\boldsymbol{\sigma} = \boldsymbol{\sigma}_T - u_a \boldsymbol{I} \tag{2.14}$$

With $\boldsymbol{\sigma}_T$ the total stress tensor, u_a the air pressure for $s > 0$ and $\boldsymbol{I}$ the identity tensor.

The model is first formulated for isotropic stress states and then it is progressively extended to triaxial stress state.

2.7.2.1. *Isotropic stress states*

Under isotropic stress conditions $(\sigma_1 = \sigma_2 = \sigma_3)$, the mechanical stress state is described using the mean net stress $p = \sigma_i$ and suction s.

Both changes in the mean net stress and in suction are assumed to produced only volumetric strains $\varepsilon_v = \varepsilon_i$. Accordingly, the space $(p - s - \varepsilon_v)$ is relevant for

the description of the model and yield limits should be defined in the plane $(p - s)$.
For saturated conditions, the Barcelona Basic Model coincides with the Modified Cam-Clay Model (Roscoe & Burland, 1968). The Modified Cam-Clay model belongs to the family of elastoplastic strain-hardening models. Accordingly, the total strain increment can be decomposed into an elastic part and a plastic part. For isotropic stress states, the increment of total volumetric strain $d\varepsilon_v$ is equal to the sum of the elastic $d\varepsilon_v^e$ and plastic $d\varepsilon_v^p$ components of the incremental volumetric strain:

$$d\varepsilon_v = d\varepsilon_v^e + d\varepsilon_v^p \tag{2.15}$$

In the elastic domain, the increment of volumetric strain associated to changes in mean net stress is given by:

$$d\varepsilon_v^e = \frac{\kappa}{1+e}\frac{dp}{p} = \frac{dp}{K} \tag{2.16}$$

where K is the slope of the unloading-reloading line and e is the void ratio. Elasticity in the Modified Cam-Clay Model is non-linear as the bulk modulus K is a function of both the void ratio and the mean net stress according to:

$$K = \frac{(1+e)p}{\kappa} \tag{2.17}$$

Once that the mean net stress reaches the preconsolidation stress (yield limit) p_0^* plastic strain is generated. The evolution of the plastic strain is then governed by the hardening law:

$$d\varepsilon_v^p = \frac{\lambda(0) - \kappa}{1+e}\frac{dp_0^*}{p_0^*} \tag{2.18}$$

where $\lambda(0)$ is the slope of saturated virgin consolidation line (see Figure 2-7). However, since the suction dependency is un-negligible in unsaturated conditions, the slope of the virgin consolidation line $\lambda(s)$ reads as follow:

$$\lambda(s) = \lambda(0)[(1-r)\exp(-\omega s) + r] \tag{2.19}$$

where r and ω are material parameters. r is related to the maximum stiffness of the soil (for an infinite suction) and ω controls the rate of increase of the soil stiffness with suction.
On the other hand, the slope κ of the loading-unloading line is supposed to be constant.
The evolution of the preconsolidation pressure $p_0(s)$ is modelled consistently with the concept of increasing the elastic domain with increasing suction:

$$p_0(s) = p_c \left(\frac{p_0^*}{p_c}\right)^{\frac{\lambda(0)-\kappa}{\lambda(s)-\kappa}} \tag{2.20}$$

where p_c is a reference net pressure. Equation 3.7 defines a yield curve in the $(p-s)$ plane called the Loading-Collapse (LC) curve, which is fundamental for the Barcelona Basic Model.
Considering suction, the hardening law of the LC curve becomes:

$$d\varepsilon_v^p = \frac{\lambda(s)-\kappa}{1+e}\frac{dp_0^*}{p_0^*} \tag{2.21}$$

And by substitution, it can be obtained:

$$d\varepsilon_v^p = \frac{\lambda(0)-\kappa}{1+e}\frac{dp_0^*}{p_0^*} \tag{2.22}$$

Corresponding to the hardening law with no suction dependence.
Under these conditions, the suction change is supposed to affect only the volumetric part of the total strain, reading therefore:

$$d\varepsilon_v^e = d\varepsilon_{vp}^e + d\varepsilon_{vs}^e = \frac{\kappa}{1+e}\frac{dp}{p} + \frac{\kappa_s}{1+e}\frac{ds}{s+u_{atm}} = \frac{dp}{K} + \frac{ds}{K_s} \tag{2.23}$$

Where $d\varepsilon_{vp}^e$ and $d\varepsilon_{vs}^e$ represent respectively the elastic volumetric strain associated to the change in net stress and the one related to the change in suction. Then κ_s is the slope of the wetting-drying line in the space $(e-s)$ and u_{atm} the atmospheric pressure. The bulk modulus for change in suction is expressed by the following equation:

$$K_s = \frac{(1+e)(s+u_{atm})}{\kappa_s} \tag{2.24}$$

Finally, a second yield curve in the space $(p - s)$ can be defined. It is called the Suction Increase curve and it defines, for a given drying path, irreversible plastic strain, after the threshold value of suction s_0 (see Figure 2-8):

$$f_{SI} \equiv s = s_0 \tag{2.25}$$

The consequential value of plastic strain is given:

$$d\varepsilon_v^p = \frac{\lambda_s - \kappa_s}{1 + e} \frac{ds_0}{s_0 + u_{atm}} \tag{2.26}$$

Accordingly, irreversible strains control the position of the LC and SI yield surfaces and the hardening of both yield surfaces is coupled. Depending on the sign of the volumetric plastic strain, hardening or softening of the yield surface will take place.

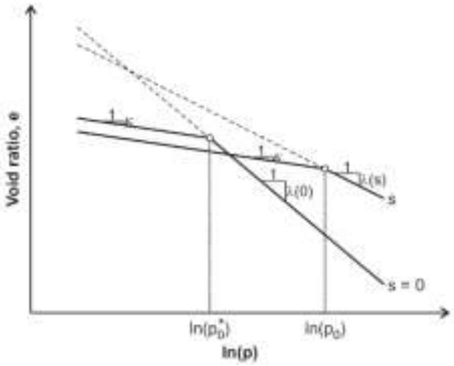

Figure 2-7 **Compression curves for saturated and unsaturated states (Alonso, Gens, & Josa, A constitutive model for partially saturated soils, 1990).**

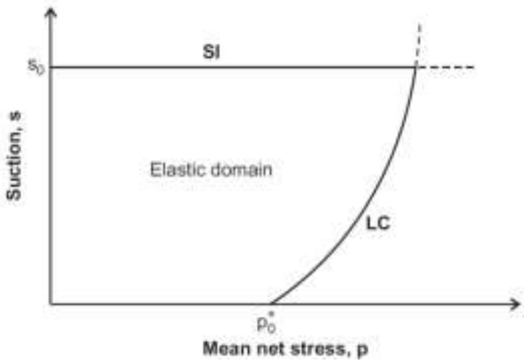

Figure 2-8 **Yield curves of the Barcelona Basic Model for isotropic stress states: Loading-Collapse (LC) and Suction Increase (SI) curves.**

2.7.2.2. ***Triaxial stress states***

Under triaxial conditions $(\sigma_1 \neq \sigma_2 = \sigma_3)$, the mechanical stress state can be described by the mean net stress p, suction s and the deviatoric stress $q = \sigma_1 - \sigma_3$ (see Figure 2-10).
In the elastic domain, the deviatoric deformation due to the deviatoric stress is given:

$$d\varepsilon_d^e = \frac{1}{3} G dq \tag{2.27}$$

where $d\varepsilon_d^e$ d is the elastic increment of deviatoric strain and G is the shear modulus. This modulus may be chosen as a constant or as a function of the bulk modulus K following:

$$G = \frac{3(1-2\nu)K}{2(1+\nu)} \tag{2.28}$$

In the $(p-q)$ plane, the yield surface is expressed (see Figure 2-9):

$$f_{LC} \equiv q^2 - M_\theta^2(p+p_s)(p_0-p) = 0 \tag{2.29}$$

With M_θ the slope of the critical state line, p_s the left intercept of yield surface and p_0 the apparent preconsolidation pressure at a suction s. p_s increases with increasing cohesion, therefore it can be given as a function of suction:

$$p_s(s) = \frac{c(s)}{tan\varphi} = \frac{c(0)+ks}{tan\varphi} \tag{2.30}$$

where $c(0)$ is the cohesion under saturated conditions and k is a parameter controlling the increase of cohesion.

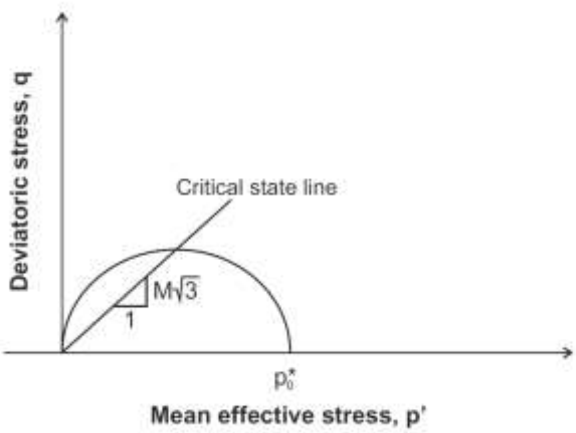

Figure 2-9 *Modified Cam-Clay Model.*

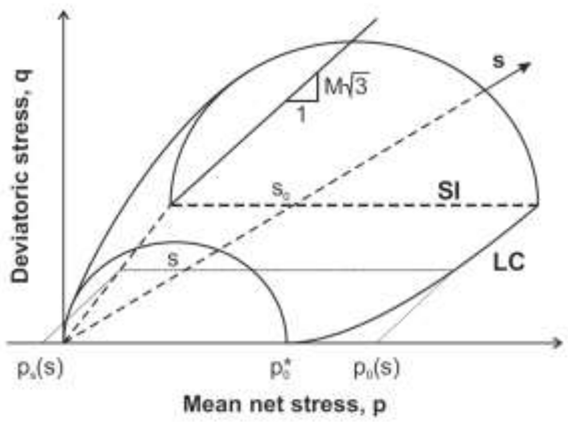

Figure 2-10 *Barcelona Basic Model*

.

2.7.2.3. *New formulation of BBM*

The following relation was introduced and implemented in LAGAMINE (Dieudonnè, 2016):

$$\kappa_s = 0 \qquad if \qquad s < s^* \tag{2.31}$$

The main concept behind this relation is that bentonite-based materials are capable to sustain high value of suction without desaturating due to their important air-entry value.
Hence, saturation is obtained before reaching the suction zero value.
As consequence, under confined conditions, the swelling stress, being generated by the saturation process, should not vary anymore as the few available experimental data show (Agus, Arifin, Tripathy, & Schanz, 2013).

2.8 CU-CTU

The simulations were carried out using a coupled thermo-hydro-mechanical double-structure constitutive framework for expansive clays based on the theory of hypoplasticity (Mašín, 2013, 2017). In the model, the hydro-mechanical coupling is accounted for at both structural levels. The water retention behaviour and the effective stress definition are specified for both levels, and they are linked to each other through double-structure coupling functions. The model can also account for the effect of variations of temperature at both structural levels.

The general model formulation can be expressed as:

$$\dot{\boldsymbol{\sigma}}^M = f_s[\boldsymbol{\mathcal{L}}:(\dot{\boldsymbol{\varepsilon}} - f_m\dot{\boldsymbol{\varepsilon}}^m) + f_d\boldsymbol{N}\|\dot{\boldsymbol{\varepsilon}} - f_m\dot{\boldsymbol{\varepsilon}}^m\|] + f_u(\boldsymbol{H}_s + \boldsymbol{H}_T)$$

where: $\boldsymbol{\mathcal{L}}$, $\boldsymbol{N}$, $\boldsymbol{H}_s$, and $\boldsymbol{H}_T$ are hypoplastic tensors; f_s, f_d, and f_u are hypoplastic scalar factors; $\dot{\boldsymbol{\varepsilon}}$ is the Euler stretching tensor; $\dot{\boldsymbol{\sigma}}^M$ is the objective effective stress rate of the macrostructure; and $\dot{\boldsymbol{\varepsilon}}^m$ is the microstructural strain rate. In the model, an anisotropic mechanical response of the macrostructure is permitted, while the microstructure can only deform isotropically.

The water retention behaviour of the macrostructure has been modelled using a bilinear hysteretic relationship between the suction and the degree of saturation (Mašín, 2013:

$$S_r^M = \chi^M = \begin{cases} 1 & \text{for} \quad s < s_e \\ \left(\dfrac{s_e}{s}\right)^\gamma & \text{for} \quad s \geq s_e \end{cases}$$

where: S_r^M is the degree of saturation of the macrostructure, χ^M is the effective stress parameter of the macrostructure, s is the suction, s_e is the air entry/expulsion value of suction, and γ is a soil parameter that can be assumed equal to 0.55 for any soil and represents the slope of the main drying/wetting curve in a $\ln S_r^M - \ln s$ plane. Conversely, the microstructure has been assumed to remain saturated at any value of suction.

In order to simulate the laboratory experiments, the single-element numerical implementation of the hypoplastic model written in C++ language has been plugged into the inhouse finite element code SIFEL. The integration of the rate formulations of the hypoplastic model is performed using a set of Runge-Kutta-Fehlberg schemes (e.g., Koudelka et al., 2017). The time-dependent problem is solved in SIFEL using a Newton-Raphson algorithm. The finite element code allows for both partly-coupled and fully-coupled solving of the hydraulic and mechanical components of the model. This feature has been improved during the simulations, so that, while test 1a and 1b were solved with the partly-coupled approach, test 1c was solved in a fully-coupled manner. Further improvements derived from the adoption of a smoothed water retention behaviour, which is reflected in the delivered final results of all tests as opposed to the preliminary ones of test 1a, obtained with the bilinear formulation. Improved approaches for the calculation of the stiffness matrix and for accelerating the convergence during the iterative calculation were also produced during the simulations.

2.9 VTT/UCLM

The general framework for the coupled thermo-hydraulic-mechanical-chemical (THMc) model developed by VTT in close cooperation with UCLM has been described in the BEACON Deliverable D3.1 Annex G (Gharbieh & Pulkkanen, 2018). The use of COMSOL Multiphysics software and the adopted model development and implementation strategy allow for flexible simulations also with subsets of the phenomena and processes considered in the THMc model framework. In WP5 Test 1b simulations, a hydro-mechanical (HM) coupled double porosity model (DPM) has been applied. The pore space has been divided into a microstructural porosity, representing the intra-aggregate space, and a macrostructural porosity, comprising both the inter-aggregate pore space inside the bentonite pellets/crushed material and the inter-pellet space. The conservation of mass is achieved by solving the mass balance equation for macrostructural water in liquid and gaseous state. Mechanical equilibrium is achieved by solving the momentum balance equation. The set of state variables are the liquid pressure, the gas pressure, and the displacement field. Resulting from the applied mixed method for solving the mechanical boundary value problem (Navarro et al., 2014), the net/effective stress is another state variable.

The swelling behaviour of the bentonite is modelled by taking into account the water mass exchange between the macrostructure and the microstructure assuming instantaneous equilibrium between the macrostructural and microstructural water chemical potentials. For defining the microstructural water potential, a state function adapted from Navarro et al. (2015) has been used to describe the relationship between micro void ratio e_{m} and the "structural" suction of the microstructure $s_{\mathrm{m,S}}$ set by the clay structure (clay mineral and exchangeable cations), see Figure 2-11. The structural suction in the microstructure can be understood as the affinity of water for the soil particles and is based on the analysis of the change of the microstructural water content. The use of the state surface approach requires the set of differential equations being extended by an ordinary differential equation (ODE) with a new internal state variable for micro void ratio.

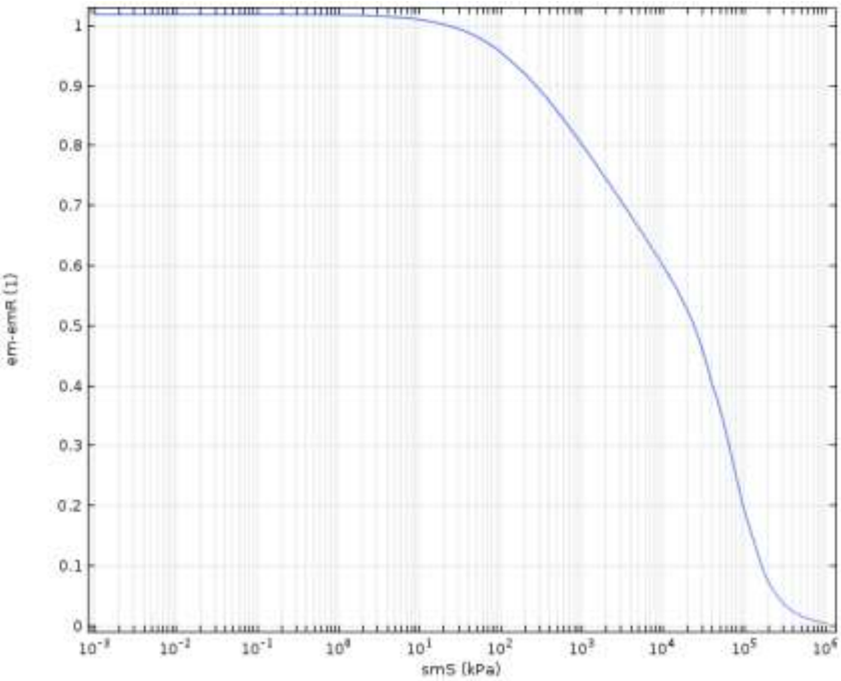

Figure 2-11 State surface defining the microstructural volumetric constitutive model. The parameter e_{mR} defines the remaining microstructural void ratio under dry conditions (adapted from Navarro et al., 2015).

The mass exchange between macrostructural and microstructural water determines directly the volumetric changes in the microstructure (assumed entirely elastic/reversible) and thus, the microstructural deformation. In addition, the mechanical model comprises macrostructural elastic deformations due to changes in mean stress and plastic deformations in accordance with the Barcelona Basic Model (BBM). The introduction of plasticity through the BBM adds the preconsolidation stress at zero suction as an additional variable to the developed modelling framework. However, the present modelling strategy deviates from the BBM insofar as elastic macrostructural deformation resulting from suction changes are disregarded. In this context, it is also noteworthy that neither suction increase/decrease yield surfaces nor coupled macro-micro strains, as formulated in the Barcelona Expansive Model (BExM), have been considered in the present simulation.

2.10 UPC

The fabric of a bentonite can be identified as a porous medium of macroparticles (clay aggregates) formed by clay platelets (Figure 2-12). From this physical fact, several constitutive models for these geomaterials have been postulated on the hypothesis of explicit consideration of two pore levels (Alonso et al. 1999; Sanchez et al. 2005; Gens et al. 2011).

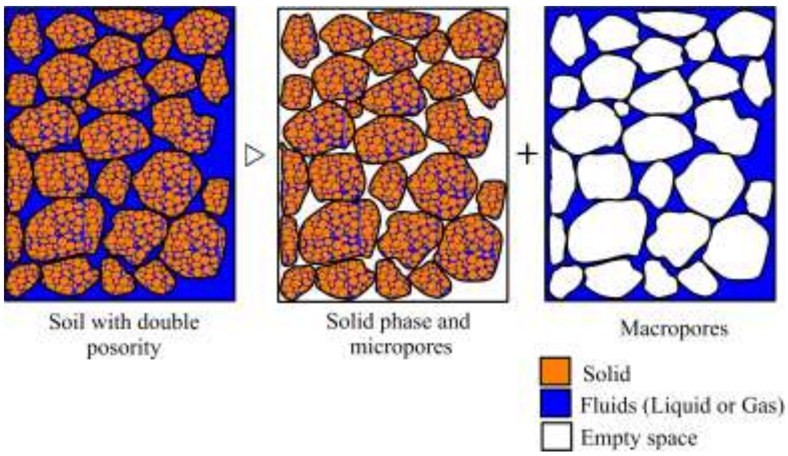

Figure 2-12 Schematic representation of the double-structure porous medium

2.10.1 Governing equations

The porous medium consist of three phases [solid (s), liquid (L) and gas (g)] and three main components [solid (s), water (w) and air (a)]. An important difference respect to the original formulation (Olivella et al. 1994) is that each structural level contains air and water in gas and liquid state. Additionally, the possibility to have unsaturated states in the micro-structural level represents a new feature with respect to the formulation of Sánchez (2004).

One of the main requirements in the coupled HM formulation is the reference of the quantities respect to the whole volume control, that is the *volume fraction concept*. Based on the structural levels of expansive clays, it is possible to define the *micro pore volume fraction* (Eq. 1), *macro pore volume fraction* (Eq. 2) and *solid volume fraction* (Eq. 3).

$$\bar{\phi}_{micro} = \frac{(V_{Pores})_{micro}}{V} \qquad \text{(Eq. 1)}$$

$$\bar{\phi}_{Macro} = \frac{(V_{Pores})_{Macro}}{V} \qquad \text{(Eq. 2)}$$

$$\bar{\phi}_{Solid} = \frac{(V_{Solid})_{micro}}{V} \qquad \text{(Eq. 3)}$$

The following governing equations present a considerable extension, therefore it is convenient a compact variable names. From now, we refer the micro-structural level with the subscript *1*, the macro-structural level with the subscript 2 and the double-structural porous media without subscript. A detailed description of the variable notation (Table 2-1) is necessary for the right understanding of the mathematical expression of the governing equations and the hydro-mechanical (HM) formulation.

Table 2-1 Variable summary

$(\cdot)_\alpha$	Subscript used to identify the structural level (1=micro, 2= macro) and/or phases (s=solid, L=liquid, g=gas)	ω, ω_α^i	Mass fraction and mass fraction of the component i in phase α
$(\cdot)^i$	Superscript used to identify the components (s=solid, w=water, a=air)	θ_α^i	Mass fraction of the component i in phase α per unit of volume of phase α
$\bar{\phi}, \phi$	Volume fraction, Porosity	S	Degree of saturation
$\rho, \tilde{\rho}$	Local and global density	j, j_α^i	Mass flux respect to the solid skeleton and mass flux respect to the solid skeleton of the component i in phase α per unit of volume of phase α

Solid mass balance equation:

$$\frac{D\bar{\phi}_2}{Dt} = \frac{\left(1-\bar{\phi}_1-\bar{\phi}_2\right)}{\rho_s}\frac{D\rho_s}{Dt} + \left(1-\bar{\phi}_1-\bar{\phi}_2\right)\frac{d\varepsilon_v^{1\to 2}}{dt} - \frac{D\bar{\phi}_1}{Dt} \qquad \text{(Eq. 4)}$$

where:

- $\varepsilon_v^{1\to 2}$ is the volumetric deformation of the macro-structural level due to change in volume of the micro-structural level.

Water mass balance equation for macrostructure:

The mass balance for water for both structural levels can be established following the approach outlined above and illustrated in Figure 2-13.

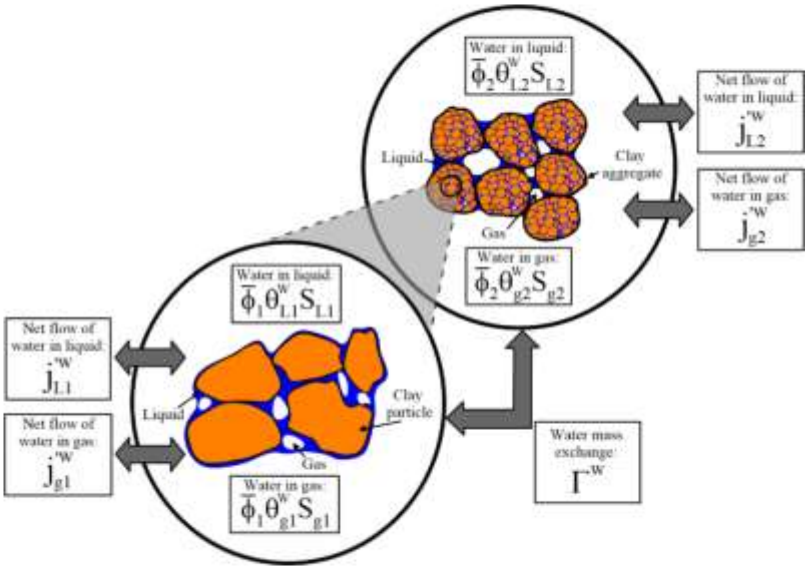

Figure 2-13 Scheme to establish the equation for the mass balance of water in a double-structure material

$$\frac{D(\theta^w_{L2}S_{L2}+\theta^w_{g2}S_{g2})}{Dt}\bar{\phi}_2+(\theta^w_{L2}S_{L2}+\theta^w_{g2}S_{g2})\left(\frac{d\bar{\varepsilon}_{v2}}{dt}\right)\nabla\cdot\left(\mathbf{j}^w_{L2}+\mathbf{j}^w_{g2}\right)=-\,\Gamma^w \quad \text{(Eq. 5)}$$

where:

- $\bar{\varepsilon}_{v2}$ is the volumetric deformation of the macro-structural level respect to the total volume of the porous medium. This term imposes a clear hydro-mechanical coupling.
- $\Gamma^w$is the term the term related to the water mass exchange between the two structural levels.

Water mass balance equation for microstructure:

$$\frac{D(\theta^w_{L1}S_{L1}+\theta^w_{g1}S_{g1})}{Dt}\bar{\phi}_1+\left(\theta^w_{L1}S_{L1}+\theta^w_{g1}S_{g1}\right)\left(\frac{d\bar{\varepsilon}_{v1}}{dt}\right)\nabla\cdot\left(\mathbf{j}^w_{L1}+\mathbf{j}^w_{g1}\right) \quad \text{(Eq. 6)}$$
$$=\Gamma^w-(\theta^w_{L1}S_{L1}+\ \theta^w_{g1}S_{g1})(1-\phi)\frac{d\rho_s}{\rho_s}$$

where:

- $\bar{\varepsilon}_{v1}$ is the volumetric deformation of the micro-structural level respect to the total volume of the porous medium.

Air mass balance equation for macrostructure:

The mass balance for air is also obtained according the procedure indicated by the Figure 2-13.

$$\frac{D\left(\theta_{L2}^{a}S_{L2}+\theta_{g2}^{a}S_{g2}\right)}{Dt}\bar{\phi}_{2}+\left(\theta_{L2}^{a}S_{L2}+\theta_{g2}^{a}S_{g2}\right)\left(\frac{d\bar{\varepsilon}_{v2}}{dt}\right)+\nabla\cdot\left(\mathbf{j}_{L2}^{a}+\mathbf{j}_{g2}^{a}\right)=-\Gamma^{a} \quad \text{(Eq. 7)}$$

Air mass balance equation for microstructure:

$$\frac{D\left(\theta_{L1}^{a}S_{L1}+\theta_{g1}^{a}S_{g1}\right)}{Dt}\bar{\phi}_{1}-\left(\theta_{L1}^{a}S_{L1}+\theta_{g1}^{a}S_{g1}\right)\left(\frac{d\bar{\varepsilon}_{v1}}{dt}\right)=\Gamma^{a}-\left(\theta_{L1}^{a}S_{L1}+\theta_{g1}^{a}S_{g1}\right)(1-\phi)\frac{d\rho_{s}}{\rho_{s}} \quad \text{(Eq. 8)}$$

Momentum balance equation:

The equation of equilibrium stresses of the double-structure porous media is given by Cauchy's expression.

$$\nabla.\boldsymbol{\sigma}+\mathbf{b}=0 \quad \text{(Eq. 9)}$$

where the body forces are given by the gravity and the global density of the medium.

The system solution requires specifying an equal number of unknown variables and equations. Thus, the state variables are as follows: solid velocity, $\dot{\mathbf{u}}$ (in three spatial direction) and the liquid and gas pressure in both structural levels, P_{L_Macro}, P_{L_micro}, P_{g_Macro} and P_{g_micro}.

Mass transfer mechanism between structural levels:

The hydraulic equilibrium between two structural levels is not assumed; that is, at each point of the domain the water potentials in the macro- and micro-structure may be different, leading to an exchange of mass water and air between them. Sánchez, (2004) and Gens *et al.*, (2011) propose a linear relationship between water exchange and suction (potential) difference.

$$\Gamma^{w}=\gamma(s_{1}-s_{2}) \quad \text{(Eq. 10)}$$

where suction is defined as

$$s=\max\left(P_{g}-P_{L},0\right) \quad \text{(Eq. 11)}$$

2.10.2 Constitutive equations

The set of balance equations has to be completed with the hydraulic and mechanical constitutive equations.

2.10.2.1. *Hydraulic constitutive equations*

The volumetric advective fluxes used in the balance equations are defined by the mass fraction of the component times the mass flow with respect to the solid phase.

$$\mathbf{j}_{\alpha}^{i} = \theta_{\alpha}^{i}\mathbf{q}_{\alpha} \qquad \text{(Eq. 12)}$$

where:

- i indicates the component (w and a) and α refers to the phase (l and g).

The generalized Darcy's law governs liquid and gas flow. This is only formulated for macro-structural level, due to the neglected advective fluxes in the micro-structural level.

$$\mathbf{q}_{\alpha 2} = -\frac{\mathbf{k}_2 k_{r_{\alpha 2}}}{\mu_{\alpha}}(\nabla P_{\alpha 2} - \rho_{\alpha 2}\,\mathbf{g}) \qquad \text{(Eq. 13)}$$

where:

- $\boldsymbol{\mu_{\alpha}}$ is the fluid viscosity, $\boldsymbol{\rho_{\alpha 2}}$ is the fluid density and $\boldsymbol{g}$ is the gravity force.

A power law defines the relative permeability, which expresses the effect of degree of saturation (or suction) on global permeability (Eq. 14). Intrinsic permeability depends on many factors such as pore size distribution, pore shape, tortuosity and porosity. Here a dependence of intrinsic permeability on porosity is adopted (Eq. 15).

$$(k_r)_{\alpha} = [(S_e)_{\alpha}]^{c} \qquad \text{(Eq. 14)}$$

$$\mathbf{k}_2 = \mathbf{k}_{o2}exp[b(\bar{\phi}_2 - (\bar{\phi}_o)_2)] \qquad \text{(Eq. 15)}$$

where:

- $\boldsymbol{c}$ is the power for relative permeability law;
- $\boldsymbol{S_e}$ is the relative saturation degree;
- $\boldsymbol{k_{o2}}$ is the initial intrinsic permeability tensor.

Finally, the retention curve relates suction (or matric potential) with degree of saturation at both structural levels. The Van Genuchten law has been used here although there are a number of alternative expressions designed to fit experimentally determined retention curves.

$$S_e = \left[1 + \left(\frac{s}{P_o}\right)^{1/(1-\lambda_o)}\right]^{-\lambda_o} \left(1 - \frac{s}{P_d}\right)^{\lambda_d} \qquad \text{(Eq. 16)}$$

where $\boldsymbol{P_o}$, $\boldsymbol{P_d}$, λ_o and λ_d are model parameters.

2.10.2.2. ***Mechanical constitutive equations***

The microstructure is the seat of the basic physical-chemical phenomena occurring at clay particle level, which is the main responsible of the expansive soils behaviour. This level plays a crucial role in the interpretation of the behaviour exhibited by expansive materials. On the other hand, deformations due to loading and collapse will have a major effect at the macrostructural level *(Mechanism LC)*. A fundamental assumption of the framework is that micro-structural behaviour is not affected by the macrostructure's state but it only responds to changes in the driving variables (i.e. stresses and suction) at local microstructural level. In contrast, plastic macro-structural strains may result from deformations of the microstructure *(Mechanism β)*. According to Eq. 17, the response of the expansive soils is accomplished by the consideration of several plastic mechanisms that can act jointly or not at different stages of the analysis.

$$\dot{\varepsilon} = \dot{\varepsilon}^e + \dot{\varepsilon}^p_\beta + \dot{\varepsilon}^p_{LC} \qquad \text{(Eq. 17)}$$

Table 2-2 Constitutive variables used for the double-structure model

	First constitutive variables FCV	**Second constitutive variables SCV**
micro-structural level	Bishop's effective stress $\boldsymbol{\sigma}'_1 = \boldsymbol{\sigma}_1 - P_{g1}\mathbf{I} + Sl_1 s_1 \mathbf{I}$	micro-suction $s_1 = \max(P_{g1} - P_{L1}, 0)$
Macro-structural level	Net stress $\boldsymbol{\sigma}''_2 = \boldsymbol{\sigma}_2 - P_{g2}\mathbf{I}$	Macro-suction $s_2 = \max(P_{g2} - P_{L1}, 0)$

The Table 2-2 shows the constitutive variables for each structural level. The fully reversible micro-structural strains obeys a non-linear elastic law. From the mean effective stress state p'_1 and suction s_1, it is possible to determine if the microstructure (clay aggregates) swell or contract. The inclusion of the macro structural level in the analysis allows the consideration of phenomena that affect the skeleton of the material (such as macro-structural collapses), which have a strong influence on the macroscopic response of expansive materials. This model is able to reproduce many of the basic patterns of behaviour observed in non-expansive soils (Alonso et al. 1990). In that sense, it is a proper way to model the macro-structural behaviour.

Elastic Behaviour

The assumption of null fabric changes at the elastic range seems physically reasonable. This means that the slips between the clay aggregates are the main factor of irreversibility at macro-structural level. This imposes geometrical restrictions that relate the elastic modulus of micro- and macro-structure.

$$\overline{K}_2 = \max\left[\frac{1+\overline{e}_2}{\overline{\kappa}_2}p_2'', (\overline{K}_2)_{min}\right] \quad \text{(Eq. 18)}$$

$$\overline{G}_2 = \frac{3(1-2\nu)}{2(1+\nu)}\overline{K}_2 \quad \text{(Eq. 19)}$$

$$K_s = \max\left[\frac{(1+\overline{e}_2)(s_2+p_{atm})}{\kappa_s}, (K_s)_{min}\right] \quad \text{(Eq. 20)}$$

$$K = K_1 = \overline{\phi}_2\overline{K}_2 \quad \text{(Eq. 21)}$$

$$G = G_1 = \overline{\phi}_2\overline{G}_2 \quad \text{(Eq. 22)}$$

Loading Collapse Mechanism (LC)

The evolution of the yield surface and its dependence of the yield surface on the stress, history variables and suction are described as in the BBm model (Alonso et al. 1990).

Mechanical interaction of the structural levels (β)

The plastic macro-structural strain induced by micro-structural effects can be evaluated by the expression:

$$d\boldsymbol{\varepsilon}_\beta = f_\beta d\overline{\boldsymbol{\varepsilon}}_1 \quad \text{(Eq. 23)}$$

Two interaction functions are defined: **mc** for microstructural contraction paths and **ms** for microstructural swelling paths. Figure 2.3 presents a generic representation of the interaction function. Several expressions have been formulated for these functions. Here, the proposal of Gens *et al.*, (2011) is adopted. The source of this structural interaction comes from the geometrical reorganization of the clay aggregates under hydro-mechanical actions.

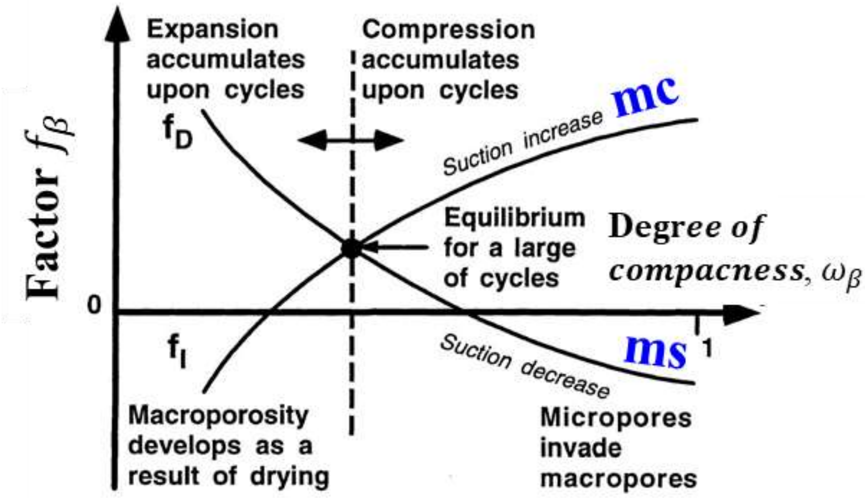

Figure 2.3. Interaction functions

Finally, the hardening of the whole double-structure medium is given by the evolution of the isotropic yield stress due to the plastic strains of the structural interaction *(mechanism β)* and macro-structure itself *(mechanism LC)*.

$$dp_o^* = \frac{(1+\bar{e}_2)p_o^*}{\lambda_{sat}-\kappa_2} d\varepsilon_v^p = \frac{(1+\bar{e}_2)p_o^*}{\lambda_{sat}-\kappa_2} (d\boldsymbol{\varepsilon}_{LC}^p + d\boldsymbol{\varepsilon}_\beta) \quad \text{(Eq. 24)}$$

3 Test 1a – Bentonite block with void

Under Test 1a denomination, two cases have been proposed. In the first case, after a classical swelling pressure test at constant volume on cylindrical bentonite block, a void is introduced on the top of the bentonite. In the second one, an initial gap is introduced on the top of the bentonite and then the constant volume swelling test started. The tests were performed by Clay Technology. Detailed can be found in SKB Report TR-14-25.
The objective of this test is to reproduce a situation that will happen in the repository when bentonite will be put in place. Residual voids at the interfaces will lead to initial heterogeneity in dry density distribution. Following the evolution of these gaps during hydration and predicting the final state of the bentonite component is the challenge proposed to the modellers.
For this first tests, 11 partners participated considering several approaches and numerical models (Table 3-1). Details on the models can be found in the deliverable D3.1 (Description of the constitutive models available at the start of the project) produced in WP3.

Table 3-1 List of partners who performed test 1a and models used

Team	Model/code	Results test1a01	Results test1a02
ICL	ICFEP	yes	yes
BGR	OpenGeoSys 5	yes	no
Claytech	Comsol/HBM	yes	yes
EPFL	Lagamine/ACMEG	yes	yes
LEI	Comsol	yes	no
Quintessa	QPAC/ILM	yes	yes
SKB	DACSAR	no	yes
ULG	Lagamine	yes	yes
CU-CTU	Sifel	yes	yes
VTT/UCLM	Comsol	no	yes
UPC	Code_Bright	Yes	yes

We have to notice that even if Comsol is used several times, the models implemented is this toolbox are quite different.

3.1 Test 1a01 – brief description of test

After mounting the specimen in the devices shown in Figure 3-1, de-ionized water is applied to the filters. The specimens have free access to water during the water saturation. When only small changes in swelling pressure with time are noticed, the water is evacuated from the filters. The upper piston is moved upwards and fixed with spacers admitting a certain volume for free swelling. After evacuation of air, the empty space and the upper filter are filled with water.

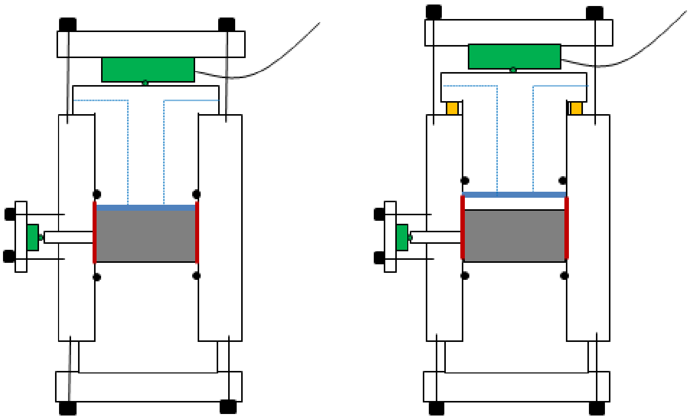

Figure 3-1 ***Test 1a01- Set-up used for the axial swelling tests. The radial pressure transducer is placed 10 mm from the bottom end of the specimen***

During saturation and homogenization water was provided as stagnant water from above only, with a water pressure of approximately 2 kPa
After finished swelling and homogenization, i.e. when no or negligibly small changes are noticed in the swelling pressure with time, the specimen is dismantled and cut in slices for determination of the water content and density distribution in the direction of swelling. Axial and radial swelling pressure are measured as could be seen on Figure 3-2.

Figure 3-2 ***Time evolution of radial and axial swelling pressure***

3.2 Test1a02 – brief description of test

The initial degree of saturation of bentonite block is very high (close to 100%) and for that reason the swelling started directly, i.e. no saturation took place in the test devices before the swelling phase. After preparation the specimen is mounted into the device with an initial gap representing 25% of the bentonite volume. Then de-ionized water is applied to the filters.

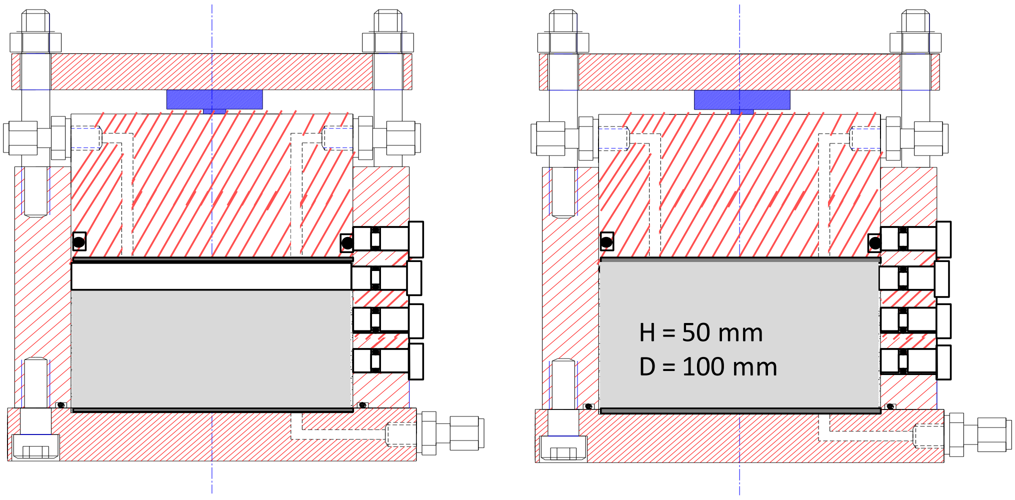

Figure 3-3 ***Set-up used for the axial swelling tests. Water is only supplied from a filter placed above the specimen***

After completed swelling and homogenization, i.e. when no or negligibly small changes were noticed in the measured swelling pressure, the specimens are dismantled and cut in slices for determination of water content and density distribution in the direction of swelling. Water was provided as stagnant water from above only, with a water pressure of approximately 2 kPa.

Axial and radial swelling pressure are measured as could be seen on Figure 3-4.

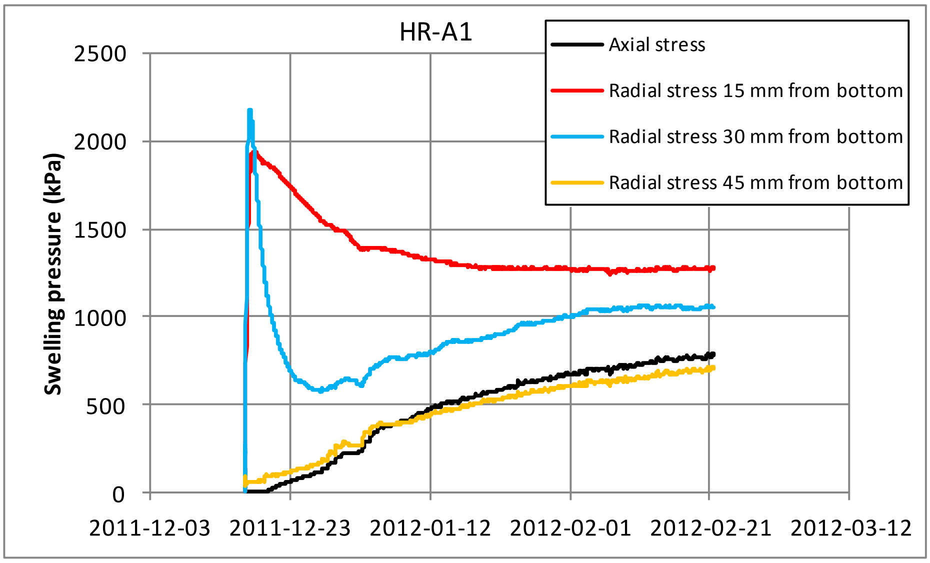

Figure 3-4 ***Time evolution of radial and axial swelling pressure***

3.3 ICL

3.3.1 Geometry and discretization

Test 1a01

The 1a01 involves a block sample of compacted MX80 bentonite, with diameter *D* = 50 mm and height *h* = 20 mm. Due to geometric symmetry around the vertical axis of the sample, half of the domain is discretised in a finite element mesh, using 8-noded quadrilateral displacement-based elements, with a pore water pressure degree of freedom at 4 corner nodes. Analysis is performed under axi-symmetric conditions. The finite element mesh is depicted in Figure 3-5.

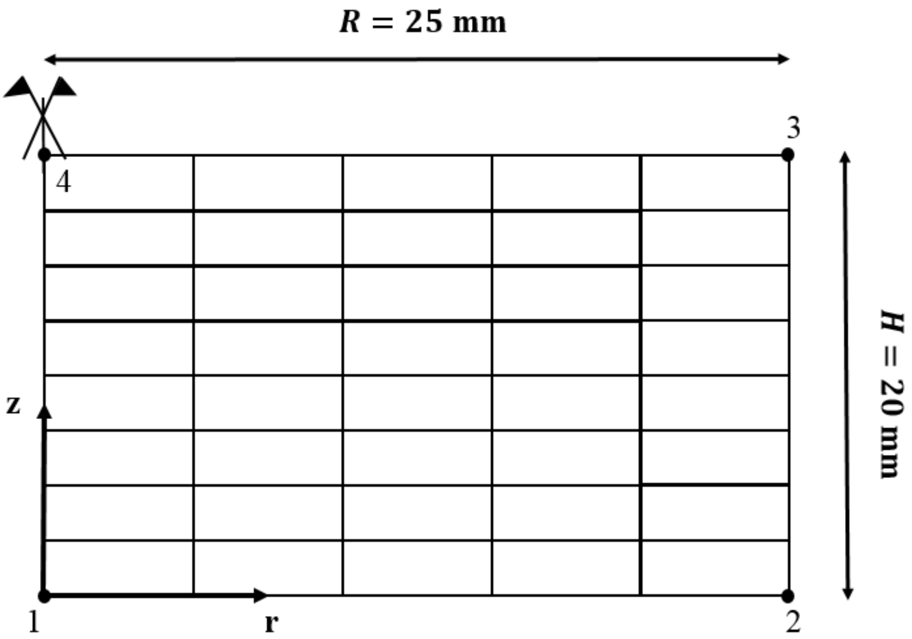

Figure 3-5 ***FE mesh employed for test 1a01.***

Test 1a02

The 1a02 Test sample is also a compacted bentonite block, with a diameter of *D* = 100 mm and a height of *h* = 40 mm. As in the Test 1a01, the geometric symmetry around the vertical axis of the sample allows half of the domain to be discretised in a finite element mesh. This is done using 8-noded quadrilateral displacement-based elements, with a pore water pressure degree of freedom at 4 corner nodes. Analysis is performed under axi-symmetric conditions. The finite element mesh is depicted in Figure 3-6.

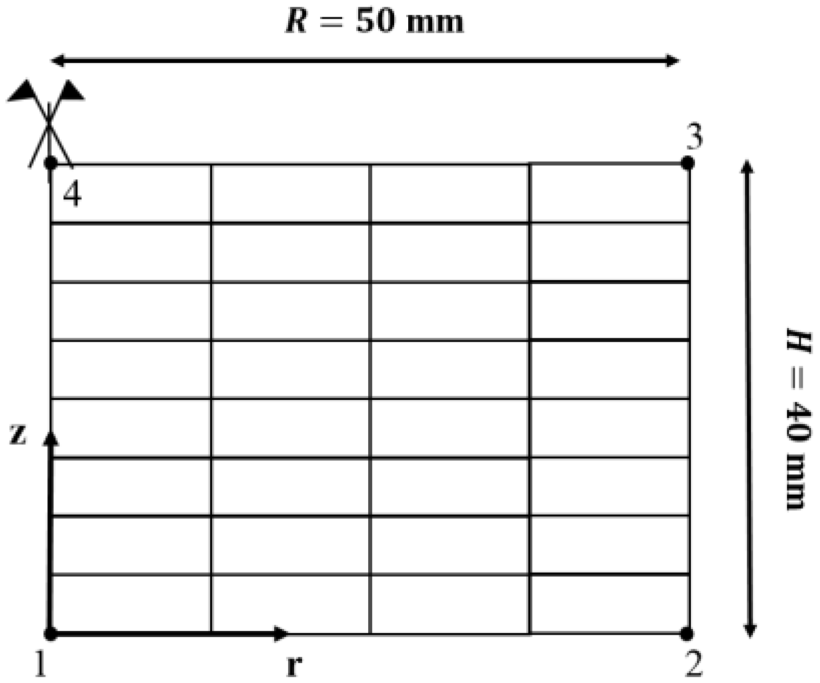

Figure 3-6 *Finite element mesh employed in the analysis of the 1a02 test.*

3.3.2 Input parameters

Table 3-2 summarises the input parameters and their values for the IC DSM constitutive model, derived for the MX 80 bentonite which was used in TEST 1a experiments. The table also gives an indication of the sources from which the model parameters need to be derived. The laboratory experiments on MX 80 bentonite, used for the derivation of IC DSM parameters, are oedometer tests of Villar (2005), isotropic compression tests of Tang et al. (2008) and triaxial tests reported in Dueck et al. (2010). The Poisson's ratio was taken from information found in Borgesson & Hernelind (2014), while the air-entry value of suction was estimated from the water retention curve reported in Marcial et al. (2008).

The soil water retention (SWR) parameters are summarised in Table 3-3.

The saturated permeability, k_{sat}, of MX 80 bentonite is taken as 3.0x10^{-13} m/s. The remaining parameters for the permeability model are summarised in Table 3-4.

Table 3-2 Summary of input parameters for IC DSM model

Parameter	Source	Value
Parameters controlling the shape of the yield surface, $\boldsymbol{\alpha_F}, \boldsymbol{\mu_F}$	Triaxail compression; relationship between dilatancy and J/p ratio	0.4, 0.9
Parameters controlling the shape of the plastic potential surface, $\boldsymbol{\alpha_G}, \boldsymbol{\mu_G}$	Triaxial compression	0.4, 0.9
Generalized stress ratio at critical state, $\boldsymbol{M_J}$	Triaxial compression, related to the angle of shear resistance ϕ'_{cs}	0.5
Characteristic pressure, $\boldsymbol{p_c}$ (kPa)	Limiting confining stress at which $p_0 = p_0^* = p_c$	1000.0
Fully saturated compressibility coefficient, $\boldsymbol{\lambda(0)}$	Fully saturated isotropic loading	0.25
Elastic compressibility coefficient, $\boldsymbol{\kappa}$	Fully saturated isotropic unloading	0.08
Maximum soil stiffness parameter, $\boldsymbol{r}$	Isotropic compression tests at constant value of suction	0.61
Soil stiffness increase parameter, $\boldsymbol{\beta}$ (1/kPa)	Isotropic compression tests at constant value of suction	0.00007
Elastic compressibility coefficient for changes in suction, $\boldsymbol{\kappa_s}$ (kPa)	Drying test and constant confining stress	0.091
Poisson ratio, $\boldsymbol{\nu}$	Triaxial compression test	0.4
Plastic compressibility coefficient for changes in suction, $\boldsymbol{\lambda_s}$	Drying test and constant confining stress	0.2
Air-entry value of suction, $\boldsymbol{s_{air}}$ (kPa)	From the retention curve	1000.0
Yield value of equivalent suction, $\boldsymbol{s_0}$ (kPa)	Usually a high value if it is not to be mobilised	10^6
Microstructural compressibility parameter, $\boldsymbol{\kappa_m}$	No direct test	0.1
Void factor, $\boldsymbol{VF}$	No direct test – potentially from MIP interpretation	0.4
Coefficients for the micro swelling function, $\boldsymbol{c_{s1}}, \boldsymbol{c_{s2}}, \boldsymbol{c_{s3}}$	No direct test – potentially from MIP interpretation	-0.1, 1.1, 5.0
Coefficients for the micro compression function, $\boldsymbol{c_{c1}}, \boldsymbol{c_{c2}}, \boldsymbol{c_{c3}}$	No direct test – potentially from MIP interpretation	-0.1, 1.1, 5.0

I

Table 3-3 Table 3-2: Summary of input parameters for SWR mode

Parameter	Value
Fitting parameter, $\boldsymbol{\alpha}$	0.000028
Fitting parameter, $\boldsymbol{m}$	1.0
Fitting parameter, $\boldsymbol{n}$	1.3
Suction at which $\boldsymbol{\Omega} = \mathbf{0.0}$ (kPa)	4×10^5

Residual degree of saturation, S_{r0}	0.15
Suction in the long term, s_0 (kPa)	4x10^5

Table 3-4 Table 3-3: Summary of input parameters for permeability model

Parameter	Value
Saturated value of permeability, k_{sat} (m/sec)	3.0x10^{-13}
Minimum value of permeability, k_{min} (m/sec)	2.0x10^{-14}
Suction s_1 (kPa)	1000.0
Suction s_2 (kPa)	20000.0

3.3.3 Initial and boundary conditions

Test 1a01

The initial dry density is 1655 kg/m^3, while the initial total axial stress is 510 kPa and the initial total radial stress is 1029 kPa. Initial suction in the sample is 48 MPa.

The simulation of Test 1a01 test is divided into four phases, each characterised by the following boundary conditions:

- *phase 1 (1st confined hydration)*, horizontal displacements are set to zero along the vertical boundaries of the mesh (i.e. 2-3 and 4-1 with reference to Figure 3-5), while vertical displacements are set to zero at the horizontal boundaries (i.e. 1-2 and 3-4), thus the volume remains constant. A gradual (reducing) change in suction is imposed on the top boundary (i.e. 3-4) until the equivalent suction reaches zero throughout the whole sample. There is no flow of water across the remaining sample boundaries in all phases of the experiment.

- *phase 2 (release)*, horizontal displacements are set to zero on the vertical boundaries (i.e. 2-3 and 4-1) and vertical displacements are set to zero on the bottom boundary (i.e. 1-2). There is now no flow of water across the top boundary of the mesh, as the simulated sample is not in contact with water at this stage. The top boundary is allowed to swell freely, with the vertical reactions at nodes on this boundary, created from the restriction of movements in phase 1, gradually reduced to zero.

- *phase 3 (free swell)*, suction is assumed to remain at zero on the top boundary, while horizontal displacements remain set to zero on the vertical boundaries and vertical displacements remain set to zero on the bottom boundary. These boundary conditions apply until the desired heave of the top boundary, which is 2.9mm, has been reached. The vertical displacement on the top boundary are tied together, in order to achieve uniform swelling of 2.9mm across the top surface.

- *phase 4 (2nd confined hydration)*, same displacement boundary conditions as in phase 1 apply for the remainder of the test, while suction is assumed to remain at zero on the top boundary.

Test 1a02

The definition of the initial conditions of this test is somewhat ambiguous, as it implies that the sample is nearly saturated and therefore has no initial saturation stage. If the simulation starts from saturated conditions, with zero suction, the IC DSM model no longer has a double structure mechanism to promote heave, as the model formulation implies that the material only has a single porosity and the subsequent swelling is very small. To alleviate this, the initial stresses in the sample are set up with a small suction of 5 MPa and zero axial and radial total stress, giving the initial degree of saturation of 95%. The initial dry density of the sample is 1655 kg/m^3.

The Test 1a02 simulation is divided into two phases, each characterised by the following boundary conditions:

- *phase 1 (free swell)*, horizontal displacements are set to zero along the vertical boundaries of the mesh (i.e. 2-3 and 4-1 with reference to Figure 3-6), while vertical displacements are set to zero at the base (i.e. 1-2 in Figure 3-6). A gradual (reducing) change in suction is imposed on the top boundary (i.e. 3-4). The sample is allowed to expand axially until a 25% strain is reached, which corresponds to a 10mm heave of the top boundary. During the expansion, the vertical displacement on the top boundary are tied together. The duration of this phase is 900 hours;

- *phase 2 (confined hydration)*, the vertical displacements at the top boundary are imposed to be zero, hence the volume is kept constant. Free access to water is maintained at the top boundary. These boundary conditions are applied for the remainder of the test. The duration of this phase is 710 hours.

3.3.4 Results/discussion

Test 1a01

Figure 3-7 compares measured and predicted evolution and magnitudes of the total axial and radial swelling stresses in Test 1a01. The peak stresses measured upon the first confined saturation are approximately 8.5 MPa for axial and 10 MPa for radial stress. The model computes a peak stress level around 9MPa both in the radial and axial direction, as it predicts an isotropic behaviour. During the first confined hydration the experimental growth rate of the radial stress is surprisingly high, in that a measured value of over 8 MPa is reached almost instantaneously. Even the axial stress seems to develop more rapidly than what numerically predicted over the first 5 MPa. After swelling, the stresses in the second confined hydration are underpredicted as it is not clear what drives the growth of the stresses given that the sample is entirely saturated at that time (as it is shown in Figure 3-8).

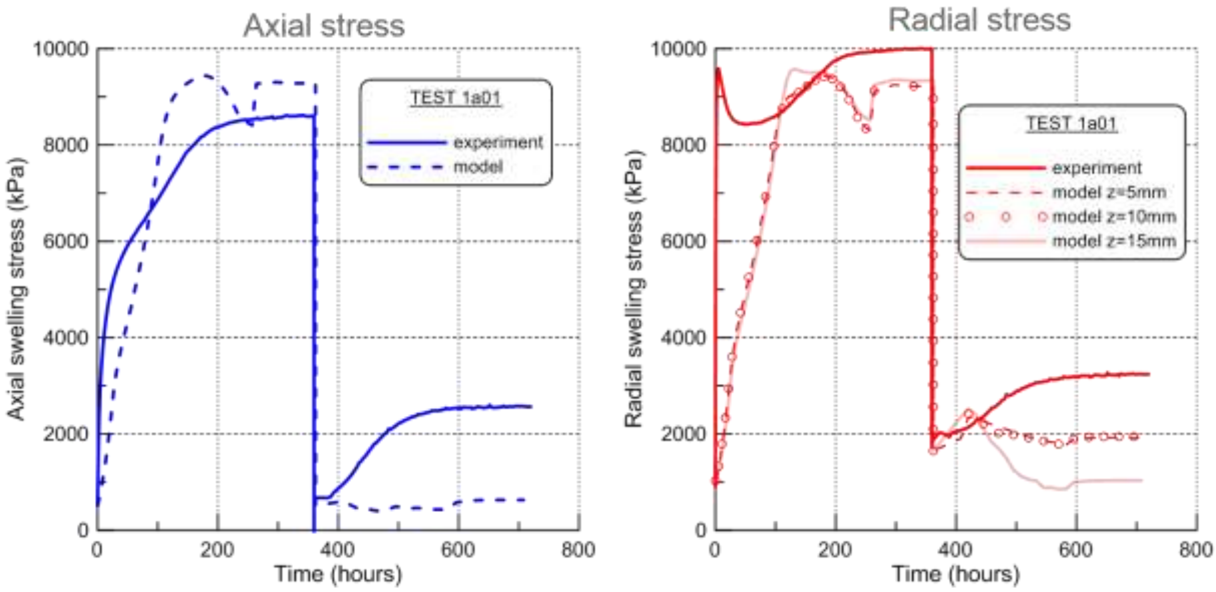

Figure 3-7 Comparison of measured and ICFEP predicted swelling pressures in TEST 1a01

Figure 3-8 presents the evolution with time of suction, degree of saturation, void ratio and water content in the middle of the sample (R=25mm) at two different heights (z=5mm, i.e. close to the bottom of the sample, and z=20mm, i.e. at the top of the sample). It should be noted that during the release phase the sample desaturates and that this allows the subsequent swelling to take place.

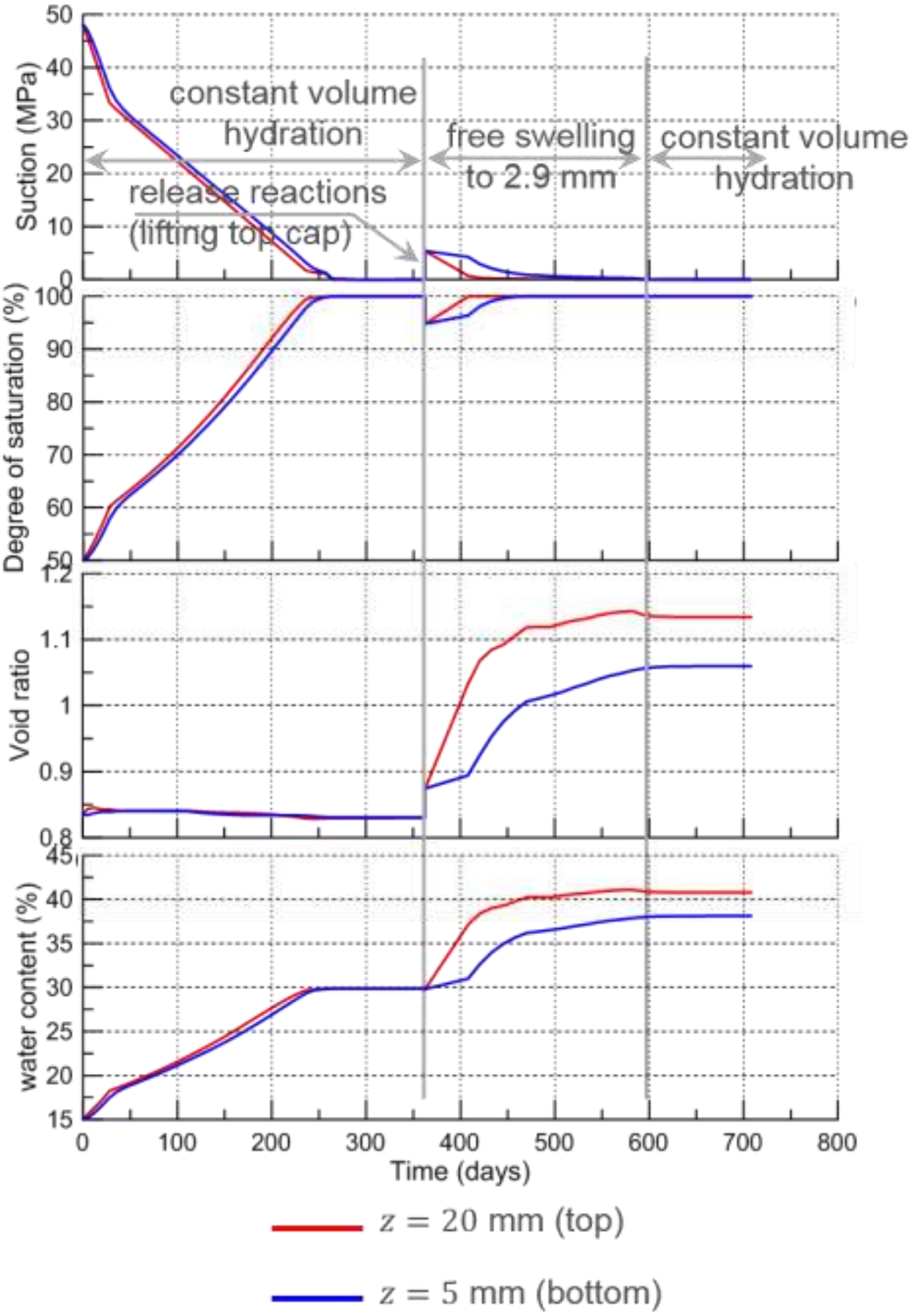

Figure 3-8 Evolution with time of suction, degree of saturation, void ratio and water content in the middle of the sample (R=25mm) at two different heights in Test 1a01

Figure 3-9 shows the predicted distributions of the void ratio and the water content along the vertical section of the sample located at R=25mm at different times during the test. The final distributions are compared to the post-mortem measurements. Overall, the latter are overpredicted in the analysis except in the top part of the sample, where they are reasonably well reproduced.

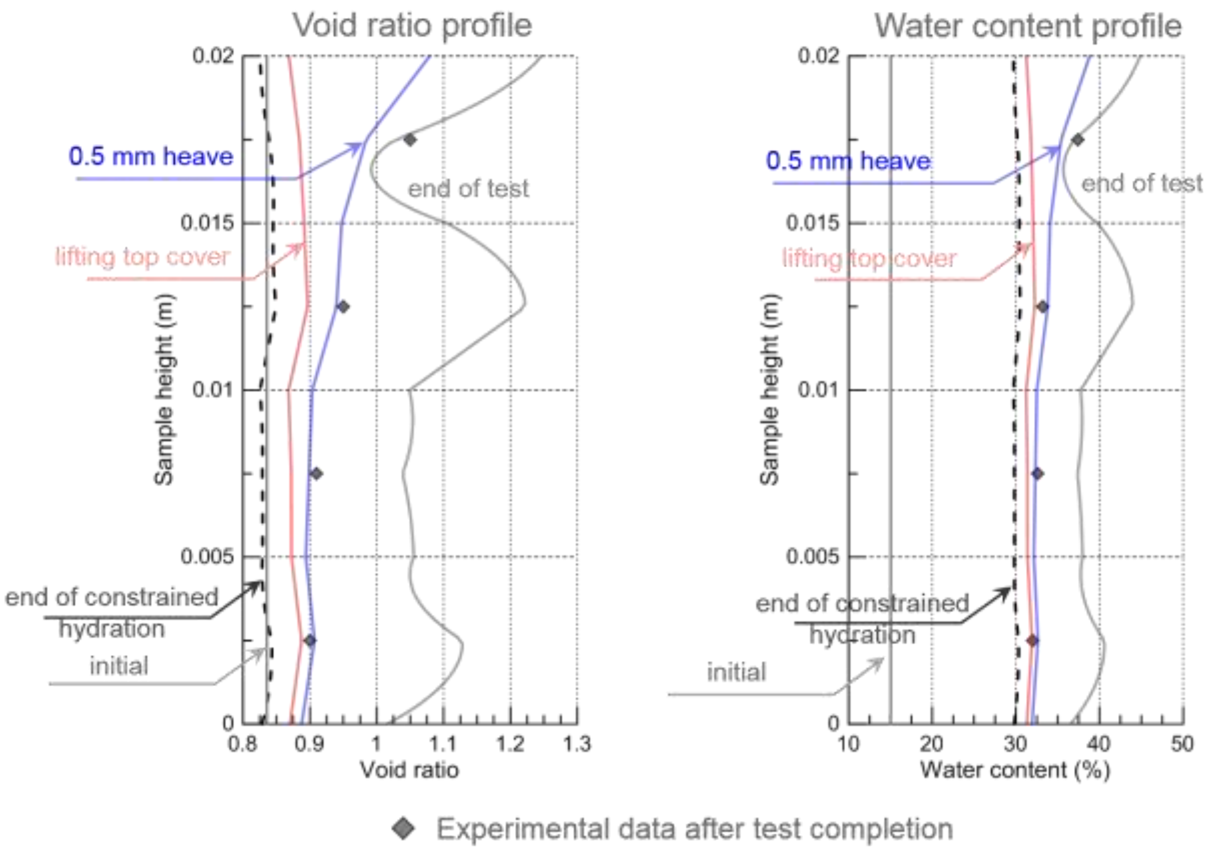

Figure 3-9 ***Final distribution of void ratio, on the left, and water content, on the right, along a vertical section of the sample used in Test 1a01***

Test 1a02

Figure 3-10 and Figure 3-11 show a comparison between measured and predicted evolution and magnitudes of the total axial and radial swelling stress, respectively. The axial stress is measured on the top boundary of the sample, while the radial stress is measured at three points located at $r = 50$mm, and $z = 15$, 30 and 40mm from the sample base. From Figure 3-10 it can be noted that the numerically computed axial stress starts developing after over 900 hours. During this period the 10mm heave of the top boundary of the specimen is reached. Nevertheless, the measurements indicate that the axial stress starts building up after only 50 hours and the swelling of the material is much faster than what the numerical analysis predicts. The magnitudes of the axial swelling pressure are also vastly different. This significant difference is difficult to interpret given that no direct information on the duration of the free swell of the sample is available. The evolution of suction in time is also not documented. On the other hand, the radial stress measurements, pictured in Figure 3-11, present a better agreement between predictions and measurements, though the model still under-estimates the measurements during the swelling phase. Overall, despite the uncertainty regarding the duration of the free-swelling phase, the general trend of the test is well-captured by the numerical model.

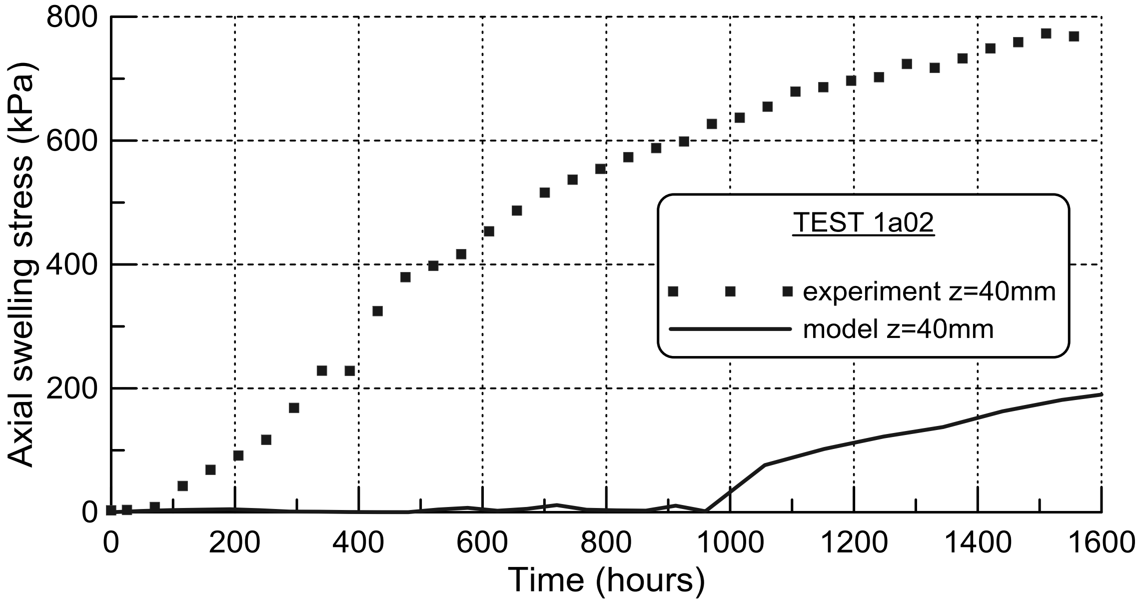

Figure 3-10 Comparison of measured and ICFEP predicted axial stress in TEST 1a02

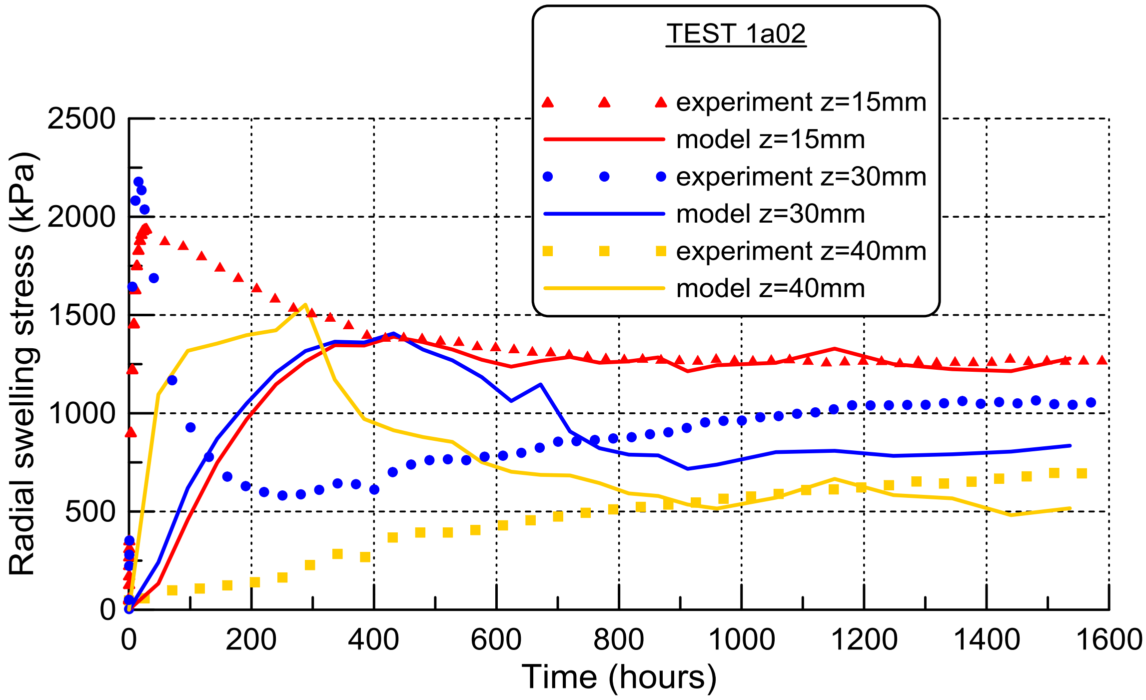

Figure 3-11 Comparison of measured and ICFEP predicted radial stress in TEST 1a02

Figure 3-12 presents the evolution with time of suction, degree of saturation, void ratio and water content at the right hand-side boundary of the sample (R=50mm) at two different heights (z=5mm, i.e. close to the bottom of the sample, and z=40mm, i.e. at the top of the sample). It can be noted that the void ratio and the water content in the top part of the sample begin to decrease as soon as the volume has been imposed as constant, which is reasonable from a physical standpoint.

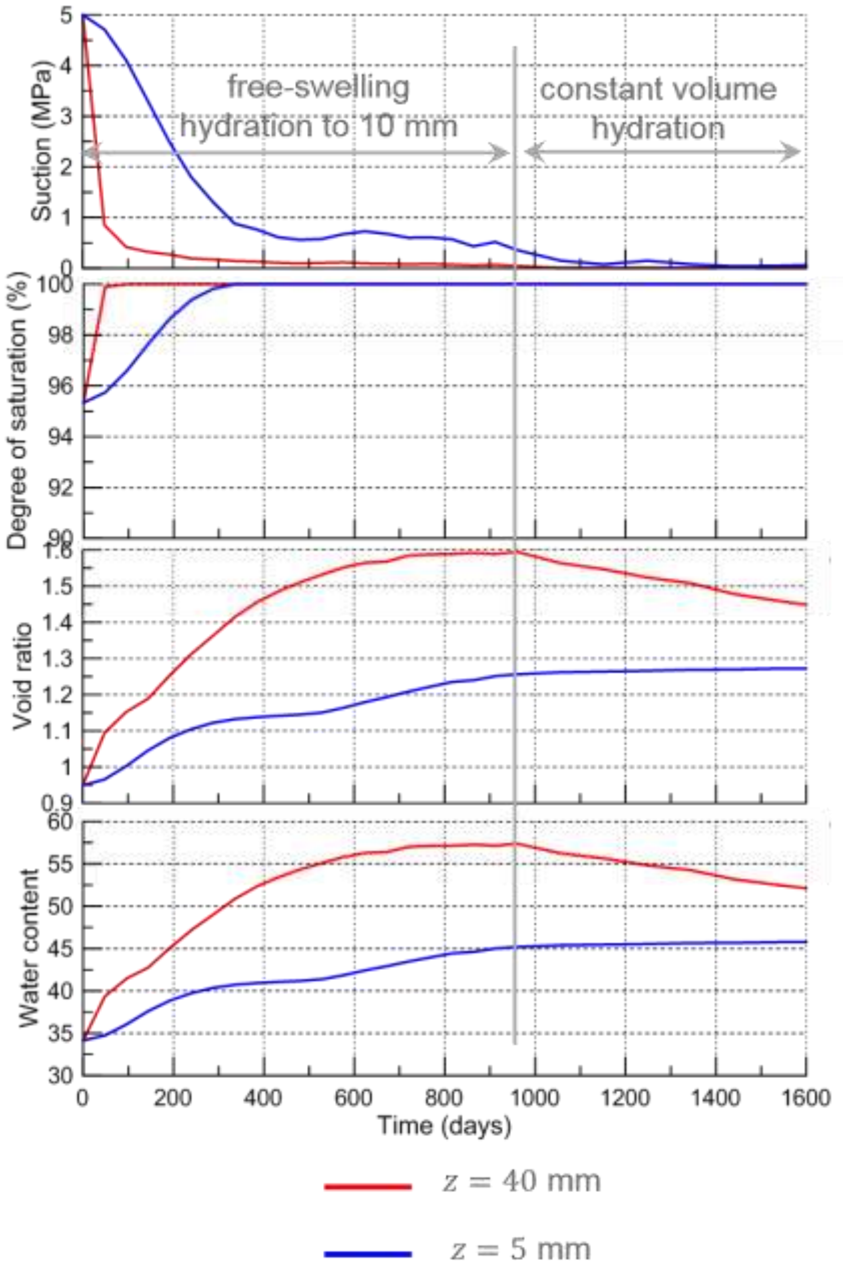

Figure 3-12 Evolution with time of suction, degree of saturation, void ratio and water content at the right hand-side boundary of the sample (R=50mm) at two different heights in Test 1a02

Figure 3-13 shows the numerically predicted distributions of void ratio and water content along the vertical section coincident with the right hand-side boundary of the mesh (R=50mm) at different times during the test. The final distributions predicted at the end of the simulation are compared to the post-mortem measurements and the obtained match is good for both void ratio and water content. Table 3-6

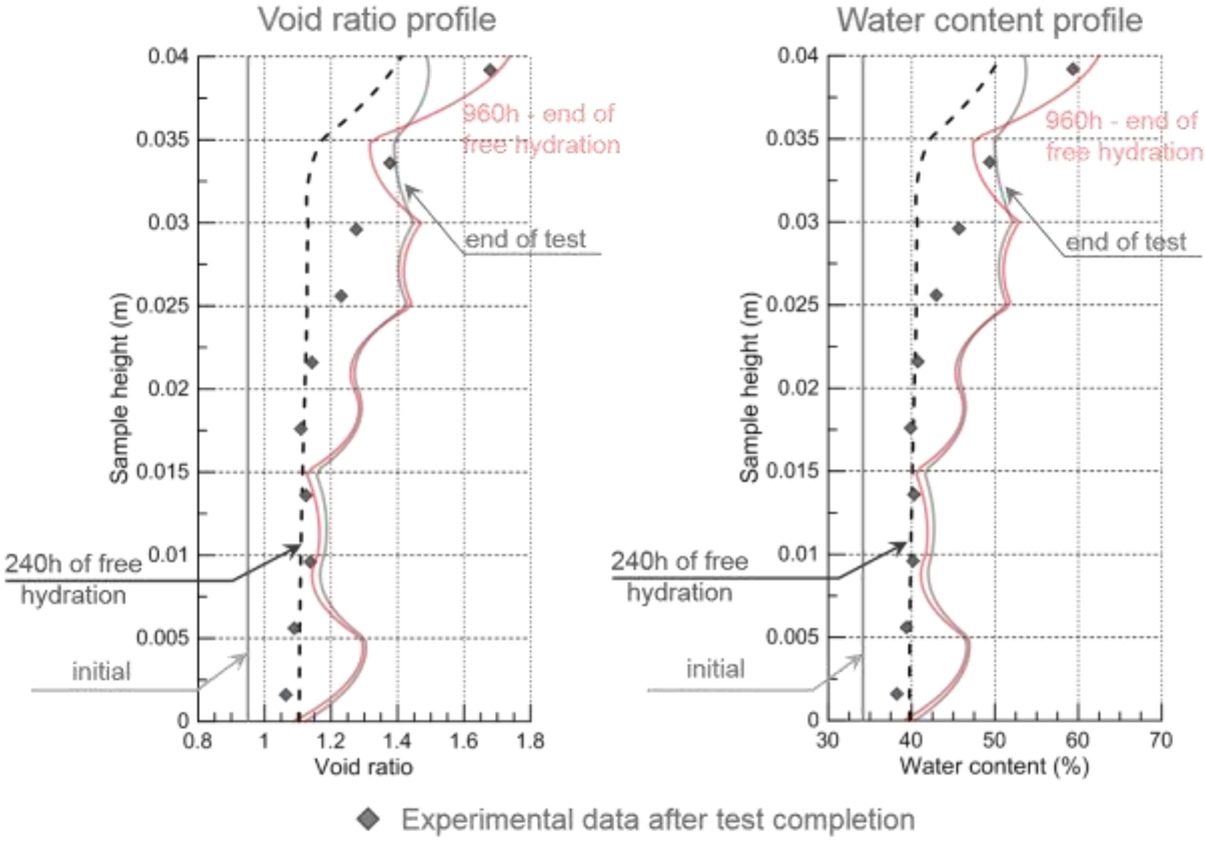

Figure 3-13 Distributions of void ratio, on the left, and water content, on the right, along a vertical section of the sample used in Test 1a02

3.4 BGR

3.4.1 Geometry and discretization

The model was setup as an axisymmetric 2D domain discretized with an unstructured FEM grid using the pre- and post-processing tool GINA (Kunz 2012). In the experiment there were two stress sensors in total, one each for the axial and radial stresses. Points were setup in the simulation domain such that the measured stresses can be compared to the simulated stresses. In order to depict the increase in volume after phase one, in the test case 1a01 the boundary condition at the top of the domain was changed from a no-deformation boundary to a constant deformation boundary at a pre-determined time taken from the experimental data. The model uses an isothermal linearly poro-elastic model under the assumption of small deformations. The hydraulic process was modelled with linear shape functions, whereas the mechanical process was modelled with quadratic shape functions. The hydraulic and the mechanical processes were sequentially (weakly) coupled in the first model run and updated with bi-directional coupling for the second model run. The discretized model domain with 1822 elements is shown in Figure 3-14.

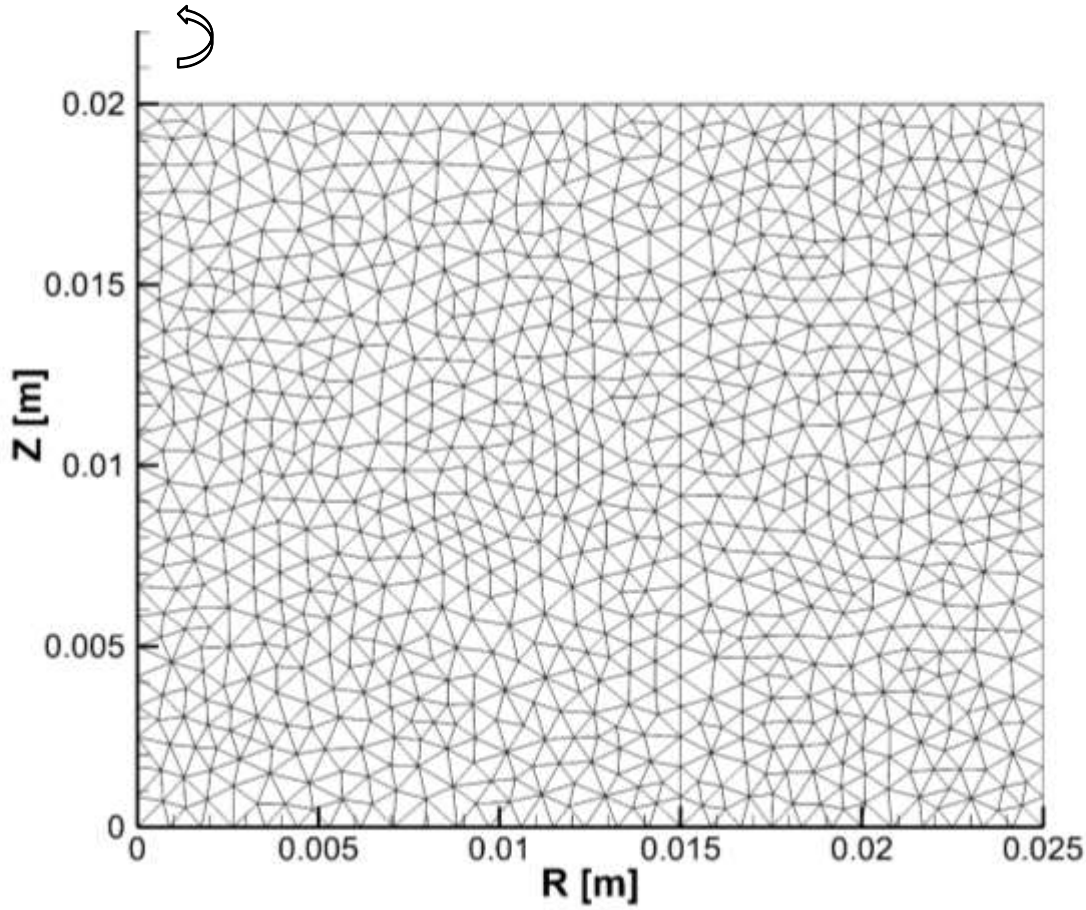

Figure 3-14 Discretized axisymmetric model domain used in the simulation for test case 1a01. The axis of symmetry is along the boundary R = 0 m. The line R = 0.015 m was to generate line-plots of parameters.

3.4.2 Input parameters

The parameters used for the Van Genuchten function in test case 1a01 is summarized in Table 3-5.

Table 3-5 Parameter values chosen for the capillary pressure – saturation curve and relative permeability for test case 1a01.

Parameter	Value	Unit	Reference
Relative permeability (k_{rel})	Cubic law of water saturation $(S^w)^3$	[-]	Åkesson et al. 2010
Gas entry pressure	43.5	MPa	Åkesson et al. 2010
Van Genuchten shape factor (m)	0.375	[-]	Åkesson et al. 2010
Residual saturation (S^w_{res})	0.0	[-]	
Maximum saturation $(S^w_{\max})$	1.0	[-]	

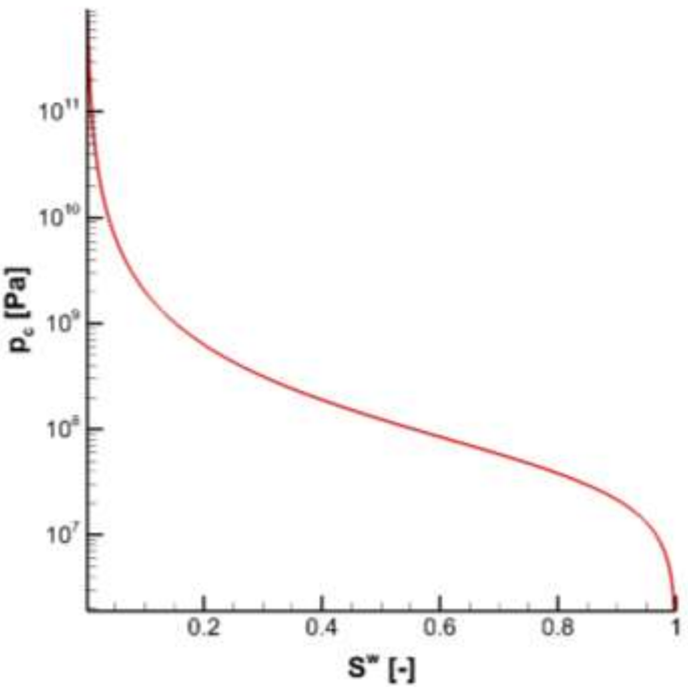

Figure 3-15 The capillary pressure – saturation curve used for test case 1a01.

The relative permeability – saturation curve follows a cubic power rule (cf. Figure 3-16) as investigated by Åkesson et al. (2010). This has been used in the simulation of both the test cases (1a01 and 1b).

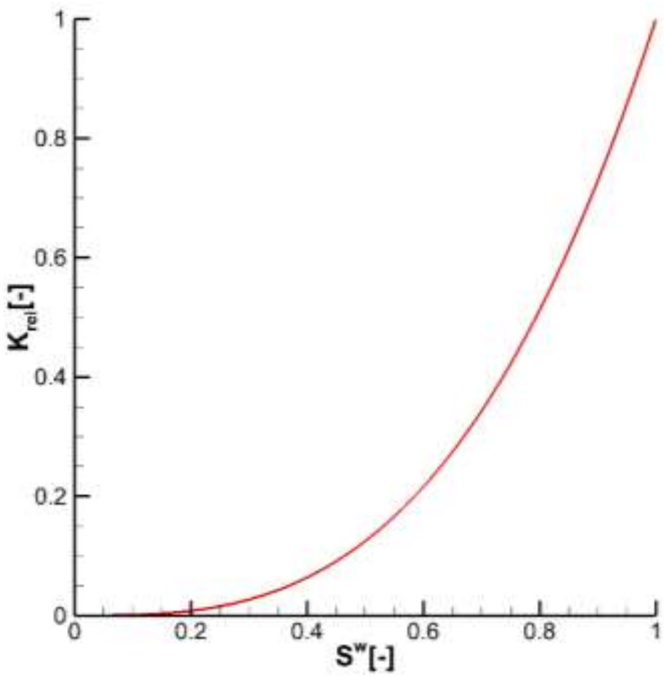

Figure 3-16 The power-law form of the relative permeability saturation curve used for both test cases.

3.4.3 Initial and boundary conditions

The initial porosity was calculated from the void ratio of 0.626 (Åkesson et al. 2010), corresponding to a porosity of 38.5%. The saturation was calculated as 0.325 from the given water content of 13% and the porosity. A pre-defined suction pressure of 275 MPa was assigned as the initial condition, which is equivalent to an initial saturation of 0.325. The swelling pressure corresponding to a dry density of 1655 kg/m^3 was taken from Dueck et al. (2014), as shown in Figure 3-17. The solid and fluid densities were specified in the BEACON Deliverable 5.1.1. The Poisson's ratio was taken from Åkesson et al. (2010) and the Young's modulus was varied in a range of 120 MPa – 200 MPa. The best fit for the measured evolution of stresses (which was distributed among the modelling groups by the task leader) was achieved at E = 150 MPa. The chosen parameters are summarized in Table 3-6.

Table 3-6: Summary of parameter values used in 1a01

Parameter	Value	Unit
Permeability $(\mathbf{K})$	2e-21	m^2
Void ratio (e)	0.626	[-]
Porosity (ϕ)	0.385	[-]

Initial saturation $\left(S_{\text{init}}^{w}\right)$	0.325	[-]
Fluid density $\left(\rho^{w}\right)$	1000	kg/m^3
Grain density $\left(\rho^{s}\right)$	2780	kg/m^3
Biot coefficient (α_{Biot})	0.6	[-]
Young's modulus (E)	150	MPa
Poisson's ratio (υ)	0.2	[-]
Max swelling pressure $\left(\sigma_{\text{max,sw}}\right)$	13	MPa

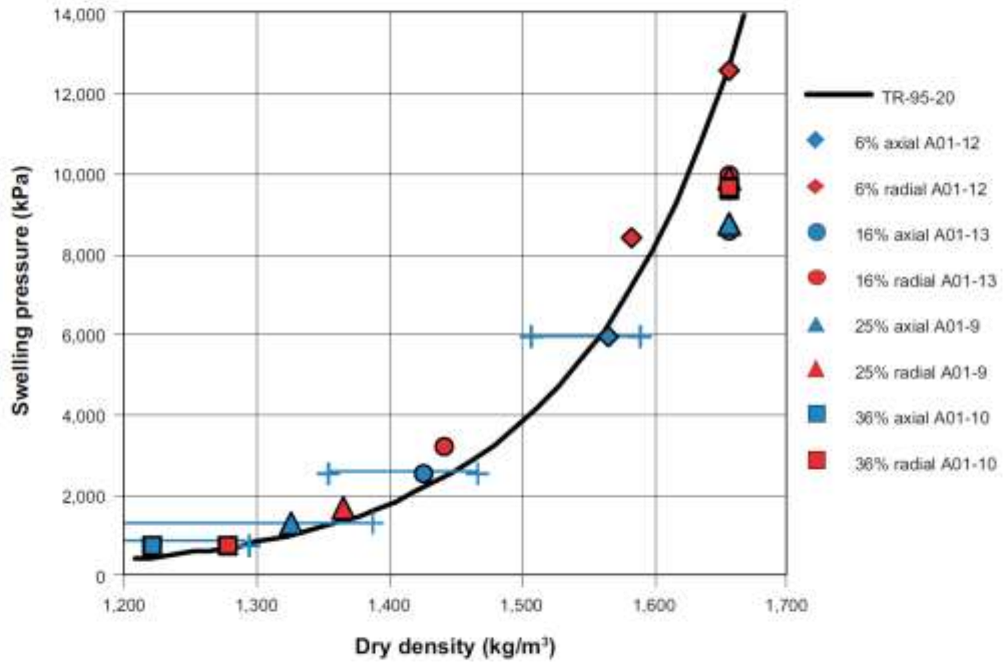

***Figure 3-17** The swelling pressure as a function of dry density. The measured swelling pressure for 1a01 is labelled A01-13 on the graph, taken from Dueck et al. (2014).*

The generalised model domain is shown schematically in Figure 3-18 to illustrate the boundary conditions. For the hydraulic boundary conditions, the model was setup with no flow boundaries on three sides and a constant fluid pressure boundary at the top of the domain equal to 2 kPa. For the mechanical boundary conditions, initially for the homogenization period (t < 360 h), deformation was allowed neither in the radial (R) nor in the axial (Z) direction. Friction at the boundaries of the experimental cell is not considered. To model the increase in volume, at the end of the homogenization period (at time t = 360 h) the no-deformation boundary along $\partial\Gamma_3$ was switched to a constant deformation boundary with a value of 2.9 mm. The boundary conditions for the test case are summarised in Table 3-7.

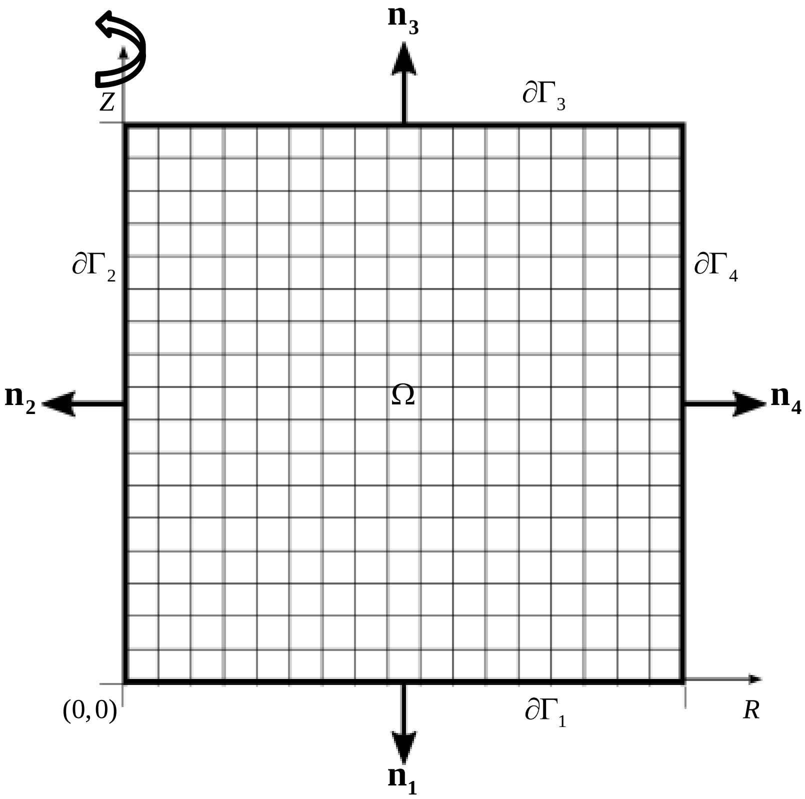

Figure 3-18 Schematic of the model domain 1a01 with boundary surfaces, the axis of symmetry and the normal directions

Table 3-7 Summary of boundary conditions for test case 1a01

Process	$\partial\Gamma_1$	$\partial\Gamma_2$	$\partial\Gamma_3$	$\partial\Gamma_4$
Hydraulic	$\mathbf{q}^w \cdot \mathbf{n}_1 = 0$	$\mathbf{q}^w \cdot \mathbf{n}_2 = 0$	$p = 2\ kPa$	$\mathbf{q}^w \cdot \mathbf{n}_4 = 0$
Mechanical	$\mathbf{u} \cdot \mathbf{n_1} = 0$	$\mathbf{u} \cdot \mathbf{n_2} = 0$	$\mathbf{u} \cdot \mathbf{n}_3 = \begin{cases} 0\ \text{mm} & t < 360\ \text{h} \\ 2.9\ \text{mm} & t > 360\ \text{h} \end{cases}$	$\mathbf{u} \cdot \mathbf{n_4} = 0$

3.4.4 Results/discussions

3.4.4.1. ***Effective Stress Time Profile at R = 25 mm, Z = 0 mm***

The temporal evolution of the effective stress at the bottom of the model domain at the above specified point is compared to the measured axial and radial stresses and shown in Figure 3-19. For this test case, initially a weak HM coupling was used in the simulations. In the weak coupling scheme the changes in the mechanical model i.e., the deformation does not affect the hydraulic mode. This model was later extended to include a bidirection HM coupling where the for each time step the hydraulic and the mechanical models are in equilibrium with each other. The prelliminary stress evolution of the updated model is shown in Figure 3-24. The following points can be inferred from the figures.

- The model can reproduce the maximum axial swelling stress developed both in the homogenization period and in the volume change period.
- The quasi-steady state behaviour in the homogenization period and also at the end of the experiment could also be captured.
- The effective stress in the axial direction is overestimated in both the homogenization and volume change phases.
- The drop in stress due to volume change at t = 360 h and the following evolution of the stress could not be simulated in the weakly coupled case, the calculated stress remains constant.
- The results from bi-directional HM coupling are qualitatively much closer to the measured stress evolution after the volume change. The stress evolution before the volume change is comparable to the weakly coulped HM case.

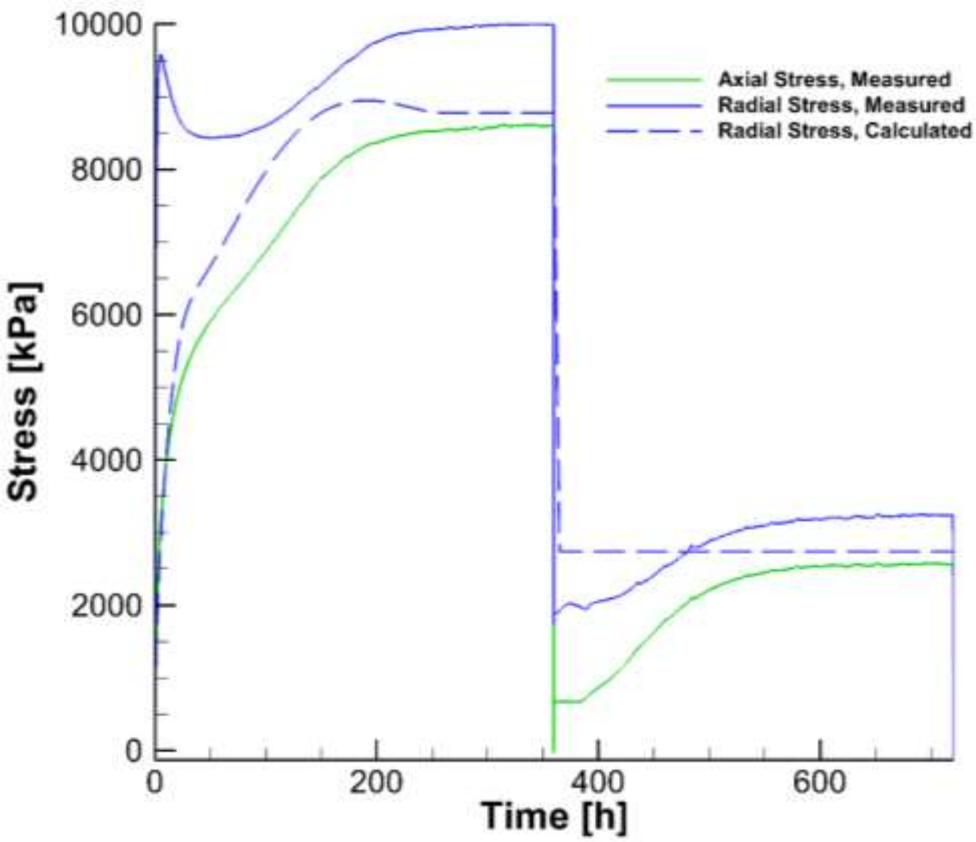

Figure 3-19 Evolution of the effective stress in the weakly coupled model of test case 1a01 at the point R = 25 mm, Z = 0 mm.

3.4.4.2. ***Water Content and Void Ratio Profiles at R = 10 mm***

In Figure 3-20 and Figure 3-22, the calculated development of the volumetric water content and the void ratio at various points in the domain is shown as a function of time for the weakly coupled HM model. The late-time contours in the previous section suggest the water content to be distributed evenly in the model. The calculated value of the water content is 0.41 and lies close to the water content range of 0.32 - 0.38 measured along the height of the probe after the experiment. The calculated void ratio, with a value of 0.7, is underestimated in comparison to the measured value range of 0.90 - 1.06 along the height of the probe.

The updated results from the bi-directionally coupled HM model are shown in Figure 3-21and Figure 3-23. The evolution of the void ratio and the gravimetric water content was markedly different than in the weakly coupled case and the values at the steady state were very close to the measured values.

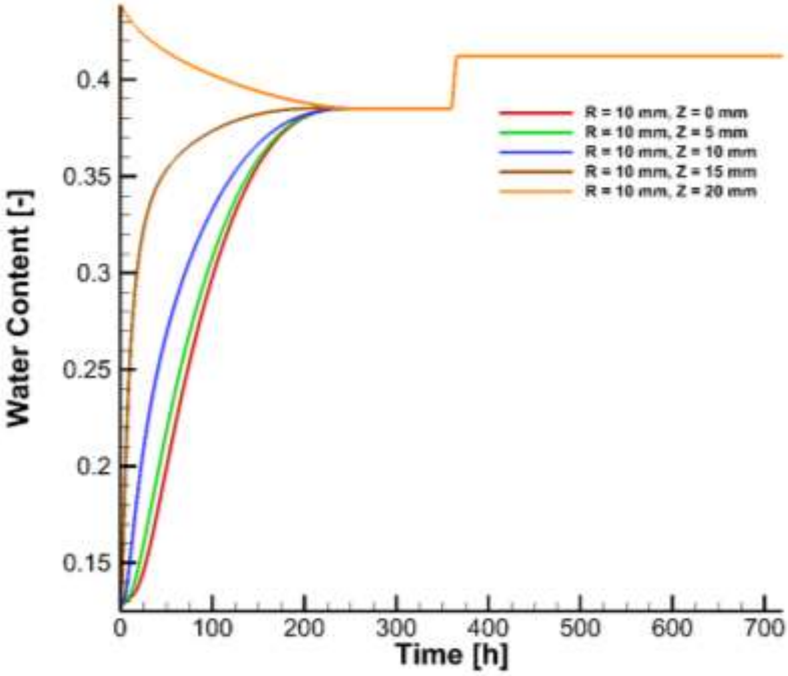

Figure 3-20 Calculated evolution of water content in the weakly coupled model of test case 1a01 at various heights along the line R = 10 mm.

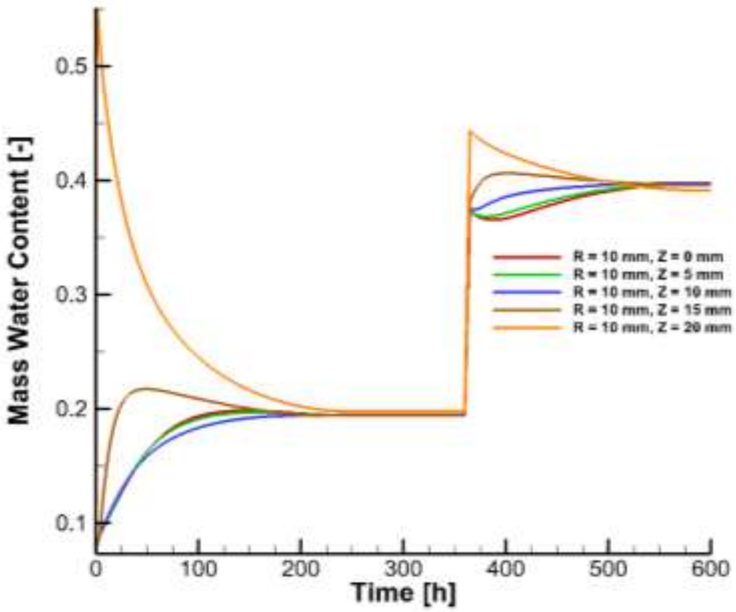

Figure 3-21 Updated calculated water content evolution in the bi-directional HM model of test case 1a01 along the line R = 10 mm.

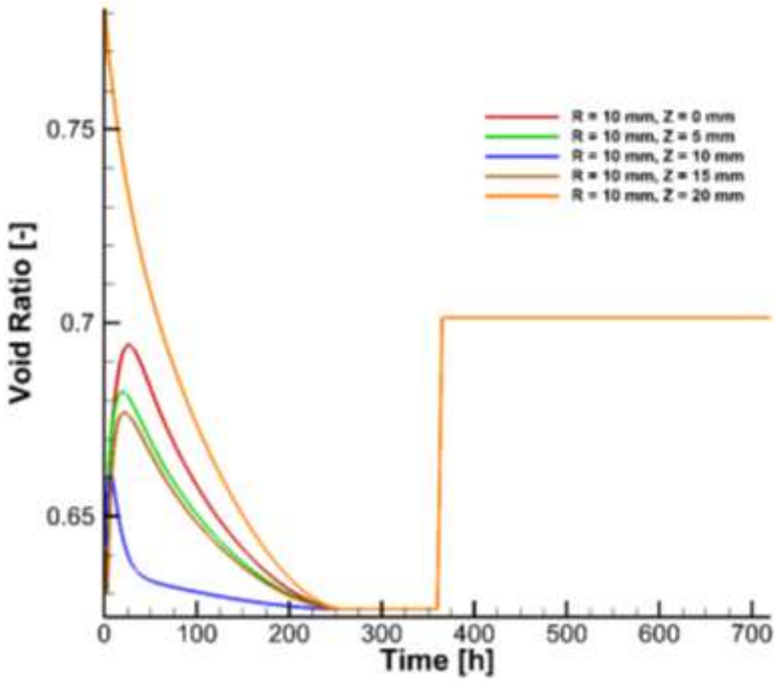

Figure 3-22 Calculated evolution of void ratio in the weakly coupled model of test case 1a01 at various heights along the line R = 10 mm.

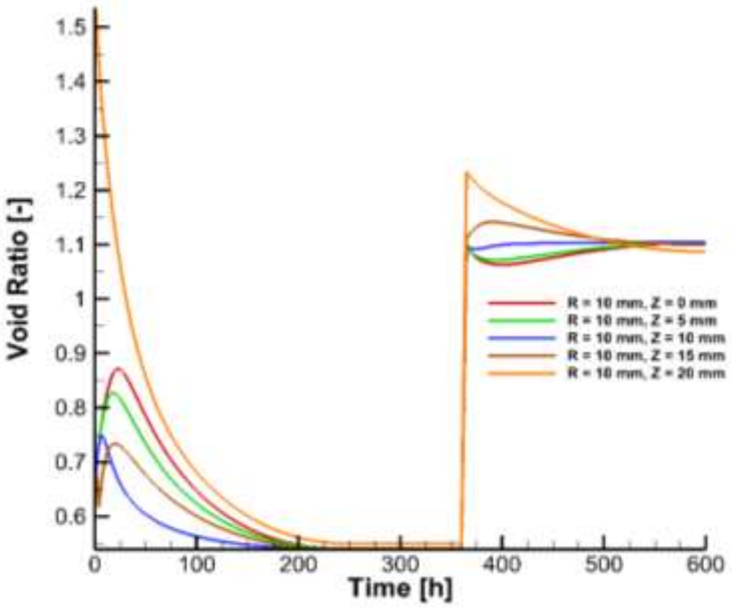

Figure 3-23 ***Updated calculated evolution of void ratio in the bi-directional HM model of test case 1a01.***

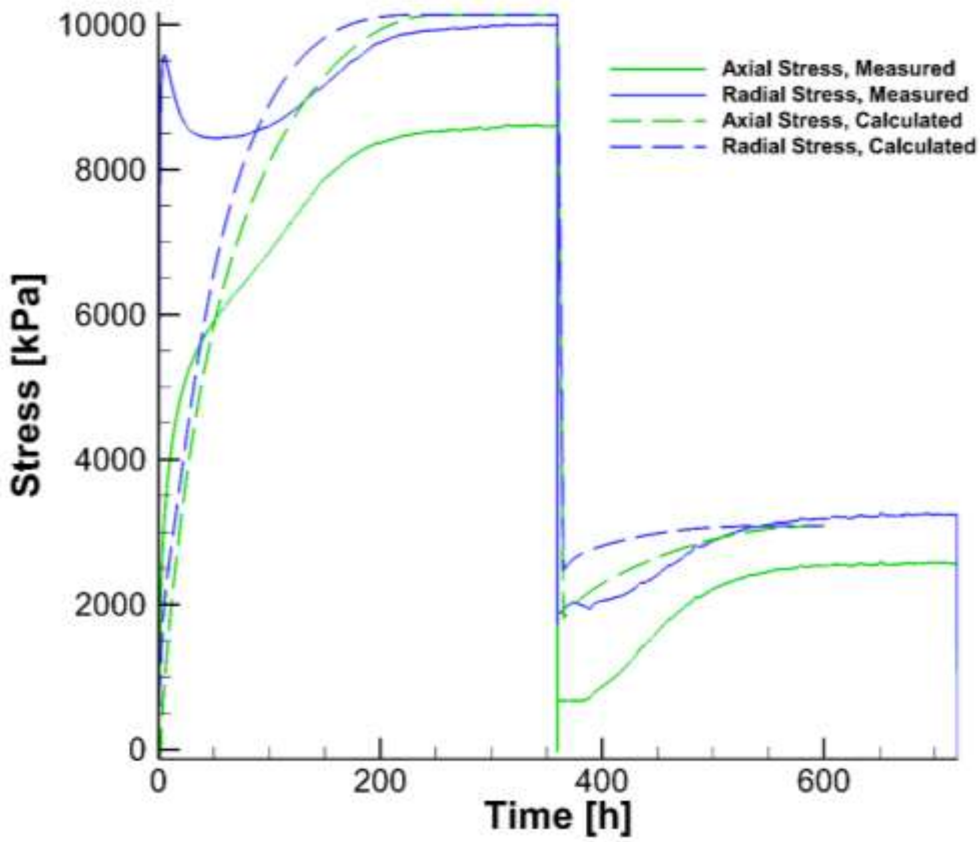

Figure 3-24 ***Updated stress evolution in the bi-directional HM model of model 1a01.***

3.4.4.3. *Water Content and Void Ratio Profiles at R = 10 mm*

In Figure 3-25 and Figure 3-27, the calculated development of the volumetric water content and the void ratio at various points in the domain is shown as a function of time for the weakly coupled HM model. The late-time contours in the previous section suggest the water content to be distributed evenly in the model. The calculated value of the water content is 0.41 and lies close to the water content range of 0.32 - 0.38 measured along the height of the probe after the experiment. The calculated void ratio, with a value of 0.7, is underestimated in comparison to the measured value range of 0.90 - 1.06 along the height of the probe.

The updated results from the bi-directionally coupled HM model are shown in Figure 3-26 and Figure 3-28. The evolution of the void ratio and the gravimetric water content was markedly different than in the weakly coupled case and the values at the steady state were very close to the measured values.

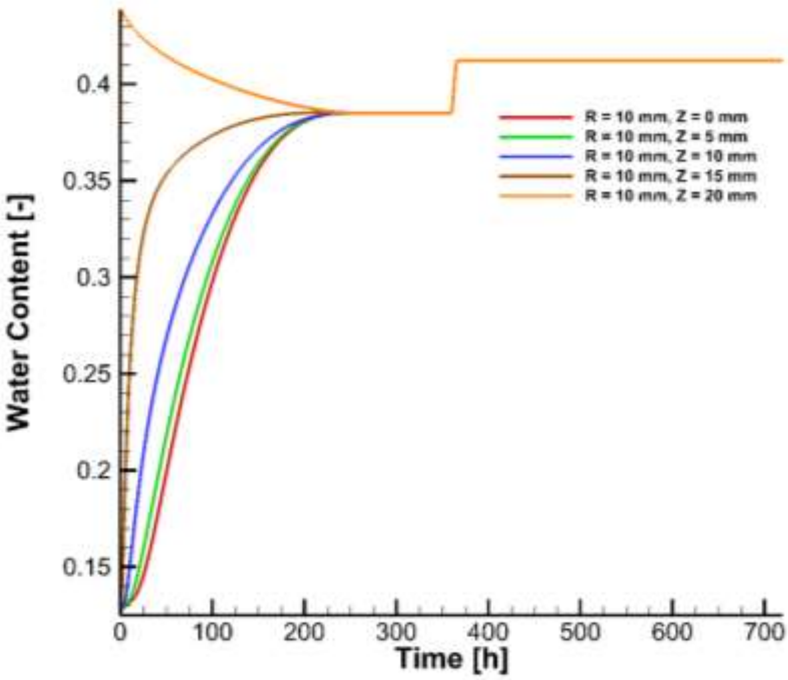

Figure 3-25 Calculated evolution of water content in the weakly coupled model of test case 1a01 at various heights along the line R = 10 mm.

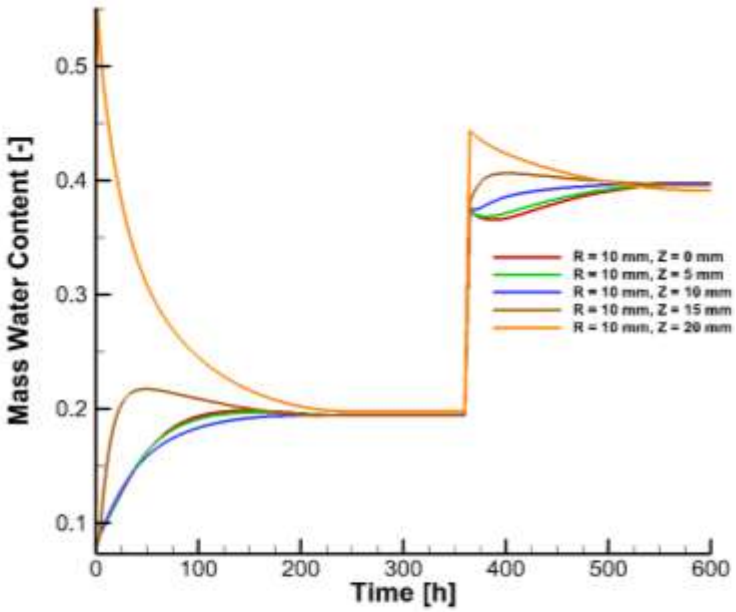

Figure 3-26 Updated calculated water content evolution in the bi-directional HM model of test case 1a01 along the line R = 10 mm.

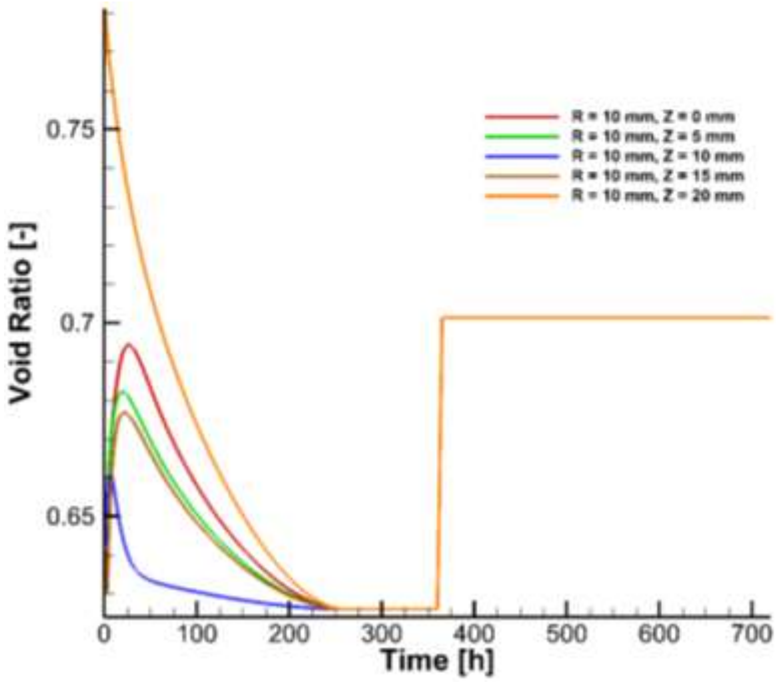

Figure 3-27 Calculated evolution of void ratio in the weakly coupled model of test case 1a01 at various heights along the line R = 10 mm.

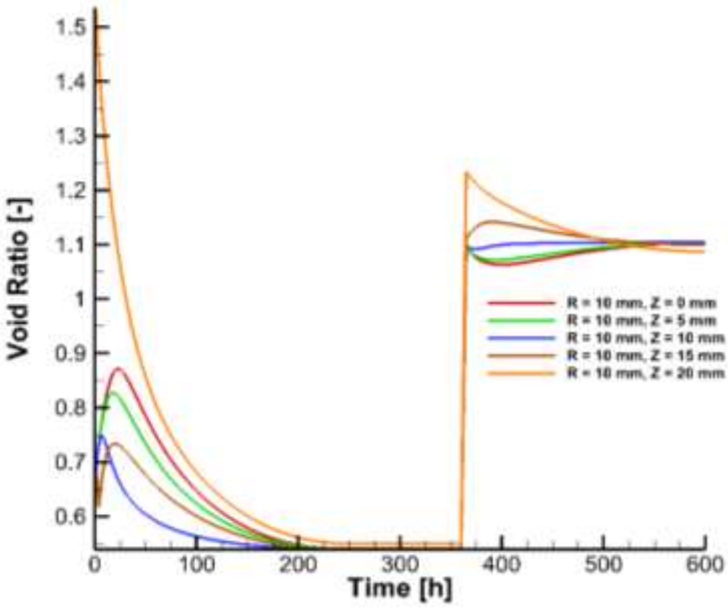

Figure 3-28 Updated calculated evolution of void ratio in the bi-directional HM model of test case 1a01.

3.5 ClayTech

3.5.1 Geometry, mesh and boundary conditions

The geometries of the two tests were both two-dimensional axisymmetric representations of the actual cylindrical geometries. Only the bentonite clay and the steel lid were included in the model, the walls and bottom of the confining steel cylinder were not. The dimensions of the geometries are shown in Figure 3-29 together with the applied boundary conditions.

Water was supplied at the top of the bentonite using a pressure dependent flux boundary condition:

$$j_l = 10^2[0.1\text{MPa} - p] \text{ kg/(m}^2\text{ s)} \quad (3\text{-}1)$$

This was set up to allow free access of water to the bentonite without causing any build-up of pore pressure.

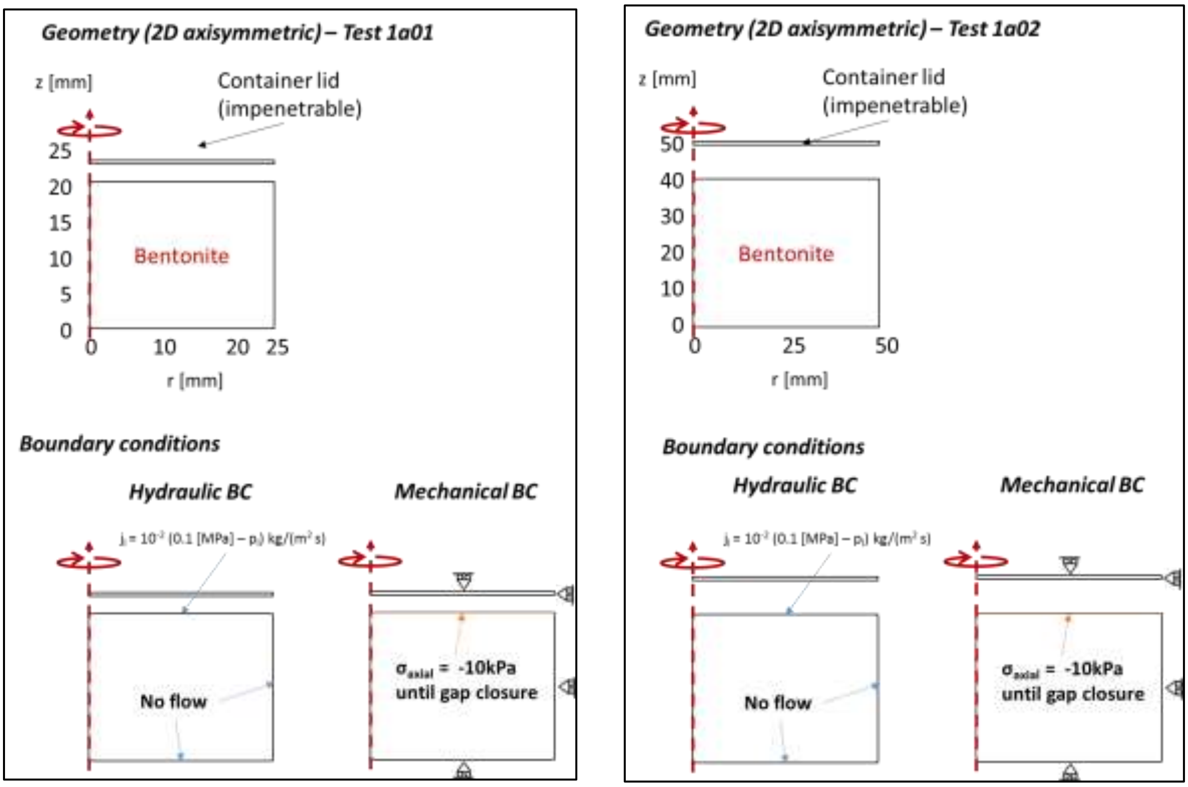

Figure 3-29. *Geometry and boundary conditions.*

In terms of the mechanical problem, all outer boundaries (i.e. walls and bottom of the bentonite clay and the steel lid) of the geometry were given roller conditions. The top of the bentonite was assigned a low axial pressure during the swelling phase (10 kPa) until the gap had filled, where after no pressure was assigned.

The geometry was meshed using quadrilateral elements with 8x20 elements in test 1a01 and 8x40 elements in test 1a02.

3.5.2 Material parameters

Two materials were used in the model – the bentonite and the steel lid. In the bentonite both hydraulic and mechanical processes were modelled, while in the steel lid only mechanical processes were considered. The bentonite material parameters are listed in Table 3-8 and Table 3-9. The clay potential curves (Ψ_H and Ψ_L) were parameterized as:

$$\Psi = 10\hat{}\left(c_2\ \rho_d^{\ 2} + c_1\ \rho_d + c_0\ \right) \text{ Pa} \qquad (3\text{-}2)$$

The mid-line and the half-allowed span were calculated as: $\Psi_M = (\Psi_H + \Psi_L)/2$ and $\Psi_{\Delta/2} = (\Psi_H - \Psi_L)/2$, respectively.

The steel lid was modelled as a linear elastic material with parameters set so that it would not deform due to the pressure exerted by the swelling bentonite. Hence, the material parameters were chosen to make the material very stiff – they are shown in Table 3-10.

Table 3-8 Hydraulic parameters

Parameter		Units	Value/Expression
Hydraulic permeability	k	m^2	$1.2 \cdot 10^{-20} \cdot e^{5.33}$
Density of water	ρ_w	kg/m^3	$998 \cdot \exp(-\alpha_w \cdot s)$
	α_w	1/Pa	4.5×10^{-10}

Table 3-9. Mechanical parameters

Parameter		Units	Value/Expression
Solid density	ρ_s	kg/m^3	2780
Initial dry density	ρ_d	kg/m^3	1631/1590[1]
Path variable derivative parameter	K	-	40
Lower clay potential curve	c_0^{low}		1.259
	c_1^{low}		4.117×10^{-3}
	c_2^{low}		-3.94×10^{-7}
Higher clay potential curve	c_0^{high}		3.325
	c_1^{high}		2.101×10^{-3}
	c_2^{high}		1.669×10^{-7}

[1]Values for test 1a01 and 1a02 respectively

Table 3-10 Material parameters of the lid (linear elastic material model)

Parameter		Units	Value/Expression
Young modulus	E	MPa	100
Poisson's ratio	v	-	0.2

Table 3-11 Contact pair properties

Parameter	Units	Value

Characteristic stiffness	E_{equ}	MPa	100
Penalty factor		MPa/m	$2x10^8$

Table 3-12 Initial conditions.

Test	Path variable (-)	Stress (MPa)	Suction (MPa)
1a01	0	0	12.1
1a02	0	0	9.4

The interaction between the bentonite and steel lid was simulated using the contact pair formulation in Comsol. The penalty method was used to solve the contact problem - the parameters used are shown in Table 3-11. The initial conditions applied to materials are shown in Table 3-12.

3.5.3 Results/discussion

The stress evolution in the models can be seen in Figure 3-30. The solid lines identify model results and the dashed lines experimental data. In the model of test 1a01 the axial stress is well reproduced, while the radial stress is a bit too high in the model. In the model of test 1a02 both the axial and radial stresses are in general a bit too high (except for the radial stress evaluated at a height of 45mm), but the early peak in the radial stresses is captured in the model. The time evolution of the modelled stresses are relatively similar to those measured,

indicating that the water-uptake process is well reproduced in the model.

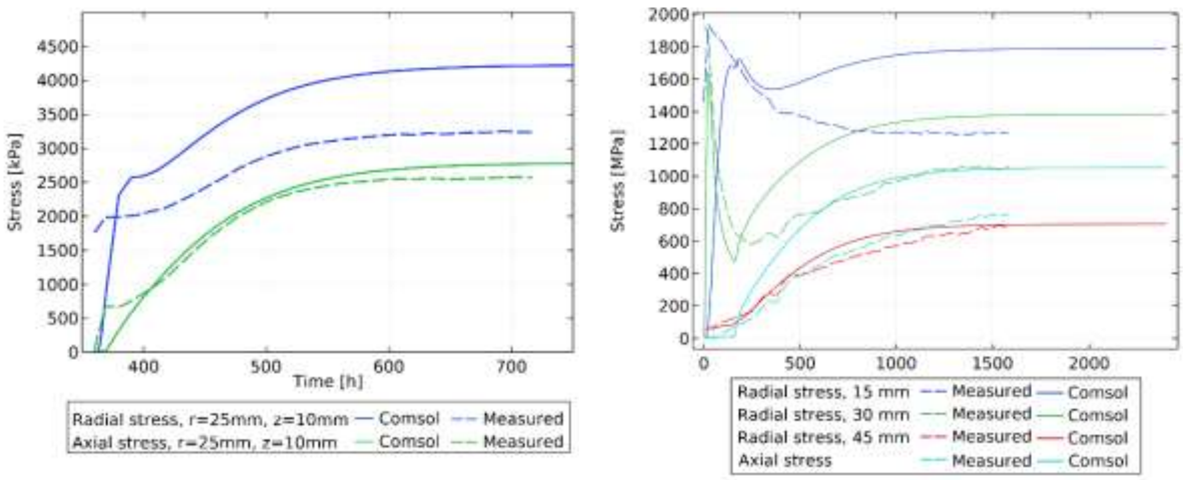

Figure 3-30. *Stress evolution in the models of test 1a01 (left) and test 1a02 (right).*

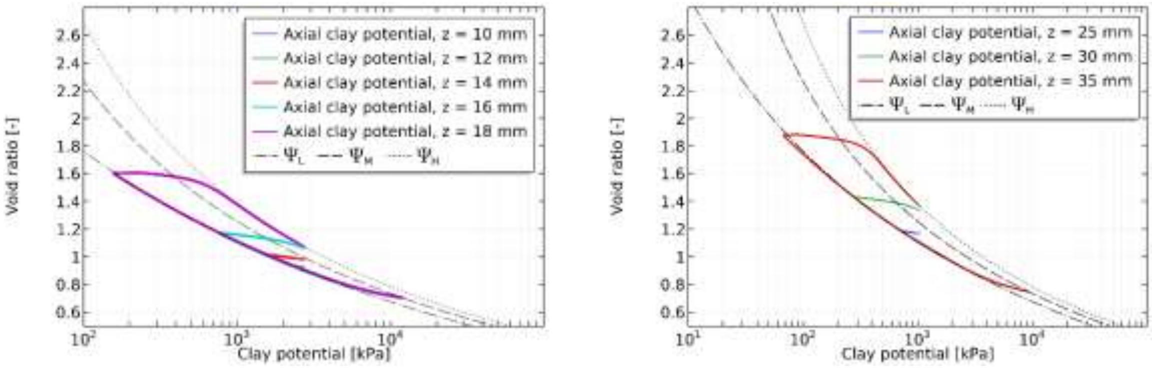

Figure 3-31. *Clay potential (axial direction) versus void ratio evolution.*

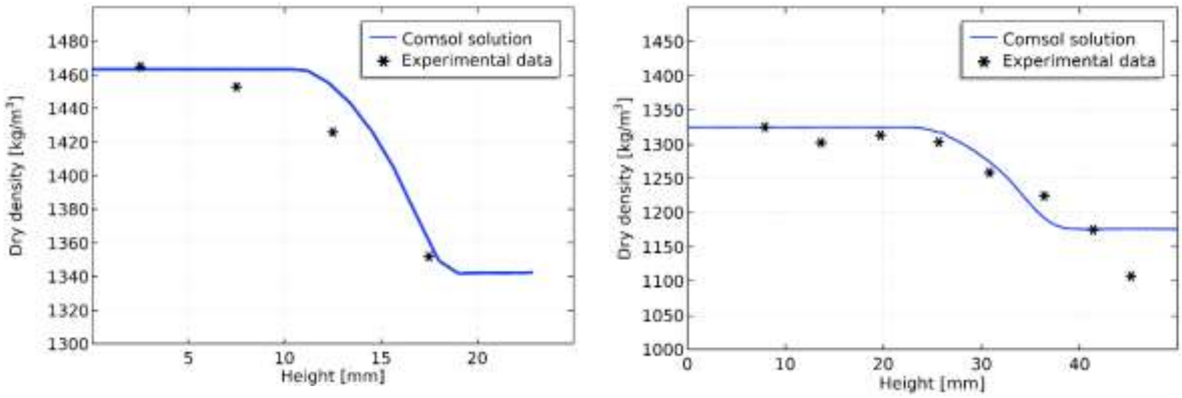

Figure 3-32. *Final state of the model (lines) and experimental data (stars).*

In Figure 3-31 the evolution in clay potential vs void ratio in several points in each model is shown. This nicely illustrates the behavior of the bentonite in the HBM model. During the initial swelling the bentonite follows the lower clay potential (lower dashed line), but during compression (which takes place when the upper part has reached the lid and is compressed by the bentonite further down) it moves towards the upper clay potential (upper dashed line).

The final dry density is shown in Figure 3-32. In both models the model results agree relatively well with experimental data, the only exception being at the top, where the models overestimate the density.

As shown, the model results agree relatively well with experimental data. The two main discrepancies are:

1. The radial stresses are in general overestimated
2. The dry density profile at the top is overestimated in the model of test 1a02

The reason that the radial stresses are overestimated may be due to the idealized geometry – for example no gap was allowed between the bentonite and the walls of the steel container. If that was present radial swelling would have occurred, possibly leading to lower radial stress.

The cause for the dry density being higher in the top part of the bentonite in the model as compared to the experiment may be that wall friction was not included in the model.

3.6 EPFL

3.6.1 Geometry and discretization

Test1a01

The initial model geometry consists of a 20x25 mm domain, representing the sample considering axisymmetric conditions, and is discretised into 100 elements (8-node quadrilateral with 4 integration points each). The finite element mesh is shown in Figure 3-33.

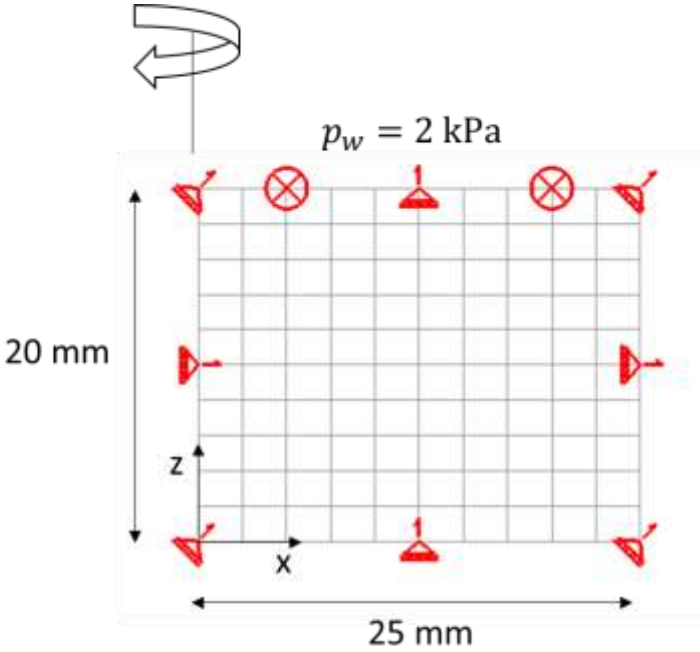

Figure 3-33. Model geometry, discretization and boundary conditions for the first stage of test 1a01. Each square represents and element which is defined with 8 nodes and contains 4 integration points.

Test1a02

The initial model geometry is shown in Figure 3-34. It consists of a 40x50 mm domain, representing axisymmetric conditions and is discretised into 100 elements (8-node quadrilateral with 4 integration points each).

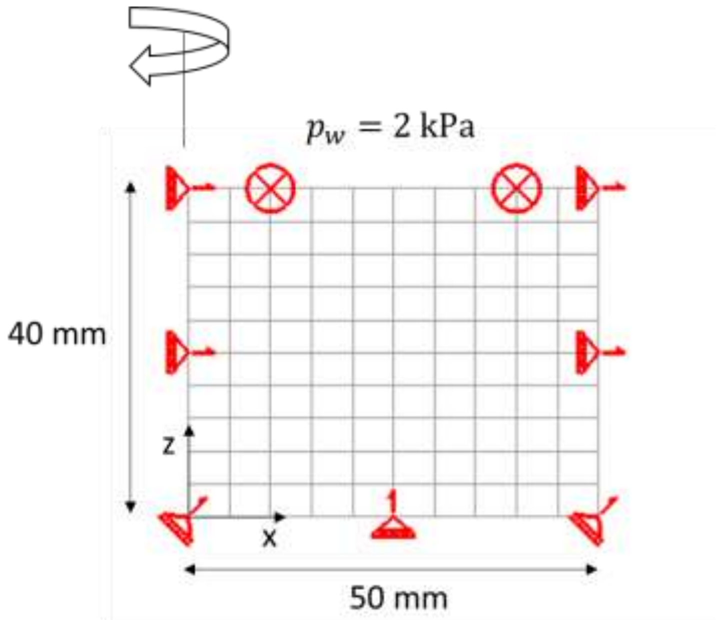

Figure 3-34 Model geometry, discretization and boundary conditions for the first stage of test 1a02. The second stage involves also constrained displacements for the top nodes which are located at h=50 mm.

3.6.2 Input parameters

The initial conditions and model parameters have been determined as follows:
Given the initial water content and dry density the value of suction at the end of the compaction phase is determined from experimental results found in the literature with similar dry density (Villar, 2005; Tang and Cui, 2010), plotted in Figure 3-35, where a degree of saturation of 45% ($w = 12\%$) is in equilibrium with a suction value of 90 MPa.

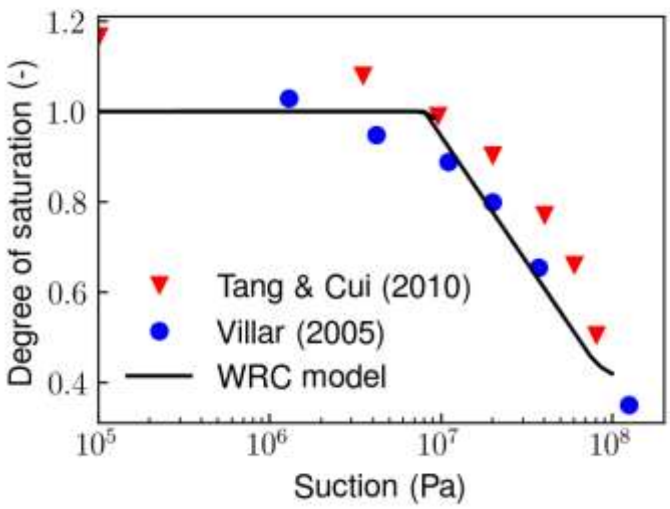

Figure 3-35 Water retention curve used in the simulations of tests 1a.

Bulk and shear moduli are set to K_{ref} =10 MPa and G_{ref} =5 MPa for a reference isotropic pressure of p' =1 MPa. The plastic compressibility parameter is set to $\beta = 5$, and the loading collapse parameter to $\gamma_s = 8$. These have been calibrated for the saturation phase, by fitting radial and axial swelling pressure at equilibrium, and the peak pressure. The remaining stages are predictions without any further attempt to calibration.

The value of permeability has been set to $k_{f0} = 10^{-20}\mathrm{m}^2$ from data reported in Borgesson et al. (1995) at a void ratio of 0.68, which yields a saturated hydraulic conductivity of $K_w = 10^{-13}\mathrm{m/s}$.

Regarding the remaining parameters, standard values for clays have been adopted. Parameters corresponding to the thermal behaviour are not used in the simulation.

The material parameters used to simulate the tests 1a are summarised in Table 3-13.

Table 3-13. Model parameters for tests 1a

Elastic parameters		
K_{ref} , G_{ref} , n^e	[MPa], [MPa], [-], [°C^{-1}]	10, 5, 1
Isotropic plastic parameters		
β_m , γ_s Ω , r^e_{iso} , p'_c	[-], [-], [-], [-], [-], [MPa] , [-]	5; 8; 0.1; 2.9; 0
Deviatoric plastic parameters		
b , d , M , g , α , a , r^e_{dev}	[-], [-], [-], [-], [-], [-], [-]	0.5, 2.0, 1.0, 0, 1, 0.001, 1
Water retention parameters		
s_{e0} , β_h , θ_T , θ_e , S_{hys}	[MPa], [-], [-], [-], [-]	8, 4, 0, 5, 1
Water flow parameters		
k_{f0}, C_{KW1}, C_{KW2}, M, N		10^{-20}, 2.9, 2.9, 5.3, 5.5

3.6.3 Initial and boundary conditions

Test1a01

The simulation of this test has been performed in three steps, whose boundary conditions are:

1. Constrained displacements in the vertical direction for the nodes situated at z=0 mm and z=20 mm. Constrained horizontal displacements in the horizontal direction for the nodes situated at x= 0 mm (symmetry axis) and x=25 mm.

2. At t=359 h, the vertical displacement of the nodes at z=20 mm is released. The remaining boundary conditions are kept invariant with respect to the first phase.
3. Once the top nodes reach z=23 mm the vertical displacements are restrained again for the top nodes (now at z=23 mm)

Throughout the entire test 2 kPa of pore water pressure at the top is imposed and air pressure is kept constant to zero.
Given the water retention curve and the initial suction, the initial effective stress is set as (isotropic):

$$p' = sS_r = 90 \times 0.45 = 40.5 \text{ MPa}$$

Where an isotropic zero net stress is assumed at the start of the simulation.
Initial yield stress is determined knowing the static compaction stress as:

$$p'_{y0}(s = 90 \text{ MPa}) = p_{comp} + sS_r = 35.6 + 90 \times 0.45 = 76.1 \text{ MPa}$$

The isotropic critical stress at suction zero is set to 2.9 MPa and the loading collapse curve parameter is $\gamma_s = 8.0$, both are found by means of calibration.

Test1a02

The simulation of this test has been performed in two steps, whose boundary conditions are:

1. The vertical displacement of the nodes at z=40 mm is free. Constrained horizontal displacements in the horizontal direction for the nodes situated at x=0 mm (symmetry axis) and x=50 mm.
2. Once the top nodes reach z=50 mm the vertical displacements are restrained for the top nodes. The remaining boundary conditions are unchanged.

Throughout the entire test pore water pressure is fixed at $p_w = 2$ kPa at the top and air pressure is kept constant to zero.
The initial conditions and parameters have been determined as follows:
Provided the initial water content and dry density, although the material is saturated, the value of suction is set to 4 MPa, in agreement with the experimental results found in the literature (see Figure 3-35). Assuming that the sample is free from external stress, the initial effective stress is isotropic and equal to the initial value of suction ($S_r = 1 \rightarrow S_r s = s$).

3.6.4 Results/discussion

Test 1a01

The swelling pressure simulated for the test 1a01 is shown in Figure 3-36 together with the experimental results. As already mentioned, the calibration was performed to fit the swelling pressure both radial and axial at the equilibrium state of the first stage (saturation stage). The remaining stages, that is, unloading, swelling, and subsequent swelling pressure, are blind predictions, since no further calibration of parameters was attempted.

Overall model performance is satisfactory, with a qualitative reproduction of the measured evolution of swelling pressure. In quantitative terms it is observed that the collapse simulated during the saturation phase is excessive. This is because of the particular shape of the loading collapse curve of the ACMEG-TS model, which is determined by means of a single parameter, γ_s and does not offer further flexibility to fit the observed behaviour. After the saturation phase, subsequent unloading and swelling stages are well reproduced in terms of axial stress.

Radial stress during the second swelling pressure phase is overestimated by the model. Nevertheless, it could be that the dimensions of the sample do not allow a very precise comparison at this scale. As a matter of fact, a better reproduction of radial stress was obtained for the test 1a02 which involved the same material and density but with larger dimensions, and was therefore simulated using the same material parameters.

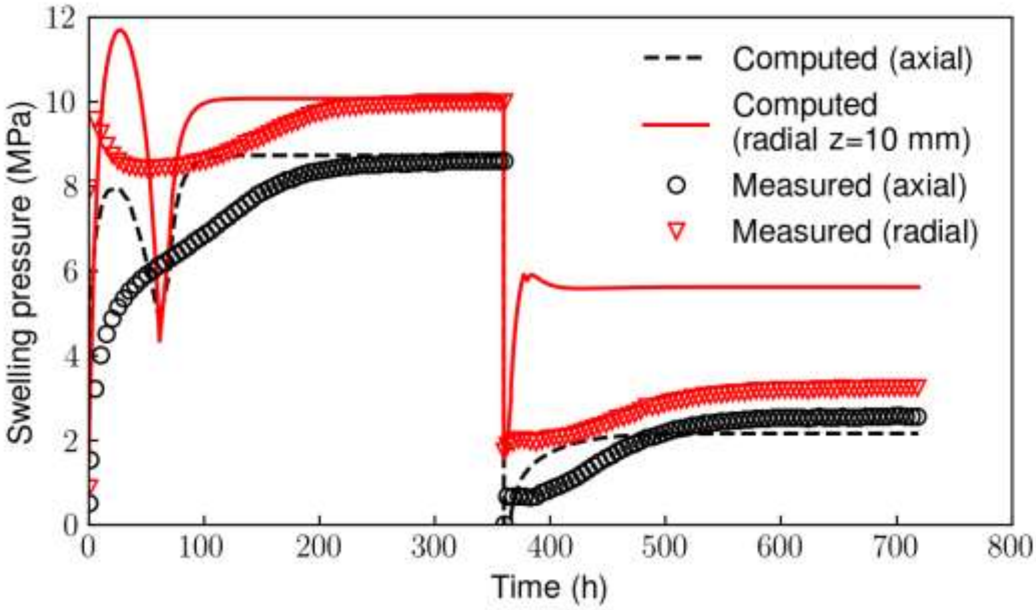

Figure 3-36 Swelling pressure results. Comparison between computed and measured data.

The comparison between the predicted void ratio and water content at the end of the test and the measured values is shown in Figure 3-37 . A trend that is in agreement with the measurements is obtained by the model. However, it is observed that the degree of heterogeneity is higher in the model than in the data obtained from dismantling. Indeed, the elements located close to the gap swell significantly, whereas the bottom elements maintained a fairly constant volume. Since the sample was saturated at the moment of dismantling, the values of void ratio e and water content w are solely related by the specific gravity G_s, as $e = G_s w$.

.

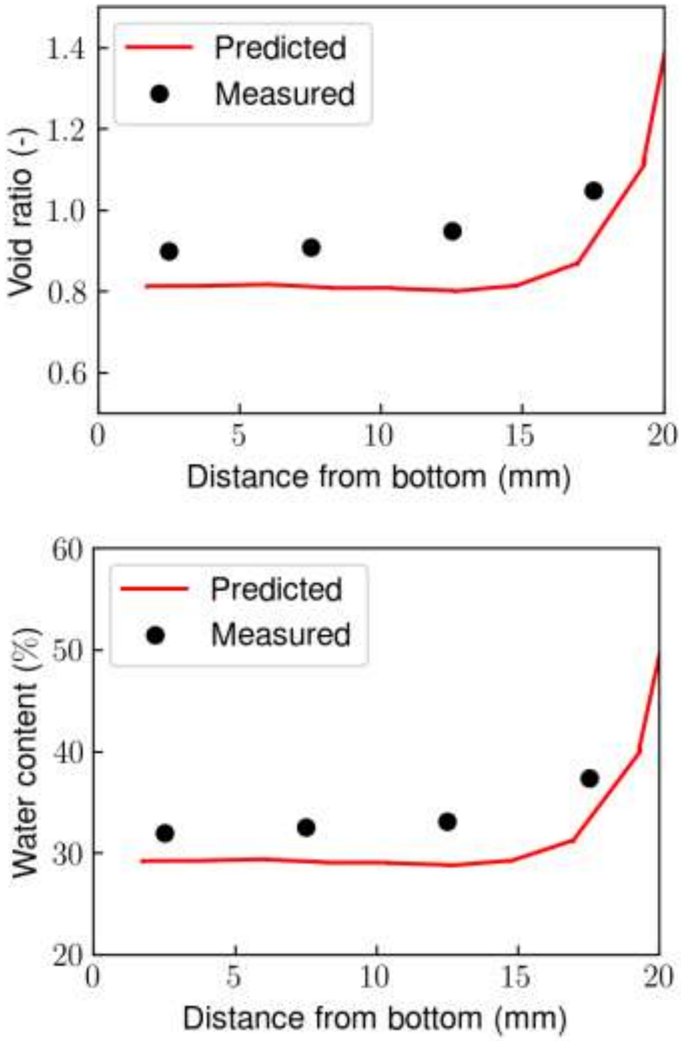

Figure 3-37 Void ratio (top) and water content (bottom) plots. comparison between measured and computed data at the end of the test.

Test 1a02

Results of the simulations for the test 1a02 in terms of swelling pressure are shown in Figure 3-38 and Figure 3-39. The particularity of this test is that swelling pressure was monitored in the radial direction at three different levels. This has the following consequence from the modelling point of view: Once the sample is let free to swell, the integration points at which stresses are computed, change their position continuously. This prevents a direct comparison of the numerical results with the experimental measurements as the latter are obtained at a fixed point.

The elements that did not change their position significantly are compared in Figure 3-38, these include the measurement of axial swelling pressure and the measurement of radial stress at 45 mm and 15 mm from bottom. Note that the sensor located at z=45 mm was not initially in contact with the bentonite sample, as this has an initial height of 40 mm. Therefore, the integration point that at the end of the simulation was closer to z=45 mm is used to compare the model output to the experimental measurements. Both initial and final values of the position at which stresses are obtained numerically are shown in the legends of Figure 3-38 and Figure 3-39.

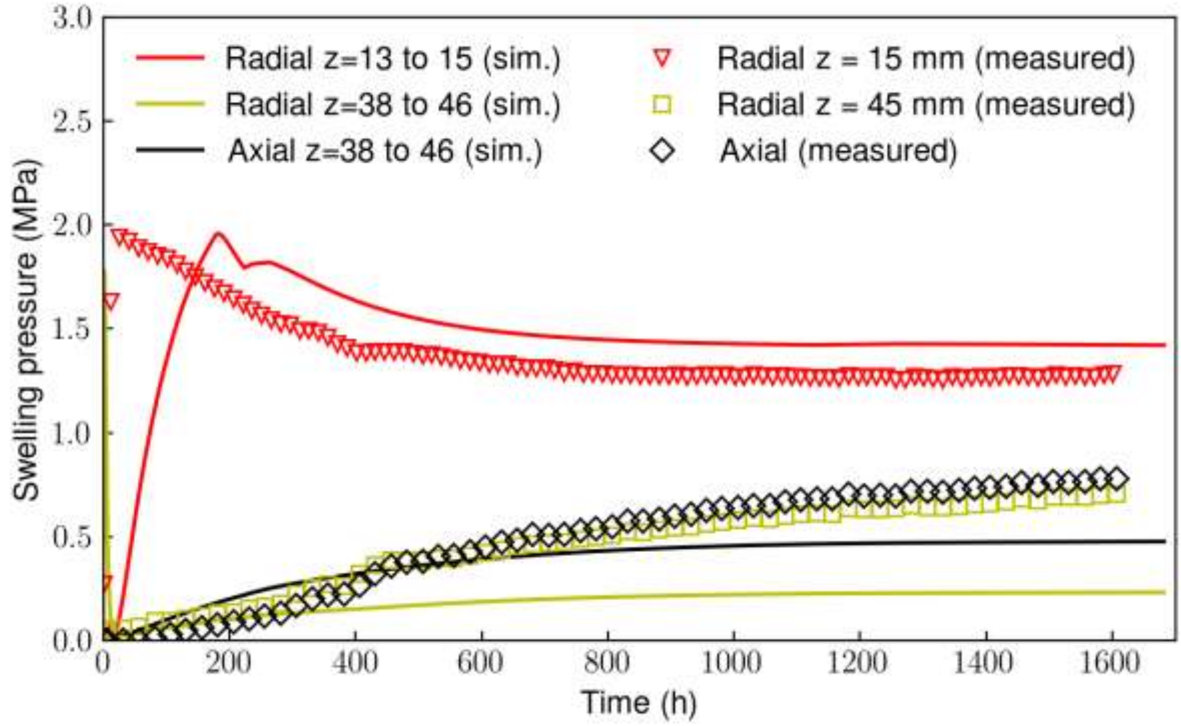

Figure 3-38 Numerical results (sim.) of radial stress around z = 15 and z = 45 and axial stress compared to the experimental measurements. Note that while the measurement points were fixed outside the sample, the numerical results are obtained at the integration points that were subjected to displacements. The initial and final positions are indicated in the legend.

In Figure 3-39 the measurements obtained at a height of z=30 mm are compared to two integration points that at different times were found at z=30mm. One had as an initial position z=30, while the other at the end of the simulation was located close to z=30 mm. Thus, these two integration points provide the envelope of stresses developed at z=30 throughout the test.

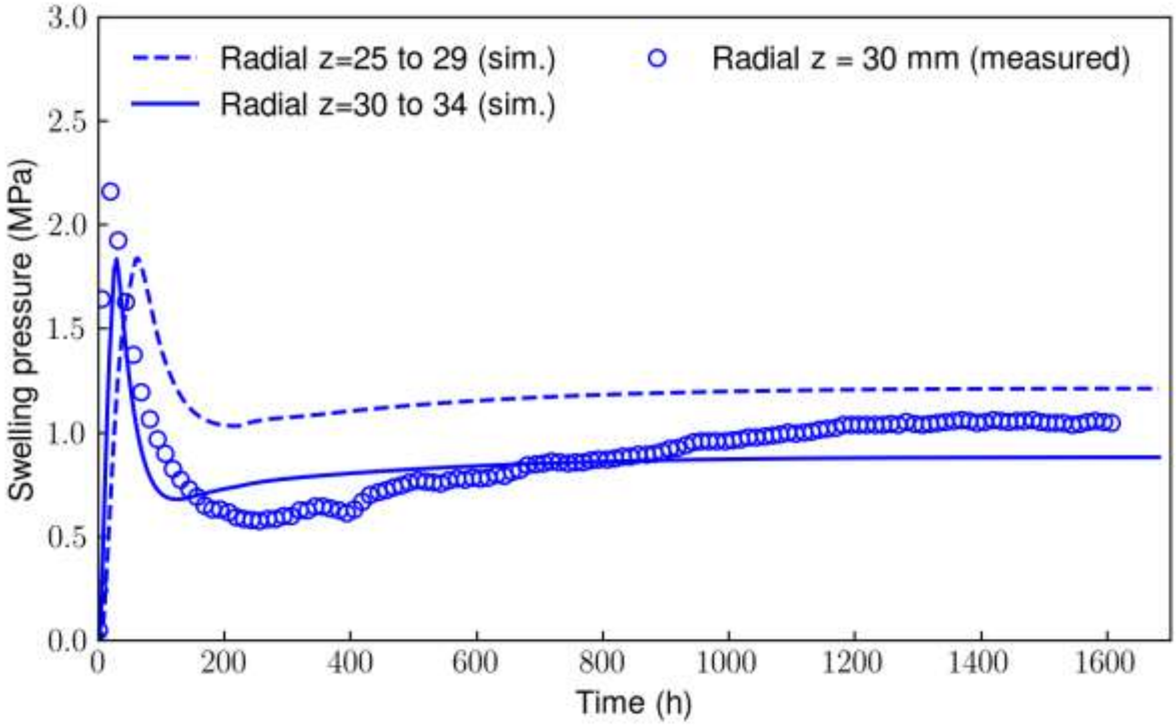

Figure 3-39 Radial swelling pressure simulated around z=30 mm for two integration points, compared with measured results at z = 30 mm. The evolution of height of the two integration points is provided in the legend.

In terms of swelling pressure, the results are in good agreement both qualitatively and quantitatively with the experimental values. This demonstrates the predictive capabilities of the model provided the results are obtained with the very same set of parameters calibrated with the saturation stage of test 1a01. Radial swelling pressures are well predicted in the bottom parts of the sample. The only noticeable difference is in the rate of pressure development at the beginning at z = 15 mm which is slower in the model compared to that measured in the experiments. Axial pressure and radial pressure at the top of the sample (after gap filling) are underestimated, nevertheless they follow a very similar trend in both cases. The simulation results corresponding to z = 45 should only be taken into account once the build-up in swelling pressure starts, since before the gap filling, no contact exists between bentonite – piston at z = 45 mm, and therefore the pressure simulated corresponds to heights below 45 mm (the initial height of the simulation point is shown in the legend of Figure 3-39).

In Figure 3-40the final state of void ratio and water content predicted from the simulation is compared to the experimental data. Since the final state of the sample was saturated the difference between the void ratio and the water content is a constant value. As in the test 1a01, the trend is similar between the model and the measured data but differing in quantitative terms, especially close to the top (z = 50 mm).

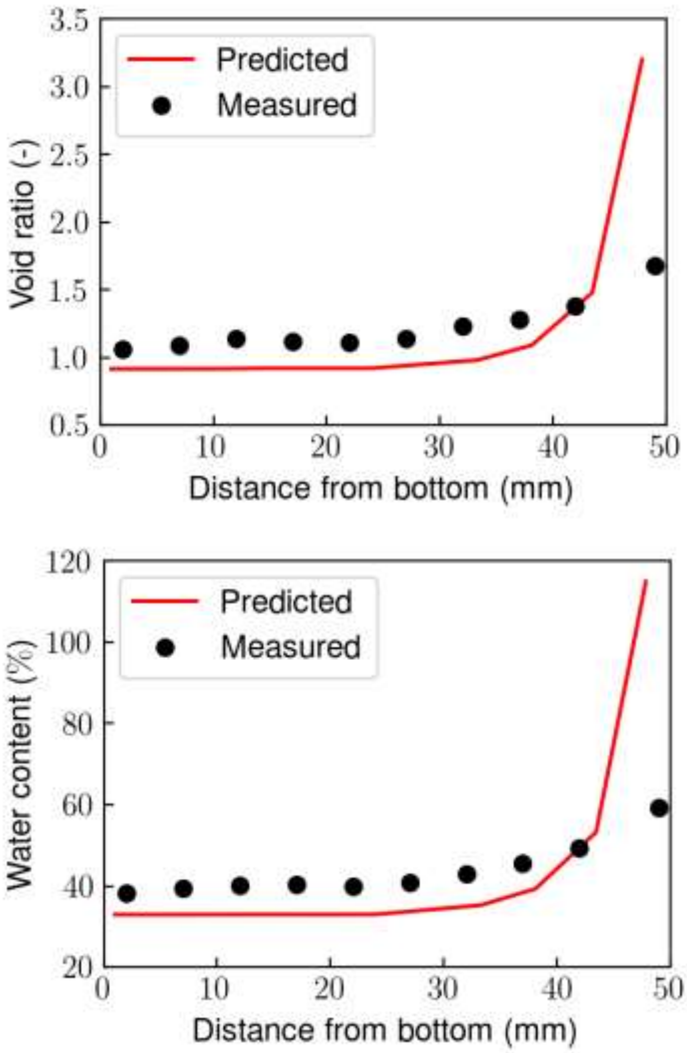

Figure 3-40 Void ratio (top) and water content (bottom). Measured versus computed values at the end of the test.

3.7 LEI

3.7.1 Geometry and discretization

This test includes two stages: a classical swelling pressure test at constant volume and an increase of accessible volume for bentonite swelling is available and water is introduced in the cell (Figure 3-41).

Dimensions for “Test 1a01” modelling were set regarding the specification:

- During step 1: cylinder with radius of 25 mm and height 20 mm;
- During step 2: cylinder with radius of 25 mm and height increasing from 20 mm to 22.9 mm.

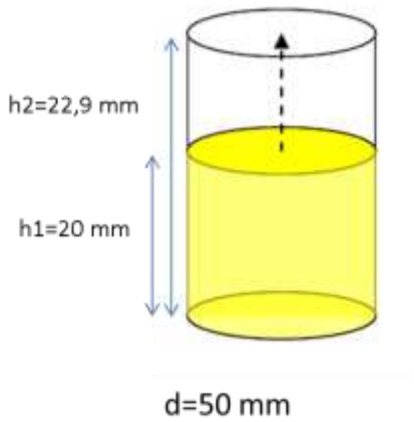

Figure 3-41. Illustration of the cell for “Test 1a01” [BEACON – D5.1.1, 2018]

3.7.1.1. *COMSOL Multiphysics model*

The COMSOL Multiphysics modelling has been done under axisymmetric conditions and analysed domain was discretized into 8548 triangular grid elements as it could be seen in Figure 3-42.

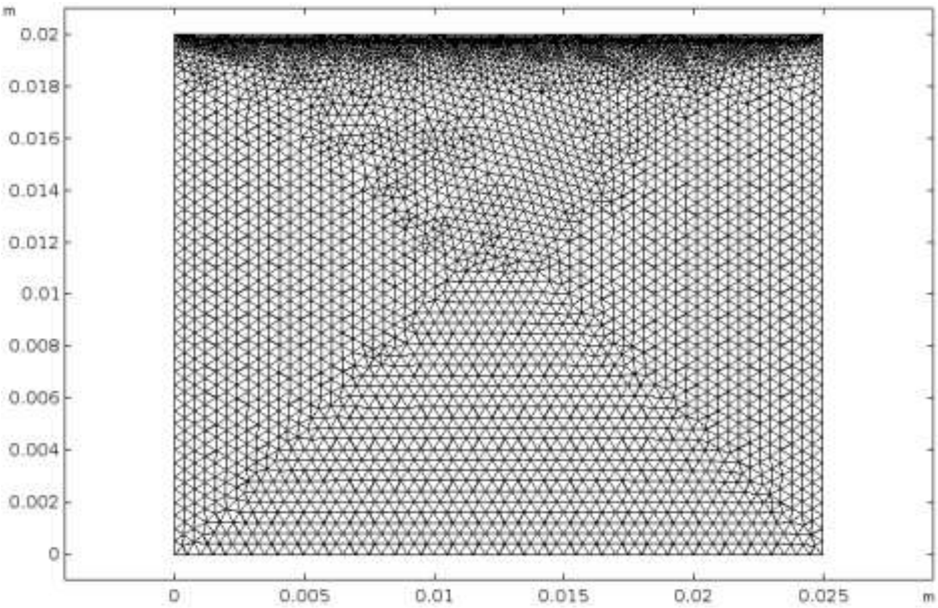

Figure 3-42. Computational grid of COMSOL Multiphysics model

3.7.1.2. ***CODE_BRIGHT model***

The CODE_BRIGHT modelling has been done under axisymmetric conditions and analysed domain was discretized into 500 rectangular grid elements as it could be seen in Figure 3-43.

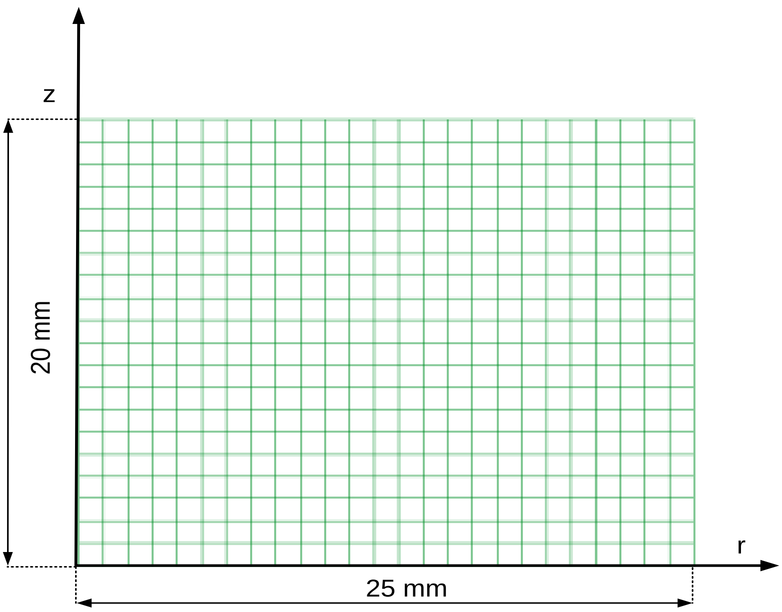

Figure 3-43. Computational grid of CODE_BRIGHT model

3.7.2 Input parameters

3.7.2.1. *COMSOL Multiphysics model*

The input parameters used for "Test 1a01" modelling are summarized in Table 3-14.

Table 3-14. Initial characteristics of materials used in the experiment

Parameter	Value
Dry density, kg/m^3	1655*
Porosity, -	0.41
Void ratio, -	0.68
Initial water content, %	13*
Initial saturation, -	0.53
Hydraulic conductivity, m/s	$K(e) = K_0 \left(\frac{e}{e_0}\right)^{\eta}$, K_0 =2.4·10^-13, e_0=1 $\eta = 5.3$ (Åkesson et al., 2010)
Water retention	$P_{entry} = A \cdot \left(\frac{e_0}{e}\right)$, A=43.5 MPa, m=0.38 (Åkesson et al., 2010)
Young modulus, MPa	3.5
Poisson ration, -	0.4 (Dagher et al., 2018)
Swelling coefficient, -	$d\varepsilon_{sw} = \beta_{sw}(dS_w - 0.25)$, β_{sw} =5.0·10^-04

*- data from specification (BEACON D51.1, 2018).

3.7.2.2. *CODE_BRIGHT model*

Part of the values of hydro-mechanical parameters for MX-80 bentonite was based on data in test specification (porosity and density) (BEACON D51.1, 2018) or values of parameters applied for COMSOL Multiphysics model (Poisson ratio, water retention and relative permeability curves). The values of other unknown parameters were based on available data on MX-80 bentonite (Åkesson, 2010; Abed, 2016; Toprak, 2015; Kristensson, 2008; Navarro, 2015). The initial values of hydro-mechanical parameters of bentonite and constitutive laws used in the analysis are summarized in Table 3-15.

Table 3-15. Initial values of hydro-mechanical parameters for bentonite and constitutive laws applied for CODE_BRIGHT modelling

Hydraulic data		
Retention curve		Van Genuchten model: $S_e = \frac{S_l - S_{rl}}{S_{ls} - S_{rl}} = \left(1 + \left(\frac{P_g - P_l}{P}\right)^{\frac{1}{1-\lambda}}\right)^{-\lambda}$ $P = P_o \frac{\sigma}{\sigma_o}$
Air entry pressure, P_0 [MPa]	43.5	
Shape function of retention curve, λ [-]	0.38	
Surface tension at 20°C, σ_0 [N·m^{-1}]	0.072	
Residual saturation, S_{lr} [-]	0	
Maximal saturation, S_{ls} [-]	1	
Intrinsic permeability		
Intrinsic permeability, 1st principal direction, $k_{11,0}$ [m^2]	$3.14 \cdot 10^{-21}$	Darcy law: $\mathbf{q}_\alpha = -\frac{\mathbf{k}k_{r\alpha}}{\mu_\alpha}\left(\nabla P_\alpha - \rho_\alpha \mathbf{g}\right)$ Kozeny's model: $\mathbf{k} = \mathbf{k}_o \frac{\varphi^3}{(1-\varphi)^2} \frac{(1-\varphi_o)^2}{\varphi_o^3}$
Intrinsic permeability, 2nd principal direction, $k_{22,0}$ [m^2]	$3.14 \cdot 10^{-21}$	
Intrinsic permeability, 3rd principal direction, $k_{33,0}$ [m^2]	$3.14 \cdot 10^{-21}$	
Reference porosity for intrinsic permeability, ϕ_0, [-]	0.405	
Liquid phase relative permeability		Van Genuchten model: $k_{rl} = \sqrt{S_e}\left(1 - \left(1 - S_e^{1/\lambda}\right)^\lambda\right)^2$
Shape function of retention curve, λ [-]	0.38	
Mechanical data		
Elastic parameters		Volumetric strains: $d\varepsilon_v^e = \frac{k_i(s)}{1+e}\frac{dp'}{p'} + \frac{k_s(p',s)}{1+e}\frac{ds}{s+0.1}$ where: $k_i(s) = k_{io}\left(1 + \alpha_i s\right)$ $k_s(p',s) = k_{so}\left(1 + \alpha_{sp} \ln p'/p_{ref}\right)$
Initial (zero suction) elastic slope for specific volume-mean stress, κ_{io} [-]	0.05	
Initial (zero suction) elastic slope for specific volume-suction, κ_{so} [-]	0.3	
Minimal bulk module, K_{min} [MPa]	1	
Poisson's ratio, v [-]	0.4	
Parameter for κ_i, a_i [-]	-0.003	
Parameter for κ_s, a_{sp} [-]	-0.147	
Reference mean stress, p_{ref} [MPa]	0.01	
Plastic parameters		The preconsolidation pressure: $p_o = p^c\left(\frac{p_o^*}{p^c}\right)^{\frac{\lambda(o)-kio}{\lambda(s)-kio}}$ where stiffness parameter: $\lambda(s) = \lambda(o)\left[(1-r)\exp(-\beta s) + r\right]$ The tensile strength: $p_s = p_{s0} + ks$ Hardening dependency on plastic volumetric strain:
Slope of void ratio - mean stress curve at zero suction, $\lambda(0)$ [-]	0.15	
Parameter defining the maximal soil stiffness, r [-]	0.75	
Parameter controlling the rate of increase of soil stiffness with suction, β [MPa^{-1}]	0.05	
Parameter that takes into account increase of tensile strength due to suction, k [-]	0.1	
Tensile strength in saturated conditions, p_{s0} [MPa]	0.1	
Reference pressure, p^c [MPa]	0.1	

Critical state line parameter, *M* [-]	1	$dp_o^* = \frac{1+e}{\lambda(0)-k_{io}} p_o^* d\varepsilon_v^p$
Non-associativity parameter, *α* [-]	0.3	
Initial void ratio, e_0 [-]	0.68	
Initial preconsolidation mean stress for saturated soil, p_0^*[MPa]	12	

3.7.3 Initial and boundary conditions

Initial and boundary conditions were the same for COMSOL Multiphysics and CODE_BRIGHT models. For the flow modelling conditions were set as follows:

- Initial conditions were set in terms of pressure head (Hp=-11 000 m) to match initial saturation of S_w=0.53.
- Constant pressure of 2 kPa was applied on model top boundary during the step 1. During step 2 constant pressure of 20 Pa was applied.
- For the bottom and side boundaries of the model domain no flow conditions were set.
- Constant temperature (20 °C) was assumed in the system.

Initial and boundary conditions for mechanical modelling were as follows:

- For the model top boundary mechanical BC was set in terms of prescribed displacement of zero during step 1 with sharp increase to 2.9 mm after 15 days of simulation.
- Prescribed (zero) displacement condition in r direction were set for side boundary of model domain. Prescribed (zero) displacement condition in z direction were set to bottom boundary.
- Initial stresses (0.11 MPa) were set in the model.

3.7.4 Results/discussion

3.7.4.1. *COMSOL Multiphysics model*

Preliminary modelling results are presented in Figure 3-44-Figure 3-48. As it could be seen from the Figure 3-44, the material was not fully saturated by the end of simulation (after 30 days).

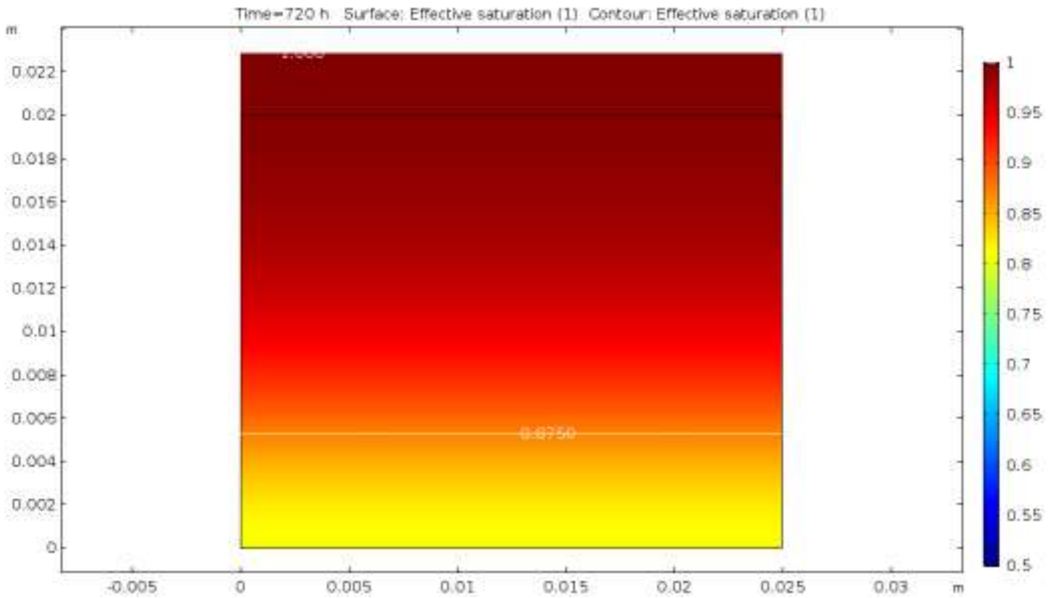

Figure 3-44. Results of water saturation distribution by the end of simulation (after 30 days)

Modelling results of axial and radial stresses (swelling pressure) are presented in Figure 3-45. As it could be seen from the figure, the trend of non-linearly increasing pressure during step 1 and step 2 observed. Modelled maximum swelling pressure was higher at the end of step 1 than of step 2. Modelled axial stress was slightly higher than radial stress through all experiment. Modelling results showed underestimated axial and radial stresses during step 1 and overestimated axial and radial stresses during step 2 in comparison to experimental results.

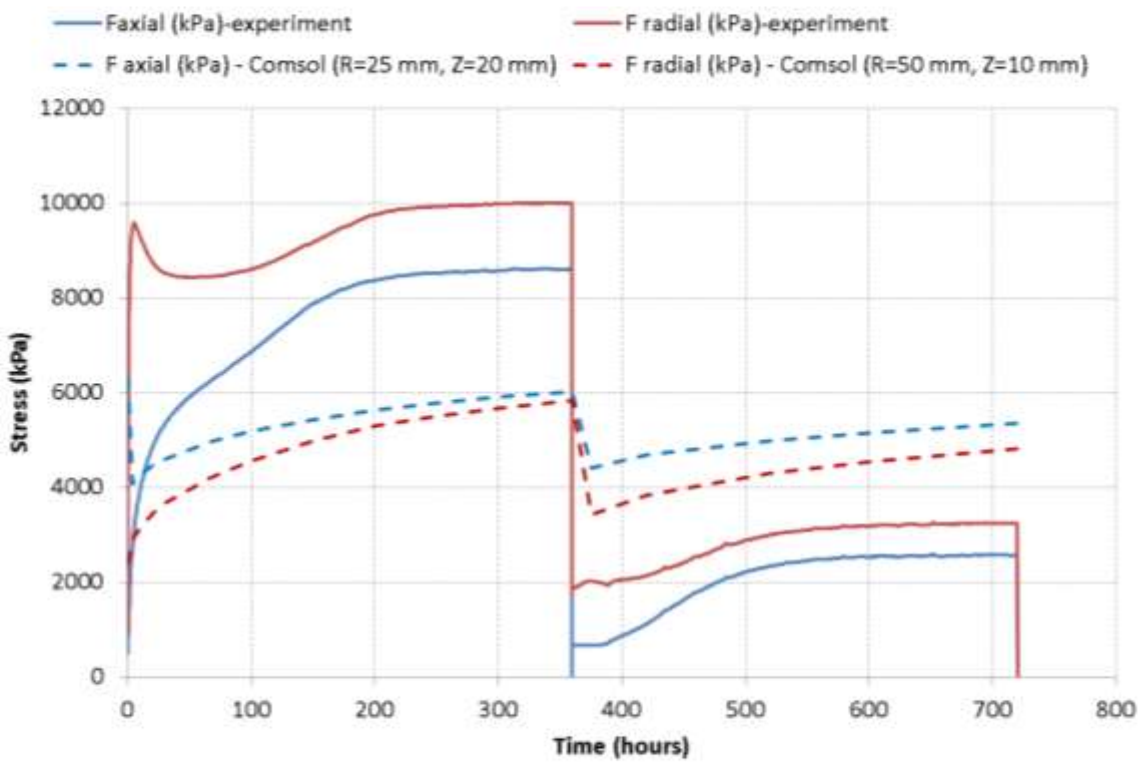

Figure 3-45. Results of swelling pressure evolution modelling and experimental results

Modelling results of dry density at particular points of specimen after step 2 are presented in Figure 3-46. As it could be seen modelled dry density at heights z=7.5 mm and 17.5 mm were in line with experimental data. More overestimated dry density in lower part of specimen (close to the bottom) was observed.

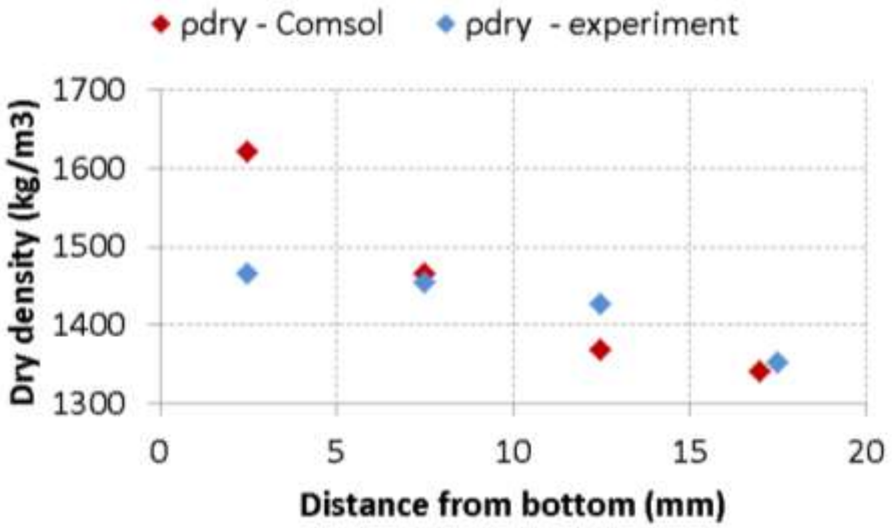

Figure 3-46. Results of dry density modelling at particular points of specimen and experimental results

Modelling results of void ratio at particular points of specimen after step 2 are presented in Figure 3-47. As it could be seen from the figure the void ratio at height z=7.5 mm were in agreement with experimental data. However the void ratio was slightly overestimated in the upper part of specimen and underestimated in the lower part of specimen.

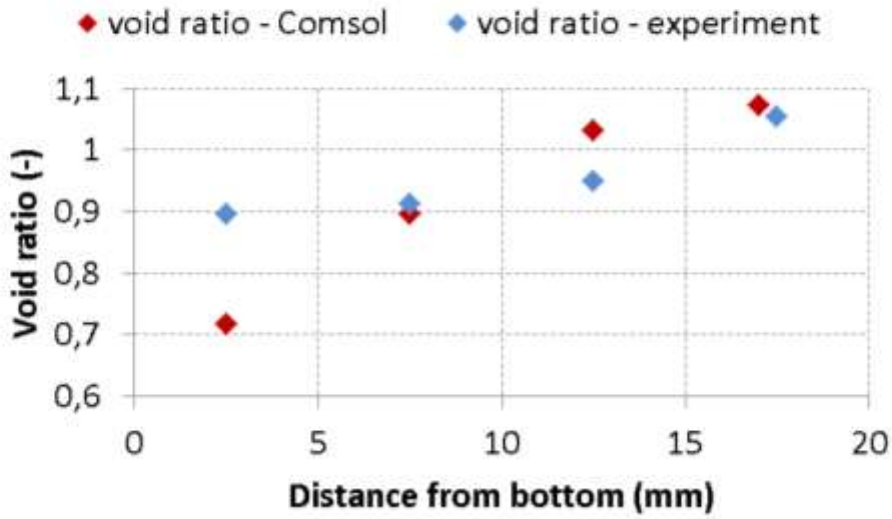

Figure 3-47. Results of void ratio at particular points of specimen and experimental results

Modelling results of water content at particular points of specimen after step 2 are presented in Figure 3-48. Modelled water content at heights z=7.5 mm, 12.5 mm and 17.5 mm were in line with experimental data. The largest difference was observed close to the bottom of specimen (where not fully saturated conditions prevail).

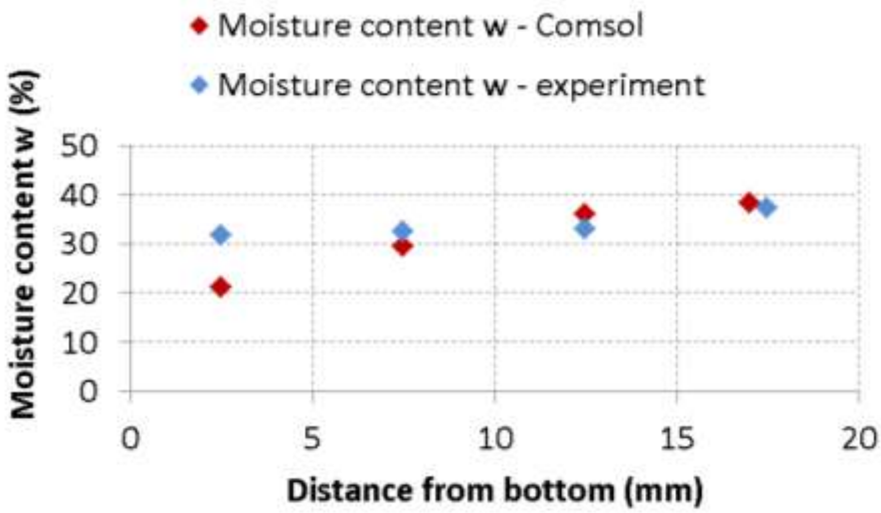

Figure 3-48. Results of water content at particular points of specimen and experimental results

In overall, it could be seen that model formulation in COMSOL Multiphysics at test modelling time led to underestimated or overestimated (to some extent) void ratio, dry density, moisture content at different parts of specimen (more significant differences for lower part of specimen) and underestimated swelling pressure for step 1 and overestimated swelling pressure for step 2.

3.7.4.2. *CODE_BRIGHT model*

Only the first step of experiment (15 days), corresponding to a classical swelling pressure test at constant volume conditions was modelled using CODE-BRIGHT.

Modelling results of bentonite saturation at five different heights of the sample is presented in Figure 3-49. The full saturation of the whole sample was predicted after ~9 days as it could be seen in the figure. The saturation was fastest on the top of the sample and took less than one day. The saturation time in the other parts of the sample took longer time.

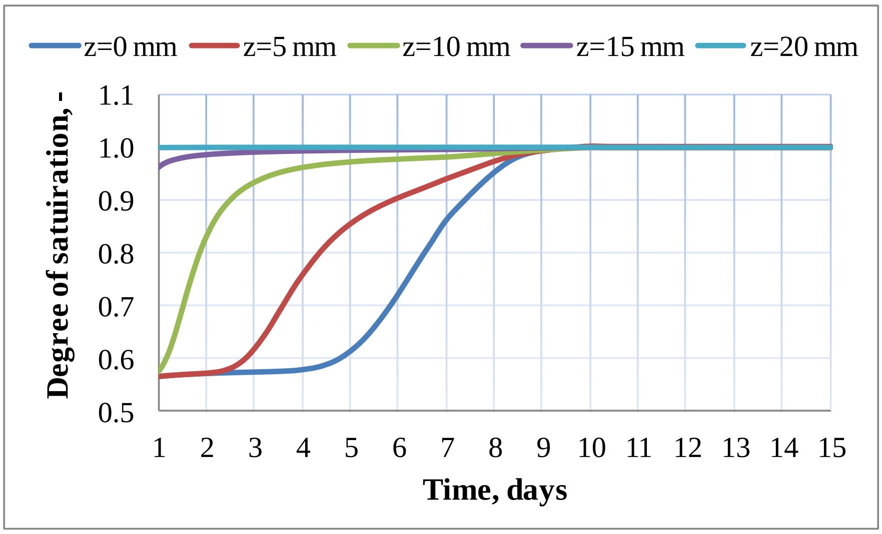

Figure 3-49. Predicted evolution of degree of saturation at five different heights of the sample (z=0 is the bottom and z=20 mm is the top of the sample)

Modelling results of axial and radial stresses (swelling pressure) are presented in Figure 3-50. Measured data during step 1 of experiment showed that profile of stresses in axial and radial directions are different. The magnitude of stresses at analysed points after step 1 differs in ~1.4 MPa (varying between ~8.6 MPa and ~10 MPa). Radial stress at z=10 mm was higher than axial stress at z=20 mm. Modelling results showed very similar profiles of stresses in axial and radial directions and almost equal magnitude of stresses (~9.6 MPa) in analysed points. However, predicted stresses at analysed points were between measured curves.

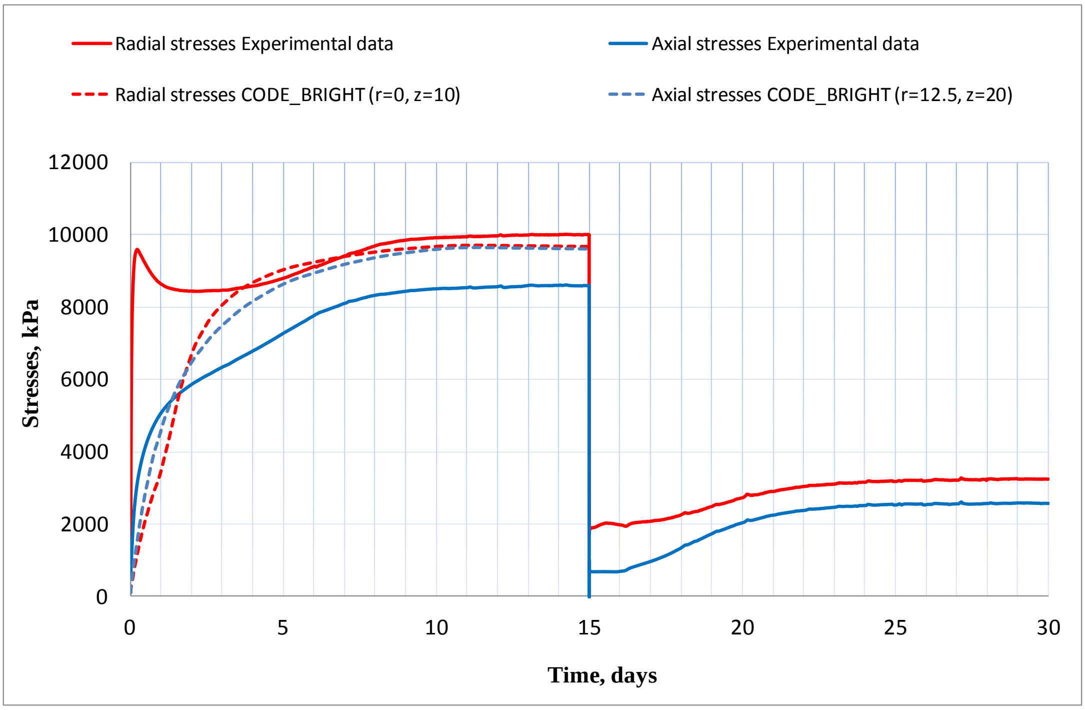

Figure 3-50. Measured (lines) and predicted (dashed lines) evolution of stresses at two different locations of the sample (z=10 is the middle and z=20 mm is the top of the sample)

Figure 3-51 shows the modelled distribution of porosity after step 1 along a line in axial direction of the sample. It was obtained that in a region near the water inlet (from z=20 mm to z=13 mm) bentonite swells (peak expansion was ~16 % from initial porosity value *n*=0.405) and it caused the compaction of analysed material in the remaining region (from z=13 mm to z=0 mm) where peak reduction of porosity was ~4.2 % from initial value *n*=0.405.

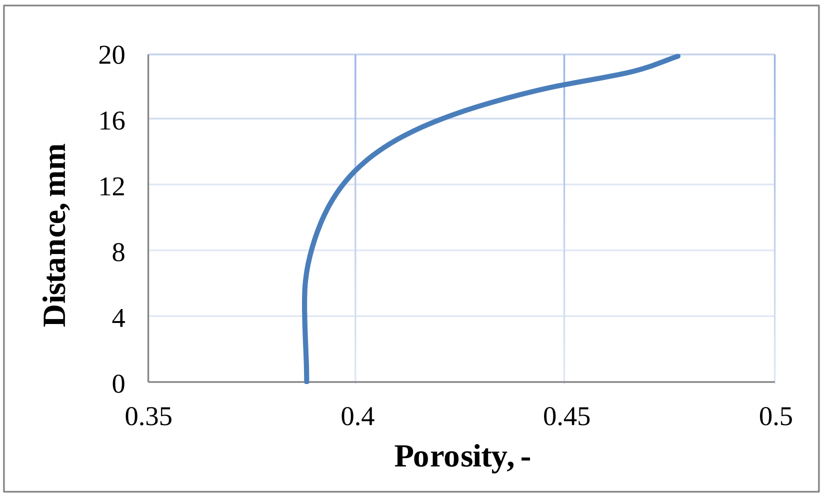

Figure 3-51. Predicted distribution of porosity after step 1 in axial direction of the sample (from the bottom (z=0 mm) to the top (z=20 mm)

3.7.4.3. *Results comparison between COMSOL Multiphysics and CODE_BRIGHT models*

Comparison of preliminary results for "Test 1a01" obtained using COMSOL Multiphysics and CODE_BRIGHT modelling tools are presented in Figure 3-52. As could be seen, current hydro-mechanical formulation in COMSOL Multiphysics underestimates stresses in analysed points during first step and overestimates stresses in second step of experiment compared to the measured data. Radial and axial stresses at analysed points predicted using CODE_BRIGHT were in between measured curves.

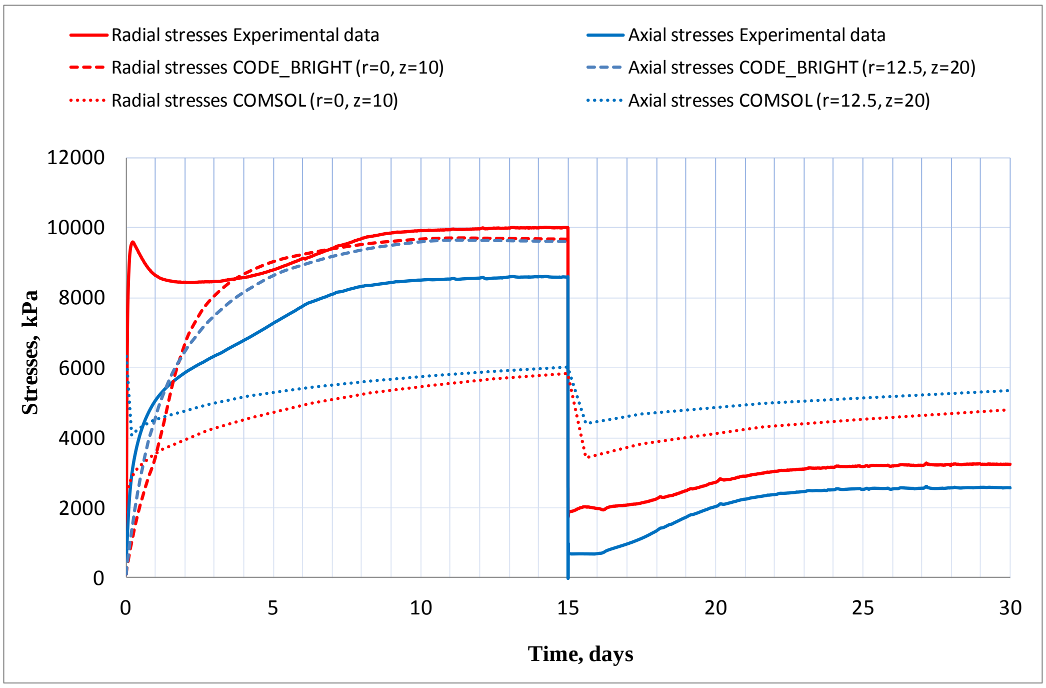

Figure 3-52. Comparison of measured (lines) stresses and modelling results for "Test 1a01" using COMSOL Multiphysics (dotted lines) and CODE_BRIGHT (dashed lines) codes

3.8 Quintessa

3.8.1 Geometry and discretization

Test1a01

A cylindrical grid is used to represent the bentonite, with height 20 mm and radius 25 mm. In the second half of the experiment, the bentonite is permitted to swell axially by 2.9 mm but this is represented by a change in boundary condition rather than any change in the grid.

Due to the axisymmetric nature of the experiment, no angular discretisation is used. There is also no radially-dependent behaviour in the model (friction is not modelled on the boundaries as the surfaces in the experiment were lubricated), but radial discretisation is included for output purposes. The grid is divided into 7 vertical and 7 radial compartments, such that the requested output points all correspond to the central coordinates of a compartment. This discretisation is illustrated in Figure 3-53. Using a finer grid increased the computation time but did not significantly affect the results.

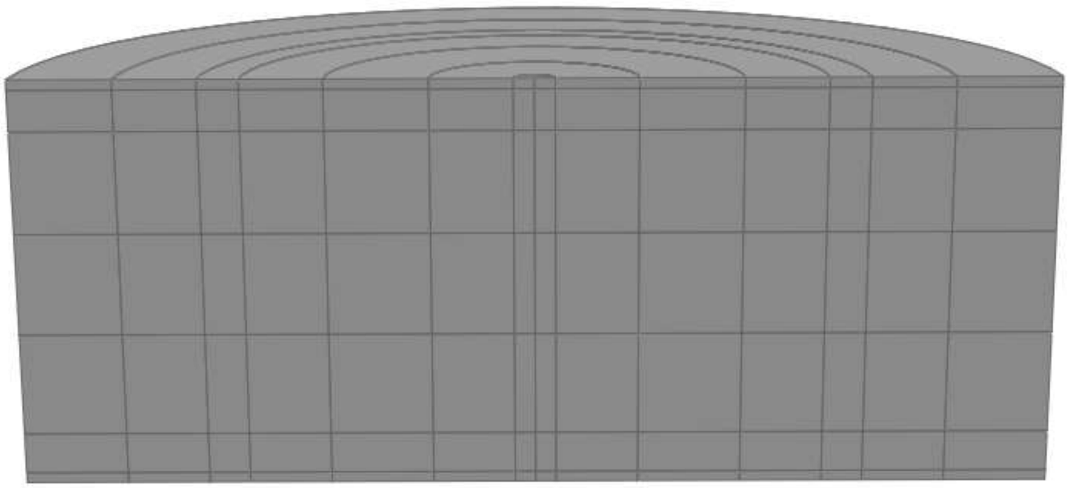

Figure 3-53 Discretisation of bentonite in the 1a01 QPAC model.

Test 1a02

The geometry is similar to 1a02 but twice as large in each dimension, with a height of 40 mm and radius 50 mm. Again, the grid is chosen to give the requested output points, resulting in a discretisation of 9 vertical compartments and 4 radial compartments. There is no radial dependence of the bentonite behaviour (again, friction has not been modelled as surfaces were lubricated) and the choice of axial discretisation did not significantly affect the results.

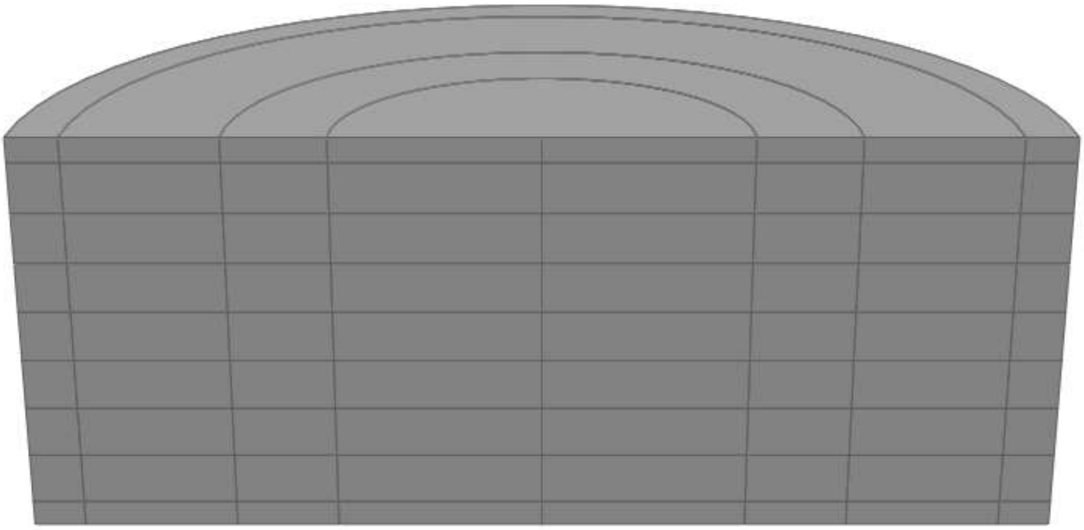

Figure 3-54 Discretisation of bentonite in the 1a02 QPAC model.

3.8.2 Input parameters

The two ILC parameters were calibrated to the swelling pressure versus dry density data provided (Figure 3-55). Otherwise, the material parameters are unchanged from those used in the model originally developed in DECOVALEX-2015, with the exception of a simplification of the intrinsic permeability. The dry density dependence of the intrinsic permeability has been removed as the lookup curve used in DECOVALEX-2015 was not general. In reality, there is likely to be some permeability dependence on dry density; a relationship for MX-80 bentonite should be used in future models.

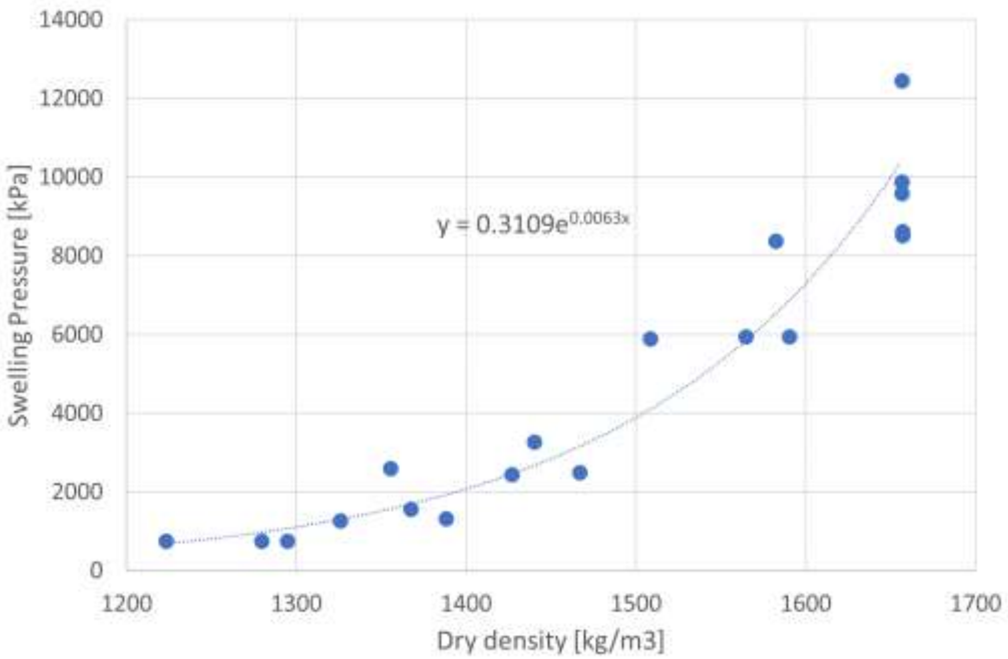

Figure 3-55 Swelling pressure versus dry density data from Dueck et al 2011, and 2014 (taken from Fig 3-6 of specification) with fitted exponential curve.

A summary of all the material parameters used is given in Table 3-16. The same parameters are used for all of the WP5 Task 1 tests.

Table 3-16 List of MX-80 parameters used in the WP5 models

Parameter	**Value**
Bentonite unit mass [Mg/m^3]	2.78
Poisson's ratio [-]	0.27
Bulk modulus at zero stress [MPa]	50
Bulk modulus scaling factor with stress [-]	30
ILC α [kPa]	0.3109
ILC $1/\beta$ [m^3/Mg]	6.3
Reference vapour diffusivity [m^2/s]	1 x 10^{-32}
Intrinsic permeability [m^2]	7.5 x 10^{-21}

3.8.3 Initial and boundary conditions

Test1a01

The initial conditions prescribed for the model consist of initial dry density, initial water content and initial stresses.

Table 3-17: Initial conditions used in the 1a01 model.

Initial Condition	Value
Initial dry density [kg/m³]	1655
Initial water content [wt%]	13
Initial stress (r, θ, z) [MPa]	0, 0, 0

The initial dry density was chosen to be the reported 1655 kg/m³ rather than the suggested 'adjusted' 1631 kg/m³ as the swelling pressure data indicate pressures up to 10 MPa, and this would not be possible in our model if the initial dry density were 1631 kg/m³ (as can be seen from Figure 3-55*).*

The bottom and side boundaries are both modelled as roller boundaries with no flow conditions. Friction between the bentonite and the container walls is neglected since the surfaces in the experiment were lubricated.

The top boundary has a constant water pressure of 0.102 MPa, i.e. a water pressure of 2 kPa above atmospheric pressure. The mechanical boundary conditions on the top boundary are specified stress. Stress perpendicular to the boundary is given by:

$$\sigma_{zz} = \begin{cases} \max\left(\dfrac{w}{1[\mathrm{mm}]} * 1[\mathrm{GPa}], 0[\mathrm{GPa}]\right) & \text{for } t < 360 \text{ [days]} \\ \max\left(\dfrac{w - 2.9[\mathrm{mm}]}{1[\mathrm{mm}]} * 1[\mathrm{GPa}], 0[\mathrm{GPa}]\right) & \text{for } t > 360 \text{ [days]} \end{cases}$$

where σ_{zz} is the vertical stress on the boundary and w is the z-component of the boundary displacement. This boundary condition acts as a zero-displacement condition during the first 360 days and then displacement up to 2.9 mm is allowed.

TEST1a02

The initial conditions prescribed for the model consist of initial dry density, initial water content and initial stresses.

Table 3-18: Initial conditions used in the 1a02 model.

Initial Condition	Value
Initial dry density [kg/m³]	1666
Initial water content [wt%]	23.7
Initial stress (r, θ, z) [MPa]	0, 0, 0

The bottom and side boundaries are both roller boundaries with no flow conditions.

The top boundary has a constant water pressure of 0.1 MPa, i.e. atmospheric pressure. The mechanical boundary conditions on the top boundary are specified stress. Stress perpendicular to the boundary is given by:

$$\sigma_{zz} = \max\left(\frac{w - 10\ [\mathrm{mm}]}{1[\mathrm{mm}]} * 1[\mathrm{GPa}], 0[\mathrm{GPa}]\right)$$

where σ_{zz} is the vertical stress on the boundary and w is the z-component of the boundary displacement. This boundary condition acts as a zero-displacement condition after 10 mm of displacement.

3.8.4 Results/discussion

TEST1a01

The evolution of total axial and radial stress in the bentonite is shown in Figure 3-56 and Figure 3-57 respectively. The general trends are well-captured by the model; both the data and model results shown an initial build-up of stress which drops once the bentonite is allowed to expand, before increasing again once the void space is filled.

The equilibrium values of axial and radial stress are reasonably well-predicted by the model, for both stages of the experiment. An axial stress of 2.3 MPa is predicted at the end of the second swelling phase compared to a measured value of 2.6 MPa, although the model does not reach this equilibrium value until about 30 days after the end of the experiment. In general, the model cannot reproduce the transient behaviour of the bentonite as well as its final state.

The model predicts a rapid initial build-up in axial swelling pressure, which is much more gradual in the data. The second swelling phase is reproduced more successfully, although there is a delay in the axial stress build-up which is not present in the data. This is discussed further under the 1a02 results, where the same effect is visible.

The experimental data also shows an initial plastic 'collapse' in radial swelling pressure which is not reproduced in the model, although the model does show similar behaviour in the second swelling phase.

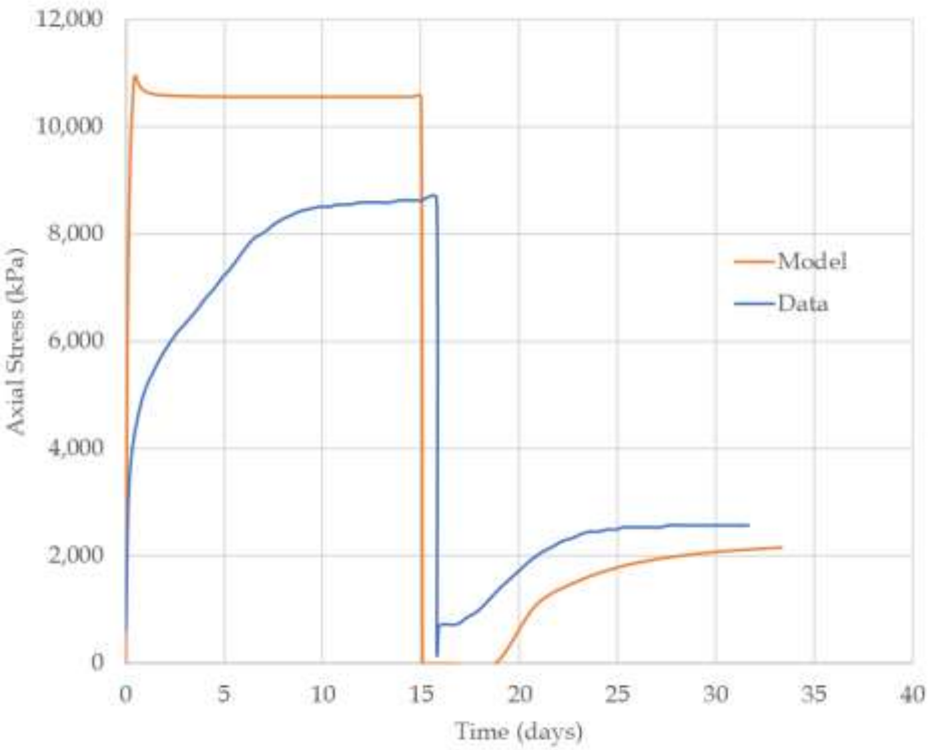

Figure 3-56: Total axial stress evolution through time in the 1a01 experiment, compared with modelled results.

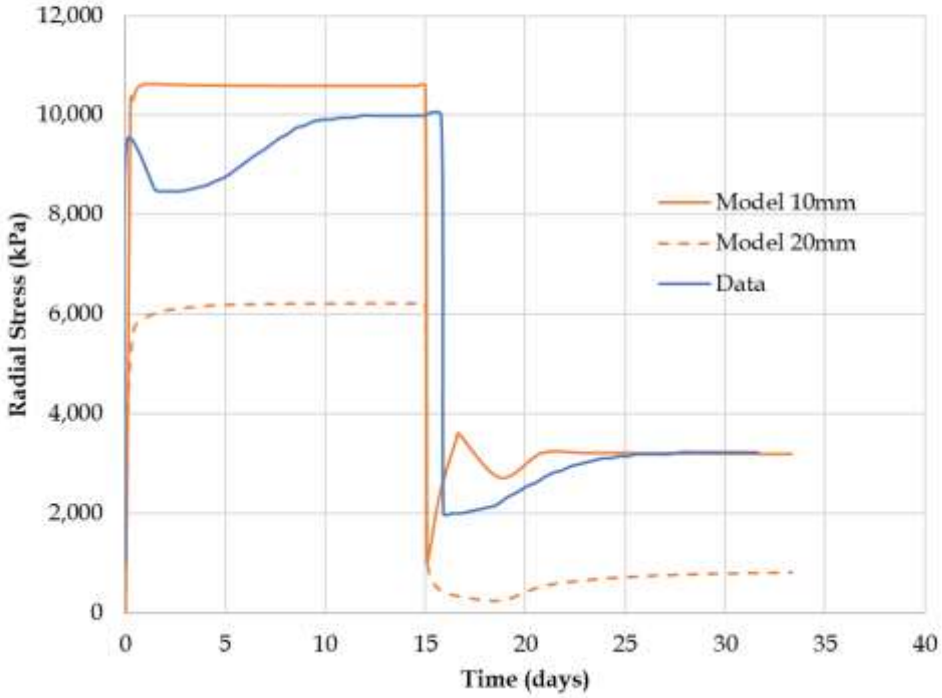

Figure 3-57: Total radial stress evolution through time in the 1a01 experiment, compared with modelled results.

Profiles of the final void ratio and water content against height are shown in Figure 3-58 and Figure 3-59.

The void ratio and water content trends are generally well-predicted by the model but with a systematic offset. The fit would be closer if the lower 'adjusted' value of initial dry density had been used in the model. This was not done as it would limit the maximum swelling pressures achievable in the bentonite. The model shows a decrease in void ratio at the top of the bentonite but since there is no data at this height, it is not clear whether this is a real phenomenon.

The ILM does not limit saturations strictly to < 1; there is an exponential relationship between suction and water content, so suction does not reach exactly zero when the bentonite is fully saturated. As discussed previously, there is some evidence that water density in bentonite inter-layers may exceed the reference value, which would support this approach. However, in this model, saturations of up to 1.4 are reached at the very top of the bentonite (they remain closer to 1 elsewhere). This does not appear to be realistic behaviour. Further work is needed to explore and constrain the behaviour of the ILM at low suctions as the fit to data is known not to be as good in this region (see Figure 2-4).

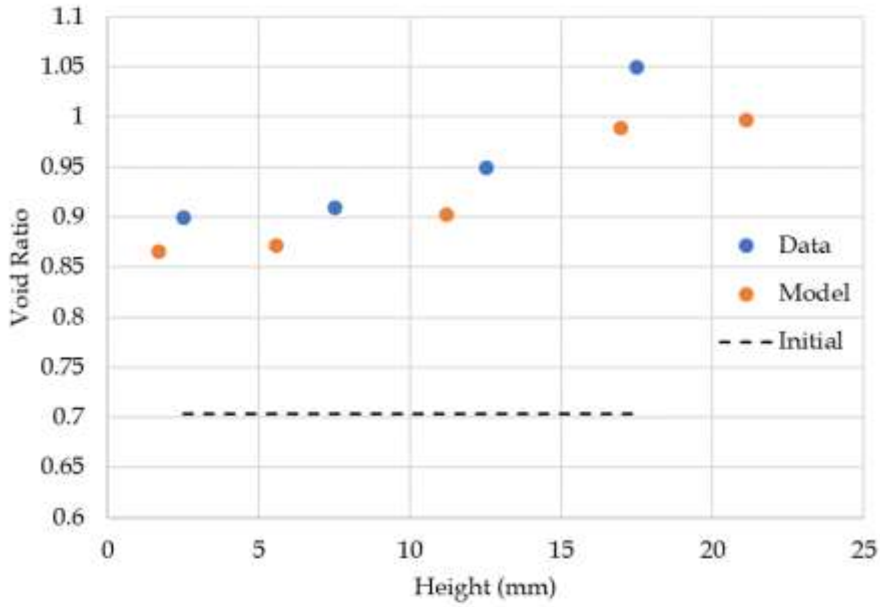

Figure 3-58: Profile of the final bentonite void ratio at different heights within the sample, for the 1a01 experiment.

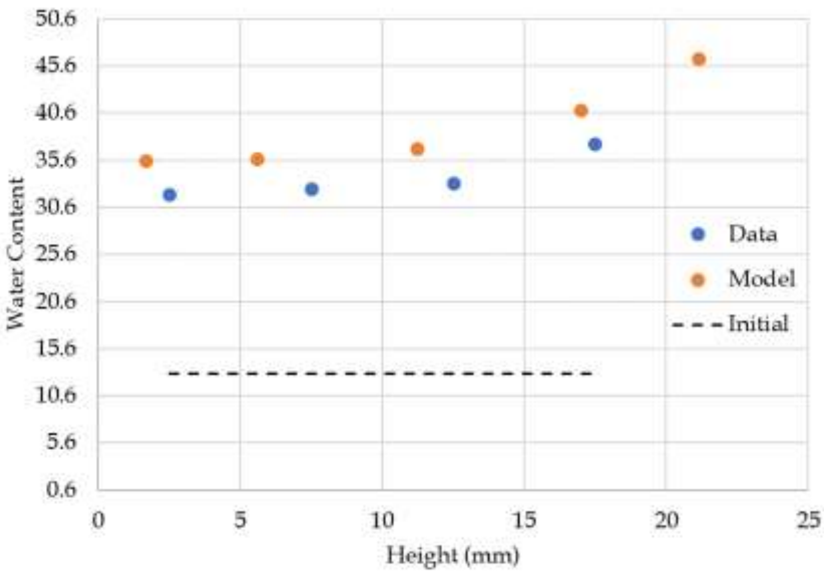

Figure 3-59: Profile of the final water content at different heights within the sample, for the 1a01 experiment.

TEST1a02

The evolution of total axial and radial stress in the bentonite is shown in Figure 3-60 and Figure 3-61 respectively.

The axial stress behaviour is similar to that of 1a02 when bentonite is allowed to swell into a void. The model predicts a large delay before stress builds up in the bentonite whilst the material freely swells into the void, whereas the experimental data shows almost instantaneous build-up of stress. Using a higher bentonite permeability reduces the time before stress build-up, but also changes other aspects of the bentonite behaviour.

This discrepancy may be due to the way in which the boundary condition is represented in the model; there is no resistive force at the top of the bentonite until the bentonite has swelled to reach the top boundary. In the experiment, the void space quickly fills with water, and in similar experiments the highly-saturated bentonite at this boundary has been observed to interact with the water to form a 'gel' rather than separate liquid and solid porous medium phases. In the first 3 days of the experiment, there is no observed stress buildup; this may be the period when gel is forming. From 3 to 16 days, there is an approximately linear increasing stress phase. By shifting the modelled results forward by 44 days, a reasonable fit to the rest of the experimental data can be obtained. Further work will be done to explore the bentonite behaviour during the initial linear stress phase.

Again, the final radial swelling pressures predicted by the model are close to the experimental data, but the transient behaviour is not as well captured. There are large peaks predicted in the radial stress which are much lower in the data. Further improvements may need to be made to the ILM to improve the distribution of stress between axial and radial directions, as radial swelling pressure data was not available for the experiments for which the ILM was initially developed.

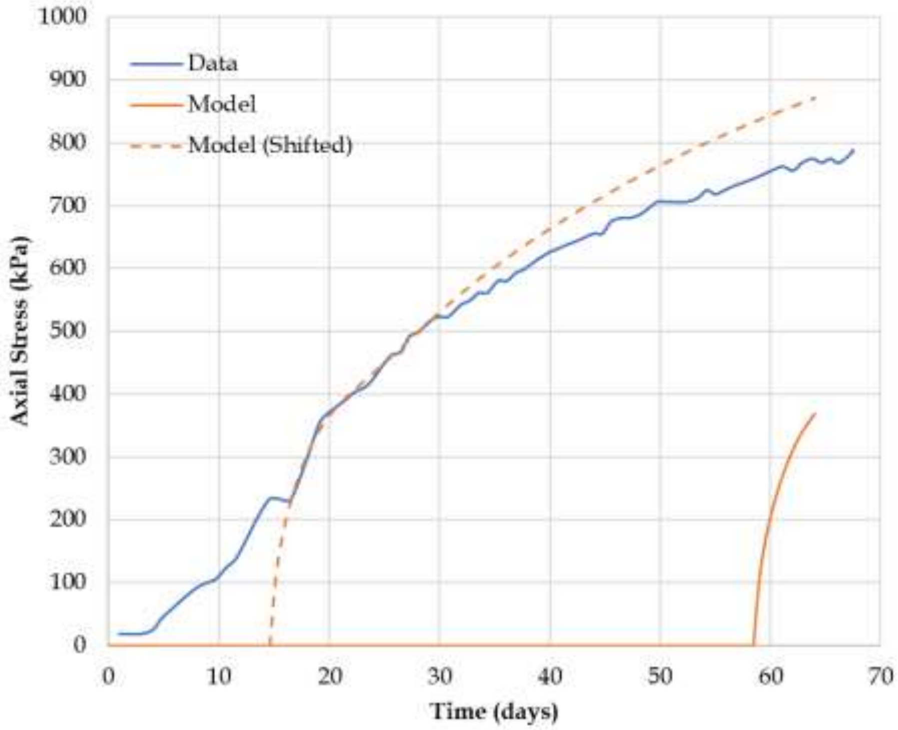

Figure 3-60: Total axial stress evolution through time in the 1a02 experiment, compared with modelled results (and model results 'shifted' forward in time by 44 days).

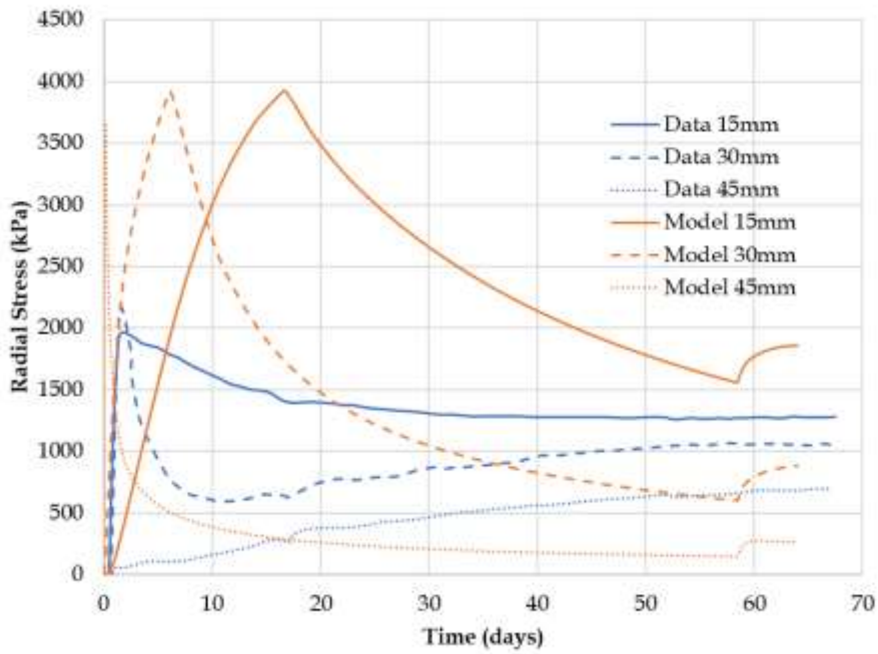

Figure 3-61: Total radial stress evolution through time in the 1a02 experiment, compared with modelled results.

Profiles of the final void ratio and water content against height are shown in Figure 3-62 and Figure 3-63.

The void ratio and water content are generally well-predicted by the model. Again, water saturations exceed 1 at the top of the bentonite.

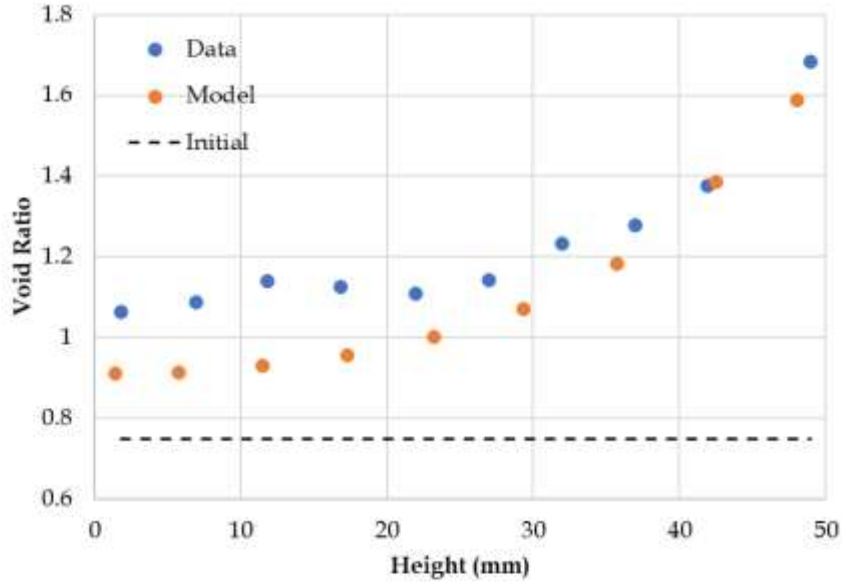

Figure 3-62: Profile of the final bentonite void ratio at different heights within the sample, for the 1a02 experiment.

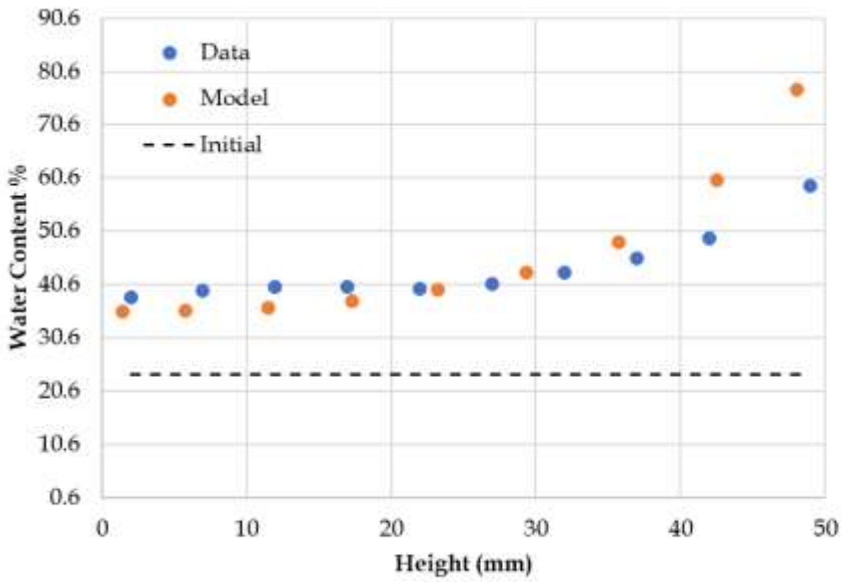

Figure 3-63: Profile of the final water content at different heights within the sample, for the 1a02 experiment.

3.9 SKB

Only Test1a02 has been modelled. Parameters, discretization and boundary conditions are related to this test.

3.9.1 Geometry and discretization

The numerical bentonite sample is divided by 25 elements in axial direction

3.9.2 Input parameters

Hydraulic parameters
A dependency of dry density on permeability coefficient is introduced (see Figure 3-64).

$$k = k_0 \left(\frac{e}{e_0} \right)^{\lambda_k}$$

e_0=0.669
k_0=4.48 10^{-15} (m/s)
λ_k=10

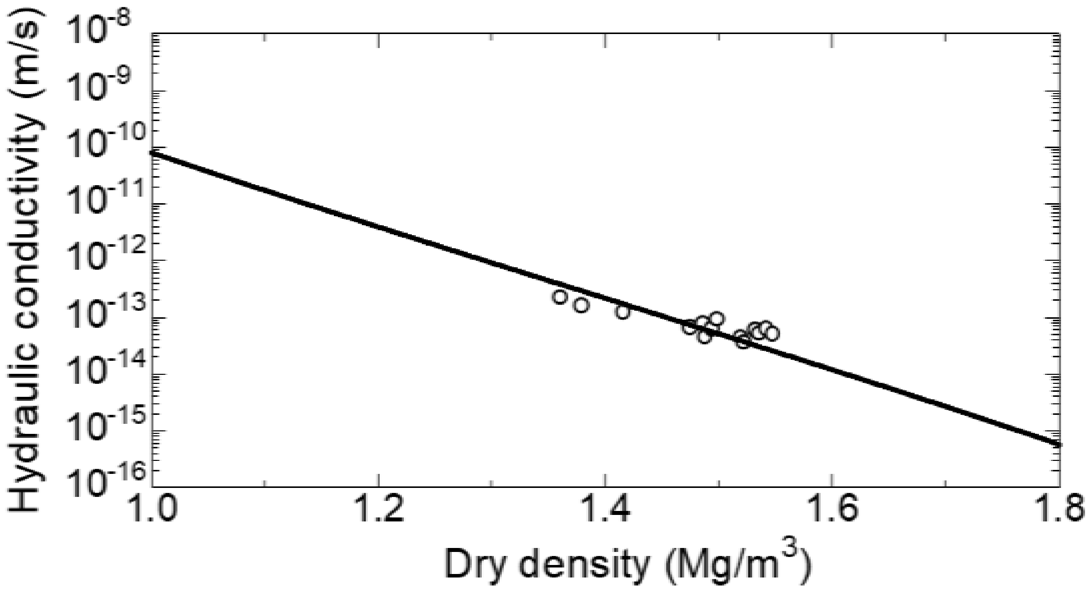

Figure 3-64 Hydraulic conductivity function of dry density

Mechanical parameters
Cam-clay model with plastic swelling concept was used in constitutive modelling of bentonite mechanical property (Figure 3-65)

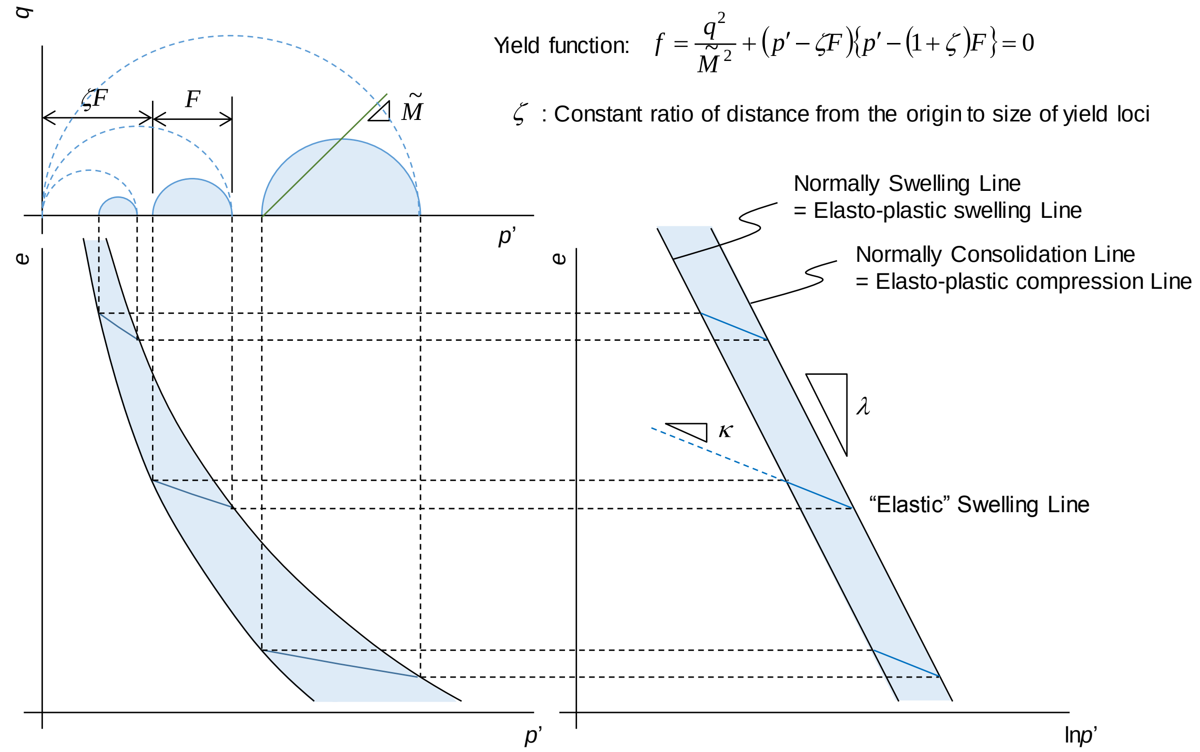

Figure 3-65 Cam-clay with plastic swelling

Parameters used for the Cam-Clay model are given below.

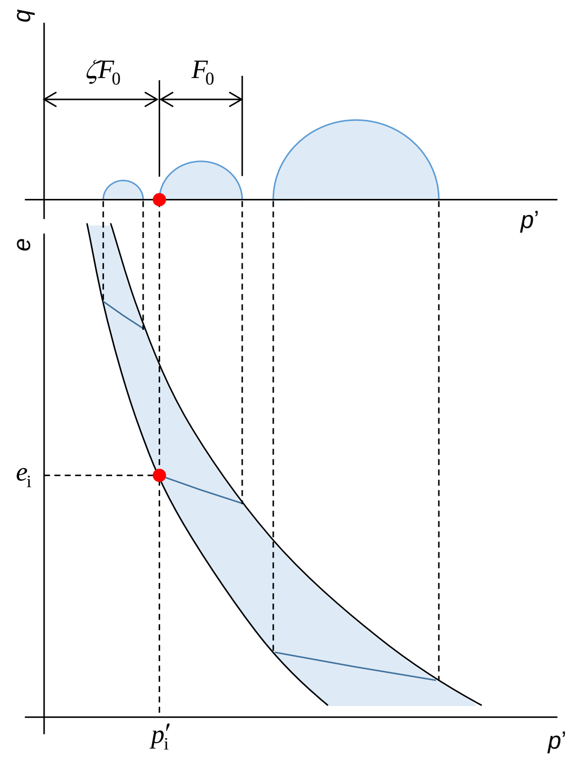

Initial values assumed in the calculation

Void ratio: $e_i = 0.669$

Effective mean stress: $p'_i = 13.0\ \mathrm{MPa}$

Size of yield loci $F_0 = 9.29\ \mathrm{MPa}$

Input parameters used in the calculation

Compression index: $\lambda = 0.150$

Swelling index: $\kappa = 0.150$

Shape parameter: $\tilde{M} = 1.0$

Poisson's ratio: $\nu' = 0.339$

Yield loci parameter: $\zeta = 1.4$

(Additional parameter to Cam-clay)

3.9.3 Initial and boundary conditions

- Displacement only in axial direction is allowed except for nodal points at bottom. If the displacement of nodal points at top surface reaches 10 mm after swelling, no more displacement is allowed.
- Only at top boundary, inflow of water is allowed by setting the water pressure. While the water pressure was initially set to be -13 MPa, it was risen up to 0 MPa in a short time and then kept to be constant until a stable condition (Figure 3-66).

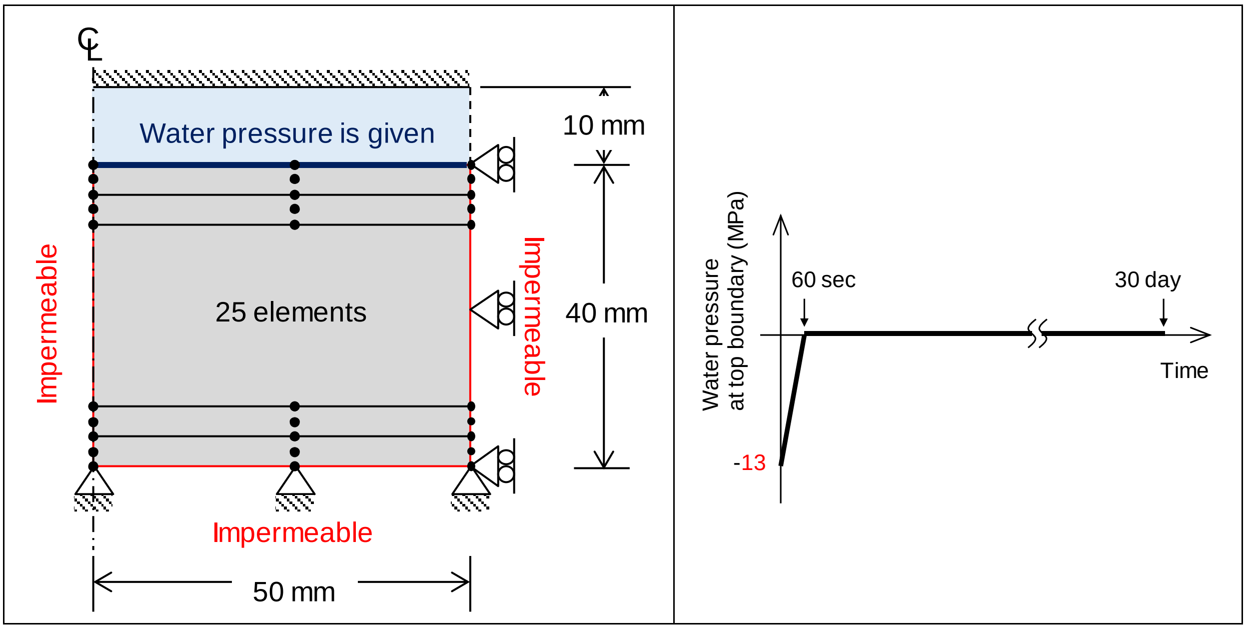

Figure 3-66 Boundary conditions for test1a02

3.9.4 Results

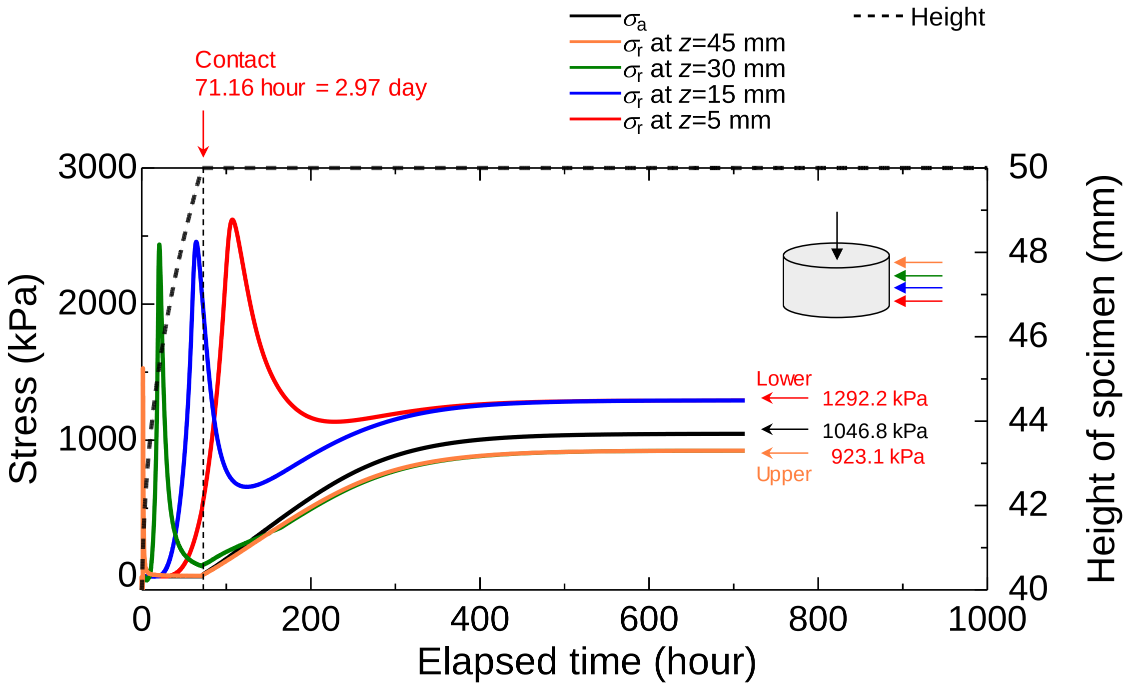

Figure 3-67 Changes in stress against time

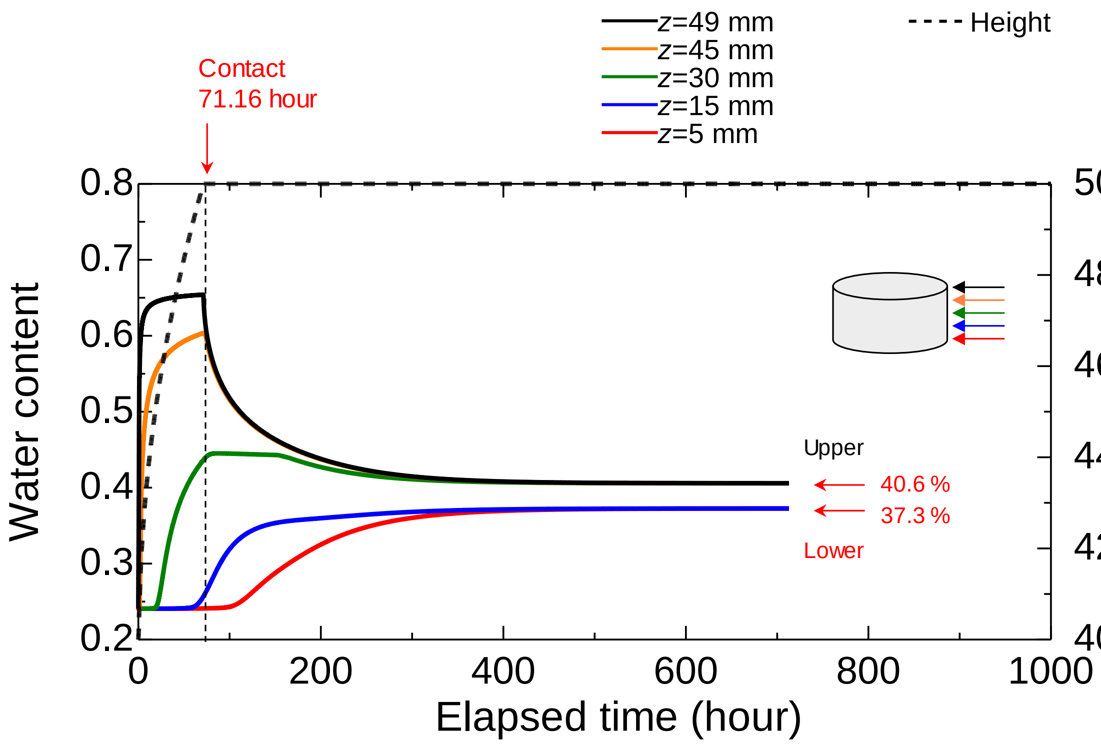

Figure 3-68 Changes in water content against time

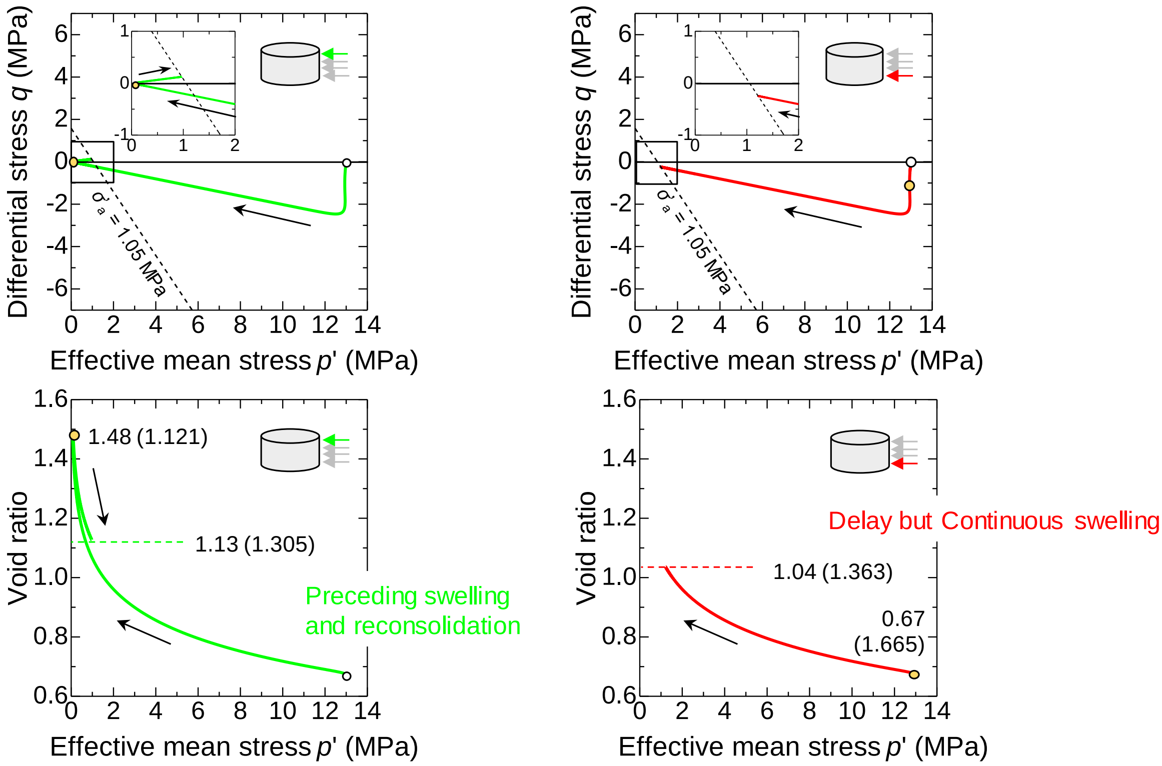

Figure 3-69 Comparison in effective stress – void ratio path between Upper and Lower parts

3.10 ULG

The finite element code Lagamine is used in order to simulate a swelling pressure test at constant volume followed with an increase of volume on a bentonite plug. The Barcelona Basic Model and the double porosity model are adopted for the mechanical and hydraulic part respectively given their robustness for the modelling of swelling soils

3.10.1 Geometry and discretization

TEST1a01

The bentonite sample consists in 50 eight-noded isoparametric elements.

In order to represent the moving piston and the water flux, a 3-nodes-zero-thickness interface element is used (Dieudonnè, 2016) (red line Figure 3-64)

The problem is assumed monodimensional and oedometer conditions are considered.

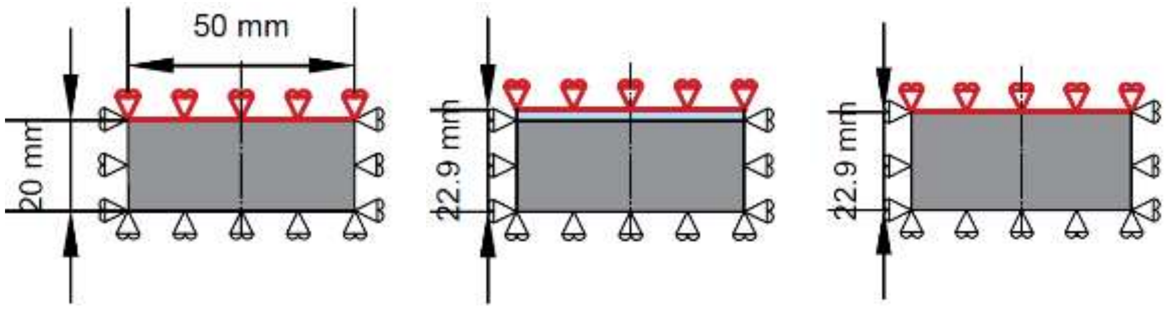

a. *Initial confined conditions*

b. *Free swelling conditions*

c. *Final confined conditions*

Figure 3-70 Schematic representation of boundary and initial conditions

The numerical simulation consists in 2 phases:

1. In the first part, the interface element is fixed at 20 mm from the bottom of the sample. Initial contact with the bentonite plug is assumed and a 2 kPa water pressure is imposed at this placed.
   Hence, the material is allowed to hydrate and to develop a swelling pressure (Figure 3-64-a).
   This first phase is concluded after 360 hours.
2. At the beginning of the second phase, the interface element is displaced instantaneously to the new position (Figure 3-64-b).
   As the simulated hydration process continues, the free swelling of the material occurs until the top plate is reached (Figure 3-64-c).
   At this point, a swelling pressure is developed.

TEST1a02

The bentonite sample consists in 81 eight-noded isoparametric elements.

In order to represent the moving piston and the water flux, a 3-nodes-zero-thickness interface element is used (Dieudonnè, 2016) (red line Figure 3-65)

The problem is assumed monodimensional and oedometer conditions are considered.

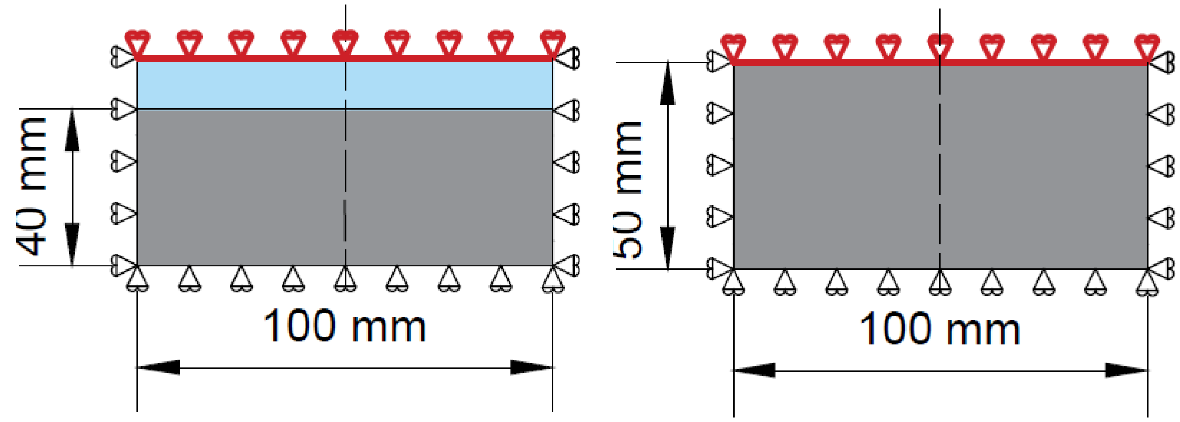

a. Free swelling saturation phase *b. Confined condition saturation phases*

Figure 3-71 Schematic representation of boundary and initial conditions

The numerical simulation consists in 2 phases:

1. In the first part, the free swelling phase takes place. The bentonite plug is hydrated at a 2 kPa water pressure from the top. Since there is no contact with the top plate, the material swells freely in the axial direction (Figure 3-65-a).
   This first phase is concluded after 660 hours since the beginning of the computation time.
2. In the second phase, the contact between the sample and the top plate has occurred (Figure 3-65-b).
   The saturation process proceeds and swelling pressure is developed.
   The time of the contact (660 hours) is considered the time 0 for the present analysis.
   The simulation is stopped at 1600 hours after the contact.

3.10.2 Input parameters

TEST1a01

The material input parameters are presented.

The hydraulic parameters (Table 1) for the water retention behaviour and permeability evolution are based on literature (Dieudonnè, 2016).

Given an initial water content equal to 13% and, consequently, the 51.3% degree of saturation, the current model suggests 55 MPa as initial suction value.

The initial permeability value is chosen to best fit the experimental results.

Table 3-19 - Selected Hydraulic parameters-

ϱ_{di}	n	C_{ads}	n_{ads}	A	n	m	K_{w0}	e_{m0}	β_0	β_1
(Mg/m^3)		(MPa^{-1})		(MPa)			(m^2)			
1.631	0.413	0.0075	1.5	0.2	2	0.2	2.0E-21	0.31	0.1	0.48

The mechanical parameters r, ω, ν, $c(0)$, k and Φ are based on literature (Dieudonnè, 2016).
κ and κ_s values are selected consistently with the data suggested in SKB Report TR-10-44.
$\lambda(0) = 0.5$ is chosen in order to keep low the ratio $\frac{\kappa_s}{\lambda(s)-\kappa}$ which controls the stress path slope in the p-s plane, assuming κ and κ_s constant in the numerical model.
The pre-consolidation pressure in saturated conditions value is selected in order to best fit the experimental results (Table 2).

Table 3-20 – Selected mechanical parameters-

ϱ_{di}	κ	κ_s	$\lambda(0)$	p_0^*	p_c	r	ω	ν	$c(0)$	k	Φ
(Mg/m^3)				(MPa)	(MPa)		(MPa^{-1})		(MPa)		°
1.631	0.100	0.300	0.50	1.6	0.0036	0.8005	0.09	0.35	0.1	0.046	25

For the interface element 2 main coefficients are required for the current model:

1. A penalty coefficient for the mechanical part K=1*10^{10};
2. A transmissivity coefficient for the hydraulic part K=1*10^{-12}.

Those coefficients are selected in order to assure the numerical stability.

TEST1a02
The material input parameters are presented.
The hydraulic parameters (Table 1) for the water retention behaviour and permeability evolution are based on literature (Dieudonnè, 2016).
For the permeability evolution, Kozeny-Karman relation is used
Given an initial water content equal to 24% and, consequently, the 88% degree of saturation, the current model suggests 6 MPa as initial suction value.
The initial permeability value is chosen to best fit the experimental results.

Table 3-21 - Selected Hydraulic parameters-

ϱ_{di}	n	C_{ads}	n_{ads}	A	n	m	K_{w0}	e_{m0}	β_0	β_1
(Mg/m^3)		(MPa^{-1})		(MPa)			(m^2)			
1.590	0.428	0.0075	1.5	0.2	3	2	8.0E-21	0.31	0.1	0.48

The mechanical parameters r, ω, ν, $c(0)$, k and Φ are based on literature (Dieudonnè, 2016).
κ and κ_s values are selected consistently with the data suggested in SKB Report TR-10-44.

$\lambda(0) = 0.5$ is chosen in order to keep low the ratio $\frac{\kappa_s}{\lambda(s)-\kappa}$ which controls the stress path slope in the p-s plane, assuming κ and κ_s constant in the numerical model.

The pre-consolidation pressure in saturated conditions value is selected in order to best fit the experimental results (Table 2).

Table 3-22 – Selected mechanical parameters-

ϱ_{di}	κ	κ_s	$\lambda(0)$	p_0^*	p_c	r	ω	ν	$c(0)$	k	Φ
(Mg/m^3)				(MPa)	(MPa)		(MPa^{-1})		(MPa)		°
1.631	0.100	0.300	0.50	1.2	0.0036	0.8005	0.09	0.35	0.1	0.046	25

For the interface element 2 main coefficients are required for the current model:

1. A penalty coefficient for the mechanical part K=1*10^{12};
2. A transmissivity coefficient for the hydraulic part K=1*10^{-9}.

Those coefficients are selected in order to assure the numerical stability.

3.11 CU-CTU

3.11.1 Geometry and discretization

The test was simulated in a two-dimensional axysimmetric setup using a structured rectangular mesh. For test 1a01, a vertical node spacing of 1.25 mm and a horizontal spacing of 12.5 mm were chosen, so that 16 rectangular elements with 83 nodes in total (including secondary nodes) were obtained. For test 1a02, a vertical node spacing of 2 mm and a horizontal spacing of 25 mm were chosen, thus obtaining 20 elements with 103 nodes in total.

The first phase of test 1a01 was simulated under a constant volume condition by introducing a spring element with very high stiffness at the top boundary. To allow for swelling in the second phase of the test, the stiffness of the spring was reduced. This reduction was achieved gradually to prevent numerical instability. In test 1a02, the entire simulation was conducted at constant volume using a very stiff spring element.

3.11.2 Input parameters

The parameters of the hypoplastic model utilised in the simulation were calibrated from experimental results obtained on the Czech B75 bentonite, and are given in Table 3-23 below.

Table 3-23 Parameters of the hypoplastic model, calibrated on the Czech B75 bentonite

Critical state friction angle of the macrostructure	φ_c	25	°
Slope of the isotropic normal compression line in $\ln\left(\frac{p^M}{p_r}\right)$ versus $\ln(1+e)$ space	λ^*	0.13	
Macrostructural volume strain in p^M unloading	κ^*	0.06	
Position of the isotropic compression line in $\ln\left(\frac{p^M}{p_r}\right)$ versus $\ln(1+e)$ space	N^*	1.73	
Stiffness in shear	ν	0.25	
Dependency of the position of the isotropic normal compression line on suction	n_s	0.012	
Dependency of the slope of the isotropic normal compression line on suction	l_s	-0.005	
Dependency of the position of the isotropic normal compression line on temperature	n_T	-0.07	
Dependency of the slope of the isotropic normal compression line on temperature	l_T	0.0	
Control of f_u and thus of the dependency of the wetting-/heating-induced compaction on the distance from the state boundary surface; control of the double-structure coupling function and thus of the response to wetting-drying and heating-cooling cycles	m	1	
Dependency of microstructural volume strains on temperature	α_s	0.00015	K^{-1}
Dependency of microstructural volume strains on p^m	κ_m	0.07	
Reference suction of the microstructure	s_m^*	-2000	kPa
Reference microstructural void ratio for reference temperature T_r, reference suction s_m^*, and zero total stress	e_m^*	0.45	
Value of f_m for compression	c_{sh}	0.002	
Air-entry value of suction for the reference macrostructural void ratio e_0^M	s_{e0}	-2700	kPa
Reference macrostructural void ratio for the air-entry value of suction of the macrostructure	e_0^M	0.50	
Reference temperature	T_r	294	K
Dependency of macrostructural air-entry value of suction on temperature	a_t	0.118	
Dependency of macrostructural air-entry value of suction on temperature	b_t	-0.000154	
Ratio of air entry and air expulsion values of suction for the water retention model of the macrostructure	a_e	1.0	
Value of λ_p corresponding to the reference void ratio e_0^M in the water retention model of the macrostructure	λ_{p0}	0.7	

In addition, the density of the solids was set at $\rho_s = 2780\,\mathrm{kg\,m^{-3}}$, and an intrinsic permeability $K = 10^{-20}\,\mathrm{m^2}$ was assumed.

3.11.3 Initial and boundary conditions

In the simulation of test 1a01, an initial void ratio $e = 0.68$ and an initial suction $s = -100\,\mathrm{MPa}$ were assigned to all elements, with the clay density set at $2780\,\mathrm{kg\,m^{-3}}$. Temperature was fixed at $T = 294\,\mathrm{K}$. The lateral and bottom boundaries were set as impervious, while free access to water was provided from the top boundary with a 2 kPa head. In the first part of the test, all boundaries are fixed, with the top boundary being constrained by a spring with very high stiffness. In the second part of the test, the spring stiffness is reduced, gradually, to a very low value to permit a swelling of 2.9 mm as prescribed by the experimental procedure.

Differently from test 1a01, an initial suction $s = -3\,\mathrm{MPa}$ was assigned in the simulation of test 1a02. All boundaries were fixed and impervious, except for the top boundary through which free access to water was provided with a 2 kPa head.

3.11.4 Results/discussion

Modelling the changing top boundary (from a fixed boundary at z = 20 mm to a fixed boundary at z = 22.9 mm) was the most challenging technical aspect of the simulation. The issue was solved by introducing a very stiff spring element at the top of the sample, which worked effectively as fixed boundary first, and then as a non-fixed boundary by greatly reducing the stiffness in the phase in which swelling was permitted. Some convergence problems arose when the stiffness of the spring was suddently changed, which were solved by adapting the stiffness more gradually.

The simulation proved successful in capturing the swelling pressure in the first phase of test 1a01 both in the axial and in the radial directions (Figure 3-66a, b). A sudden increase of the pressure after ~220 days of simulation was observed in the preliminary runs of the simulation, caused by the chosen bilinear formulation of the water retention curve, which presents a discontinuity upon saturation. This has been resolved in subsequent simulations by adopting a smoothed formulation. In the second part of the simulation of test 1a02, the swelling pressures are underpredicted because the sample does not swell enough to reach the top boundary at its new location. The lower-than-expected swelling can be attributed to the isotropic deformation of the microstructure predicted by the hypoplastic model, which is inconsistent with the one-dimensional deformation in the experimental condition. Overcoming this issue is the object of current research. The smaller swelling capability of the model is reflected also in the results of test 1a02 (Figure 3-66c, d), which show swelling pressure developing later than expected in the axial direction, due to slower swelling, and remaining at smaller values than those measured experimentally. Similarly, in the radial direction, even though the time trend of the pressure could be captured with an appropriate choice of the value of permeability, the simulated values remained smaller than the measured ones at any time.

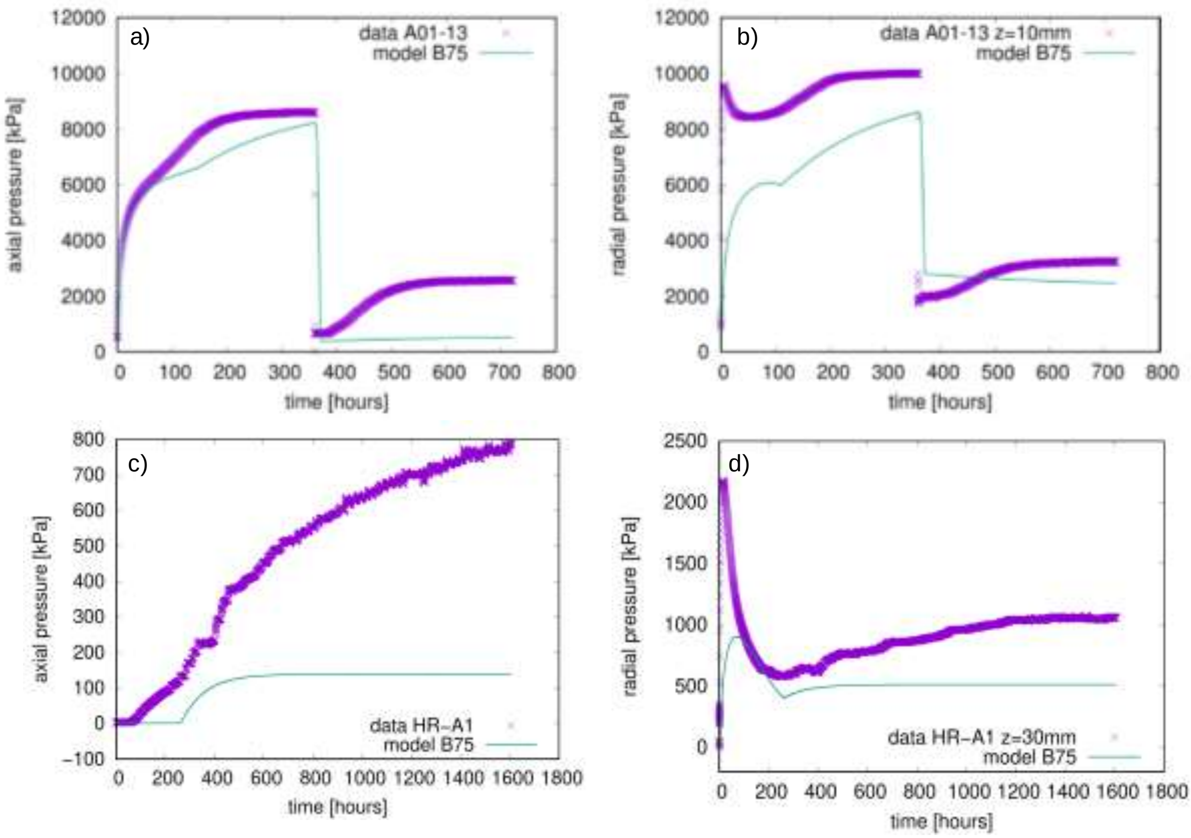

Figure 3-72 Summary of the results of test 1a: a) axial pressure, and b) radial pressure at 10 mm from the bottom of the sample in test 1a01; c) axial pressure, and d) radial pressure at 30 mm from the bottom of the sample in test 1a02.

3.12 VTT/UCLM

3.12.1 Geometry and discretization

3.12.2 Input parameters

3.12.3 Initial and boundary conditions

3.13 UPC

3.13.1 Geometry and discretization

Test 1a01

This test includes two stages: the first corresponds to the classic swelling pressure test at constant volume where both radial and axial stresses are measured. The second stage refers to a free swelling of the sample under hydration

The sample is cylindrical with a diameter of 50mm and a height of 20mm.

The problem has been discretized by an axisymmetric mesh with the same dimensions as the sample.

Test 1a02

Another swelling pressure test has been carried out with a larger device with 100mm diameter and 50mm height. A free swelling test is performed directly in the device due to the presence of a gap at the top of the sample.

The discretization used an axisymmetric mesh with the same dimensions as the sample.

3.13.2 Input parameters

Test 1a01

The material used for the sample is MX-80 bentonite powder. The powder is compacted into the intended density and geometry. The double structure node has been used to represent the behaviour of the material. The hydraulic and mechanical parameters are listed in Table 3-24 and Table 3-25.

Table 3-24 Hydraulic parameters

Hydraulic Model			
Constitutive law	Analytic expression	Parameter	Value
Retention curve	Van Genuchten's expression $S_e = \left(1 + \left(\frac{s}{P_0}\right)^{\frac{1}{1-\lambda}}\right)^{-\lambda}$	$P_0(MPa)$ λ	43.5(1) 0.48(1)
Intrinsic permeability	Kozeny's expression $k_j = k_0 exp^{b(\phi_j - \phi_0)}$	$K_0(m^2)$ ϕ_0 b	2.2e-21(1) 0.38(1) 8(1)
Relative liquid conductivity	Power law $k_r = A(S_e)^B$	A B S_{ls} S_{rl}	1(1) 3(1) 1(1) 0(1)
Leakage parameter	$\Gamma^w = \gamma(\Psi_1 - \Psi_2)$	γ (kg/s/m3/MPa)	4.0e-7(3)

Table 3-25 Mechanical parameters

Mechanical model BExM			
Constitutive law	Analytic expression	Parameter	Value
BBM Elastic part	$d\varepsilon_v^e = -\frac{\kappa}{1+e_M}\frac{dp}{p} - \frac{\kappa_s}{1+e_M}\frac{ds}{s+p_{atm}}$	κ κ_s	0.12(1) 0.03(1)
Yield locus	$p_0 = p_c\left(\frac{p_0^*}{p_c}\right)^{\frac{\lambda_{(0)}-\kappa}{\lambda_{(s)}-\kappa}}$ $\lambda(s) = \lambda(0)\,(r + (1-r)e^{-\beta s})$	$p_0^*(MPa)$ $p_c(MPa)$ r $\lambda(0)$ $\beta(MPa^{-1})$)	10(3) 0.5(3) 0.6(3) 0.15(3) 0.2(3)

BExM Microstructure	$K_m = \dfrac{1+\overline{e_m}}{\kappa_m}\hat{p}$	κ_m	0.06(3)
Interaction function	$f_s = f_{s0} + f_{si}\left(1 - \dfrac{p}{p_0}\right)^{ns}$	f_{s0} f_{si} n_s	-2 1(3) 2.5(3)

TEST1a02

The same parameters as in test 1a01 are used with the exception of the water retention curve. As the initial degree of saturation is very high, a modified curve is used in this test in order to reproduce a large initial suction. The modified water retention curves are plotted in Figure 3-67.

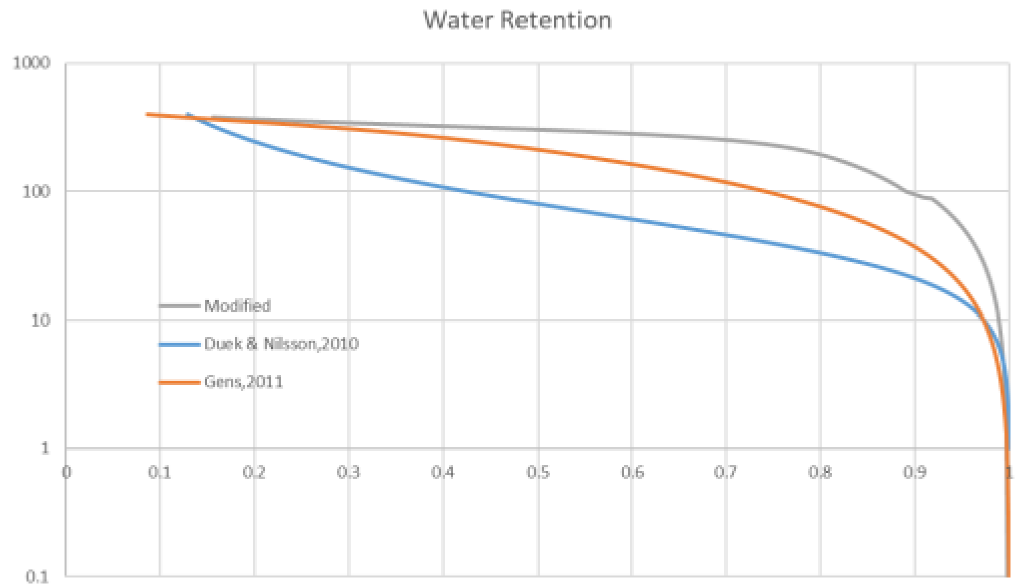

Figure 3-73 Water retention curves

3.13.3 Initial and boundary conditions

Test 1a01

The initial conditions of the sample are presented in Table 3-26 and Table 3-27.

Table 3-26 initial properties of the sample

Test 1a01	Radius(mm)	Height(mm)	Dry density (kg/m³)	Water content(%)	Particle density (kg/m³)
	25	20	1655	13	2780

Table 3-27 Initial conditions

Total porosity	Micro porosity	Macro porosity	Macro Suction (MPa)	Micro Suction (MPa)
0.40	0.24	0.16	55	80

The boundary conditions of the first stage corresponds to that of a standard swelling pressure test. For the second phase, a bilinear elastic model represents the behaviour of the gap (Figure 3-68). The model ensures a very soft material before the gap is closed; subsequently, a very large stiffness is set. Hydraulic (constant water pressure) conditions are applied at the top of the sample.

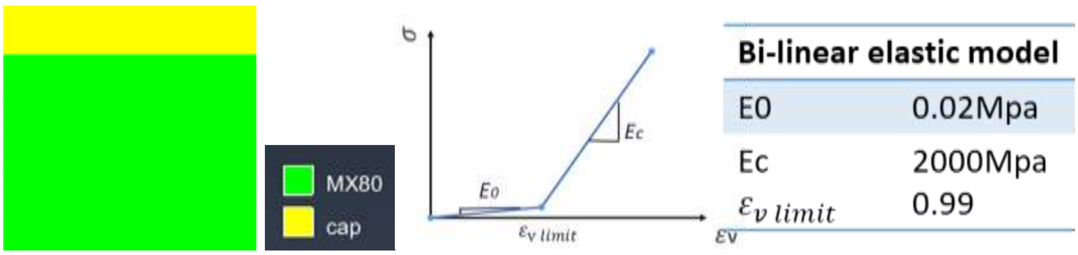

Figure 3-74 Material plot of the test and the corresponding parameters for the gap material

Test 1a02

The initial water content of 23.7% corresponds to an initial suction of 13 MPa. The initial properties of the sample are listed in Table 3-28 and Table 3-29.

Table 3-28 Initial properties of the sample

Initial w (%)	Initial density(kg/m³)	Constant Radius (mm)	Initial height (mm)	Final height (mm)
23.7	1666	50	40	50

Table 3-29 Initial conditions of the sample

Total porosity	Micro porosity	Macro porosity	Macro Suction (MPa)	Micro Suction (MPa)
0.40	0.24	0.16	13	13

The boundary conditions correspond to the fixed displacements of a swelling pressure test. Constant water content is prescribed at the top of the sample. The gap material is modelled in the same way as described on Figure 3-68.

3.13.4 Results/discussion

TEST1a01

The results of the distribution of water content, dry density, void ratio in the final state are presented and compared with the experiment results in the following figures.

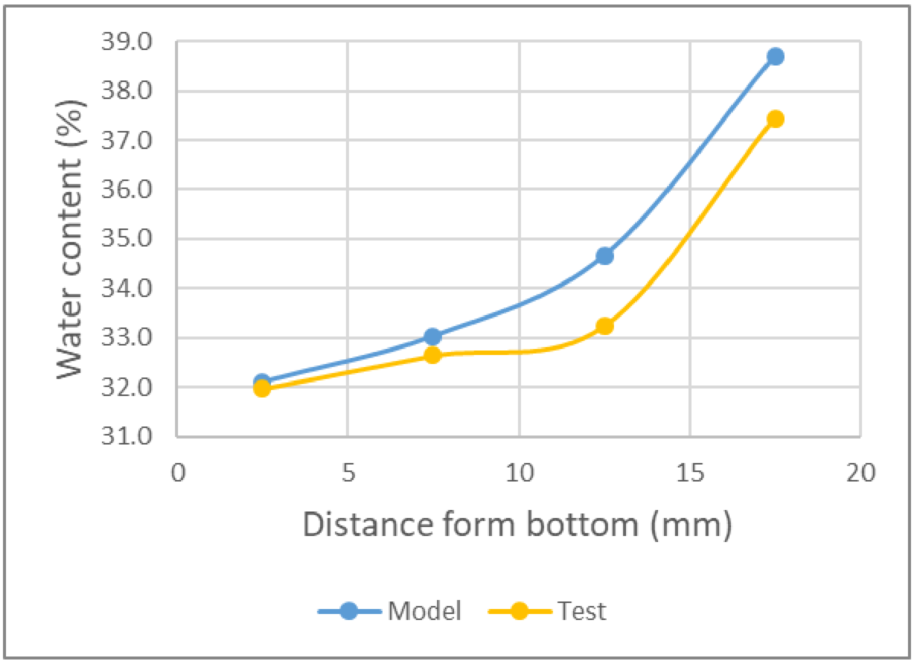

Figure 3-75 Distribution of water content along specimen height

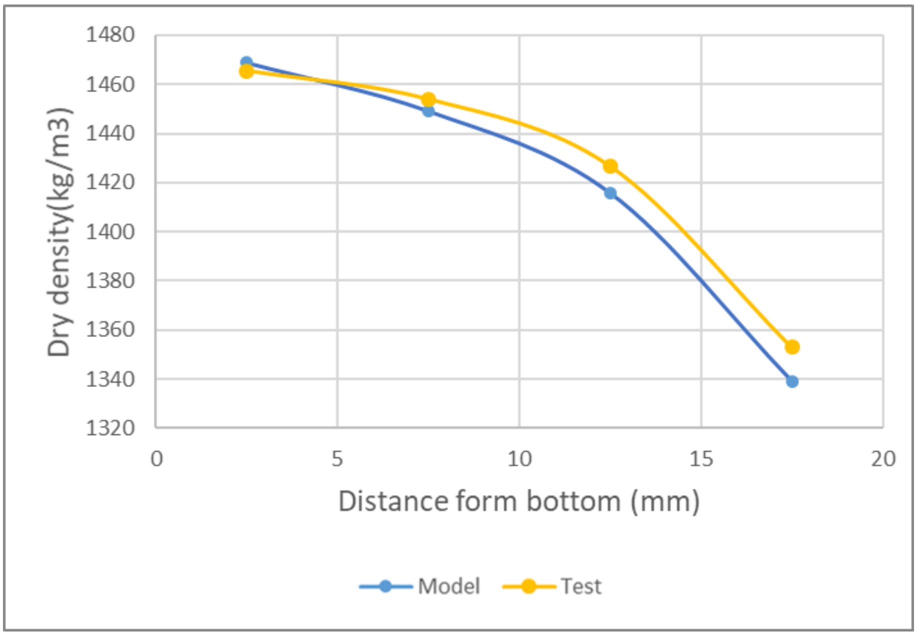

Figure 3-76 Distribution of dry density over specimen height

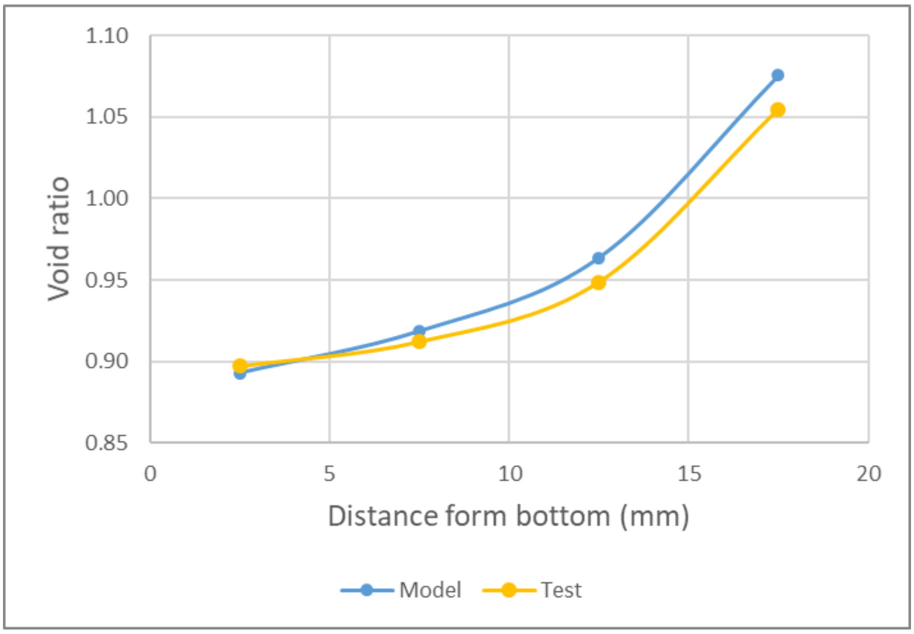

Figure 3-77 Distribution of void ratio over specimen height

It can be noted that the final state is well reproduced from the numerical model. Dry density reduces with height because of the large swelling developed in this region that it is not fully recovered. As the sample is totally saturated, the water content follows the dry density distribution.

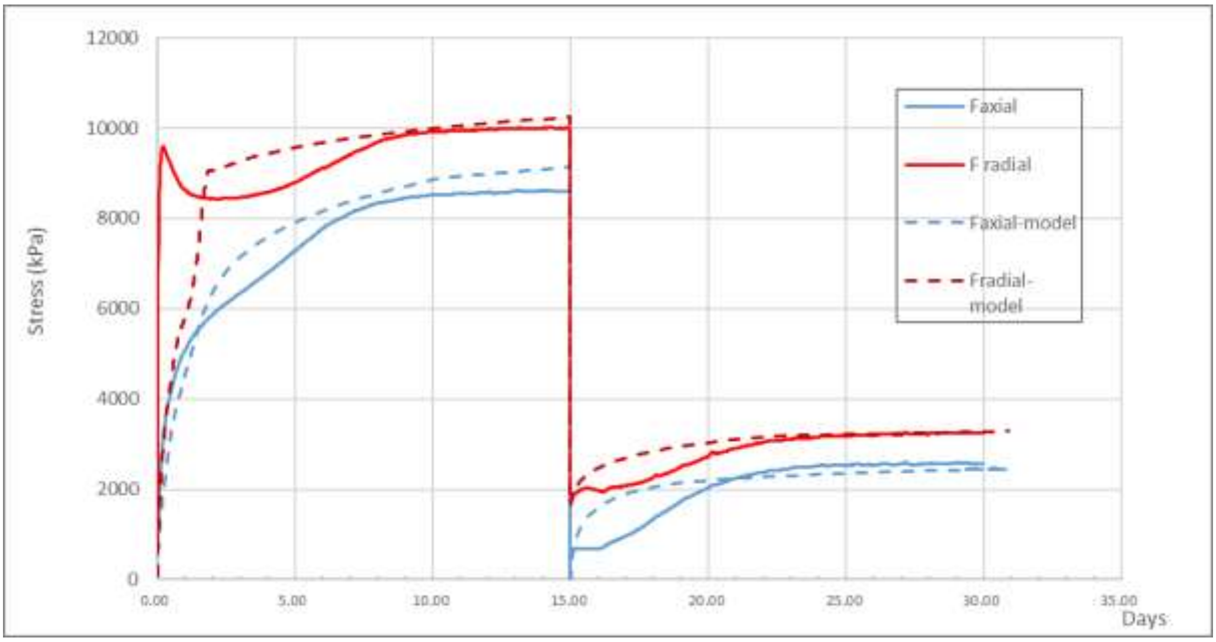

Figure 3-78 Time evolution of the swelling stress. Solid lines are observations and dashed lines are modelling results

The swelling stress results are collected in Figure 3-72. During the first phase, stresses develop under constant volume conditions. As a result, the stresses reach a very high value, up to 10 MPa. The radial stress is higher with a peak at the beginning. From the simulation, the trend of both radial stress and axial stress correspond well to the test and the final stresses reach about the same level. However, there is no computed peak at the beginning because the swelling developed more progressively in the numerical model. When the upper piston is withdrawn, the axial stress decreases directly to zero but there is a residual radial stress around 1.8 MPa. The evolution of computed stresses and their final value are similar to observations in this second stage.

TEST1a02

The axial displacement of the top of the sample is shown in Figure 3-73. It can be observed that displacement ceases when the sample reaches the top cap and the gap is closed.

Figure 3-79 Contour plot and time evolution of the axial displacement

Radial swelling stresses at the three heights and the axial swelling stress are shown and compared with observations in Figure 3-74. A rather satisfactory agreement is obtained including the peaks in the early development of radial stresses.

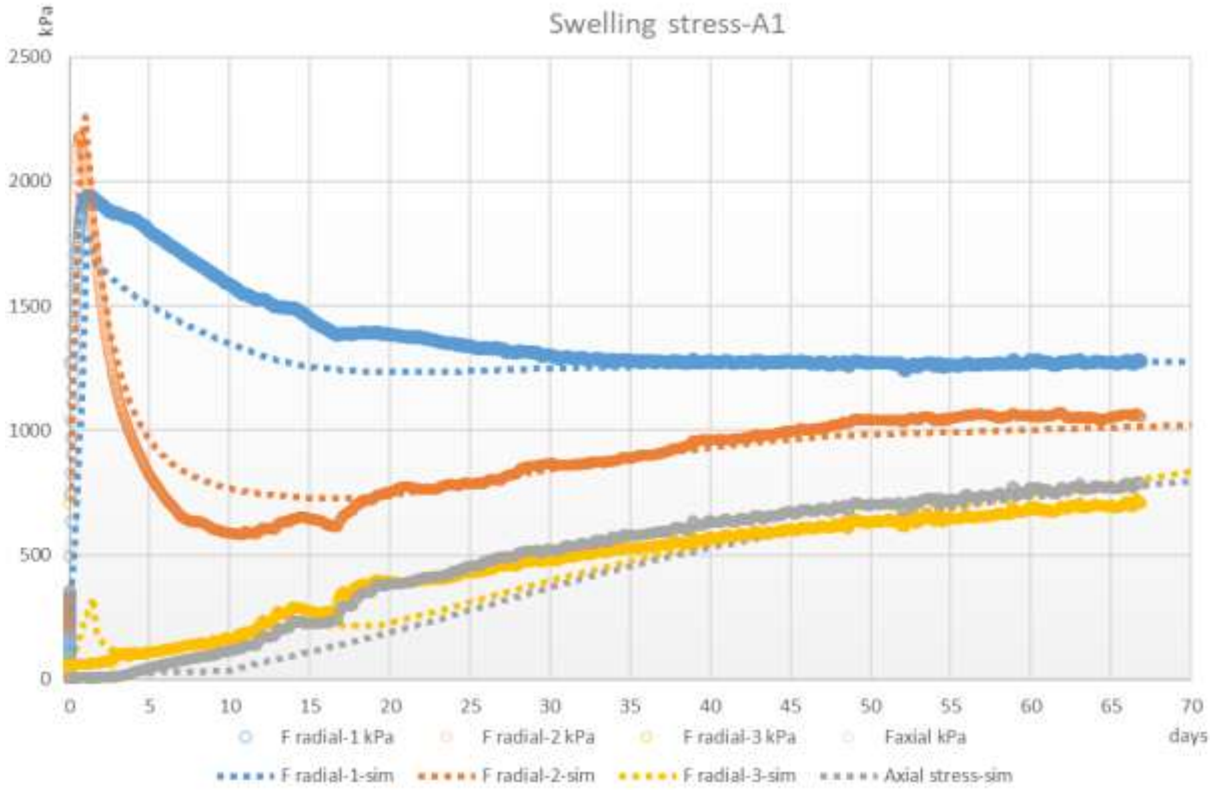

Figure 3-80 Time evolution of the swelling stresses. Solid lines are observations and dashed lines are modelling results

Distributions of water content, void ratio and dry density at the end of the test are shown in Figure 3-75 to Figure 3-77 together with the experimental results.

The general trend of the results is well captured although some quantitative differences can be noted. As the specimen is saturated, dry density and water content distributions are directly related.

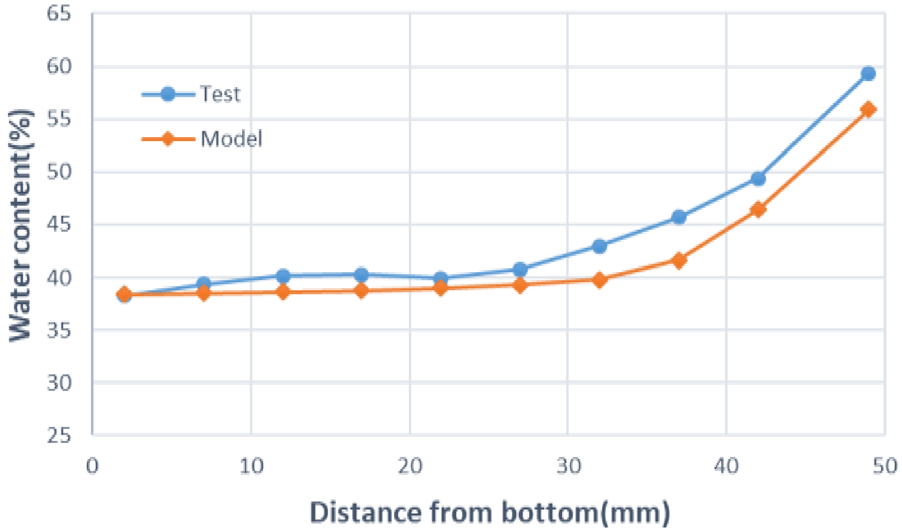

Figure 3-81 Distribution of water content along specimen height

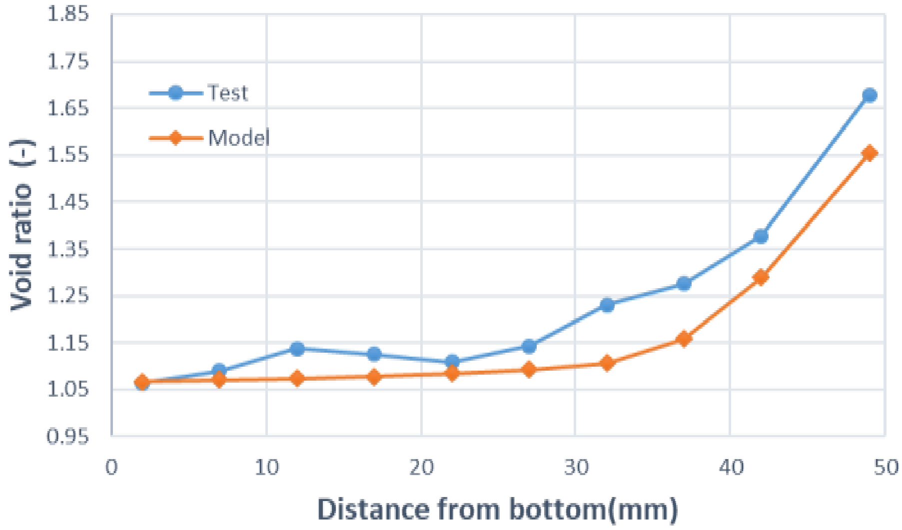

Figure 3-82 Distribution of void ratio along specimen height

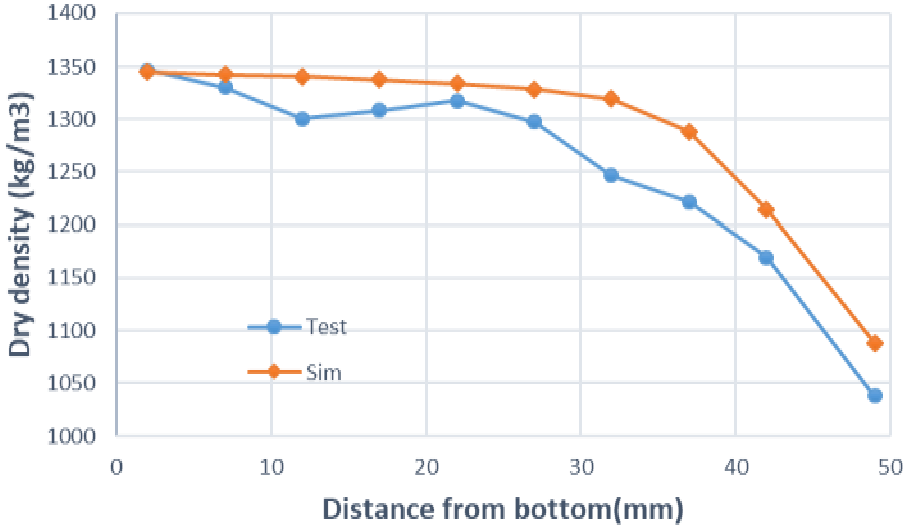

Figure 3-83 Distribution of dry density along specimen height

3.14 Synthesis of results test 1a

A comparison between all the results obtained by the participants have been made on several quantities. The comparisons are built to show where are the difficulties encountered by the models and what is well captured by them.
Several points of view are retained for the analysis:

- An analysis in relation with the main indicators for the repository applications: how the model deals with the homogenisation of the material after full saturation? Is the swelling pressure in the range of what it is expected at the end? Are the characteristic times well reproduced by the model?
- An analysis in relation with the capacity of the model to reproduce the different physical processes. Is it possible to identify the strengths and the weaknesses of each model?
- The boundary and initial conditions play an important role in the simulation. Was it necessary to accommodate the specified values given in the test description?

The idea of this comparison is not to make a ranking but really try to identify where to improve the models in link with WP3.
Another aspect is to compare the parameters used by the different groups. Some arguments will be proposed to explain the differences and if some specific experiments are needed in link with WP4.

3.14.1 Results test1a01

3.14.1.1. *Axial and radial pressure*

On Figure 3-78, simulated axial pressure evolutions are compared with the measurement. It can be seen that most of the models reproduce very well the swelling pressure reached at the end of the first stage. This first stage correspond to a classical swelling pressure test at constant volume for a homogeneous block. Nevertheless, the way to reach this swelling pressure is not unique and the results show a certain dispersion. As often, the transient phase of bentonite saturation tests is difficult to reproduce with models.
In the second phase of the test, a void is introduced of the top of the sample. This test is interesting in link with the situation encountered in repository with the technological voids. The final swelling pressure is less well reproduced than in the first stage. Only, 4 models have been able to reach a final pressure close to the measured one. As before, the way followed to reach the final state is not well represented.

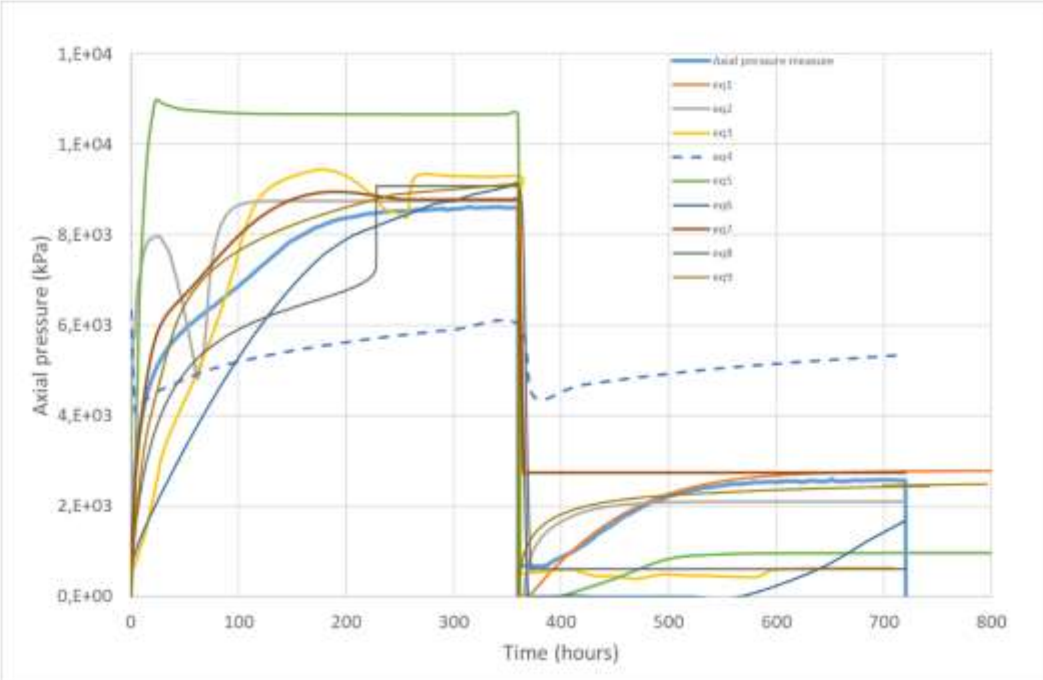

Figure 3-84 Axial pressure evolution test1a01

The situation for the radial pressure seems worse than for the axial one. This can be seen of Figure 3-79 and Figure 3-80. Radial pressure is presented at three different heights 5, 10 and 15 mm. Due to the fact that only one sensor was used of the height, a mean pressure radial has been calculated based on the numerical results and compared with the measure. There is a poor accuracy on the swelling pressure reached at the end of the two stages and especially for the second stage.

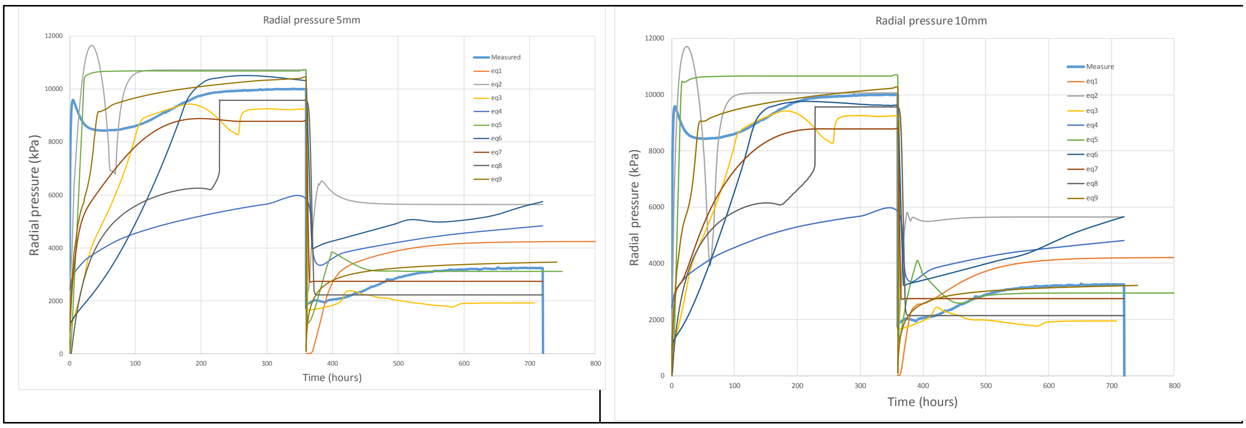

Figure 3-85 Radial pressure evolution at z=5mm and z=10 mm test1a01

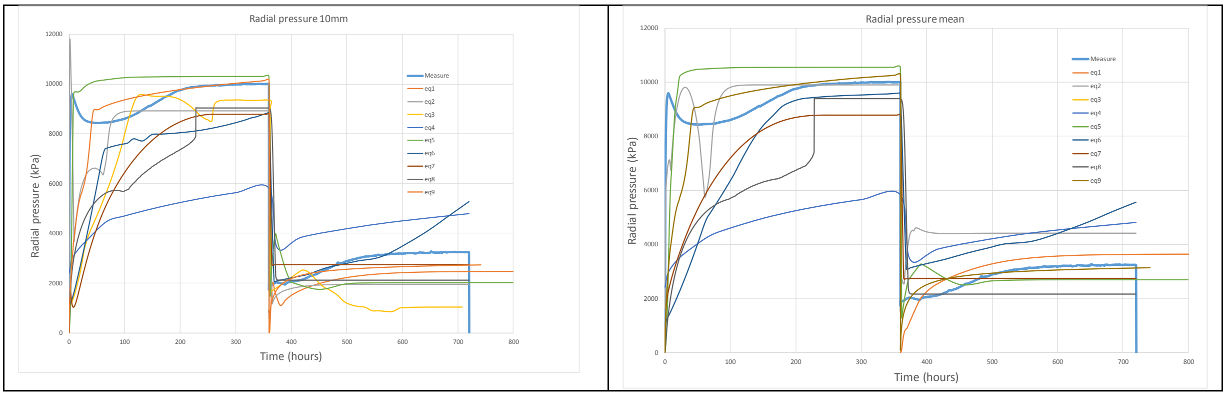

Figure 3-86 Radial pressure evolution at 15 mm and mean radial pressure on the height of the sample test1a01

3.14.1.2. ***Water content***

On Figure 3-81, water content evolution at a height of 17.5mm is shown. This figure indicates clearly the differences between the models to catch the transient phase. Nevertheless, final water content is close to the measure for most of the participants. It can be seen that the initial condition is not identical for all the simulation. It is particularly interesting to see that despite this initial difference, the final water content is not far from the measurement.

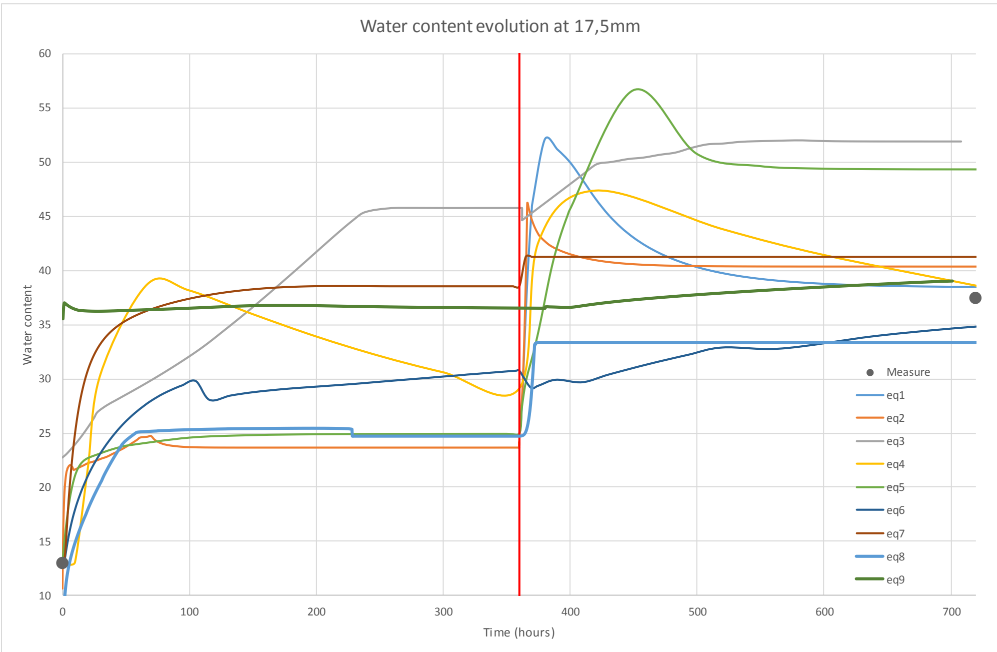

Figure 3-87 Water content evolution at z=17,5mm, comparison with initial and final values test1a01

On Figure 3-82, water content profiles at the end are shown and compared to the post mortem measure. In most cases, the trend was obtained by the models with lower values at the sample bottom and higher values on the top where the gap was introduced. Nevertheless, a certain dispersion is observed close to the base of the sample.

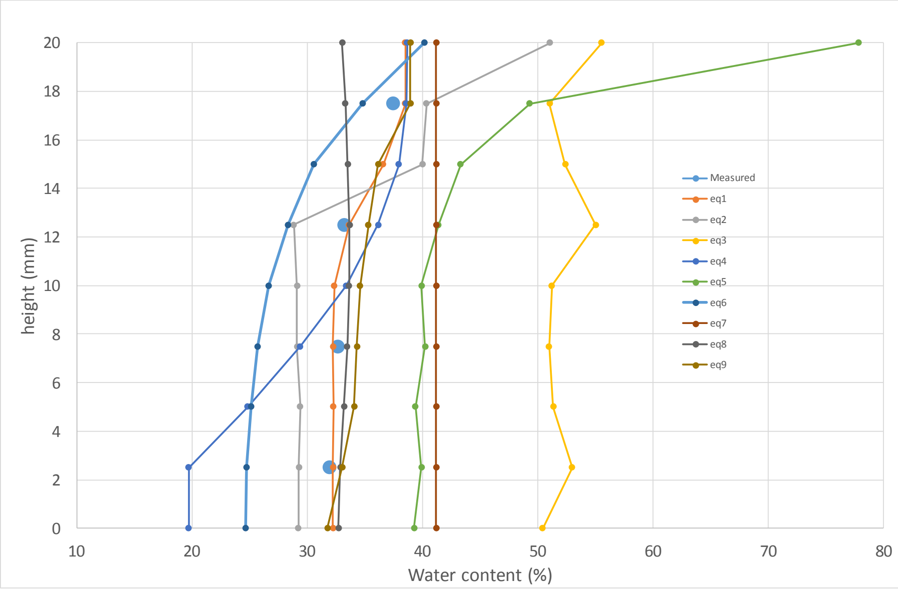

Figure 3-88 Water content profile at the end of the test along the sample axis test1a01

The same kind of analysis can be made on the void ratio profiles at the end of the test (Figure 3-83).

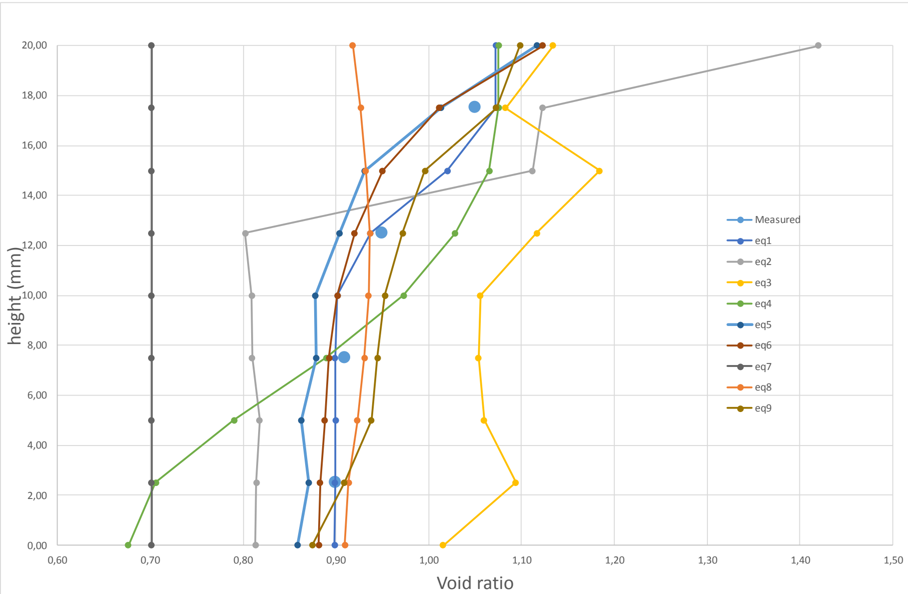

Figure 3-89 Void ratio profiles at the end of the test1a01

3.14.2 Results test1a02

3.14.2.1. *Axial and radial pressure*

The Figure 3-84 shows the comparison between the radial pressure measured and the simulations. It can be seen a high dispersion of the results. Unlike the previous test, both transient phase and final value of swelling pressure are not well captured by the models. In this test, the heterogeneity is introduced at the beginning with an initial gap on the top of the sample. Due to the gap, the pressure sensor recorded a signal several hours after the start of the test. In the simulations, we can see that some models do not catch this first phase, pressure is growing up immediately. At the end, all the results indicated a stabilized state but mainly with different swelling pressure.

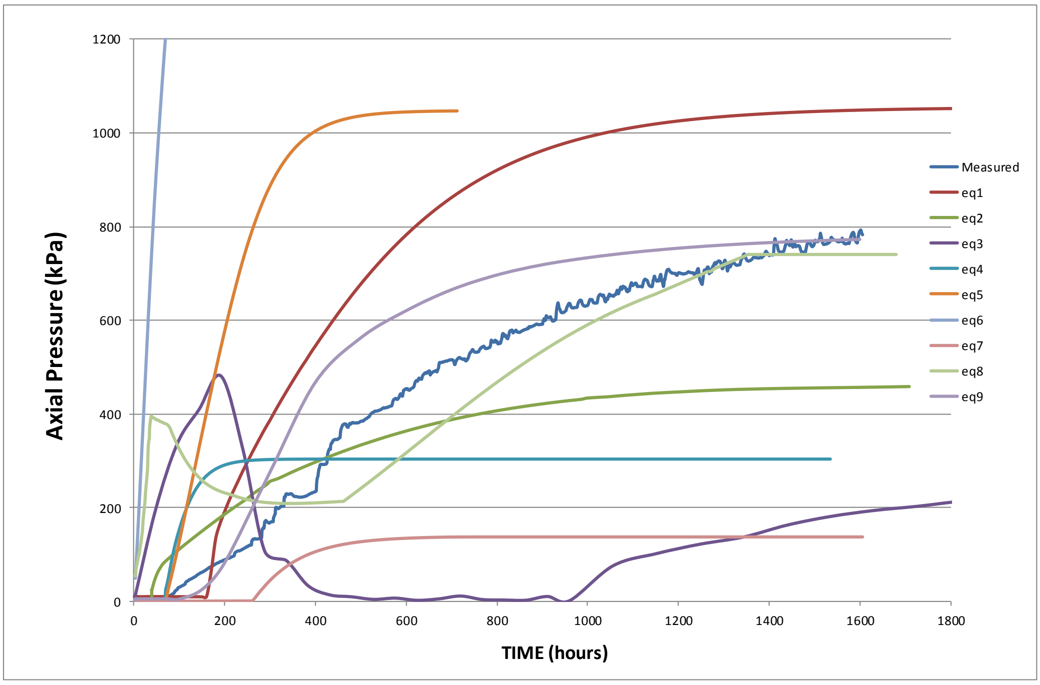

Figure 3-90 Axial pressure evolution and comparison with measure test1a02

This situation is confirmed by the results obtained for the radial pressure evolutions taken at different levels of the sample and compared with the measurement (see Figure 3-85and Figure 3-86). Even if the dispersion of the results is obvious, the trend of time evolution is quite similar to the one observed. This can be seen on Figure 3-86a which proposes radial pressure evolution at z=30mm at the early stage before 100 hours. The measurement shows a rapid increase of pressure at the beginning followed by a quick decrease. After a while, the radial pressure increases again but with a slow kinetic. This behaviour is well capture by most of the numerical results, showing that main physical processes are included in the models.

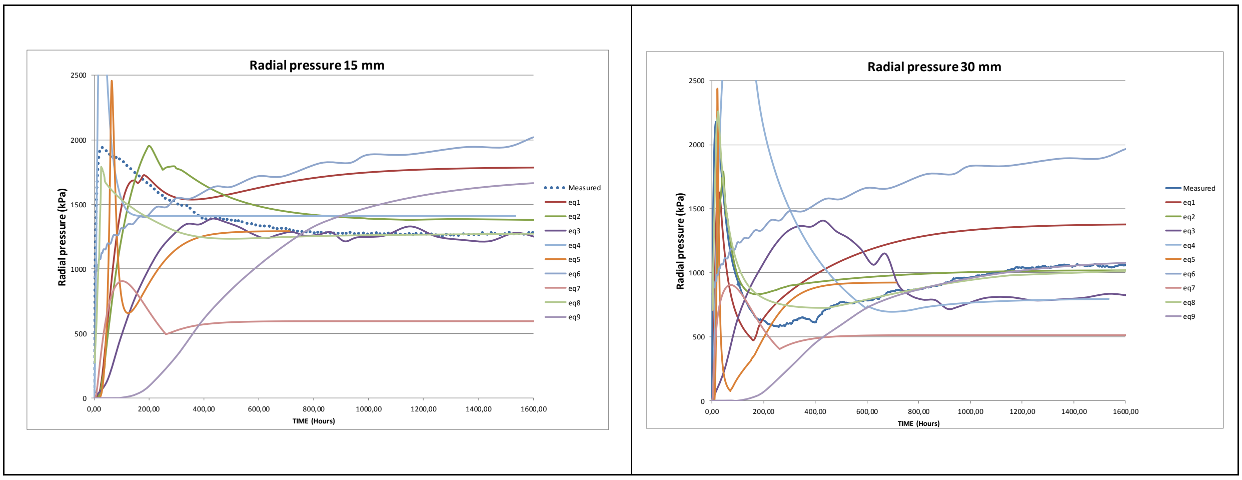

Figure 3-91 Radial pressure at z=15mm and z=30mm, comparison with measure test1a02

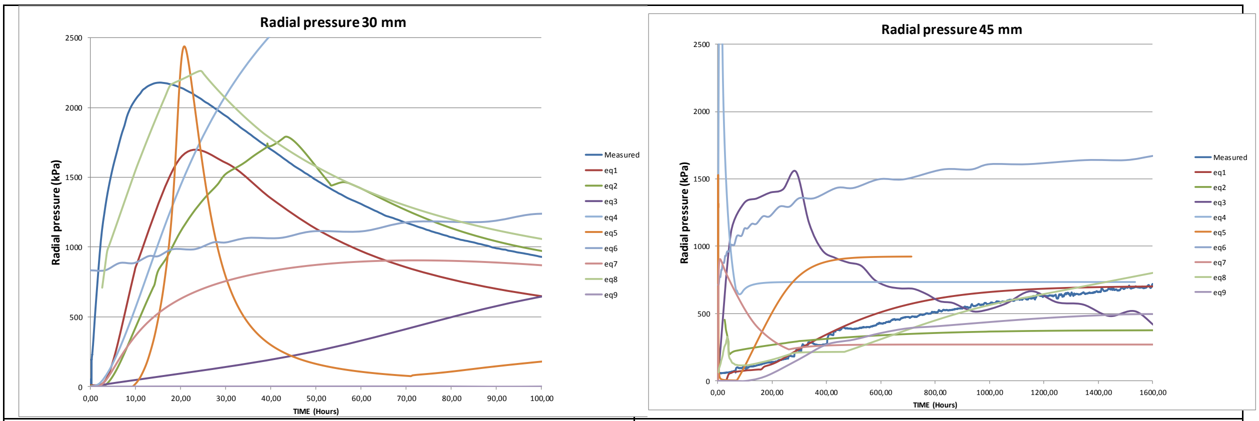

(a) (b)

Figure 3-92 (a) Radial pressure at z=30mm before 100 hours and (b) Radial pressure at z=45mm test1a02

3.14.2.2. *Water content*

Despite the dispersion of the results on pressure, the water content estimated by most of the modellers at the end of the test is very close to the measure. This can be seen on Figure 3-87 where the profile of water content are presented at the end of the test and on Figure 3-88. This last figure illustrates the significant differences during saturation phase but a good convergence of values at the end. The transient phase seems still difficult to capture. Models predict both monotonic or going through a maximum at the early times.

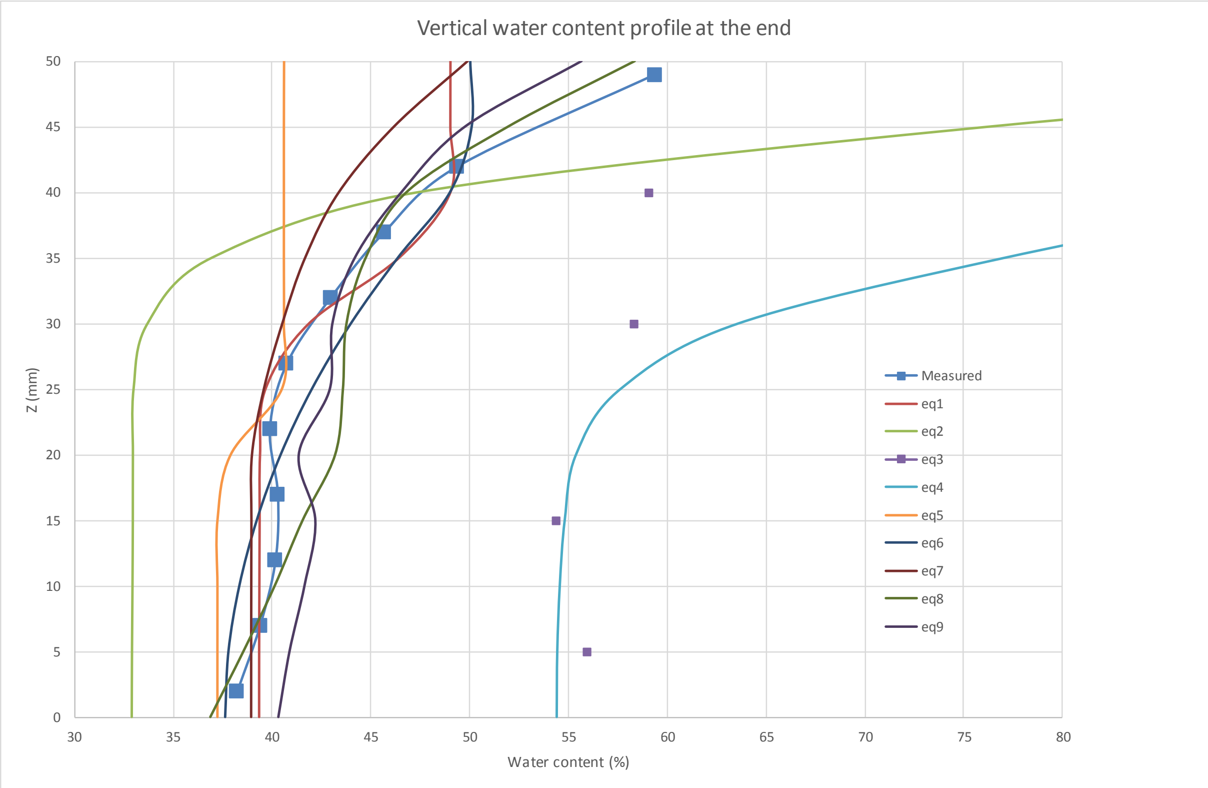

Figure 3-93 Vertical profile of water content at the end of the test1a02, comparison with measure

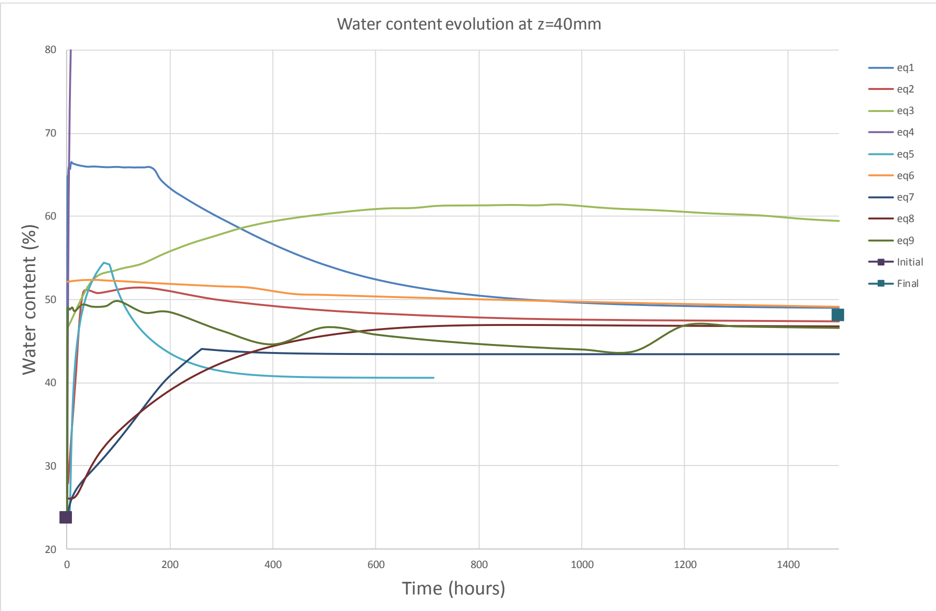

Figure 3-94 Water content evolution at z=40mm test1a02

At the end of the test, despite the stability of pressure, it can be seen that the homogeneity of the sample is not reached. This can be observed on Figure 3-89. Void ratio is not uniform in sample with a large difference between the top (where the gap was introduced) and the bottom. Dry density on the top is around 1040 kg/m³ and at the bottom around 1350 kg/m³. Models predicted the good trend of dry density (or void ratio) evolution along the sample.

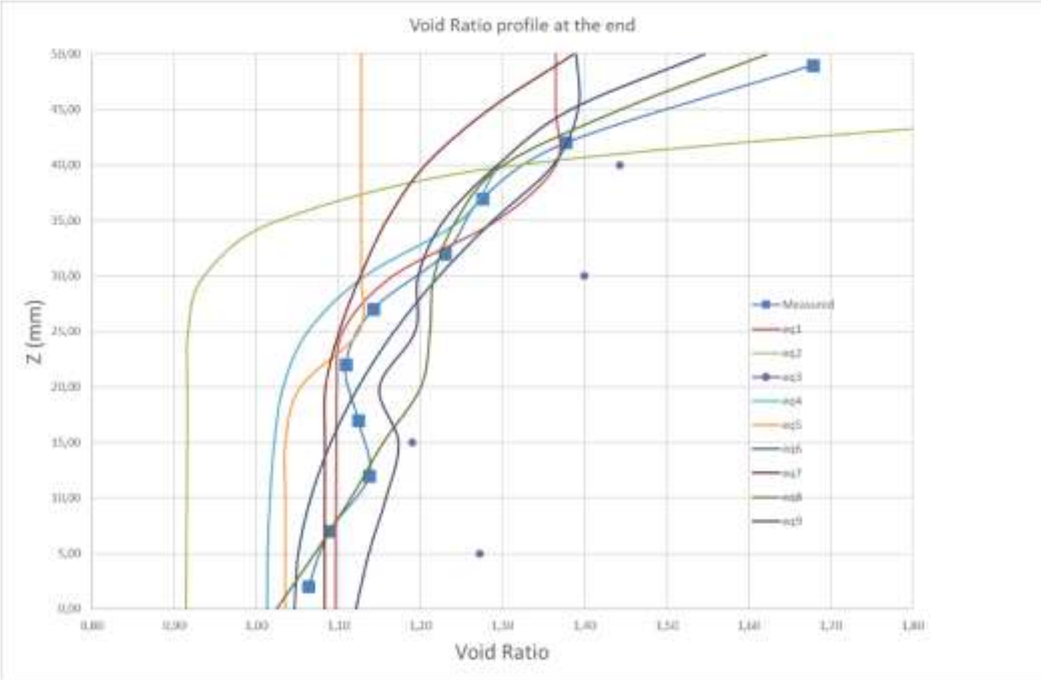

Figure 3-95 Void ratio profile at the end of the test1a02

3.15 Discussion

The comparisons made between the measure and the results of simulations for both axial pressure and mean radial pressure just at this end of the first stage of TEST1a01 showed that the values predicted by the models are very close to the measurements (Figure 3-96). This part of the experiment is in fact a classical swelling pressure test at constant volume. This shows that the main physical processes involved in bentonite swelling are well captured by the models, despite the diversity of the approaches used.

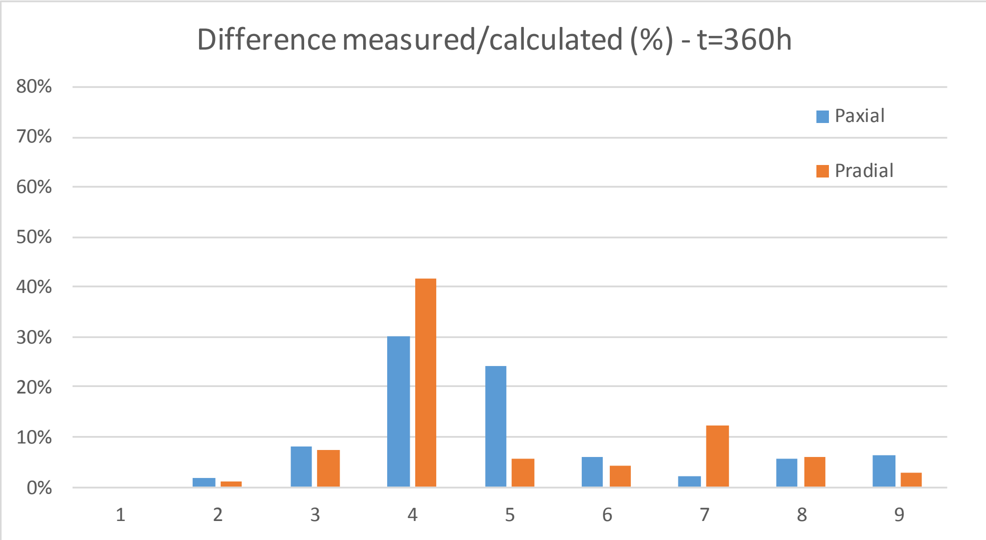

Figure 3-96 Evaluation of error between simulation and measure for test1a01 after 360h

On the contrary, when an initial void is present in contact with the swelling material, the situation seems much more difficult to handle. This can be observed on Figure 3-97 for test1a01 and on Figure 3-98 for test1a02. Most of the models had difficulties to reproduce both axial and radial pressure at the end of the swelling phase.

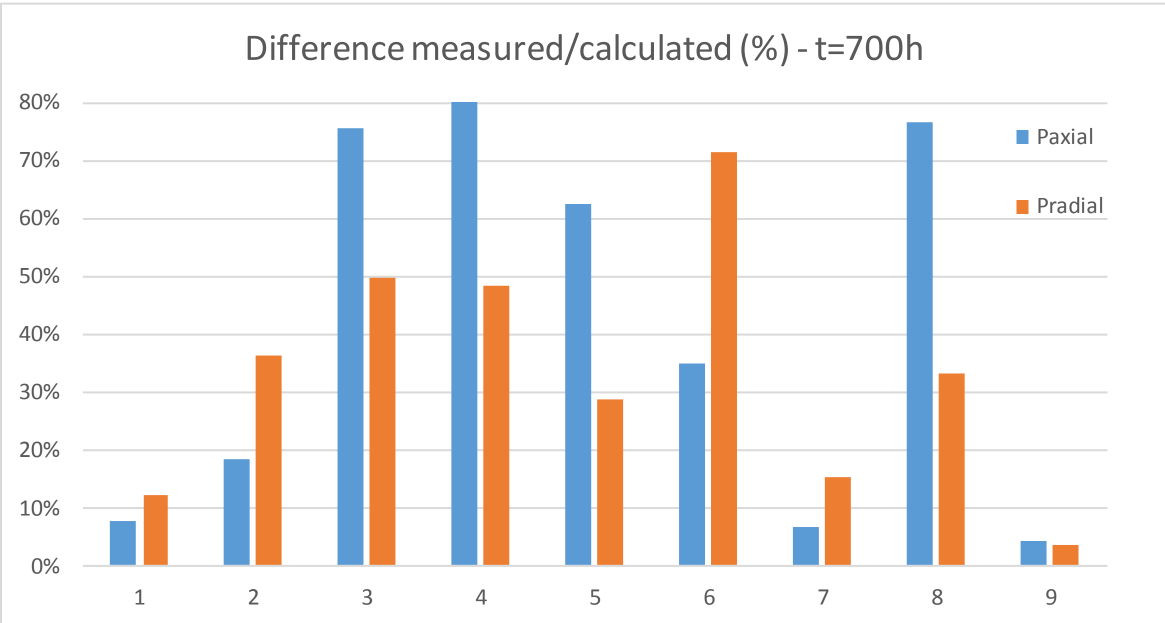

Figure 3-97 Evaluation of error between simulation and measure for test1a01after 700h

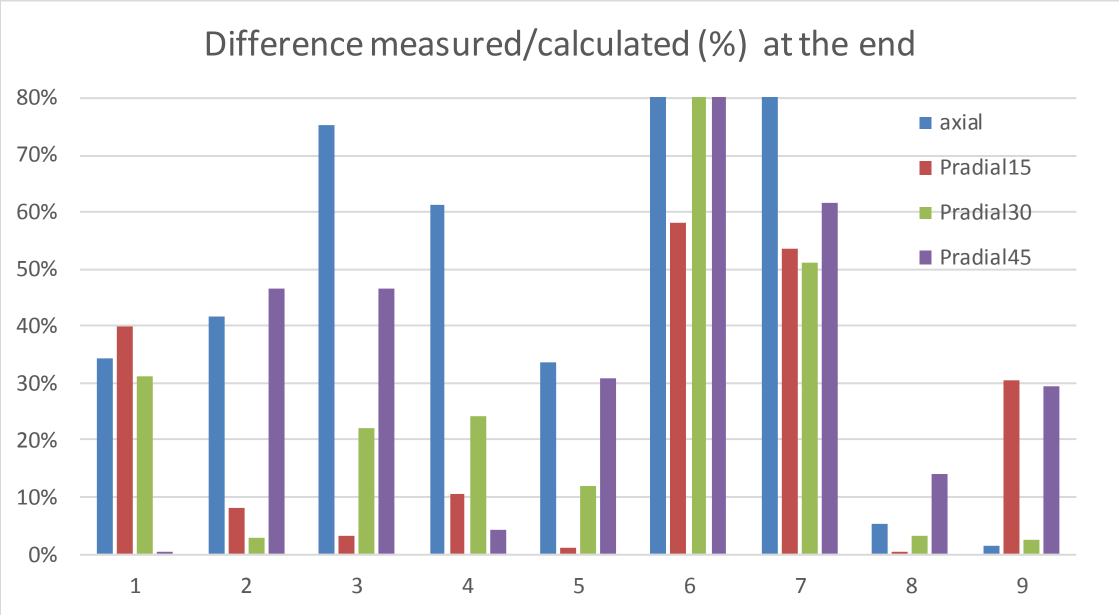

Figure 3-98 Evaluation of error between simulation and measure for test1a02 at the end

One of the difficulty identified by some groups on the test1a02 was induced by an initial water saturation close to 100%. In this case, the model could encounter problems to develop a swelling pressure.

Both tests showed that models had difficulties to reproduce the transient phase. First, the path followed to reach the final state is most of the time different from one group to another. One of the indicator explored was the duration to reach a stabilized state on axial pressure. In Table 3-30, the measurements are compared to the time obtained with the models. This is another way to illustrate the difficulty to predict the transient phase ons this kind of swelling tests.

Table 3-30 Time to reach the final axial swelling pressure for test1a01 for the two stages

	Measured	eq1	eq2	eq3	eq4	eq5	eq6	eq7	eq8	eq9
First step	242		103	263	360	100	360	250	228	320
Second step	600	620	494	595	700	550	700	365	374	725
Difference - step 1			57,44%	8,68%	48,76%	58,68%	48,76%	3,31%	5,79%	32,23%
Difference - step 2		3,33%	17,67%	0,83%	16,67%	8,33%	16,67%	39,17%	37,67%	20,83%

4 Test1b – Pellets mixture

The objective of this test is to follow the evolution of pellets mixture during hydration. The initial state is heterogeneous due to the used of high-density pellets. Small size grains of bentonite separate them from each other. In this kind of mixture, heterogeneities could be due to: difference of density between pellets and powder, irregular distribution of pellets or voids at the interfaces.
This test has been developed by CEA (France). For this test 10 partners participated with a large variety of approaches.

Table 4-1 List of partners who performed test 1a and models used

Team	Model/code
ICL	ICFEP
BGR	OpenGeoSys 5
Claytech	Comsol/HBM
EPFL	Lagamine/ACMEG
LEI	Comsol/Code_Bright
ULG	Lagamine
CU-CTU	Sifel
VTT/UCLM	Comsol
UPC	Code_Bright
Quintessa	QPAC/ILM

4.1 Brief description of the test1b

The test is a constant-volume swelling test. The material is composed with 70% of 32mm pellets and 30% of crushed pellets. They are arranged layer by layer in the cell, with a target for the dry density of about 1.52g / cm3 (see Figure 4-1).

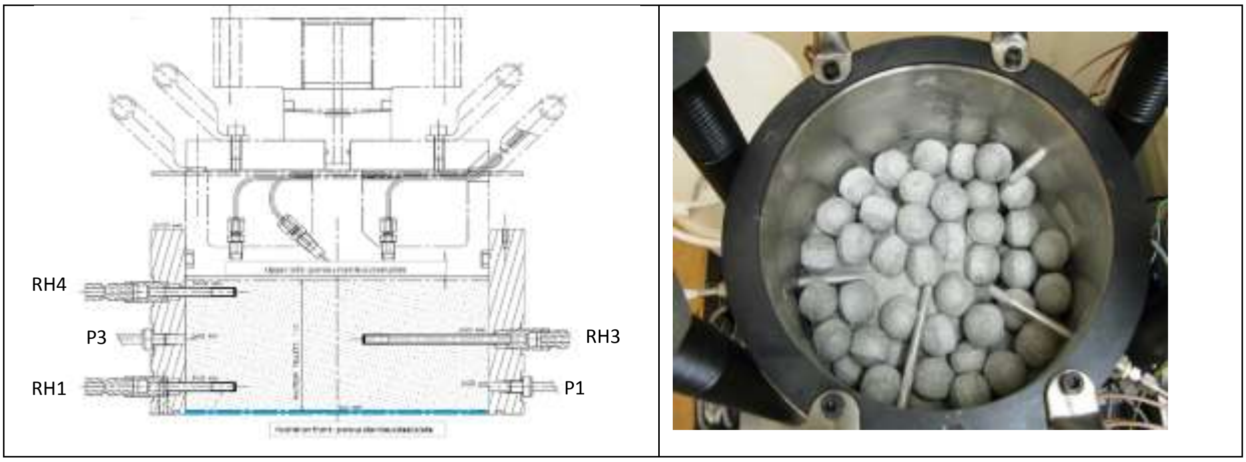

Figure 4-1 Set-up used for the swelling test. Photo of the pellets mixture during installation

Water is in contact with the lower face of the sample with a pressure differential of about 10kPa. The upper face is at atmospheric pressure. Swelling pressure (axial and radial) and water inflow are monitored. The test is continued even after stabilisation of both water flow and pressure (Figure 4-2). After more than 3 years, the test has been dismantled. Post mortem analysis gives access to some of the characteristics of the material after saturation such as dry density map, water content, pore size distribution…

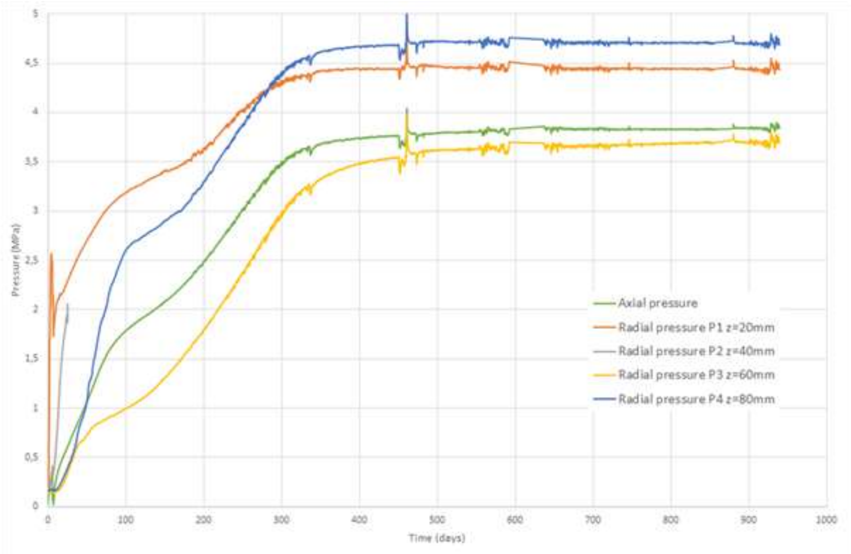

Figure 4-2 Axial and radial pressure during the test

4.2 ICL

4.2.1 Geometry and discretization

Test 1b involves a sample of compacted MX80 bentonite pellets, a diameter *D* = 240 mm and a height *h* = 105.15 mm.
Due to geometric symmetry around the vertical axis of the sample, half of the domain is discretised in a finite element (FE) mesh, using 8-noded quadrilateral displacement-based elements, with a pore water pressure degree of freedom at 4 corner nodes. Analysis is performed under axi-symmetric conditions.

4.2.2 Input parameters

Table 4-2 summarises the input parameters and their values for the IC DSM constitutive model and gives an indication of the sources from which the model parameters need to be derived. In the absence of element laboratory tests on mixtures of pellets, the input parameters were derived for the MX 80 bentonite which was used in TEST 1a experiments, with the following exceptions: the values for the elastic compressibility coefficient for changes in suction, κ_s, the microstructural compressibility parameter, κ_m, and the Void Factor VF, were adjusted so that the final swelling pressures computed were comparable to the final swelling pressures measured experimentally (Figure 4-3).

The laboratory experiments on MX 80 bentonite, used for the derivation of the remaining IC DSM parameters, are oedometer tests of Villar (2005), isotropic compression tests of Tang et al. (2008) and triaxial tests reported in Dueck et al. (2010). The Poisson's ratio was taken from information found in Borgesson & Hernelind (2014).

The parameters for the non-hysteretic soil water retention (SWR) model are summarised in Table 4-3. They were obtained from retention tests on 80/20 MX80 pellets/powder mixture by Molinero Guerra et al. (2018). The desaturation value of suction, s_{des}, was estimated to be 500.0 kPa and the same value was used as the air-entry value of suction, s_{air}, in the IC DSM constitutive model.

The saturated permeability, k_{sat}, of MX 80 bentonite is taken as $3.0\text{x}10^{-13}$ m/s. The remaining paramters for the permeability model are summarised in Table 4-4. As a verification for the input parameters, the computed and measured relative humidity (RH) at different elevations within the sample are compared in Figure 4-3 and are found to be in good agreement.

Table 4-2 Summary of input parameters for IC DSM model

Parameter	Source	Value
Parameters controlling the shape of the yield surface, $\boldsymbol{\alpha_F}, \boldsymbol{\mu_F}$	Triaxail compression; relationship between dilatancy and J/p ratio	0.4, 0.9
Parameters controlling the shape of the plastic potential surface, $\boldsymbol{\alpha_G}, \boldsymbol{\mu_G}$	Triaxial compression	0.4, 0.9
Generalized stress ratio at critical state, $\boldsymbol{M_J}$	Triaxial compression, related to the angle of shear resistance ϕ'_{cs}	0.5
Characteristic pressure, $\boldsymbol{p_c}$ (kPa)	Limiting confining stress at which $p_0 = p_0^* = p_c$	1000.0
Fully saturated compressibility coefficient, $\boldsymbol{\lambda(0)}$	Fully saturated isotropic loading	0.25
Elastic compressibility coefficient, $\boldsymbol{\kappa}$	Fully saturated isotropic unloading	0.08
Maximum soil stiffness parameter, $\boldsymbol{r}$	Isotropic compression tests at constant value of suction	0.61
Soil stiffness increase parameter, $\boldsymbol{\beta}$ (1/kPa)	Isotropic compression tests at constant value of suction	0.00007
Elastic compressibility coefficient for changes in suction, $\boldsymbol{\kappa_s}$ (kPa)	Drying test and constant confining stress	0.035
Poisson ratio, $\boldsymbol{\nu}$	Triaxial compression test	0.4
Plastic compressibility coefficient for changes in suction, $\boldsymbol{\lambda_s}$	Drying test and constant confining stress	0.2
Air-entry value of suction, $\boldsymbol{s_{air}}$ (kPa)	From the retention curve	500.0
Yield value of equivalent suction, $\boldsymbol{s_0}$ (kPa)	Usually a high value if it is not to be mobilised	10^6
Microstructural compressibility parameter, $\boldsymbol{\kappa_m}$	No direct test	0.005
Void factor, $\boldsymbol{VF}$	No direct test – potentially from MIP interpretation	0.05
Coefficients for the micro swelling function, $\boldsymbol{c_{s1}}, \boldsymbol{c_{s2}}, \boldsymbol{c_{s3}}$	No direct test – potentially from MIP interpretation	-0.1, 1.1, 5.0
Coefficients for the micro compression function, $\boldsymbol{c_{c1}}, \boldsymbol{c_{c2}}, \boldsymbol{c_{c3}}$	No direct test – potentially from MIP interpretation	-0.1, 1.1, 5.0

Table 4-3 Summary of input parameters for SWR model

Parameter	Value
Fitting parameter, $\boldsymbol{\alpha}$ (1/kPa)	0.00007
Fitting parameter, $\boldsymbol{m}$	0.85

Fitting parameter, n	1.6
Parameter Ω	Degree of saturation dependent
Residual degree of saturation, S_{r0}	0.085
Suction desaturation, s_{des} (kPa)	500.0
Suction in the long term, s_0 (kPa)	4x10^5

Table 4-4 Summary of input parameters for permeability model

Parameter	Value
Saturated value of permeability, k_{sat} (m/sec)	3.0x10^{-13}
Minimum value of permeability, k_{min} (m/sec)	3.0x10^{-15}
Suction s_1 (kPa)	1000.0
Suction s_1 (kPa)	20000.0

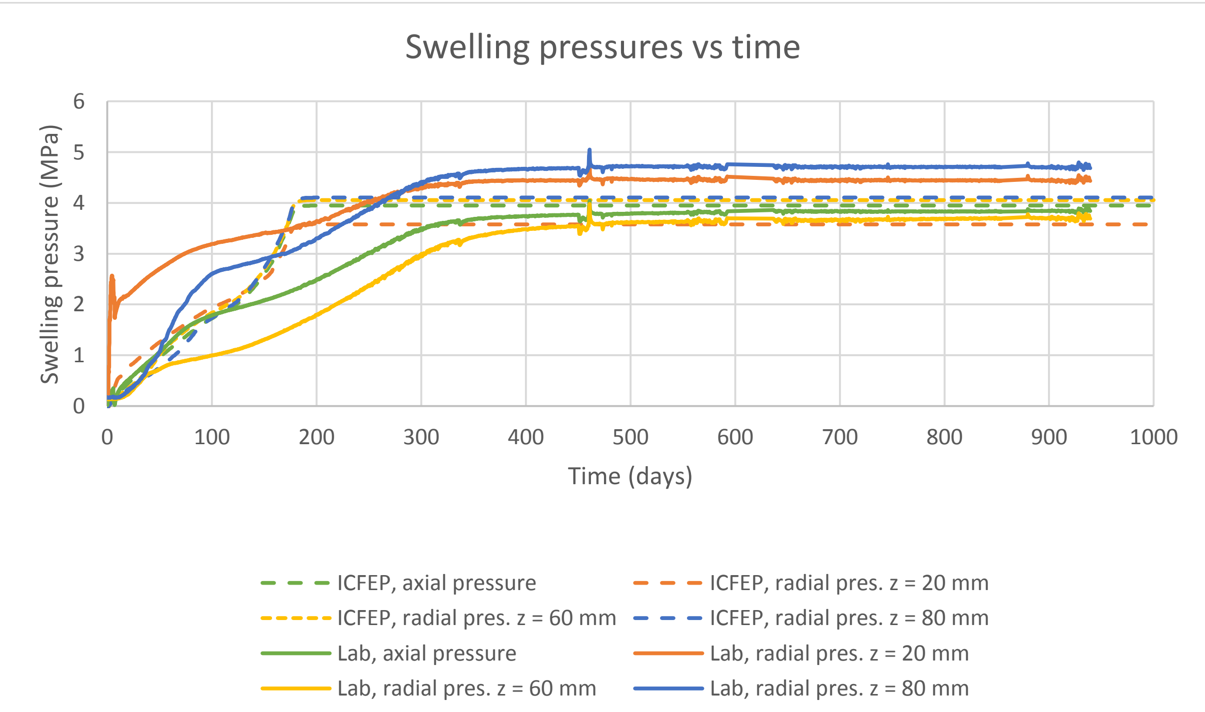

Figure 4-3 Comparison between numerical predictions and experimnetal measurements of swelling pressures

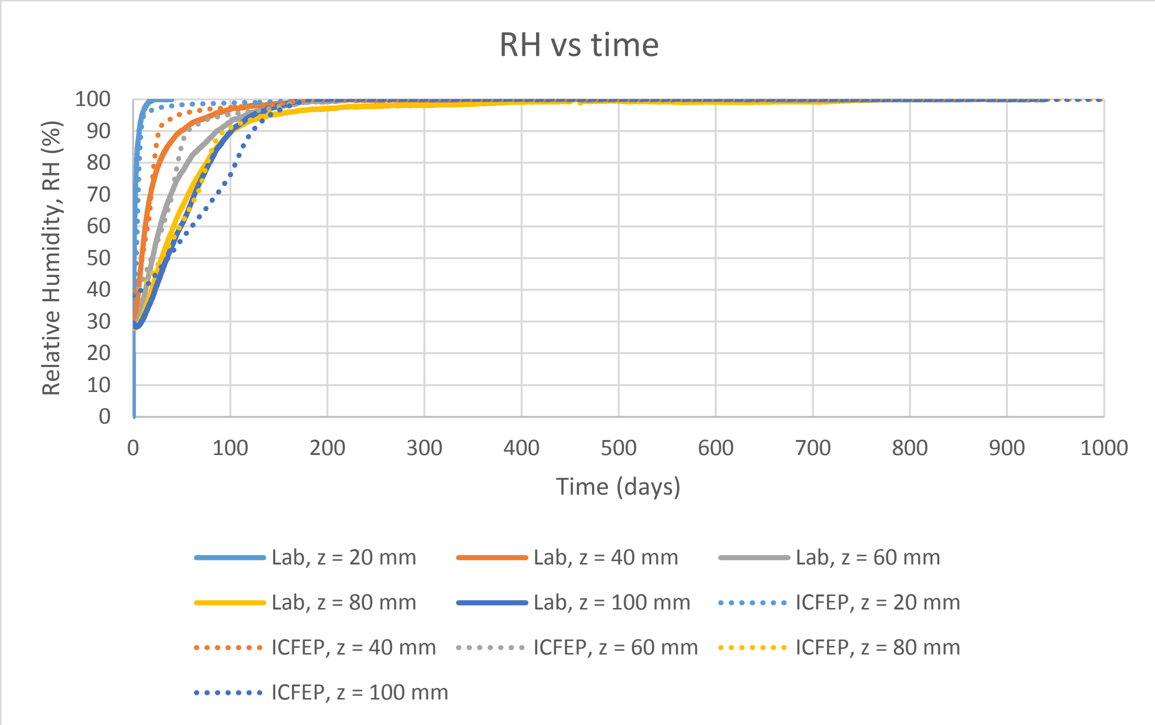

Figure 4-4 Comparison between numerical predictions and experimnetal measurements of Relative Humidity (RH)

4.2.3 Initial and boundary conditions

The initial dry density is 1520 kg/m^3 and the initial void ratio is 0.824. The initial total axial and radial stresses are 10 kPa and the initial suction is 103 MPa, corresponding to an initial degree of saturation of 14.6%.
Zero horizontal and vertical displacements are imposed on the vertical and horizontal boundaries of the FE mesh throughout the analysis. A dual boundary condition (precipitation) is prescribed on the bottom boundary, imposing either an inflow of water, q_n, to match the water inflow measured during the test, or a constant pore water pressure, p_{fb}, equal to 10 kPa of compressive pressure, in accordance with the pressure differential imposed in the test.

At the beginning of each increment the pore water pressure at boundary nodes is compared to p_{fb} and if found to be more tensile, an infiltration boundary condition is applied, employing the specified flow rate, q_n. Infiltration is also applied when at the beginning of the increment the flow rate across the boundary exceeds the prescribed value. Alternatively, if the pore pressure at the beginning of the increment is more compressive than p_{fb}, then a constant pore water pressure equal to the latter is imposed. In order to maintain the prescribed pore pressure at the boundary, a portion of the specified infiltration is applied.

4.2.4 Results/discussion

Figure 4-5 presents the evolution of axial and radial swelling pressures with time predicted by the numerical analysis. Axial swelling pressure is evaluated at the top boundary of the FE mesh (top of the cell), whereas radial swelling pressures are evaluated at the right-hand side vertical boundary (cell wall) at different elevations z from the bottom. The final axial swelling pressure is of magnitude comparable to the one measured experimentally (see also Figure 4-3), but it is reached sooner than in the experiment. The radial swelling pressures follow an evolution with time similar to the evolution of the axial swelling pressure, and increase slightly in magnitude with elevation.

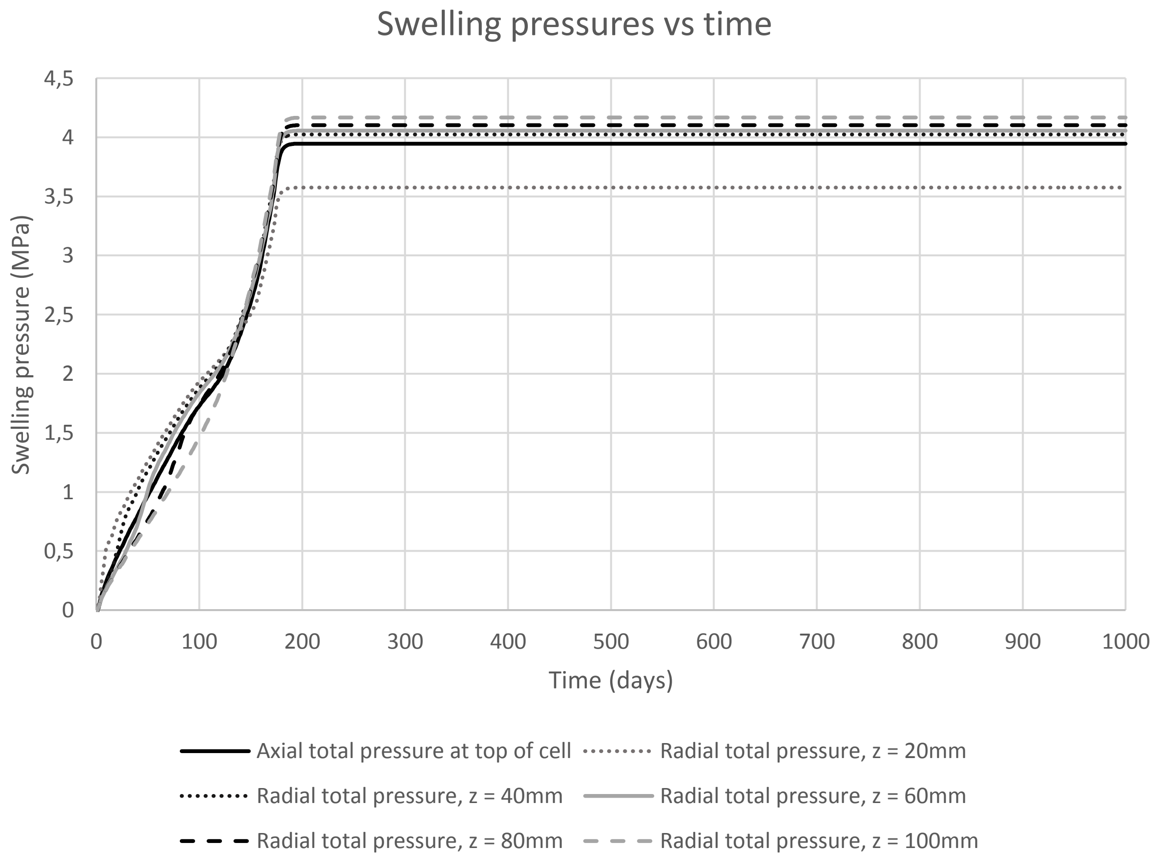

Figure 4-5 Evolution of swelling pressures with time predicted by the analysis

Figure 4-6 presents the evolution of void ratio with time predicted by the numerical analysis at the left-hand side vertical boundary (middle of the cell, R = 120 mm) at different elevations, z. At the beginning of the analysis, the lower part of the sample (elevations 10 and 30 mm) swells, thus increasing the void ratio and forcing the remaining part of the sample (elevations 50, 70 and 100 mm) to contract. The swelling at the lower part of the sample reaches a maximum, shortly after swelling of the middle part (elevation 50 mm) starts to occur. With time, the top part of the sample starts swelling too, while the bottom is forced to contract. When full saturation is achieved, the initial swelling at z = 10 mm has been almost entirely reverted by subsequent contraction (caused by the sample swelling at higher elevations). At z = 30 and 50 mm, overall swelling is marked at full saturation. The higher the elevation the smaller the final magnitude of swelling. At z = 70 and 100 mm, overall contraction is measure at full saturation, with larger final contraction corresponding to higher elevation.

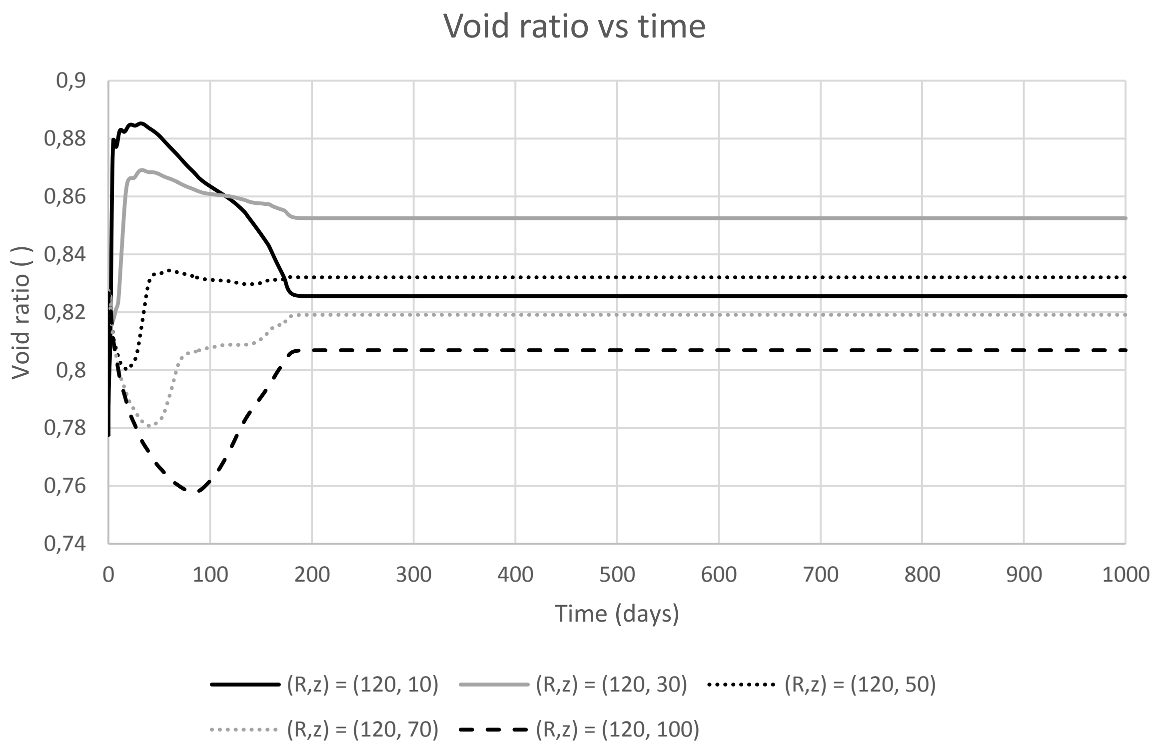

Figure 4-6 ***Evolution of void ratio with time predicted by the analysis***

In Figure 4-7 the evolution of gravimetric water content predicted with time at R = 120 mm at different elevations, z, is presented. The water content starts increasing almost immediately at z = 10 mm, reaches a maximum value few days later and then starts decreasing slightly, as the void ratio at the same elevation starts decreasing too (Figure 4-6). It reaches a final value at the same time as the void ratio reaches a plateau. A similar evolution with time is observed at z = 30 mm, although the decrease from the maximum value of water content is a lot less pronounced and almost imperceptible. For the remaining of elevations examined, water content reaches its final value monotonically, with higher elevations marking a change in water content at later stages of the analysis. The final values of water content at different elevations are slightly different, in accordance with the final void ratios at the same elevations.

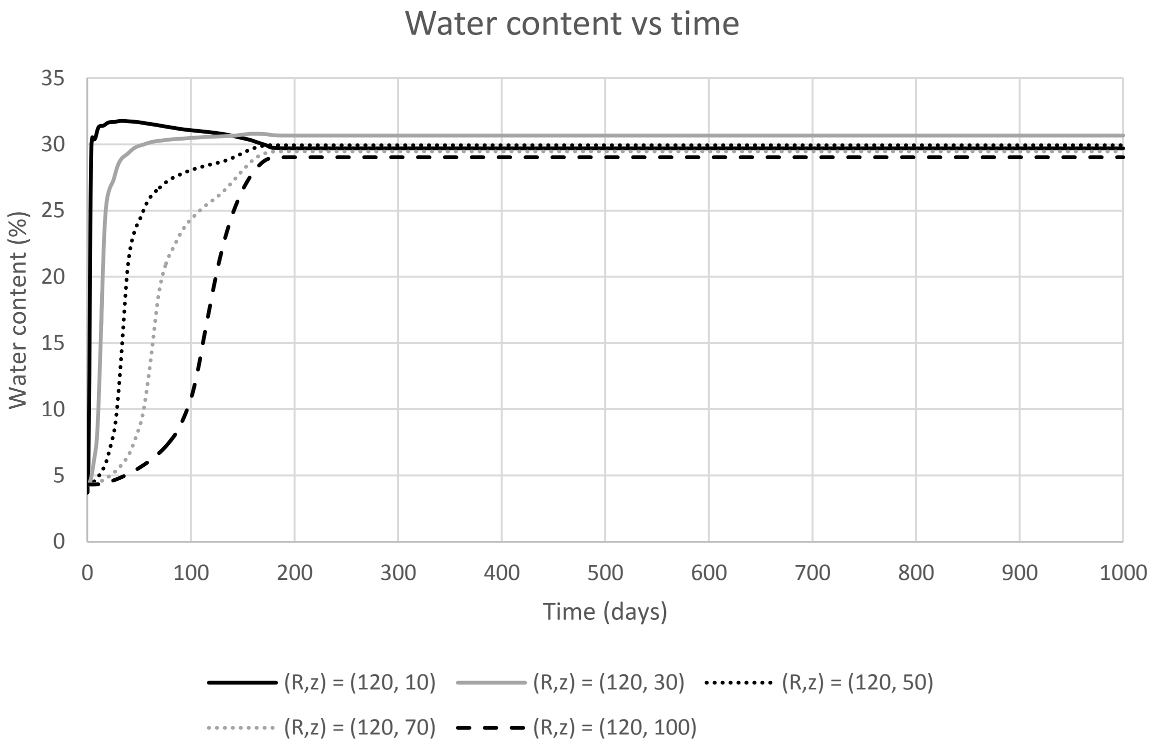

Figure 4-7 Evolution of water content with time predicted by the analysis

The evolution of degree of saturation predicted with time at different points (co-ordinates R, z) in the sample, is presented in Figure 4-8. As the model is currently unable to account for horizontal heterogeneities within the sample, co-ordinate R becomes irrelevant in the discussion of the numerical results. It can be observed in Figure 4-8 that the degree of saturation changes monotonically towards the final value of 100% and that changes are faster at lower elevations. After about 180 days, the whole sample is fully saturated. At this point the evolution of swelling pressures, void ratio and water content with time ceases (see Figure 4-5, Figure 4-6, Figure 4-7).

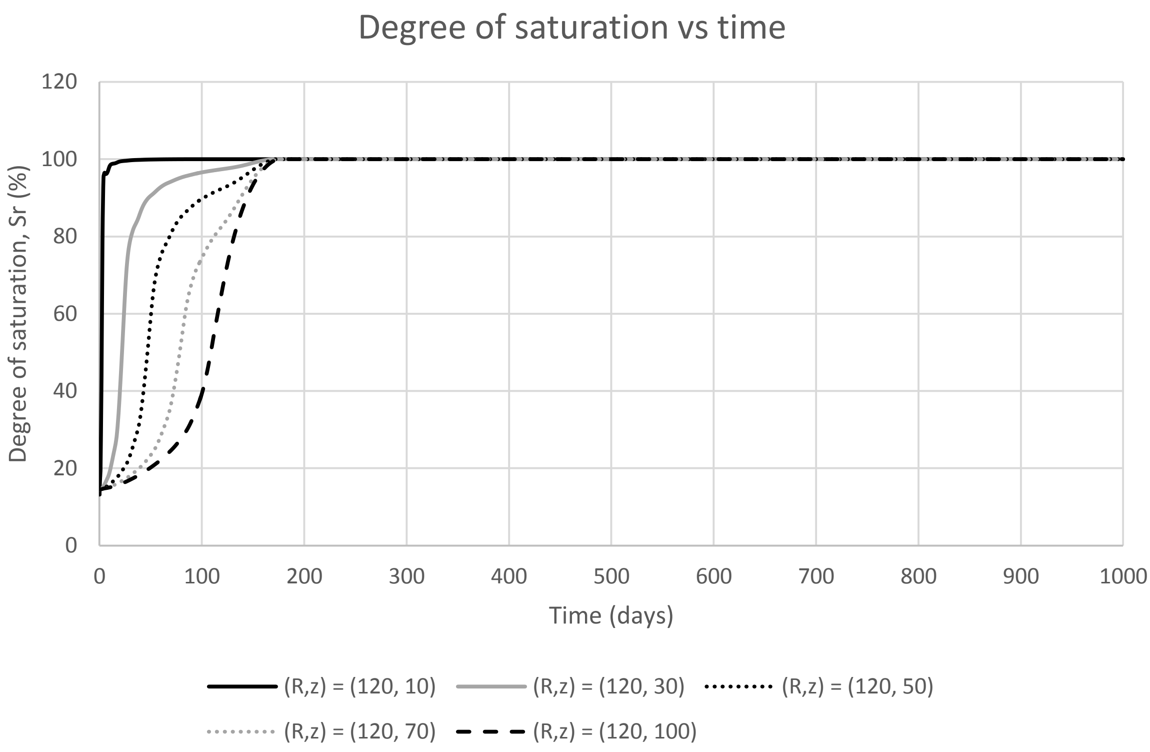

Figure 4-8 Evolution of degree of saturation with time predicted by the analysis

Finally, Figure 4-9 shows the final distribution of dry density and water content. The numerical results is in good agreement with the post-mortem measurements, however the dry density is overpredicted at the bottom of the sample (z=10mm) and the water content is underpredicted. This indicates that the final void ratio was locally under-predicted.

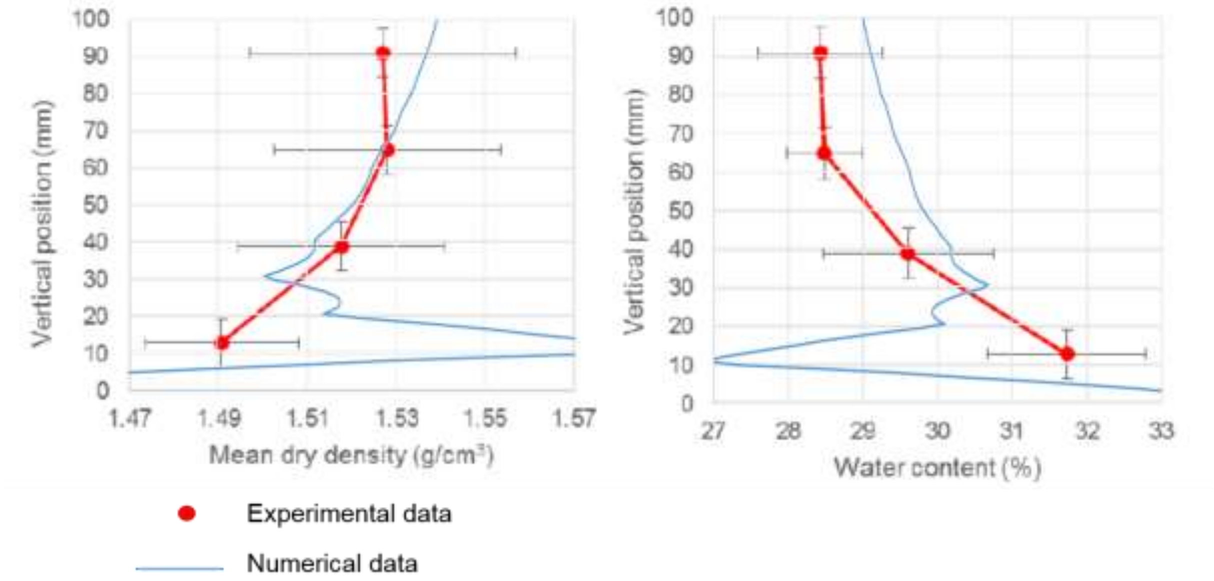

Figure 4-9 Final distribution of dry density, on the left, and water content, on the right

4.3 BGR

4.3.1 Geometry and discretization

The model for test case 1b was set up similar to test case 1a01. The axial symmetry was used to reduce model dimensions and the measurement points were set up to obtain the output as specified in the test case document (BEACON deliverable 5.1.1). The model geometry and the unstructured grid used for the simulation are shown in Figure 4-10. In the experiment, the radial stresses were measured with pressure sensors at the fllowing locations:

- P1: R = 240 mm, Z = 20 mm,
- P2: R = 240 mm, Z = 40 mm,
- P3: R = 240 mm, Z = 60 mm,
- P4: R = 240 mm, Z = 80 mm.

These points were also setup in the simulation domain to provide stress output for comparison. The simulation was done under the assumption of a homogeneous medium without distinctly resolving the pellets and the crushed pellets. This was done for two reasons. Firstly, a distinct configuration of pellets and crushed pellets is a unique system. A simulation of the discrete system requires deterministic data on the position and arrangement of pellets. Therefore, it would prove difficult to transfer data and understanding obtained from discrete simulation of a single experiment to other similar systems. Deriving generic inferences describing the behaviour of pellets-mixture systems would require a series of experiments. This was not available for the current experiment. Secondly, simulating discrete pellet-mixture systems in repository-scale models is computationally resource intensive. From the viewpoint of compuational efficiency using a homogenized system with estimated equivalent parameters was an efficient way to capture the behaviour of the system. The discretized model domain with 2050 elements is shown in Figure 4-10.

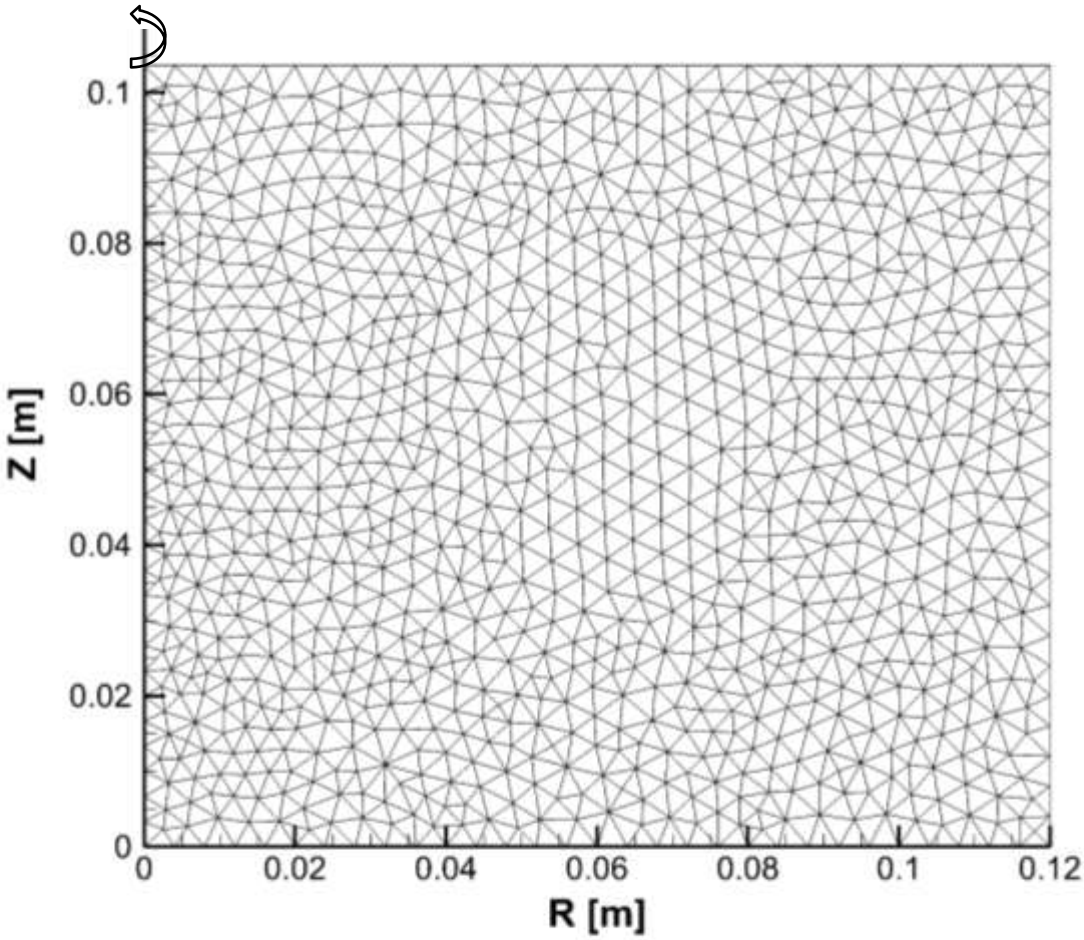

Figure 4-10 Discretized axisymmetric model domain used in the simulation for test case 1b. The axis of symmetry is along the boundary R = 0 m.

4.3.2 Input parameters

The initial values of parameters of the bentonite mixture were taken from the test case document (BEACON Deliverable 5.1.1) when available. The parameters are summarized in the Table 4-5. Assumptions behind certain parameter values are remarked in the following section.

Table 4-5 Parameter set used in the simulation of test case 1b.

Parameter	Value	Unit
Permeability $(\mathbf{k})$	1.5e-21	m^2
Void ratio (e)	0.801	[-]
Porosity (ϕ)	0.445	[-]
Initial saturation $\left(S^w_{\text{init}}\right)$	0.14	[-]
Fluid density $\left(\rho^w\right)$	1000	kg/m^3
Grain density $\left(\rho^s\right)$	2780	kg/m^3
Biot coefficient (α_{Biot})	0.16	[-]
Young's modulus (E)	70	MPa
Poisson's ratio (υ)	0.35	[-]
Max swelling pressure $\left(\boldsymbol{\sigma}_{\text{max,sw}}\right)$	5.8	MPa

The pellet mixture is expected to have two distinct scales at which the re-saturation process occurs. The resaturation of the porespace within a pellet is expected to be a slower process compared to the resaturation of the porespace between pellets. However, the model used for 1b accounted for the behaviour in a homogenized model without differentiation of the spatial scales of porosity. This model was assigned a permeability as given in Table 4-5. The permeability was varied as a function of the porosity according to the following relation

$$\mathbf{k}_{\text{new}} = \mathbf{k}_0 \left(\frac{\phi - \phi_0}{\phi_0 - \phi_{\text{crit}}} \right)^{\lambda} \tag{18}$$

Where $\mathbf{k}_0$ is the initial permeability, ϕ_0, ϕ and ϕ_{crit} are the initial, current and critical (minimum) porosities and λ is the exponent. The current porosity was a function of the volumetric strains calculated from (9). The exponent was chosen to be 10, based on Åkesson et al. (2010) and personal communication from other modelling teams while discussing the simulation results of test case 1a01. The critical porosity was chosen to be an arbitrarily small non-zero number (1e-24). The Young's modulus is taken to be less than that in test case 1a01 (150 Mpa) under the assumption that the pellet mixture is mechanically less elastic than the bentonite plug. The Poisson's ratio was assumed to be 0.35. The Biot coefficient which yielded the best fit suggests a very weak HM coupling. Back calculations from the Biot's coefficient yield a grain compressibility which is in the same order of magnitude as the compressibility of the porous skeleton. This corresponds to the conceptual understanding of the water uptake process in a double-structure porosity medium. Since the compressibility of the grain is comparable to the compressibility of the porous skeleton, it might have implications to the rate of swelling under confined conditions, but, this is not considered in the current numerical model.

The development of swelling pressure was assumed to be of a constant rate and linearly proportional to the change in saturation. The maximum swelling pressure providing the best fit to the measured data was higher than the swelling pressure suggested in the test case document for the measured dry density (ref. Figure 4-11). This might suggest a stress-path dependency of the maximum swelling pressure; since the upper parts of the domain would experience compaction before resaturation, the swelling pressure in those regions would be higher.

In comparison to test case 1a01 where the change in porosity was calculated in post processing and the permeability was kept constant, for this test case, the two functions eq. (9) and eq. (18) were implemted in the code and newly calculated every time step.

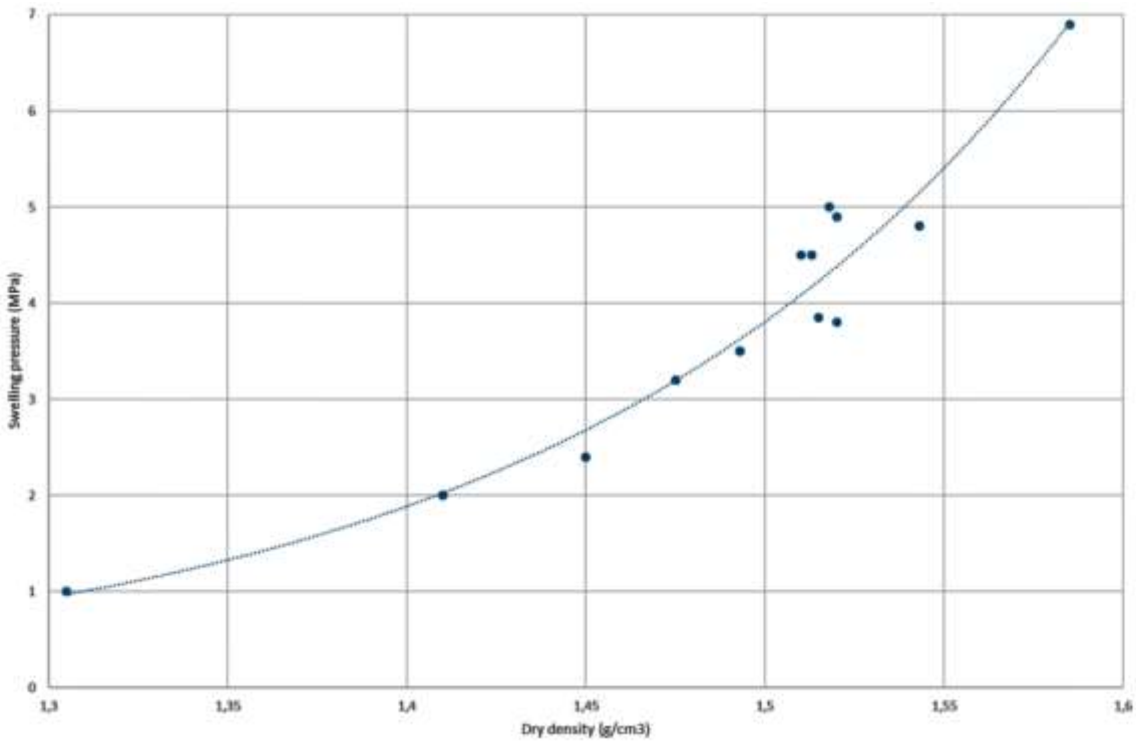

Figure 4-11 Swelling pressure as a function of dry density. Taken from BEACON Deliverable 5.1.1 (Decimal separator is the comma).

4.3.3 Initial and boundary conditions

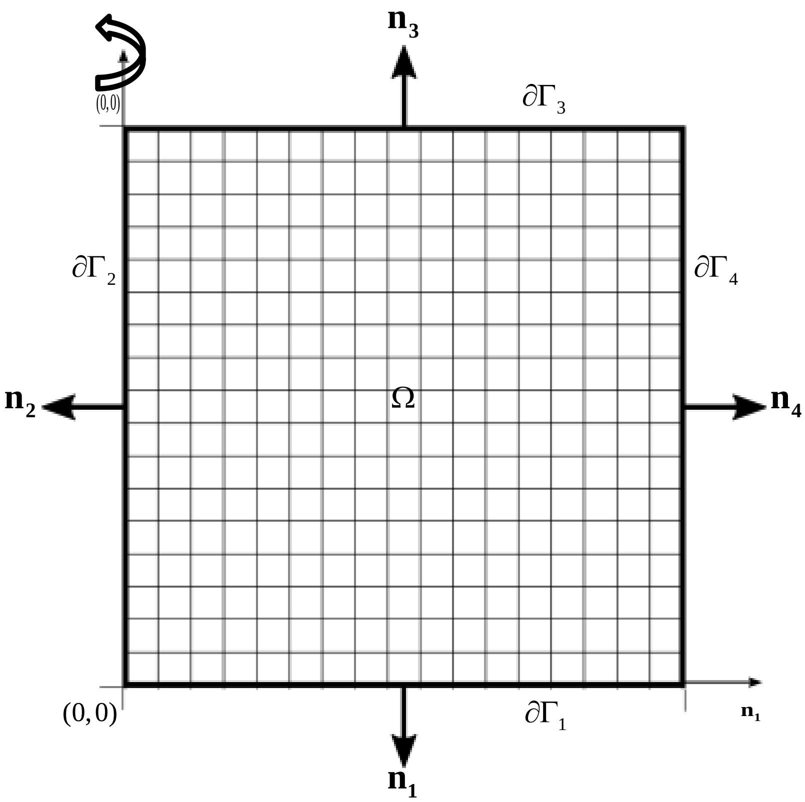

Figure 4-12 Schematic of the model domain with boundary surfaces, the axis of symmetry and the normal directions.

The schematic model domain, the axis of symmetry, the boundary surfaces and normal directions are depicted in Figure 4-12 and summarized in Table 4-6.

Table 4-6 Tabular summary of the boundary conditions for test case 1b, based on Figure 4-12

Process	$\partial\Gamma_1$	$\partial\Gamma_2$	$\partial\Gamma_3$	$\partial\Gamma_4$
H	$p = 10\ kPa$	$\mathbf{q}^w \cdot \mathbf{n}_2 = 0$	$\mathbf{q}^w \cdot \mathbf{n}_3 = 0$	$\mathbf{q}^w \cdot \mathbf{n}_4 = 0$
M	$\mathbf{u} \cdot \mathbf{n}_1 = 0$	$\mathbf{u} \cdot \mathbf{n}_2 = 0$	$\mathbf{u} \cdot \mathbf{n}_3 = 0$	$\mathbf{u} \cdot \mathbf{n}_4 = 0$

4.3.4 Results/discussion

4.3.4.1. *Saturation, Void Ratio and Water content profiles*

The void ratio and water content profiles of the model domain at lines Z = 20 mm and Z = 60 mm for the requested times are given in Figure 4-13 and Figure 4-14, respectively.

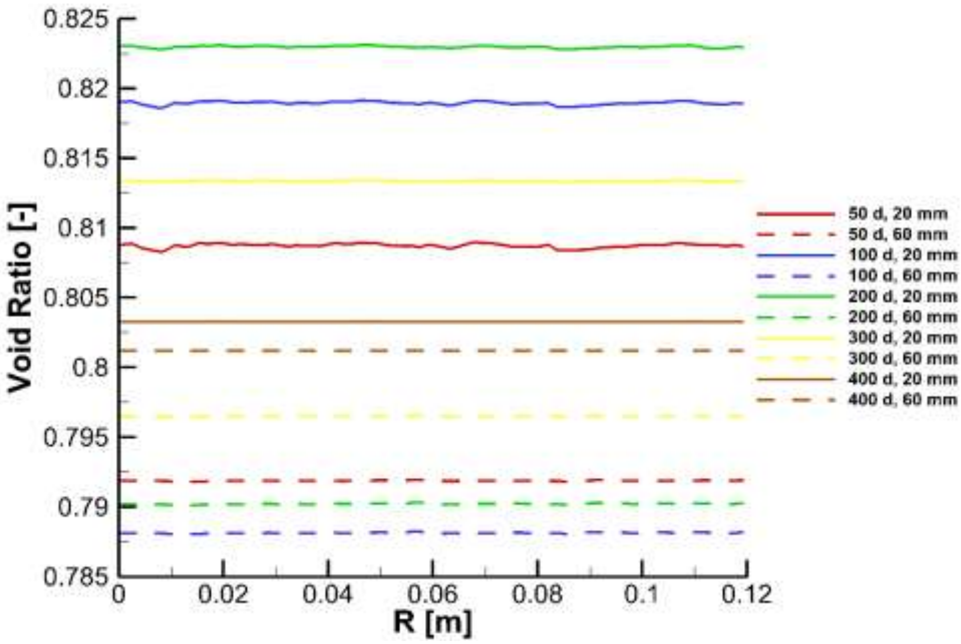

Figure 4-13 Calculated voids ratio profiles at Z = 20 mm and Z = 60 mm for various times.

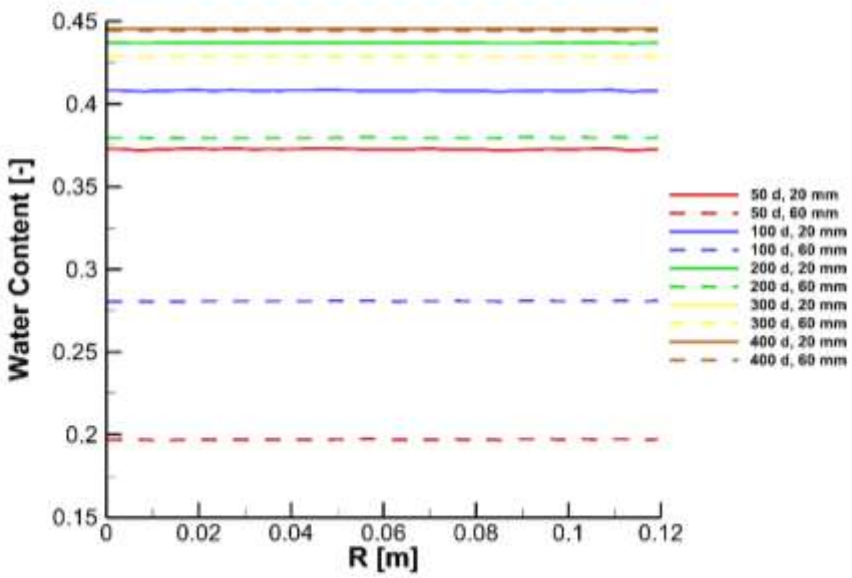

Figure 4-14 Calculated water content profiles at Z = 20 mm and Z = 60 mm for various times.

The temporal evolution of the saturation, void ratio and water content at the requested output points are shown in Figure 4-15, Figure 4-16 and Figure 4-17, respectively. The saturation and water content curves show a monotonic increase with time, achieving a maximum at steady state. The void ratio suggests that the lower parts of the system experience an increase in voids, due to the uptake of water, during the early times before being compacted by the swelling process. The void ratio in the upper parts of the model domain suggests that these parts experience compaction from the swelling process occuring at lower levels before the saturation front reaches the upper parts of the domain and the swelling process begins.

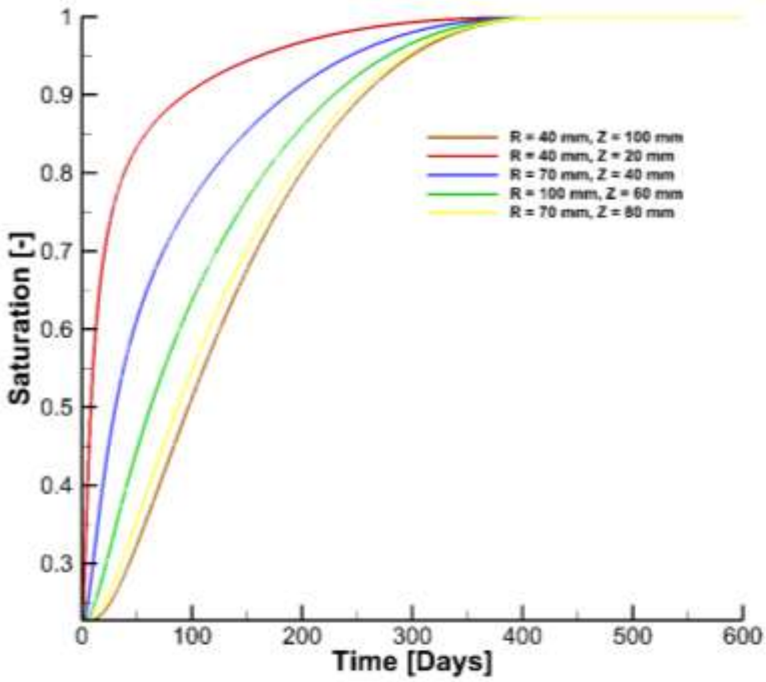

Figure 4-15 Calculated evolution of saturation at different points in the domain.

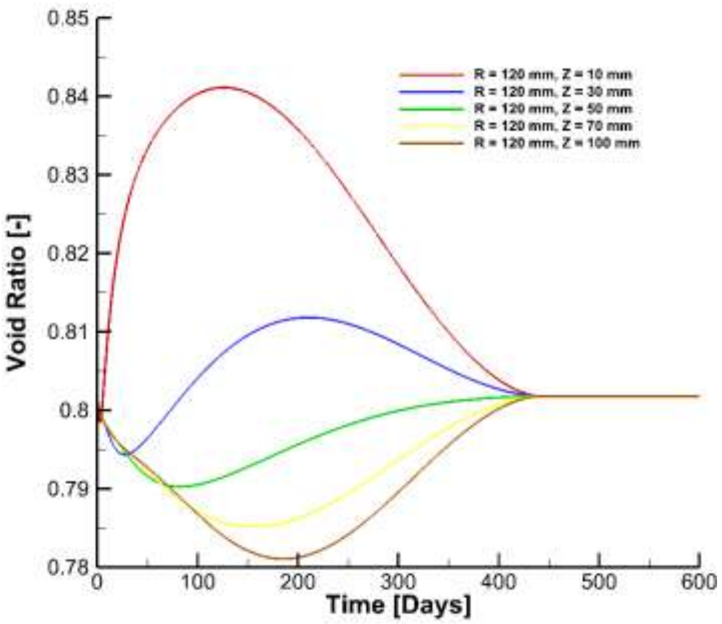

Figure 4-16 Calculated evolution of void ratio at different points in the domain.

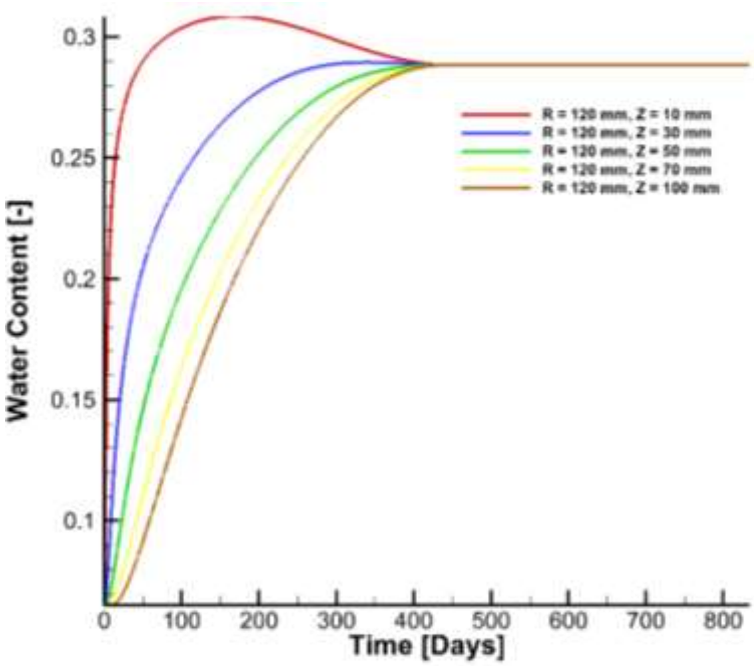

Figure 4-17 Calculated evolution of water content at different points in the model domain.

4.3.4.2. ***Stress Profiles***

The evolution of the effective radial stresses along the outer edge of the model domain at various heights is shown in Figure 4-18. The evolution of the effective axial stress at the top of the model domain is shown in Figure 4-19. In Figure 4-20 a comparison between the measured and simulated stresses is shown.

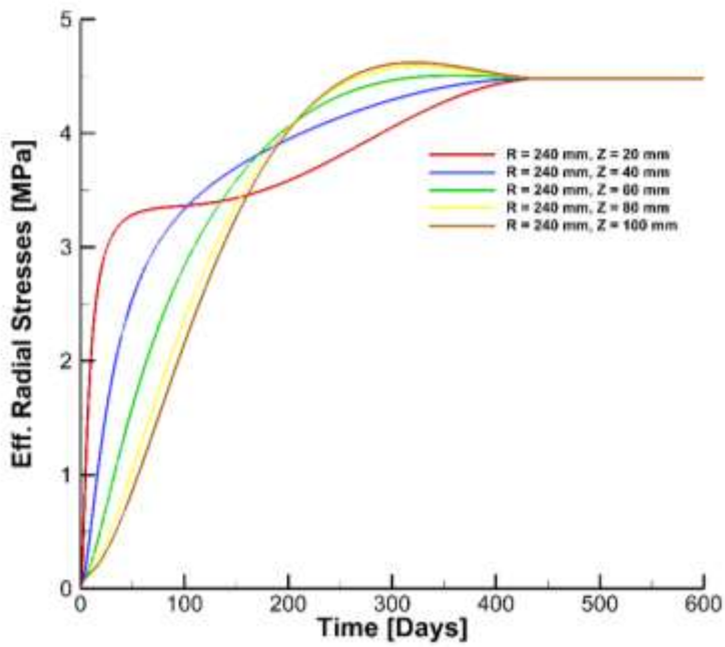

Figure 4-18 Calculated evolution of effective radial stress at different points in the model domain.

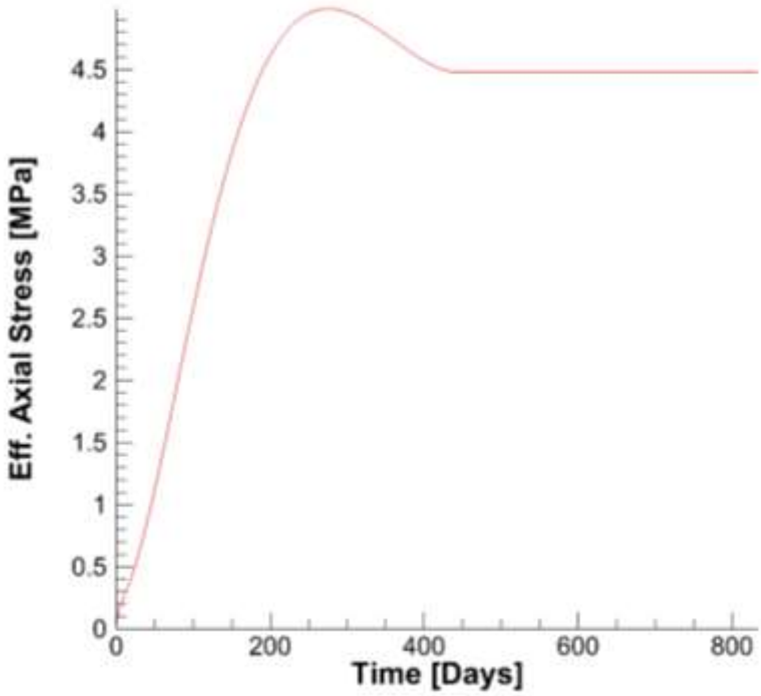

Figure 4-19 Calculated evolution of effective axial stress at the top of the model domain, Z = 103.6 mm.

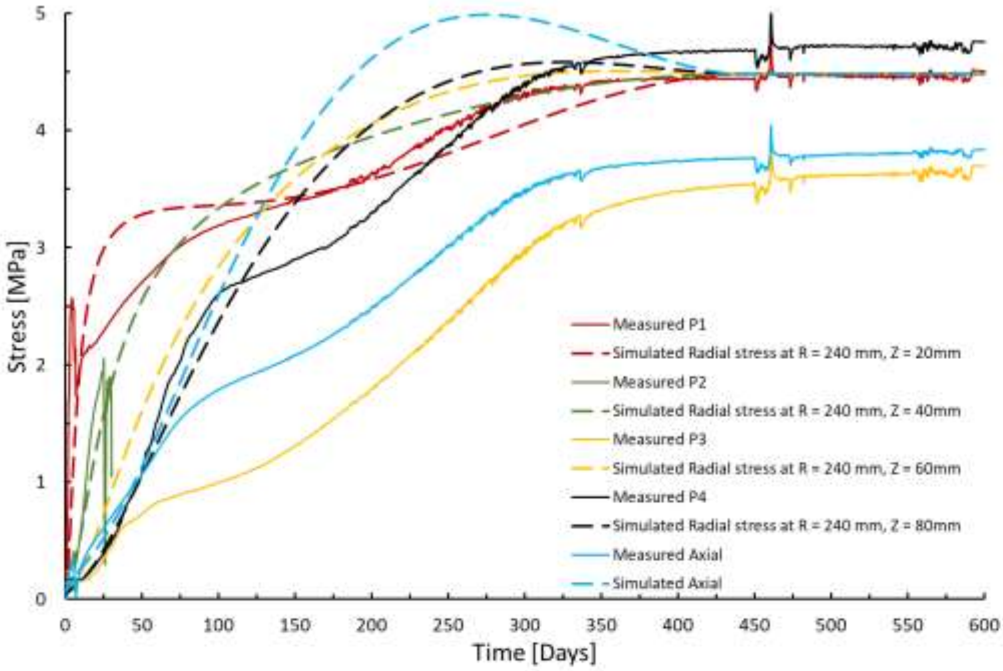

Figure 4-20 Comparison of measured and simulated stresses.

The following observations can be made based on the comparison of the measured and simulated data:

- The measured data suggests no clear trend in the stress evolution along the height. This inference is made based on to the measurements of sensor P3, which recorded lower stresses than P1.
- The repsonse of P3 is also the slowest, suggesting a non-homogenous saturation process in the system (e.g. the existence of a preferential flow barrier)
- Although P2 failed very early on, the early evolution of the other three sensors appear to show a trend which is followed by the model.
- All measured curves show an apparent decrease in the rate of swelling stress at approximately 100 days. This might suggest either that the constant-volume swelling process is of a variable rate or that the energy built up in the system due to the swelling stresses is dissipated at that point in time (e.g. compaction, local rearrangement of pellets or local deformation).
- The early time evolution of all the measured stress curves, except P3, are reproduced well in the model. The biggest deviation is seen in the axial stresses. The measured axial stress is much smaller than the simulated axial stress. This might suggest an axial elongation of the test cell or a deformation in the axial direction. The early-time volume increase of the test cell mentioned in the test case document might be one of the reasons. The total length of the cell was increased by 1.55 mm which might have caused the low measured axial stress.

The model can reproduce the early-time measured stresses qualitatively and quantitatively well. The steady state stress of the simulated system depends on the maximum swelling pressure which is a model input. This parameter was chosed to be 5.8 MPa and yields the steady state stress value of the sensor P1. Due to the elastic model used, all points in the model domain attain the same stress value at steady state.

The model concept for unsaturated flow represents the total stresses as the total equivalent external force action on both the porous skeleton and the pore water. The initial capillary pressure in the system, calculated from the capillary pressure – saturation relationship, the saturation as a function of water content and the porosity, are very high. A part of the capillary force is transferred to the solid skeleton as effective stress during the saturation process (controlled by Bishop's parameter and the Biot coefficient). However, in the experimental setup, although the sensors fitted measure the total stresses, it is still unclear whether the stresses measured in unsaturated conditions are the same total stresses as defined by the effective stress concept used in the model. It is therefore assumed that in case of partial saturation, the effective stresses are the same as the total stresses. Hence the effctive stresses were chosen intentionally for the comparison.

4.4 ClayTech

4.4.1 Geometry and discretization

The total length of the geometry and the section area were set to 0.10515 m and 0.0452 m^2, respectively.

The geometry was discretized in 21 elements, thereby making the initial length of each element approximately 5 mm (Figure 4-21). The time increment was 25 seconds for the first 10 days and was thereafter increased to 250 seconds.

4.4.2 Input parameters

A new parametrization of the clay potential functions was made since the functions used previously were less relevant for a void ratio level below approximately 0.7. The new functions were based on the previous functions for void ratios 0.8, 1.0, 1.2 …3.0, and on two water retention curves for free swelling conditions, and for initial water content of 0 and 64 %, respectively, presented by Dueck and Nilsson (2010), see Figure 4-22Figure 4-22 (left).

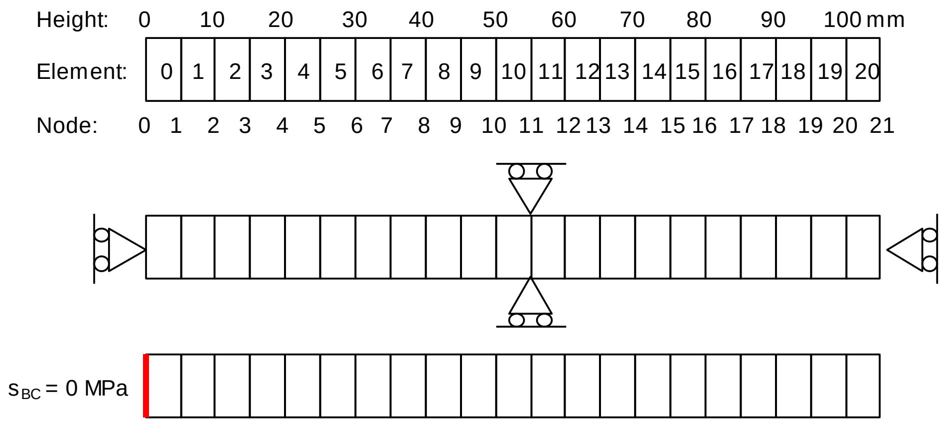

Figure 4-21 Model geometry and discretization (upper). Boundary conditions: mechanical (middle) and hydraulic (lower).

The new functions were fitted on the following form:

$$\Psi = exp(c_3 e^3 + c_2 e^2 + c_1 e + c_0) \tag{4-1}$$

The following coefficients were found for the lower curve (Ψ_L): c_3= -0.0838; c_2=1.1904; c_1= -6.3234; and c_0=5.7035. The corresponding coefficients for the higher curve (Ψ_H) were found to be c_3=-0.1463; c_2=1.6239; c_1=-6.6382; c_0= 6.6008. The mid-line and the half-allowed span were calculated as: $\Psi_M = (\Psi_H + \Psi_L)/2$ and $\Psi_{\Delta/2} = (\Psi_H - \Psi_L)/2$, respectively. It should be noted that the conversion of the water content data of the water retention curves to void ratio values was made with a constant water density value (1000 kg/m^3), and not by taking any compressibility into account. These functions are therefore likely to be revised.

The K parameter was set to 40, a value which was adopted for water saturated conditions (Börgesson et al. 2018).

The γ parameter was set to 7, in line with the definitions proposed by Åkesson et al. (2018).

The water density parameters ρ_0 and β were set to 998 kg/m^3 and 4.5·10^{-4} MPa^{-1}, respectively. The particle density ρ_s was set to 2780 kg/m^3.

The hydraulic conductivity was adopted from Åkesson et al. (2010) and calibrated for the current test results:

$$K(e, S_l) = {S_l}^3 \cdot 4.8 \cdot 10^{-13} e^{5.33}\ [m/s] \tag{4-2}$$

It should be noted that this is a factor 2 higher than the original parametrisation.

The vapor diffusion tortuosity, included in (2-32), was set to the value 0.5.

4.4.3 Initial and boundary conditions

The experimental initial RH level (i.e. suction) and the final pressure level are illustrated in Figure 4-22 (right) against the initial micro void ratio and void ratio, respectively, and compared with the adopted clay potential functions. It can be noted that both points were found in the lower part of the adopted interval. The initial path variable value (both axial and radial) was therefore set to -0.5.

The initial dry density was set to 1520 kg/m³ which corresponds to a void ratio of 0.829. The initial stress (both axial and radial) was set to 0.1 MPa. The initial water content was set to 4.23 %. With the adopted material parameters, this corresponded to a micro void ratio of 0.128 and an initial suction value of 180 MPa.

The geometry was mechanically confined in all directions, and a hydraulic boundary condition (s_{BC}=0 MPa) was applied at one of the short ends of the geometry (Figure 4-21).

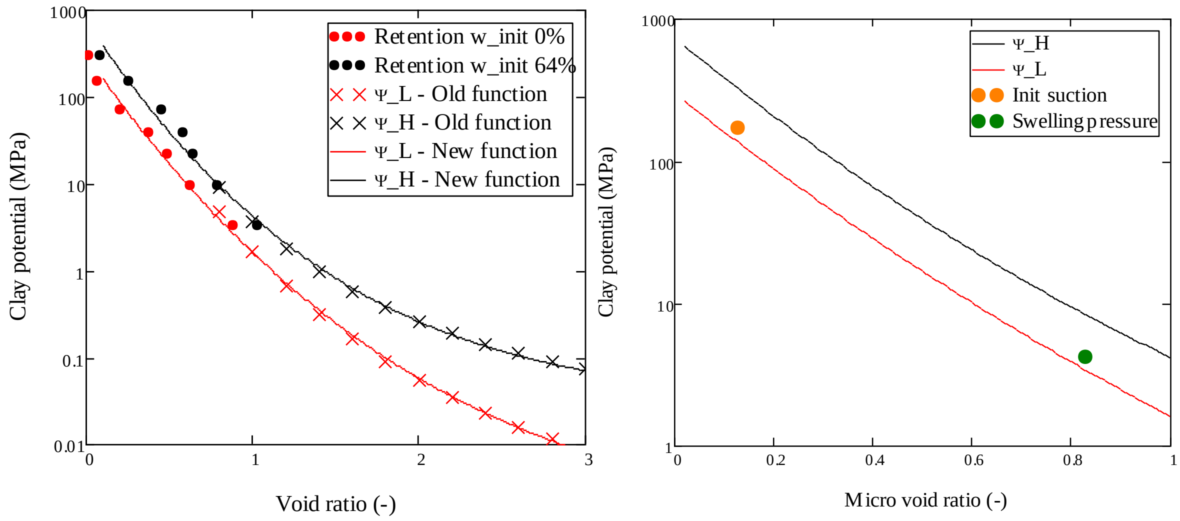

Figure 4-22 Adoption of new set of clay potential functions (left): water retention data (•), old Ψ functions (χ), and new Ψ functions (lines). Comparison of new Ψ functions with initial and final points of the analysed test (right).

4.4.4 Results/discussion

4.4.4.1. *Results*

A comparison of modelled and experimental results is shown in Figure 4-23. It can be noted that the measured evolution of the RH, as well as the overall time-scale of hydration, was fairly well mimicked by the model. This agreement was largely enabled by the inclusion of both Darcy´s law and vapor diffusion. Especially the results from the RH sensors located far from the hydraulic boundary could not be matched without the inclusion of vapor diffusion.

The build-up of radial stresses was fairly well mimicked by the model, especially for the P1 and P4 sensors, although the final levels were slightly higher than the measured levels. Concerning the P3 sensor, the measured stress level was significantly lower than both the model and all the other operational sensors. The measured build-up of the axial stress was also markedly lower than the modelled evolutions. The measured trend for the cumulative water uptake was fairly well mimicked by the model, although the measured volume was slightly higher than the modelled volume.

Modelled axial profiles of radial and axial stresses at different times are shown in Figure 4-24. It can be noted that the radial stresses initially were lower at the far end from the hydraulic boundary, but that this changed with time so that the highest radial stresses were found at the far end when saturated conditions were reached. The axial stresses were naturally the same through the entire geometry.

Modelled evolutions of void ratio, water content and degree of saturation at different positions are shown in Figure 4-25, while modelled axial profiles of void ratio and water content at different times are shown in Figure 4-26.

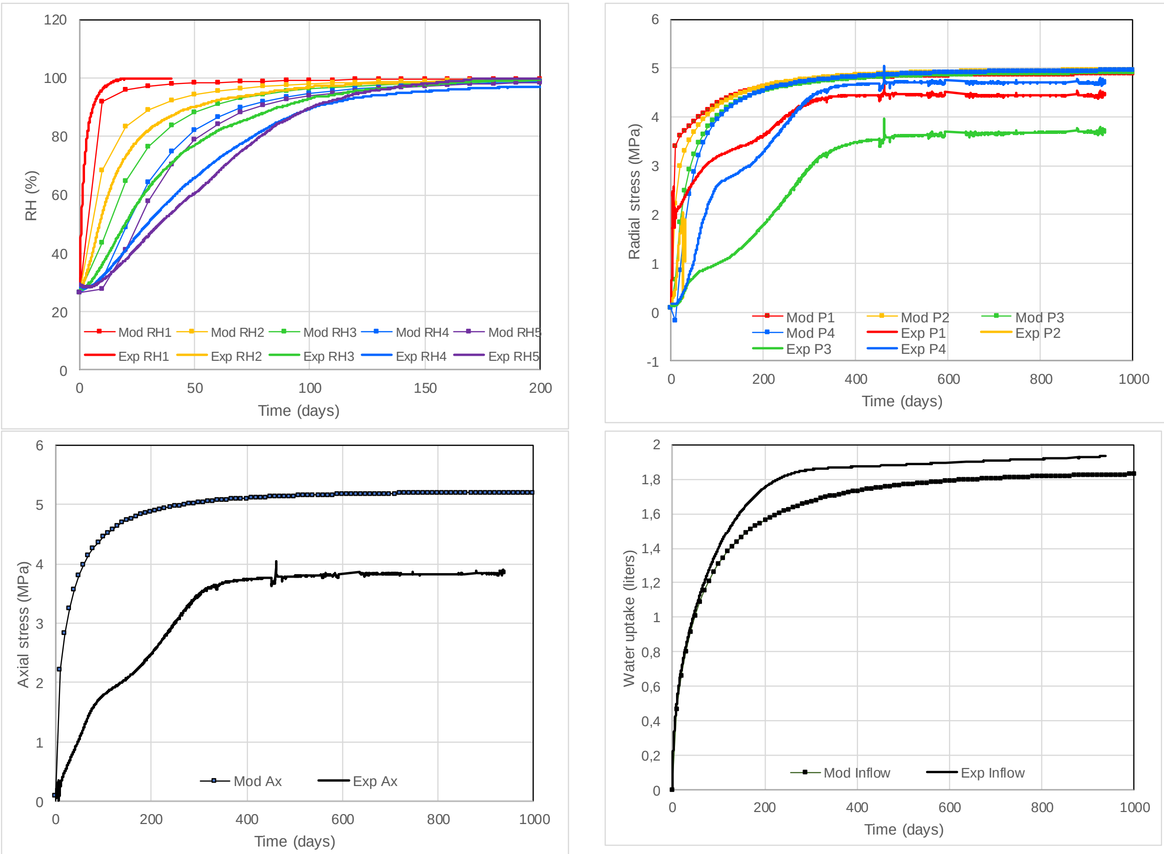

Figure 4-23 ***Modelled (symbols) and experimental (solid lines) evolutions of RH (upper left), radial stress (upper right), axial stress (lower left) and water uptake (lower right).***

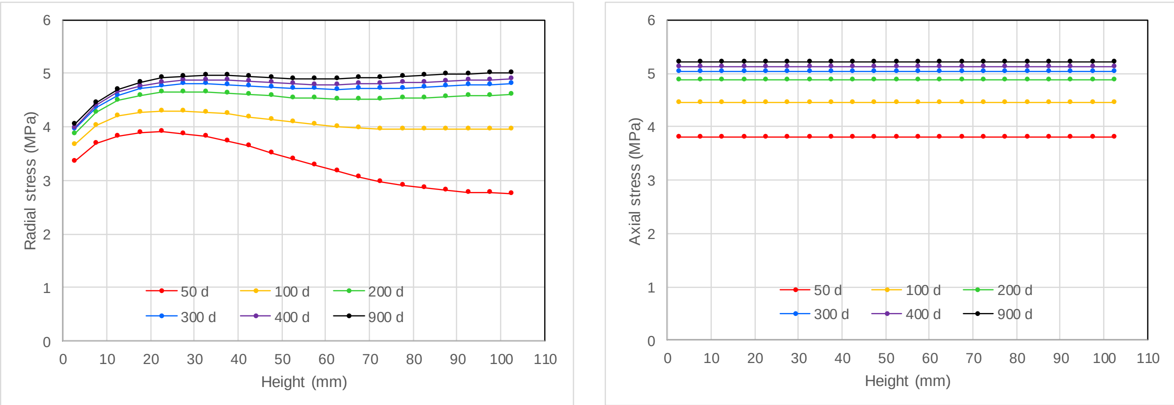

Figure 4-24 Modelled axial profiles of radial stress (left) and axial stress (right) for different times.

The initial evolution and profiles of the void ratio showed that the bentonite close to the hydraulic boundary swelled and increased in void ratio, while the inner parts were compressed and decreased in void ratio. The trends subsequently changed direction so that bentonite close to the boundary was compressed whereas, the inner parts (more than 60 mm from the boundary) swelled.

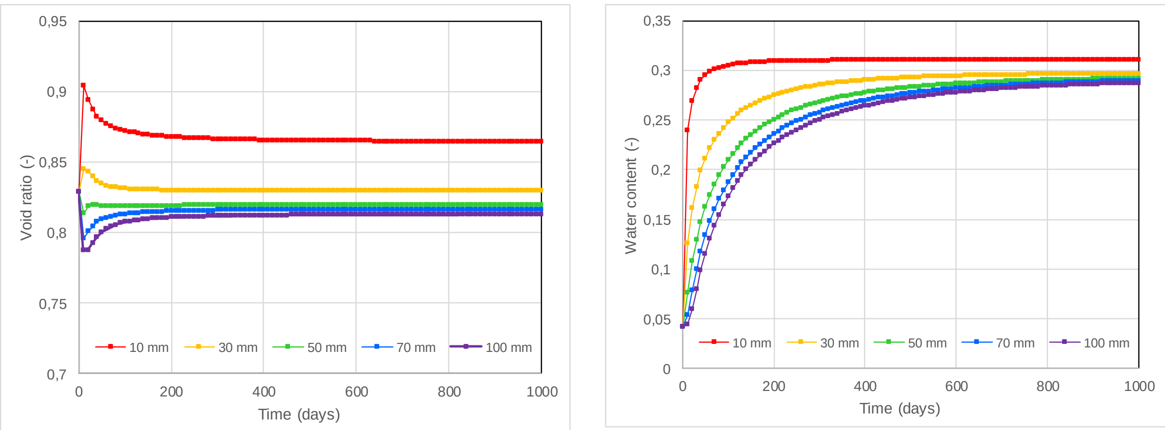

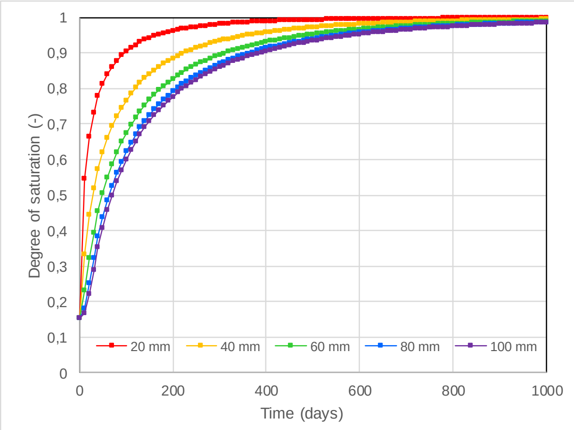

Figure 4-25 Modelled evolution of void ratio (upper left), water content (upper right) and degree of saturation (lower left).

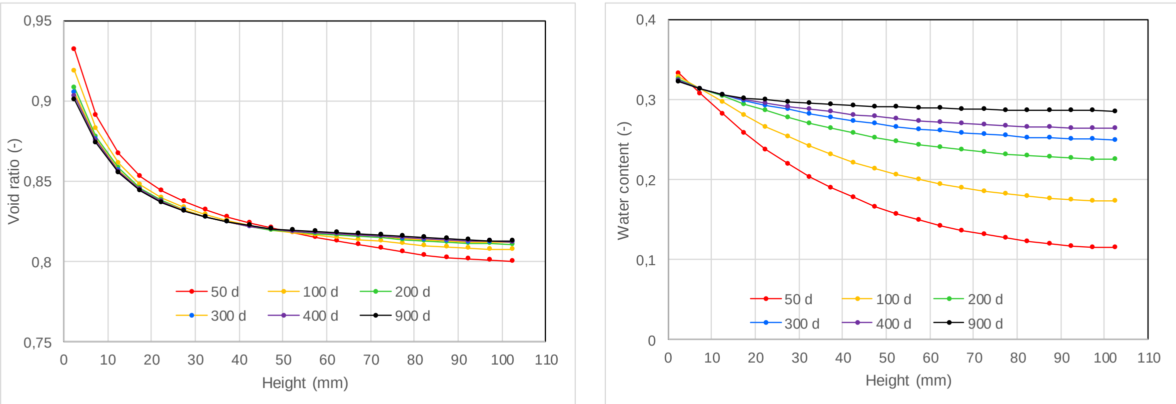

Figure 4-26 Modelled axial profiles of void ratio (left) and water content (right) for different times.

The evolution and profiles of water content and the degree of saturation generally reflected the water uptake from the hydraulic boundary so that both w and S_l increased from their initial levels to a level corresponding to saturated conditions.

4.4.4.2. *Discussion*

The overall mechanism of the model is illustrated in Figure 4-27. This shows stress paths in the Ψ-e_m plane for the elements at the two ends of the geometry (no. 0 and 20), and both the axial (Ψ1) and the radial (Ψ2) clay potential are shown in each graph. Each variable was found within the allowed span of the clay potential and changed from the initial suction value to the final swelling pressure value. Close to the hydraulic boundary (no 0) the stress condition was fairly isotropic but was later on more anisotropic; first with Ψ_1 lower than Ψ_2, reflecting the swelling of the element, and finally with Ψ_1

higher than Ψ_2, reflecting the compression. Far from the hydraulic boundary (no 20) the initial compression meant that Ψ_1 exceeded Ψ_2, but this difference was levelled out during the subsequent swelling of this part.

The behaviour in the Ψ-e_m plane is thus similar to the behaviour in water saturated homogenisation problems and is largely controlled by equations (2-20) and (2-27). In addition, an important feature for the models is that the suction value reduces to zero when the difference between the void ratio and the micro void ratio decreased to zero (i.e. the saturation degree increases to unity, and this is controlled by equations (2-24) and (2-26).

Nevertheless, the presented model still displays at least one limitation: namely that the interaction functions Eq (2-23) to (2-26) does not include any path dependence. For instance, the $\partial\sigma_1/\partial\varepsilon_1{}^i$- derivative should exhibit a higher value (stiffer behaviour) for unloading conditions than for loading conditions. The absence of such a path dependence make the calculations of increments in axial stress (A2-5) and strains (A2-6) more simple than they otherwise would be.

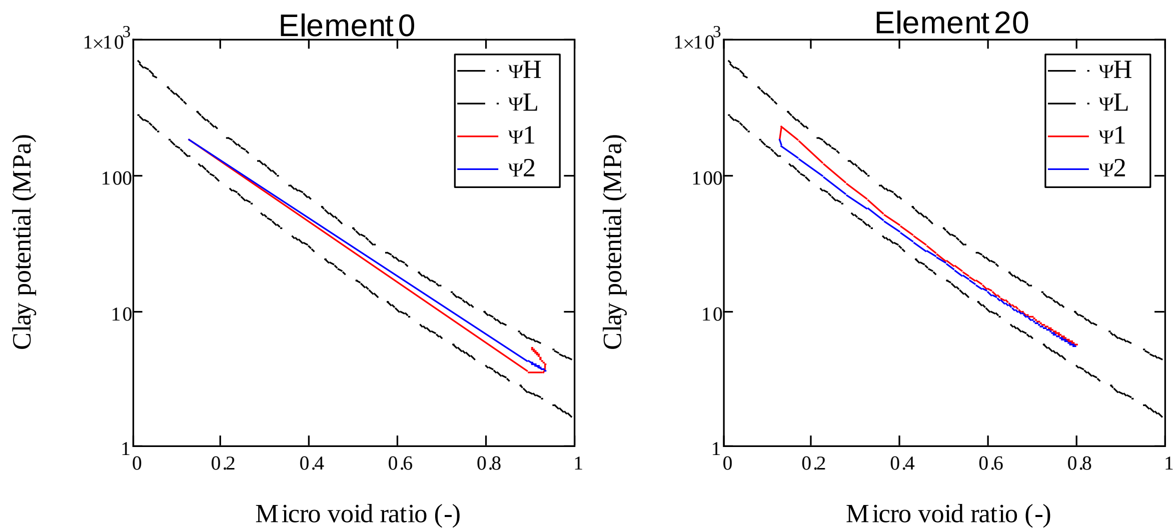

***Figure 4-27** Stress paths in Ψ-e_m plane, axial (red lines) and radial (blue lines). Left graph shows stress path for element closest to the hydraulic boundary. Right graph shows path for element most distant from boundary.*

4.5 EPFL

4.5.1 Geometry and discretization

The geometry of the model for the test 1b consists of a 120x105 mm domain, representing axisymmetric conditions. This domain is discretised into 100 finite elements (8-node quadrilateral with 4 integration points each). A sketch of the model geometry and its mesh is shown in Figure 4-28.

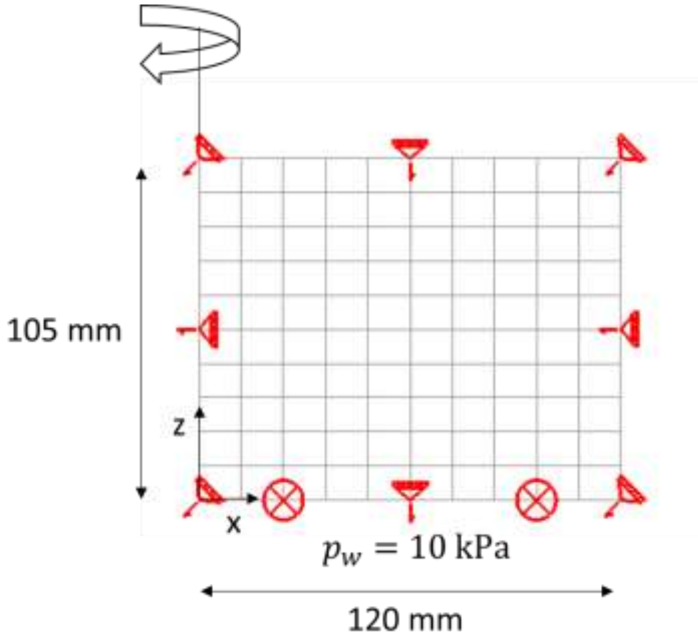

Figure 4-28 Model geometry, mesh, and boundary conditions for the model of the test 1b

4.5.2 Input parameters

Bulk and shear moduli are set to K_{ref} =19 MPa and G_{ref} =10 MPa for a reference isotropic pressure of p'_{ref} =1 MPa. The plastic compressibility parameter is set to $\beta = 6$ and the loading collapse parameter to $\gamma_s = 4$. These have been calibrated using measurements of the steady-state swelling pressure, by fitting radial and axial swelling pressure at equilibrium. Parameters obtained from the calibration are slightly different to those used in the tests 1a, which is likely due to the initial fabric of the material.
The value of permeability has been set to $k_{f0} = 10^{-20}\mathrm{m}^2$ derived from data reported in Borgesson et al. (1995) at a void ratio of 0.68, which yields a saturated hydraulic conductivity of $K_w = 10^{-13}\mathrm{m/s}$. This value remains the same as with the tests 1a.
Regarding the remaining parameters, standard values for clays have been adopted.

Material parameters of the model are summarised in Table 4-7.

Table 4-7 Model parameters used for the simulation of test 1b

Elastic parameters		
K_{ref} , G_{ref} , n^e	[MPa], [MPa], [-], [°C^{-1}]	19, 10, 1
Isotropic plastic parameters		
β_m , γ_s , r^e_{iso} , p'_c , Ω	[-], [-], [-], [-], [-], [MPa] , [-]	6; 4; 0.01; 1.8; 0
Deviatoric plastic parameters		
b , d , M , g , α , a , r^e_{dev}	[-], [-], [-], [-], [-], [-], [-]	0.5, 2.0, 1.0, 0, 1, 0.001, 1
Water retention parameters		
s_{e0} , β_h , θ_T , θ_e , s_{hys}	[MPa], [-], [-], [-], [-]	5, 7.7, 0, 0, 1
Water flow parameters		
k_{f0},C_{KW1},C_{KW2}, M, N	[m^2], [-], [-], [-], [-]	10^{-20}, 2.9, 2.9, 5.3, 5.5

Regarding mechanical parameter, i.e. elastoplastic parameters, the elastic moduli, initial preconsolidation pressure and the loading collapse curve parameter have been changed with respect to the tests 1a. Although in both tests the material was MX-80 bentonite, the initial fabric and compaction conditions are different and could justify this change.

The water retention curve parameters have been calibrated using a test on a similar mixture of MX-80 pellets reported by Molinero-Guerra et al. (2016). The experiments were also performed on a mixture with a void ratio of around 0.8 as in the present case, showing a similar water content in hygroscopic conditions. The experimental results and the corresponding model of water retention used are shown in Figure 4-29. A water content of 4% corresponds to the initial relative humidity measured in the test (RH = 30%). Parameters accounting for temperature, hysteresis and volume change effects on water retention have not been taken into account.

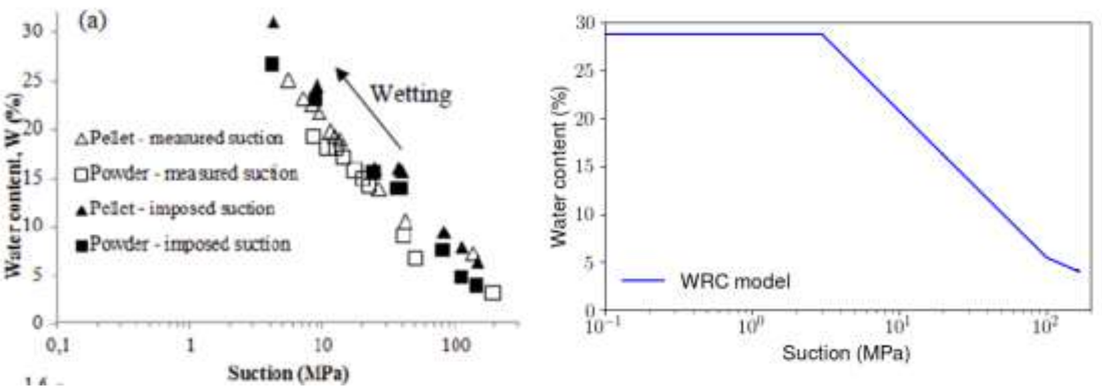

Figure 4-29 Left: (From Molinero-Guerra et al. 2016) Water retention reported in a MX-80 mixture of pellets and powder at void ratio of 0.8. Right: ACMEG model of water retention used for the simulations.

4.5.3 Initial and boundary conditions

All external nodes in the vertical boundaries are constrained in the horizontal direction and all nodes in horizontal boundaries are constrained in the vertical direction.
The initial suction s_0 in the entire domain has been set in accordance with the relative humidity RH measured at the beginning of the stage. This has been obtained applying the Kelvin's law, which relates total suction s and RH:

$$s = -\frac{RT\rho_w}{M_w}\ln(RH) \tag{24}$$

with R = 8.314 J/mol K; Mw=18.016 kg/kmol; ρ_w=1000 kg/m^3; and T is the temperature which is taken as T=296ºK. Accordingly, for a relative humidity of RH=30% a value of total suction s =165 MPa is obtained. Assuming that osmotic suction can be disregarded, an initial water pressure of -165 MPa has been set as initial condition, while air pressure is set to 0. The bottom (z=0) boundary has been fixed to a water pressure of 10 kPa according to the experimental setup. The remaining boundaries are set to no flow conditions.

4.5.4 Results/discussion

As in the tests 1a, the results are presented using the convention that z=0 corresponds to the bottom of the sample, which is where water uptake takes place.
Swelling pressure that resulted from the model is shown in Figure 4-30, as well as some of the experimental results. It can be seen that the model overestimates the magnitude of the axial stress measured by a difference of 1 to 2 MPa. It is also observed that while the maximum swelling pressure measured corresponds to the radial stress at z=80 mm, in the model the highest pressure is obtained in the axial direction. Excessive collapse is also predicted by the model which was not observed in the experiment.
Nevertheless, the trend of swelling pressure is reasonable, with a sharp initial increase for the bottom part that resembles the experimental measurements. Steady state is reached at about the same time as observed in the experiment. Moreover, the magnitude of swelling pressure in radial direction is well captured for the steady state. The results suggest that modifications to the formulation should aim at avoiding the collapse behaviour observed.

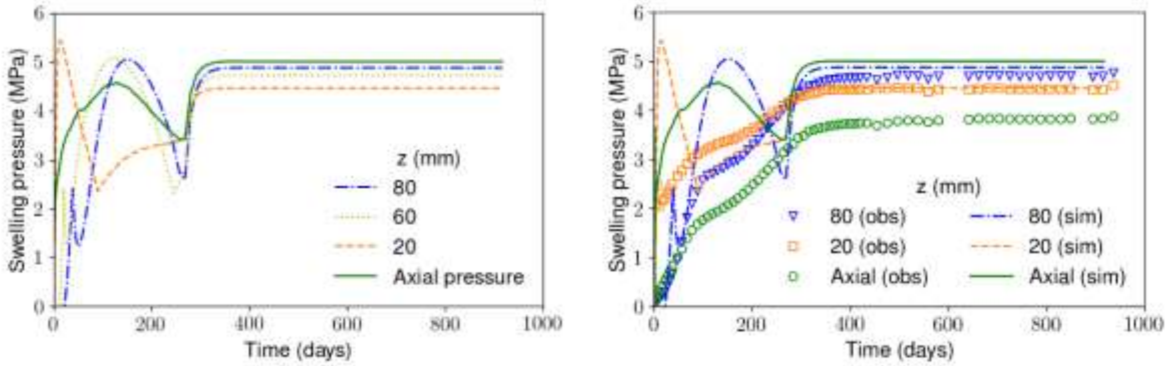

Figure 4-30 Left: Radial swelling pressure results at 3 different heights and axial pressure simulated. Right: Comparison of simulation (sim) with experimental results (obs in the legend) at two heights and axial measurement.

To understand the development of swelling pressure as observed in Figure 4-30 it is necessary to examine the stress paths in the planes suction-mean effective stress and void ratio which are the fundamental state variables of the mechanical model. These are represented in Figure 4-31 together with the swelling pressure (total stress) – suction plane. Initial effective stress is exclusively due to the initial suction and degree of saturation of the material, which upon wetting tends to decrease as observed in the effective stress path.

The initial decrease of effective stress results in an increase of void ratio due to elastic unloading as observed in the plane void ratio – effective stress. Subsequent reduction of suction eventually results in reaching the yield stress in the plane effective stress – suction. At this point the material densifies (void ratio decreases) in order to compensate the decrease of suction. The void ratio and stress at which this process happens varies with depth (see Figure 4-31). Indeed the elements situated at the bottom of the sample intially expand, whereas the upper elements are compressed by such developed strains. Therefore the elements at different depths are wetted under different initial void ratios and lead to different amount of collapse for each of them. Thus, swelling pressure in the upper part is higher because the density of the material at the moment of wetting is higher. Upon reaching saturation, the collapse process ceases and the material experiencies an elastic increase in void ratio due to the decrease in effective stress.

This plastic process is the reason why the final state of the sample is heterogeneous in terms of void ratio and stresses. Note that because the yield surface is formulated in terms of mean effective stress, the axial stress that is developed corresponds to that needed to maintain overall null deformation of the sample for different radial stress in depth. As radial stress develops progressively with depth, the vertical stress is the result of the overall collapse behaviour of the sample. In this case the axial stress is higher than the radial one due to the specific yield surface (loading collapse) used. Such yield curve would only predict lower axial stress if the collapse is even higher and can be obtained increasing γ_S (eq. 11). However, despite decreasing axial stress, the collapse obtained in that case would lead to unrealistic swelling pressures.

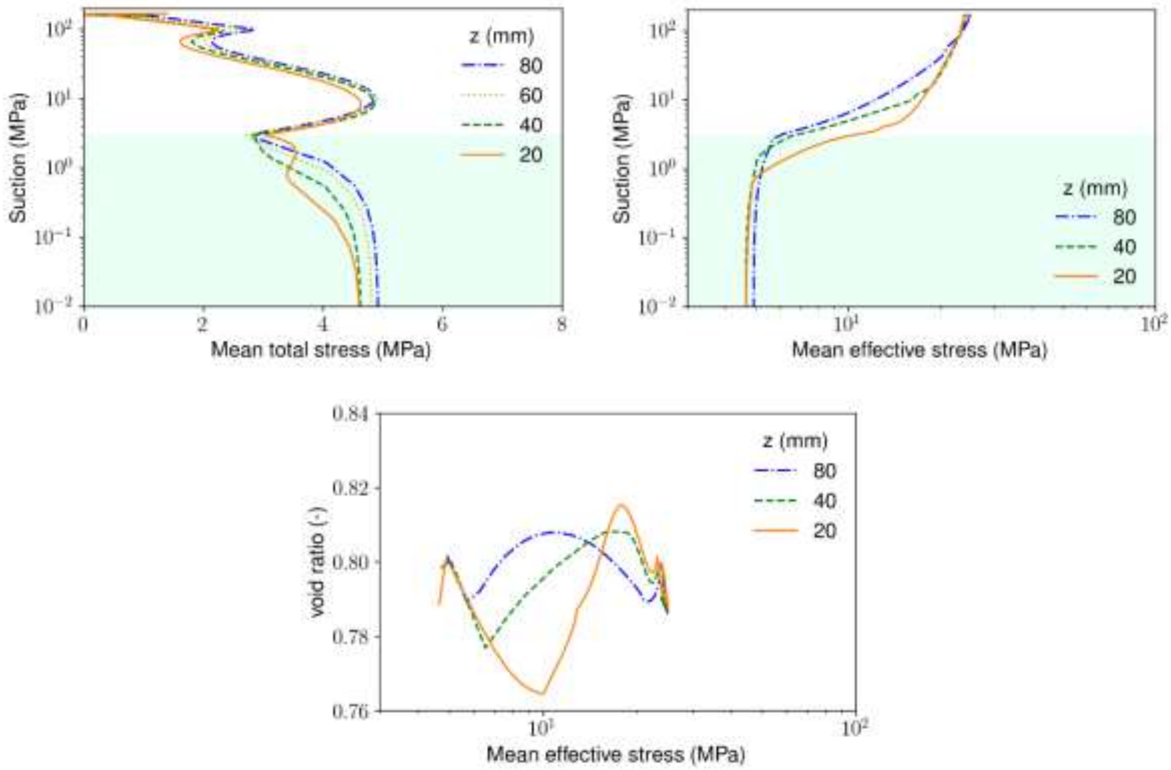

Figure 4-31 Stress paths obtained during the test, shadowed zone corresponds to a saturated state. Upper left: In terms of mean total stress and suction. Upper right: In terms of effective stress and suction. Bottom: Void ratio evolution as a result of effective stress changes.

The evolution of relative humidity measured is compared in Figure 4-32 with that obtained from the simulations. The agreement is satisfactory and provides validation of the water flow model and its parameters, which remained unchanged from tests 1a.

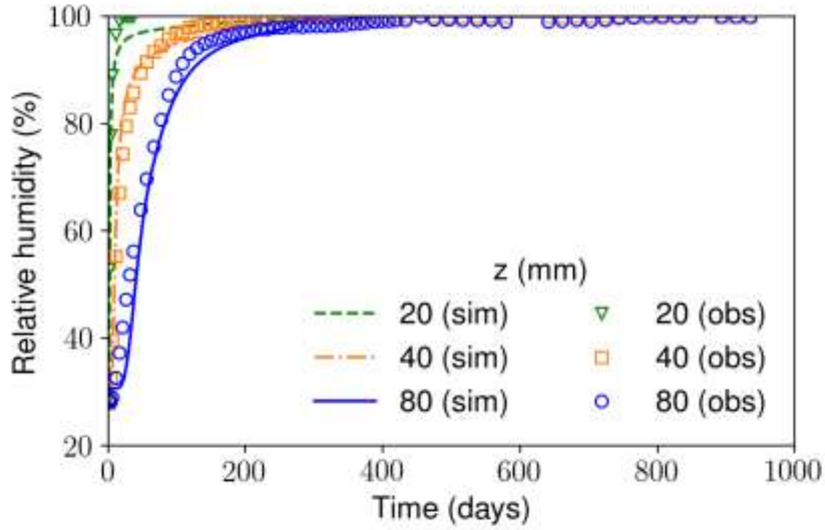

Figure 4-32 Comparison of relative humidity simulated (sim) with the measurements (obs) form 3 sensors at variable height.

Water uptake by the model is shown in Figure 4-33 in terms of water content and degree of saturation. The model reaches complete saturation between 300 and 400 days, in agreement with the experimental observations.

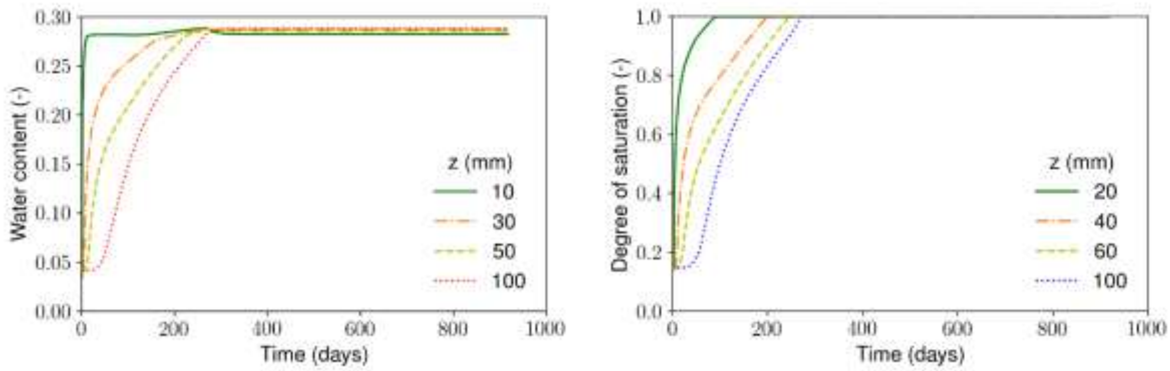

Figure 4-33 Left: Simulated water uptake in terms of water content at different positions. Right: Evolution of the degree of saturation at different positions.

Void ratio evolution is shown in Figure 4-34. It can be seen that before the steady state is reached, the sample undergoes collapse at different heighs. The final state is denser at the bottom of the sample with a rather homogeneous state in the upper part.

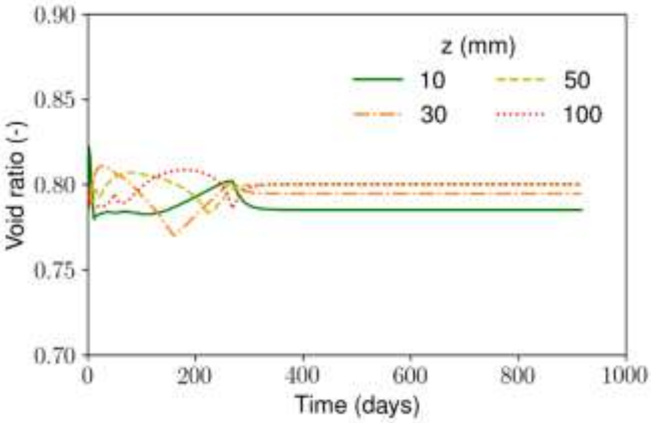

Figure 4-34 Predicted evolution of void ratio with time at different positions. Initial void ratio is 0.8.

The predicted values of dry density are compared to the measurements after the dismantling of the test in Figure 4-35. The values are within the range of the measurements, except for the zone between 40 mm and 20 mm heigh, where the trend of the simulations deviates from the one that was measured. This is most likely due to the excessive collapse that is obtained during the saturation phase (see Figure 4-34).

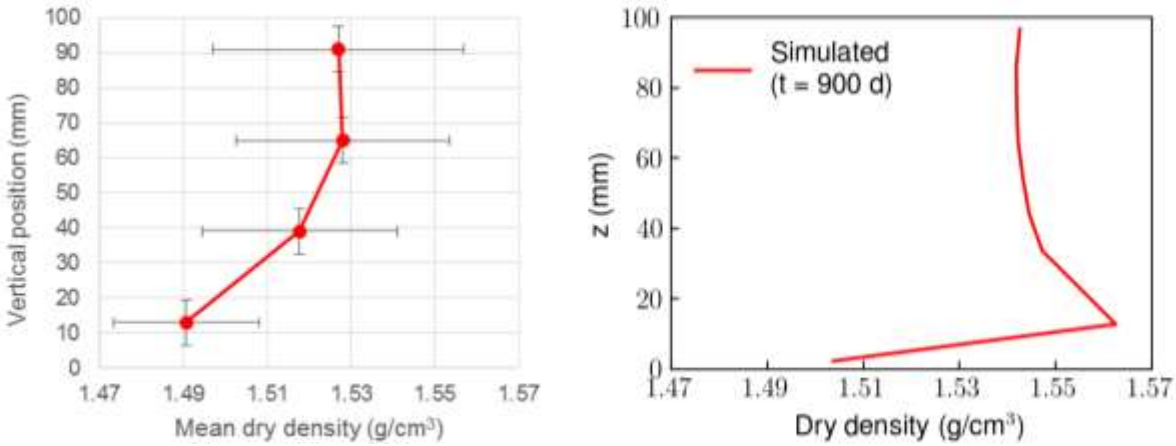

Figure 4-35 Measured values of dry density after the dismantling (left) compared to the model predictions (right).

4.6 LEI

The objective of the experiment was to study the swelling behaviour of a MX-80 pellet/crushed pellet mixture. Pellets are roughly spherical with a diameter of 32 mm. Swelling pressure tests were carried out using constant volume cells of the following dimensions: height - 105.15 mm, radius – 120 mm. The illustration of experimental cell with pellets and crushed pellets is given in Figure 4-36.

Figure 4-36. Illustration of the 240 mm diameter cell at installation (Beacon D5.1.1, 2018)

For the modelling of hydro-mechanical behaviour of bentonite pellets and crushed pellets mixture "Single pellet model" was developed. Taking into consideration the observations of "Single pellet model" the equivalent material and its effective parameters were proposed.

4.6.1 Geometry and discretization

4.6.1.1. *COMSOL Multiphysics model*

The modelling of the mixture of pellets and crushed pellets was performed in two steps. First of all the analysis of water saturation and swelling was carried out on smaller scale (single pellet model). Later the larger scale model (cell scale) was developed for modelling of the swelling pressure resulting from wetting of this mixture. The mixture of pellets and crushed pellets was described as equivalent material with effective parameters. The observations from "Single pellet model" were considered for the justification of effective parameters values for equivalent material model.

Single pellet model

The conceptual model of single pellet is presented in Figure 4-37. It consists of two materials with significantly different characteristics. The geometry of pellet and surrounding crushed pellet material was simplified. Pellet was assumed to be spherical (r=16 mm) and the surrounding crushed pellet material was assumed to be cylinder around it (axisymmetric geometry) (r=18 mm, h=34 mm). The dimensions were evaluated considering that the volumes of pellet and crushed pellet material are equal that is in line with given specification of proportion 70 % (pellets) and 30 % (crushed pellets) by mass.

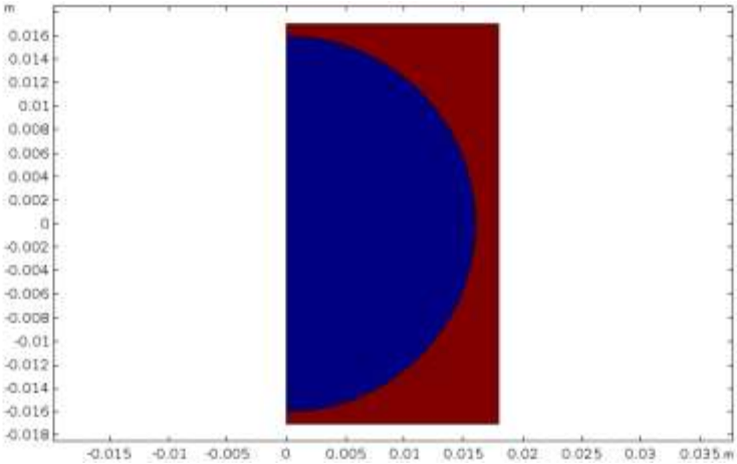

Figure 4-37. Conceptual model of single pellet model: pellet (blue), crushed pellet material (brown)

The numerical model of coupled HM processes consisted of hydraulic process model based on Richard's equation, modified linear swelling model and the model for the evaluation of porosity change.

Equivalent material model

The geometry for computational model of equivalent material was set as the cell geometry (r=120 mm, h=105.15 mm). The modelling has been done under axisymmetric conditions and analysed domain was meshed with 1886 triangular grid elements as could be seen in Figure 4-38

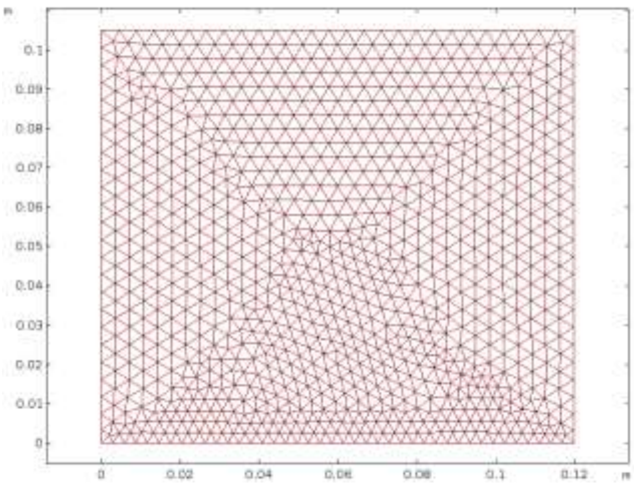

Figure 4-38. Computational grid of COMSOL Multiphysics model

4.6.1.2. *CODE_BRIGHT model*

Equivalent material approach was applied for the analysis of the behaviour of pellets and crushed pellets mixture during water saturation. The modelling has been done under axisymmetric conditions and analysed domain was meshed with 480 rectangular grid elements as could be seen in Figure 4-39.

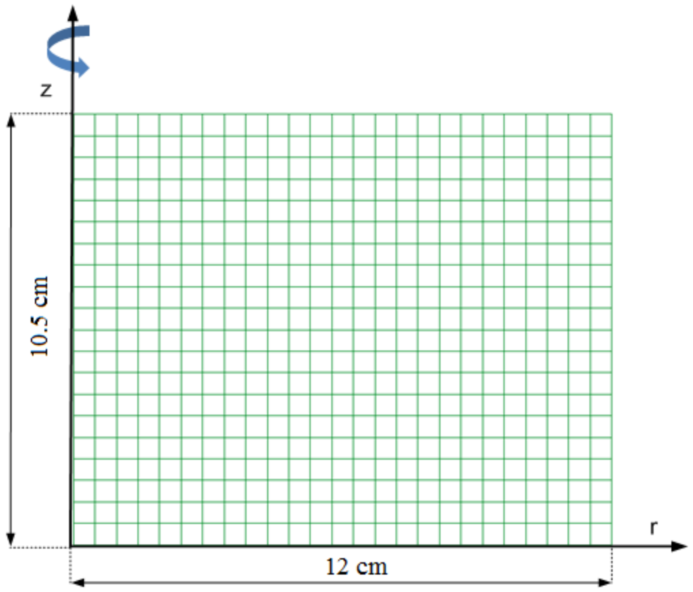

Figure 4-39. Computational grid of CODE_BRIGHT model

4.6.2 Input parameters

4.6.2.1. *COMSOL Multiphysics model*

Initial characteristics of pellets and crushed pellets are summarized in Table 4-8.

Table 4-8. Initial characteristics of materials used in the experiment

Parameter	Pellets	Crushed pellets	Mixture
Clay density (g/cm^3)	2780(*)		
Total dry mass per constituent, g	5052.455 (*)	2177.236 (*)	7229.691
Initial gravimetric water content, %	4.090(*)	4.550(*)	4.23 (*)
Initial dry density(g/cm^3)	2152.436	930.668	1.543 (*)

Parameter	Pellets	Crushed pellets	Mixture
Initial porosity, -	0.225	0.665	0.445 (*)
Initial void ratio, -	0.29	1.98	0.802
Initial saturation, -	0.38	0.0636	0.1465(*)

* - data from specification (Beacon D5.1.1, 2018).

Single pellet model

The input data required for bentonite saturation modelling are:

- Water retention curve (dependency of saturation versus suction (capillary pressure));
- saturated permeability;
- relative permeability;
- initial and residual saturation of material.

The parameters required for bentonite swelling modelling are:

- Young's modulus *E* or bulk modulus *K*;
- Poisson ratio;
- Swelling coefficient.

Water retention

For the pellet material water retention curve was selected to be represented by van Genuchten relationship, which is governed mainly by parameters such as air entry pressure P_{entry} and pore size parameter m. For highly compacted pellets (porosity n=0.225) the parameters in terms of P_{entry} and m were not available.

According to (Åkesson et al., 2010) for MX-80 bentonite compacted to have total porosity n=0.38 (e=0.629) P_{entry} and m were reported to be 43.5 MPa and 0.38, respectively. Water retention curve was not available for such dense pellet material (n=0.225, e=0.29) during the study. However, compaction of sample to lower dry density will decrease significantly the macroporosity and P_{entry} is expected to be determined by microporosity mainly. Thus the water retention curve parameters were assumed to be the same as for compacted material of porosity n=0.38.

The crushed bentonite material is of high porosity (n=0.665, e=1.98) thus it is reasonable to expect its fast saturation and piping phenomena. Considering this the air entry pressure is expected to be much lower in comparison with the pellets. The entry pressure P_{entry}=0.5 MPa and m=0.26 were reported in (Åkesson et al., 2010) for MX-80 material of high porosity (n=0.64, e=1.78). Considering this the van Genuchten relationship parameters for crushed pellet material were selected as P_{entry}=0.1 MPa and parameter m=0.2705 to give the estimated initial saturation of 0.0636 at initially measured suction of 171 MPa.

Some data on estimated water retention curves for MX-80 bentonite of different density (1.5 g/cm^3, 1.6 g/cm^3, 1.7 g/cm^3, 1.8 g/cm^3) is provided in (Villar, 2004). Tested material however does not cover the densities of interest (0.93 g/cm^3; 2.15 g/cm^3). The results provided in (Villar, 2004) showed that for the material of the higher density the entry pressure and parameter m are higher, thus selected values are in line with these observations.

Permeability

It has been reported that permeability (hydraulic conductivity) of saturated bentonite is a function of initial density. As it is provided in (Åkesson et al., 2010) the saturated hydraulic conductivity is a function of void ratio as follows:

$$K(e) = K_0 \left(\frac{e}{e_0}\right)^{\eta}, \tag{17}$$

$$k_s = \frac{K\mu}{\rho_w g}, \tag{18}$$

where K_0=2.40·10^{-13} m/s, e_0=1, η=5.33.

Exponential dependency was also reported in (Åkesson et al., 2010) such as:

$$k(n) = k(n_0) \cdot exp[b \cdot (n - n_0)], \tag{19}$$

where parameter b can be estimated as $4 \cdot \eta$.

Taking into consideration these dependencies (eq. 17, 19) the calculated saturated permeability for dense pellet would be 3.311·10^{-23} m^2 and 3.360·10^{-23} m^2 with an average value of 3.335·10^{-23} m^2.

Taking into consideration dependencies (eq. 17, 19) the calculated saturated permeability for loose crushed pellets would be 3.892·10^{-19} m^2 and 9.469·10^{-19} m^2 with an average value of 6.680·10^{-19} m^2.

Relative permeability for pellet was assumed to follow van Genuchten-Mualem relationship (eq. 9). The relative permeability for crushed pellet material was assumed to be independent of saturation degree as the crushed bentonite material is of high porosity and its fast saturation and piping phenomena are expected.

Initial saturation of pellet was estimated to be 0.38 in Table 4-8, while the residual saturation was assumed zero. Initial saturation of crushed pellets was estimated to be 0.0636 (Table 4-8), while the residual saturation was assumed zero.

Young's modulus E (bulk modulus K) and Poisson ratio

The average bulk modulus *K*=20 MPa of bentonite-buffer was reported in (Åkesson et al., 2010). With Poisson ratio υ=0.4 ((Åkesson et al., 2010; Rutquist et al, 2014), this corresponds to Young's modulus of 12 MPa. Poisson's ratio (*v*) is the conventional elastic parameter, defined as the negative ratio between the transverse strain and the axial strain for uniaxial compression tests. A value *v*=0.4 has been chosen.

Swelling coefficient

It is known that swelling is a complex process and bentonite macroscopic behaviour upon water uptake is strongly dependent on mineralogy, dry density, void ratio and local conditions. During saturation more dense material (pellet) undergoes larger volumetric deformations in comparison to loose material. During water uptake in pellet surrounded by other material the swelling process occurs neither in strictly confined nor free swell conditions. The material of the lower density has impact on the mechanical boundary of swelling pellet. On the other hand, crushed pellet material is also influenced by mechanical load from swelling pellet. Taking into consideration that the swelling pressure non-linear dependency on void ratio (dry density), the swelling coefficient was assumed to reflect partly this trend for the materials of different porosities, i.e. dense material has more swelling potential:

$$\beta = A \cdot n^{-4.2}, \tag{20}$$

where A=0.002.

Considering changing boundary conditions from mechanical point of view averaged swelling coefficient values were selected for the pellet and crushed pellet material. The averaged (geometric mean) swelling coefficient was assigned for pellet and crushed pellet material considering swelling coefficient at their initial porosity (0.225; 0.665) and expected final porosity (averaged porosity of a mixture, 0.445): 0.25 and 0.025, respectively.

Equivalent material model

The effective parameters for equivalent material model taking into consideration the modelling results of single pellet model.

Water retention

For the material with effective parameters values the water retention behaviour was assumed to be controlled by the pellet saturation, thus air entry pressure was assumed to be equal to that of pellet (P_{entry}=43.5 MPa) with parameter *m* estimate to be equal to 0.582 to correspond to initial saturation of 0.15.

Permeability

Saturated permeability value for equivalent material was taken as geometric mean of the values for different materials in "Single pellet model" ($4.72 \cdot 10^{-21}$ m^2). Relative permeability for pellet was assumed to follow van Genuchten-Mualem relationship (eq. 9).

Young's modulus E (bulk modulus K) and Poisson ratio

The same values for Poisson ratio (υ=0.4) and average bulk modulus *K*=20 MPa was taken the same as used for single pellet model.

Swelling coefficient

Swelling coefficient was taken as geometric mean of parameter values used for different materials in "Single pellet model" ($\beta = 0.08$).

4.6.2.2. CODE_BRIGHT model

Part of the values of hydro-mechanical parameters for equivalent material was based on data in test specification (porosity and density) (Beacon D5.1.1, 2018) or values of parameters applied for COMSOL Multiphysics model (Poisson ratio, water retention and relative permeability curves). The values of other unknown parameters were based on available data on MX-80 compacted bentonite or pellets (Åkesson, 2010; Abed, 2016; Toprak, 2015; Kristensson, 2008; Navarro, 2015). The values of hydro-mechanical parameters of equivalent material and constitutive laws used in the analysis are summarized in Table 4-9.

Table 4-9. Values of hydro-mechanical parameters for equivalent material and constitutive laws applied for CODE_BRIGHT modelling

Hydraulic data		
Retention curve		Van Genuchten model:
Air entry pressure, P_0 [MPa]	43.5	$S_e = \frac{S_l - S_{rl}}{S_{ls} - S_{rl}} = \left(1+\left(\frac{P_g - P_l}{P}\right)^{\frac{1}{1-\lambda}}\right)^{-\lambda}$
Shape function of retention curve, λ [-]	0.582	
Surface tension at 20°C, σ_0 [N·m^{-1}]	0.072	
Residual saturation, S_{lr} [-]	0	$P = P_o \frac{\sigma}{\sigma_o}$
Maximal saturation, S_{ls} [-]	1	
Intrinsic permeability		
Intrinsic permeability, 1st principal direction, $k_{11,0}$ [m^2]	$4.72 \cdot 10^{-21}$	Darcy law:
Intrinsic permeability, 2nd principal direction, $k_{22,0}$ [m^2]	$4.72 \cdot 10^{-21}$	$\mathbf{q}_\alpha = -\frac{\mathbf{k}k_{r\alpha}}{\mu_\alpha}\left(\nabla P_\alpha - \rho_\alpha \mathbf{g}\right)$
Intrinsic permeability, 3rd principal direction, $k_{33,0}$ [m^2]	$4.72 \cdot 10^{-21}$	Kozeny's model:
Reference porosity for intrinsic permeability, ϕ_0, [-]	0.445	$\mathbf{k} = \mathbf{k}_o \frac{\varphi^3}{(1-\varphi)^2} \frac{(1-\varphi_o)^2}{\varphi_o^3}$
Liquid phase relative permeability		Van Genuchten model:
Shape function of retention curve, λ [-]	0.582	$k_{rl} = \sqrt{S_e}\left(1-\left(1-S_e^{1/\lambda}\right)^\lambda\right)^2$
Mechanical data		
Elastic parameters		Volumetric strains:
Initial (zero suction) elastic slope for specific volume-mean stress, κ_{io} [-]	0.05	$d\varepsilon_v^e = \frac{k_i(s)}{1+e}\frac{dp'}{p'} + \frac{k_s(p',s)}{1+e}\frac{ds}{s+0.1}$
Initial (zero suction) elastic slope for specific volume-suction, κ_{so} [-]	0.09	where:
Minimal bulk module, K_{min} [MPa]	10	$k_i(s) = k_{io}\left(1+\alpha_i s\right)$
Poisson's ratio, ν [-]	0.4	$k_s(p',s) = k_{so}\left(1+\alpha_{sp} \ln p'/p_{ref}\right)$
Parameter for κ_i, a_i [-]	0	
Parameter for κ_s, a_{sp} [-]	-0.145	
Reference mean stress, p_{ref} [MPa]	0.01	
Plastic parameters		The preconsolidation pressure:
Slope of void ratio - mean stress curve at zero suction, $\lambda(0)$ [-]	0.18	$p_o = p^c\left(\frac{p_o^*}{p^c}\right)^{\frac{\lambda(o)-kio}{\lambda(s)-kio}}$
Parameter defining the maximal soil stiffness, r [-]	0.8	where stiffness parameter:
Parameter controlling the rate of increase of soil stiffness with suction, β [MPa^{-1}]	0.02	$\lambda(s) = \lambda(o)\left[(1-r)\exp(-\beta s) + r\right]$
Parameter that takes into account increase of tensile strength due to suction, k [-]	0.1	The tensile strength: $p_s = p_{s0} + ks$
Tensile strength in saturated conditions, p_{s0} [MPa]	0	Hardening dependency on plastic volumetric strain:
Reference pressure, p^c [MPa]	0.01	

Critical state line parameter, *M* [-]	1.07	$dp_o^* = \frac{1+e}{\lambda(0)-k_{io}} p_o^* d\varepsilon_v^p$
Non-associativity parameter, *α* [-]	1	
Initial void ratio, e_0 [-]	0.8	
Initial preconsolidation mean stress for saturated soil, p_0^*[MPa]	3	

4.6.3 Initial and boundary conditions

Initial and boundary conditions were the same for COMSOL Multiphysics and CODE_BRIGHT models. For the flow modelling conditions were set as follows:

- Initial suction (~171 MPa) was estimated using Kelvin's law from the measurements of relative humidity (~28 %);
- Initial porosity for pellets and crushed pellets 0.225 and 0.665, respectively (Single pellet model), for mixture representing equivalent material – 0.445;
- Initial water saturation for pellets and crushed pellets 0.0636 and 0.38, respectively (Single pellet model), for mixture representing equivalent material – 0.15;
- For the top and side boundaries of both models no flow conditions were set;
- For the bottom boundary a constant water pressure condition was imposed *p*=10 kPa;
- Constant temperature (21.5 °C) was assumed in the system.

Initial and boundary conditions for swelling modelling were as follows:

- Initial stresses (0.15 MPa) were set in the model based on the experimental data;
- For the top, bottom and side boundaries of both models prescribed displacement of 0 were set.

4.6.4 Results/discussion

4.6.4.1. *COMSOL Multiphysics model*

Single pellet model

Preliminary modelling results are presented in Figure 4-40. As it could be seen from the figures, the crushed pellet material became saturated quite quickly and provided access of water to pellet. Within such model configuration and with current data set the pellet became fully water saturated after ~230 days.

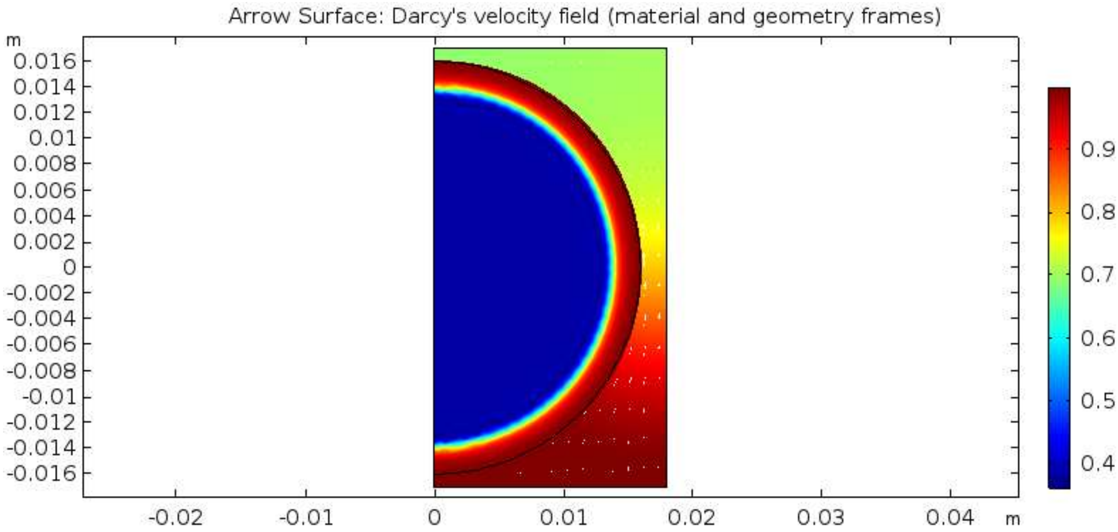

a) after 10 days

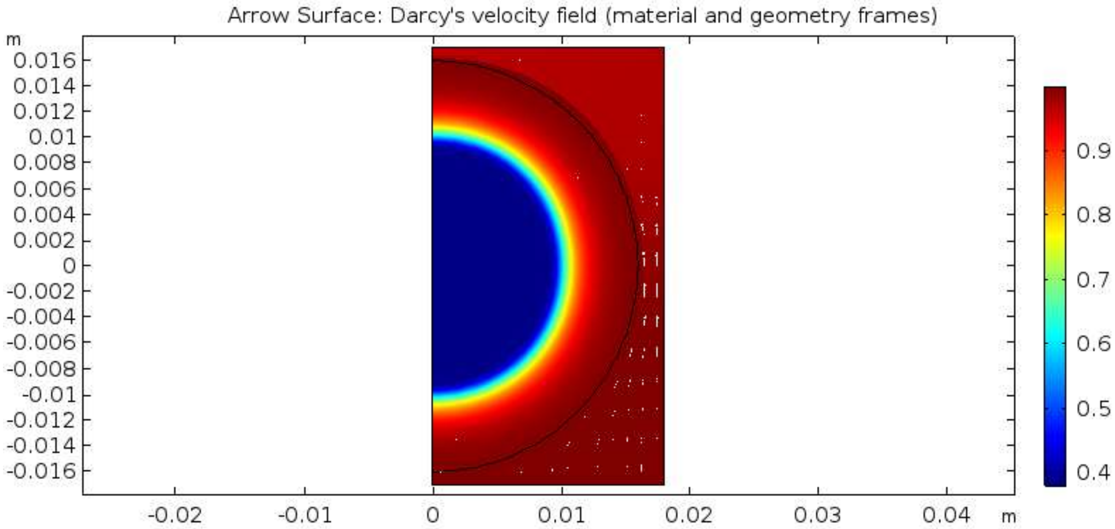

b) after 50 days

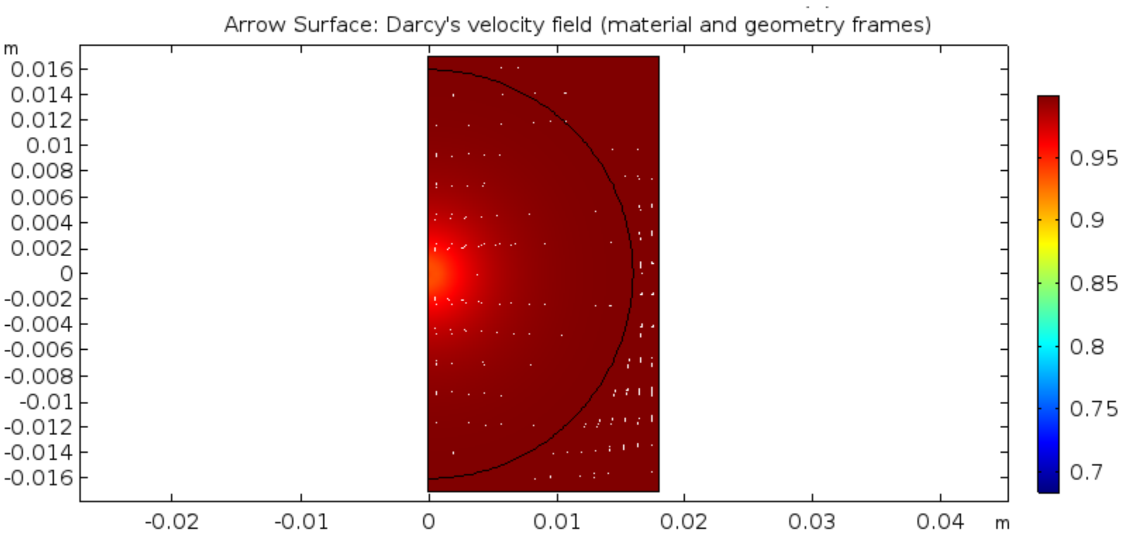

after 200 days

Figure 4-40. Water saturation in single pellet model at different times

Results on water saturation at point 1 (r=18 mm, z=20 mm) and point 2 (r=18 mm, z=34 mm) in crushed pellet material are presented in Figure 4-41. As it could be seen from the results, the point 1 became fully saturated earlier (after app. 70 days), while for the upper point 2 it took slightly more time to became fully saturated.

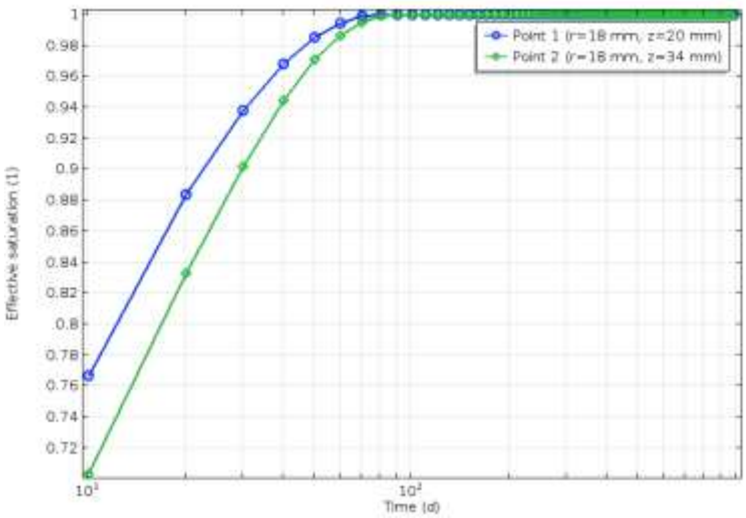

Figure 4-41. Time dependent water saturation at points 1 and 2 in crushed pellet material at two different heights

Figure 4-42 presents the dependency of average saturation in different components (pellet and crushed pellet material) considering in the system three different sets of water retention for crushed pellet material (a) P_{entry}=0.1 MPa, m=0.2705; b) P_{entry}=1 MPa, m=0.3505; c) P_{entry}=10 MPa, m=0.4955). As it could be seen in the figures, despite of different water retention data sets for crushed pellet material the full saturation of total system was achieved after ~200 days. This observation supported the assumption on decisive nature of the pellet for equivalent material water retention curve parameters.

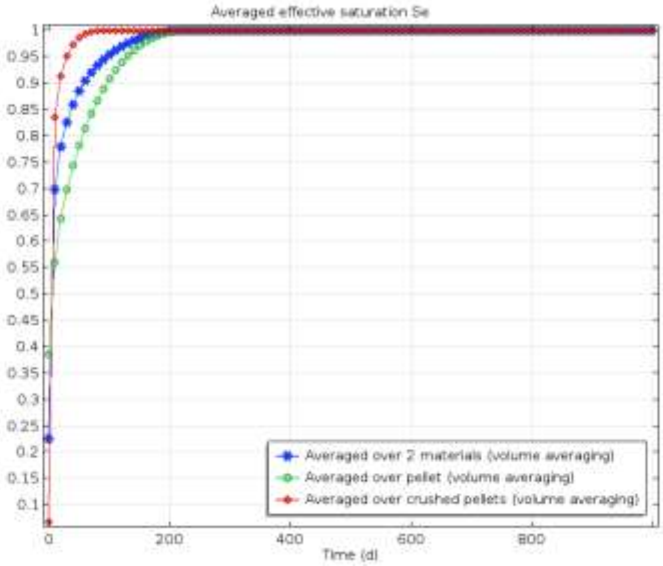

a) P_{entry}=0.1 MPa, m=0.2705

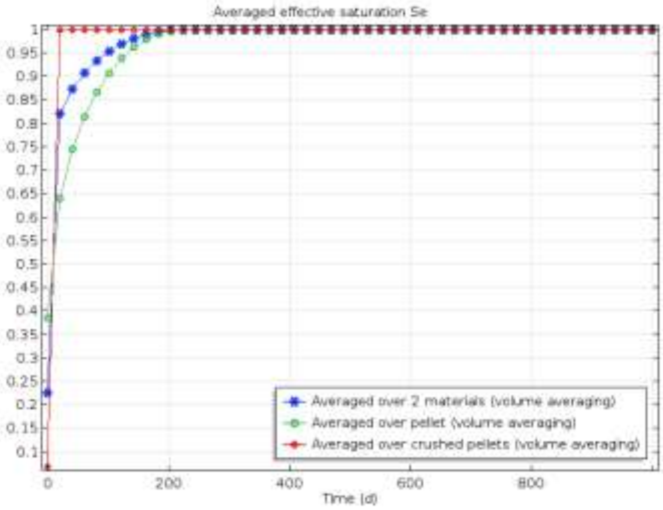

b) P_{entry}=1 MPa, m=0.3505

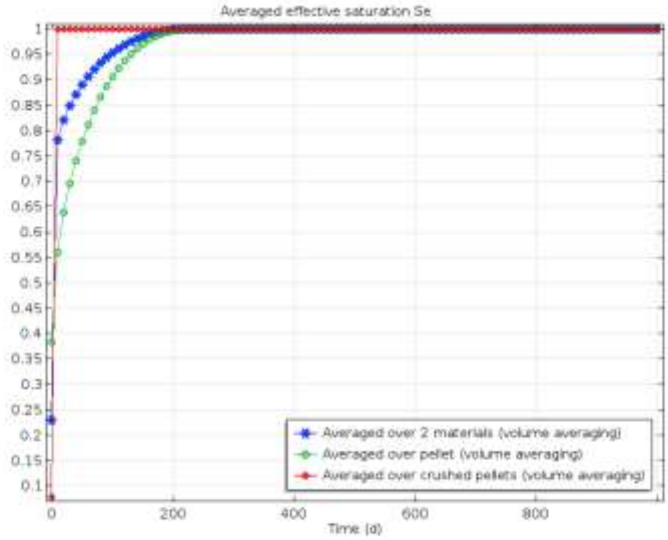

c) P_{entry}=10 MPa, m=0.4955

Figure 4-42. Time dependent water saturation (average) of single components and total system

The averaged pressures on the top and side boundaries are provided in Figure 4-43. As it is shown in the Figure 4-43 the buildup of pressure could be seen within ~ 200 days. After app. 200 days from the start of wetting a constant average pressure observed. Based on these observations it was expected that the swelling pressure from pellet will be dissipated in the crushed pellet material surrounding it and finally will induce the pressure on the other pellets of this order of magnitude.

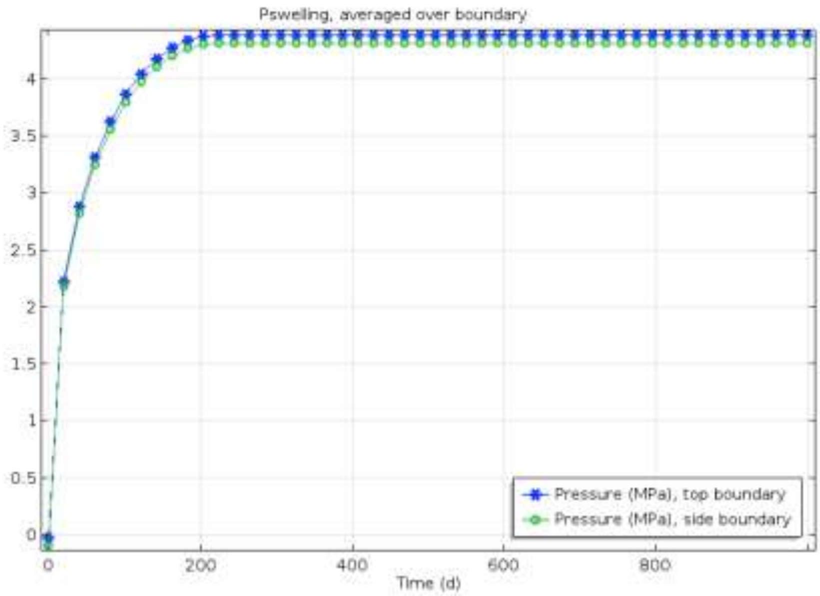

Figure 4-43. Axial and radial swelling pressures (averaged over top and side boundaries)

Equivalent material model

Preliminary modelling results on the saturation of equivalent material are presented in Figure 4-44.

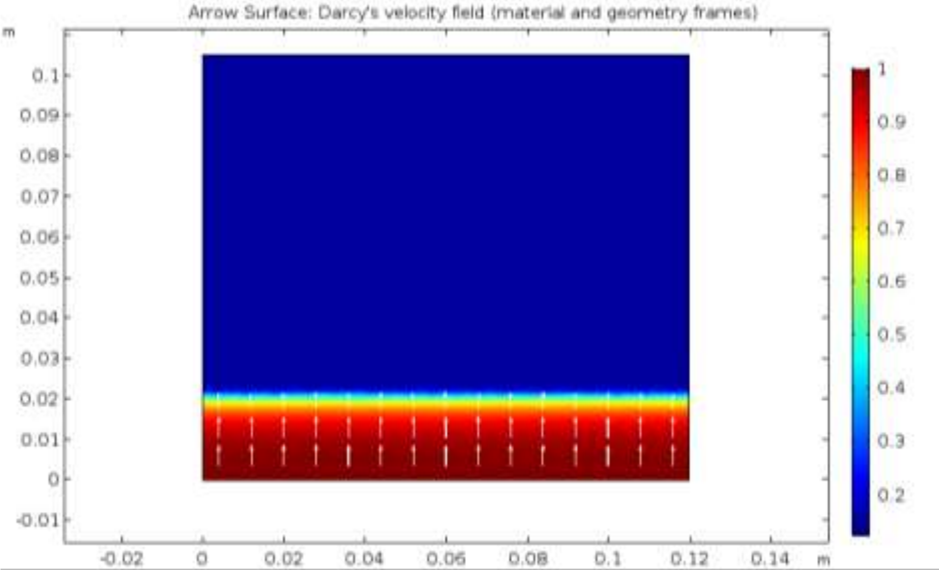

a) after 10 days

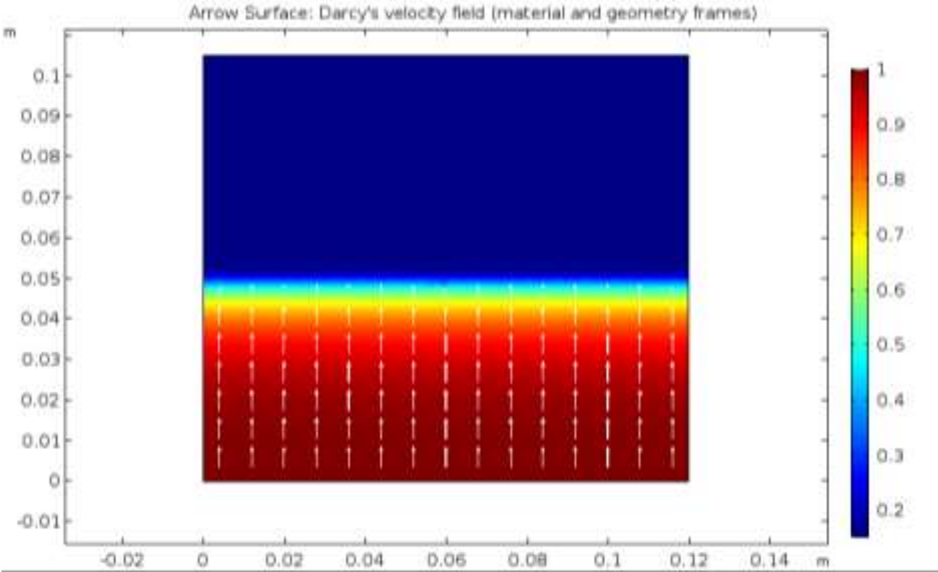

b) after 50 days

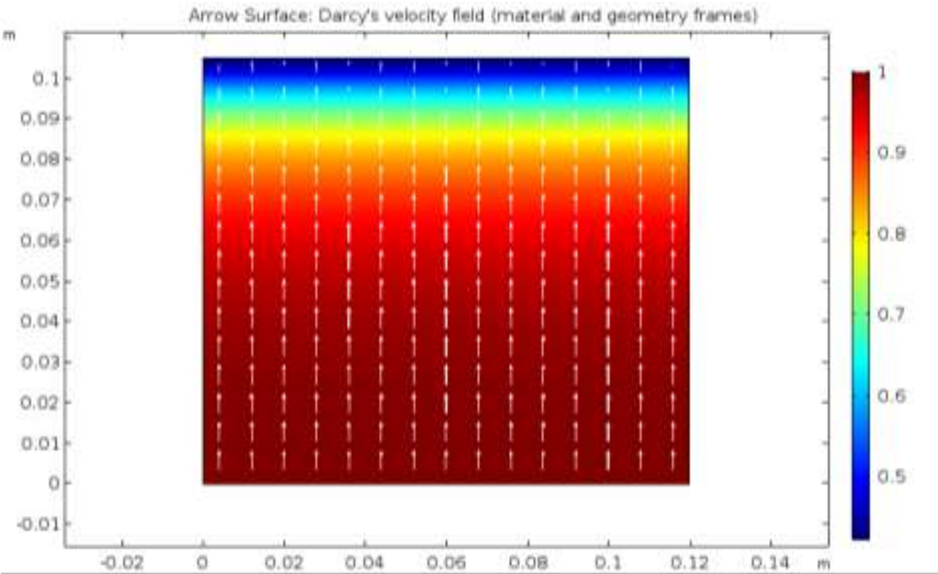

c) after 200 days

Figure 4-44. Saturation of equivalent material

As it could be seen from the figures, due to such model configuration (one equivalent material) the saturation proceed more or less evenly from the bottom. It was observed that such equivalent system with selected effective parameters became fully saturated after ~280 days.

The peak swelling pressure of ~4 MPa was observed in all monitored points (r=120 mm, z=20 mm, 60 mm, 80 mm) and middle point on the cell top (r=0 mm, z=105.15 mm) (Figure 4-45). The pressure buildup firstly appeared at the points closer to the bottom and then in the upper points. This order is expected with saturation proceeding from the lower part of cell and with uniformly distributed material in the cell.

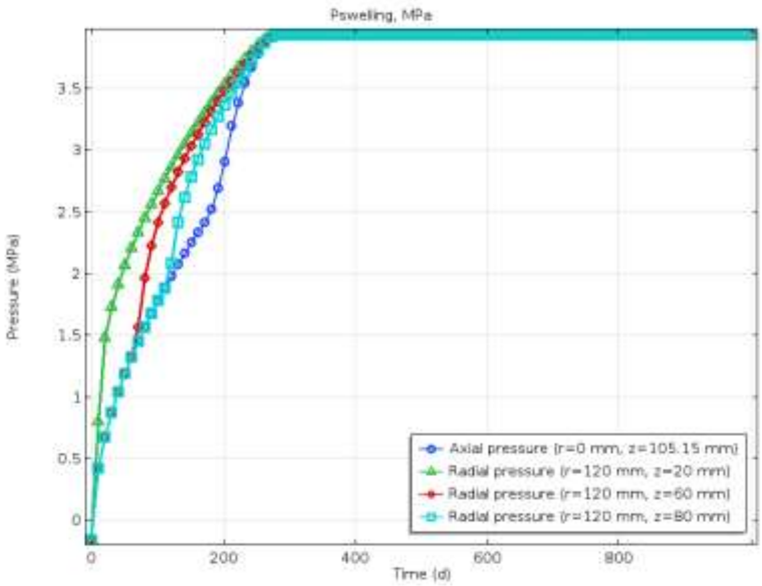

Figure 4-45. Time dependent swelling pressure evolution in the monitoring points (r=120 mm, z=20 mm, 60 mm, 80 mm), middle point on the top cell (r=0 mm, z=105.15 mm)

Comparison of swelling pressure modelling results and experimental data is provided in Figure 4-46.

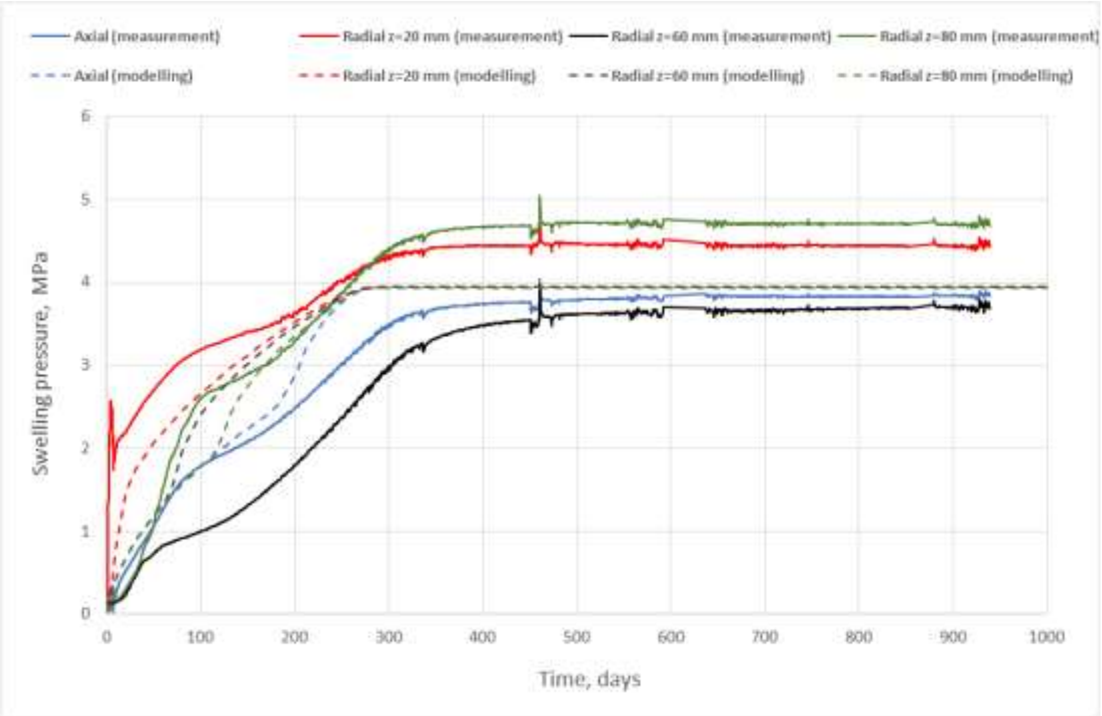

Figure 4-46. Measured (lines) and modelled (dashed lines) evolution of swelling pressures at different locations of the sample: axial pressure (r=0 mm, z=105.15 mm) and radial pressure at points (r=120 mm, z=20 mm), (r=120 mm, z=60 mm), (r=120 mm, z=80 mm)

It could be seen from the results, that modelling results of axial pressure showed a good agreement with measurements till app. 200 days after the beginning and later the model output overestimated measured swelling pressure. Modelling of radial swelling pressure at point closest to the bottom (r=120 mm, z=20 mm) showed that model output underestimated the measured pressure during all analysed period. Modelling results of radial swelling pressure at point (r=120 mm, z=60 mm) overestimated the swelling pressure during app. 400 days, while during the next period it overestimated the measured swelling pressure values only to limited extent. On the other hand modelling of radial swelling pressure at point (r=120 mm, z=80 mm) showed good correlation with the measured values up to 300 days from the beginning of water uptake. While for the rest of analysed time the numerical model over predicted swelling pressure to some limited extent.

4.6.4.2. ***CODE_BRIGHT model***

Predicted hydration behaviour of equivalent material at four different heights of the sample is presented in Figure 4-47. In the same figure measured data from the experiment are presented as well. The initial relative humidity of ~28 % corresponds to the initial suction of 171 MPa according to the Kelvin equation. With selected water retention curve this corresponds to initial saturation of 0.15. Figure 4-47 indicates that full saturation of the sample is predicted after ~220 days and its correlate well with measured date (~200 days, except measured data at height z=80 mm, blue line). However the relative humidity profiles differs between modelled and measured data.

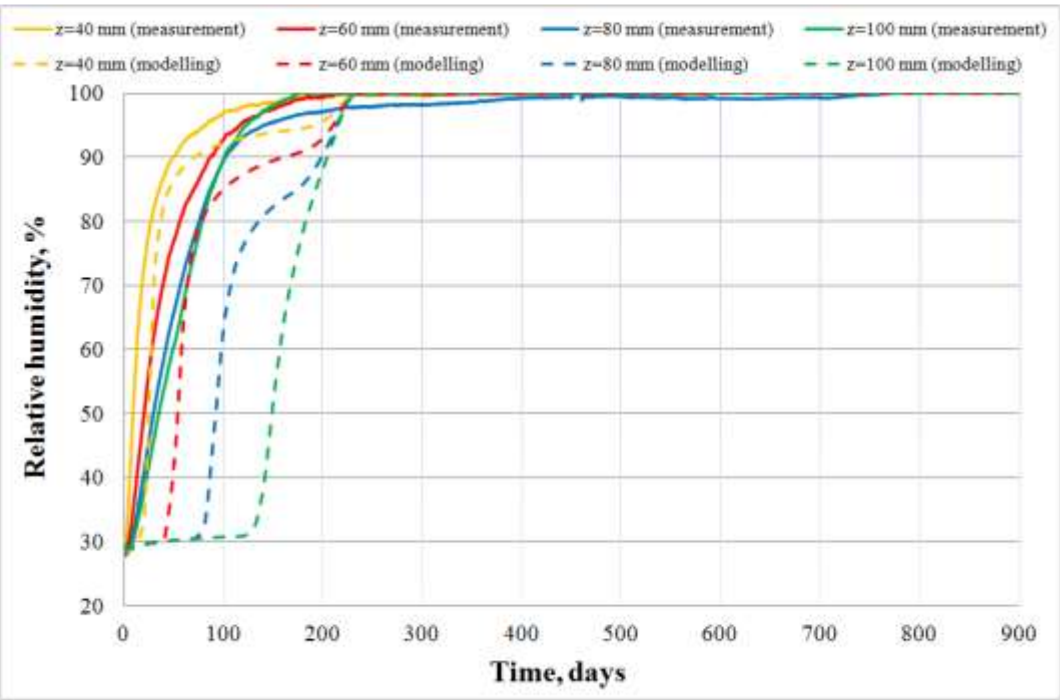

Figure 4-47. Measured (lines) and predicted (dashed lines) evolution of relative humidity at four different heights of the sample (z=0 is the bottom and z=105 mm is the top of the sample)

A consequence of material hydration is swelling. The swelling under confined conditions produces stress increase. Figure 4-48 shows the evolution of total stresses at selected points of the sample. Measured data showed that continuous increases in stress intensity have last about 400 days and magnitude of stresses at analysed points differs in ~1 MPa (varying between ~3.7 MPa and ~4.7 MPa). Axial stress at z=105 mm was higher than radial stress at z=40 mm, but it was lower than radial stresses at z=20 mm and z=80 mm. Modelling results of equivalent material showed the shorter increase in stress intensity (~250 days) and almost equal magnitude of stresses (~4.2 MPa) in analysed points. However, predicted stresses at analysed points were between measured curves.

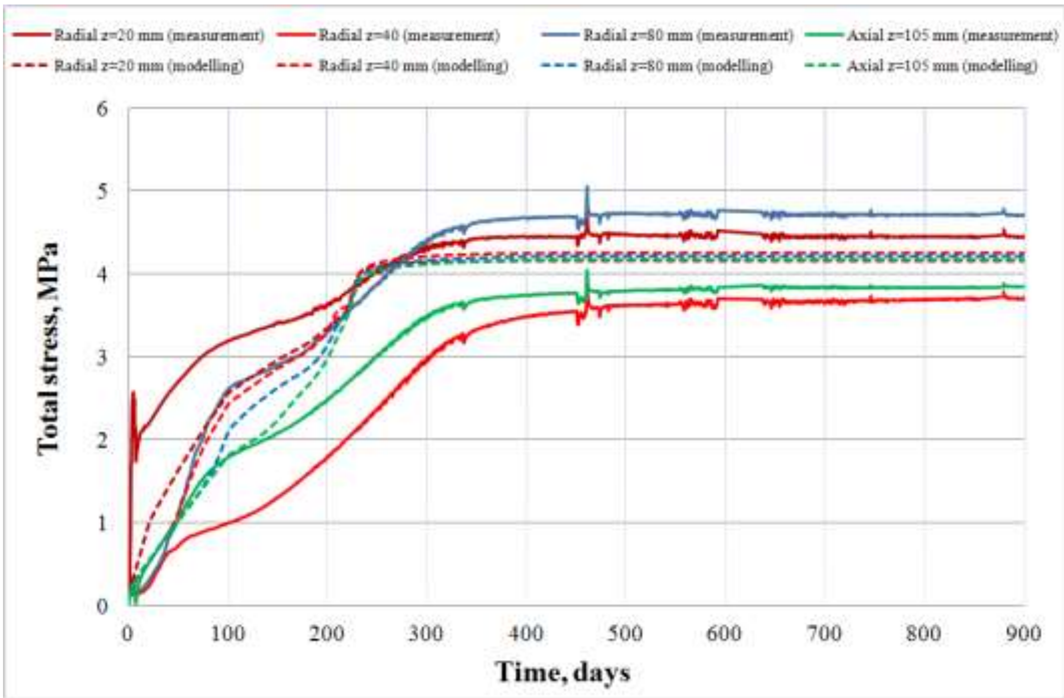

Figure 4-48. Measured (lines) and predicted (dashed lines) evolution of total stress at four different locations of the sample (z=0 is the bottom and z=105 mm is the top of the sample)

Due to swelling of analysed material the porosity was locally changed. Figure 4-49 shows the modelled distribution of porosity along a line in axial direction of the sample at different times. It was obtained that in a region near the water inlet (from z=0 mm to z=40 mm) material swells (peak expansion was ~9 % from initial porosity value n=0.445) and it caused the compaction of analysed material in the remaining region (from z=40 mm to z=105 mm) where peak reduction of porosity was ~4.5 % from initial value n=0.445.

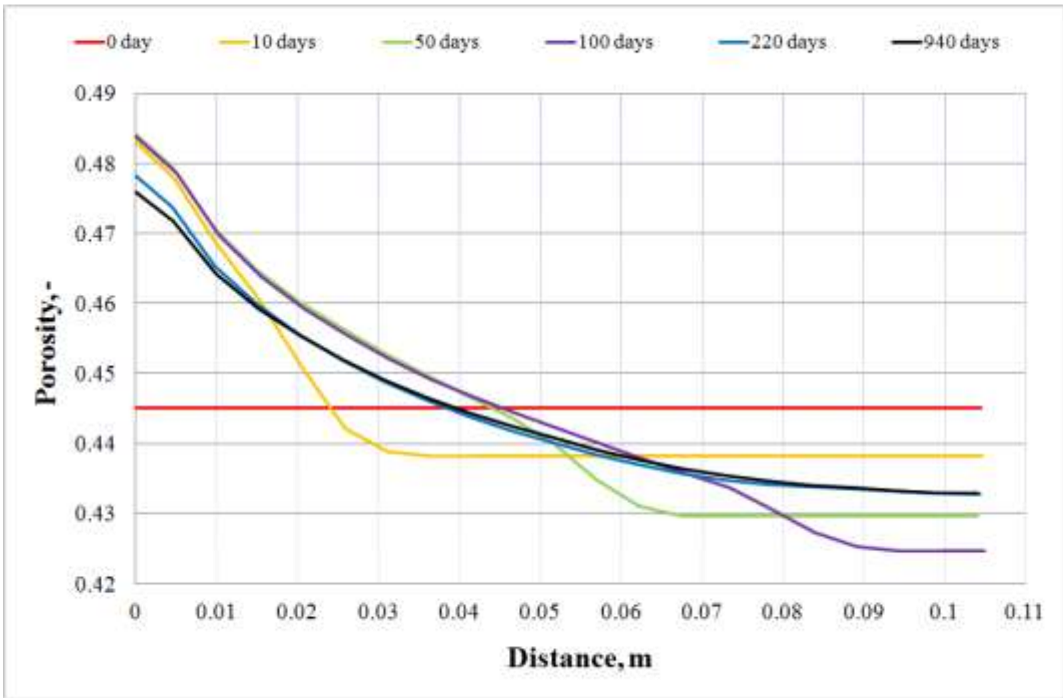

Figure 4-49. Predicted distribution of porosity in axial direction of the sample (from the bottom (z=0 mm) to the top (z=105 mm)) at different times

4.6.4.3. ***Results comparison between COMSOL Multiphysics and CODE_BRIGHT models***

Comparison of the results for equivalent material approach obtained using COMSOL Multiphysics and CODE_BRIGHT modelling tools are presented in Figure 4-50. Obtained stress profiles were similar between both codes, and difference on peak stresses was ~0.3 MPa. However the results of both modelling tools were between maximal and minimal values measured in the "Test 1b" as it could be seen in Figure 4-46 and Figure 4-48.

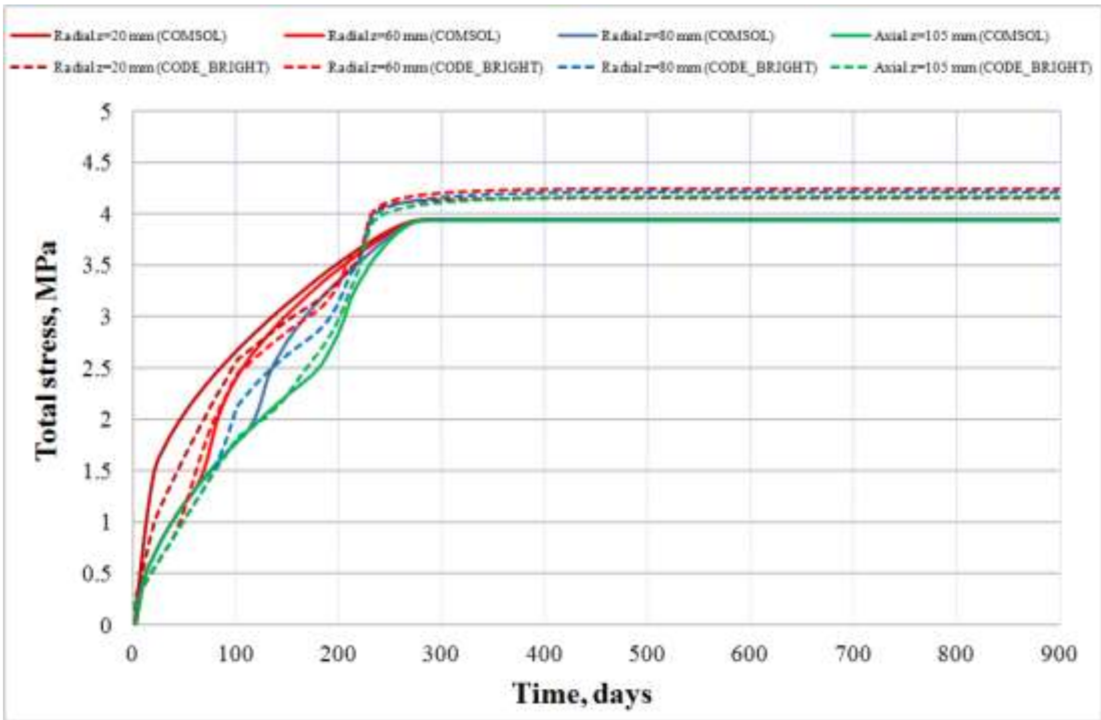

Figure 4-50. Comparison of modelling results for equivalent material approach using COMSOL Multiphysics (lines) and CODE_BRIGHT (dashed lines) codes

4.7 Quintessa

4.7.1 Geometry and discretization

Similarly to the Test 1a models, a 2D cylindrical grid is used to represent the bentonite. This has height 105.15 mm and radius 120 mm. According to the experiment description, the initial height of the bentonite is 103.6 mm and the height after some adjustment in the beginning of the test is 105.15 mm. It is unclear how this height adjustment was carried out and over what time period, so the adjusted height has been used in the initial conditions.

The bentonite is discretised into 13 radial and 11 axial compartments, as shown in Figure 4-51. It is unclear whether friction has been minimised in the experiment, but it has not been included in the model, so there is no radial dependence.

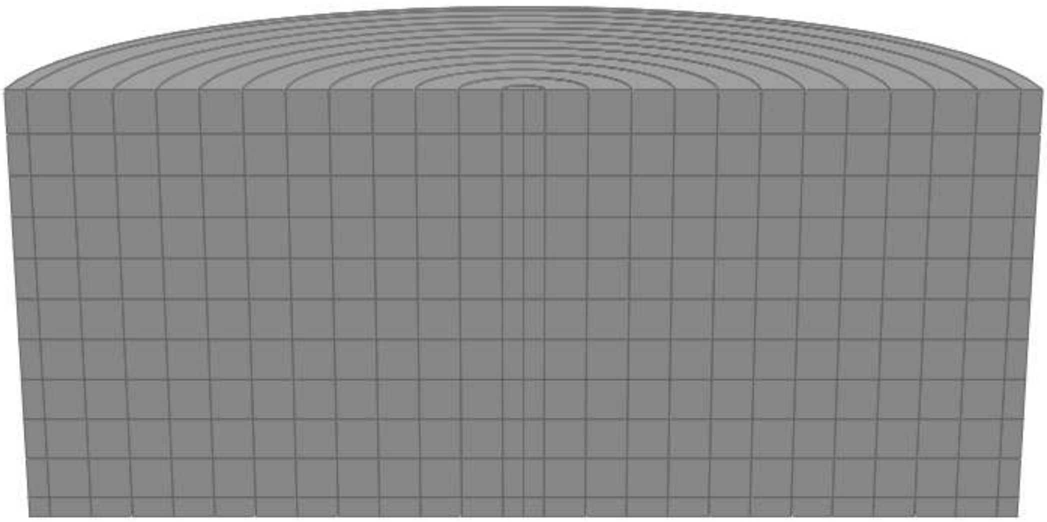

Figure 4-51 Discretisation of bentonite in the 1b QPAC model.

4.7.2 Input parameters

The input parameters are unchanged from those presented in Table 3-16.
An additional 'swell delay' parameter of 0.15 y^{-1} has been introduced to represent the granular bentonite, as discussed in Section 4.7.4.

4.7.3 Initial and boundary conditions

The initial conditions prescribed for the model consist of initial dry density, initial water content and initial stresses. The bentonite pellets and powder are treated as a bulk material, so the properties listed are the averaged properties of the pellets and powder, by volume.

The averaged dry density used is that for the 'adjusted' volume.

Table 4-10 Initial conditions used in the 1b model.

Initial Condition	Value
Initial dry density [kg/m^3]	1517
Initial water content [wt%]	4.23
Initial stress (r, θ, z) [MPa]	0, 0, 0

The top and side boundaries are both roller boundaries with no flow conditions.

The bottom boundary is a roller boundary with a constant water pressure of 0.11 MPa, i.e. 10 kPa above atmospheric pressure.

4.7.4 Results/discussion

The evolution of total axial and radial stress in the bentonite is shown in Figure 4-52 and Figure 4-53 respectively.

As with Tests 1a, the final values of axial and radial stress are predicted more successfully than the transient behaviour. The model predicts much less variation in radial swelling pressure with height than is seen in the experiment, but this may be due to inhomogeneity of the bentonite in the experiment – there appears to be no logical correlation between height and radial swelling pressure for the three data points.

It can be seen from Figure 4-54 that although the water inflow is well represented in the model, the swelling pressure is much quicker to build up than the experimental data suggests. The discrepancy may be explained by the treatment of the powder and pellets mixture as a bulk material.

In an attempt to account for this difference, an additional parameter was added to the model to introduce a 'delay' between the water content 'seen' by the swelling equations, compared to the water content 'seen' by the hydraulic equations. This represents water that may quickly enter the experiment through void spaces between the pellets, before being later sucked into the bentonite pellets, causing them to swell. This somewhat improved the fit to experimental data, although it is still not a good representation of the transient behaviour (see Figure 4-52).

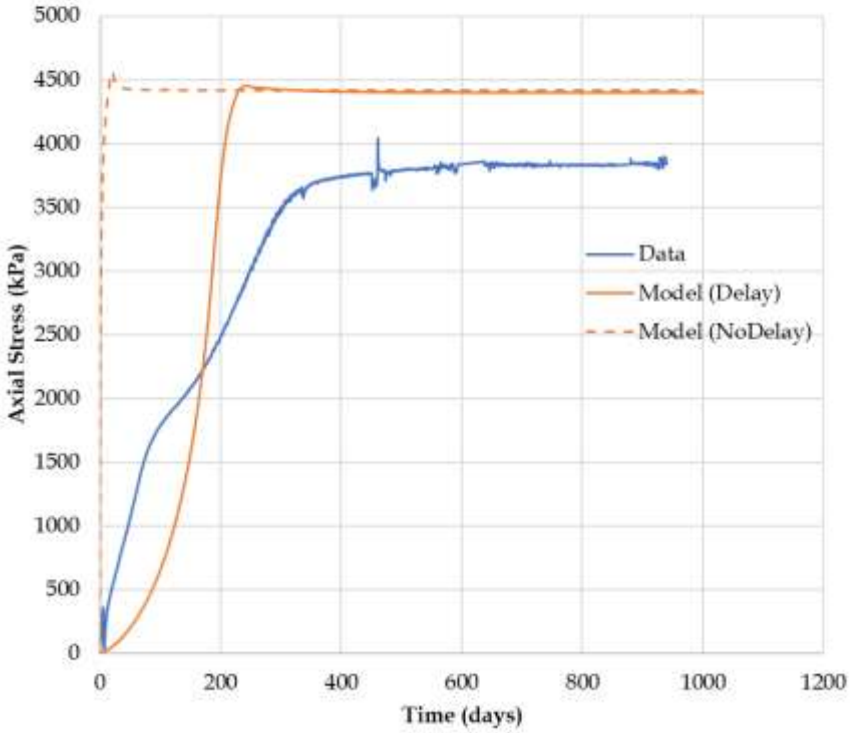

Figure 4-52 Total axial stress evolution through time in the 1b experiment, compared with modelled results (with and without a delay term in the water content used for swelling).

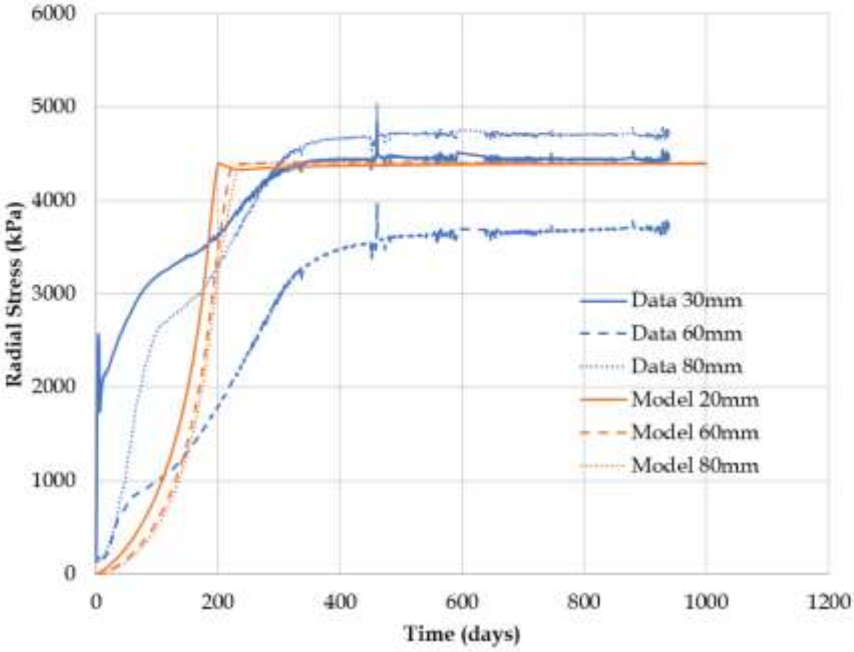

Figure 4-53 Total radial stress evolution through time in the 1b experiment, compared with modelled results (with a delay term in the water content used for swelling).

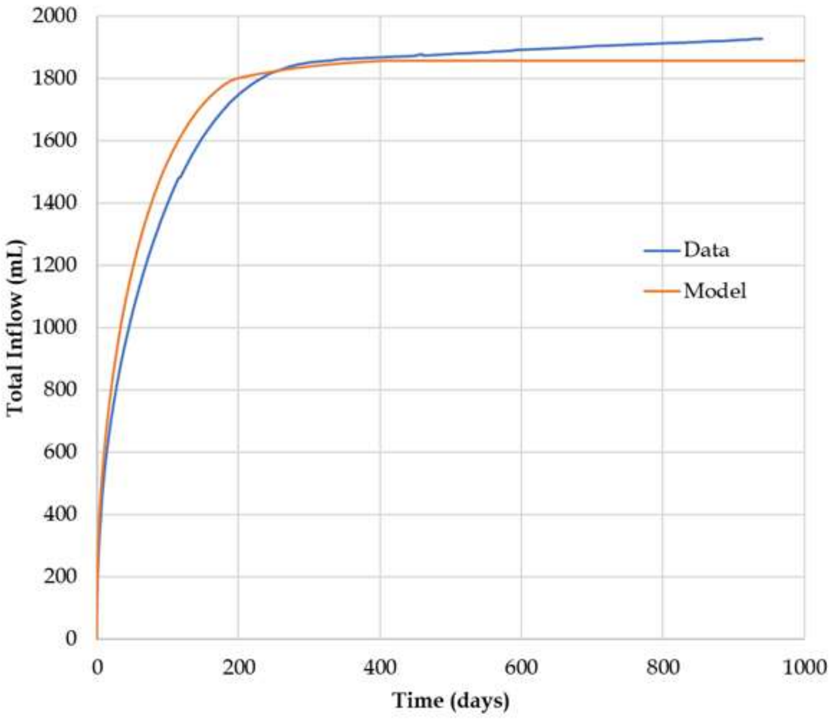

Figure 4-54 Total water inflow through time for the 1b experiment, compared with modelled results (with a delay term in the water content used for swelling).

Profiles of the final void ratio and water content against height are shown in Figure 4-55 and Figure 4-56.

The magnitudes of void ratio and water content are well-predicted, although the distributions with height are flatter than the experimental data. This may be due to the slightly faster saturation in the model.

Unlike the previous models, the water saturation reaches but does not exceed 1.

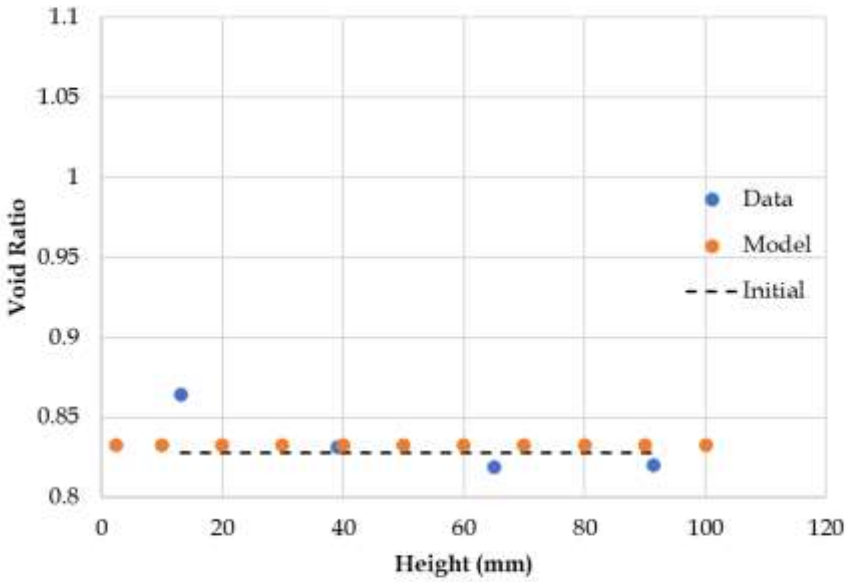

Figure 4-55 Profile of the final bentonite void ratio at different heights within the sample, for the 1b experiment.

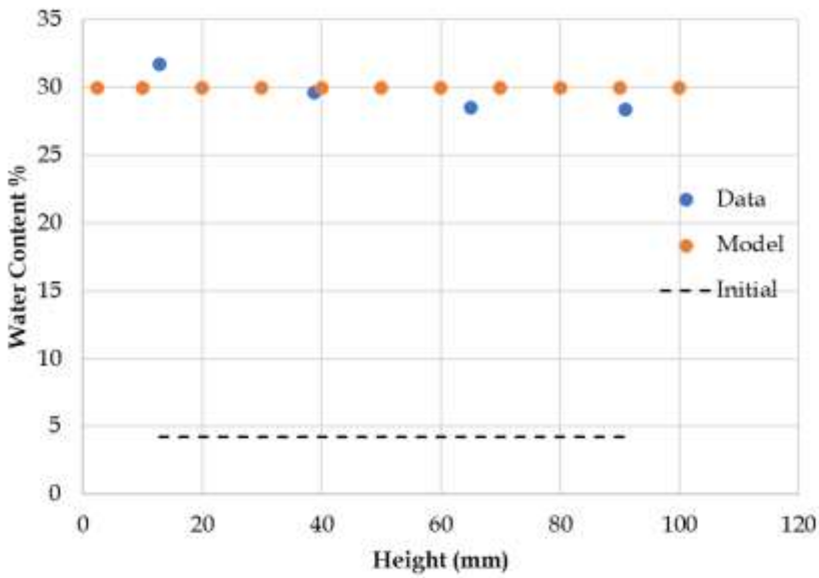

Figure 4-56 Profile of the final water content at different heights within the sample, for the 1b experiment.

4.8 ULG

4.8.1 Geometry and discretization

The numerical bentonite sample consists in 25 eight-noded isoparametric elements. The problem is assumed monodimensional.

4.8.2 Input parameters

4.8.2.1. *Hydraulic parameters*

The available data for compacted MX-80 bentonite are used for water retention behaviour.
The proposed water retention model is validated against experimental data on wetting paths under confined conditions and for different dry densities for MX-80 bentonite studied by Villar (2004a). Samples of MX-80 bentonite were uniaxially compacted to different dry densities and water contents. After equalization, a hole was drilled in the samples and a relative humidity sensor was installed in order to measure the sample relative humidity.
The corresponding suction was obtained using Kelvin's law.
Figure 4-57 represents the experimental data in the (s-Sr) plane together with the model predictions. The calibrated parameters are: C_{ads} = 0,0075 MPa^{-1}, n_{ads} = 1,5, A = 0,2 MPa, n = 3 and m = 0,15. As observed in Figure 4-57, the degrees of saturation estimated by the water retention model compare favourably with the measured degrees of saturation. In addition, the evolution of the air entry value is consistent with the data obtained by Seiphoori et al. (2014).

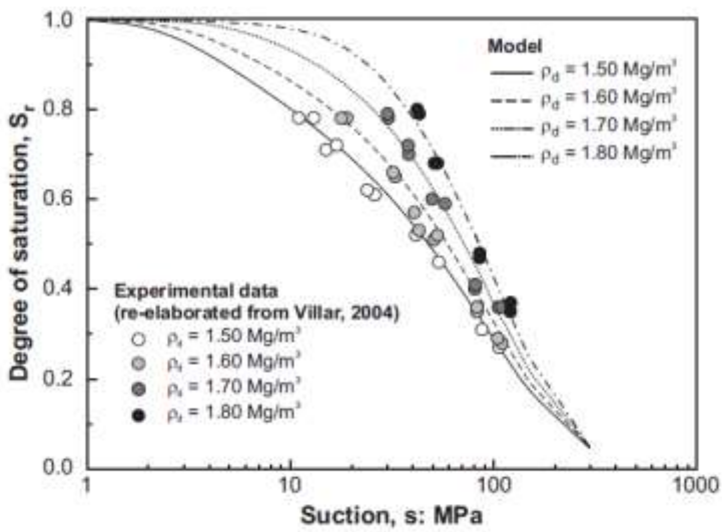

Figure 4-57 Comparison between experimental data (re-elaborated from Villar (2004a)) and model predictions on MX-80 bentonite compacted at four different dry densities..

The porosity is derived from the dry density provided by the experiment's report, and consequently the void ratio is obtained.
The reference permeability is selected in order to best fit the experimental results.

Table 4-11. Selected hydraulic parameters

ϱ_{di}	C_{ads}	n_{ads}	A	n	m	K_{w0}	n	e_{m0}	β_0	β_1
(Mg/m^3)	(MPa^{-1})		(MPa)			(m^2)				
1.52	0.0075	1	0.2	3	0.2	6.0E-19	0.453	0.31	0.1	0.48

4.8.2.2. ***Mechanical parameters***

The considered material is MX-80 bentonite compacted to a dry density equal to 1.52 Mg/m³.

Table 4-12. Selected mechanical parameters

ϱ_{di}	κ	κ_s	$\lambda(0)$	p_0^*	p_c	r	ω
(Mg/m^3)				(MPa)	(MPa)		(MPa^{-1})
1.52	0.06	0.07	0.12	0.30	0.12	0.55	0.075

The input parameters (see Table 4-12) were calibrated in order to best fit the target results presented in the report.
The preconsolidation pressure for saturated state p_0^* was selected by an iterative procedure in order to reproduce the results of swelling stress tests performed by Gatabin (Gatabin, Guillot, & Bernachy, 2016) (see Figure 4-58).

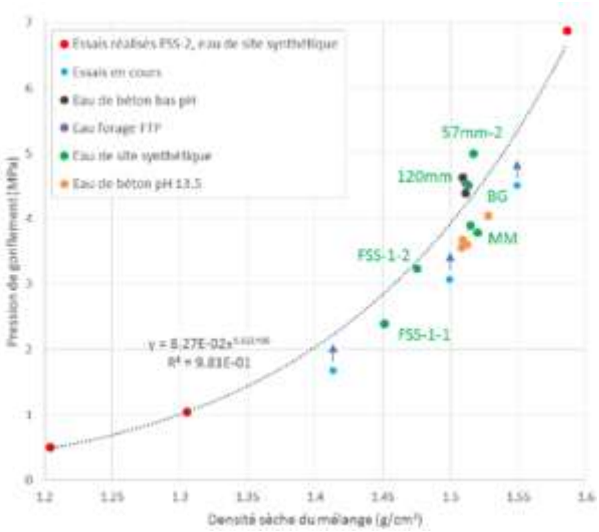

Figure 4-58 Dry density VS Maximum swellling pressure in a swelling stress test (Gatabin, Guillot, & Bernachy, 2016)

4.8.3 Initial and boundary conditions, discretization

The numerical bentonite sample consists in 25 eight-noded isoparametric elements.

The problem is assumed monodimensional and oedometer conditions are considered [Figure 4-1].

The strong heterogeneity of the material is well-recognized, but for sake of simplicity, in this modelling strategy, the sample is considered homogeneous, presenting the same hydro-mechanical properties and state in the entire domain.

Initial uniform suction is considered with a value equal to 171 MPa.

The hydration of the sample is provided from the bottom end [red line Figure 4-59] assuming a suction decrease from 171 MPa (-171 MPa of pore water pressure) to -0.01 MPa (0.010 MPa pore water pressure) occurring in 1000 seconds.

In order to reproduce the test conditions (i.e. atmospheric pressure at the top face), an additional finite element is placed on the top end (FMILC) with a fixed pore water pressure equal to 0.1 MPa, which allows water flux [Blue line Figure 4-59].

Finally, the sample is subjected to an initial confining stress values of 0.02 MPa axially (vertically) and 0.2 MPa radially (horizontally).

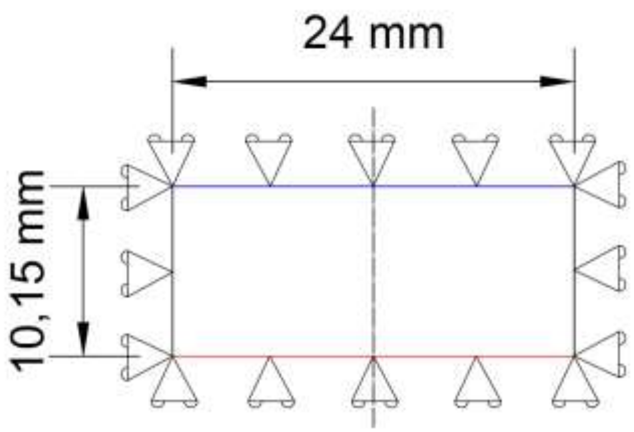

Figure 4-59 Test conditions description

4.8.4 Results/discussion

The measurements at 80 mm height are selected as reference. At this height all the measurement tools did not present any malfunctions during the whole experiment. Moreover, the measurements point is quite far from the bottom end, where the water is injected. Because of all these reasons, the measured quantities are considered reliable.
The relative humidity is translated into suction via the Kelvin equation.
The stress path resulting from the experimental results are presented in the p-s plane [Figure 4-60]:

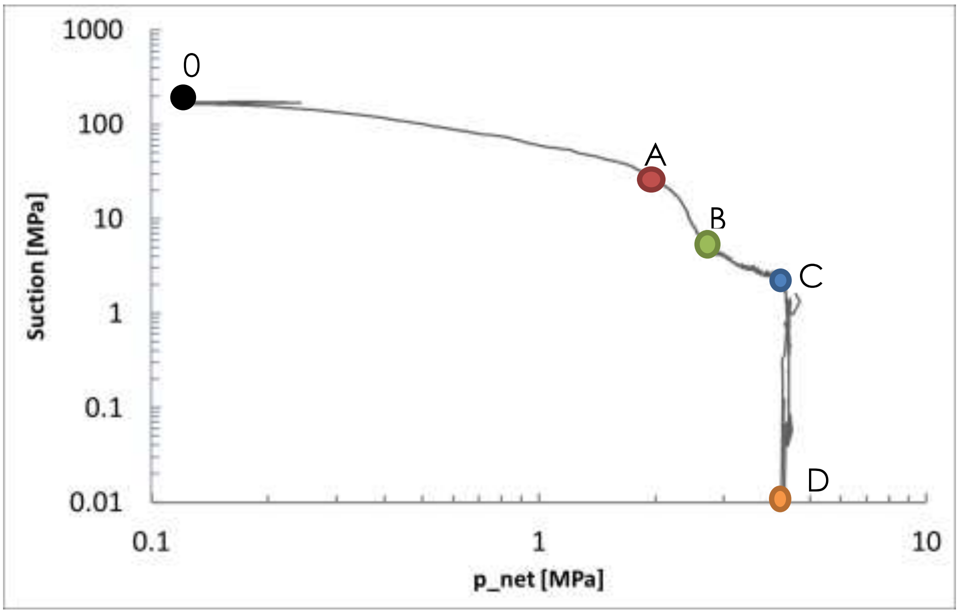

Figure 4-60 Experimental stress path in p-s plane

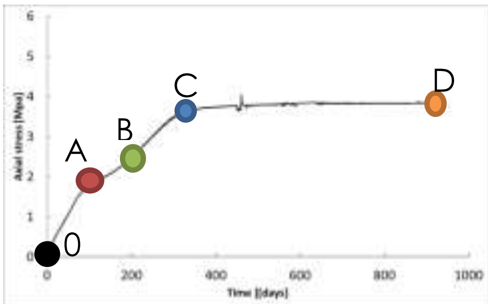

Figure 4-61 Experimental axial stress at 80 mm from the bottom end

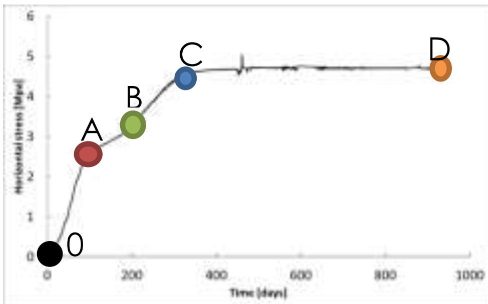

Figure 4-62 Experimental horizontal stress at 80 mm from the bottom end

The experimental results are consistent with literature [Figure 4-61, Figure 4-62]. According to (Villar M., 2004) the development of the swelling pressure in pellets/powder mixtures shows three phases: a first one with a quick swelling pressure increase (from point 0 to point A, Figure 4-60, Figure 4-61, Figure 4-62), a second one with either a quasi-constant level or even a decrease of the swelling pressure (from point A to point B), and the last one with a new increase of the swelling pressure (from point B to point C). The interaction between micro and macrostructure accounts for this pattern. At saturation and for equal density, precompacted samples and pellets/powder samples display the same swelling pressure.

When the BBM is used in constant volume conditions, the swelling stress can be obtained by integrating equation 2.23:

$$p(s) = p_A \left(\frac{s_A + u_{atm}}{s_B + u_{atm}}\right)^{\frac{\kappa_s}{\kappa}} \tag{4.1}$$

In this way [Eq 4.1], the developed swelling pressure is a monotone function of suction.

Neglecting the above-mentioned micro-macro interaction, it can be assumed that until point A [red dot Figure 4-60], the behaviour of the material is elastic, controlled by the ratio κ_s/κ.

From point A to point C [blue dot Figure 4-60], the material undergoes to plastic behaviour, with the stress path being controlled by the ratio $\frac{\kappa_s}{(\lambda(s)-\kappa)}$. The change of the curves slopes is due to the variation of $\lambda(s)$ with suction, assumed κ_s and κ constant.

From point C to point D [orange dot Figure 4-60], the stress is constant with the decreasing suction, therefore this point can be assumed as the air entry value.

Given the importance of the suction in the problem, in the following a comparison between the experimental and numerical results is presented Figure 4-63:

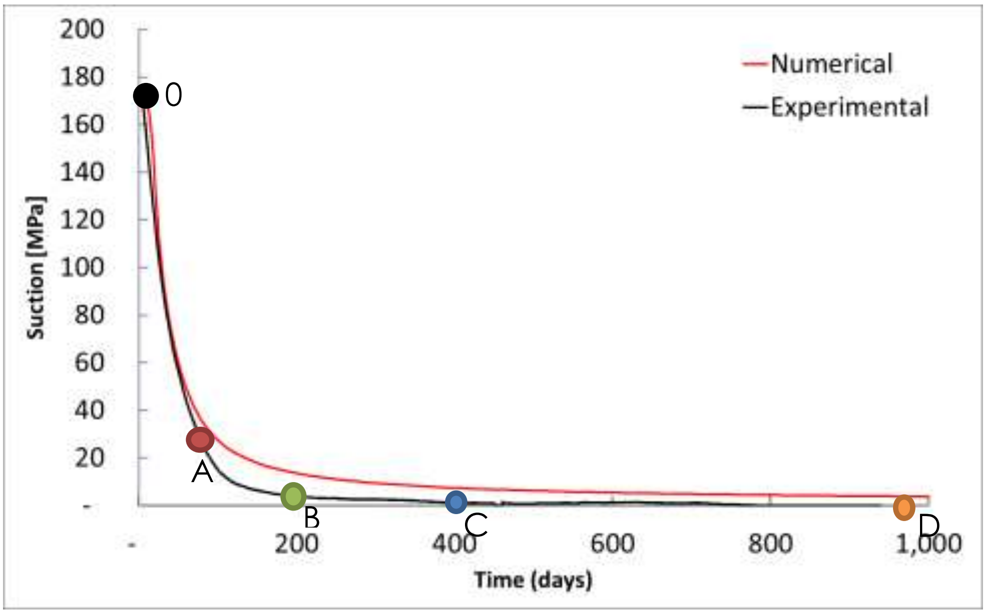

Figure 4-63 ***Experimental vs Numerical suction history at 80 mm from the bottom end***

The selected permeability law evolution fits very well the experimental results in the first phase. Then, the numerical suction decreases slowlier than the experimental one. This is due the progressive decrease of the permeability given by the progressive decrease of the macro-pores [Eq. 2.13] resulting from the adopted micro-porosity evolution law [Eq. 2.12].

On the other hand, experimental results from (Cui, 2017)show that when the full saturation is approached, the volume of the large-pore void ratio increases [Figure 4-64] resulting in an increased water permeability. Unluckily, this latter aspect is not captured in the present model and gives as result slower saturation process.

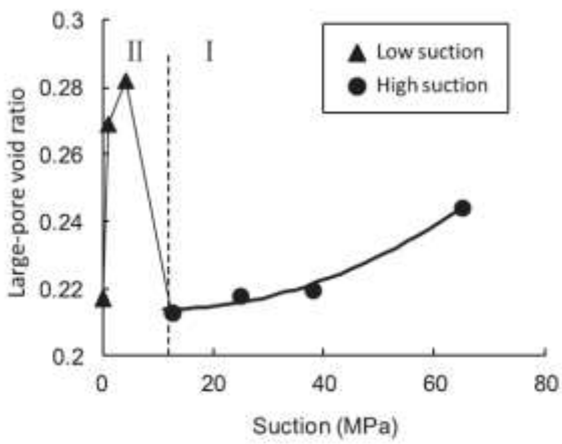

Figure 4-64 ***Changes of large-pores void ratio (diameter larger than 2 mm) with suction (Cui, 2017)***

Although neglecting this fundamental aspect, by back-analysing the stress path in the p-s plane, the mechanical parameters can be found.

The matching between the curves is considerably good [Figure 4-65].

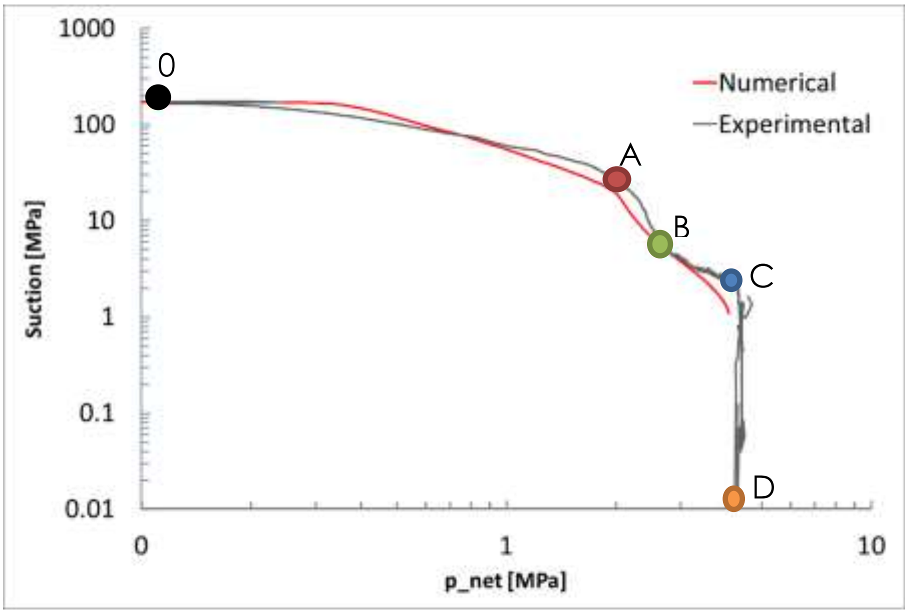

Figure 4-65 Experimental vs Numerical stress path in p-s plane.)

Because of the adopted modelling strategy, the difference into the saturation process time is directly translated in a mismatching of the swelling pressure development time.
Until point A [Figure 4-66], the numerical and experimental results are quite corresponding. Successively, the time evolution of the process diverges, resulting into a strong delay for the numerical results.
Finally, the steady value of the swelling stress is quite similar in the two cases.

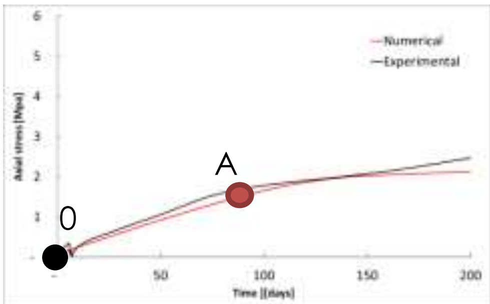

Figure 4-66 Experimental vs Numerical axial stress at 80 mm from the bottom end (until day 200)

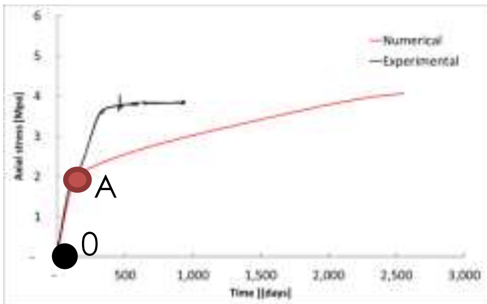

Figure 4-67 Experimental vs Numerical axial stress at 80 mm from the bottom end (until day 3000)

4.9 CU/CTU

4.9.1 Geometry and discretization

The test was simulated in a two-dimensional axysimmetric setup using a structured mesh. A vertical node spacing of 3.125 mm and a horizontal one of 6 mm were chosen, thus obtaining 33 rectangular elements with 168 nodes in total (including secondary nodes).

4.9.2 Input parameters

The pellets were not simulated individually. Instead, an equivalent, homogeneous double-structure medium was chosen for the simulations. The parameters of the model are identical to those used in the simulation of test 1a and are recalled in Table 4-13 below.

Table 4-13 Parameters of the hypoplastic model, calibrated on the Czech B75 bentonite

Critical state friction angle of the macrostructure	φ_c	25	°
Slope of the isotropic normal compression line in $\ln\left(\frac{p^M}{p_r}\right)$ versus $\ln(1+e)$ space	λ^*	0.13	
Macrostructural volume strain in p^M unloading	κ^*	0.06	
Position of the isotropic compression line in $\ln\left(\frac{p^M}{p_r}\right)$ versus $\ln(1+e)$ space	N^*	1.73	
Stiffness in shear	ν	0.25	
Dependency of the position of the isotropic normal compression line on suction	n_s	0.012	
Dependency of the slope of the isotropic normal compression line on suction	l_s	-0.005	
Dependency of the position of the isotropic normal compression line on temperature	n_T	-0.07	
Dependency of the slope of the isotropic normal compression line on temperature	l_T	0.0	
Control of f_u and thus of the dependency of the wetting-/heating-induced compaction on the distance from the state boundary surface; control of the double-structure coupling function and thus of the response to wetting-drying and heating-cooling cycles	m	1	
Dependency of microstructural volume strains on temperature	α_s	0.00015	K^{-1}
Dependency of microstructural volume strains on p^m	κ_m	0.07	
Reference suction of the microstructure	s_m^*	-2000	kPa
Reference microstructural void ratio for reference temperature T_r, reference suction s_m^*, and zero total stress	e_m^*	0.45	

Value of f_m for compression	c_{sh}	0.002	
Air-entry value of suction for the reference macrostructural void ratio e_0^M	s_{e0}	-2700	kPa
Reference macrostructural void ratio for the air-entry value of suction of the macrostructure	e_0^M	0.50	
Reference temperature	T_r	294	K
Dependency of macrostructural air-entry value of suction on temperature	a_t	0.118	
Dependency of macrostructural air-entry value of suction on temperature	b_t	-0.000154	
Ratio of air entry and air expulsion values of suction for the water retention model of the macrostructure	a_e	1.0	
Value of λ_p corresponding to the reference void ratio e_0^M in the water retention model of the macrostructure	λ_{p0}	0.7	

In addition, the density of the solids was set at $\rho_s = 2780\ \mathrm{kg\ m^{-3}}$. Values of intrinsic permeability K in the range $10^{-22} - 10^{-19}\ \mathrm{m}^2$ were explored to find the best match with the experimental values.

4.9.3 Initial and boundary conditions

An initial void ratio $e = 0.829$ and an initial suction $s = -170\ \mathrm{MPa}$ were assigned to all elements to simulate the pellets as an equivalent, homogeneous double-structure medium. Temperature was fixed at $T = 294\ \mathrm{K}$. The lateral and bottom boundaries were set as impervious, while free access to water was provided from the top boundary with a 10 kPa head. Deformations of the sample were prevented at all boundaries.

4.9.4 Results/discussions

As shown by Figure 4-68, the simulation was able to capture the final values of both the axial and the radial pressures. However, the development of the pressure through time could not be captured together with the evolution of the relative humidity. In fact, a low value of permeability was necessary to simulate the development of the swelling pressures satisfactorily, but such value provided, at the same time, low and unrealistic values of relative humidity. Conversely, satisfactory values of permeability to simulate the evolution of relative humidity would result in a very quick (within days) development of swelling pressures.

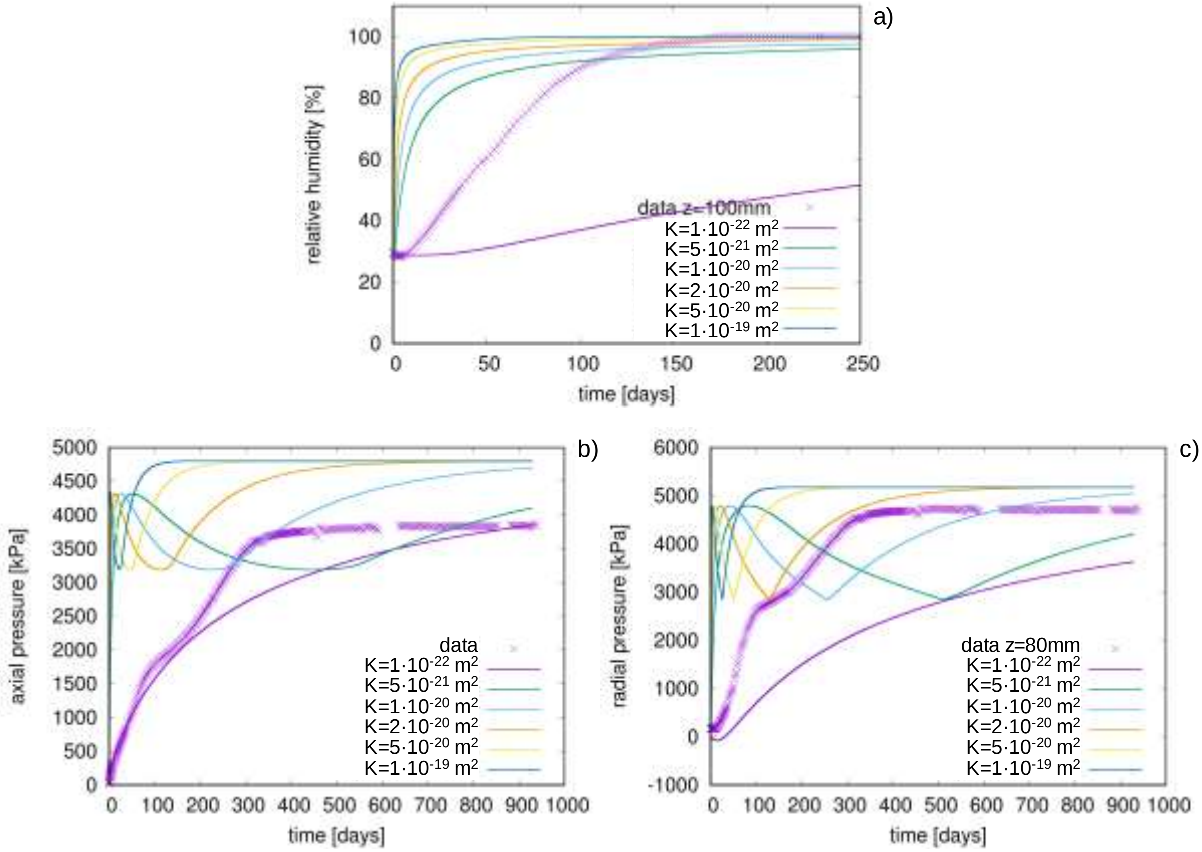

Figure 4-68 Summary of the results of test 1b: a) relative humidity as a function of the chosen intrinsic permeability K; b) axial, and c) radial pressure at 80 mm from the bottom of the sample.

4.10 VTT/UCLM

4.10.1 Input parameters

Since the studied test set up resembles somewhat a compacted bentonite block due to the crushed pellet material filling the inter-pellet space and the resulting high density, the same values for the set of model parameter as used in previous simulations of compacted bentonite blocks have been utilized. The parameters used for modelling Test 1b are listed in Table 4-14 below.

Table 4-14 Model parameters used for Test 1b

Parameter	Symbol	Value, units	Reference
Hydraulic model			
Molar mass of water	$M_{\mathrm{mol,w}}$	$18.02\ \frac{\mathrm{g}}{\mathrm{mol}}$	--
Density of liquid water	ρ_{w}	$10^3\ \frac{\mathrm{kg}}{\mathrm{m}^3}$	--
Constitutive parameter for van Genuchten model	α_{VG}	$1.149 \cdot 10^{-7}\ \mathrm{Pa}^{-1}$	Navarro et al. (2015)
Constitutive parameter for van Genuchten model	m_{VG}	0.733	Navarro et al. (2015)
Reference intrinsic permeability for liquid water	$K_{\mathrm{int,L,ref}}$	$2.34 \cdot 10^{-21}\ \mathrm{m}^2$	Adapted from Gens et al. (2011)
Parameter of exponential law of intrinsic permeability for liquid water	$b_{\mathrm{int,L}}$	9.91	Navarro et al. (2017) (adapted from Gens et al., 2011)
Reference macrostructural porosity for intrinsic permeability for liquid water (exponential law)	$\phi_{\mathrm{M,ref}}$	0.0465	Navarro et al. (2017) (adapted from Gens et al., 2011)
Temperature	T	$293.15\ \mathrm{K}$	
Dynamic viscosity of liquid water	μ_{L}	$661.2 \cdot 10^{-3} \cdot (T-229)^{-1.562}\ \mathrm{Pa}\cdot\mathrm{s}$ Temperature T in K	Ewen and Thomas (1989)
Reference density of water vapour	ρ_{V0}	$\frac{\mathrm{e}^{0.06374\cdot(T-273.15\ \mathrm{K})\,-\,1.634\cdot10^{-4}\cdot(T-273.15\ \mathrm{K})^2}}{194.1}\ \frac{\mathrm{kg}}{\mathrm{m}^3}$ Temperature T in K	Ewen and Thomas (1989)

Molar mass of air (21 vol% oxygen and 78 vol% nitrogen)	$M_{\mathrm{mol,A}}$	$28.97\ \frac{\mathrm{g}}{\mathrm{mol}}$	--
Binary diffusion coefficient of water vapour	D_{V}	$5.9\cdot10^{-6}\cdot T^{2.3}\cdot {P_{\mathrm{G}}}^{-1}\ \frac{\mathrm{m}^2}{\mathrm{s}}$ Temperature T in K Gas pressure P_{G} in Pa	Pollock (1986)
Tortuosity factor for water vapour	τ_{V}	1	Olivella and Gens (2000)
Mechanical model			
Poisson's ratio	ν	0.33	Toprak et al. (2013)
Reference stress (LC curve)	p^c	10^4 Pa	Toprak et al. (2013)
Slope of critical state line	M	1.07	Toprak et al. (2013)
Increase in cohesion with suction	k	0.1	Kristensson and Åkesson (2008)
Elastic stiffness parameter for slope in $e_{\mathrm{M}}-\ln(p)$ diagram for zero macrostructural matric suction	κ_0	0.1	Adapted from Toprak et al. (2013)
Minimum bulk modulus	K_{min}	$1.5\cdot10^6$ Pa	
Plastic stiffness parameter for slope in $e_{\mathrm{M}}-\ln(p)$ diagram for zero macrostructural matric suction	λ_0	0.3	Toprak et al. (2013)
Plastic parameter for slope in $e_{\mathrm{M}}-\ln(p)$ diagram for varying macrostructural matric suction	r_{sM}	0.8	Toprak et al. (2013)
Plastic parameter for slope in $e_{\mathrm{M}}-\ln(p)$ diagram for varying macrostructural matric suction	β	$2\cdot10^{-8}\ \mathrm{Pa}^{-1}$	Toprak et al. (2013)

4.10.2 Initial and boundary conditions

The initial and boundary conditions for Test 1b are given in Table 4-15.

Table 4-15 Initial and boundary conditions for Test 1b

Test 1b	Swelling pressure tests for Pellets mixture
Processes:	• Hydraulic (H) • Mechanical (M)
Physics:	• Macro water (MW) mass balance • Mechanical equilibrium • Water vapour (V): Yes • Dissolved air (AL): Yes • Gravity effects: No
State variables:	• Liquid pressure (P_{L}) • Displacement field ($\boldsymbol{u}$) • Net/effective stress ($\boldsymbol{\sigma}$) • Pre-consolidation stress for zero suction (p_0^*) • Internal variable for micro void ratio ($e_{\mathrm{m,inst}}^*$)
Initial conditions (IC):	Hydraulic: • $P_{\mathrm{L,init}} = -1.73 \cdot 10^8$ Pa (from initial RH) Mechanical: • $\sigma_{\mathrm{r,init}} = \sigma_{\varphi\mathrm{,init}} = \sigma_{\mathrm{z,init}} = 10^3$ Pa • $\tau_{\mathrm{rz,init}} = 0$ Pa • $p_{0,\mathrm{init}}^* = 2.35 \cdot 10^6$ Pa Microstructural: • $e_{\mathrm{m,init}} = 0.094$ $\left(e_{\mathrm{TOT,init}} = 0.83\right)$
Boundary conditions (BC):	Hydraulic: • $P_{\mathrm{L,bottom}} = 1.1 \cdot 10^5$ Pa (Dirichlet BC) on bottom boundary • $-\hat{\boldsymbol{l}}_{\mathrm{MW}} \cdot \boldsymbol{n} = 0\ \frac{\mathrm{kg}}{\mathrm{m^2 s}}$ (no water flow) on top and lateral boundary • $P_{\mathrm{G,top}} = 10^5$ Pa (Dirichlet BC) on top boundary • $-\hat{\boldsymbol{l}}_{\mathrm{A}} \cdot \boldsymbol{n} = 0\ \frac{\mathrm{kg}}{\mathrm{m^2 s}}$ (no air flow) on bottom and lateral boundary Mechanical: • $\boldsymbol{u} \cdot \boldsymbol{n} = 0$ m (roller) on top, bottom and lateral boundary

Geometry:

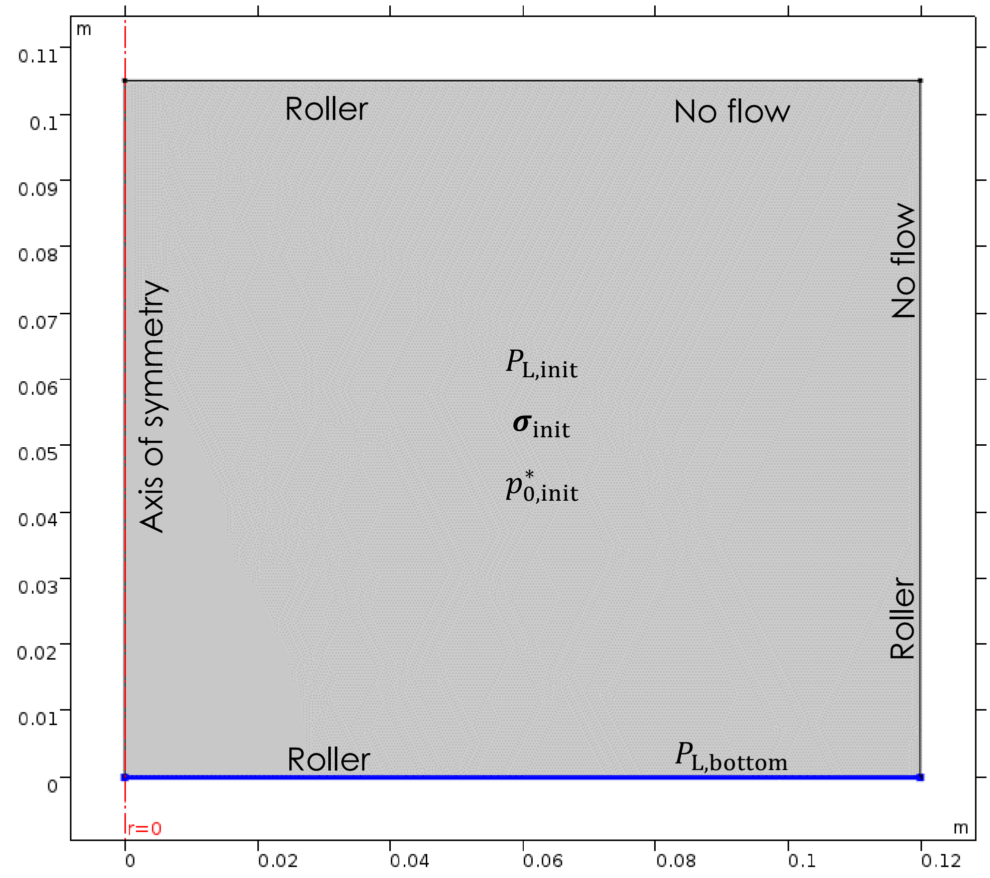

4.10.3 Results/discussion

Figure 4-69 represents the evolution of stresses with time, measured both radially at the heights of 20, 60 and 80 mm and axially. The signal of the radial stress sensor at a height of 40 mm was lost early in the test, so its results have not been plotted. The general evolution as well as the final values for the radial stresses at a height of 80 mm and for the axial stress are captured somewhat well, while radial stresses at a height of 20 mm and 60 mm are under and overestimated, respectively.

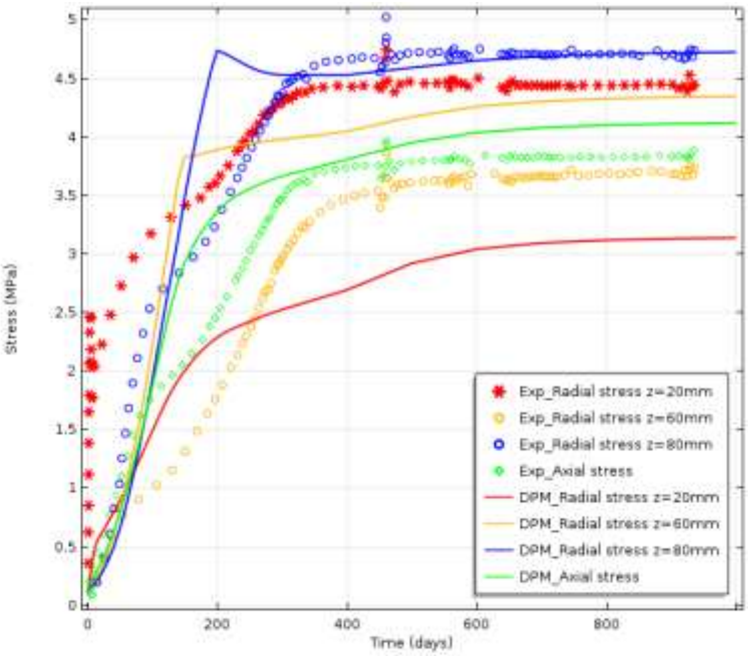

Figure 4-69 Temporal evolution of radial and axial stresses.

The simulated water inflow evolution is satisfactory, if compared to the experimental results (Figure 4-70).

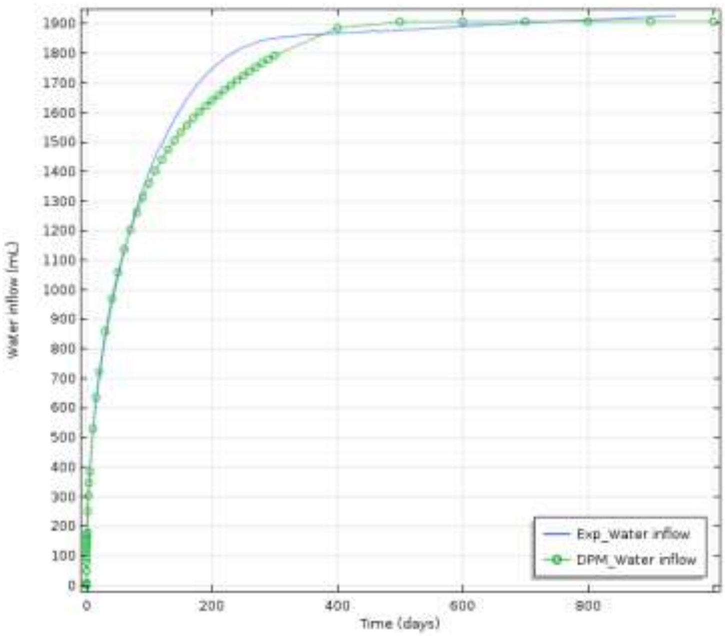

Figure 4-70 Temporal evolution of the water inflow.

In a post-mortem analysis, the water content and dry density at different vertical positions at the end of the test has been measured and mean values and standard deviations have been determined. The comparison with the numerical results shows that the simulation curves of the final water content (Figure 4-71) and the final dry density (Figure 4-72) lay inside the experimentally determined standard deviation, except for the slightly overestimation of the dry density at the top of the sample. The general trends suggested by the experimental values of the final water content and dry density have been reasonably captured by the model.

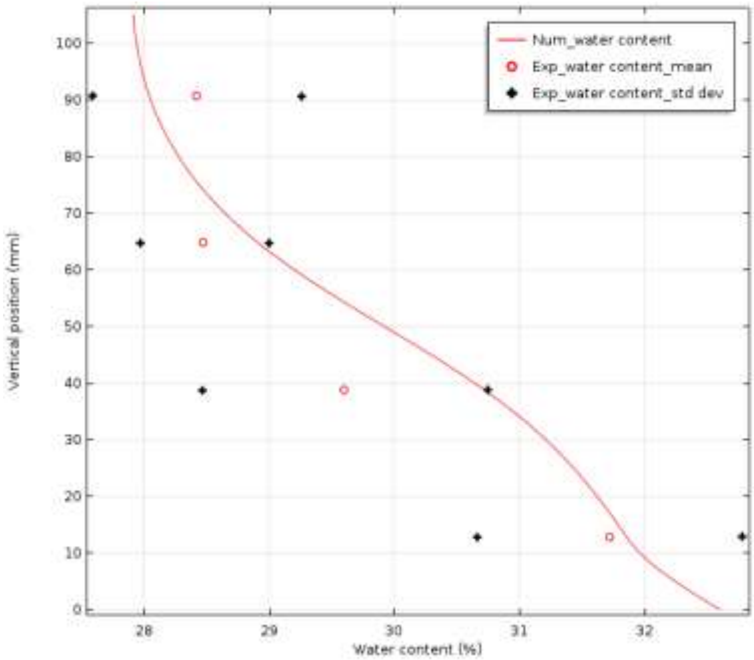

Figure 4-71 Comparison between experimental post-mortem data for the vertical water content distribution and numerical results.

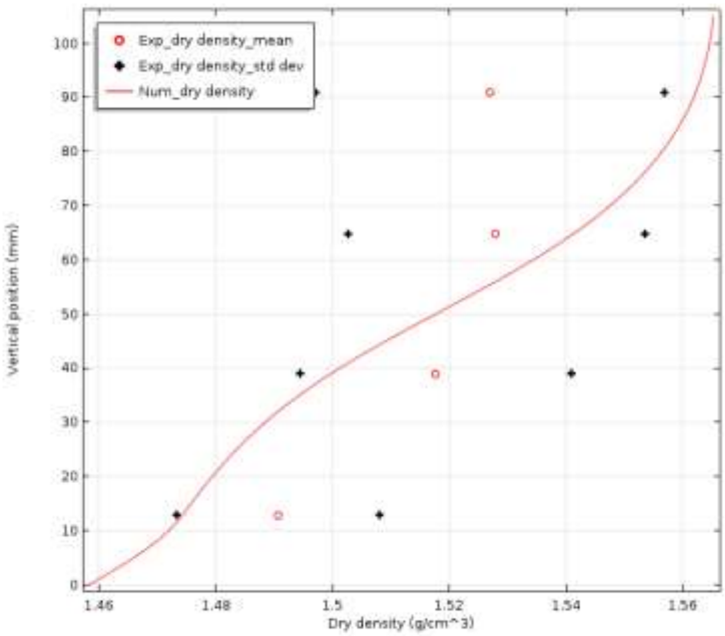

Figure 4-72 Comparison between experimental post-mortem data for the vertical dry density distribution and numerical results.

Although the results obtained are satisfactory, it is advisable to reconsider the scope of a conceptual model based on two functional levels, that is, on a double porosity continuum approach. Especially for configurations, in which a pellet filling does not contain crushed pellet material or other types of granules or fines in the inter-pellet space, the DPM approach may not be able to take into account adequately the additional functional level, that is the inter-pellet porosity. Modelling such configurations on basis of a DPM could require choices of inconsistent parameter values. To overcome these difficulties, our research group is currently working on a new development based on a triple porosity conceptual model for bentonite pellet fillings.

4.11 UPC

4.11.1 Geometry and discretization

The test has been performed by CEA (France) to study the behaviour of a mixture of whole pellets and crushed pellets. The sample is set up in a device that consists of a confining cylinder, a fixed base and mobile piston. A force sensor is interposed between the piston and the upper flange to measure the axial swelling stress. Four more sensors are installed to record the radial stress at four levels. In addition, five relative humidity sensors are placed at different locations inside the bentonite.
The problem is discretized by an axisymmetric mesh with the same dimensions as the specimen in the test.

4.11.2 Input parameters

The double structure model has been used to represent the behaviour of the mixture. The parameters are listed in Table 4-16 and Table 4-17.

Table 4-16 Hydraulic parameters

Hydraulic Model				
Constitutive law	Analytic expression	Parameter	Micro(4)	Macro(1)
Retention curve	Modified Van Genuchten's expression	$P_0(MPa)$ λ_0 $P_d(MPa)$ λ_d	**378.95** **0.899** **750** **3.5**	**40** **0.48**
Intrinsic permeability	Kozeny's expression $k_j = k_0 exp^{b(\phi_j - \phi_0)}$	$K_0(m^2)$ ϕ_0 b	9.6e-14(2) 0.4(2) 8(2)	
Relative liquid conductivity	Power law $k_r = A(S_e)^B$	A B S_{ls} S_{rl}	1(1) 3(1) 1(1) 0(1)	
Leakage parameter	$\Gamma^w = \gamma(\Psi_1 - \Psi_2)$	γ (kg/s/m3/ MPa)	**2.0e-7(2)**	

(1) Duek & Nilsson,2010 (2) Note DO, 2018 (3) Sánchez,2004(4)Gens,2011

Table 4-17 Mechanical parameters

Mechanical model BExM			
Constitutive law	Analytic expression	Parameter	Value
BBM Elastic part	$d\varepsilon_v^e = -\frac{\kappa}{1+e_M}\frac{dp}{p} - \frac{\kappa_s}{1+e_M}\frac{ds}{s+p_{atm}}$	κ κ_s	0.12(1) 0.03(1)
Yield locus	$p_0 = p_c\left(\frac{p_0^*}{p_c}\right)^{\frac{\lambda_{(0)}-\kappa}{\lambda_{(s)}-\kappa}}$ $\lambda(s) = \lambda(0)\,(r + (1\text{-}r)e^{-\beta s})$	$p_0^*(MPa)$ $p_c(MPa)$ r $\lambda(0)$ $\beta(MPa^{-1}))$	10(3) 0.5(3) 0.6(3) 0.15(3) 0.2(3)
BExM Microstructure	$K_m = \frac{1+\overline{e_m}}{\kappa_m}\hat{p}$	κ_m	0.06(3)
Interaction function	$f_s = f_{s0} + f_{si}\left(1 - \frac{p}{p_0}\right)^{ns}$	f_{s0} f_{si} n_s	-2 1(3) 2.5(3)

(1) Duek & Nilsson,2010 (2) Noiret, 2016 (3) Sánchez,2016

4.11.3 Initial and boundary conditions

The initial parameters are listed in the Table 4-18 and Table 4-19. Two different water retention curves are selected for the macro and microstructure. The entire pellet porosity is included in the micro porosity. There are both macro and micro pores in the powder which are calculated with the formula from Romero, 1999.

Table 4-18 initial properties of the sample

Initial w (%)	Initial density(kg/m3)	Constant Radius (mm)	Initial height (mm)	%pellet	%crushed pellet
4.23	1.54	120	105	69.88	30.12

Table 4-19 initial parameters of the sample

Total porosity	Micro porosity	Macro porosity	Macro Suction (MPa)	Micro Suction (MPa)
0.453	0.221	0.224	205	305

A fixed mechanical boundary is used during the test and the water is introduced from the lower surface under constant water pressure of 10 kPa. Throughout the test, the hydraulic and mechanical condition stay constant.

4.11.4 Results/discussion

The evolution of degree of saturation is shown in Figure 4-73. As the water is supplied from the bottom, the saturated process evolves from the lower sections upwards.

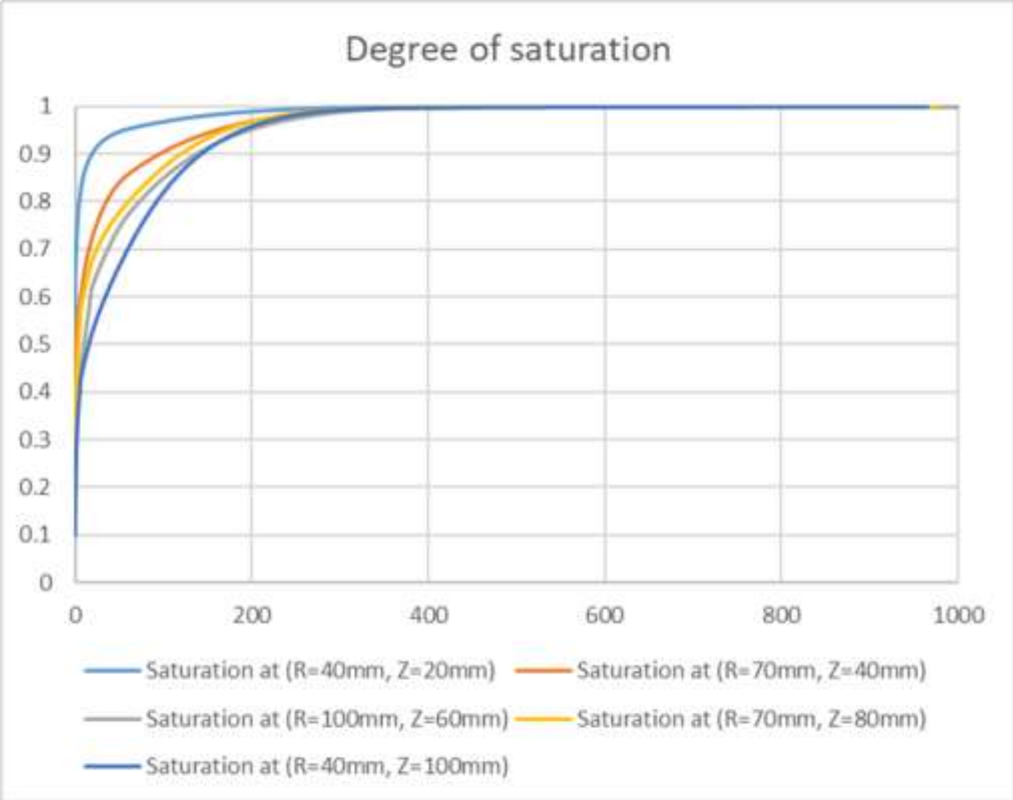

Figure 4-73 Time evolution of degree of saturation

The swelling stress at different heights have been collected and compared with the test results inFigure 4-74. The interchange between two porosity levels contribute to the computed variations of swelling stress. Figure 5.4Figure 4-75shows that the final water content is well reproduced by the numerical model.

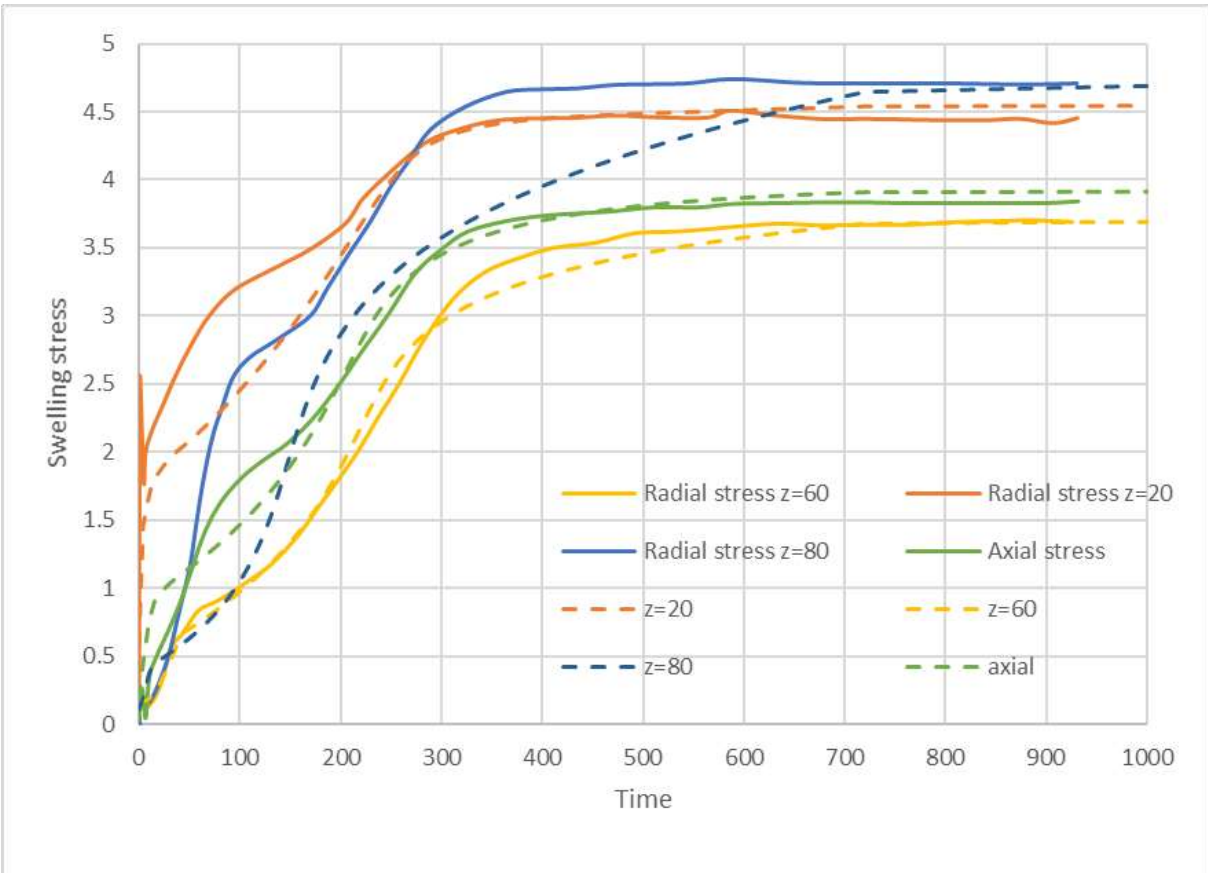

Figure 4-74 Time evolution of swelling stresses. Solid lines are modelling results and dashed lines are experimental observations.

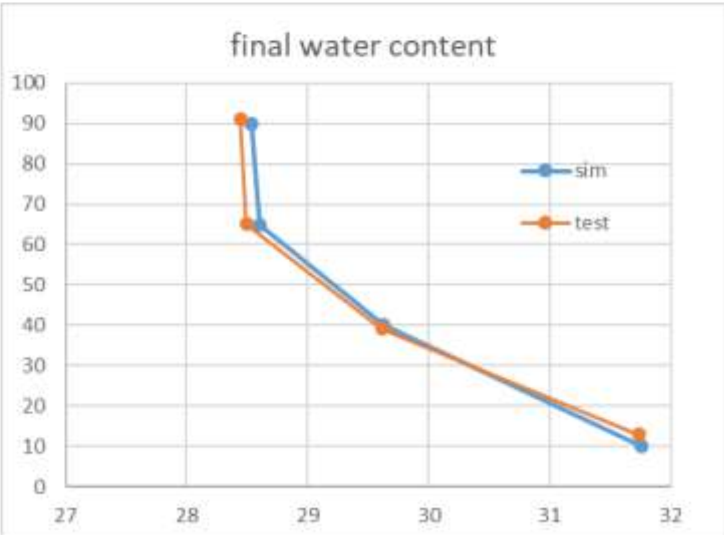

Figure 4-75 Distribution of water content along the specimen height

The water intake is also plotted and compared with the test results (Figure 4-76). The simulation results show a faster water intake at the beginning of the test. The relative humidity is plotted in Figure 4-77. Again, the computed relative humidity increases somewhat faster than observations.

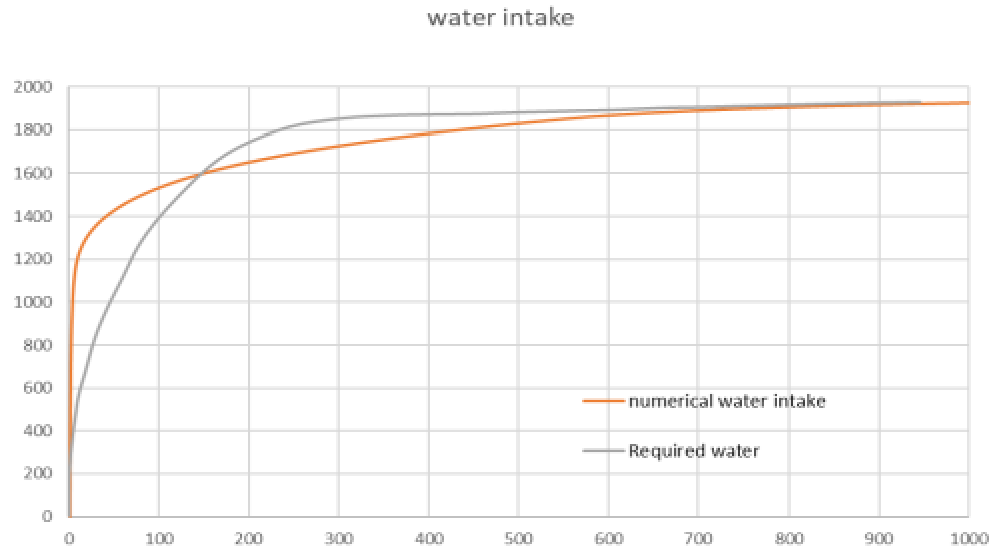

Figure 4-76 Time evolution of water intake

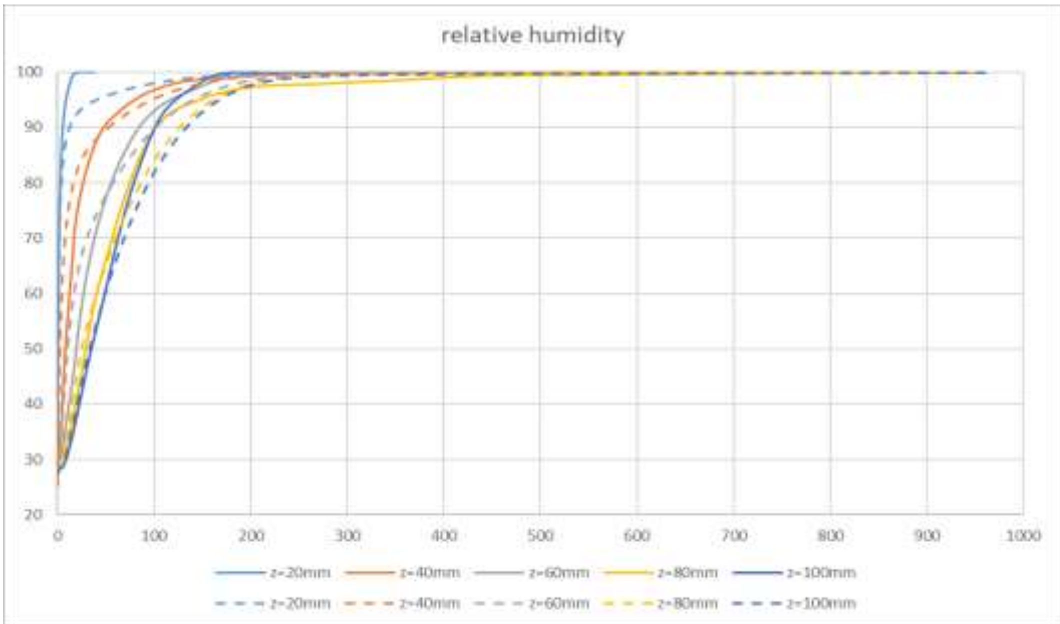

Figure 4-77 Time evolution of relative humidity. Solid lines are modelling results and dashed lines are experimental observations

4.12 Synthesis of results

In this test, the swelling material was constituted with a pellets mixture. The models used to simulate do not integrate the heterogeneities inherent to this type of mixture. The models were very similar to those used for bentonite block evolutions.

4.12.1 Axial pressure and radial pressure

Figure 4-78 show a comparison between the axial pressure measured during the test and the numerical results. In a first analysis, most of the models seem to overestimate the axial pressure and especially the final value when bentonite is fully saturated. Final swelling pressure observed is about 3.8 MPa and simulations give a range between 3.7 and 5.2 MPa. Nevertheless, when the analysis of the final value is made in regard of the swelling data given in D5.1.1 tests specifications, all the models are in the good range. This can be explained partially by the fact that with this kind of pellet mixture some residual uncertainties remain on the initial dry density. As a small deviation on this value induces a large difference on the final swelling pressure, this could be one explanation for this overestimation.

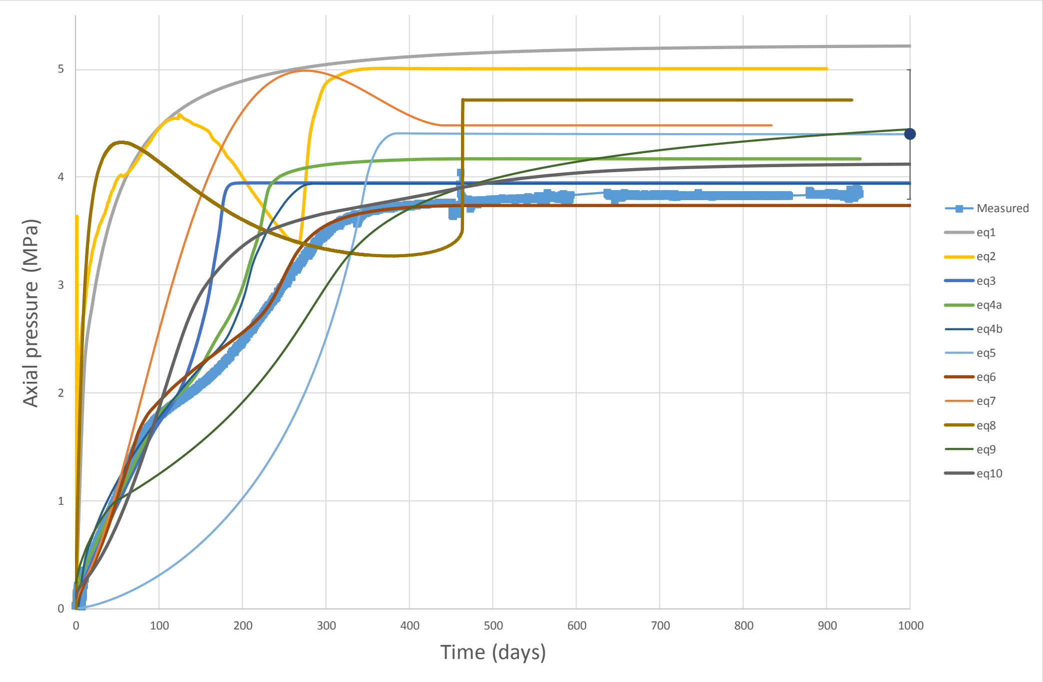

Figure 4-78 Axial pressure, comparison between measurement and modelling results

Even if some numerical results are still far from the measurement during the transient phase, most of the evolution curves are close to the measurement and capture the trend. The variations in the slope of the curve indicating several phases of swelling are present in most of the numerical result with a reasonable accuracy in terms of pressure values. Despite the presence of pellets, this test is very classical. It is a swelling pressure test at constant volume with an initial water content relatively low. Independently of the presence of pellets, models have been developed and calibrated for this kind of situation. It should be noticed that some numerical results are very close to the measure.

Figure 4-79, Figure 4-80 and Figure 4-81 show the evolution of radial pressure at three positions on the height of the sample at 20, 60 and 80mm.

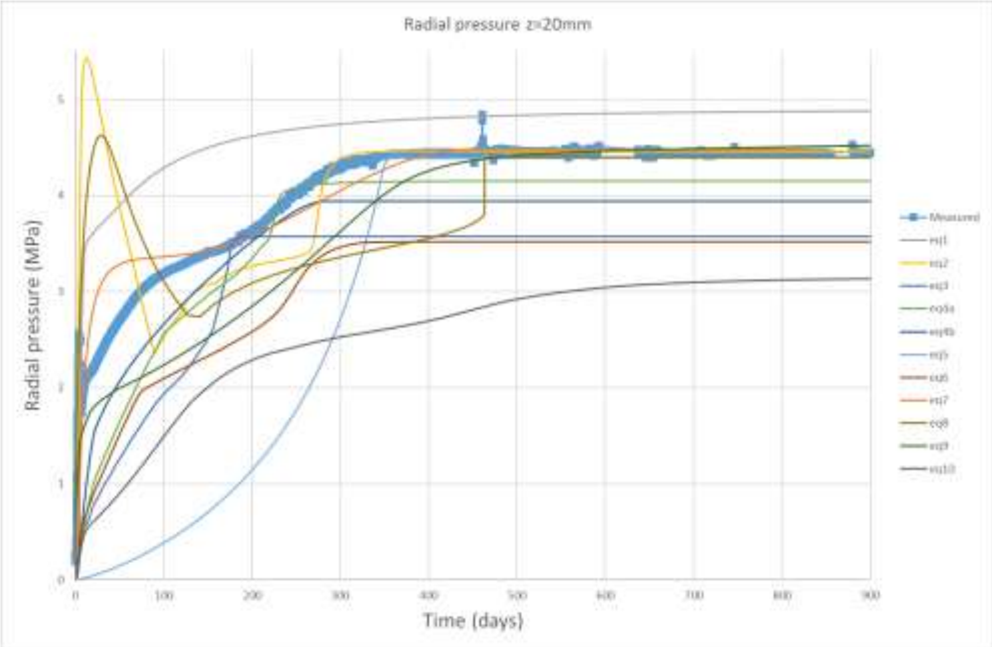

Figure 4-79 Radial pressure at z=20mm, comparison between measurement and modelling results

The analysis is very similar to the one on the axial pressure. Most of the numerical results are in the good range of values and the trend is well capture by the majority of the models. It was not possible to reproduce the differences observed between the different heights. It should confirm that the size of the sensor compare to the size of the pellets could lead to some uncertainties in the measure. For example, if a high density pellets is in face of the sensor, pressure which is assumed to be representative of a level is certainly overestimate (see for example results at z=20mm). If the sensor is in face of powder, the pressure is certainly underestimated (see for example results at z=60mm).

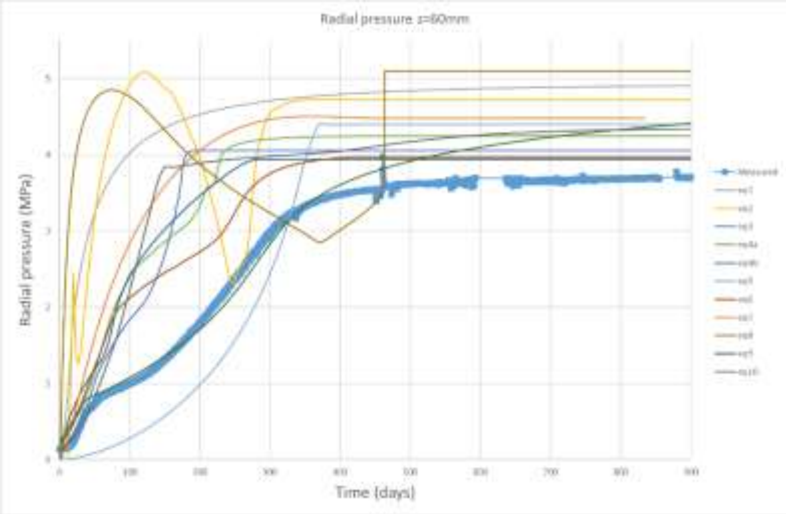

Figure 4-80 Radial pressure at z=60mm, comparison between measurement and modelling results

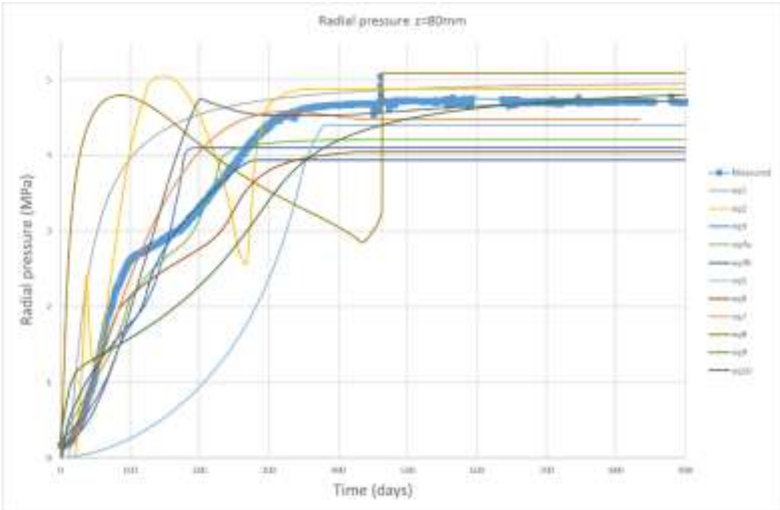

Figure 4-81 Radial pressure at z=80mm, comparison between measurement and modelling results

4.12.2 Dry density

The dry density profile at the end of the test are presented on Figure 4-82. If most of the final values are in the range of what was measured during the post mortem analysis, it could be seen that the profile are quite different. It is interesting to notice that despite the duration of the test (~1000 days), a certain heterogeneity in dry density is still present. This situation is reproduce by most of the models. Few of them predict a uniform distribution of dry density iver the height.

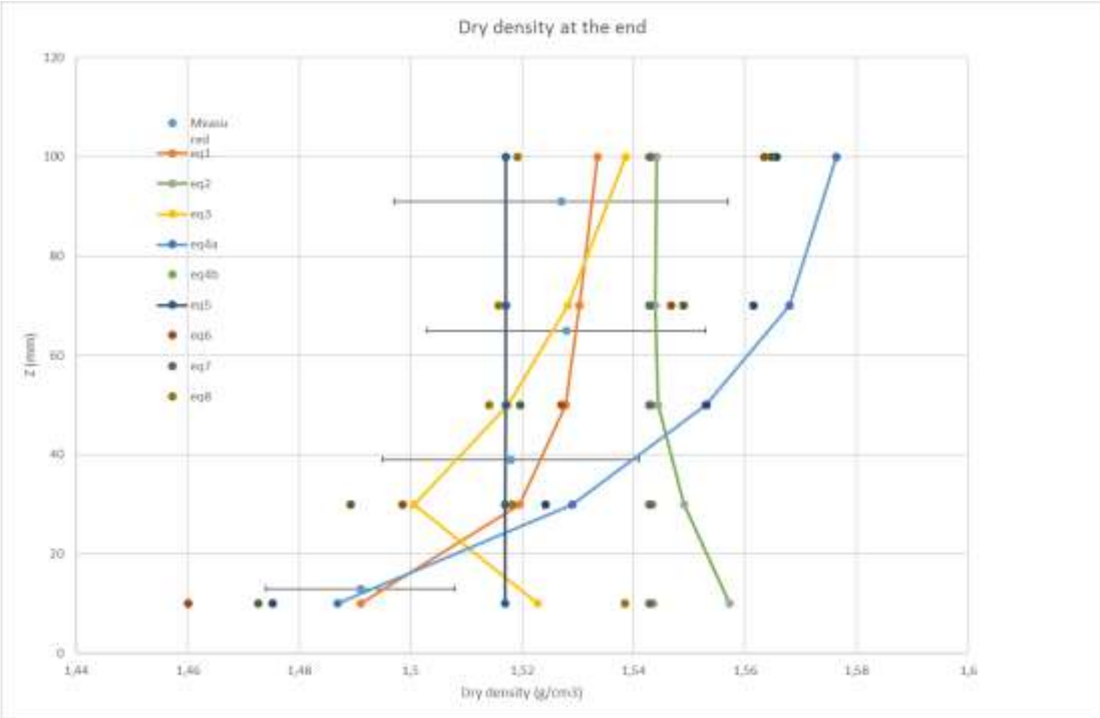

Figure 4-82 Vertical dry density profile at the end

The evolution of dry density at three locations shows as usual large differences in the transient phase and especially at the beginning of the test, far from the stable state (see Figure 4-83 and Figure 4-84).

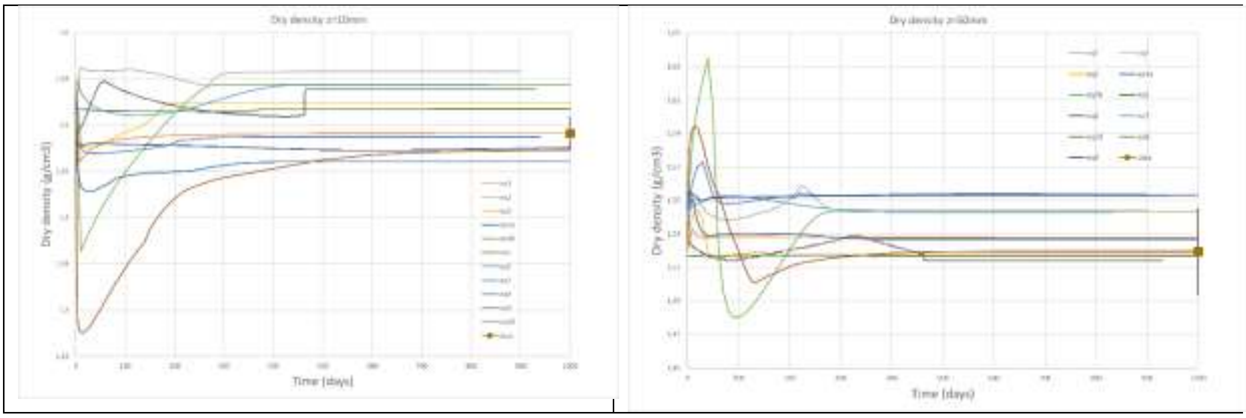

Figure 4-83 Dry density evolution at z=10mm and z=50mm

Non monotonic evolutions are observed but not always in the same trend which is difficult to explain based on physical processes arguments, especially with such a high amplitude of variation.

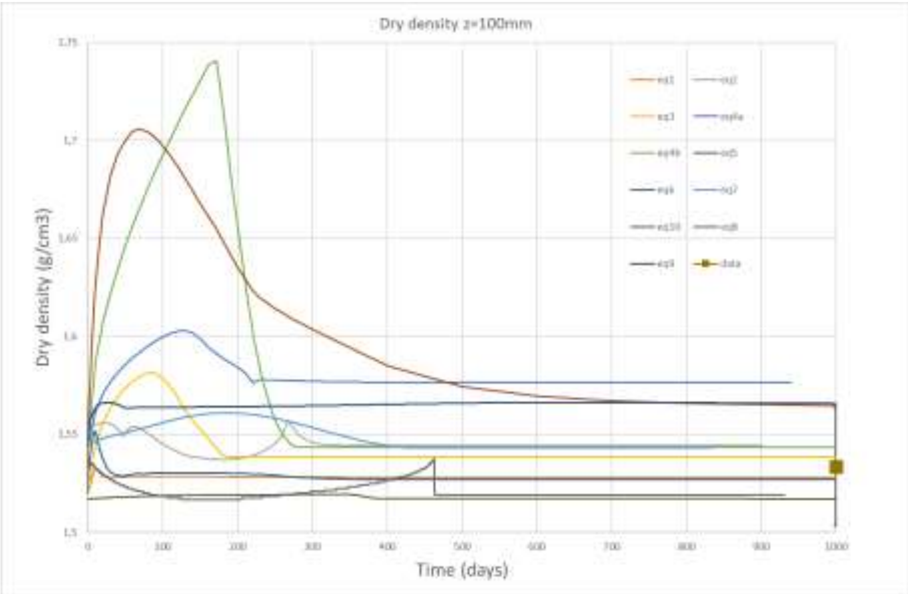

Figure 4-84 Dry density evolution at z=100mm

4.12.3 Water content

Water content profiles at different heights show interesting behaviour. All the models seems to give almost the same evolution of water content through the sample especially close to the base and at the middle of the sample. This result tends to show that models capture the saturation transient well. Close to the base, saturation and water content evolution are certainly correlate to water injection. The more dispersive results have been obtained near the top of the sample where behaviour is more driven by capillarity effects.

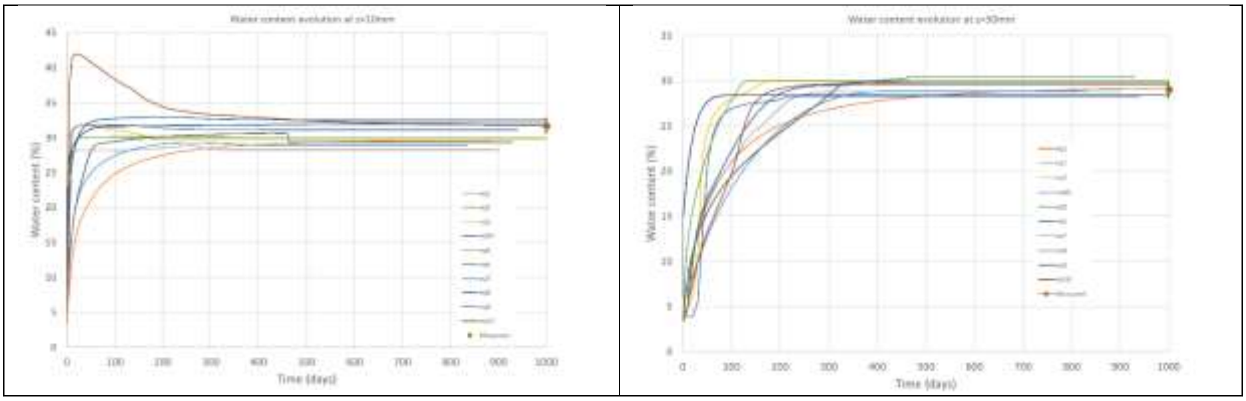

Figure 4-85 Water content evolution at z=10 and 50mm

The time to reach the final value at z=100mm is quite different for the participants compared to the other locations.
At the end of the test, all the models are very close to the water content measured during the post-mortem analysis.

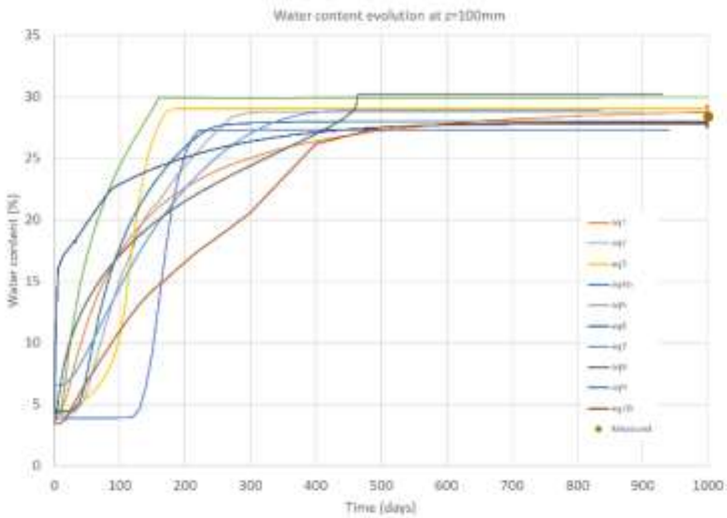

Figure 4-86 Water content evolution at z=100mm

As a global remark, the hydraulic part of the problem seems to be well reproduced by all the models.

4.13 Discussion

Comparison between the final values of pressure measured axially and radially with the simulations seems to indicated large differences depending on the location in the sample (Figure 4-87). This could be induced by low numerical accuracy in some cases but also by dispersion in the measurement due to the fact that pellets size is important in regards of the size of the sensors.

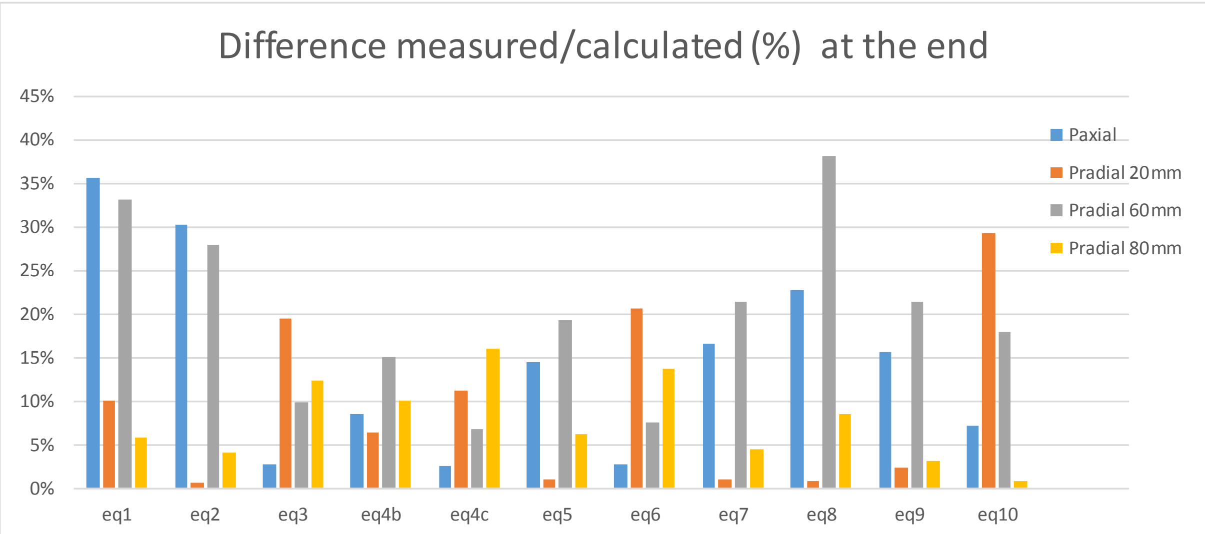

Figure 4-87 Evaluation of error between simulation and measure on pressure

However, a combination between the variability of dry density coming from the post mortem analysis and the reference swelling pressure curves obtained on the same kind of pellets mixture for several dry density (Figure 4-88b) shows that the values obtained by the models are in the good range (Figure 4-88a).

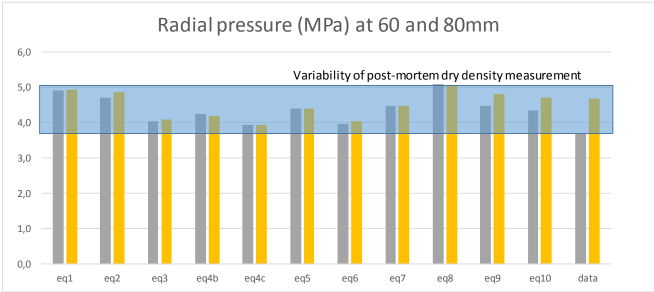

(a)

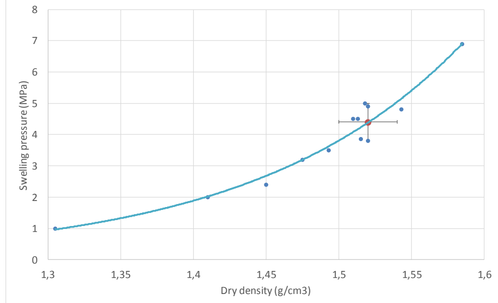

(b)

***Figure 4-88** (a) Radial pressure at 60 and 80mm from bottom,(b) Swelling pressure function of dry density forMX-80 pellets mixture*

The predict time to reach a stabilized state is presented in Table 4-20 (estimated on 3% of the final value for the axial pressure). Some dispersion is observed with underestimation or overestimation of the duration of the transient phase. This is consistent with the graph Figure 4-78 where a large dispersion is observed during hydration.

***Table 4-20** Time to reach the final axial swelling pressure for test1a01 for the two stages*

	Meas	eq1	eq2	eq3	eq4b	eq4c	eq5	eq6	eq7	eq8	eq9	eq10
Time	366	330	300	178	260	262	370	324	389	463	772	600
Difference model-measurement		9,8%	18,0%	51,3%	28,9%	28,4%	1,1%	11,5%	6,3%	26,5%	110,9%	63,9%

On the other hand, Figure 4-89 illustrates that transient phase seeing from an hydraulic point of view seems well capture by the model. Water uptake by the sample or relative humidity evolution estimated at several locations in the sample are in good agreement with the measurements.

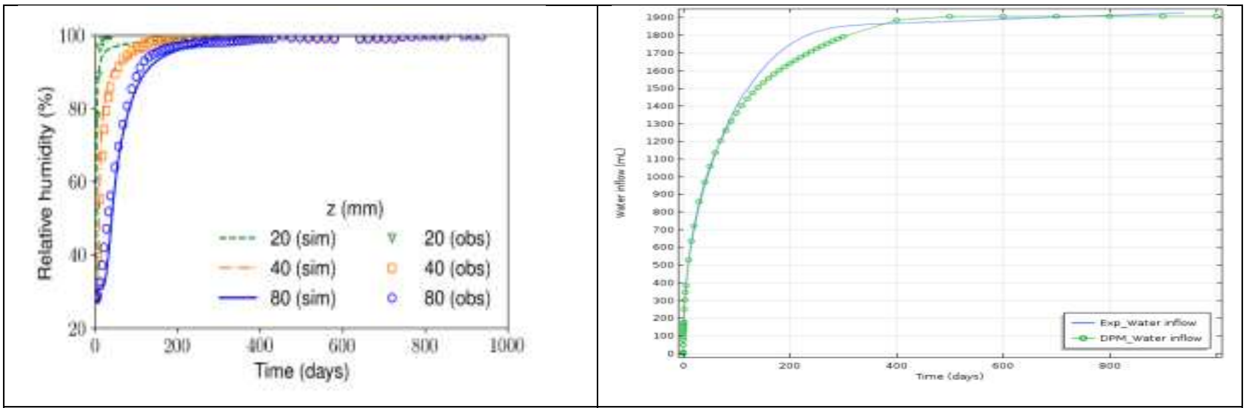

(a) (b)

Figure 4-89 ***(a) relative humidity evolution results compared to observations, (b) water uptak by the sample during the test, comparison model/measurement***

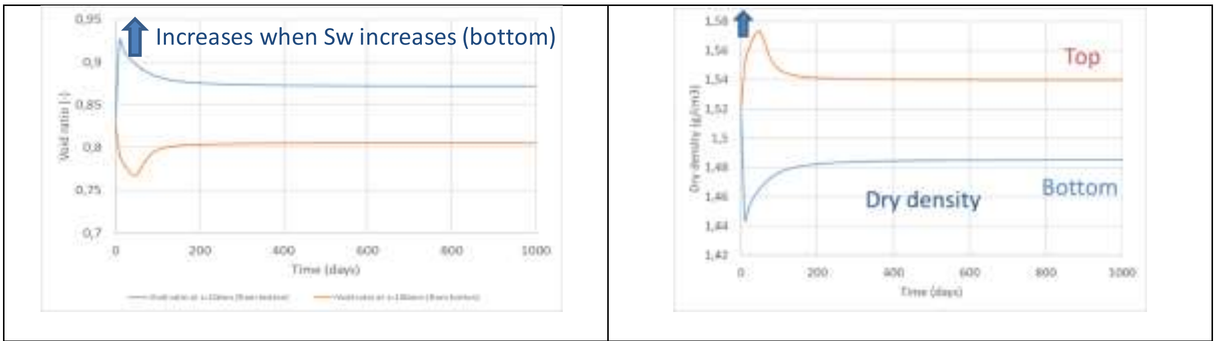

(a) (b)

Figure 4-90 ***Example of modelling results on void ratio and dry density evolution at the top and the bottom of the sample***

Results on test 1b show how models can help in the comprehension of the physical processes and the behaviour of the swelling material during hydration. Figure 4-90 illustrates this by presenting void ratio and dry density evolution on the top and bottom of the sample. In this test, water was supplied at the bottom. As soon as there is contact between water and the material, swelling started and induced an increase of void ratio and a decrease of dry density locally close to the bottom. On the other hand, swelling pressure developed at the bottom tends to compress the overall sample. This leads to an increase of the dry density and a decrease of void ratio at the top.

5 Test1c – Bentonite block and pellets mixture

This test is composed of two layers of bentonite with high contrast of dry density between them. Pellets mixture are placed on the top of a bentonite block. The objective of the test is to study the evolution of this heterogeneous structure during hydration. It could be representative of a situation in a repository where voids around compacted blocks are filled with pellets (like in KBS3 concepts). The test has been developed by POSIVA (Finland). For this last test, ten partners proposed results (see Table 5-1).

Table 5-1 List of partners who performed test 1a and models used

Team	Model/code
ICL	ICFEP
BGR	OpenGeoSys 5
Claytech	Comsol/HBM
EPFL	Lagamine/ACMEG
LEI	Comsol/Code_Bright
Quintessa	QPAC/ILM
CU-CTU	Sifel
UPC	Code_Bright
ULG	Lagamine
VTT/UCLM	Comsol

5.1 Brief description of the test1c

Bentonite block sample was compacted directly into the cell to dry density value of 1808 kg/m^3. Pellets mixture is poured into the cell on the top of the compacted block without external compaction (Figure 5-1). In this constant volume cell, the saturating solution is injected from the top under constant head of 10 kPa. One bottom circuit port of the cell was open to atmosphere over the saturation period.

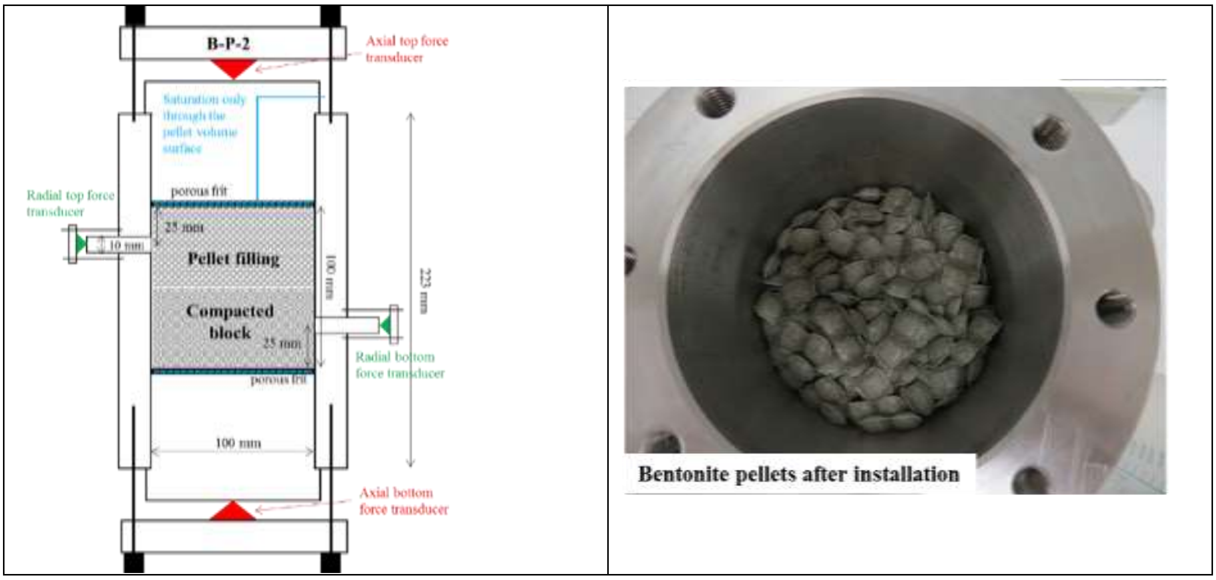

Figure 5-1 **Experimetal set-up, view of the cell after pellets installation**

Test was terminated after 672 days. Although the stability of the pressure in both directions (axial and radial) was reached, the test continued over a period of about 1 year (Figure 5-2).

Post-mortem analysis was performed in the axial and radial directions. Profiles of water content and dry density have been produced.

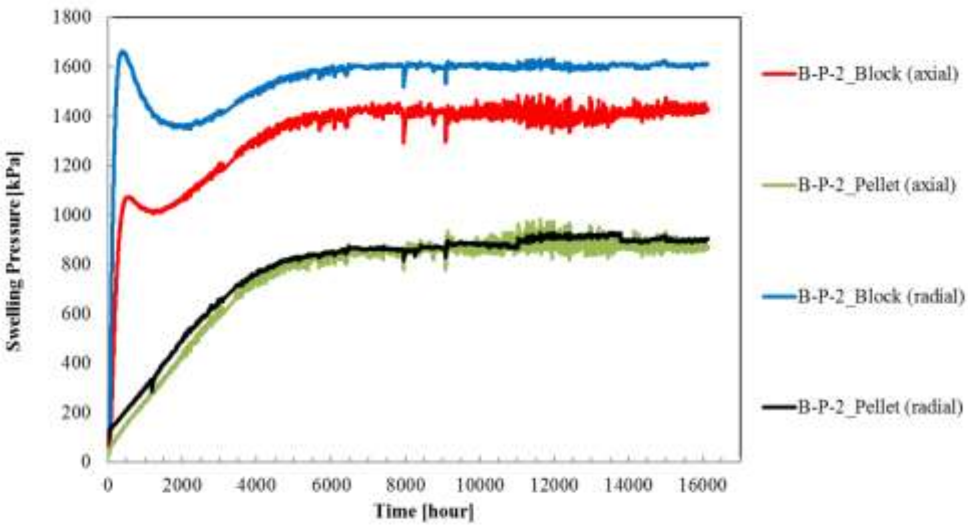

Figure 5-2 **Swelling pressure in radial and axial directions function of time**

5.2 ICL

5.2.1 Geometry and discretisation

The Test 1c sample has a diameter of *D* = 100 mm and a height of *h* = 100 mm. The MX-80 bentonite block is located below the pellets and occupy the first 48.5mm of the height of the specimen. As in previous tests, the geometric symmetry around the vertical axis of the sample allows half of the domain to be discretised in a finite element mesh. This is done using 8-noded quadrilateral displacement-based elements, with a pore water pressure degree of freedom at 4 corner nodes. Analysis is performed under axi-symmetric conditions. The employed mesh comprises 200 finite elements organised in 20 rows of ten elements each.

5.2.2 Input parameters

Two materials are employed in the experiment: compacted MX-80 bentonite and pellets. The former is characterised as in Tests 1a01 and 1a02, while the latter is characterised as in Test 1b.

5.2.3 Initial and boundary conditions

The compacted bentonite block has an initial dry density of 1808 kg/m^3, the initial water content is 16.3% and the initial degree of saturation is 85%, corresponding to the initial suction of 10.5 MPa. The pellets have an initial dry density of 904 kg/m^3, the initial water content is 15.3% and the initial degree of saturation is 20%, corresponding to the initial suction of 59MPa. For both materials the initial total axial and radial stresses are 10 kPa.

The volume of the sample is constant throughout the experiment, therefore the horizontal displacements are imposed to be zero on the two vertical boundaries and the vertical displacements are imposed to be zero on the two horizontal boundaries. A final pore water pressure of 10kPa, corresponding to the constant hydraulic head present in the experiment, is imposed on the top boundary.

5.2.4 Results/discussion

Figure 5-3 and Figure 5-4 show a comparison between measured and predicted evolution and magnitudes of the total axial and radial swelling stresses, respectively. The axial stress is measured on the top boundary of the sample for the pellets and on the bottom boundary for the block. Meanwhile, the radial stress is measured at two points located at $r = 50$mm, and $z = 25$

and $z = 95$ from the sample base, respectively for the block and for the pellets. In terms of axial stress, the measurements in the block are well reproduced from about 3000 hours of the test duration onwards. The numerical prediction presents some small oscillations in the initial phase of the analysis and the measurements are underestimated. This could be caused by a rapid dissipation of suction throughout the sample. On the other hand, the axial stress in the pellets is overestimated in the simulation, however this is due to equilibrium throughout the sample, which is inevitable in numerical analysis.

In terms of the radial stress, the outcome of the analysis is in good agreement with the measurements both in the block and in the pellets. As for the axial stress, some oscillations are present within the first 2000 hours of test duration. As observed in the Tests 1a, the growth of the stress in the block is surprisingly high and cause of this remains unknown. This is not reproduced in the model. Nevertheless, it can be noted from Figure 5.2, that the pellets are less expansive than the compacted bentonite.

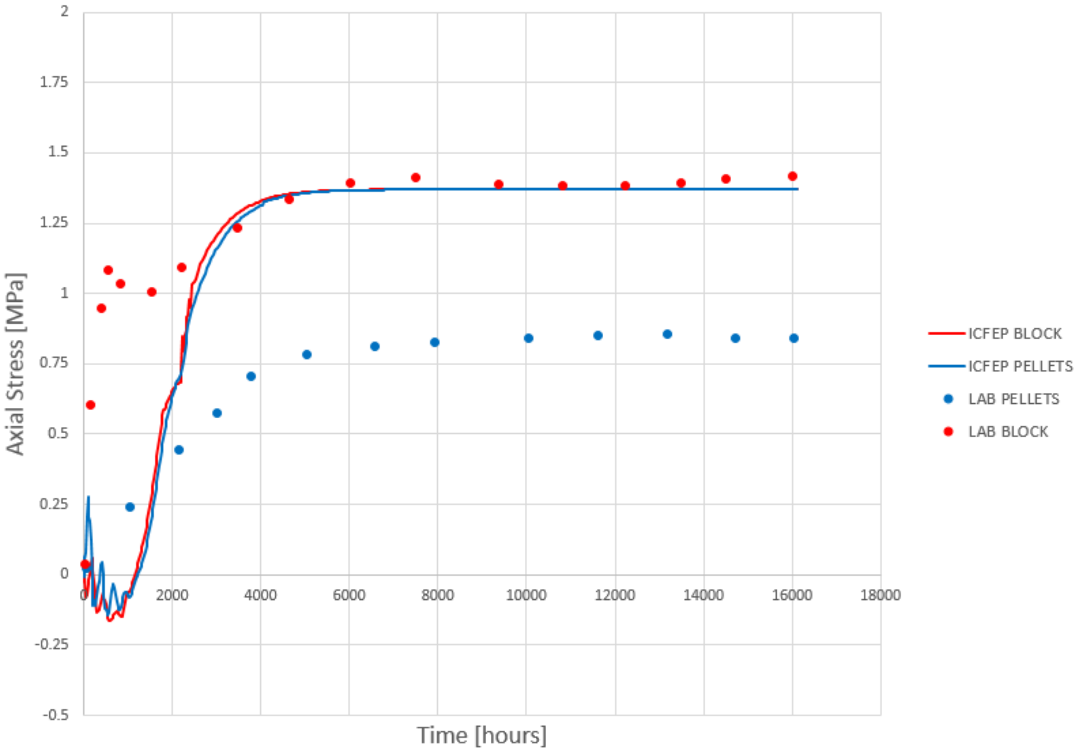

Figure 5-3 Comparison of measured and ICFEP predicted axial stress in TEST 1C

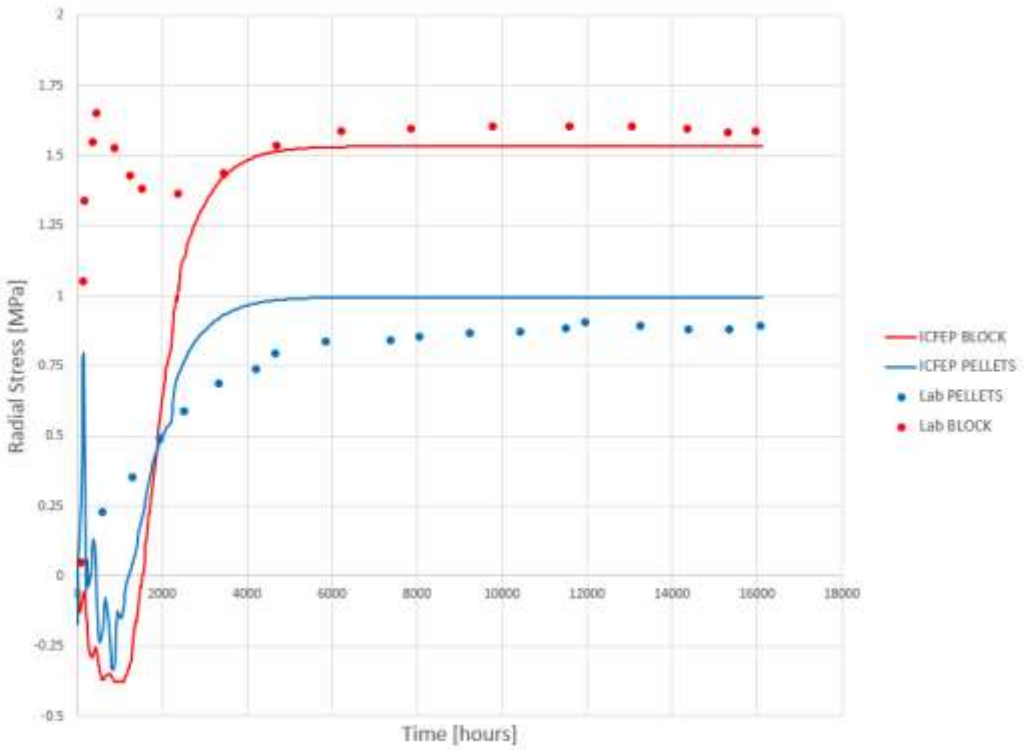

Figure 5-4 Comparison of measured and ICFEP predicted radial stress in TEST 1C

Figure 5-5 and Figure 5-6 show the distributions of dry density and water content along a vertical section of the sample taken along the left hand-side boundary of the mesh, i.e. the centre of the sample. The profiles are shown at different times: 50, 100, 200, 300, 400 and 670 days (i.e. the end of the test). It can be noted that the dry density is very different in the two materials, as the block is twice as dense as the pellets. In the proximity of the interface between the two materials, at $z = 48.5$mm from the bottom of the sample, the dry density changes rapidly with the z coordinate in order to be continous along the height of the sample. It can also be noted that the dry density does not change throughout the test, as the final distribution presents values similar to those at the beginning of the experiment because the volume is constant. The temporary changes in dry density take place in the block while its level of suction is reducing towards zero and remains stable afterwards.

The same observations made for the dry density profiles apply to those of the water content pictured in Figure 5-6. In fact, the water content is computed from the void ratio using the following relationship: $w = (e \cdot S_r)/\rho_s$, where $\rho_s = 2.78\, kg/m^3$ is the particle density adopted for both the block and the pellets.

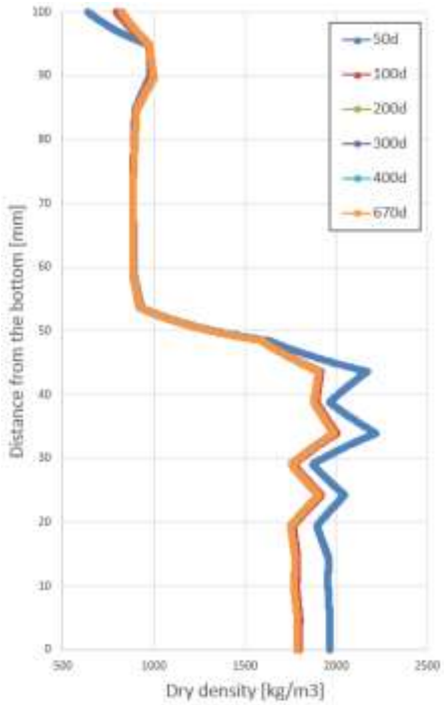

Figure 5-5 Distributions of dry density along a vertical section at different times in the analysis of TEST1C

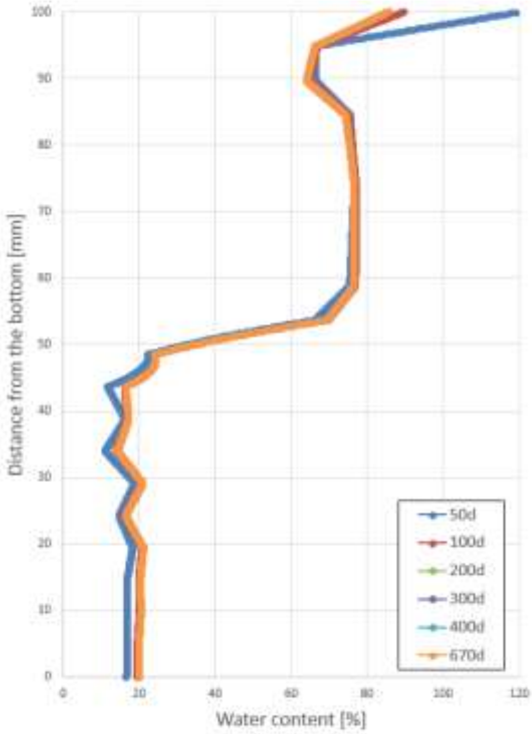

Figure 5-6 Distributions of water content along a vertical section at different times in the analysis of TEST 1C

5.3 BGR

5.3.1 Geometry and discretization

The model was setup as an axisymmetric heterogeneous domain. The pellets and the block were modelled as two different materials with their own set of hydraulic and mechanical parameter sets. The pellets were not resolved explicitly but instead the pellets were modelled as a homogeneous material with estimated equivalent properties. There were 4 stress sensors in total in the experimental setup, one radial stress sensor each in the block and pellet region on the wall on the experimental cell and one axial stress sensor each on the top (pellet region) and bottom (block region) of the cell. These points were setup in the simulation domain to provide stress output for comparison. The discretized model domain with 2391 elements is shown in Figure 5-7.

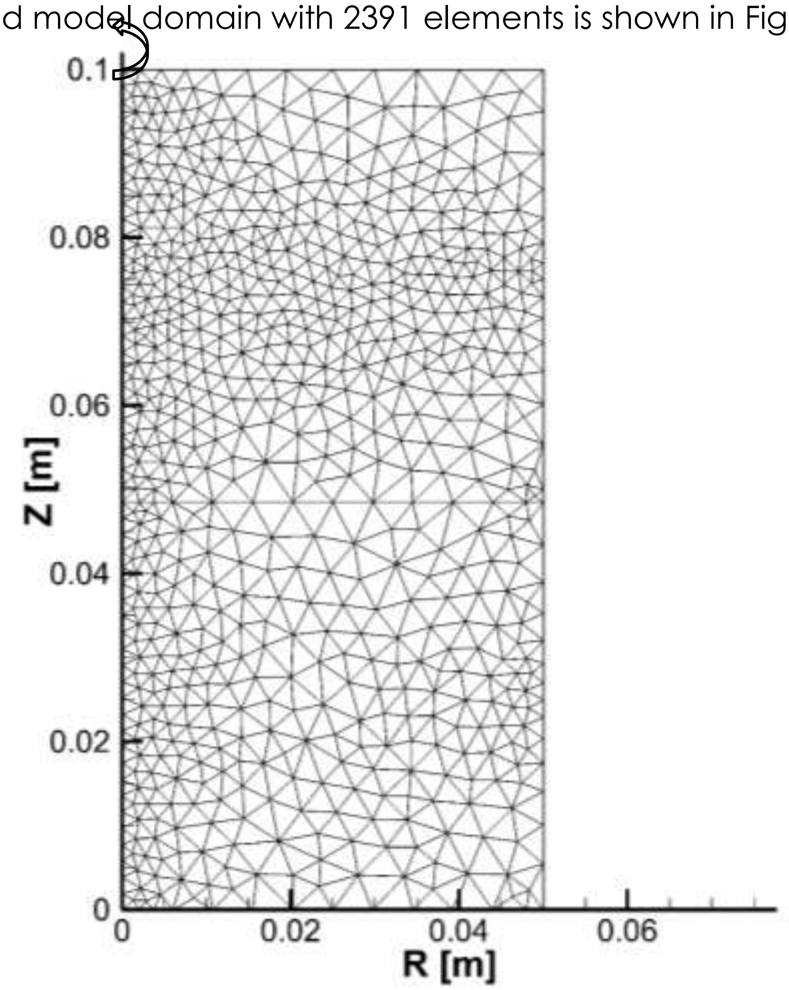

Figure 5-7 Discretized axisymmetric model domain used in the simulation for test case 1c. The axis of symmetry is along the boundary R = 0 m. The boundary between pellets and blocks is shown as a line at Z = 0.0485 m. Pellets are above this line and the block is situated below.

5.3.2 Input parameters

In test case 1c, the lower part of the experimental cell was installed with a bentonite block, which was compacted in the cell. The block was initially at 80% water saturation. The upper part of the cell was filled with bentonite pellets without any mechanical compaction. The pellet system was initially at 20% water saturation. Data about the initial state of the system was scarce and observation about the initial HM state of the system was missing, especially regarding equilibrium and processes occurring at the interface between the block and the pellets. Hence, a decision was taken during the model setup to establish capillary pressure equilibrium between the pellet and block systems in order to avoid transfer of water from the block to the pellets. Other options regarding setup of the initial state of the system at the block-pellet interface were not explored. Equilibrium was established by adjusting the entry pressure of the pellet system so that both the block and pellet systems were at the measured saturation levels and in HM equilibrium with each other for one value of capillary pressure in the entire model domain. The two curves used are depicted in Figure 5-8. The parameter set is given in

Table 5-2.

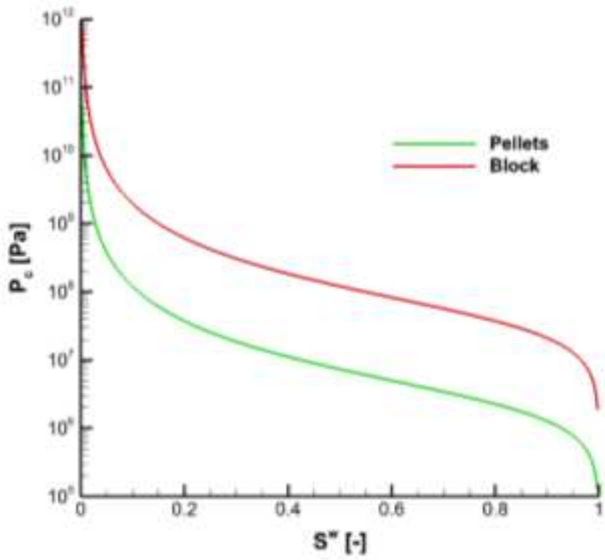

Figure 5-8 Capillary pressure – saturation curves used for the two materials in test case 1c.

Table 5-2 Parameter values chosen for the capillary pressure – saturation curve and relative permeability for test case 1c.

Parameter	Value		Unit	Reference
	Pellet	Block		
Relative permeability (k_{rel})	Cubic law of water saturation $(S^w)^3$		[-]	Åkesson et al. 2010
Pellet entry pressure	2.576	42.5	MPa	Fitted for capillary pressure equlibrium
v.G. shape factor (m)	0.375		[-]	Åkesson et al. 2010
Residual saturation (S^w_{res})	0.0		[-]	
Maximum saturation (S^w_{max})	1.0		[-]	

5.3.3 Initial and boundary conditions

Choice of boundary and initial conditions for this test case was particularly difficult due to the lacking mechanical characterization of both the block and pellet systems. The block was compacted in-situ to a dry density of 1808 kg/m^3. Therefore the swelling pressure was estimated from the swelling pressure graph of experiment 1a01 (Figure 3-17). Based on the figure the chosen value is of the swelling pressure for the given dry density is plausible. The mechanical parameters of the block were estimated based on its dry density and experience gained from test case 1a01. With a dry density of 904 kg/m^3, the pellet system was half as dense as the block system. Therefore, the elasticity paramters were adjusted appropriately. The swelling pressure of the pellets system was also set very low based on the swelling pressure curve of the FSS type mixture (ref. Figure 4-11). The permeabilities of the two materials were set up to be identical. The parameters used for the simulation are summarised in Table 5-3.

Table 5-3 Parameter set used in the simulation of test case 1c.

Parameter	Value		Unit
	Block	Pellet	
Permeability Ω	1.0e-20	1.0e-20	m^2
Void ratio (e)			[-]
Porosity (ϕ)	0.36838	0.69156	[-]
Initial saturation $\left(S_{\text{init}}^{w}\right)$	0.8	0.2	[-]
Fluid density $\left(\rho^{w}\right)$	1000		kg/m^3
Grain density $\left(\rho^{s}\right)$	2780		kg/m^3
Biot coefficient (α_{Biot})	0.1		[-]
Young's modulus (E)	80	40	MPa
Poisson's ratio (υ)	0.1		[-]
Max swelling pressure $\left(\boldsymbol{\sigma}_{\text{max,sw}}\right)$	11	1	MPa

Since the block was compacted in-situ into the experimental cell, the friction of the material to the walls of the cell was expected to influence the developement of the stresses. The difference in the measured axial stresses between the pellet and block systems also suggested a presence of friction between the block and the cell. Two possible approaches to model friction between the wall of the cell and the bentonite are either by using a constant friction force or a friction force based on the radial stresses. However, the functionality required to simulate friction was not available in OGS at the time of the simulation of the test case. Therefore the behaviour of the model under the influence of friction was approximated by a no-deformation (no-slip) boundary, thus preventing the movement of the block at the outer boundary in the Z direction. The boundary conditons are shown schematically in Figure 5-9 and summarised in Table 5-4.

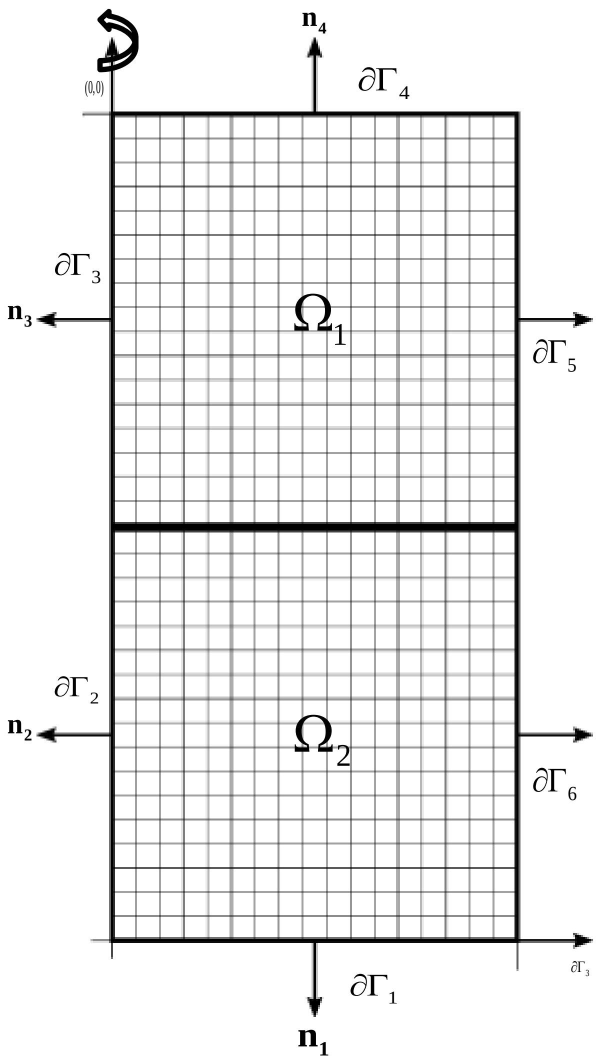

Figure 5-9 Schematic of the model domain for test case 1c showing 2391 elements in two distinct regions; the pellets region (Ω_1) and block subdomain (Ω_2). The interface between the two, the boundary surfaces, the axis of symmetry and the normal directions are also shown.

Table 5-4 Tabular summary of the boundary conditions for test case 1b, based on Figure 5-9

Process	$\partial\Gamma_1$	$\partial\Gamma_2$	$\partial\Gamma_3$	$\partial\Gamma_4$	$\partial\Gamma_5$	$\partial\Gamma_6$
H	$p = 10\,kPa$	$\mathbf{q}^w \cdot \mathbf{n}_2 = 0$	$\mathbf{q}^w \cdot \mathbf{n}_3 = 0$	$\mathbf{q}^w \cdot \mathbf{n}_4 = 0$	$\mathbf{q}^w \cdot \mathbf{n}_5 = 0$	$\mathbf{q}^w \cdot \mathbf{n}_6 = 0$
M	$\mathbf{u} \cdot \mathbf{n}_1 = 0$	$\mathbf{u} \cdot \mathbf{n}_2 = 0$	$\mathbf{u} \cdot \mathbf{n}_3 = 0$	$\mathbf{u} \cdot \mathbf{n}_4 = 0$	$\mathbf{u} \cdot \mathbf{n}_5 = 0$	$\mathbf{u} = 0$

5.3.4 Results/discussion

The results are documented according to the test case specification document and are shown here as figures in subsequent sections. The following general observations can be made regarding the measured stress evolution

- Both the axial and radial stress sensors of the experiment pick up compressive stresses from the beginning of the experiment. This could be due to the pre-stress loads which could have possibly compacted the sample before the saturation began.
- If the previous assumption regarding the pre-stress loads holds, then a water transfer from the block to the pellets due to the mechanical load at the pellet-block interface could be expected.
- It is not known whether the water exchange process achieved equlibrium before the start of the experiment. Considering that such an exchange would be dominated by capillary forces, it would mean that the system was unlikely to be at equilibrim owing to the longer time scales of capillary-force driven systems. It is also not known whether and how much influence this could have possibly had on the measured stress evolution.
- For the pellet region, there is clearly no indication of the stress evolution typically observed in resaturation experiments in bentonite such as in 1a01 and 1b. Reasons for this behaviour is not clearly apparent from the avilable data either of the experimental setup or of the measurements.

5.3.4.1. *Axial and Radial Stresses*

In this experiment, the axial stress measured at the bottom was different than the axial stress measured at the top. This suggests an additional process providing the reaction force opposing the axial stress evolution in the block region in such a way that the stresses are not transferred to the pellets. Considering that the block was compacted in the experimental cell, friction with the cell wall could have been the process responsiblefor this effect. Although the simulated model substituted friction with a zero-deformation (or no-slip) boundary in the Z direction, the results obtained showed the general trend observed in the experiment, i.e., the model achieved different axial stresses at the top and the bottom of the domain. But the axial stress at the top of the domain was still higher than the axial stress at the bottom. The evolution of stresses are shown in Figure 5-10 and Figure 5-11.

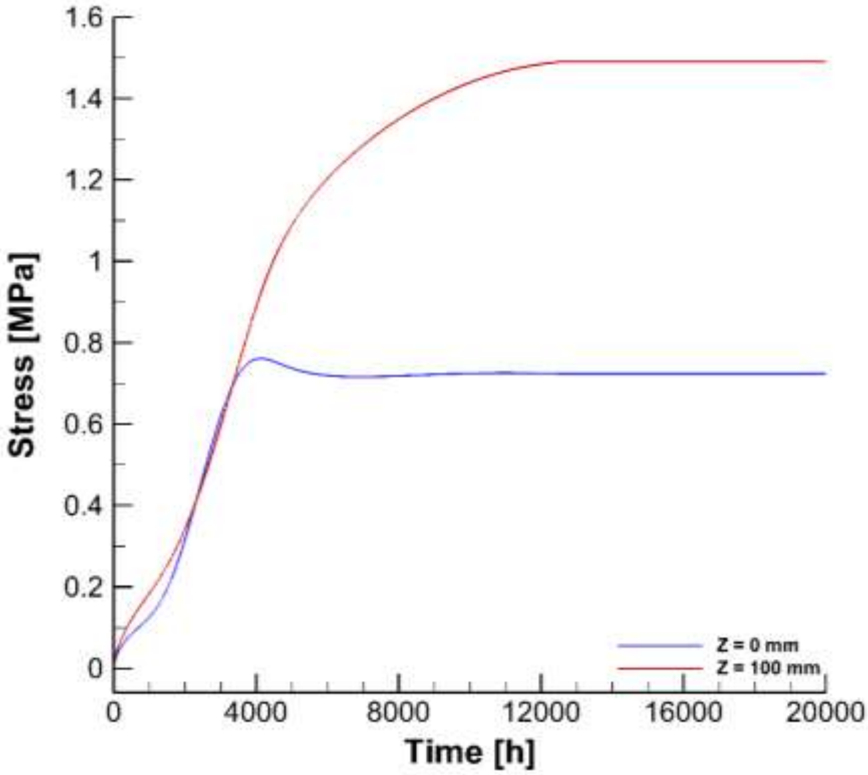

Figure 5-10: Simulated axial stresses at the top and bottom of the domain at R = 50 mm.

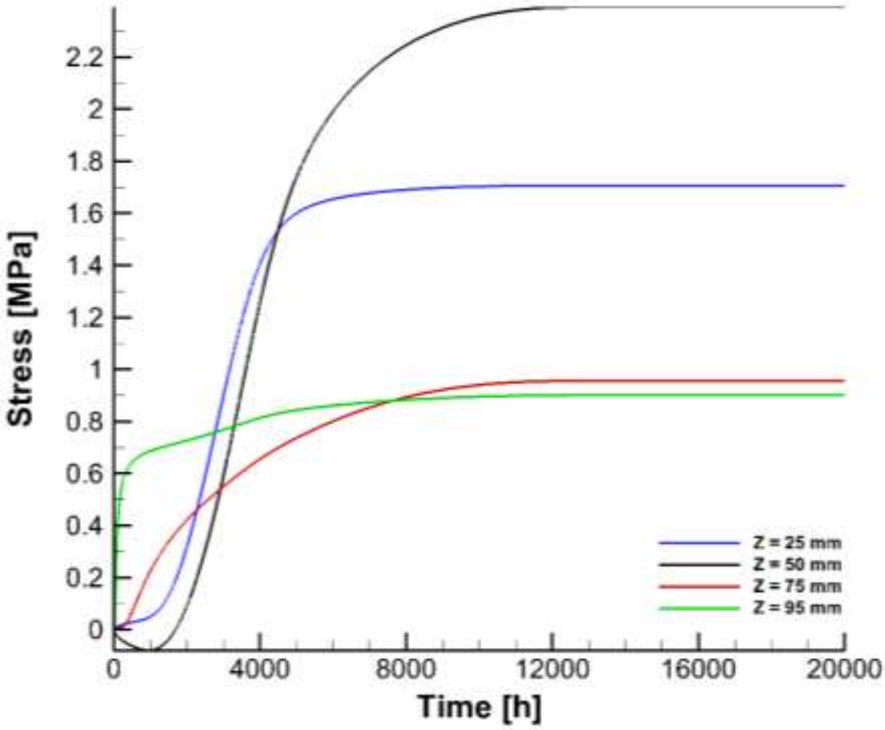

Figure 5-11: Simulated radial stresses at the wall of the experimental cell (R = 100 mm)

5.3.4.2. *Dry Density and Water Content*

The dry density and water content were documented at different levels along the Z axis at two particular points along the R axis. The block undergoes compression initially from the staturation and swelling of the pellet region and hence an increase in dry density in the early time. The block then undergoes a decrease in in dry density as the saturation front advances into the block region. The pellets undergo the same process in reverse chronological order. The pellets first experience a decrease in dry density due to the advancing saturation front and later a drastic increase due to the compression caused by the saturation and swelling of the block. The temporal variation of the water content follows the temporal change in pore-space. However, the measured values are not met by the simulation. The evolution of the dry density and water content are shown in the Figure 5-12 and Figure 5-13.

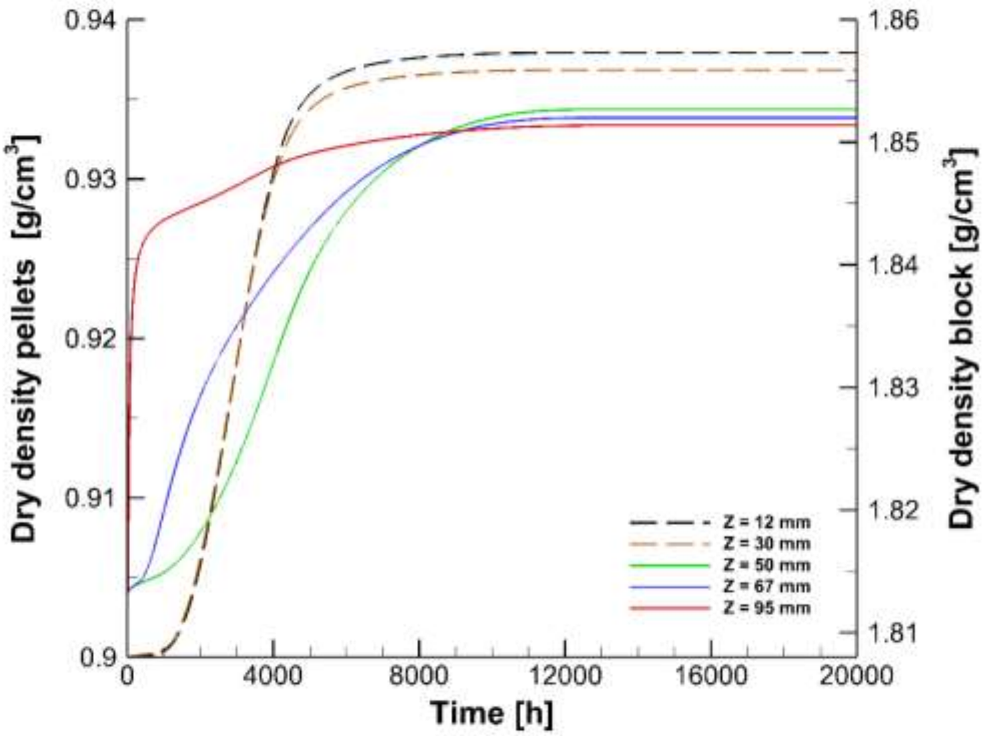

Figure 5-12: Dry density evolution at selected points in the Z direction at R = 50 mm

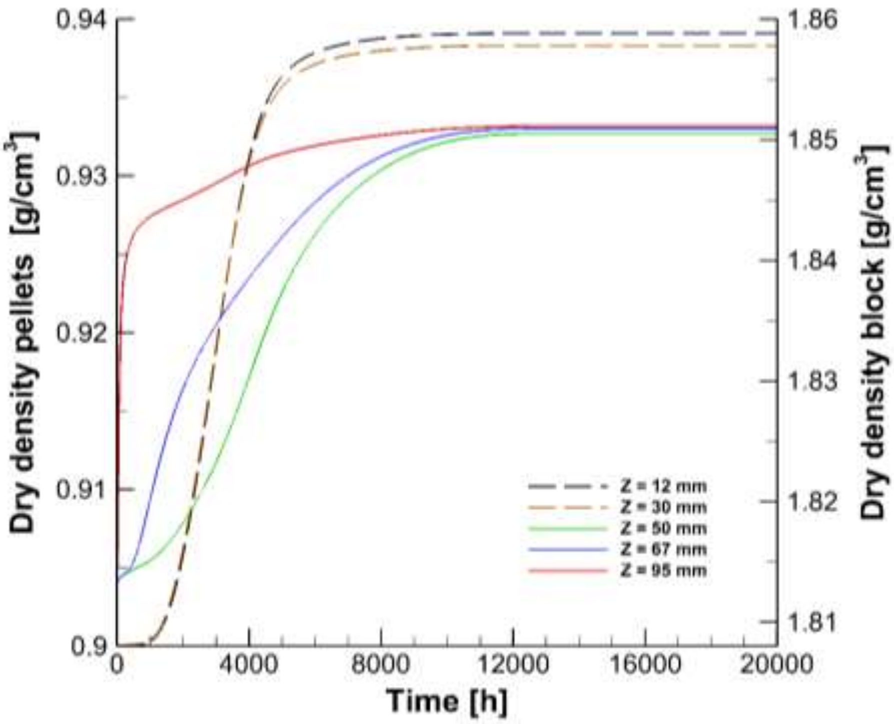

Figure 5-13: Dry density evolution at selected points in the Z direction at R = 90 mm.

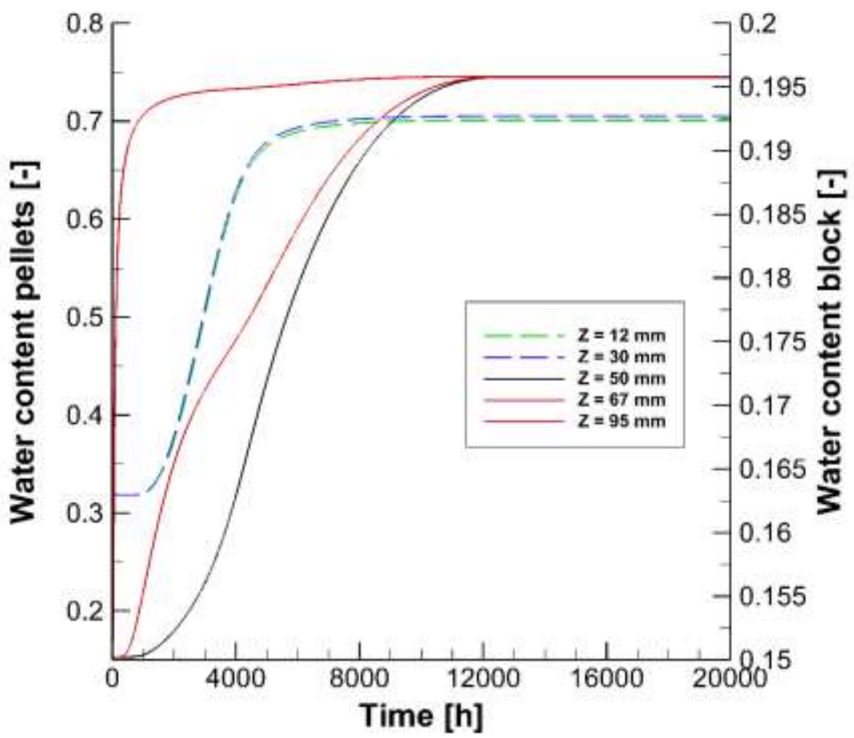

Figure 5-14: Water content evolution at selected points in the Z direction at R = 50 mm.

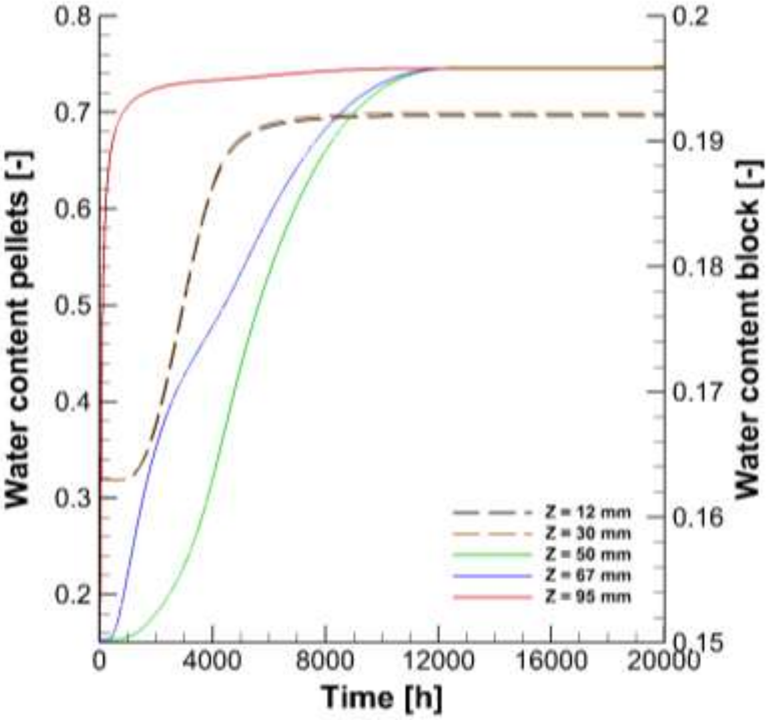

Figure 5-15: Water content evolution at selected points in the Z direction at R = 90 mm.

The changes in dry density and the water content is extremely low compared to the measured values. For the simulation of this experiment several parameter sets were tried in order to find the approximate system behaviour. The choice of paramters however was always made considering the phenomenology of the system, such as, the stiffness of the pellet system compared to that of the block, the HM coupling from to the Biot coefficient, the capillary pressure saturation curves and the swelling pressures. The approximate system behaviour was achieved for a very weak HM coupling. It is to be emphasized that although an effort was made to capture the behaviour of the system, the model was purely elastic and lacked possible additional processes, such as plasticity and wall friction,which could have possibly better described the observed phenomenology. Considering these points, the best fit in a linearly poro-elastic model was achieved for a very weak HM coupling.

In a linearly elastic HM process in such a system, the strains are completely recovered at steady state. The strain at steady state is the strain caused by the pressure of water according to the effective stress principle. This principle is extended to consider the swelling stresses as stated in (2). In the current model, the system was initially free of total stresses. The only non-recoverable contribution to the stresses is that from the swelling pressure. The changes in porosity and permeability are direct or implicit functions of the volumetric strains which are inturn controlled by the deformations from the HM coupling and the evolution of swelling pressure. These contributions are very small due to the following reasons.

- The HM coupling was chosen to be very weak.
- The swelling pressure development in the pellets is taken up by the large initial porosity.
- The swelling pressure development in the block is very weak since the block is already at 80% saturation initially.

Therefore the claculated dry density and water content show very weak variation in comparison to the measured data. The temporal evolution of these quantities, however, fits the phenomenologically expected behaviour of the system.

5.4 ClayTech

Test 1c is described as an unsaturated 1D axial homogenisation problem, *with* wall friction. The problem was simplified by representing the pellets filling as water saturated throughout the calculation.

5.4.1 Geometry and discretization

The total length of the geometry and the radius was set to 0.1 m and 0.05 m, respectively.

The geometry was discretized in 20 elements, thereby making the initial length of each element 5 mm. The 10 elements most closely located to the hydraulic boundary (element no 0 to 9) were assigned properties corresponding to pellets, while the other 10 elements (no 10 to 19) were assigned properties corresponding to the compacted block.

The time increment was 3600 seconds.

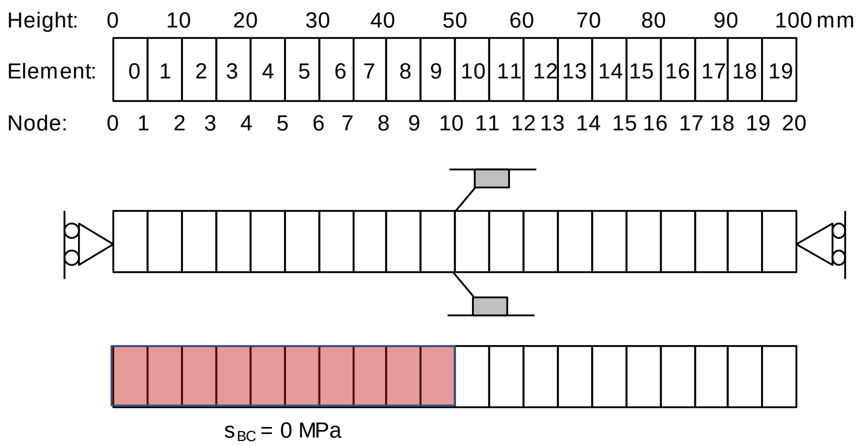

Figure 5-16 Model geometry and discretization (upper). Boundary conditions: mechanical (middle) and hydraulic (lower)

5.4.2 Material parameters

The material parameter values used were generally the same as for the test 1b case except for friction and the hydraulic conductivity.

The friction angle was set to φ=7°. This value is generally consistent with independent measurements (e.g. Dueck et al. 2014). The shear module describing the elastic part was set to K_s=500 MPa/m by simple testing.

The hydraulic conductivity was adopted from Åkesson et al. (2010) and calibrated in the same way as for saturated conditions:

$$K(e, S_l) = {S_l}^3 \cdot 1.2 \cdot 10^{-13} e^{5.33} \; [m/s] \tag{5-1}$$

No representation of vapor diffusion was included in this model.

5.4.3 Initial and boundary conditions

The initial conditions were based on the initial dry densities, which for the block and pellets was 1808 and 904 kg/m^3, respectively, and corresponding void ratio were based on a particle density of 2780 kg/m^3 (Table 5-5). In addition, the initial water content in the blocks was 16.3 %, whereas the pellets were assumed to be water saturated from the beginning with zero suction, from which followed that the initial water content was 74.5 %. The initial path variable (both axial and radial) was set low (-0.9), which together with the clay potential function meant that the initial swelling pressure for the pellets was 0.057 MPa. The block was assumed to have the same initial stress level, which meant than initial suction for this material was 22.3 MPa.

The overall mechanical boundary condition for the bentonite was that the total axial strain was equal to zero. The suction value in the pellets-material was kept equal to zero throughout the calculation.

Table 5-5 Initial material properties and initial conditions

Material	Void ratio (-)	Water content (%)	Path variables (-)	Stresses (MPa)	Suction (MPa)
Pellets	2.075	74.5	-0.9	0.057	0
Blocks	0.538	16.3	-0.9	0.057	22.3

5.4.4 Results/discussion

A comparison of modelled and experimental stresses is shown in Figure 5-17. This shows that the modelled stresses were generally overestimated, although the timescale of the build-up of stresses and the radial stress in the top end were quite accurate. As expected, the model resulted in a noticeable difference between the axial stresses at the top and the bottom.
The final distributions of axial and radial stresses are shown in Figure 5-18 (left). This illustrates the profile of axial stresses along the specimen, which was caused by the wall friction. It also shows that the radial stresses exceeded the axial stresses in the lower part, which was in agreement with the experimental data, and that the radial stresses were lower than the axial in the upper part, which however was contrasted by the apparent isotropic conditions in the experiment.

The overall mechanism of the model is illustrated in Figure 5-18 (right). This shows stress paths in the axial Ψ-e_m plane for the elements at the two ends of the geometry (no. 0 and 19). Both stress paths were found within the allowed span of the clay potential. In the lower end, it decreased from the initial suction value down to the final axial stress, in the upper end it increased from the initial swelling pressure up to the final axial stress. The final difference between these points were caused by the wall friction.

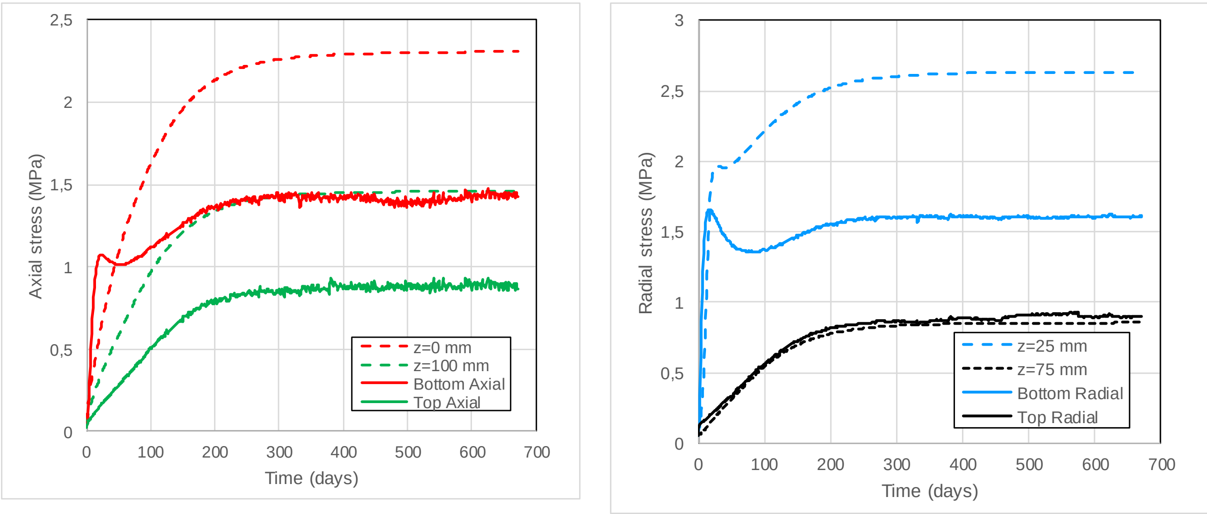

Figure 5-17 Evolution of axial stresses (left) and radial stresses (right).

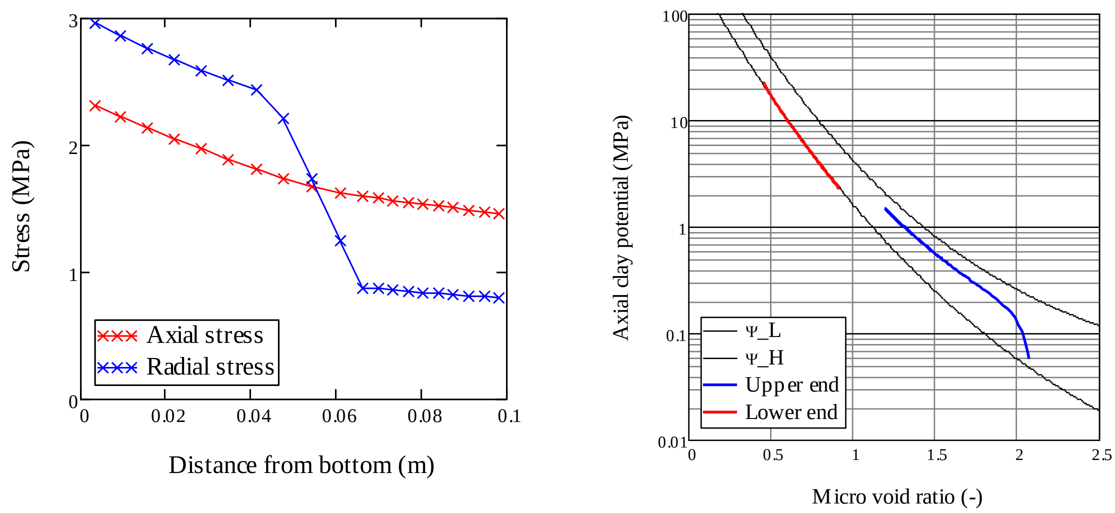

Figure 5-18 Final stress distribution (left), stress paths (right).

Modelled profiles of dry density and water content at different times are shown in Figure 5-19 together with experimental data. The final profiles were in quite good agreement with the experimental data, although it can be noted that the overall dry density level was slightly overestimated. To some extent this was caused by the simplification of initially dividing the geometry in two parts with equal length, but according to the task description (see Tab 5-3) there was also a minor discrepancy between the initial and determined dry density.

The discrepancy between the modelled and measured stresses is further illustrated in Figure 5-20. This shows a compilation of final stress states (pressure versus dry density) for the different test cases analysed within Task 1. Each state is marked as an interval between two points defined for the highest stress and dry density, and correspondingly the lowest stress and dry density. In addition, the upper and lower lines for the clay potential function used in this task are shown for comparison. It can clearly be seen that the final stress states for test 1a01, 1a02 and 1b are generally found within the interval described by the clay function. The data for test 1c on the other hand are to a large extent found outside and below this interval. The reason for this discrepancy is not known.

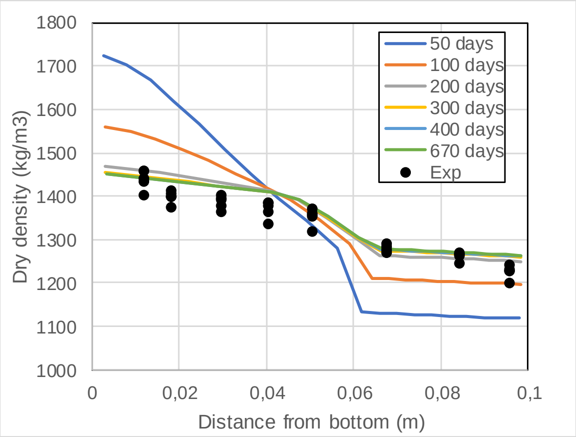

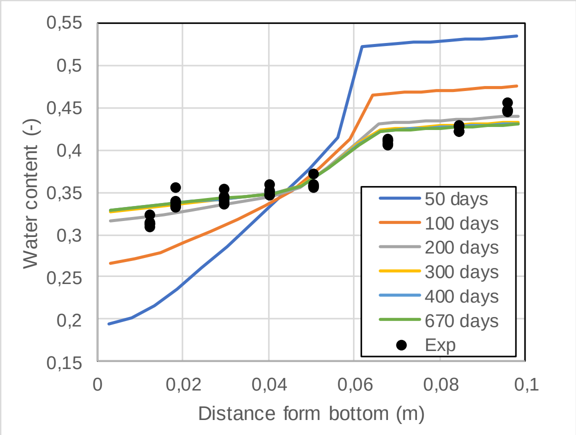

Figure 5-19 Distributions of dry density (left) and water content (right).

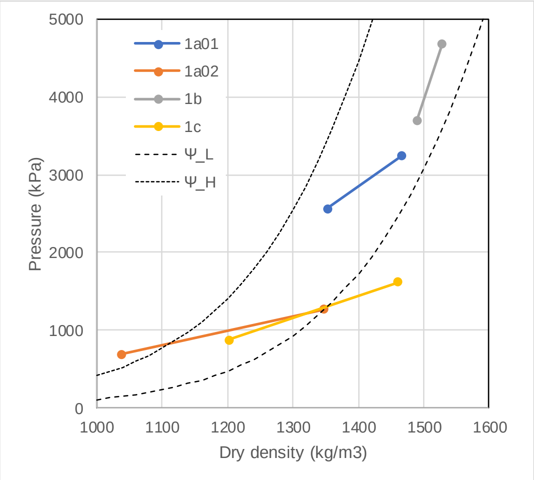

Figure 5-20 Final stress states for the different test cases in Task 1.

5.5 EPFL

5.5.1 Geometry and discretization

The model geometry consists of a 2D axisymmetric domain of 100x50 mm. The volume of pellet material and block material is considered to be the same, with the division at z = 50mm. Both materials are idealised as an equivalent continuum. In line with the previous models, the geometry consists of 100 elements, which therefore have a size of 10x5 mm and should verify the REV scale once the material is saturated and homogeneous. A sketch of the finite element model is shown in Figure 5-21.

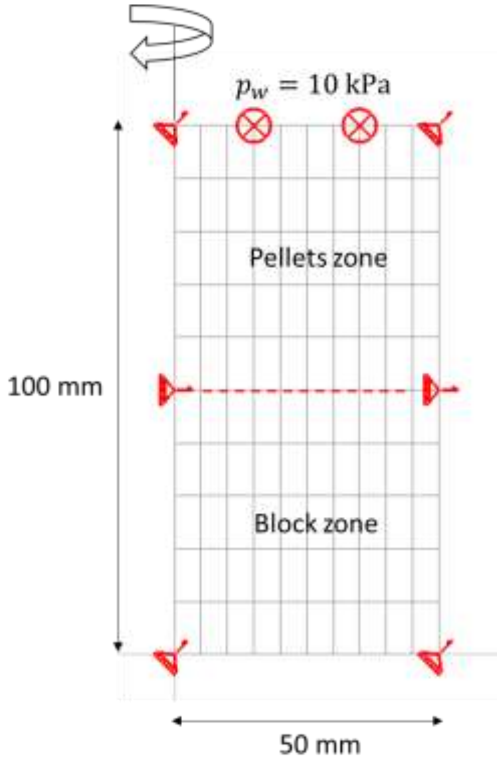

Figure 5-21 Model geometry, discretization and boundary conditions of the test 1c.

5.5.2 Input parameters

The parameters of the bentonite block zone have been defined according to the test 1a. Since there is no characterization of the pellet material (e.g. oedometric tests, water retention curve), the parameters have been adjusted to give reasonable results in the simulation of the swelling pressure measured during the test. These are summarized in Table 5-6 and Table 5-7.

Table 5-6 ACMEG Model parameters for the bentonite pellets zone

Elastic parameters		
K_{ref} , G_{ref} , n^e	[MPa], [MPa], [-], [°C^{-1}]	15, 7.5, 1,
Isotropic plastic parameters		
β_m , γ_s , r^e_{iso} , p'_c , Ω	[-], [-], [-], [-], [-], [MPa] , [-]	5; 2.8; 0.01; 0.55; 0
Deviatoric plastic parameters		
b , d , M , g , α , a , r^e_{dev}	[-], [-], [-], [-], [-], [-], [-]	0.5, 2.0, 1.0, 0, 1, 0.001, 1
Water retention parameters		
s_{e0} , β_h , θ_T , θ_e , S_{hys}	[MPa], [-], [-], [-], [-]	0.1, 7.5, 0, 0, 1
Water flow parameters		
k_{f0}, C_{KW1}, C_{KW2}, M, N	[m^2], [-], [-], [-], [-]	10^{-19}, 2.9, 2.9, 5.3, 5.5

Table 5-7 ACMEG and water flow model parameters for the bentonite block zone

Elastic parameters		
K_{ref} , G_{ref} , n^e ,	[MPa], [MPa], [-], [°C^{-1}]	15, 7.5, 1
Isotropic plastic parameters		
β_m , γ_s , r^e_{iso} , p'_c , Ω	[-], [-], [-], [-], [-], [MPa], [-]	5; 23; 0.01; 1.45; 0
Deviatoric plastic parameters		
b , d , M , g , α , a , r^e_{dev}	[-], [-], [-], [-], [-], [-], [-]	0.5, 2.0, 1.0, 0, 1, 0.001, 1
Water retention parameters		
s_{e0} , β_h , θ_T , θ_e , S_{hys}	[MPa], [-], [-], [-], [-]	10, 9, 0, 0, 1
Water flow parameters		
k_{f0}, C_{KW1}, C_{KW2}, M, N	[m^2], [-], [-], [-], [-]	10^{-20}, 2.9, 2.9, 5.3, 5.5

5.5.3 Initial and boundary conditions

While there is evidence that indicates that the lateral friction between the bentonite material and the apparatus was significant (high differences in axial swelling pressure between the top and the bottom measurements), at this stage no attempt was made to simulate this effect.

Water pressure is fixed at 10 kPa at the upper boundary. Vertical displacements are fixed in the horizontal lines delimiting the domain whereas horizontal displacements are fixed for the lines delimiting the vertical domain. An initial water content of 16.3% and 15.3% was reported for the block and pellets, respectively. According to the MX-80 WRC data shown in Figure 1, this corresponds to an initial suction of around 65 MPa, which is set as negative water pressure of 65 MPa in the entire domain (block and pellets). The initial effective stress is, as for tests 1a and 1b, set according to the initial degree of saturation and suction, whose values are given by the water retention curve.

5.5.4 Results/discussion

The swelling pressure results obtained for the 1c model are shown in Figure 5-22 (Radial stresses) and Figure 5-23 (Axial stresses). In the same figures, the experimental results are also shown for comparison purposes.

The model does not perform well for this case. There are several causes for this:

i) The initial dry density of the blocks zone implies a very high degree of saturation which in turns involves a high value of initial effective stress (45 MPa). The yield surface (loading collapse curve) cannot adapt this value while having reasonable values of initial increase in swelling pressure.
ii) The fabric of the pellets is initially bimodal, and it can be expected a significant difference between the pore size of the micro structure and the pore size of the macro structure. A possible interpretation of the homogenisation process could be as follows. Initially, water flow mainly occurs through the macro structure, allowing to reach the block zone while the pellets (micro structure) have not been fully hydrated themselves. Hence, the block starts to swell towards the pellets zone producing compression of the pellets. The model cannot predict block hydration before the pellets are hydrated, resulting in a confinement of the block and the development of significant swelling pressure especially at the beginning of the simulation.
iii) In the current version of our model, the final value of swelling pressure is very much related to the preconsolidation pressure of each material. However, a low value of preconsolidation pressure, that would be needed to predict a lower swelling pressure, would result in an excessive and sharp decrease of effective stress and hence, unrealistic collapse. This is because of the loading collapse curve formulation, which was initially developed with low activity clays in mind, and does not offer a proper flexibility to adapt to large variations in suctions.

With the above considerations in mind, and because no additional information such as the water retention curve or oedometric tests, the philosophy for parameter estimation has been to keep the elastoplastic parameters as similar as possible to tests 1a (block zone) and test 1b (for the pellets zone). This allows to better define the scope of improvement of the model for such complex cases.

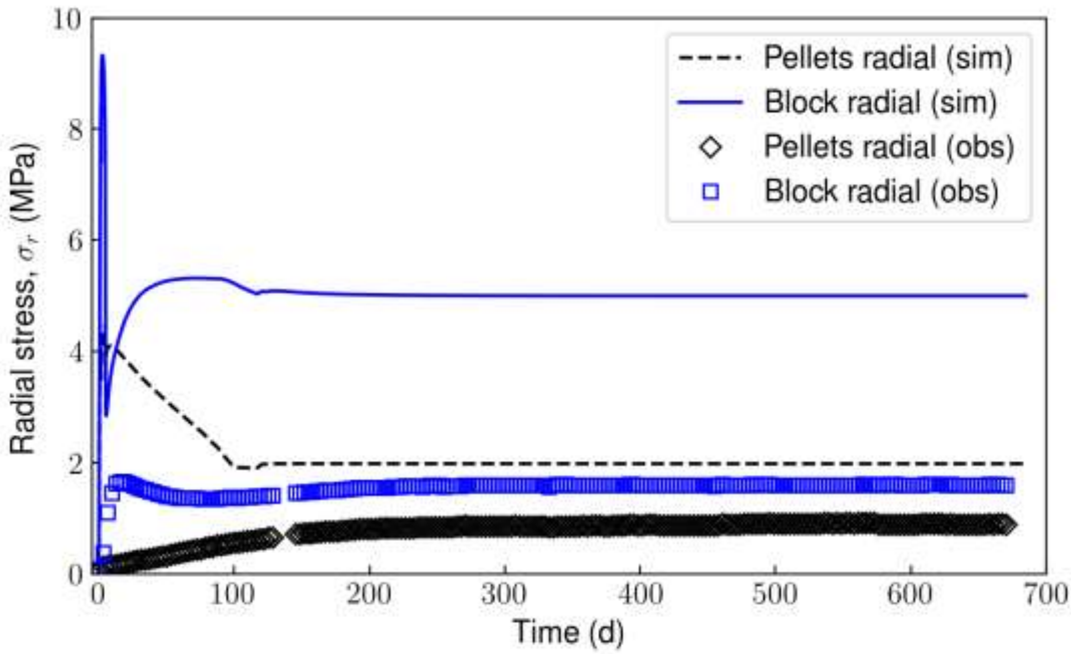

Figure 5-22 ***Radial swelling pressure simulated for the test 1c (sim) compared to the experimental data (obs).***

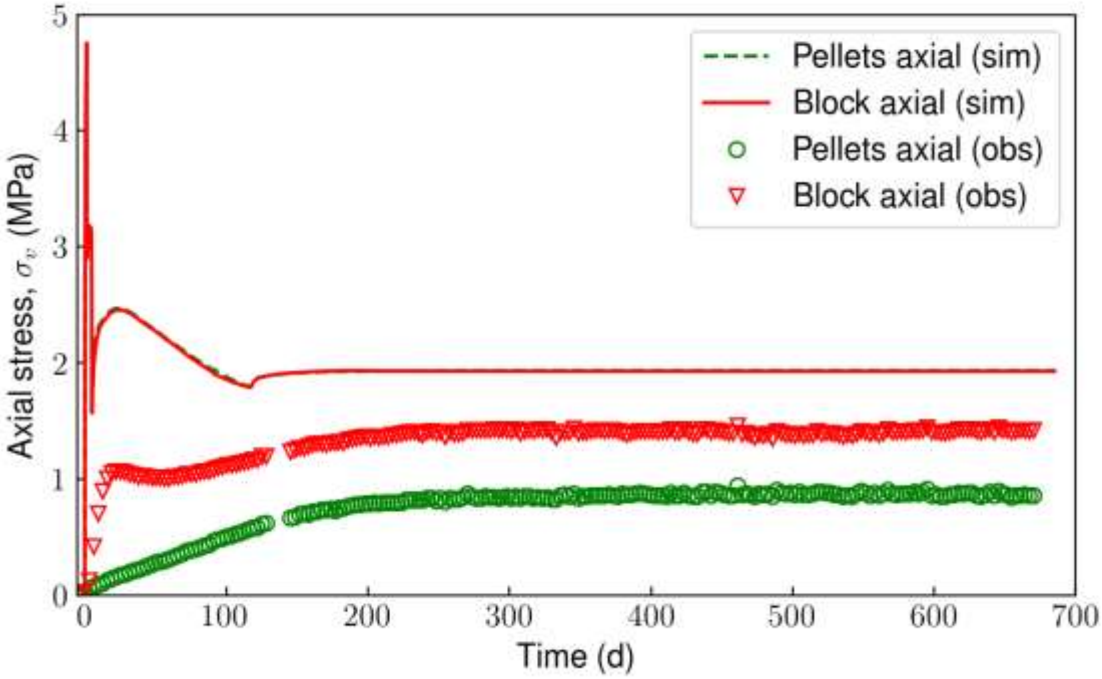

Figure 5-23 Axial swelling pressure simulated for the test 1c (sim) compared to the experimental data (obs).

The final dry density that is predicted by the model is shown in Figure 5-24. While the dry density of the pellets increased and the one of the block decreased, the results of the simulations predict a much lower degree of homogenisation than that observed from the dismantling of the test.

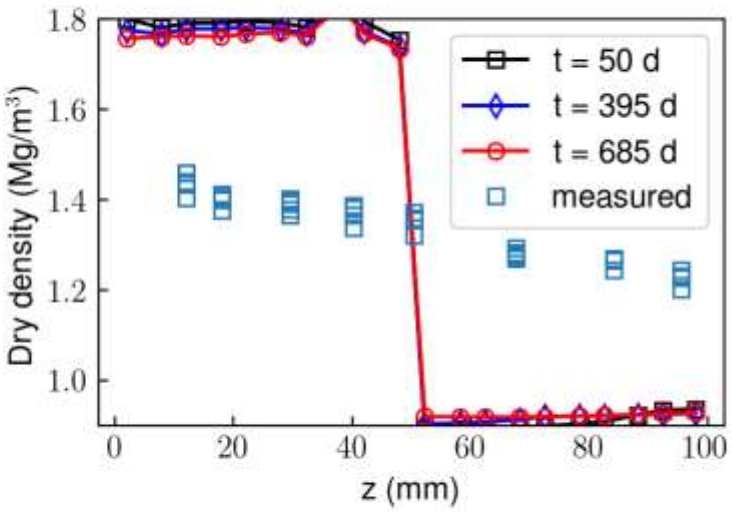

Figure 5-24 Predicted distribution of dry density at different time steps (t = 685 days corresponds to the end of the simulation) compared to the dismantling data.

5.6 LEI

5.6.1 Geometry and discretization

Test was performed in a constant-volume cell with a 100 mm diameter and a height of 100 mm. Initial block height was 48.5 mm and initial height of pellet zone was 51.5 mm. The modelling has been done under axisymmetric conditions and analysed domain was discretized into 3947 triangular grid elements as it could be seen in Figure 5-25. Pellets of high density with surrounding air were modelled as equivalent porous media. Final block height was 63.7 mm and final height of pellet zone was 37.4 mm.

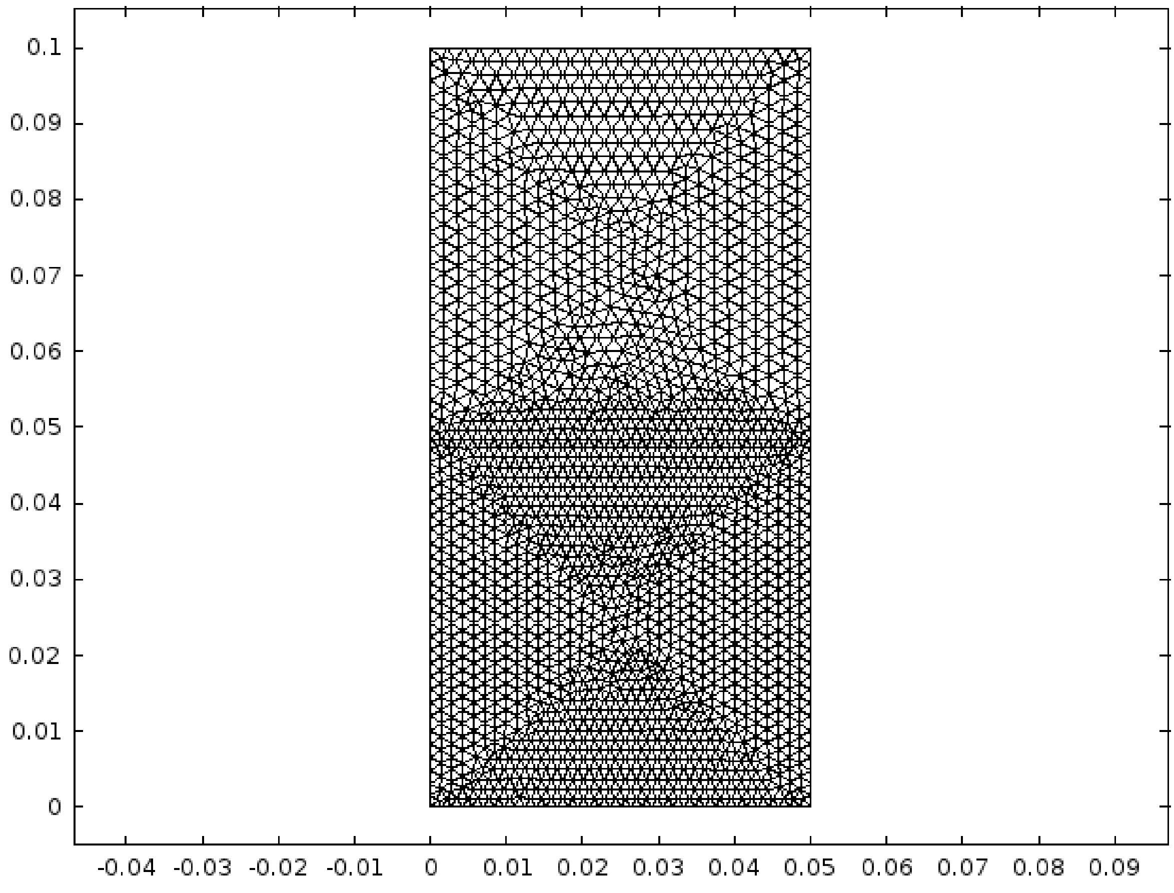

Figure 5-25. Computational grid of COMSOL Multiphysics model

5.6.2 Input parameters

The input parameters used for "Test 1c" modelling are summarized in Table *5-8*. Considering the overall dry density of pellet zone, it was assumed that wetting pellets will swell into the void space around pellets, but there will be no overall swelling induced stress of a pellet zone as a whole. The pellet zone was assumed to be weaker from mechanical point of view as the interface of block and pellet zone was expected to be moved into the pellet zone (considering the final heights of zones).

Table 5-8. Initial characteristics of materials used in the experiment

Parameter	Block zone	Pellet zone
Dry density, kg/m^3	1808*	904*
Porosity, -	0.35	0.675
Void ratio, -	0.53	2.075
Initial water content, %	16.3*	15.3*
Initial saturation , -	0.83*	0.21*
Hydraulic conductivity, m/s	$K(e) = K_0 \left(\frac{e}{e_0}\right)^{\eta}$, K_0 =2.4·10^{-13}, e$_0$=1 $\eta = 5.3$	$K(e) = K_0 \left(\frac{e}{e_0}\right)^{\eta}$, K_0 =2.4·10^{-13}, e$_0$=1 $\eta = 5.3$
Relative permeability	van Genuchten	$k_{rel} = 1$
Water retention	$P_{entry}(e) = 2 \cdot \Psi(e)$,** $\Psi = 19.14\ MPa$, m=0.38,	$P_{entry}(e) = 2 \cdot \Psi(e)$,** $\Psi = 0.01\ MPa$, m=0.2705,
Young modulus, MPa	5	2
Poisson ration	0.4	0.4
Swelling coefficient	no swelling assumed	$d\varepsilon_{sw} = \beta_{sw} dS_w$, β_{sw} =0.95

* - data from specification (Beacon D5.1.1, 2018).

** - Ψ - total suction at saturation. Ψ taken from in (Seiphoori et al., 2014) for MX-80 granular bentonite as a function of void ratio $\Psi(e) = 248.21 \cdot exp(-4.78 \cdot e)$.

5.6.3 Initial and boundary conditions

For the modelling initial and boundary conditions were set as follows:

- Initial conditions were set in terms of pressure head (Hp=-2659 m and Hp=-204 m) to match initial saturation of S_w=0.83 and S_w=0.2 for block zone and pellet zone, respectively.

- Constant pressure of 10 kPa was applied on model top boundary.
- For the bottom and side boundaries of the model domain no flow conditions were set.
- Prescribed (zero) displacement condition in r direction were set for side boundary of model domain.
- Prescribed (zero) displacement condition in z direction were set to the top and bottom boundary.

5.6.4 Results/discussion

Preliminary modelling results on swelling pressure and experimental measurement data are presented in Figure 5-26. Radial stresses were measured at the midpoints of the block and pellet zones, 25 and 75 mm.

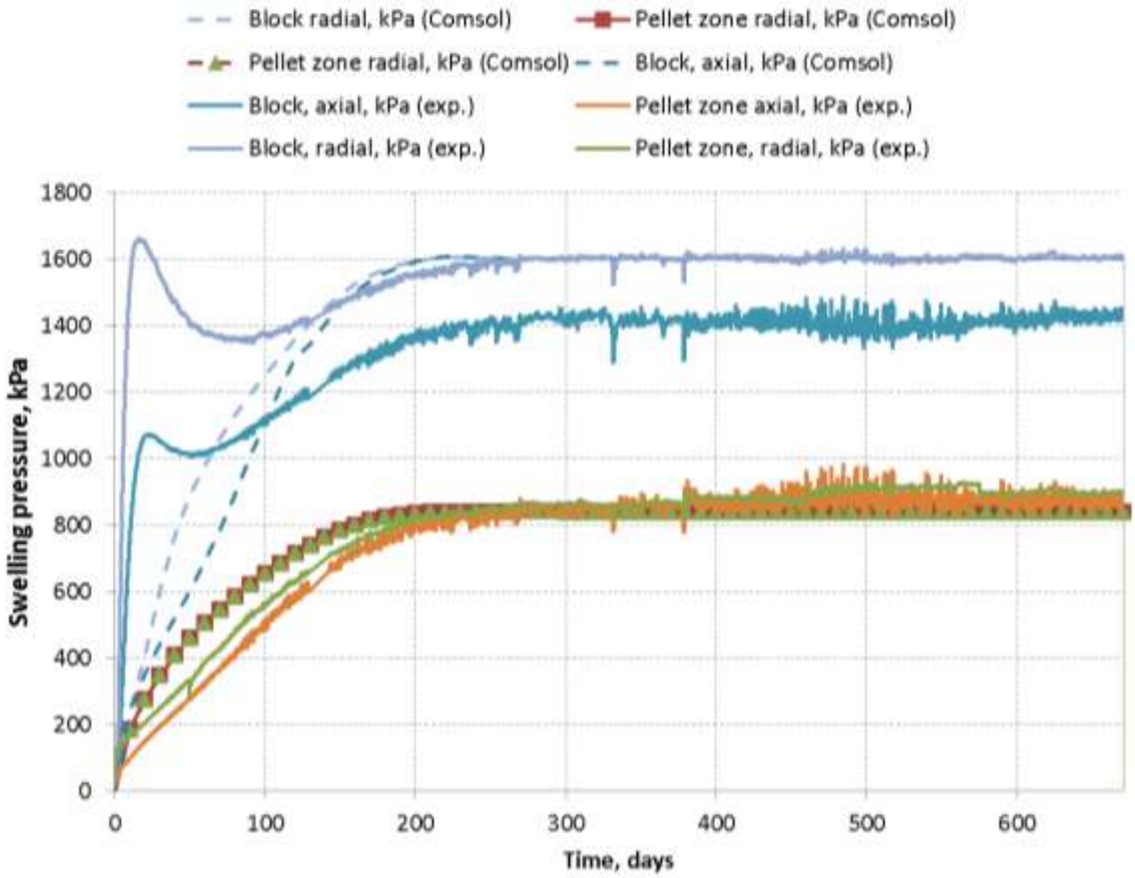

Figure 5-26. Axial and radial swelling pressures (modelling results and experimental measurements)

As it could be seen in figure the modelled block stresses (radial and axial) were of similar trend while measured block radial stress was higher than the axial stress. Modelled swelling pressure of bentonite block zone was in agreement with measured radial stress in the longer time. Measured peak in the short term (during first 50 days) were not captured with current model formulation. Preliminary modelling results on pellet zone response were in agreement with measurements.

Distribution of modelled displacements for “Test 1c” is presented in Figure 5-27. As it could be seen, the zero displacements occurred at the top and bottom part of specimen. The largest displacements were estimated to be around interface between bentonite block and pellet zone.

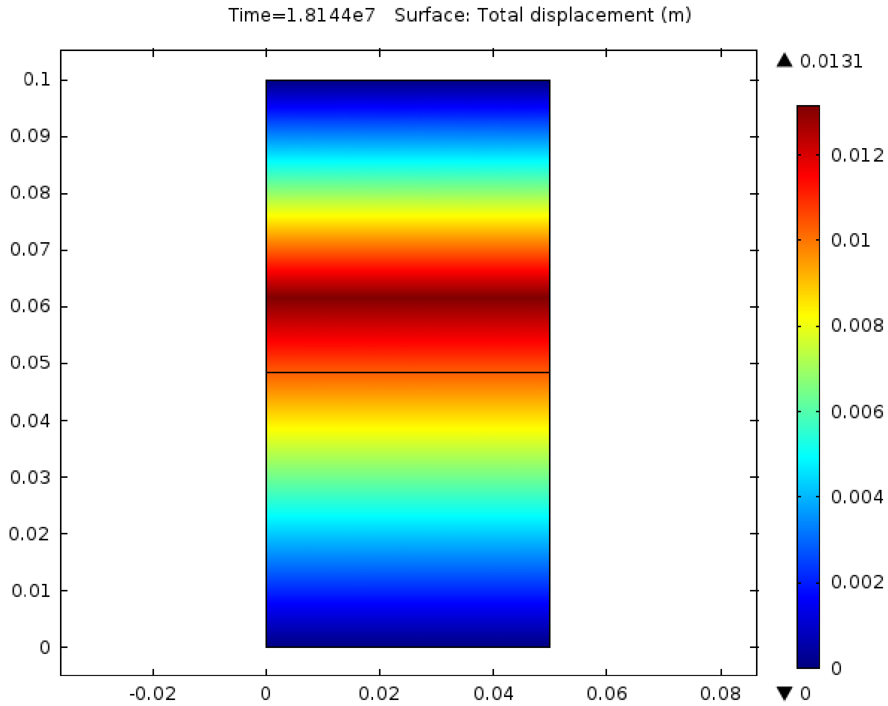

Figure 5-27. Distribution of modelled displacements for “Test 1c”

5.7 Quintessa

5.7.1 Geometry and discretization

As with the previous models, a 2D cylindrical grid is used to represent the bentonite. Due to the boundary conditions used, there is radial as well as axial dependence in the bentonite behaviour.

The bentonite has height 100 mm and radius 100 mm. This is discretised into 25 axial and 5 radial compartments as shown in Figure 5-28.

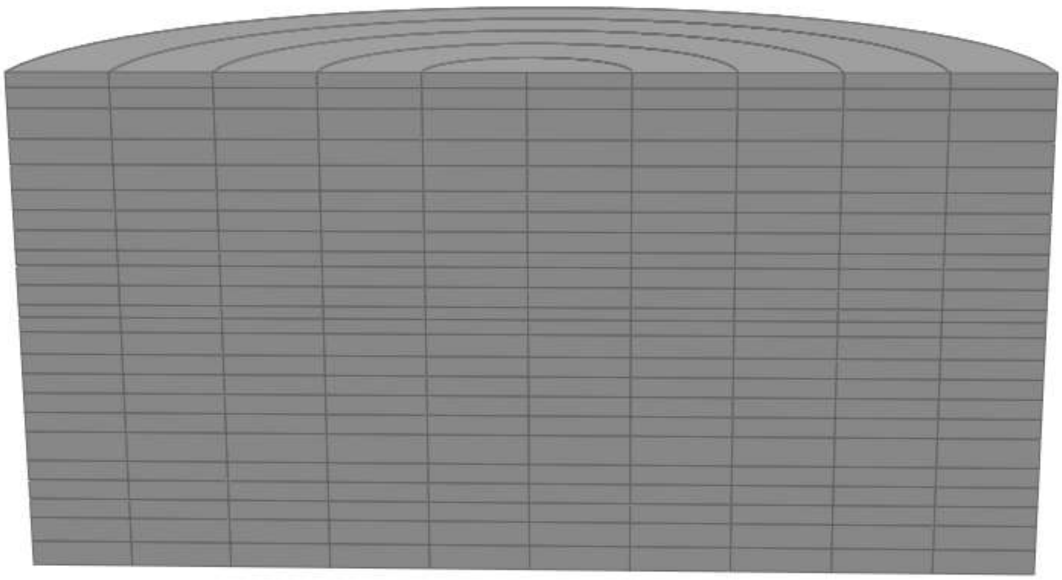

Figure 5-28 ***Discretisation of bentonite in the 1c QPAC model.***

5.7.2 Input parameters

The input parameters are unchanged from those presented in Table 3-16.

From the data, there are signs that friction is a key process in the experiment – for example, different axial stress throughout the height of the sample. An additional coefficient of friction parameter (μ) was therefore required for this model. This was calibrated using axial stress data from the experiment, which resulted in a coefficient of friction of approximately 0.36 (or, equivalently, a friction angle of 20°).

5.7.3 Initial and boundary conditions

The initial conditions prescribed for the model consist of initial dry density, initial water content and initial stresses. In the model, these are defined separately for the bottom half of the grid (corresponding to the bentonite block) and the top half of the grid (corresponding to the bentonite pellets).

The pellets are treated as a bulk material with an averaged dry density which accounts for void space between the pellets.

Table 5-9 Initial conditions used in the 1c model.

Initial Condition	Bentonite Block	Bentonite Pellets
Initial dry density [kg/m^3]	1808	904
Initial water content [wt%]	16.3	15.3
Initial stress (r, θ, z) [MPa]	0, 0, 0	0, 0, 0

The top and bottom boundaries are both roller boundaries. The top boundary has a no flow condition. The bottom boundary has a constant water pressure of 0.11 MPa, i.e. 10 kPa above atmospheric pressure.

The outer boundary has a no flow condition. A friction condition is applied to constrain the displacement along the boundary. For simplicity, a linear coefficient of friction is used (dependence on bentonite saturation, for example, is not considered).

5.7.4 Results/discussion

The evolution of total axial and radial stress in the bentonite is shown in Figure 5-29 and Figure 5-30 respectively.

The inclusion of friction is key for calculating different axial stresses in the top pellets region and bottom block region of the bentonite. This also causes radial variation in stresses, so results are presented at the centre and outer regions of the bentonite.

As with previous models, the equilibrium stresses are predicted more successfully than the transient stress behaviour, but the key behaviour is captured. In the block region, the model predicts high initial axial and radial stress peaks which are not as prominent in the data. This is similar to the behaviour of the 1a02 model.

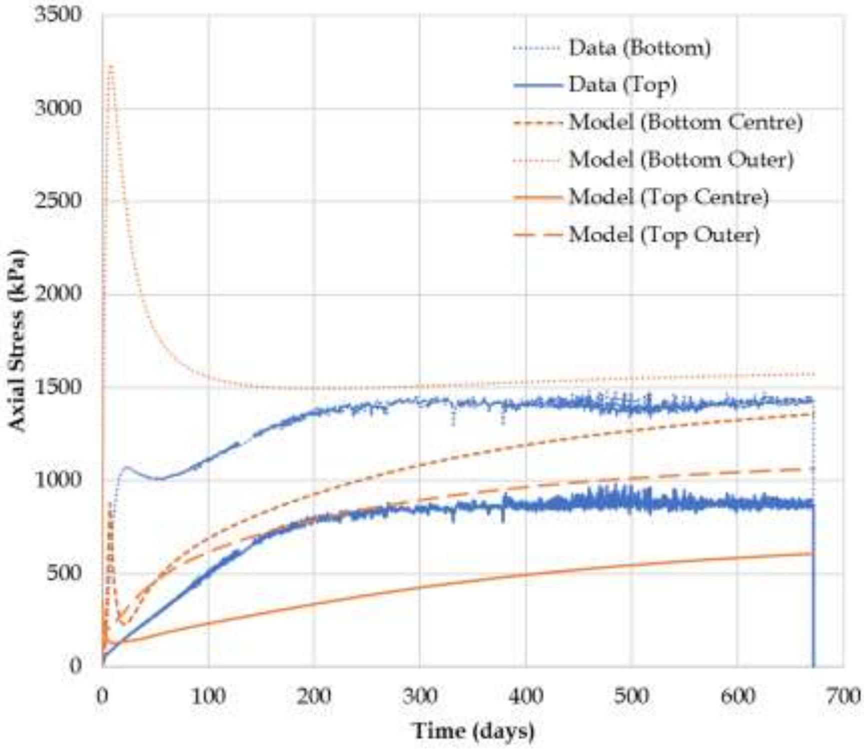

Figure 5-29: Total axial stress evolution through time in the 1c experiment, compared with modelled results.

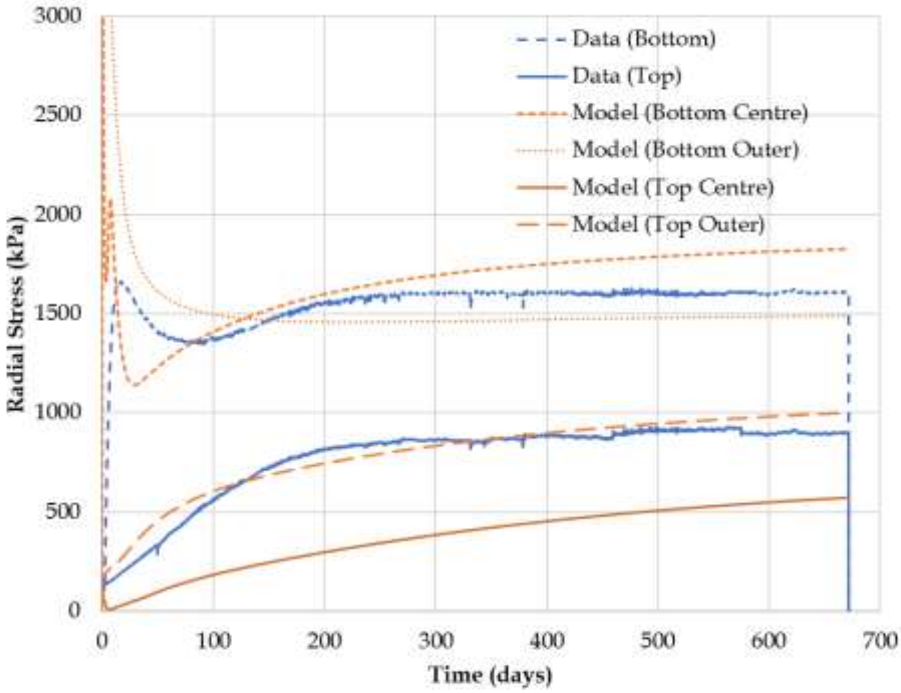

Figure 5-30: Total radial stress evolution through time in the 1c experiment, compared with modelled results.

Profiles of the final void ratio and water content against height are shown in Figure 5-31 and Figure 5-32.

The experimental data shows slight differences between measurements at the North, East, South and West of the bentonite sample due to some azimuthal heterogeneity. Some radial dependence of the void ratio and water content profiles can be seen in the model and experimental data. Results presented here are for the centre of the bentonite.

Void ratio results without friction are presented for comparison. The inclusion of friction in the model can be seen to make a significant difference to the bentonite behaviour. Without friction, the bentonite block swells and easily compresses the pellets, leading to a low dry density at the bottom of the sample and a flat profile in the pellet region. With friction, the model appears to behave more like the experiment, with a more continuously decreasing dry density profile with height.

Water saturation reaches a maximum of approximately 1.05 in the model.

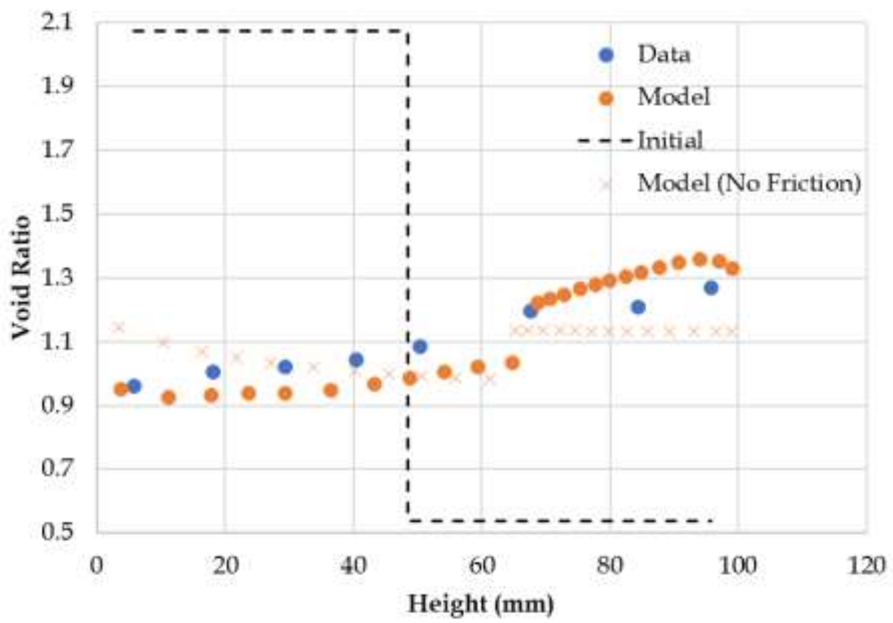

***Figure 5-31** Profile of the final bentonite void ratio at different heights within the sample, for the 1c experiment.*

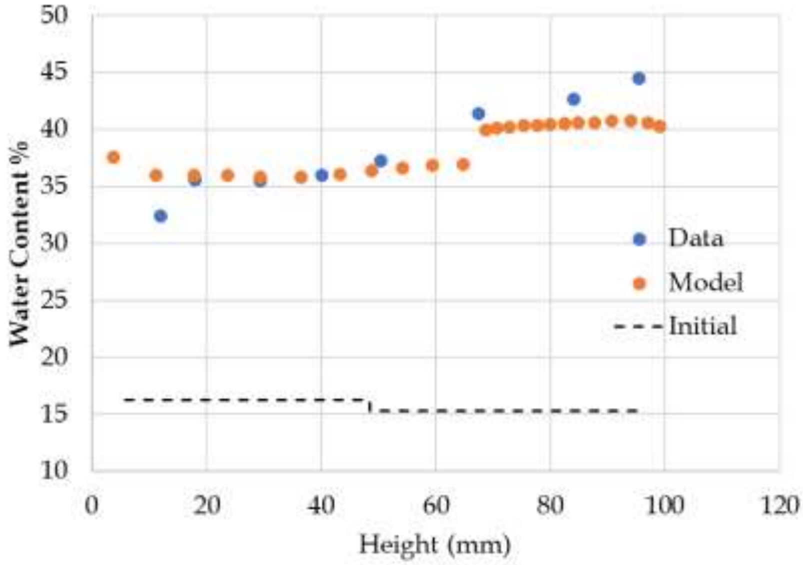

Figure 5-32 Profile of the final water content at difference heights within the sample, for the 1c experiment.

5.8 ULG

5.8.1 Geometry and discretization

The numerical bentonite sample consists in 200 eight-noded isoparametric elements. The problem is assumed bidimensional.

5.8.2 Input parameters

5.8.2.1. *Parameters for bentonite pellets layer*

The available data for this density of MX-80 bentonite pellets mixture are very few. The permeability evolution process in bentonite pellet mixture involves a number of complex phenomena. As a result of the very large pores of the assembly, its initial permeability turns out to be very high.
Therefore, the inter-pellets porosity represents a preferential pathway for hydration for the bottom block and the pellets themselves.
Considering the pellets-layer, as the test begins, it is assumed that the inter-pellets porosity is very quickly saturated.
In these conditions, considering the very low density, the pellets are able to be hydrated and by hydration they swell in a quasi-free swelling condition increasing their permeability.
As a consequence, the inter-pellets porosity volume decreases, but the overall permeability of the assembly remains high.
To the authors knowledge, at the present state, a model which takes into account all these strictly coupled phenomena does not exist, therefore, a constant permeability is selected as a first approximation and the pellets-layer is considered saturated since the beginning of the test.

The unsaturated material considered for WP5_b is MX-80 bentonite pellet-powder mixture (70/30 proportion) compacted to a dry density equal to 1.52 Mg/m^3.
The mechanical input parameters (see Table 5-10) were calibrated on experimental data provided by (Molinero, et al., 2019).
The characterisation was performed via suction controlled oedometer tests carried out for the compressibility investigation [Figure 5-33]. Both constant-volume and swell-consolidation methods were applied for the swelling pressure determination. The vapor equilibrium technique was used for suction control.

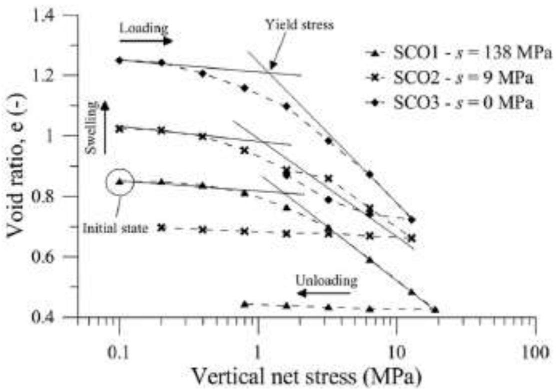

Figure 5-33 oedometer tests on MX80 pellet and powder mixture compacted to a dry density of 1.49 Mg/m³ (Molinero Guerra, Experimental and numerical characterizations of the hydro-mechanical behavior of a heterogeneous material : pellet/powder bentonite mixture, 2019)

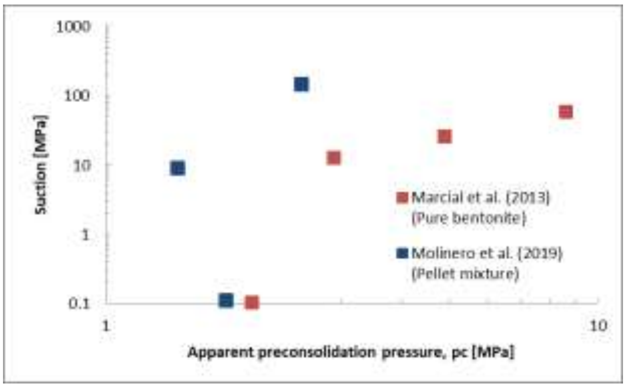

Figure 5-34 Yield stress versus suction for compacted bentonite with initial void ratio of 0.559 (Marcial, 2003), and pellet/powder mixture with initial void ratio of 0.859 (Molinero Guerra, Experimental and numerical characterizations of the hydro-mechanical behavior of a heterogeneous material : pellet/powder bentonite mixture, 2019)

It can be noticed that the pellet mixture apparent preconsolidation pressure is less sensitive to suction with respect to pure bentonite compacted block [Figure 5-34].
In Table 3-1, the selected mechanical parameters are presented and their functions are depicted in ***Figure 5-35*** and Figure 5-36 [Equations 2.19 and 2.20].

Table 5-10 Selected mechanical parameters for WP5_b

λ(0)	r	ω	p0*	pc	κ	κs
[-]	[-]	[-]	[MPa]	[MPa]	[-]	[-]
0.2	0.75	1.00E-07	1.86	0.93	0.06	0.07

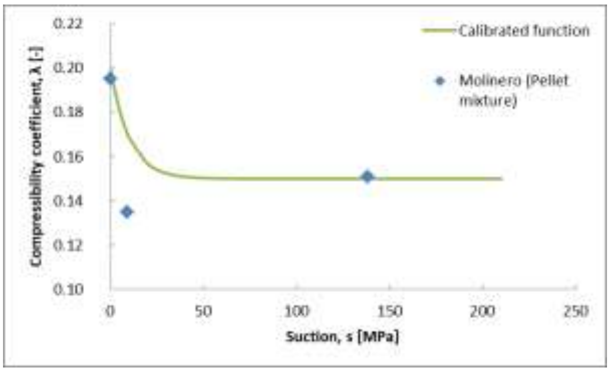

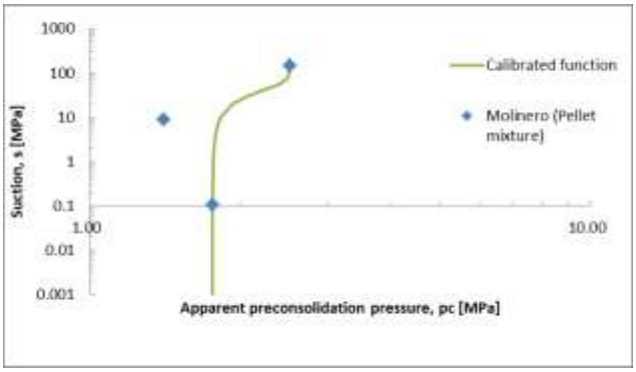

Figure 5-35 Selected compressibility index λ(s) evolution with suction

Figure 5-36 Selected apparent preconsolidation evolution with suction.

An oedometer test in saturated conditions has been modelled in order to test the feasibility of these set of data for the current pellets-mixture (ρ_{di}=0.904

Mg/m3). The mechanical data representing the mixture of WP5_b are denoted as ***reference pellets***.

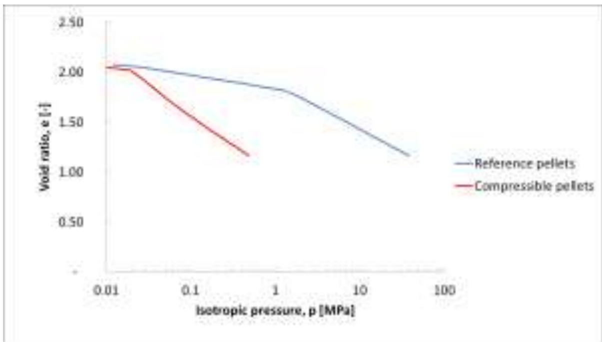

Figure 5-37 Numerical results: void ratio VS isotropic pressure for the considered sets of parameters.

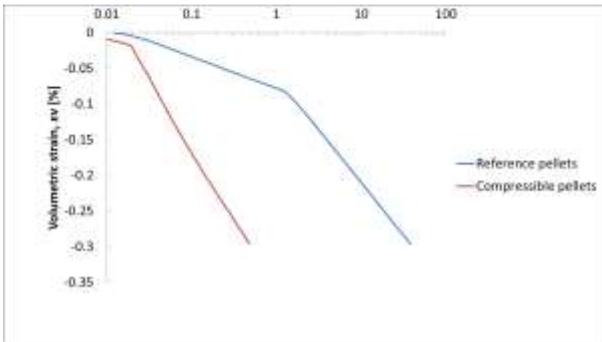

Figure 5-38 Numerical results: volumetric strain VS isotropic pressure for the considered sets of parameters

The experimental results of WP5_c underlined that the pellets layer undergo to a deformation of 28% (51.5mm to 37.4 mm at the end of the test). Therefore, the same displacement on the bottom has been imposed.

The numerical outcomes for the reference pellets parameters show that in order to obtain 28% of strain, an isotropic pressure of 30 MPa is needed [Figure 5-37 and Figure 5-38]. This value is not comparable with the axial pressure measured in the test WP5_c.

Considering the different nature of the mixture, which does not involve crushed pellets between the pellets and a much lower dry density (0.904 Mg/m3 with respect to 1.51 Mg/m3 of WP5_b), the mechanical parameters have been modified [Table 5-11].

The **compressible pellets** parameters present a lower preconsolidation pressure, given the lower degree of compaction, and lower stiffness, considering the inter-pellets space.

The numerical results show that a pressure lower of 1 MPa is required for the 28% of strain. These values are comparable with the experimental results reported for WP5_c. The mechanical parameters of the compressible pellets case are considered in the following analysis [Table 5-11].

Table 5-11 Reference and compressible mechanical parameters

	λ(0)	p0*	κ
	[-]	[MPa]	[-]
Reference	0.200	1.860	0.060
Compressible	0.258	0.020	0.100

5.8.2.2. ***Parameters for bentonite block layer***

The available data for compacted MX-80 bentonite are used for water retention behaviour.

The proposed water retention model is validated against experimental data on wetting paths under confined conditions and for different dry densities for MX-80 bentonite studied by (Villar M., 2004). Samples of MX-80 bentonite were uniaxially compacted to different dry densities and water contents. After equalization, a hole was drilled in the samples and a relative humidity sensor was installed in order to measure the sample relative humidity.

The corresponding suction was obtained using Kelvin's law.

Figure 5-39 represents the experimental data in the (s-Sr) plane together with the model predictions. The calibrated parameters are reported in [Table 5-12]. As observed in Figure 5-39, the degrees of saturation estimated by the water retention model compare favourably with the measured degrees of saturation. In addition, the evolution of the air entry value is consistent with the data obtained by Seiphoori et al. (2014).

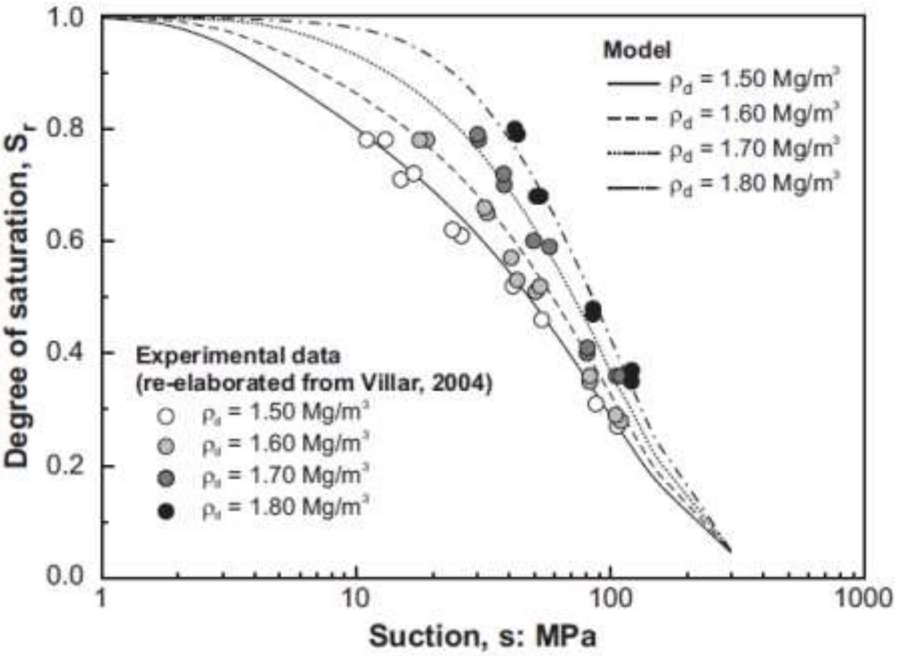

Figure 5-39 Comparison between experimental data (re-elaborated from Villar (2004a)) and model predictions on MX-80 bentonite compacted at four different dry densities

The porosity is derived from the dry density provided by the experiment's report, and consequently the void ratio is obtained.

The reference permeability is selected in order to best fit the experimental results concerning the stabilisation of the swelling pressure.

Table 5-12 Selected hydraulic parameters for the bottom bentonite block

ϱ_{di}	C_{ads}	n_{ads}	A	n	m	K_{w0}	n	e_{m0}	β_0	β_1
(Mg/m^3)	(MPa^{-1})		(MPa)			(m^2)				
1.808	0.0075	1.5	0.2	3	0.15	3.8E-20	0.350	0.31	0.1	0.48

The considered material is MX-80 bentonite compacted to a dry density equal to 1.808 Mg/m3.

Table 5-13 Selected mechanical parameters

ϱ_{di}	κ	κ_s	$\lambda(0)$	p_0^*	p_c	r	ω
(Mg/m^3)				(MPa)	(MPa)		$(MPa^{-1}))$
1.808	0.05	0.0275	0.20	0.15	0.0158	0.5	0.09

The input parameters (see

Table 5-13) were calibrated in order to best fit the experimental data [Figure 5-40] and the target results presented in the report.

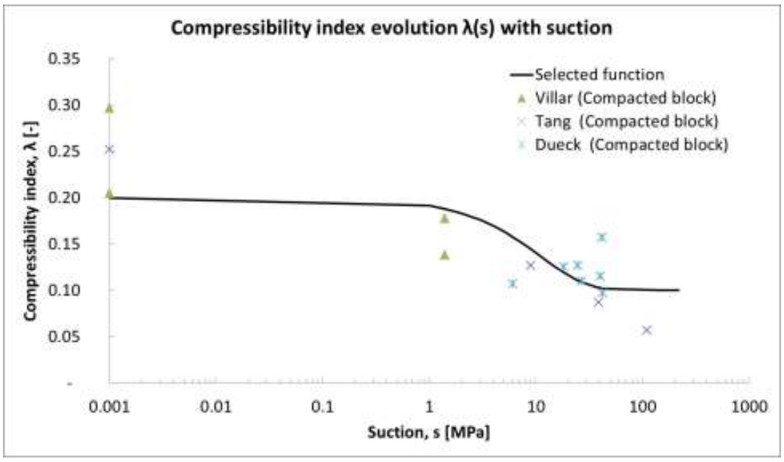

Figure 5-40 Selected compressibility index λ(s) evolution with suction

Formulation for κ_s evolution

The swelling behaviour is one of the most fundamental properties of compacted bentonites. Figure 5-41 presents the evolution of void ratio with suction for a sample of granular MX-80 bentonite compacted to an initial dry density of 1.519 Mg/m3 and subjected to wetting path in free swelling conditions (Seiphoori, Laloui, Ferrari, Hassan, & Khushefati, 2016).

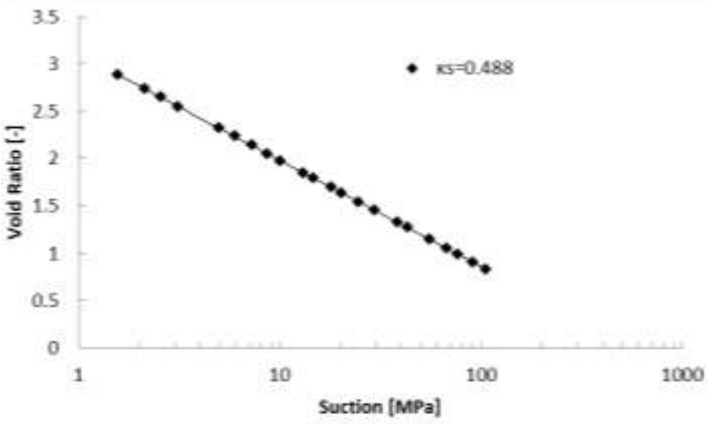

Figure 5-41 (Seiphoori, Laloui, Ferrari, Hassan, & Khushefati, 2016) - Free volume swelling of granular MX80 bentonite: evolution of void ratio versus suction

Upon wetting under unconfined conditions, the material shows a gradual increase in volume, with a quasi-linear response in the (lns-e) plane, whose slope is denoted κ_s.

It is observed that the maximum increase in void ratio occurs at suction values lower than 4.8 MPa where the void ratio has reached e=3.

For the entire range, more than 50% of the total swelling in terms of the void ratio occurs for suction values less than 4.8 MPa.

The maximum volume change behaviour in this range of suction is attributed to the subdivision of smectite particles caused by the inclusion of water molecules in the bentonite particles in a hydration path ((Saiyouri, Hicher, & Tessier, 2000); (Seiphoori, Ferrari, & Laloui, Water retention behaviour and microstrucmicrostructural, 2014)).

This modification at the particle state is a function of the total suction.

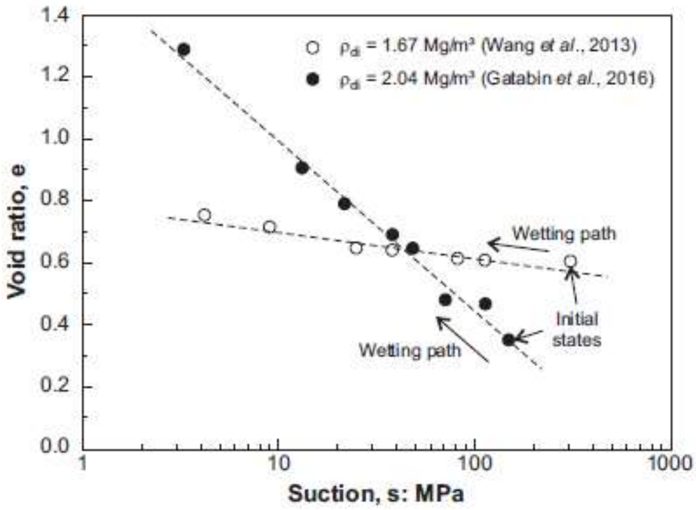

***Figure 5-42** (Wang, Tang, Cui, Barnichon, & Ye, A comparative study on the hydro-mechanical behavior of compacted bentonite/sand plug based on laboratory and field infiltration tests., 2013) & (Gatabin, Guillot, & Bernachy, F.T. Caractérisation bentonite - Rapport final, 2016)- Free volume swelling of granular MX80 bentonite and sand: evolution of void ratio with suction*

Figure 5-42 shows the evolution of void ratio for a mixture of MX-80 bentonite and sand compacted to two different dry densities and wetted under free swelling conditions ((Wang, Tang, Cui, Barnichon, & Ye, A comparative study on the hydro-mechanical behavior of compacted bentonite/sand plug based on laboratory and field infiltration tests., 2013) (Gatabin, Guillot, & Bernachy, F.T. Caractérisation bentonite - Rapport final, 2016)). The increase of the slope for increasing dry density is evident (κ_s= 0.24 for ρ_{di}= 2.04 Mg/m^3 against κ_s= 0.039 for ρ_{di}= 1.67 Mg/m^3). This behaviour can be explained by the larger amount of clay particles (the scale at which the swelling processes take place) in the denser material.

Let us now consider the case of wetting under stress (Figure 5-43). (Dueck & Nilsson, Thermo-Hydro-Mechanical properties of MX-80, 2010) presented controlled-suction oedometer tests on compacted MX-80 bentonite. The tests were carried out on MX-80 bentonite samples compacted to a dry density of 1.74 Mg/m^3 for different values of applied confining stress, namely 2 MPa, 10 MPa and 20 MPa. The slopes κ_s of the 3 curves are respectively 0.129, 0.036 and 0.016, decreasing for increasing applied stress. Consequentially, the final swelling of the samples is maximum for the lowest applied stress and minimum for the highest, underlining the strong stress dependence of bentonite swelling potential.

It is worth to be noticed that when the value of 20 MPa confining stress is applied, the material undergoes to compaction going from 1.74 Mg/m^3 to

1.87 Mg/m^3. As previously stated, for higher density, higher κ_s is expected but the effect of confining stress is prevalent.

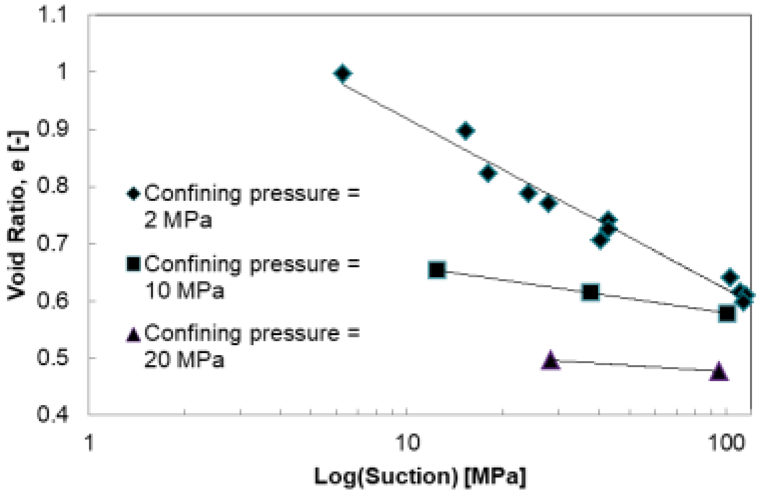

Figure 5-43 (Dueck & Nilsson, Thermo-Hydro-Mechanical properties of MX-80, 2010)-Swelling test at different constant loads on MX-80 bentonite blocks

When the BBM is used in constant volume conditions, the swelling stress can be obtained by integrating equation 3.1 and 3.2:

$$p(s) = p_A \left(\frac{s_A + u_{atm}}{s_B + u_{atm}}\right)^{\frac{\kappa_s}{\kappa}} \quad \text{(Elastic state)} \quad (3.1)$$

$$p(s) = p_A \left(\frac{s_A + u_{atm}}{s_B + u_{atm}}\right)^{\frac{\kappa_s}{\lambda(s)-\kappa}} \quad \text{(Plastic state)} \quad (3.2)$$

The previous equations relate the swelling stress increase to the suction decrease via the exponent κ_s.

It is worth to be noticed that bentonite based materials do not reach the maximum swelling pressure when the suction level is equal to zero but when the full saturation occurs.

Moreover, bentonites are able to sustain a high level of suction without desaturating (i.e. high air entry value).

Therefore, along a saturation path, the material is saturated before reaching zero suction.

Consequentially, the use of BBM overestimates the swelling pressure because does not take into account the previous features.

In order to avoid such overestimation and tackle the stress dependence characteristic of κ_s the following equation is introduced [Equation 3.3]:

$$\kappa_s(p) = \kappa_{s0} * \exp(-\alpha_p * p) \quad (3.3)$$

$$\kappa_s(p) = 0.275 * \exp(-3.5 * 10^{-7} * p) \quad (3.4)$$

The parameter a_p is calibrated in order to reproduce the target results in terms of stress and deformation of the bottom block [Equation 3.4].
It Is assumed that the top pellets layer does not participate to the swelling pressure development of the mixture for two main reasons:

- experimental results suggest that dry density and swelling pressure during hydration are directly linked. Given the initial dry density of ρ_d=0.904 Mg/m^3 , this assembly does not develop a relevant swelling pressure (even after the compaction due to the bottom block swelling, because the full saturation occurs before the compaction);
- the full saturation of the layer is approximately 30 days not comparable with the swelling stress stabilisation and the overall test duration. The swelling stress development is assumed to be controlled by the bottom block only.

5.8.3 Initial and boundary conditions

For further details on the experimental conditions, see the experimental report provided by BEACON.
The numerical bentonite sample consists in 200 eight-nodes isoparametric elements.
The problem is assumed bidimensional and oedometer conditions are considered [Figure 5-44].
The strong heterogeneity of the pellets-mixture material is well-recognized, but for sake of simplicity, in this modelling strategy, the top pellets layer is considered homogeneous, presenting the same hydro-mechanical properties and state in the entire domain and constant permeability, as well as the bottom bentonite block layer.
Initial uniform suction is considered:

- with a value equal to 0 MPa (initial full saturation) for the top pellets-layer;
- with a value equal to 23 MPa (saturation equal to 84%) for the bottom block-layer;

The hydration of the sample is provided from the top end [blue line Figure 5-44Figure 5-44] assuming a pressure evolution from 0 MPa to 0.01 MPa (0.010 MPa pore water pressure) occurring in 9000 seconds.

Finally, the sample is subjected to an initial confining stress values of 0.03 MPa axially (vertically) and 0.09 MPa radially (horizontally).

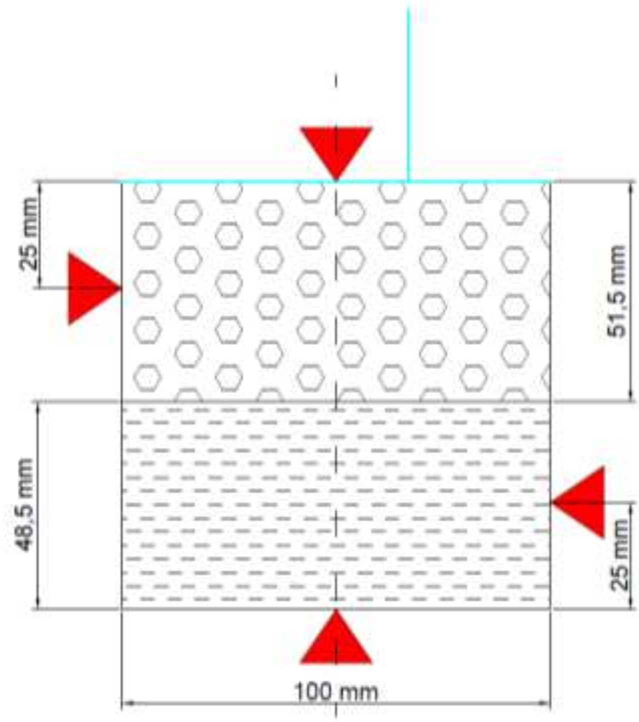

Figure 5-44 Test conditions description

Interface element

An interface element is modelled in order to reproduce friction on the lateral wall of the cell. For further details, refer to (Cerfontaine, Dieudonne', Radu, Collin, & Charlier, 2015).

In the current modelling strategy, the total stress formulation is selected for the mechanical constitutive model of the interface element.

5.8.4 Results/discussion

It can be observed that the measured experimental axial swelling pressures on top and bottom sensors differ of approximately 600 kPa [Figure 5-45]. Therefore, the role of friction in the experimental test is not negligible.

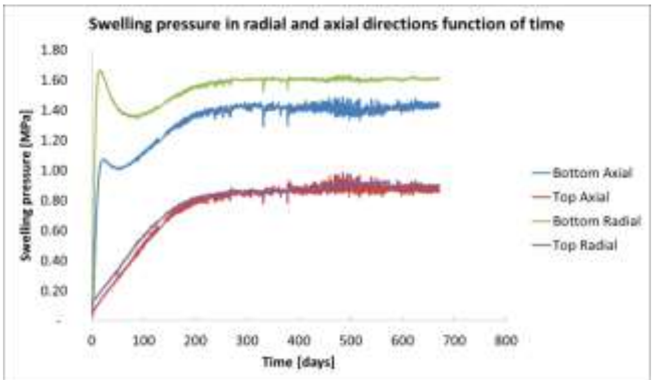

Figure 5-45 Swelling pressure in radial and axial directions function of time

In the following, a comparison between two limit cases is considered:

- Sliding case, in which the sample is free to swell and consequentially displace without any friction with the cell wall;
- Sticking case, in which the sample boundary is fixed to the cell wall and cannot displace with respect to this.

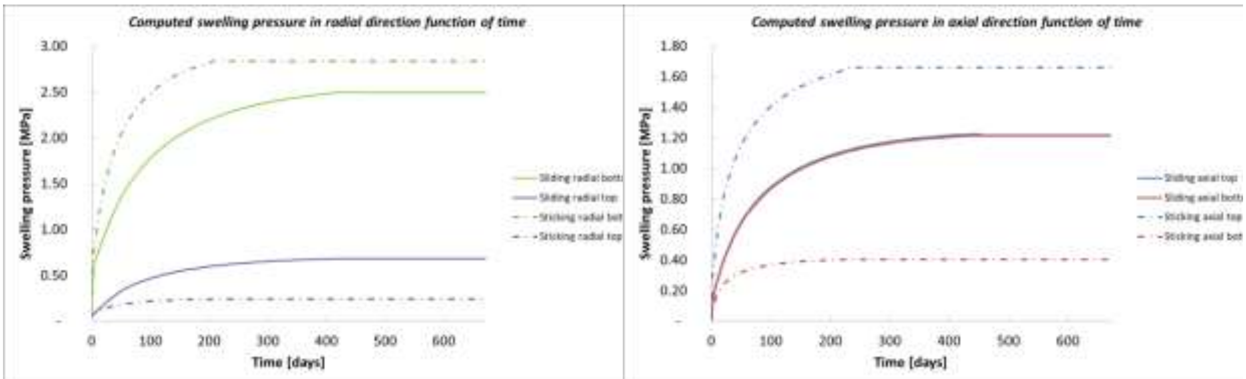

Figure 5-46 Comparison between sliding and sticking cases: computed swelling pressure in radial and axial directions function of time

For the sliding case, the top and bottom axial swelling pressures coincide [Figure 5-46], whereas for the sticking case they differ of 800 kPa.
For the sliding case, the obtained axial stress is comparable with the experimental results.
For both cases, the interface between the block and pellet layers reproduces consistently the experimental results [Figure 5-47].

For the sticking case, the elements stuck to the cell wall undergo to shear deformation [Figure 5-47].

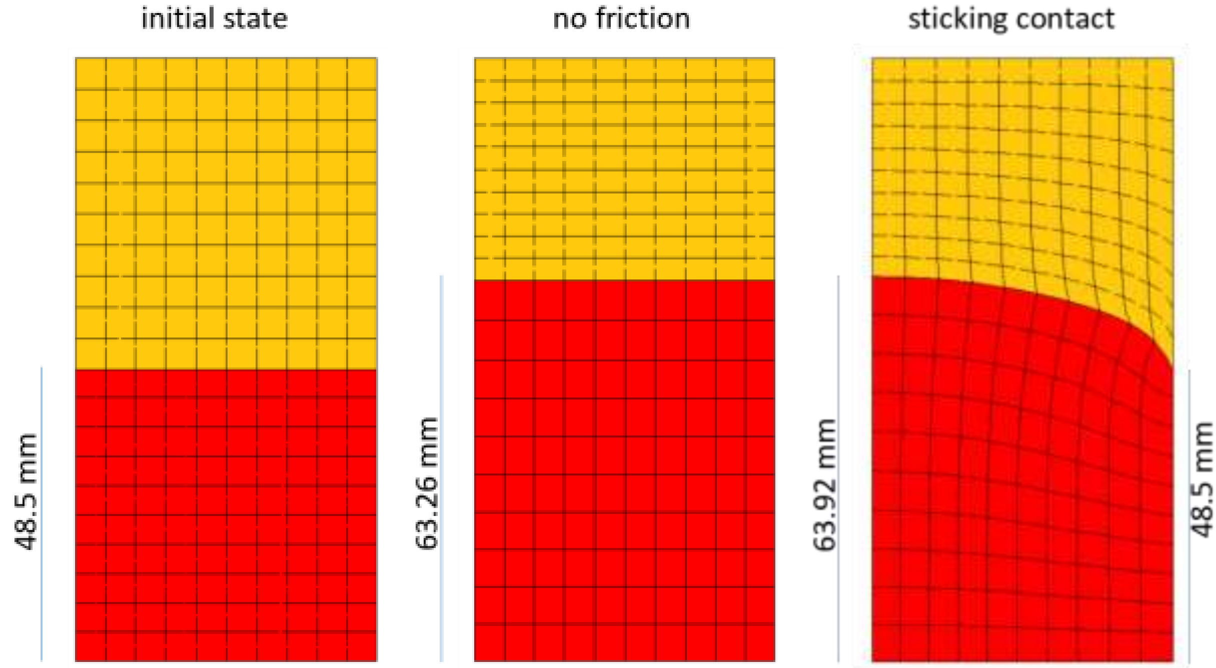

Figure 5-47 Comparison between sliding and sticking cases: initial state and computed deformation at the end of the simulation

An intermediate case is considered. Friction is modelled only to the boundary of the bentonite bottom block. A friction coefficient μ=0.170 is selected [Table 5-14].

Table 5-14 Interface parameters

Penalty coefficient in the normal direction	Penalty coefficient in the longitudinal direction	Friction angle φ [°]	Friction coefficient μ
10^9	10^9	9.65	0.170

The axial swelling pressure numerical results can be favourably compared with the experimental ones [Figure 5-48].
On the other hand, the obtained radial swelling pressures result not corresponding to the experimental ones.

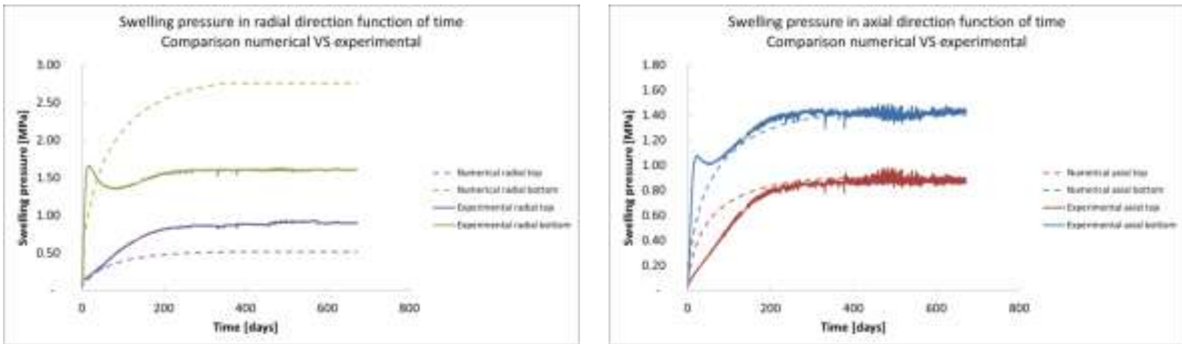

Figure 5-48 Comparison between experimental and numerical results swelling pressure in radial and axial directions function of time

The numerical predictions of water content and dry density compare favourably with the experimental results at the end of the test [Figure 5-49].

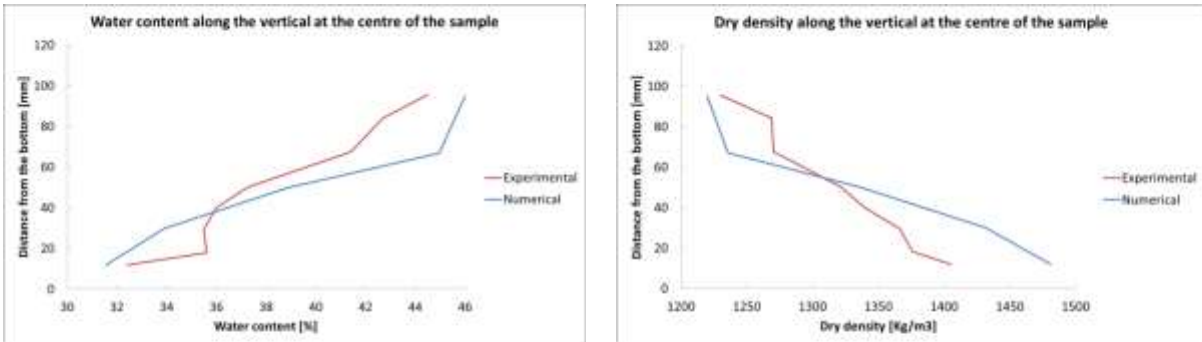

Figure 5-49 Comparison between experimental and numerical result:s water content and dry density along the vertical at the centre of the sample after dismantling

5.9 CU-CTU

5.9.1 Geometry and discretization

The test was simulated in a two-dimensional axysimmetric setup using a structured mesh. A vertical node spacing of 5 mm and a horizontal one of 1.25 mm were chosen for both the bentonite block (bottom layer) and the pellets (top layer). In total, 40 rectangular elements with 165 nodes (including secondary nodes) were obtained. Slightly differently from the experimental condition, the two layers were modelled with equal thickness (50 mm).

5.9.2 Input parameters

The pellets were not simulated individually. An equivalent, homogeneous double-structure medium was chosen to simulate the pellet layer. The parameters of the hypoplastic model for both the pellet layer and the bentonite block were calibrated on the Czech B75 bentonite and are given in Table 5-15 below. These parameters are identical to those used in the simulations of test 1a and 1b.

Table 5-15 Parameters of the hypoplastic model, calibrated on the Czech B75 bentonite

Critical state friction angle of the macrostructure	φ_c	25	°
Slope of the isotropic normal compression line in $\ln\left(\frac{p^M}{p_r}\right)$ versus $\ln(1+e)$ space	λ^*	0.13	
Macrostructural volume strain in p^M unloading	κ^*	0.06	
Position of the isotropic compression line in $\ln\left(\frac{p^M}{p_r}\right)$ versus $\ln(1+e)$ space	N^*	1.73	
Stiffness in shear	ν	0.25	
Dependency of the position of the isotropic normal compression line on suction	n_s	0.012	
Dependency of the slope of the isotropic normal compression line on suction	l_s	-0.005	
Dependency of the position of the isotropic normal compression line on temperature	n_T	-0.07	
Dependency of the slope of the isotropic normal compression line on temperature	l_T	0.0	
Control of f_u and thus of the dependency of the wetting-/heating-induced compaction on the distance from the state boundary surface; control of the double-structure coupling function and thus of the response to wetting-drying and heating-cooling cycles	m	1	
Dependency of microstructural volume strains on temperature	α_s	0.00015	K^{-1}
Dependency of microstructural volume strains on p^m	κ_m	0.07	
Reference suction of the microstructure	s_m^*	-2000	kPa
Reference microstructural void ratio for reference temperature T_r, reference suction s_m^*, and zero total stress	e_m^*	0.45	
Value of f_m for compression	c_{sh}	0.002	
Air-entry value of suction for the reference macrostructural void ratio e_0^M	s_{e0}	-2700	kPa
Reference macrostructural void ratio for the air-entry value of suction of the macrostructure	e_0^M	0.50	
Reference temperature	T_r	294	K
Dependency of macrostructural air-entry value of suction on temperature	a_t	0.118	
Dependency of macrostructural air-entry value of suction on temperature	b_t	-0.000154	

Ratio of air entry and air expulsion values of suction for the water retention model of the macrostructure	a_e	1.0	
Value of λ_p corresponding to the reference void ratio e_0^M in the water retention model of the macrostructure	λ_{p0}	0.7	

In addition, the density of the solids was set at $\rho_s = 2780\ \mathrm{kg\ m^{-3}}$.

Besides for the initial condition (see next section), the bentonite block and the pellet layer were only differentiated by the value of intrinsic permeability: for the block, a value of $5 \cdot 10^{-22}\ \mathrm{m^2}$ was chosen, while for the pellet a larger value, $10^{-19}\ \mathrm{m^2}$ was adopted to account for the comparatively larger permeability of the inter-pellet voids.

5.9.3 Initial and boundary conditions

For the pellet layer, it was not possible to assign, to the void ratio, an initial value comparable to that of the experimental condition. The required high value would have lied outside of the state boundary surface prescribed by the hypoplastic formulation, and modelling would not have been possible. The largest admissible void ratio in the simulation, $e = 1.30$, was assigned to the pellet layer as initial value, together with an initial suction $s = -60\ \mathrm{MPa}$, so as to approach the initial degree of saturation in the experimental condition. For the bentonite block layer, an initial void ratio $e = 0.538$ (corresponding to the experimental condition) and an initial suction $s = -10\ \mathrm{MPa}$ were assigned. Temperature was fixed at $T = 294\ \mathrm{K}$. The lateral and bottom boundaries were set as impervious, while free access to water was provided from the top boundary with a 10 kPa head. Deformations of the sample were prevented at all boundaries.

5.9.4 Results/discussion

With the appropriate choice of initial condition to overcome the significantly different initial void ratio that had to be assigned to the pellet layer, the results of the simulation match with the experimental ones satisfactorily (Figure 5-50).

Since the adopted model does not account for the friction between the sample and the lateral boundary of the experimental device, the axial pressures at the top and at the bottom of the sample coincide (Figure 5-50a). In the delivered result, the simulation was tuned so as to match the axial pressure at the sample bottom. At the same time, a good match with the radial pressure in the top layer could be achieved (Figure 5-50b), while that in the bottom layer resulted significantly overpredicted. Among the many trials preformed, a ratio between the permeabilities in the two layers of 200:1 and a value of permeability in the bentonite block set at $5 \cdot 10^{-22}\ \mathrm{m}^2$ provided the best results in terms of the shape of the temporal evolution of the pressures.

In addition, it is worth noting that negative radial pressures are recorded in the initial phase of the simulation, which in reality would correspond to null pressure with detachment of the sample from the lateral walls of the experimental device. This is expected on the basis of the high initial void ratio of the simulated material, which would undergo an initial collapse upon wetting. This behaviour was not recorded in the experiment, since the actual void ratio of the pellets was much smaller (while the overall void ratio was larger), thus the pellets quickly swelled into the inter-pellet voids and generated swelling pressures.

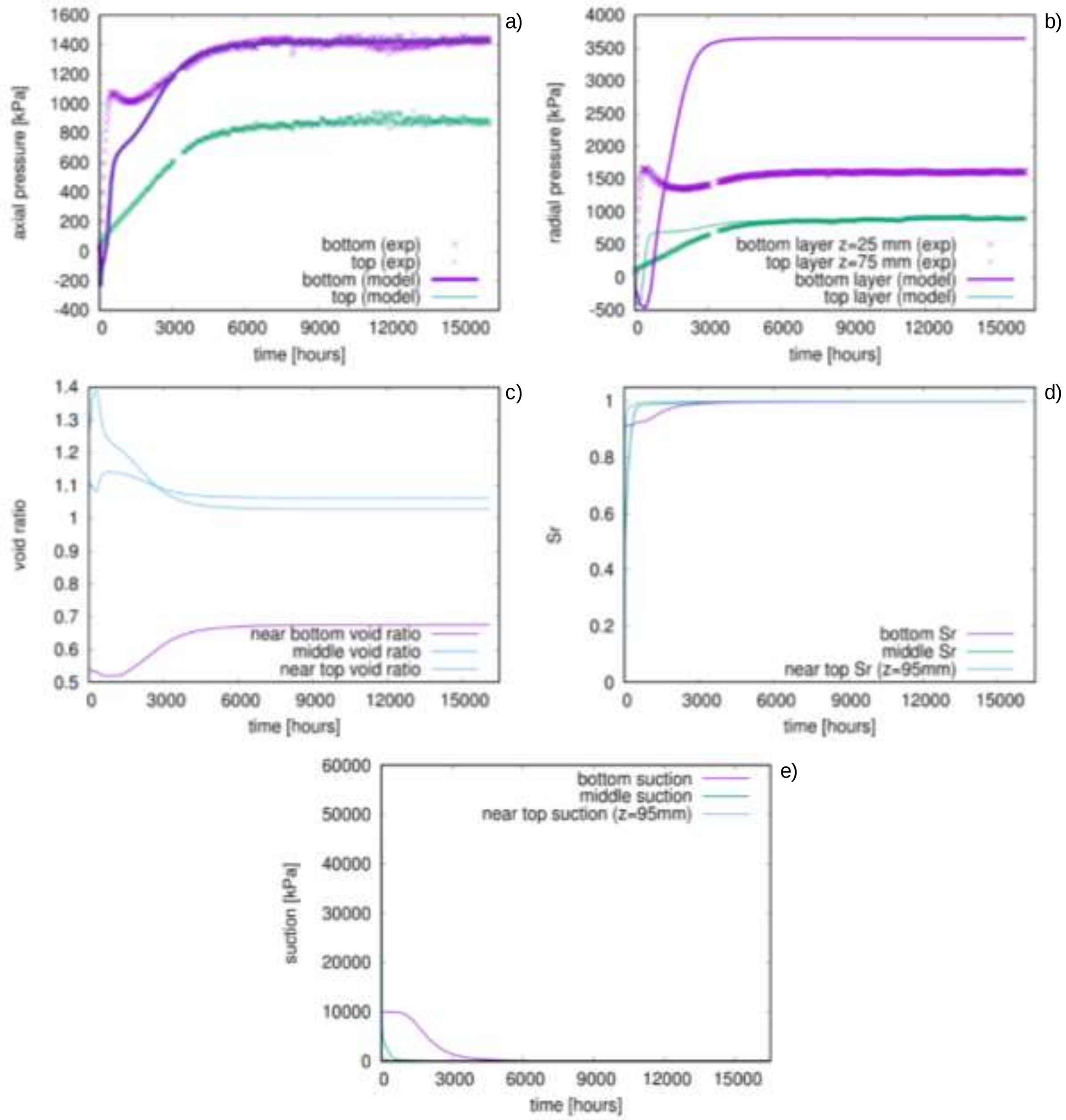

Figure 5-50

Figure 3. Summary of the results of test 1c: a) axial pressure at the top and at the bottom of the sample; b) radial pressure at 25 mm from the bottom (in the bentonite block layer) and at 75 mm from the bottom of the sample (in the pellet layer); c) void ratio, d) degree of saturation, and e) suction near the bottom of the sample (in the bentonite block layer), in the middle (at the base of the pellet layer), and near the top of the sample (in the pellet layer)

5.10 UPC

5.10.1 Geometry and discretization

The test is performed in a constant-volume cell with 100mm diameter and a height of 100mm, equipped with two axial piston at the top and bottom. The top part of the sample is constituted by bentonite pellets whereas a compacted block forms the lower part. Two radial sensors are set at the midpoints of block and pellet zones in order to measure the stresses. At the end of the test, the water content is measured in the centre and four other locations of the sample. The water intake is through a porous disc at the top of the pellets zone. The test was terminated after 672 days when both axial and radial stresses had reached a stationary condition.
No lateral friction was considered in the analysis reported here.

5.10.2 Input parameters

The bentonite block is compacted directly into the cell under to a dry density of 1808kg/m3 and a height of 48.5mm.The MX-80 pellets with pillow shape are placed on the top of block directly until reaching a total height of 100 mm. Two double structure material are defined for the block and pellets regions with the parameters listed in Table 5-16 and Table 5-17.

Table 5-16 Mechanical parameters for block and pellets

Hydraulic Model			block		pellet	
Constitutive law	Analytic expression	Parameter	Micro	Macro	Micro(4)	Macro(1)
Retention curve	Modified Van Genuchten's expression $S_e = \left[1+\left(\frac{s}{P_0}\right)^{\frac{1}{1-\lambda_0}}\right]^{-\lambda_0} \left(1-\frac{s}{P_d}\right)^{\lambda_d}$ $S_e = \left(1+\left(\frac{s}{P_0}\right)^{\frac{1}{1-\lambda}}\right)$	$P_0(MPa)$ λ_0 $P_d(MPa)$ λ_d	280 0.85 900 2.5	35(1) 0.45(1)	280 0.85 900 2.5	50 0. 065 600 4
Intrinsic permeability	Kozeny's expression $k_j = k_0 exp^{b(\phi_j-\phi_0)}$	$K_0(m^2)$ ϕ_0 b	5.5e-19(1) 0.4(1) 6(1)		1e-18(1) 0.4(1) 8(1)	
Relative liquid conductivity	Power law $k_r = A(S_e)^B$	A B S_{ls} S_{rl}	1(1) 1.5(1) 1(1) 0(1)		1(2) 3(2) 1(2) 0(2)	
Leakage parameter	$\Gamma^w = \gamma(\Psi_1 - \Psi_2)$	γ (kg/s/m3/ MPa)	1.0e-8(2)		5.0e-7(2)	

(1) POSIVA 2012 (2) Gens,2009 (3) Sánchez,2016

Table 5-17 Mechanical parameters for block and pellets

Mechanical model BExM				
Constitutive law	Analytic expression	Parameter	block	pellet
BBM Elastic part	$d\varepsilon_v^e = -\frac{\kappa}{1+e_M}\frac{dp}{p} - \frac{\kappa_s}{1+e_M}\frac{ds}{s+p_{atm}}$	κ κ_s	0.06(1) 0.03(1)	0.03(3) 0.02(3)
Yield locus	$p_0 = p_c\left(\frac{p_0^*}{p_c}\right)^{\frac{\lambda_{(0)}-\kappa}{\lambda_{(s)}-\kappa}}$ $\lambda(s) = \lambda(0)\,(r + (1-r)e^{-\beta s})$	$p_0^*(MPa)$ $p_c(MPa)$ r $\lambda(0)$ $\beta(MPa^{-1}))$	0.75(1) 0.01(1) 0.8(1) 0.15(1) 0.2(1)	0.15(2) 0.01(2) 0.6(2) 0.15(2) 0.22(2)
BExM Microstructure	$K_m = \frac{1+\overline{e_m}}{\kappa_m}\hat{p}$	κ_m	0.04(3)	0.03(2)
Interaction function	$f_s = f_{s0} + f_{si}\left(1-\frac{p}{p_0}\right)^{ns}$	f_{s0} f_{si} n_s	0(1) 1(1) 2(1)	0 1 2

(1) POSIVA 2012 (2) Gens,2009 (3) Sánchez,2016

5.10.3 Initial and boundary conditions

The initial conditions for the two materials are indicated in Table 5-18 and Table 5-19. The displacements were fixed throughout whereas the hydraulic condition of free water was prescribed at the top of the sample. The initial degree of saturation are 85% and 21% respectively in the block and pellet region.

Table 5-18 Initial properties of block and pellets

	Initial w(%)	Initial ρ_d(kg/m^3)	Constant radius(mm)	Initial height(mm)
Block	16.3	1808	100	48.5
Pellets	15.3	904	100	51.5

Table 5-19 Initial conditions for block and pellets

Initial parameters	Initial porosity	Macro porosity	Micro porosity	Initial macro suction(MPa)	Initial micro suction(MPa)
Block	0.347	0.132	0.215	50	82
Pellets	0.674	0.56	0.114	180	220

5.10.4 Results/discussion

The computed evolution of degree of saturation is shown in Figure 5-51. It developed more rapidly closer to the upper boundary in the pellets region where water ingress takes place. In the block region there is a slight decrease at the beginning as some of the water is sucked by the pellets.

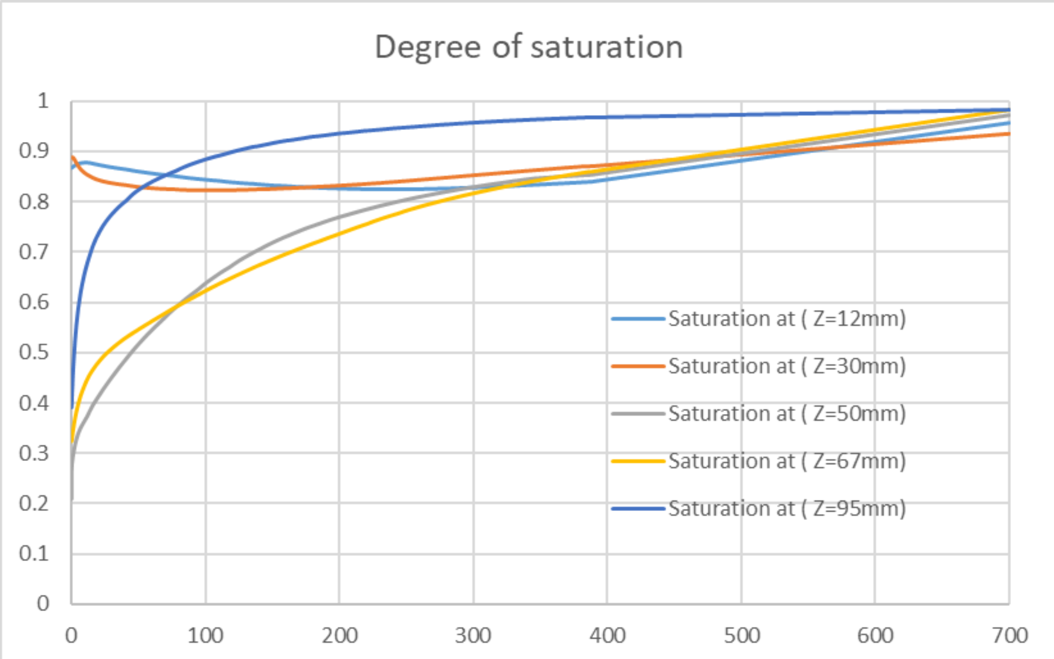

Figure 5-51 Degree of saturation function with time for different depths

Computed and observed evolutions of swelling radial stresses are shown in Figure 5-52. The measured stress is systematically higher in the block zone than in the pellet zone. There is a peak in the block zone that the analysis also reproduces. The stress evolution in the pellets zone is well reproduced. Figure 5-53 shows the evolution of axial stresses. The experimental observations show quite different values of axial stress at the two ends of the sample due to lateral friction. Only one curve is computed in the analysis because friction is not considered. It can be observed that the calculated values are intermediate between the two observed ones.

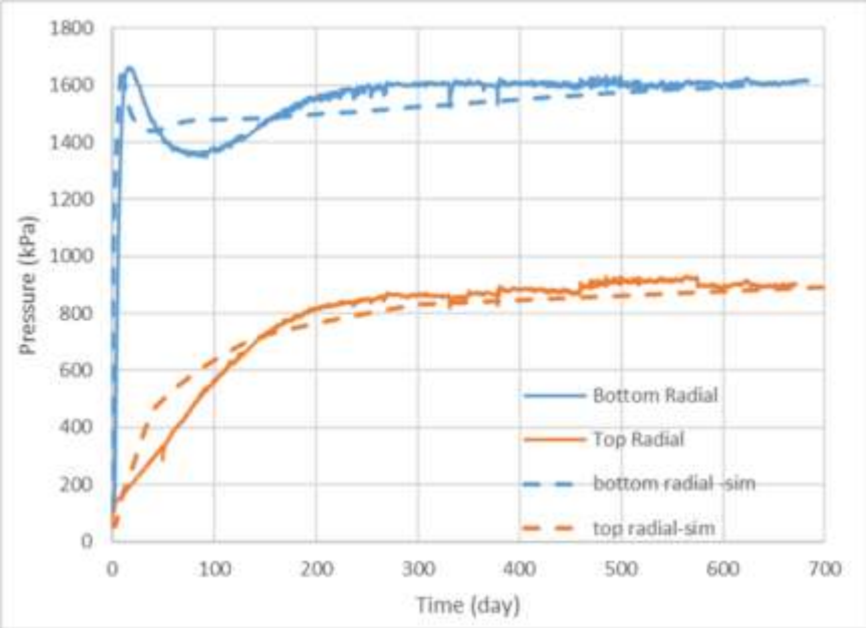

***Figure 5-52** Swelling pressure in radial direction as a function of time. Solid lines are modelling results and dashed lines are experimental observations.*

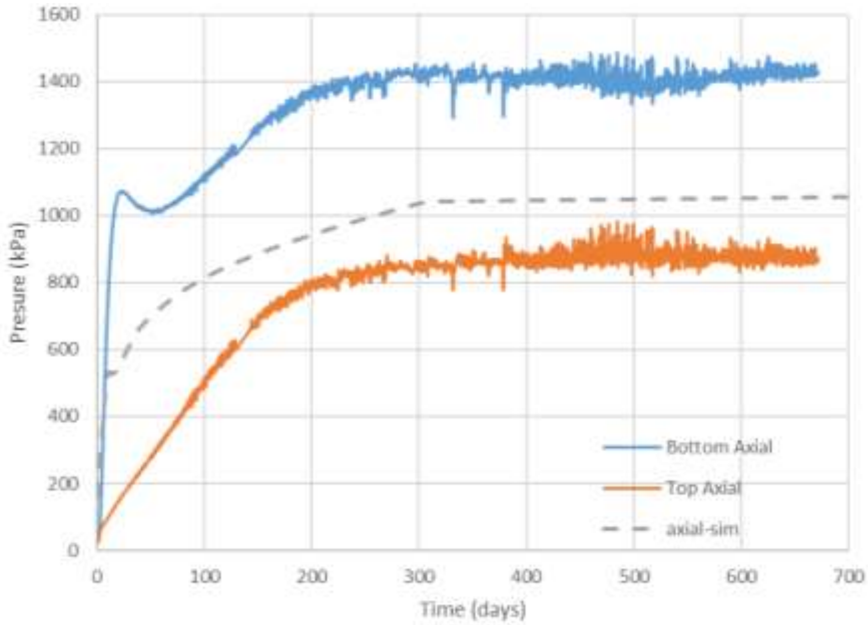

***Figure 5-53** Swelling pressure in axial direction as a function of time. Solid lines are modelling results and dashed lines are experimental observations.*

The water content plot (Figure 5-54) refers to the final state of the mixture. From the experimental results, five sets of the results are collected at different location. Naturally, there is only a single set of modelling results. Results and observations agree satisfactorily. The computed distribution of dry density

(Figure *5-55*) also captures quite well the observed final distribution of the specimen although the degree of homogenization is somewhat underestimated.

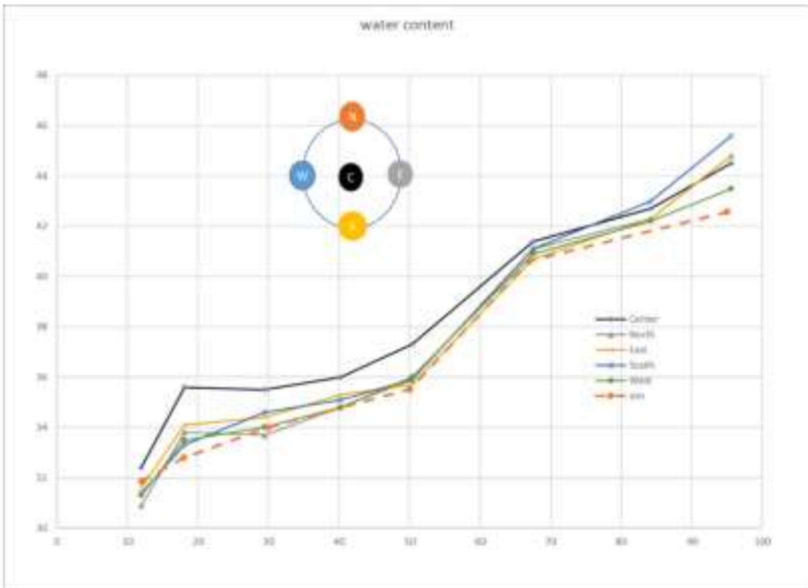

Figure 5-54 Water content along different vertical locations

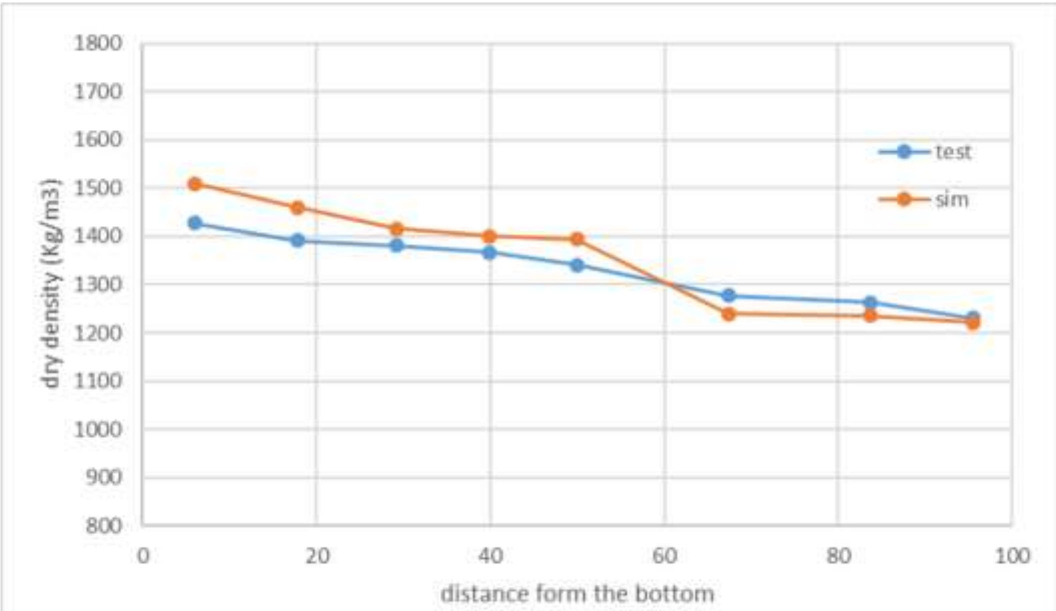

Figure 5-55 Dry density distribution along sample length

5.11 Synthesis of results

This test is a sort of combination of the two previous tests. Two layers composed one with pellets and the other by a bentonite block are introduced in the cell. The large initial difference of dry density leads to consider an important homogenisation during the saturation. One of the particularities of this test is the measurement of pressure on the top and on the bottom of the sample. The measure shows a significative difference between the two side of the sample. This difference is certainly due to the initial contrast of density between the top and bottom of the sample but also to the friction at cell wall.

Among the 9 participants, five of them introduced in their models some friction on the lateral boundary, allowing a difference of pressure between the top and the bottom.

5.11.1 Axial pressure on top and base of the sample

Figure 5-56 shows the results obtained of the top of the sample. This is the pressure measure on the face in contact with the pellets mixture. For most of the participants, the pressure at the top seems overestimated by the model. However, some results are very close to the measure and represent well, both final value and global evolution of the pressure.

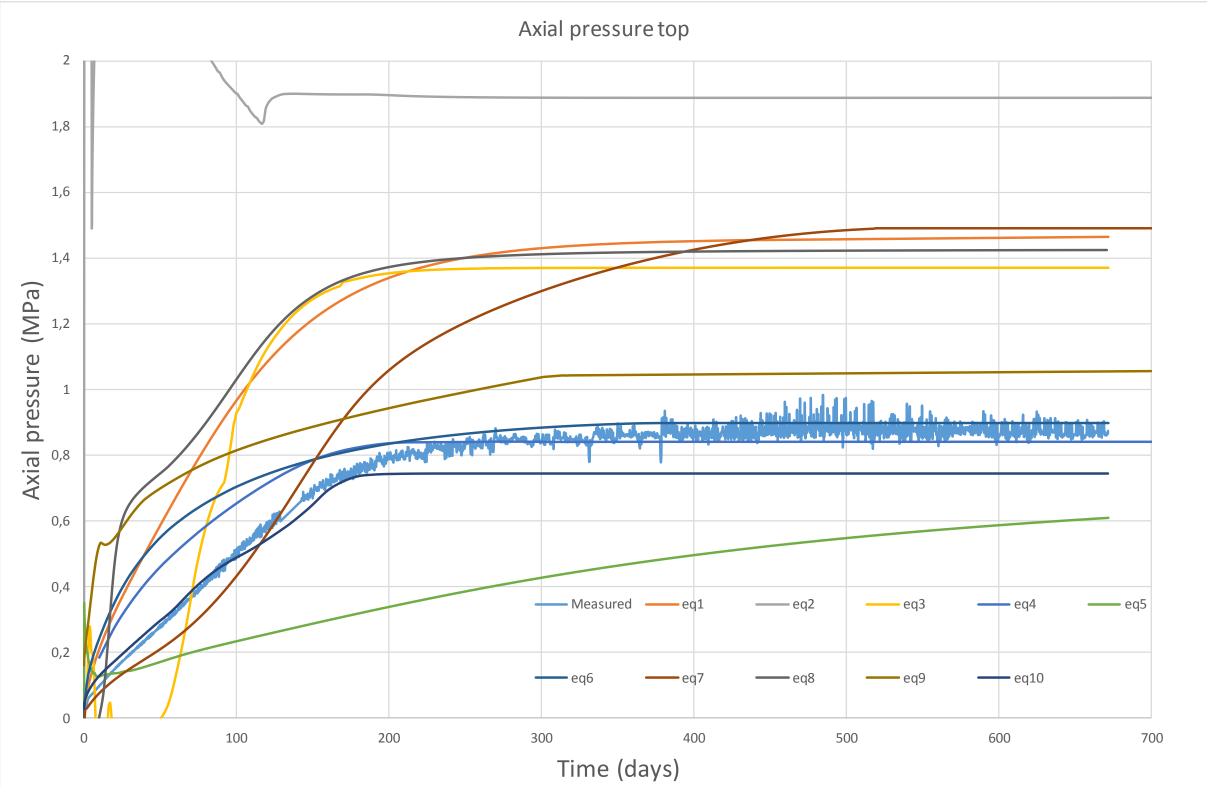

Figure 5-56 Axial pressure evolution at the top of the sample

The results on pressure predicted at the bottom (see Figure 5-57) are more dispersive than on the top. As in the test 1b, the behaviour of the bentonite seems to be more difficult to handle on the face where there is no water supply. Certainly, saturation is driven more by capillary effects and hydromechanical coupling should be more important in proccesses evolution far from the injection point.

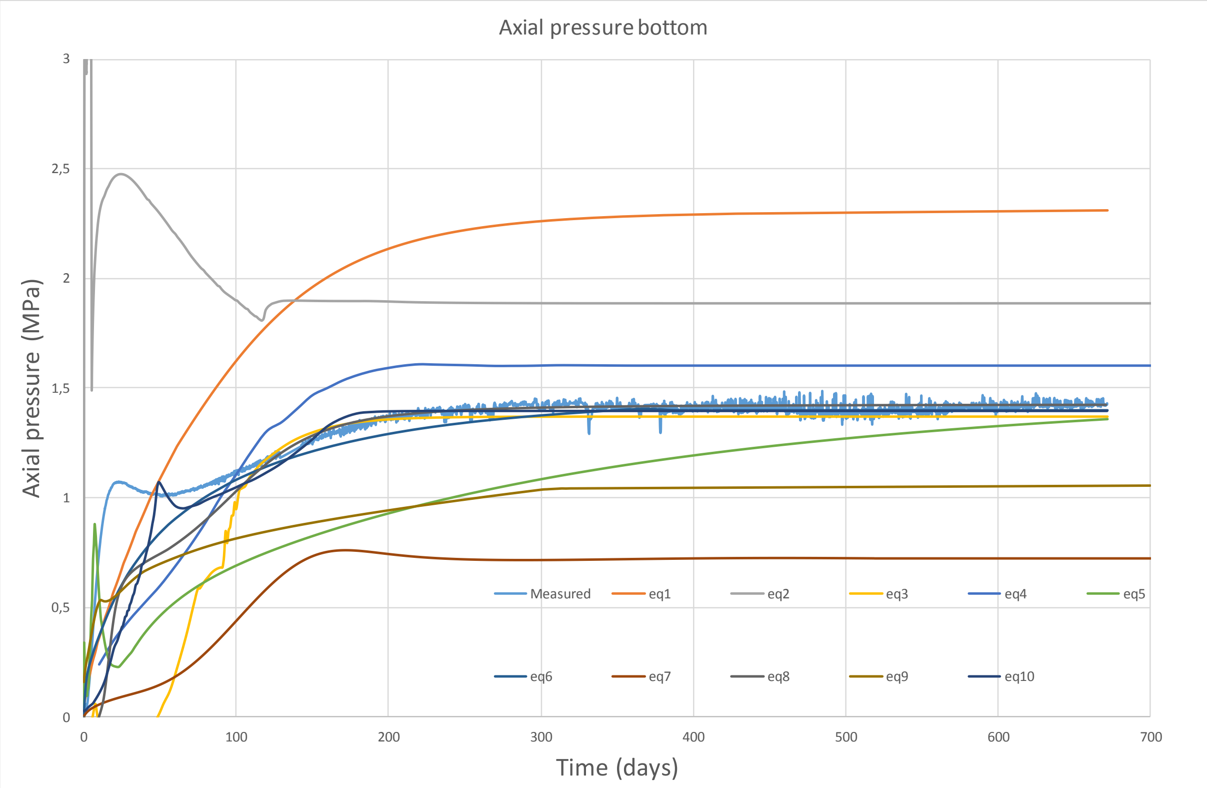

Figure 5-57 Axial pressure evolution at the bottom of the sample

The comparison between the top and the bottom pressure shows a higher pressure on the block size and a lower one on the pellets side (see Figure 5-59). This illustrates that homogeneity of the material is not reach in this experimental configuration. This behaviour can be well reproduced by some of the model as it can be seen on Figure 5-59.

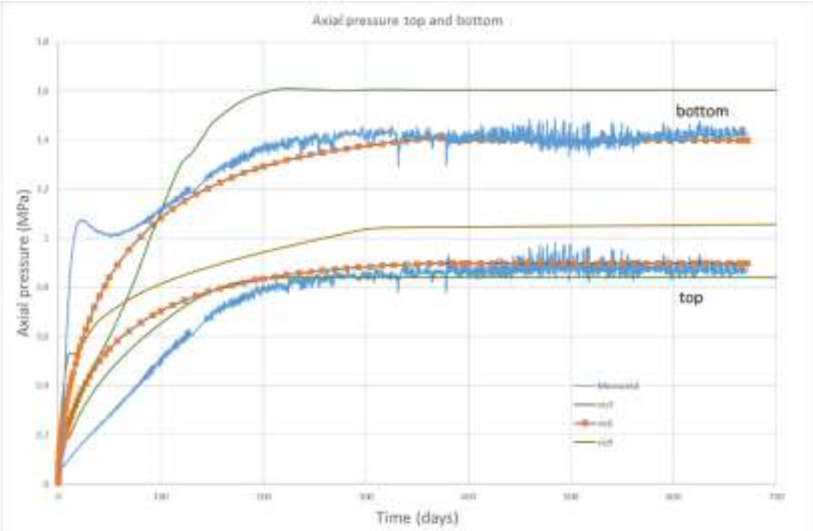

Figure 5-58 Axial pressure evolution on the top and bottom: measure and selected numerical results

5.11.2 Radial pressure evolution

Figure 5-59 and Figure 5-60 presented the radial pressure evolution at the level of the bentonite block and at the level of the pellets mixture. As for the axial pressure, the numerical results are more dispersive in the bentonite block. Most of the models give a very good representation of radial pressure evolution at the pellets mixture level.

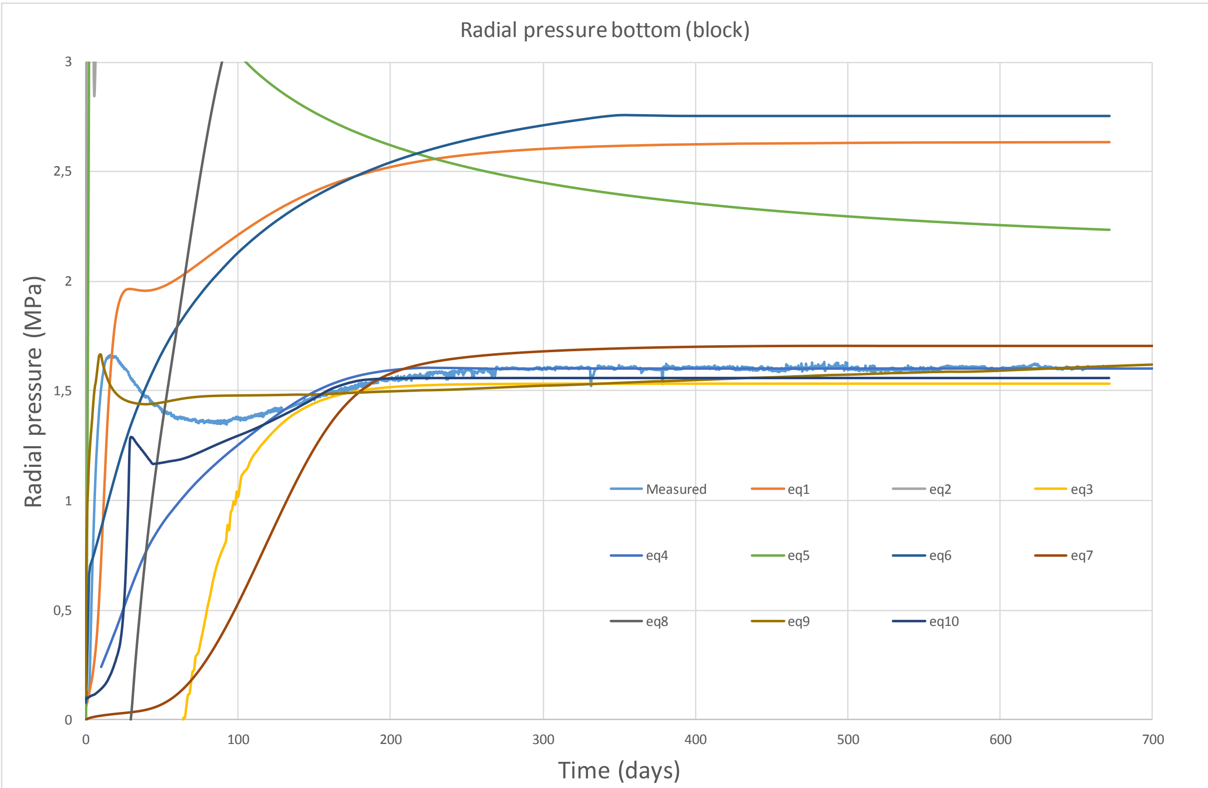

Figure 5-59 Radial pressure evolution at z=25mm (block level)

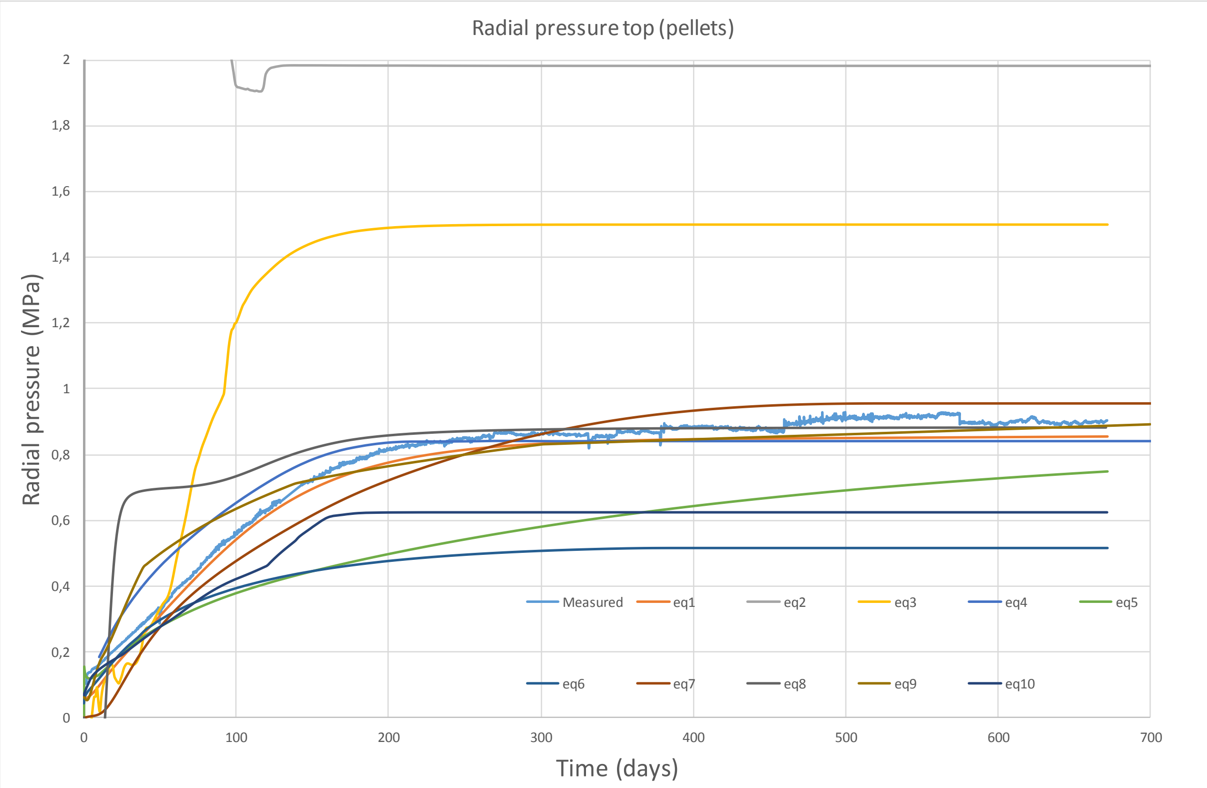

Figure 5-60 Radial pressure evolution at z=75mm (pellets mixture level)

5.11.3 Water content and dry density

As it can be seen of Figure 5-61, Figure 5-62 and Figure 5-63 water content profiles at three heights are spread out and sometimes very far from post-mortem measurements. A fast increase of water content is observed at the top where water is injected and at the middle of the cells at the interface between pellets and block. It seems that pellets mixture allow a quick transfer of water from the top to the block part. In the block, as expected, the water content evolves more slowly.

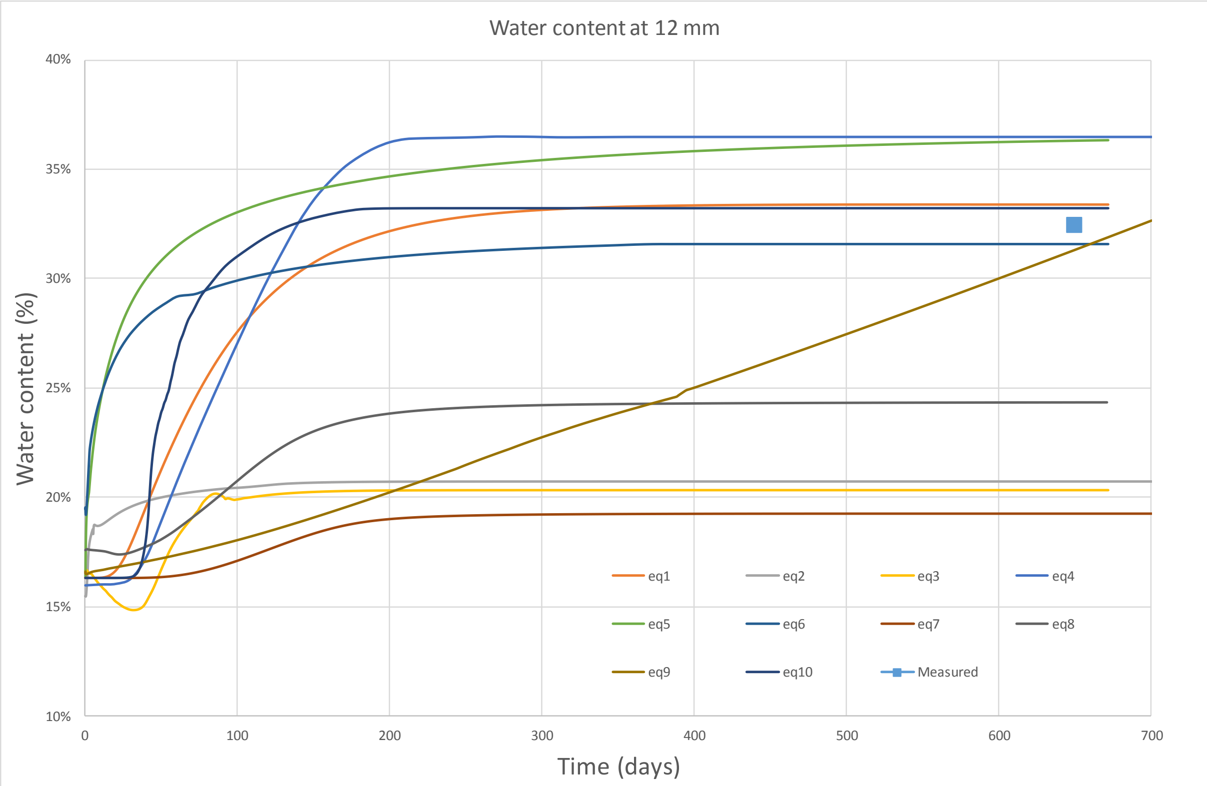

Figure 5-61 Water content evolution at z=12mm

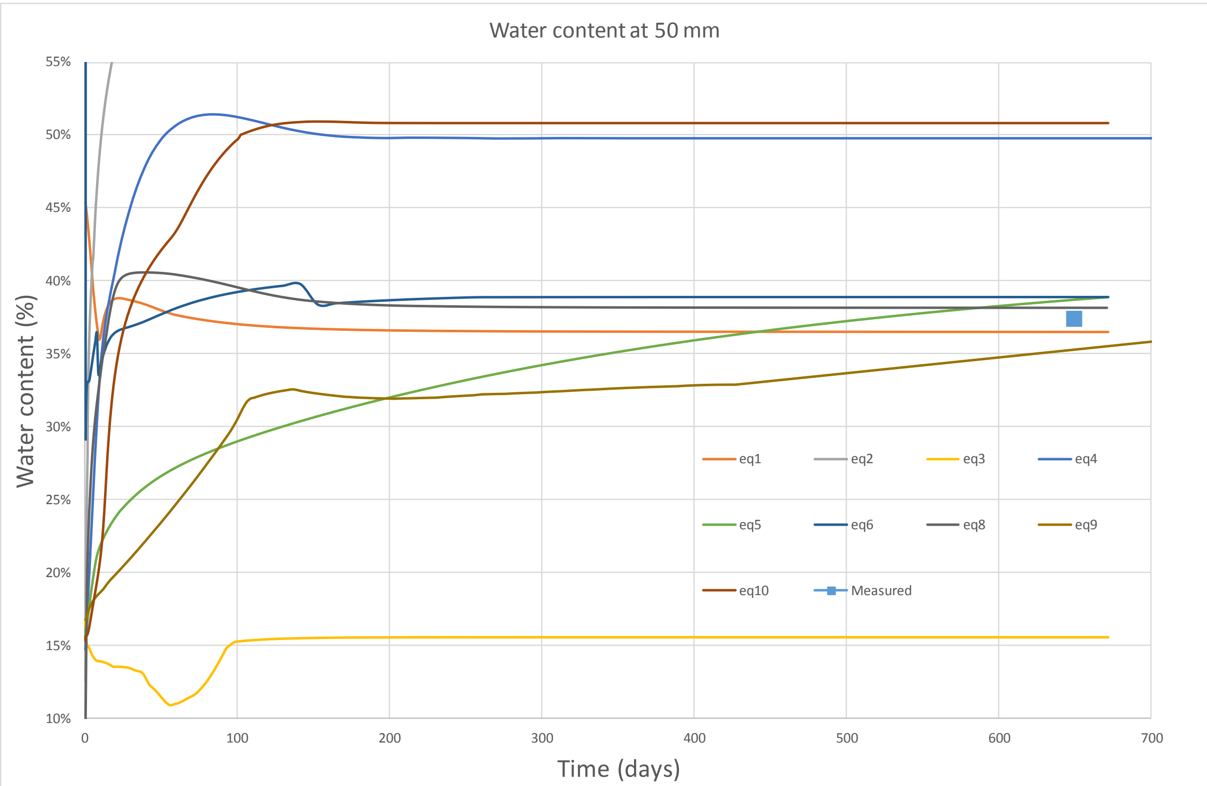

Figure 5-62 Water content evolution at z=50mm

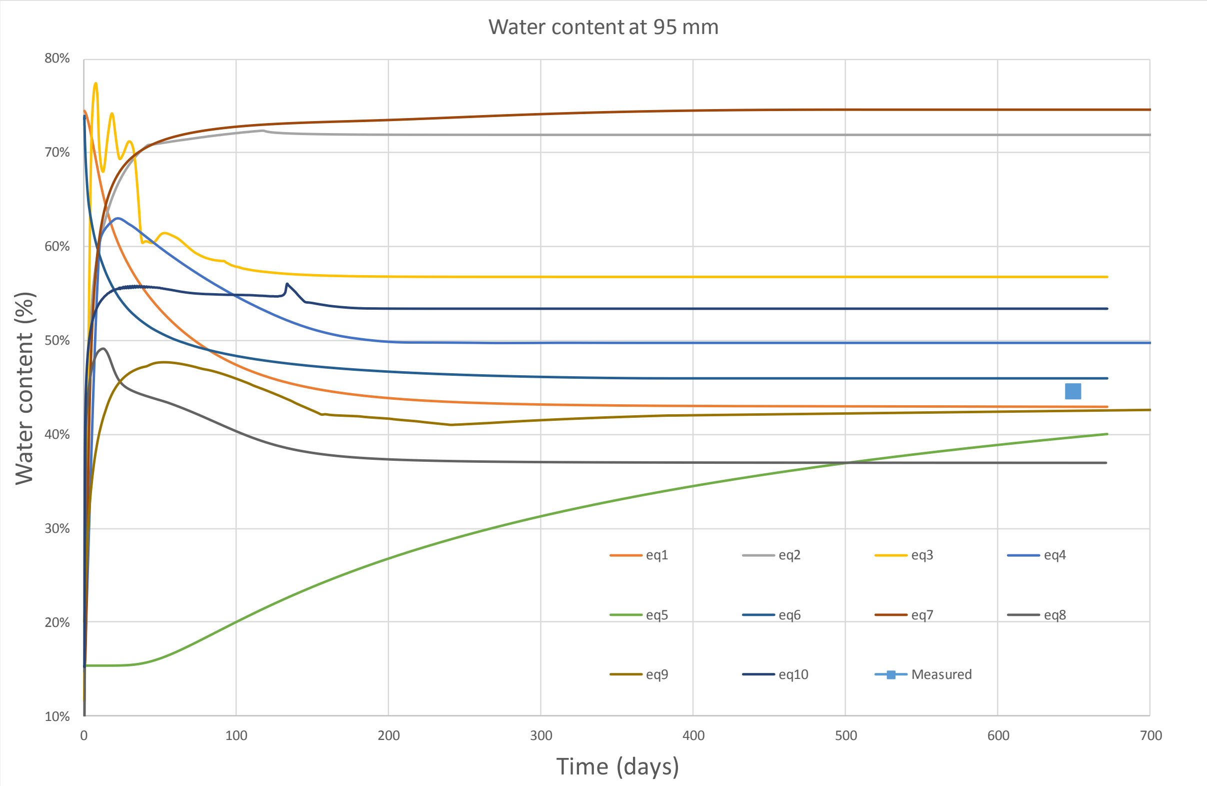

Figure 5-63 Water content evolution at z=90mm

Numerical values at the final state obtained by some models are very close to the measure. This can be seen on Figure 5-63. What it is surprising, arethe initial values retained by modellers for the water content. In some cases, those values are really different from the specifications. Water content for the initial material is constant and about 15%. This difference is certainly due to numerical problem and especially to the constrast of properties betwenn the two layers.

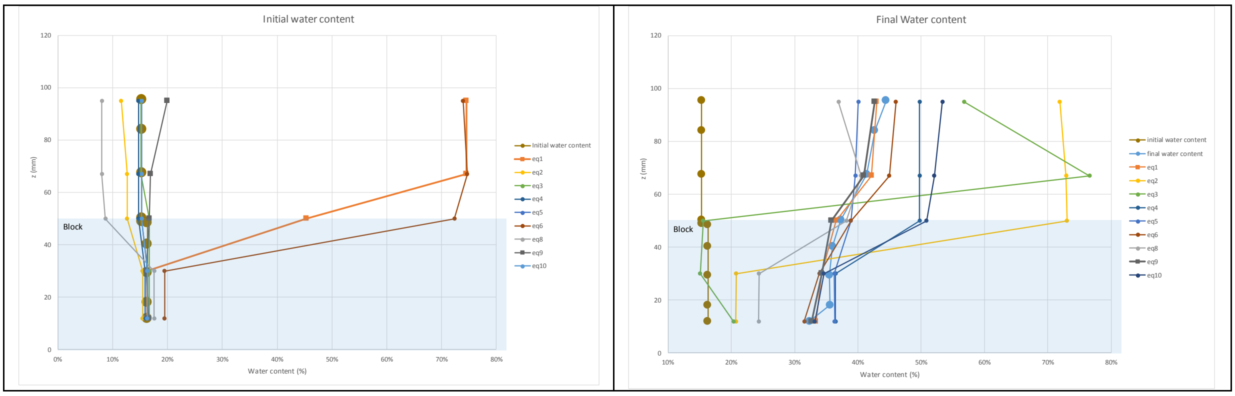

Figure 5-64 Initial and final water content profiles

Same kind of analysis could be done for dry density at the final state and concerning the initial conditions applied by the different partners.

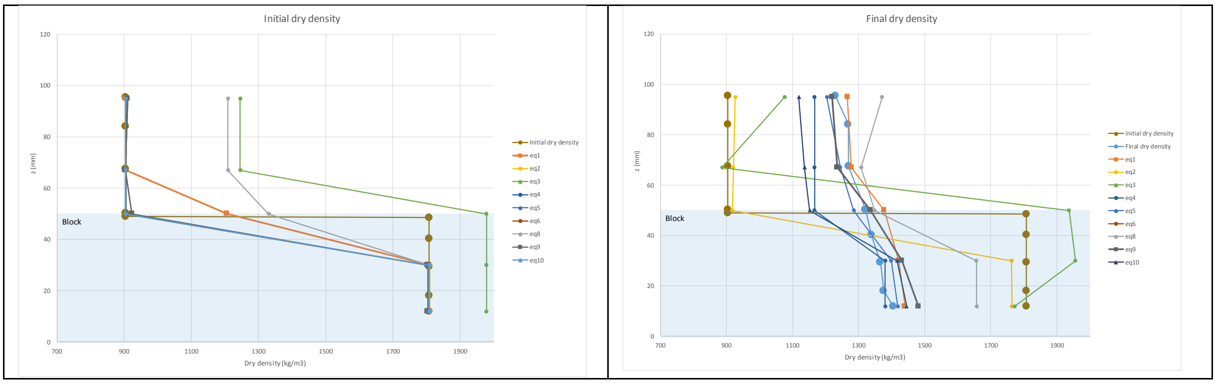

Figure 5-65 Initial and final dry density profiles

5.12 Discussion

As in most of test cases, a large discrepancy appears on the transient phase on several variables such as water content, dry density or total stress. The duration of the transient phase (estimated when the pressure reached 3% of the final value) seems also difficult to predict with accuracy (see table below).

Table 5-20 Time to reach a steady state on axial pressure (top) and value of pressure

	Eq1	Eq2	Eq3	Eq4	Eq5	Eq6	Eq7	Eq8	Eq10	Data
Time (days)	265	117	172	170	610	269	425	211	170	288
Paxial value (Mpa)	1.4	1.8	1.3	0.85	0.6	0.9	1.4	1.4	0.7	0.87

Despite the fact that pellets mixture is represented by a homogeneous media, the behaviour seems well capture by all the model.

In this test, the role of friction was highlighted by the fact that the stress has been measured on both side of the sample, top and bottom. Differences has been observed on the measurements and to predict similar behaviour, it has been necessary to introduce friction in the model. However, assumptions retained by participants are not always the same. For example, comparison of friction angle shows choices between 7 and 20°. One of the difficulty was to associate a saturation state to the friction processes. Changes during hydration influences certainly this parameter.

The post mortem analysis indicates that the final state is not homogeneous with a higher dry density on the lower part (initial block) and a lower dry density where the pellets mixture has been put. Results from one simulation are presented on Figure 5-66. They show the evolution of dry density at different locations in the sample and illustrate the decrease of dry density in the block part and the increase in the pellets part. The model predicted that the final state is not homogeneous and seems not to evolve anymore. The slopes of the curves indicate that a steady state has been reached.

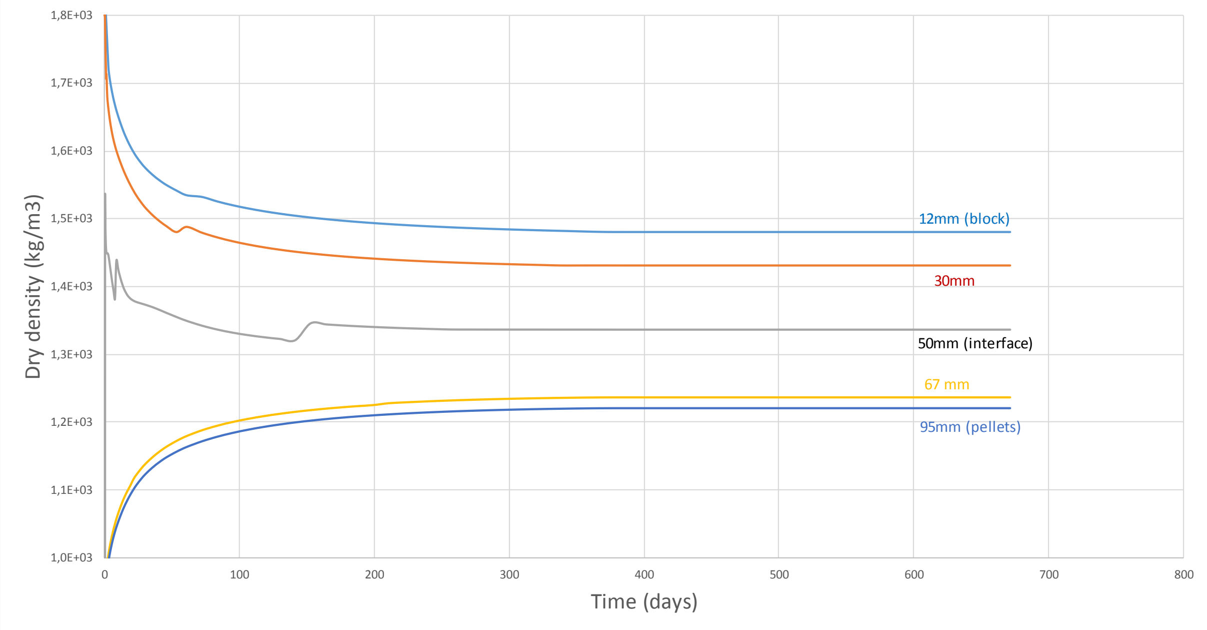

Figure 5-66 Example of dry density evolution from one model at different locations

6 Synthesis

This aim of the first task of WP5 was to confront the models with "simple" laboratory tests. The choice of the tests has been motivated by the fact that each of them illustrates some situation where initial heterogeneity can be identified.

- The first tests (tests1a) explored the role of a void in contact of the swelling clay block.
- The second test (test1b) introduced a pellets mixture where heterogeneities are inherent to the mixture itself.
- The third test combine block and pellets mixture introducing a high-density layer and a low-density layer.

It could be noted that all the tests reproduce at small scales situations that could be encountered in the underground repository context.

Eleven groups participated to this task with several types of approaches. The strength of this exercise was that different constitutive models have been used.

As it has been shown in deliverable 3.1 "description of constitutive models available at the start of the project" and in the description of the models presented in this document, a large variety of constitutive models and computer codes have been used. For example, most of the groups involved made the choice to use double structure models for mechanical or/and hydraulic behaviour. The basic idea is to manage two levels of porosity (micro and macro) and to define mass exchanges and mechanical dependency between these two levels. The choices made by the different groups are summarised in Table 6-1.

Table 6-1 Constitutive models used by the partners

Feature	ClayTech	CU/CTU	BGR	EPFL	ICL	Quintessa.	ULg	UPC	VTT/UCLM
Double structure/porosity Mechanical	Y	Y	N	N	Y	N	N	Y	Y
Double structure/porosity Hydraulic	Y	Y	N	N	N	N	Y	Y	Y

One of the difficulty identified in this first task of WP5, was to compare the parameters used for each case by the involved groups. Implementations of models are slightly different and coupling between mechanical and hydraulic processes make difficult some relevant comparisons.

Based on the results obtained in this first stage of the project, the main lessons that can be learned from this phase are:

- *Swelling pressure measurements*: Most of the models are able to reproduce "classical" swelling pressure tests at constant volume. Stress distribution at the end are in the expected range deduced from the experimental data (dry density/swelling pressure curves) and observation on the specific test.
- *Transient phase:* Major differences have been found concerning the path followed by the models to reach the finalized stable state. Most of the time comparisons between the measurements and the model predictions show discrepancies even if the global trend is reproduced. For example, models are able to simulate complex physical processes such as structural collapse during the hydration but these processes are either underestimated or overestimated.

- *Duration of transient phase: Comparison between time necessary to reach the final swelling pressure measured and the one predicted by the models, shows differences that can reach more than 50%.*
- *Hydraulic/mechanical behaviour:* Hydraulic evolution of material during hydration seems better capture by model in terms of final water content or water inflow than mechanical behaviour. This can be seen for example on Figure 5-64 or Figure 4-89.
- *Heterogeneities:* Based on the feedback from the test 1a, 1b and 1c, the most difficult situation to model is certainly when a gap is introduced in the cell as in test 1a01 (second part) and test 1a02. This particular point needs more investigations.
- *Friction:* Role of friction has been highlighted in test 1c due to the fact that axial pressure has been measured on the two bases of the swelling clay cylinder. The importance of friction is certainly due to the scale of the test and the heterogeneity of the structure. At small scales surface/volume ratio is high and the role of friction has to be considered. For large-scale component, the ratio S/V is much lower and importance of friction is certainly reduced. When two layer are present is the cell with high contrast of density, displacements along the lateral interfaces are significant due to the swelling. This is the case for test 1c but also for test 1a due to the presence of gaps on the top of the sample.
- *Pellets Mixture:* Treatment of pellets mixture as a homogeneous media with mean properties seems to be a reasonable approach. Some specific characterizations should be done for low density mixture as in test 1c.

7 References

Abed A., Laitinen M., Lämsä J., Harjupatana T., Sołowski W. T., Kataja M., 2016. Hydro-mechanical modelling of MX-80 bentonite: one dimensional study. In proceedings of 3rd European Conference on Unsaturated Soils – "E-UNSAT 2016", Paris, France, September 12-14, 2016

Agus S. S. [et al.] 2013. Swelling pressure – suction relationship of heavily compacted bentonite–sand mixtures, Acta Geotechnica 8. - 2013. - pp. No. 2, 155–165.

Åkesson M, Börgesson L, Kristensson O, 2010. SR-Site Data report – THM modelling of buffer, backfill and other system component. SKB TR-10-44, Svensk Kärnbränslehantering AB.

Åkesson M, Kristensson O, Malmberg D, 2018. The Hysteresis Based Material model. Deliverable (D3.1) Beacon Report. February 2018.

Alonso E., Gens A., Josa A., 2013. A constitutive model for partially saturated soils. Géotechnique, 40(3), 1990, P.: 405–430.A. Szymkiewicz. Modelling Water Flow in Unsaturated Porous Media Accounting for Nonlinear Permeability and Material Heterogeneity., 238 p.

Alonso EE, Gens A, Josa A., 1990. A constitutive model for partially saturated soils. Géotechnique. 1990;40(3):405–30.

Alonso E. E. [et al.] 2005. Expansive bentonite–sand mixtures in cyclic controlled-suction drying and wetting. Engineering Geology. - 3 : Vol. 81.

Alonso EE, Vaunat J, Gens A., 1999. Modelling the mechanical behaviour of expansive clays. Eng Geol. 54:173–83.

Audiguier M., Geremew Z. et Cojean R., 2008. Relations enter les microstructures de deux sols argileux de la région parisienne et leur sensibilité au retrait gonflement, LCPC.

BEACON D3.1, 2018. Description of the constitutive models available at the start of the project. Conceptual bases, mathematical description and capabilities and shortcomings

BEACON D5.1.1, 2018. Specifications for BEACON WP5: testing, verification and validation of models. Step 1- verification cases.

Bishop AW., 1959. The principle of effective stress. Teknisk Ukeblad; 39:859–863.

Borgesson L., L.E. Johannesson, T. Sandén, J. Hernelind. 1995. Modelling of the physical behaviour of water saturated clay barriers. Laboratory tests, material models and finite element application. SKB Technical report 95-20.

Börgesson L, Hernelind J, 2014. Modelling of bentonite block compaction P-14-10", SKB.

Börgesson L, Hernelind J, Åkesson M, 2018. EBS TF - THM modelling. Homogenisation task. SKB P-18-05. Svensk Kärnbränslehantering AB.

Brooks R. N. et Corey A., 1964. T. Hydraulic properties of porous media, Colorado State University Hydrology Paper No. 3.

Charlier R., 1987. Approche unifiée de quelques problèmes non linéaires de mécanique des milieux continus par la méthode des éléments finis. PhD Thesis, Université de Liège in Department ArGEnCo, Liège, Belgium.

Collin F, Li XL, Radu JP, and Charlier R., 2002. Thermo-hydro-mechanical coupling in clay barriers. Engineering Geology. 64(2-3):179-193.

Cui Y. J. 2017. On the hydro-mechanical behaviour of MX80 bentonite-based materials, Journal of Rock Mechanics and Geotechnical Engineering. - 2017. - pp. 565-574

Dagher E.E., Nguyen T.S. & Infante Sedano J.A. 2018. Development of a mathematical model for gas migration (two-phase flow) in natural and engineered barriers for radioactive waste disposal. From: Norris, S., Neeft, E.A.C. & Van Geet, M. (eds) Multiple Roles of Clays in Radioactive Waste Confinement, Geological Society, London, Special Publications, 482.

Daniel D. E. 1982. Measurement of hydraulic conductivity of unsaturated soils with thermocouple psychrometers.: Soil Science Society of America Journal, 1982. - Vol. 20.

Dieudonné A.-C., 2016. Hydro-mechanical behaviour of compacted bentonite: from micro-scale analysis to macro-scale modelling. Université of Liège.

Dixon D. A., Graham J., Gray M. N., 1999. Hydraulic conductivity of clays in confined tests under low hydraulic gradients,Canada Geotechnique, Vol. 36.

Dueck A, 2004. Hydro-mechanical properties of a water unsaturated sodium bentonite. PhD thesis, Lund University.

Dueck A, Goudarzi R, Börgesson L, 2011. Buffer homogenization, status report. SKB TR-12-02, Svensk Kärnbränslehantering AB.

Dueck A, Nilsson U, 2010. Thermo-Hydro-Mechanical properties of MX-80. Results from advanced laboratory tests. SKB TR-10-55, Svensk Kärnbränslehantering AB.

Dueck A, Goudarzi R, Börgesson L, 2014. Buffer homogenisation, status report 2. SKB TR-14-25, Svensk Kärnbränslehantering AB.

Dueck A, Börgesson L, Kristensson O, Malmberg D, Åkesson M 2018. Bentonite homogenization. Laboratory study, model development and modelling of homogenisation processes. Svensk Kärnbränslehantering AB. In progress.

Ewen J, Thomas HR.1989. Heating unsaturated medium sand. 10.1680/geot.1989.39.3.455

Francois B. and Laloui L., 1988. ACMEG-TS: A constitutive model for unsaturated soils under non-isothermal conditions. International Journal for Numerical and Analytical Methods in Geomechanics, 2008. 32:1955-1988.

Fredlund D. G. et Rahardjo H., 1993. Soil mechanics for unsaturated soils Wiley.

Gatabin C. [et al.], 2006. ESDRED Project –Module 1. Selection and THM characterisation of the buffer material. Commissariat à l'Energie Atomique.

Gatabin C., Guillot W. et Bernachy, 2016. F. F.T. Caractérisation bentonite - Rapport final, Technical report, Commissariat à l'Energie Atomique (CEA).

Gens A. et Alonso E. E., 1992. A framework for the behaviour of unsaturated expansive clays, Canadian Geotechnical Journal 29. pp. No. 6, 1013–1032.

Gens A, Valleján B, Sánchez M, Imbert C, Villar MV, Van Geet M., 2011. Hydromechanical behaviour of a heterogeneous compacted soil: experimental observations and modelling. Géotechnique. 61(5):367–86.

Gens, A., Sánchez, M., Guimaraes, L. D. N., Alonso, E. E., Lloret, A., Olivella, S., ... & Huertas, F., 2009. A full-scale in situ heating test for high-level nuclear waste disposal: observations, analysis and interpretation. Géotechnique, 59(4), 377.

Howell P, Kozyreff G, Ockenden J, 2009. Applied Solid Mechanics. Cambridge University Press, Cambridge.

Gharbieh H, Pulkkanen V. 2018. THcM model status at VTT. EC-BEACON Deliverable D3.1 Annex G.

Ghiadistri GM, 2019. Constitutive modelling of compacted clays for applications in nuclear waste disposal. PhD thesis, Imperial College London.

Hujeux J.C., 1979. Calcul numérique de problèmes de consolidation élastoplastique. PhD Thesis, Ecole Centrale, Paris, France.

Jacinto AC, Villar M, Ledesma A, 2012. Influence of water density on the water retention curve of expansive clays. Géotechnique 62(8):657-667.

Kolditz, O.; Bauer, S.; Bilke, L.; Böttcher, N.; Delfs, J. O.; Fischer, T. et al., 2012. OpenGeoSys. An open-source initiative for numerical simulation of thermo-hydro-mechanical/chemical (THM/C) processes in porous media. In Environ Earth Sci 67 (2), pp. 589–599. DOI: 10.1007/s12665-012-1546-x.

Komine H. 2004. Simplified evaluation on hydraulic conductivities of sand–bentonite mixture backfill : Applied Clay Science. - Vol. 26.

Koudelka T, Krejčí T, Kruis J., 2017. Numerical modelling of expansive clays. In: Fuis V (Ed.), Engineering Mechanics 2017, 23rd Intl. Conf., Brno University of Technology, Brno, Czech Republic, ISBN 978-80-214-5497-2.

Kristensson O., M. Åkesson, 2008. Mechanical modeling of MX-80 – Quick tools for BBM parameter analysis. Physics and Chemistry of the Earth, Parts A/B/C, Volume 33, 2008, P.:S508-S515.

Kunz, H., 2012. GINA_OGS. In O. Kolditz, U. J. Görke, H. Shao, W. Wang (Eds.): Thermo-hydro-mechanical-chemical processes in fractured porous media. Benchmarks and examples. Berlin, Heidelberg [u.a.]: Springer (Lecture Notes in Computational Science and Engineering, 86), pp. 353–355.
Lewis, R. W.; Schrefler, B. A., 1998. The finite element method in the static and dynamic deformation and consolidation of porous media. 2nd ed. Chichester, New York: John Wiley.
Lloret, A.; Villar, M. V., 2007. Advances on the knowledge of the thermo-hydro-mechanical behaviour of heavily compacted "FEBEX" bentonite. In Physics and Chemistry of the Earth, Parts A/B/C 32 (8-14), pp. 701–715. DOI: 10.1016/j.pce.2006.03.002.
Lloret, A.; Villar, M. V.; Sánchez, M.; Gens, A.; Pintado, X.; Alonso, E. E., 2003. Mechanical behaviour of heavily compacted bentonite under high suction changes. In Géotechnique 53 (1), pp. 27–40. DOI: 10.1680/geot.53.1.27.37258.
Lloret A., Villar M. V. et Pintado X., 2002. Ensayos THM: Informe de síntesis. Internal report CIEMAT.
Marcial D., 2003. Comportement hydromécanique et microstructural des matériaux de barrière ouvragée. Ph.D. thesis, ENPC.
Mašín D, 2013. Coupled Thermohydromechanical Double-Structure Model for Expansive Soils. J. Eng. Mech. 143(9):04017067.
Mašín D, 2017. Double structure hydromechanical coupling formalism and a model for unsaturated expansive clays. Eng. Geol. 165:73-88.
Molinero-Guerra A., Mokni N., Cui Y.J., Tang A.M., Aimedieu P., Delage P., Bernier F. and Bornet M., 2016. Water retention properties and microstructure of bentonite pellets/powder mixture.
Molinero Guerra A, Mokni N, Cui YJ, Tang AM, Delage P, Aimedieu P, Bernier F, Bornert M, 2018. Experimental characterisations of the hydro-mechanical behaviour of a pellet/powder bentonite mixture. 7th Int. Conf. Unsat. Soils, HK.

Molinero A. G. [et al.], 2019. Characterization of water retention, compressibility and swelling properties of a pellet/powder bentonite mixture, Engineering geology - Vol. 248.
Molinero Guerra A., 2019. Experimental and numerical characterizations of the hydro-mechanical behavior of a heterogeneous material: pellet/powder bentonite mixture, phD Ecole des Ponts ParisTech.

V. Navarro, L. Asensio, Á.Yustres, X. Pintado, 2014. J. Alonso. An elastoplastic model of bentonite free swelling. Engineering Geology, Volume181, 2014, P.: 190-201.

Navarro V, Asensio L, Alonso J, Yustres Á, Pintado X. 2015. Multiphysics implementation of advanced soil mechanics models. 10.1016/j.compgeo.2014.03.012

Navarro V, Asensio L, De la Morena G, Pintado X, Yustres Á. 2015. Differentiated intra- and inter-aggregate water content models of MX-80 bentonite. 10.1016/j.clay.2015.10.015

Navarro V, Yustres Á, Asensio L, De la Morena G, González-Arteaga J, Laurila T, Pintado X. 2017. Modelling of compacted bentonite swelling accounting for salinity effects. 10.1016/j.enggeo.2017.04.016

Nermoen, A.; Korsnes, R. I.; Hiorth, A.; Madland, M. V., 2015. Porosity and permeability development in compacting chalks during flooding of nonequilibrium brines. Insights from long-term experiment. In J. Geophys. Res. Solid Earth 120 (5), pp. 2935–2960. DOI: 10.1002/2014JB011631

Noiret, A., S. Bethmont, J.-M. Bosgiraud and R. Foin, 2016. - DOPAS Work Package 4 Deliverable 4.8 FSS Experiment Summary Report (http://www.posiva.fi/files/4416/DOPAS_D4_8_FSS_Experiment_Summary_Report_31082016.pdf)

Olivella S, Carrera J, Gens A, Alonso EE.,1994. Non-isothermal multiphase flow of brine and gas through saline media. Transp Porous Media. 1994;15(3):271–93.

Olivella S, Gens A. 2000. Vapour transport in low permeability unsaturated soils with capillary effects. Transport in Porous Media 40, No. 2, 219-241

Pollock DW. 1986. Simulation of Fluid Flow and Energy Transport Processes Associated With High-Level Radioactive Waste Disposal in Unsaturated Alluvium. 10.1029/WR022i005p00765

Posiva, 2012. Safety case for the disposal of spent nuclear fuel at Olkiluoto. Features, events and processes 2012 (No. POSIVA--12-7). Posiva Oy.

Potts DM, Zdravkovic L, 1999. Finite element analysis in geotechnical engineering: theory. Thomas Telford, London.

Potts DM, Zdravkovic L, 2001. Finite element analysis in geotechnical engineering: application. Thomas Telford, London.

Quintessa, 2013. QPAC: Quintessa's General-Purpose Modelling Software. Quintessa report QRS-QPAC-11, available from https://www.quintessa.org/software/QPAC

Richards, L. A., 1931. Capillary Conduction of Liquids Through Porous Mediums. In Physics 1 (5), pp. 318–333. DOI: 10.1063/1.1745010.

Roscoe KH, Burland JB, 1968. On the generalised stress-strain behaviour of 'wet clay'. In: Heyman J, Leckie FA (eds) Engineering plasticity. Cambridge University Press, Cambridge, pp 535-609

Rutquist J. et al., 2014. Modeling of Coupled Thermo-Hydro-Mechanical Processes with Links to Geochemistry Associated with Bentonite-Backfilled Repository Tunnels in Clay formations. Rock Mechanics and Rock Engineering, 47, 2014, P.: 167-186.

Saiyouri N., Hicher P. Y. et Tessier D., 2000. Microstructural approach and transfer water modelling in highly compacted unsaturated swelling clays. Mechanics of Cohesive-Frictional Materials. - Vol. 5.

Sánchez M., 2004. Thermo-Hydro-Mechanical coupled analysis in low permeability media. PhD Thesis, Universitat Politecnica de Catalunya, Spain. 2004.

Sanchez M, Gens A, Guimarães L, Olivella S., 2005. A double structure generalized plasticity model for expansive materials. Int J Numer Anal Methods Geomech. 2005;29(8):751–87.

Seiphoori A., Ferrari A. and Laloui L., 2014. Water retention behaviour and microstructural evolution of MX-80 bentonite during wetting and drying cycles. Géotechnique, Volume 64(9), 2014, P.: 721-734.

Seiphoori A. [et al.], 2016. Water retention and swelling behaviour of granular bentonites for application in Geosynthetic Clay Liner (GCL) systems. Soils and Foundations.

Tang AM, Cui YJ, Barnel N, 2008. Compression-induced suction change in a compacted expansive clay. 1st European Conference on Unsaturated Soils, E-UNSAT 2008, 369-374. CRC Press, Durham, United Kingdom.

Tang A. M. and Cui Y. J., 2010. Effects of mineralogy on thermo-hydro-mechanical parameters of MX80 bentonite. Journal of Rock Mechanics and Geotechnical Engineering. (1): 91–96.

Thatcher KE, Bond AE, Robinson P, McDermott C, Fraser Harris AP, Norris S, 2016. A new hydro-mechanical model for bentonite resaturation applied to the SEALEX experiments. Environmental Earth Sciences 75(11) doi: 10.1007/s12665-016-5741-z

Thatcher KE, 2017. FEBEX-DP: THM modelling. Contractor report to RWM QRS-1713A-R2

E. Toprak, S. Olivella, X. Pintado, 2015. THM modeling of Onkalo project (Finland)-final disposal of radioactive spent nuclear fuel. In international Symposium on Energy Geotechnics SEG 2015, Barcelona, Spain, June 2-4, 2015.

E. Toprak, N. Mokni, S. Olivella, X. Pintado, 2013. Thermo-Hydro-Mechanical Modelling of Buffer. POSIVA report 2012-47, Eurajoki, Finland, 2013.

UPC, 2017. CODE-BRIGHT users guide, Universitat Politècnica de Catalunya, Barcelona, Spain, 2017.

Van Geet M., Volckaert G. et Roels S., 2005. The use of microfocus X-ray computed tomography in characterising the hydration of a clay pellet/powder mixture, Applied Clay Science. - Vol. 29.

Van Genuchten MT, 1980. A closed-form equation for predicting the hydarulic conductivity of unsaturated soils. Soil Sci. Soc. Am. J., **44**, 892-898.

Villar M. V., 2004. MX-80 Bentonite. Thermo-Hydro-Mechanical Characterisation Performed at CIEMAT in the Context of the Prototype Project. CIEMAT report CIEMAT/DIAE/54540/2/04, 2004.

Villar M. V. 2005. MX-80 Bentonite. Thermo-hydro-mechanical characterisation performed at CIEMAT in the context of the prototype project. Informes técnicos Ciemat 1053.

Villar M. V. 2004. Thermo-Hydro-Mechanical Characteristics and Processes in the Clay Barrier of a High Level Radioactive Waste Repository. State of the Art Report Ciemat, 2004.

Wang X., H. Shao, W. Wang, J. Hesser, O. Kolditz, 2015. Numerical modeling of heating and hydration experiments on bentonite pellets. Engineering Geology, Volume 198, 2015, P.: 94-106.

Wang Q, Tang AM, Cui Y-J, Delage P, Gatmiri B, 2012. Experimental study of the swelling behaviour of bentonite/clay-stone mixture. Eng Geol 124:59-66. doi:10.1016/j.en.geo.2011.10.003

Wang Q, Cui Y-J, Tang AM, Barnichon J-D, Saba S, Ye W-M, 2013. Hydraulic conductivity and microstructure changes of compacted bentonite/sand mixture during hydration. Eng Geol 164:67-76, doi:10.1016/j.cageo.2010.10.011

Wang Q. [et al.], 2013. A comparative study on the hydro-mechanical behavior of compacted bentonite/sand plug based on laboratory and field infiltration tests, Engineering Geology,. - Vol. 162.

Wang Q. [et al.], 2013. Investigation of the hydro-mechanical behaviour of compacted bentonite/sand mixture based on the BExM model, Computers and Geotechnics,

Wang Q. [et al.], 2013. The effects of technological voids on the hydro-mechanical behaviour of compacted bentonite–sand mixture, Soils and Foundations 53. pp. No. 2, 232–245.

Wheeler S. J. et Karube D., 1995. Constitutive modelling, Proceedings of the First International Conference on Unsaturated Soils. - Paris, 1995.

8 Appendix

8.1 Claytech

8.1.1 Appendix 1 Comsol implementation

The equation system describing the model to implement in COMSOL is given below together with brief comments relating to the implementation of the different parts. The implementation of the mechanical material model (providing the stress as a function of independent variables) is outlined in the latter part of this appendix.

Balance of solid mass: $\dot{\phi} = (1-\phi)\,\dot{\varepsilon}_v$

The solid mass balance has been implemented as a user input equation to provide the updating scheme for the porosity.

Balance of water mass: $\dot{\rho}_w\phi + \rho_w\phi\,\mathrm{div}(\dot{\boldsymbol{u}}_w - \dot{\boldsymbol{u}}_s) + \rho_w\dot{\varepsilon}_v = f_w$

The water mass balance has been implemented by use of a generic partial-differential-equation-input option.

Balance of forces: $\mathrm{div}\boldsymbol{\sigma} + \boldsymbol{b} = \boldsymbol{0}$

COMSOL's available option for accounting for the force balance was used.

Constitutive equation for flow of water in the porous media: $\dot{\boldsymbol{u}}_w - \dot{\boldsymbol{u}}_s = \tilde{\boldsymbol{q}}(s)$

Darcy's law was implemented in connection with defining the water mass balance as a user input.

Constitutive equation for the water density: $\rho_w = \tilde{\rho}_w(s) = \rho_{w0}\exp(-\beta s)$.

This was implemented by the user input option.

Constitutive equation for the stresses, mechanics: $d\boldsymbol{\sigma} = d\tilde{\boldsymbol{\sigma}}(d\boldsymbol{u}_s, ds, \boldsymbol{f})$

This was implemented using the available "General stress-strain relation"-option.

Mechanical material model implementation

GENERAL STRESS-STRAIN RELATION

The **General stress-strain relation** socket implements a stress-strain relation computing a second Piola-Kirchhoff stress tensor given the current Green-Lagrange strain together with a material property vector and a vector of stored states. The expected external material function signature is:

```
int eval(double *e,            // Green-Lagrange strain, input
         double *s,            // Second Piola-Kirchhoff stress, output
         double *D,            // Jacobian of stress with respect to strain,output
         int *nPar,            // Number of material model parameters, input
         double *par,          // Material model parameters, input
         int *nStates,         // Number of states, input
         double *states) { }   // States, input/output
```

The e and s tensors are given in Voigt order; that is., the components in e are $\{e_{xx}, e_{yy}, e_{zz}, e_{yz}, e_{xz}, e_{xy}\}$ and similarly for s. The Jacobian D is a 6-by-6 matrix of partial derivatives of components of s (rows) with respect to components of e (columns); the matrix is stored in row-major order.

The implementation of the material model into COMSOL is performed by using the available user defined 'General stress-strain relation socket' which is described above. Using the input in form of

$$(\boldsymbol{\varepsilon}^0, \boldsymbol{\varepsilon}^1, s^0, s^1, \boldsymbol{\sigma}^0, \boldsymbol{f}^0)$$

and material parameter values, the output,

$$(\boldsymbol{\sigma}^1, \boldsymbol{f}^1, \mathbb{C}^1),$$

should be calculated within the module. A superscripted 0 means that the variable belongs to the state at the beginning of the current time step and variables with 1 as a superscript belong at the end of the current time step.

Within the module the internal variable $\boldsymbol{f}$ and stress $\boldsymbol{\sigma}$ are updated from the known state, 0, to the unknown state, 1. Due to the nonlinearity of the model the updating is accomplished by integration of the incremental relations (described in the next section),

$$\boldsymbol{f}^1 = \boldsymbol{f}^0 + \int_{\boldsymbol{f}^0}^{\boldsymbol{f}^1} d\boldsymbol{f}^* = \boldsymbol{f}^0 + \int_{\boldsymbol{\varepsilon}^0}^{\boldsymbol{\varepsilon}^1} \frac{\partial \boldsymbol{f}}{\partial \boldsymbol{\varepsilon}} d\boldsymbol{\varepsilon}^* \text{ and } \boldsymbol{\sigma}^1 = \boldsymbol{\sigma}^0 + \int_{\boldsymbol{\sigma}^0}^{\boldsymbol{\sigma}^1} d\boldsymbol{\sigma}^* \qquad \text{(A1-1)}$$
$$= \boldsymbol{\sigma}^0 + \int_{\boldsymbol{\varepsilon}^0}^{\boldsymbol{\varepsilon}^1} \mathbb{C} d\boldsymbol{\varepsilon}^* + \int_{s^0}^{s^1} \mathbf{1} ds^* .$$

The integration is approximated using a Euler forward scheme with sub-incrementation, i.e.

$$\boldsymbol{f}^1 \approx \boldsymbol{f}^0 + \sum_{\alpha=1}^{N} \left.\frac{\partial \boldsymbol{f}}{\partial \boldsymbol{\varepsilon}}\right|_{\alpha-1} \Delta\boldsymbol{\varepsilon}_\alpha \text{ and} \qquad \text{(A1-2)}$$
$$\boldsymbol{\sigma}^1 \approx \boldsymbol{\sigma}^0 + \sum_{\alpha=1}^{N} \mathbb{C}|_{\alpha-1} \Delta\boldsymbol{\varepsilon}_\alpha + \sum_{\alpha=1}^{N} \mathbf{1} \Delta s_\alpha .$$

Here the final solution at 1 is obtained by performing subsequent updating from 0 to 1 in N substeps. The Jacobians are calculated at the beginning of the sub step (Euler forward) which is indicated by the notation $<\cdot>|_{\alpha-1}$.
In the implementation the variables are subsequently updated to the state at the end of the α^{th} sub-step according to:

$$\left.\begin{aligned} {\boldsymbol{f}^0}_\alpha &= {\boldsymbol{f}^0}_{\alpha-1} + \left.\frac{\partial \boldsymbol{f}}{\partial \boldsymbol{\varepsilon}}\right|_{\alpha-1} \Delta\boldsymbol{\varepsilon}_\alpha \\ {\boldsymbol{\sigma}^0}_\alpha &= {\boldsymbol{\sigma}^0}_{\alpha-1} + \mathbb{C}|_{\alpha-1} \Delta\boldsymbol{\varepsilon}_\alpha + \mathbf{1}\Delta s_\alpha \end{aligned}\right\} \text{for } \alpha = 1, 2 \cdots N \qquad \text{(A1-3)}$$

where ${\boldsymbol{f}^0}_0 = \boldsymbol{f}^0$ and ${\boldsymbol{\sigma}^0}_0 = \boldsymbol{\sigma}^0$. The convergence criterion, which determines whether the solution should be accepted or not, is based on that the chosen norm of the difference in the stress solution from using N and $N/2$ subincrements should be less than a given tolerance, i.e.

$$\sqrt{\left(\boldsymbol{\sigma}^0{}_N - \boldsymbol{\sigma}^0{}_{N/2}\right) \cdot \left(\boldsymbol{\sigma}^0{}_N - \boldsymbol{\sigma}^0{}_{N/2}\right)} < tol \,. \tag{A1-4}$$

If the criterion is fulfilled, the solution is accepted as the updated state, i.e. $\boldsymbol{f}^1 = \boldsymbol{f}^0{}_N$ and $\boldsymbol{\sigma}^1 = \boldsymbol{\sigma}^0{}_N$.
If the criterion is not fulfilled for $N \leq N_{MAX}$, where N_{MAX} is to be specified by the user, the module sends out an erroneous (NaN) stress component so that COMSOL decreases the time step taken from the known state and the integration procedure described above restarts.

Incremental form of the mechanical material model
The mechanical material model may be expressed as,

$$\boldsymbol{\sigma} = \tilde{\boldsymbol{\sigma}}(\boldsymbol{\varepsilon}, \boldsymbol{f}, s), \tag{A1-5}$$

and the time derivative can then be written,

$$\dot{\boldsymbol{\sigma}} = \frac{\partial \boldsymbol{\sigma}}{\partial \boldsymbol{\varepsilon}} \dot{\boldsymbol{\varepsilon}} + \frac{\partial \boldsymbol{\sigma}}{\partial \boldsymbol{f}} \dot{\boldsymbol{f}} + \frac{\partial \boldsymbol{\sigma}}{\partial s} \dot{s} \,, \tag{A1-6}$$

where,

$$\frac{\partial \boldsymbol{\sigma}}{\partial \boldsymbol{\varepsilon}} = \frac{\partial \boldsymbol{\sigma}}{\partial \boldsymbol{\psi}} \frac{\partial \boldsymbol{\psi}}{\partial \boldsymbol{\varepsilon}} \quad \text{and} \quad \frac{\partial \boldsymbol{\sigma}}{\partial \boldsymbol{f}} = \frac{\partial \boldsymbol{\sigma}}{\partial \boldsymbol{\psi}} \frac{\partial \boldsymbol{\psi}}{\partial \boldsymbol{f}} \,. \tag{A1-7}$$

The ingoing derivatives are given by,

$$\frac{\partial \boldsymbol{\sigma}}{\partial \boldsymbol{\psi}} = -\mathbb{I}, \tag{A1-8}$$

where $\mathbb{I}$ = denotes the fourth order unit tensor,

$$\frac{\partial \boldsymbol{\psi}}{\partial \boldsymbol{\varepsilon}} = \frac{\partial \psi_M}{\partial \varepsilon_v} \mathbf{1} \otimes \mathbf{1} + \frac{\partial \psi_{\Delta/2}}{\partial \varepsilon_v} \boldsymbol{f} \otimes \mathbf{1} \,, \tag{A1-9}$$

$$\frac{\partial \boldsymbol{\psi}}{\partial \boldsymbol{f}} = \psi_{\Delta/2} \mathbb{I} \,,$$

$$\dot{\boldsymbol{f}} = \frac{\partial \boldsymbol{f}}{\partial \boldsymbol{\varepsilon}} \dot{\boldsymbol{\varepsilon}} \,,$$

and

$$\frac{\partial \boldsymbol{\sigma}}{\partial s} = \mathbf{1} \,. \tag{A1-10}$$

Using all the above gives,

$$\dot{\boldsymbol{\sigma}} = \left[-\frac{\partial\psi_M}{\partial\varepsilon_v}\mathbf{1}\otimes\mathbf{1} - \frac{\partial\psi_{\Delta/2}}{\partial\varepsilon_v}\boldsymbol{f}\otimes\mathbf{1} - \psi_{\Delta/2}\frac{\partial\boldsymbol{f}}{\partial\boldsymbol{\varepsilon}}\right]\dot{\boldsymbol{\varepsilon}} + \mathbf{1}\dot{s} = \mathbb{C}\dot{\boldsymbol{\varepsilon}} + \mathbf{1}\dot{s}\,, \tag{A1-11}$$

when expressed on index free notation and

$$\begin{aligned}\dot{\sigma}_{ij} &= \left[-\frac{\partial\psi_M}{\partial\varepsilon_v}\delta_{ij}\delta_{kl} - \frac{\partial\psi_{\Delta/2}}{\partial\varepsilon_v}f_{ij}\delta_{kl} - \psi_{\Delta/2}\left(\frac{\partial\boldsymbol{f}}{\partial\boldsymbol{\varepsilon}}\right)_{ijkl}\right]\dot{\varepsilon}_{kl} + \delta_{ij}\dot{s} \\ &= C_{ijkl}\dot{\varepsilon}_{kl} + \delta_{ij}\dot{s}\,,\end{aligned} \tag{A1-12}$$

when expressed on index notation.

Matrix format

In COMSOL second order tensors are represented by column arrays where components are given in Voigt order. It should be noted that in the implementation the "shear components" of the stiffness matrix, $[\mathbb{C}]$, are given by $C_{1111} \cdot ratio$, where $ratio$ is to be specified by the user.

$$[\boldsymbol{\sigma}] = \begin{bmatrix}\sigma_{11}\\\sigma_{22}\\\sigma_{33}\\\sigma_{23}\\\sigma_{13}\\\sigma_{12}\end{bmatrix}, \qquad [\boldsymbol{f}] = \begin{bmatrix}f_{11}\\f_{22}\\f_{33}\\0\\0\\0\end{bmatrix}, \qquad [\boldsymbol{\varepsilon}] = \begin{bmatrix}\varepsilon_{11}\\\varepsilon_{22}\\\varepsilon_{33}\\\varepsilon_{23}\\\varepsilon_{13}\\\varepsilon_{12}\end{bmatrix} \tag{A1-13}$$

$$[\mathbb{C}] = \begin{bmatrix}C_{1111} & \cdots & C_{1112}\\ \vdots & \ddots & \vdots\\ C_{1211} & \cdots & C_{1212}\end{bmatrix} = \begin{bmatrix}[\mathbb{c}] & [0]\\ [0] & [\mathbb{d}]\end{bmatrix}$$

$$[\mathbb{c}] = \begin{bmatrix} -\frac{\partial\psi_M}{\partial\varepsilon_v} - \frac{\partial\psi_{\frac{\Delta}{2}}}{\partial\varepsilon_v}f_{11} - \psi_{\Delta/2}\frac{\partial f_{11}}{\partial\varepsilon_{11}} & -\frac{\partial\psi_M}{\partial\varepsilon_v} - \frac{\partial\psi_{\Delta/2}}{\partial\varepsilon_v}f_{11} & -\frac{\partial\psi_M}{\partial\varepsilon_v} - \frac{\partial\psi_{\Delta/2}}{\partial\varepsilon_v}f_{11} \\ -\frac{\partial\psi_M}{\partial\varepsilon_v} - \frac{\partial\psi_{\Delta/2}}{\partial\varepsilon_v}f_{22} & -\frac{\partial\psi_M}{\partial\varepsilon_v} - \frac{\partial\psi_{\frac{\Delta}{2}}}{\partial\varepsilon_v}f_{22} - \psi_{\Delta/2}\frac{\partial f_{22}}{\partial\varepsilon_{22}} & -\frac{\partial\psi_M}{\partial\varepsilon_v} - \frac{\partial\psi_{\Delta/2}}{\partial\varepsilon_v}f_{22} \\ -\frac{\partial\psi_M}{\partial\varepsilon_v} - \frac{\partial\psi_{\Delta/2}}{\partial\varepsilon_v}f_{33} & -\frac{\partial\psi_M}{\partial\varepsilon_v} - \frac{\partial\psi_{\Delta/2}}{\partial\varepsilon_v}f_{33} & -\frac{\partial\psi_M}{\partial\varepsilon_v} - \frac{\partial\psi_{\Delta/2}}{\partial\varepsilon_v}f_{33} - \psi_{\Delta/2}\frac{\partial f_{33}}{\partial\varepsilon_{33}} \end{bmatrix}$$

$$[\mathbb{d}] = C_{1111} \cdot ratio \begin{bmatrix}1 & 0 & 0\\0 & 1 & 0\\0 & 0 & 1\end{bmatrix}$$

Further details on this implementation is presented in Dueck et al. (2018).

8.1.2 Appendix 2 Numerical solution 1b

General scheme

A numerical solution was developed for analysing the processes in Test 1b. The test geometry was simplified as a 1D axial homogenisation problem without any wall friction. The geometry was discretized as an array of n elements with equal initial length, from here on denoted with index i ranging from 0 to n-1 (Figure A2-1), and of an array of n+1 nodes with index i ranging from 0 to n. The confinement of the specimen implied that the radial strain of each element was zero. In axial direction the total length was constant which implied that the sum of the axial strains was zero. A hydraulic boundary condition with a specified suction value was applied at the end of the first element (Figure A2-1).

The problem was discretized in time with a specified time increment Δt. The calculation was performed iteratively so that the following seven steps were made during each time step:

i. Water content increments (Δw^i) were calculated from suction gradients, Darcy´s law, vapor diffusion relation and water mass balance for a given time increment.
ii. Increments in axial stress ($\Delta\sigma_1$) and strains ($\Delta\varepsilon_1^i$) were calculated from interaction functions, water content increments, and the conditions that the axial stress increment was homogenous, and that the sum of axial strains was zero.
iii. Micro void ratio increments (Δe_m^i) were calculated from increments in axial strains and water contents.
iv. Path variable increments (Δf_1^i and Δf_2^i) were calculated from axial strain increments, strain relations and path variable equations.
v. Radial stress ($\Delta\sigma_2^i$) increments were calculated from Δe_m^i, Δf_2^i, $\Delta\varepsilon_1^i$ and Δw^i.
vi. Suction increments (Δs^i) were calculated from Δe_m^i and Δw^i.
vii. All variables and coordinates (x^i) were updated.

The first six steps are described in more depth below.

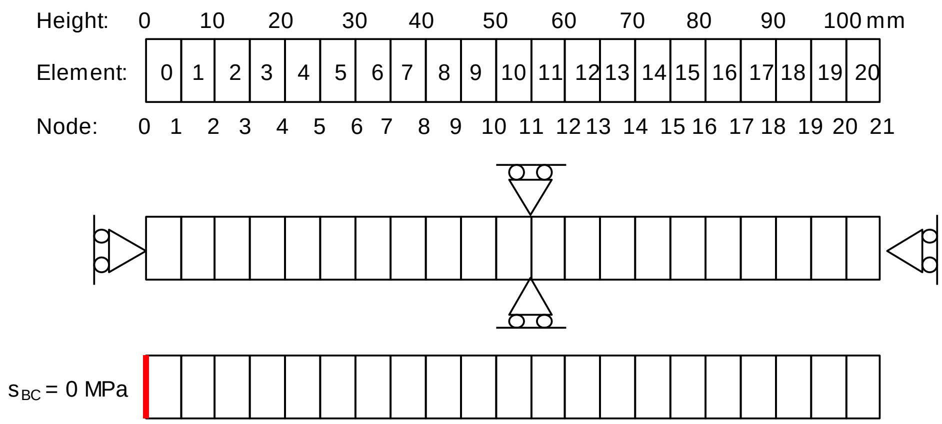

Figure A2-1. *Model geometry and discretization (upper). Boundary conditions: mechanical (middle) and hydraulic (lower).*

Water content

The mass flow rate (J) for node 1 to n-1 was calculated from the suction gradient, the section area (A) and average values of void ratio, saturation degree ($S_l = e_m/e$) and suction for two adjacent elements:

$$J^i = D\left[\frac{e^i + e^{i-1}}{2}, \frac{S_l^i + S_l^{i-1}}{2}, \frac{s^i + s^{i-1}}{2}\right] \cdot \frac{s^i - s^{i-1}}{\frac{x^{i+1} - x^{i-1}}{2}} \cdot A \qquad \text{(A2-1)}$$

The flow coefficient D was calculated as the sum of the contribution from both vapor diffusion (2-35) and advective liquid flow (2-31):

$$D(\bar{e}, \bar{S}_l, \bar{s}) = \frac{\bar{e}}{1+\bar{e}} \cdot (1 - \bar{S}_l) \cdot D_m^w \frac{M_w}{RT} \frac{\rho_v(\bar{s})}{\rho_w(\bar{s})} + \rho_w(\bar{s}) \cdot K_H(\bar{e}, \bar{S}_l) \qquad \text{(A2-2)}$$

K_H is a function of void ratio and the degree of saturation, see Eq (4-2), whereas the density of water is a function of suction, Eq (2-21).

The corresponding mass flow rate for node 0 was calculated in a similar way, for half the length of the first element, and by taking the boundary suction into account. For node n the mass flow rate was zero. The increment in water content was calculated from the difference between the mass flow rate in and out from each element, the time increment and the solid mass of each element (m_s):

$$\Delta w^i = \left(J^i - J^{i+1}\right) \cdot \frac{\Delta t}{m_s} \qquad \text{(A2-3)}$$

Axial stress and strains

Increments in axial stress and strains could be calculated from interaction functions, water content increments, and the conditions that the axial stress increment was homogenous, and that the sum of axial strains was zero. This was based on the interaction functions (2-23) for element i.

Both sides of this equation were first divided with the $\partial\sigma_1/\partial{\varepsilon_1}^i$- derivative. Each term was then added together for all elements, i.e. i = 0 to n-1:

$$\sum_{i=0}^{n-1}\left(\frac{\partial{\sigma_1}^i}{\partial\varepsilon_1}\right)^{-1} d\sigma_1 = \sum_{i=0}^{n-1} d\varepsilon_1^i + \sum_{i=0}^{n-1}\frac{\partial{\sigma_1}^i}{\partial w}\left(\frac{\partial{\sigma_1}^i}{\partial\varepsilon_1}\right)^{-1} dw^i \tag{A2-4}$$

The sum of the stains on the right side is equal to zero, whereas the stress differential ($d\sigma_1$) is the same for all elements. This means that the stress increment could be calculated by dividing the remaining sum on the right side, which included the water content increments, with the sum of the inverse of the $\partial\sigma_1/\partial{\varepsilon_1}^i$- derivatives:

$$\Delta\sigma_1 = \sum_{i=0}^{n-1}\frac{\partial{\sigma_1}^i}{\partial w}\left(\frac{\partial{\sigma_1}^i}{\partial\varepsilon_1}\right)^{-1}\Delta w^i \cdot \left(\sum_{i=0}^{n-1}\left(\frac{\partial{\sigma_1}^i}{\partial\varepsilon_1}\right)^{-1}\right)^{-1} \tag{A2-5}$$

Finally, the strain increment of each element, was calculated from (2-23):

$$\Delta\varepsilon_1^i = -\frac{\partial{\sigma_1}^i}{\partial w}\left(\frac{\partial{\sigma_1}^i}{\partial\varepsilon_1}\right)^{-1}\Delta w^i + \left(\frac{\partial{\sigma_1}^i}{\partial\varepsilon_1}\right)^{-1}\Delta\sigma \tag{A2-6}$$

Micro void ratio

An expression for calculating micro void ratio increments could be derived through differentiation of several relations:

First, the thermodynamic relation (2-18) for the axial direction:

$$ds + d\left(\frac{\sigma_1}{\alpha}\right) = d\Psi_1 \tag{A2-7}$$

Second, the relation for the water density (2-21):

$$ds = \frac{de_m}{\beta e_m} - \frac{dw}{\beta w} \tag{A2-8}$$

Third, the relation for the contact stress:

$$d\left(\frac{\sigma_1}{\alpha}\right) = \frac{1}{\alpha}d\sigma_1 - \frac{\sigma_1}{\alpha^2}\left(\frac{\partial\alpha}{\partial e_m}de_m + \frac{\partial\alpha}{\partial e}de\right) \tag{A2-9}$$

Fourth, the clay potential function (2-19):

$$d\Psi_1 = \left(\frac{d\Psi_M}{de_m} + f_1 \frac{d\Psi_{\Delta/2}}{de_m}\right) de_m + \Psi_{\Delta/2} \frac{df_1}{d\varepsilon_1^m} d\varepsilon_1^m \tag{A2-10}$$

Fifth, the relation between void ratio and axial strain:

$$de \;= (1 + e_0) d\varepsilon_1 \tag{A2-11}$$

And finally, the strain relation (2-27):

$$d\varepsilon_1^m \;= d\varepsilon_1 \tag{A2-12}$$

By combining these six relations ((A2-7) to (A2-12)) together with the interaction function (2-23), the following expression for the micro void ratio increment could be derived:

$$\Delta e_m = \frac{\left[\Psi_{\Delta/2} \frac{df_1}{d\varepsilon_1^m} + \frac{\sigma_1}{\alpha^2} \frac{\partial \alpha}{\partial e} (1 + e_0) - \frac{1}{\alpha} \frac{\partial \sigma_1}{\partial \varepsilon_1}\right] \Delta \varepsilon_1 + \left[\frac{1}{\beta w} - \frac{1}{\alpha} \frac{\partial \sigma_1}{\partial w}\right] \Delta w}{\left[\frac{1}{\beta e_m} - \frac{\sigma_1}{\alpha^2} \frac{\partial \alpha}{\partial e_m} - \frac{d\Psi_M}{de_m} - f_1 \frac{d\Psi_{\Delta/2}}{de_m}\right]} \tag{A2-13}$$

Path variables

Increments in path variables was calculated from the definition (2-14) and the strain relations (2-27):

$$\Delta f_1 = -K[1 - \Phi(\gamma_1)\gamma_1 + \mathrm{sgn}(\Delta\varepsilon_1) f_1] \cdot \Delta\varepsilon_1 \tag{A2-14}$$

$$\gamma_1 = \frac{|f_1 - f_2|}{2} + \mathrm{sgn}(\Delta\varepsilon_1) \frac{f_1 + f_2}{2}$$

$$\Delta f_2 = -K[1 - \Phi(\gamma_2)\gamma_2 + \mathrm{sgn}(-\xi\Delta\varepsilon_1) f_2] \cdot -\xi\Delta\varepsilon_1 \tag{A2-15}$$

$$\gamma_2 = \frac{|f_1 - f_2|}{2} + \mathrm{sgn}(-\xi\Delta\varepsilon_1) \frac{f_1 + f_2}{2}$$

The non-diagonal elements of the strain relation (ξ) were calculated as (2-28).

Radial stress

The increment in radial stress could be calculated with a modified set of relations used for the micro void ratio increments: i) Eq (A2-7), but with σ_2 and Ψ_2 instead of σ_1 and Ψ_1; ii) Eq (A2-8); iii) Eq (A2-9), but with σ_2 instead of σ_1; iv) (A2-10) but with f_2 and Ψ_2 instead of f_1 and Ψ_1, and with df_2 instead of $df_1/d\varepsilon_1^m \cdot d\varepsilon_1^m$; and v) Eq (A2-11). Taken together the following relation between increments in radial stress, micro void ratio, axial strain, water content, and radial path variable could be derived:

$$\Delta\sigma_2 = \alpha\left(\frac{\sigma_2}{\alpha^2}\frac{\partial\alpha}{\partial e_m} + \frac{d\Psi_M}{de_m} + f_2\frac{d\Psi_{\Delta/2}}{de_m} - \frac{1}{\beta e_m}\right)\Delta e_m + \frac{\sigma_2}{\alpha}\frac{\partial\alpha}{\partial e}(1+e_0)\Delta\varepsilon_1 + \frac{\alpha}{\beta w}\Delta w + \alpha\Psi_{\Delta/2}\Delta f_2 \quad \text{(A2-16)}$$

Suction

Finally, a relation for the suction increment was derived from (A2-8):

$$\Delta s = \frac{\Delta e_m}{\beta e_m} - \frac{\Delta w}{\beta w} \quad \text{(A2-17)}$$

8.1.3 Appendix 3 Numerical solution 1c

General scheme

A numerical solution was developed for analysing the processes in Test 1c. The test geometry was simplified as a 1D axial homogenisation problem with lateral wall friction. The geometry was discretized as an array of n elements with equal initial length, from here on denoted with index i ranging from 0 to n-1 (Figure A3-1), and of an array of n+1 nodes with index i ranging from 0 to n. The confinement of the specimen implied that the radial strain of each element was zero. In axial direction the total length was constant which implied that the sum of the axial strains was zero. The influence of wall friction on the axial stress balance was also included in the model. A hydraulic boundary condition with zero suction value was applied over half of the geometry, which was a simplification that represented an assumed rapid hydration of the pellets material (Figure A3-1).

The problem was discretized in time with a specified time increment Δt. The calculation was performed iteratively so that the following seven steps were made during each time step:

i. Water content increments (Δw^i) were calculated from suction gradients, Darcy´s law and the water mass balance for a given time increment.
ii. The increment of the displacement of node 1 (Δu^1) was calculated from the water content increments, the constitutive equations, the stress balance, *and* the condition that the Δu^n displacement increment was zero.
iii. Increments in axial strains ($\Delta\varepsilon_1^i$), axial and radial stresses ($\Delta\sigma_1^i$ and $\Delta\sigma_2^i$) and shear stresses ($\Delta\tau^i$) were calculated from the Δu^1-value and the abovementioned water content increments, constitutive equations and stress balance.
iv. Micro void ratio increments (Δe_m^i) were calculated from increments in axial strains and water contents.
v. Path variable increments (Δf_1^i and Δf_2^i) were calculated from axial strain increments, strain relations and path variable equations.
vi. Suction increments (Δs^i) were calculated from Δe_m^i and Δw^i.
vii. All variables and coordinates (x^i) were updated.

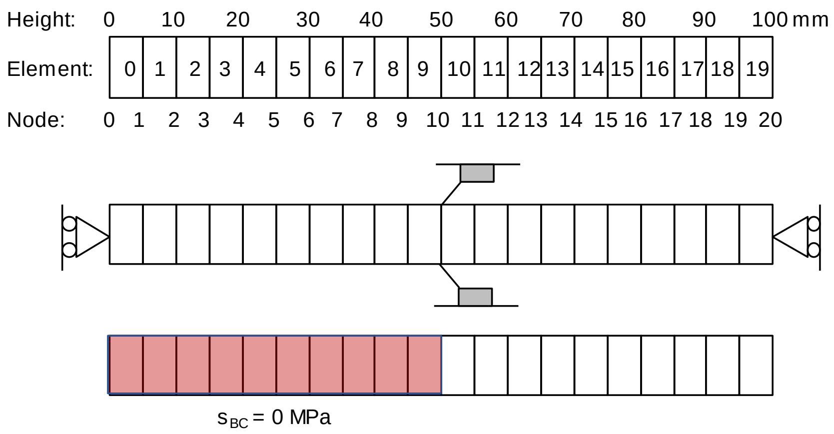

Figure A3-1. *Model geometry and discretization (upper). Boundary conditions: mechanical (middle) and hydraulic (lower).*

The first three of these steps differed from the calculation steps presented in Appendix 2 and are described in more depth below. The solutions used for the representing the pellets as water saturated throughout the calculation are also described at the end of this Appendix.

Water content increments

The water mass flow rate and the increment in water content were calculated in a similar way as for Test 1b (see Appendix 2), but in this case only advective liquid flow was included. The mass flow rate (J) for node 1 to n-1 was calculated from the suction gradient, the section area (A) and the average value of the water density and the hydraulic conductivity for two adjacent elements:

$$J^i = \frac{\rho_w^i + \rho_w^{i-1}}{2} \cdot \frac{K_H^i + K_H^{i-1}}{2} \cdot \frac{s^i - s^{i-1}}{\frac{x^{i+1} - x^{i-1}}{2}} \cdot A \qquad \text{(A3-1)}$$

K_H was calculated from the void ratio and the degree of saturation, see Eq (4-2), whereas the density of water from the suction value, Eq (2-21). The corresponding mass flow rate for node 0 was calculated in a similar way, for half the length of the first element, and by taking the boundary suction into account. For node n the mass flow rate was zero.

Stress balance and zero axial strain

The mechanical boundary conditions implied that: i) the stress balance Eq (2-29) should be fulfilled, and ii) that the sum of the axial strains was zero. The second condition implied that if the displacement at the node 0 was zero ($u^0 = 0$) then the displacement at node n should also be zero ($u^n = 0$). Based on this, a method was developed in which the displacement increment of the first node (Δu^1) was assumed. From this followed that the strain increment ($\Delta\varepsilon_1^0$) of the first element could be calculated. Together with the water content increment Δw^0, this meant that the stress increments $\Delta\sigma_1^0$, $\Delta\sigma_2^0$ and $\Delta\tau^0$ could be calculated. Based on some of these increments (i.e. $\Delta\sigma_1^0$, $\Delta\tau^0$, $\Delta\varepsilon_1^0$ and Δu^1), the stress balance and the water content increment of the second element (Δw^1) it was possible to calculate the strain increment for the second element ($\Delta\varepsilon_1^1$). An iterative calculation could thus be derived (Figure A3-2) in which the displacement increment of node n was defined as a function of the displacement increment of node 1, i.e. $\Delta u^n(\Delta u^1)$. The overall equation system could thus be solved by finding the root of this function (i.e. $\Delta u^n = 0$). Two major equations were derived in order to perform these calculations: for the strain increment ($\Delta\varepsilon_1^i$) and for the radial stress increment ($\Delta\sigma_2^i$), respectively.

Strain increments

The strain increment equation is based on the stress balance Eq (2-29). For two adjacent element (with indices i-1 and i) this can be expressed as:

$$\frac{\sigma_1^i - \sigma_1^{i-1}}{l_\Delta^{i-1}} + \frac{2}{r} \cdot \frac{\tau^i + \tau^{i-1}}{2} = 0 \tag{A3-2}$$

where l_Δ^{i-1} denotes the average length of the elements $\left(l^i + l^{i-1}\right)/2$. This can be expressed in incremental form:

$$\Delta\sigma_1^i - \Delta\sigma_1^{i-1} + \frac{l_\Delta^{i-1}}{r} \cdot \left[\Delta\tau^i + \Delta\tau^{i-1}\right] + \frac{\Delta l_\Delta^{i-1}}{r} \cdot \left[\tau^i + \tau^{i-1}\right] = 0 \tag{A3-3}$$

where Δl_Δ^{i-1} is related to the strain increments of the two elements: $\left(\Delta\varepsilon_1^i + \Delta\varepsilon_1^{i-1}\right) \cdot l_{init}/2$.

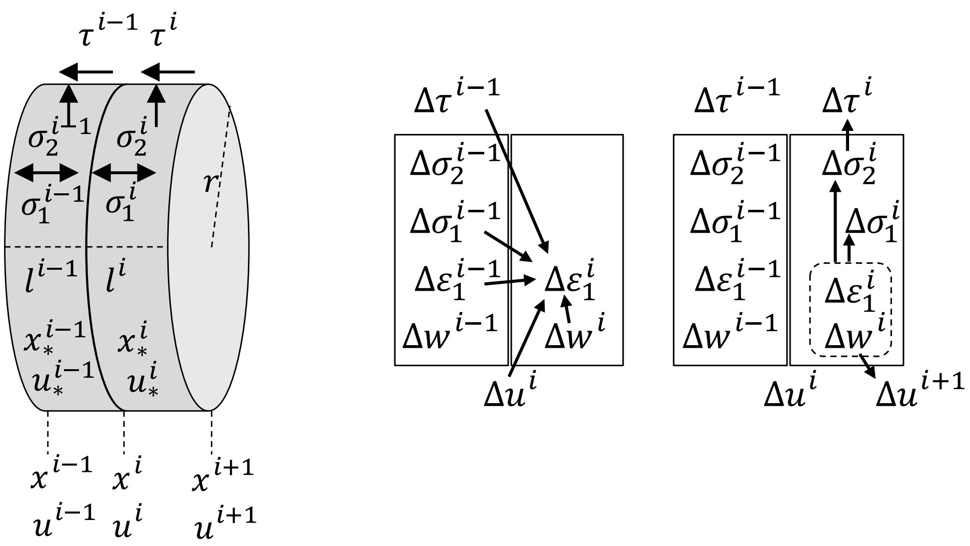

Figure A3-2. *Notation of quantities associated with elements and nodes (left). Schematic illustration of iterative integration used for calculating stress and strain increments (right).*

The shear stress increment as defined as (2-30) is utilized for element i:

$$\Delta\tau^i = \begin{cases} \Delta u_*^i \cdot K_s \quad \text{if } \left|\tau^i\right| < \sigma_2^i \cdot \tan(\varphi) \vee \tau^i \cdot \Delta u_*^i < 0 \\ \operatorname{sign}\left(\Delta u_*^i\right) \cdot \Delta\sigma_2^i \cdot \tan(\varphi) \quad \text{otherwise} \end{cases} \tag{A3-4}$$

where the displacement increment Δu_*^i is representative for the element i:

$$\Delta u_*^i = \Delta u^i + \frac{\Delta\varepsilon_1^i \cdot l_{init}}{2} \tag{A3-5}$$

The stress increments are given as partial derivatives with respect to the strain and the water content:

$$\Delta\sigma_1^i = \frac{\partial\sigma_1}{\partial\varepsilon_1}\Delta\varepsilon_1^i + \frac{\partial\sigma_1}{\partial w}\Delta w^i \tag{A3-6}$$

$$\Delta\sigma_2^i = \frac{\partial\sigma_2}{\partial\varepsilon_1}\Delta\varepsilon_1^i + \frac{\partial\sigma_2}{\partial w}\Delta w^i \tag{A3-7}$$

The first of these is the interaction function, whereas the second is defined in the next section.

By combining the first row in equation (A3-4) with equation (A3-3), (A3-5) and (A3-6) the following expression can be derived in which $\Delta\varepsilon_1^i$ can be calculated from $\Delta\varepsilon_1^{i-1}$, Δw^i, $\Delta\sigma_1^{i-1}$, Δu^i and $\Delta\tau^{i-1}$:

$$\Delta\varepsilon_1^i = \frac{\Delta\sigma_1^{i-1} - \frac{\partial\sigma_1}{\partial w}\Delta w^i - \frac{l_\Delta^{i-1}}{r}\cdot\left[K_s\cdot\Delta u^i + \Delta\tau^{i-1}\right] - \Delta\varepsilon_1^{i-1}\cdot\frac{l_{init}}{2r}\cdot\left[\tau^i + \tau^{i-1}\right]}{\frac{\partial\sigma_1}{\partial\varepsilon_1} + \frac{l_\Delta^{i-1}}{r}\cdot K_s\cdot\frac{l_{init}}{2} + \frac{l_{init}}{2r}\cdot\left[\tau^i + \tau^{i-1}\right]} \tag{A3-8}$$

$$\text{if} \qquad \left|\tau^i\right| < \sigma_2^i \cdot \tan(\varphi) \ \vee \ \tau^i \cdot \Delta u_*^i < 0$$

Correspondingly, by combining the second row in equation (A3-4) with equation (A3-3), (A3-5) and (A3-7) the following expression is obtained:

$$\Delta\varepsilon_1^i = \frac{\Delta\sigma_1^{i-1} - \frac{\partial\sigma_1}{\partial w}\Delta w^i - \frac{l_\Delta^{i-1}}{r}\cdot\left[\operatorname{sign}(\Delta u_*^i)\cdot\tan(\varphi)\cdot\frac{\partial\sigma_2}{\partial w}\Delta w^i + \Delta\tau^{i-1}\right] - \Delta\varepsilon_1^{i-1}\cdot\frac{l_{init}}{2r}\cdot\left[\tau^i + \tau^{i-1}\right]}{\frac{\partial\sigma_1}{\partial\varepsilon_1} + \frac{l_\Delta^{i-1}}{r}\cdot\left[\operatorname{sign}(\Delta u_*^i)\cdot\tan(\varphi)\cdot\left(\frac{\partial\sigma_2}{\partial\varepsilon_1}\right)\right] + \frac{l_{init}}{2r}\cdot\left[\tau^i + \tau^{i-1}\right]} \tag{A3-9}$$

otherwise

Radial stress increment

The derivation of the radial stress increment and its governing partial derivatives (Eq. (A3-7)) is based on the thermodynamic relation:

$$s + \frac{\sigma}{\alpha} = \Psi_M + f \cdot \Psi_{\Delta/2} \tag{A3-10}$$

From this follows that the difference between $\sigma_1$and σ_2 can simply be calculated as:

$$\sigma_1 - \sigma_2 = \alpha \Psi_{\Delta/2} \cdot (f_1 - f_2) \tag{A3-11}$$

Both sides of this equation are differentiated as:

$$\Delta\sigma_1 - \Delta\sigma_2 = \alpha\Psi_{\Delta/2} \cdot (\Delta f_1 - \Delta f_2) + \Delta\alpha\Psi_{\Delta/2} \cdot (f_1 - f_2) \tag{A3-12}$$

The first term on the right-hand side can be developed in terms of stain increments:

$$(\Delta f_1 - \Delta f_2) = \frac{\partial f_1}{\partial \varepsilon_1^m} \cdot 1 \cdot \Delta\varepsilon_1 - \frac{\partial f_2}{\partial \varepsilon_2^m} \cdot (-\xi) \cdot \Delta\varepsilon_1 = \left(\frac{\partial f_1}{\partial \varepsilon_1^m} + \xi \frac{\partial f_2}{\partial \varepsilon_2^m}\right) \cdot \Delta\varepsilon_1 \tag{A3-13}$$

Note that ξ is positive, and that the $\partial f_2/\partial\varepsilon_2^m$-derivative is calculated for the negative sign of $\Delta\varepsilon_1$. The second term is developed in terms of stain increments and micro void ratio increments:

$$\Delta\alpha\Psi_{\Delta/2} = \left[\frac{\partial\alpha}{\partial e_m}\Psi_{\Delta/2} + \alpha\frac{\partial\Psi_{\Delta/2}}{\partial e_m}\right] \cdot \Delta e_m + \frac{\partial\alpha}{\partial e}\Psi_{\frac{\Delta}{2}} \cdot (1 + e_0\ ) \cdot \Delta\varepsilon_1 \tag{A3-14}$$

Taken together, the difference between the stress increments can also be expressed in terms of strain increments and micro void ratio increments:

$$\Delta\sigma_1 - \Delta\sigma_2 = \frac{\partial q}{\partial\varepsilon_1} \cdot \Delta\varepsilon_1 + \frac{\partial q}{\partial e_m} \cdot \Delta e_m \tag{A3-15}$$

where the partial derivatives are defined as:

$$\frac{\partial q}{\partial \varepsilon_1} = \alpha\Psi_{\frac{\Delta}{2}} \cdot \left(\frac{\partial f_1}{\partial \varepsilon_1^m} + \xi\frac{\partial f_2}{\partial \varepsilon_2^m}\right) + (f_1 - f_2)\frac{\partial\alpha}{\partial e}\Psi_{\frac{\Delta}{2}} \cdot \left(1 + e_0\ \right) \tag{A3-16}$$

$$\frac{\partial q}{\partial e_m} = (f_1 - f_2)\left[\frac{\partial\alpha}{\partial e_m}\Psi_{\Delta/2} + \alpha\frac{\partial\Psi_{\Delta/2}}{\partial e_m}\right]$$

Correspondingly, the micro void ratio increment can be expressed in terms of strain increments and water content increment (see Appendix 2).

$$\Delta e_m = \frac{\partial e_m}{\partial \varepsilon_1} \cdot \Delta\varepsilon_1 + \frac{\partial e_m}{\partial w} \cdot \Delta w \tag{A3-17}$$

where the partial derivatives are defined as:

$$\frac{\partial e_m}{\partial \varepsilon_1} = \frac{\Psi_{\Delta/2} \dfrac{df_1}{d\varepsilon_1^m} + \dfrac{\sigma_1}{\alpha^2} \dfrac{\partial \alpha}{\partial e}(1+e_0) - \dfrac{1}{\alpha} \dfrac{\partial \sigma_1}{\partial \varepsilon_1}}{\dfrac{1}{\beta e_m} - \dfrac{\sigma_1}{\alpha^2} \dfrac{\partial \alpha}{\partial e_m} - \dfrac{d\Psi_M}{de_m} - f_1 \dfrac{d\Psi_{\Delta/2}}{de_m}} \tag{A3-18}$$

$$\frac{\partial e_m}{\partial w} = \frac{\dfrac{1}{\beta w} - \dfrac{1}{\alpha} \dfrac{\partial \sigma_1}{\partial w}}{\dfrac{1}{\beta e_m} - \dfrac{\sigma_1}{\alpha^2} \dfrac{\partial \alpha}{\partial e_m} - \dfrac{d\Psi_M}{de_m} - f_1 \dfrac{d\Psi_{\Delta/2}}{de_m}}$$

Finally, Equation (A3-15) and (A3-17) are combined with the interaction function:

$$\Delta\sigma_1 = \frac{\partial \sigma_1}{\partial \varepsilon_1} \Delta\varepsilon_1 + \frac{\partial \sigma_1}{\partial w} \Delta w \tag{A3-19}$$

from which the radial stress increment can be expressed in terms of strain increments and water content increments:

$$\Delta\sigma_2 = \frac{\partial \sigma_2}{\partial \varepsilon_1} \Delta\varepsilon_1 + \frac{\partial \sigma_2}{\partial w} \Delta w \tag{A3-20}$$

where the partial derivatives are defined as:

$$\frac{\partial \sigma_2}{\partial \varepsilon_1} = \frac{\partial \sigma_1}{\partial \varepsilon_1} - \frac{\partial q}{\partial \varepsilon_1} - \frac{\partial q}{\partial e_m} \cdot \frac{\partial e_m}{\partial \varepsilon_1} \tag{A3-21}$$

$$\frac{\partial \sigma_2}{\partial w} = \frac{\partial \sigma_1}{\partial w} - \frac{\partial q}{\partial e_m} \frac{\partial e_m}{\partial w}$$

It should be noted the second strain increment equation (A3-9) includes the signs of the displacement increment Δu_*^i and the strain increment $\Delta\varepsilon_1^i$ (through the $\partial\sigma_2/\partial\varepsilon_1$-derivative), which means that these signs have to be guessed before-hand. In this work, this was handled by simply testing all four combinations.

Solution for water saturated pellets

The homogenisation process was simplified by assuming that the pellets filling was water saturated from the beginning, and by maintaining zero suction (s=0) conditions in this part of the geometry throughout the calculation. Since the stress increments could be expressed in terms of the strains only, in contrast to Equations (A3-6) and (A3-7):

$$\Delta\sigma_1^i = \frac{d\sigma_1}{d\varepsilon_1}\Delta\varepsilon_1^i \tag{A3-22}$$

$$\Delta\sigma_2^i = \frac{d\sigma_2}{d\varepsilon_1}\Delta\varepsilon_1^i \tag{A3-23}$$

this meant that the strain increment equations in (A3-8) and (A3-9) could be simplified by eliminating the term related to the water content increment in each case:

$$\Delta\varepsilon_1^i = \frac{\Delta\sigma_1^{i-1} - \frac{l_\Delta^{i-1}}{r}\cdot\left[K_s\cdot\Delta u^i + \Delta\tau^{i-1}\right] - \Delta\varepsilon_1^{i-1}\cdot\frac{l_{init}}{2r}\cdot\left[\tau^i + \tau^{i-1}\right]}{\frac{\partial\sigma_1}{\partial\varepsilon_1} + \frac{l_\Delta^{i-1}}{r}\cdot K_s\cdot\frac{l_{init}}{2} + \frac{l_{init}}{2r}\cdot\left[\tau^i + \tau^{i-1}\right]} \tag{A3-24}$$

$$\text{if} \qquad \left|\tau^i\right| < \sigma_2^i\cdot\tan(\varphi) \ \vee \ \tau^i\cdot\Delta u_*^i < 0$$

$$\Delta\varepsilon_1^i = \frac{\Delta\sigma_1^{i-1} - \frac{l_\Delta^{i-1}}{r}\cdot\Delta\tau^{i-1} - \Delta\varepsilon_1^{i-1}\cdot\frac{l_{init}}{2r}\cdot\left[\tau^i + \tau^{i-1}\right]}{\frac{\partial\sigma_1}{\partial\varepsilon_1} + \frac{l_\Delta^{i-1}}{r}\cdot\left[\mathrm{sign}(\Delta u_*^i)\cdot\tan(\varphi)\cdot\left(\frac{\partial\sigma_2}{\partial\varepsilon_1}\right)\right] + \frac{l_{init}}{2r}\cdot\left[\tau^i + \tau^{i-1}\right]} \tag{A3-25}$$

otherwise

The stress-strain derivative in Equation (A3-22) can be evaluated from the thermodynamic relation for saturated conditions:

$$s + \sigma_1 = \Psi_M + f_1\cdot\Psi_{\Delta/2} \tag{A3-26}$$

Due to the simplifying condition that s=0, this means that equation can be differentiated as:

$$d\sigma_1 = \frac{d\Psi_M}{de}de + f_1\cdot\frac{d\Psi_{\frac{\Delta}{2}}}{de}de + \Psi_{\Delta/2}\cdot\frac{df_1}{d\varepsilon_1}d\varepsilon_1 \tag{A3-27}$$

Finally, together with the relation between the strain and the void ratio $(d\varepsilon_1 = de/(1+e_0))$, this means that the stress-strain derivative can be expressed as:

$$\frac{d\sigma_1}{d\varepsilon_1} = \left(\frac{d\Psi_M}{de} + f_1\cdot\frac{d\Psi_{\frac{\Delta}{2}}}{de}\right)(1+e_0) + \Psi_{\Delta/2}\cdot\frac{df_1}{d\varepsilon_1} \tag{A3-28}$$

The corresponding derivative for the radial stress (A3-23) is even simpler since the radial path variable is constant ($df_2 = 0$), which yields:

$$\frac{d\sigma_2}{d\varepsilon_1} = \left(\frac{d\Psi_M}{de} + f_2 \cdot \frac{d\Psi_{\frac{\Delta}{2}}}{de} \right) (1 + e_0) \tag{A3-29}$$

It should be noted that the second strain increment equation for saturated conditions (A3-25) can be used directly without assuming the sign of the strain increment $\Delta\varepsilon_1^i$ (due to the independence of sign in the $\partial\sigma_2/\partial\varepsilon_1$-derivative). Due to the simplification with zero suction conditions, it could also be safely assumed that the displacement increment Δu_*^i was negative throughout the simulation.